CHEMICAL SEPARATION

IN

ELECTROSTATIC PRECIPITATORS

by

© R.L.R. Salcedo

A thesis submitted to the Faculty of Graduate Studies and Research in partial fulfilment of the requirements for the degree of Doctor of Philosophy.

Department of Chemical Engineering

McGill University

Montreal

August, 1981

ABSTRACT

This work was carried out to investigate the mechanisms of solid-solid separation in electrostatic precipitators. The separation of mixtures of pure compounds from each other and the components of an industrial dust has been studied in a wire-and-duct type laboratory-scale electrostatic precipitator. Particle size distribution affected the separation most, but both the dielectric constant and electrical resistivity of the dust can be important. Operating voltage and air velocity in the precipitator also affected the separation along the precipitator length. The Southern Research Institute (SRI) computer model of precipitator performance gave reasonable predictions of separation under conditions of negligible re-entrainment.

An apparently unique relationship between separation and recovery was experimentally observed with components which do not re-entrain appreciably; a similar behaviour is theoretically predicted from the Deutsch Equation of collection efficiency or the SRI model.

RESUME

Ce travail a été accompli afin d'étudier les mechanismes de séparation des phases solide-solide dans des précipitateurs électrostatiques. La séparation de mélanges de composés purs ainsi que des composants d'une poussière industrielle a été étudiée en laboratoire à l'aide d'un précipitateur électrostatique de plaques parallèles. La séparation est affectée en majeure partie par la distribution de grosseur des particules mais aussi par la constante diélectrique et la résistivité de la poussière. Le voltage d'opération ainsi que la vitesse de l'air influencent le degré de séparation en fonction de la longueur du précipitateur. Le modèle numérique SRI pour la simulation de l'efficacité d'un précipitateur a donné des résultats acceptables pour la prédiction du degré de séparation en cas de réentrainement négligeable. Une relation apparemment unique entre les taux de séparation et de recouvrement a été observée experimentalement pour les composants qui ne réentrainent de façon aprécieable; un comportement similaire est théoriquement predit par l'Equation de Deutsch sur l'efficacité ou par le modèle SRI.

ACKNOWLEDGEMENTS

I wish to express my appreciation to the following people:

Professor R.J. Munz for his advice, guidance, and support throughout this work;

Dr. H.J. White for his dedicated interest and helpful comments; Dr. J.R. McDonald of SRI, Alabama, for providing some literature relevant to this work;

Professor M.E. Weber, Professor J.R. Grace and Professor P. Reilly for their helpful comments;

The Departments of Physical Chemistry and Chemical Engineering of the Noranda Research Centre, Pointe Claire, Quebec for use of the bulk resistivity cell and for providing the industrial dust used in this work;

Messrs. A. Krish, A. Gagnon, H. Alexander, J. Dumont and W. Hoogendoorn, for their invaluable assistance with equipment and instrumental problems;

The Department of Metallurgical Engineering of McGill University, for use of the X-Ray Sedigraph and other equipment, in particular Professor J. Finch, Mrs. M. Riendeau and Mr. M. Leroux;

Dr. A. Garcia-Rejon, Dr. S.S. Treiber, Dr. T. Obot, and my colleagues B. Huang, K. Khant and P. Lafleur for their advice on several aspects of this project;

Mr. M. Ross of the McGill Institute of Occupational Health and Safety, for preparing the electron microphotographs;

Mrs. H. Rousseau and Mrs. D. Ross for the excellent typing of the manuscript;

Mr. V. Jariwala for help in producing the drawings;

The Natural Sciences and Engineering Research Council of Canada, for its financial support;

My Parents and Family, for their continuous support, encouragement and love;

Luisa, for everything, and Joao, for being there.

TABLE OF CONTENTS

	Page
ABSTRACT	i
RESUME	ii
ACKNOWLEDGEMENTS	iii
TABLE OF CONTENTS	v
LIST OF FIGURES	xii
LIST OF TABLES	xxvii
CHAPTER 1 INTRODUCTION	1
References	5
CHAPTER 2 FUNDAMENTALS OF ELECTROSTATIC PRECIPITATION	6
2.1 Introduction	6
2.2 Corona Generation and Space-Charge Effects	6
2.3 Electric Field in Parallel-Type Precipitators	13
2.3.1 Corona-Onset Voltage and Field Intensity	13
2.3.2 Electrostatic Field	17
2.3.3 Corona Current and Space-Charge	19
2.4 Particle Charging	30
2.4.1 Field Charging	30
2.4.2 Diffusion Charging	35
2.4.3 Combined Field and Diffusion Charging	38
2.4.4 Comparison with Experimental Data	44
2.5 Particle Collection	51
2.5.1 Introduction	51
2.5.2 Theoretical Migration Velocity	54
2.5.3 Collection Efficiency Equation	58

2.6 Dust Resistivity 69
2.7 Dust Adhesion and Re-entrainment 76
2.8 The SRI Electrostatic Precipitator Performance Computer Model 87
2.8.1 General Description 87
2.8.2 Experimental Verification 97
References 101

CHAPTER 3 LITERATURE REVIEW ON SELECTIVE PRECIPITATION 112

3.1 Variables Affecting Solid-Solid Segregation in ESP's 112
3.2 Observed Solid-Solid Segregation in ESP's 115
3.2.1 Power Plants 115
3.2.2 Iron and Steel Industry 119
3.2.3 Cement Industry 127
3.2.4 Pulp and Paper Industry 128
3.2.5 Non-Ferrous Metals Industry 129
3.2.5.1 Zinc and Lead Smelters 129
3.2.5.2 Aluminium Production 131
3.2.5.3 Copper Smelters 134
3.2.6 Municipal Incinerators 138
3.2.7 Petroleum Industry 138
3.3 Quantitative Definition of Segregation (Separation) 138
3.4 Conclusions 143
References 146

CHAPTER 4 EXPERIMENTAL EQUIPMENT 150

4.1 General Description 150
4.2 Electrical Characteristics 157
4.3 Gas Flow Characteristics 160

4.4 Particle Generation and Feeding 166
4.4.1 General Considerations 166
4.4.2 The Tafa Dust Feeder 168
4.4.3 The Vibrating Screw Feeder 168
4.4.4 The Wright Dust Feeder 171
4.4.5 The Fluidized Bed Feeder (FBF) 174
4.5 Safety Precautions 175
References 177

CHAPTER 5 CHARACTERIZATION OF POWDERS AND EXPERIMENTAL TECHNIQUES 179

5.1 Choice of Powders 179
5.2 Dust Sampling 181
5.2.1 General Considerations 181
5.2.2 Sampling Trains 183
5.2.2.1 Outlet Sampling Train 183
5.2.2.2 Inlet Sampling Trains 187
5.2.3 Dust Concentration Gradients at the ESP Inlet and Sedimentation Effects 188
5.3 Size Analysers and Analysis 196
5.3.1 General Considerations 196
5.3.2 Particle Size Analysers 198
5.3.2.1 The Optical Microscope 198
5.3.2.2 The X-Ray Sedimentometer 206
5.3.2.3 The Andersen Cascade Impactor 208
5.3.3 Particle Size Statistics 210
5.4 Size Distributions at the ESP Inlet 223
5.4.1 Cupric Oxide, Magnesium Oxide and Titanium Dioxide 223
5.4.2 Aluminium Oxide (Alumina) 231
5.4.3 The Industrial (Noranda) Dust 239

5.5 Dielectric Constant 251
5.6 Bulk Electrical Resistivity 261
5.7 Chemical Analyses 271
5.8 Particle Collection Experiments 277
References 283

CHAPTER 6 - PRECIPITATION OF PURE COMPOUNDS: EXPERIMENTAL RESULTS, THEORETICAL PREDICTIONS AND DISCUSSION 288

6.1 Introduction 288
6.2 Precipitation of Cupric Oxide 290
6.2.1 Global Collection Efficiencies 290
6.2.2 Collection Efficiencies as Function of ESP Length 295
6.2.3 Collection Efficiencies as Function of Particle Size 305
6.3 Precipitation of Magnesium Oxide 313
6.3.1 Global Collection Efficiencies 313
6.3.2 Collection Efficiencies as Function of ESP Length 315
6.3.3 Collection Efficiencies as Function of Particle Size 318
6.4 Precipitation of Titanium Dioxide 322
6.4.1 Global Collection Efficiency 322
6.5 Precipitation of Alumina 322
6.5.1 Global Collection Efficiencies 322
6.5.2 Collection Efficiency as Function of ESP Length 324
6.5.3 Uncertainties in the SRI Simulation 326
6.5.3.1 Abnormal Charging Near Corona Wires 326
6.5.3.2 Dielectric Constant 327
6.5.3.3 Particle Shape 328
6.6 Conclusions 333
References 335

CHAPTER 7 BEHAVIOUR OF MIXTURES OF PURE COMPOUNDS. EXPERIMENTAL RESULTS, THEORETICAL PREDICTIONS AND DISCUSSION 336

7.1 Introduction 336
7.2 Mixtures of CuO/MgO 337
7.2.1 Interaction Effect 337
7.2.2 Effect of Air Velocity 347
7.2.3 Effect of Electric Field 352
7.2.4 Effect of Relative Concentration 354
7.2.5 Re-entrainment of CuO in Mixtures with MgO 361
7.2.6 Conclusions 361
7.3 Mixtures of TiO_2/CuO 363
7.4 Mixtures of TiO_2/MgO 370
7.5 Mixtures of CuO/MgO/TiO_2 376
7.6 Mixtures of the Coarser Oxides with Alumina 384
7.6.1 Mixtures of CuO/Al_2O_3 386
7.6.2 Mixtures of MgO/Al_2O_3 393
7.6.3 Mixtures of TiO_2/Al_2O_3 396
7.7 Conclusions 400
References 403

CHAPTER 8 PART I PRECIPITATION OF THE INDUSTRIAL COPPER REACTOR (NORANDA) DUST. EXPERIMENTAL RESULTS, THEORETICAL PREDICTIONS AND DISCUSSION 404

8.1 Introduction 404
8.2 Precipitation of the Overall Dust 406
8.3 Segregation of Copper from Lead, Zinc and Cadmium 413
8.3.1 Global Elemental Collection 413
8.3.2 Elemental Collection and Separation as Function of ESP Length 417
8.4 Uncertainties in the SRI Simulation 421
8.4.1 Dielectric Constant 421
8.4.2 Particle Size Distribution 423

8.5 Conclusions 428
References 429

PART II SEPARATION AND RECOVERY (COLLECTION) 430

8.6 Experimental Results 430
8.7 Theoretical Considerations 436
8.7.1 Separation Nomograph 436
8.7.2 Comparison with SRI Results and Experimental Data 443
8.8 Conclusions 449

CHAPTER 9 CONCLUSIONS AND RECOMMENDATIONS 451

9.1 Conclusions 451
9.2 Contributions to Knowledge 454
9.3 Recommendations for Future Research 455

NOMENCLATURE 457

APPENDIX A I/Ø DATA FOR THE SRI COMPUTER MODEL A1
References A17

APPENDIX B B1

B.1 Electrical Characteristics of Laboratory-Scale ESP with Clean Plates B1
B.2 Gas Flow Characteristics B7
B.3 Calibration of Tafa Feeder with Copper Oxide B12
B.4 Calibration Curve of Wright Feeder Rotameter B21
References B25

APPENDIX C C1

C.1 Calibration Curve of Sampling Rotameter C1

C.2 Velocity Profiles and Sampling Points at the ESP Outlet C1

C.3 Particle Size Statistics: Conversion of Number to Weight Basis C4

C.4 Effect of Sedimentation in Changing the Inlet Size Distribution C15

C.5 Use of the X-Ray Sedimentometer C18

C.6 Optical Microscope Raw Data for the Coarser Oxides C21

C.7 The Wright Feeder - Minicyclone System C21

References C36

LIST OF FIGURES

Figure		Page
2.1	Partial grid showing nomenclature used in the numerical analysis of the electrical conditions, McDonald et al. (1977)	24
2.2	Nomenclature used in the numerical analysis of the electrical conditions in wire-duct precipitators, McDonald et al. (1977)	24
2.3	a) Theoretical and experimental potential profiles along a line from a point midway between the wires to the plate, McDonald et al. (1977)	27
	b) Theoretical and experimental profiles along a line from the corona wire to the plate, McDonald et al. (1977)	27
	c) Theoretical and experimental electric field at the plate as a function of displacement, McDonald et al. (1977)	27
2.4	Electric field lines for partially charged particle in electric field, McDonald et al. (1978 c)	40
2.5	a, b, c, d) Comparison of charging theories with the experimental results of Hewitt (1957), in Smith et al. (1975)	47
2.6	Comparison of charging theories (Eqs. 2.30 and 2.32) with the experimental data of McDonald et al. (1980 a)	50

2.7	Relation between effective migration velocity and particle diameter for different gas velocities with flat and tulip electrodes in a pilot plant, in Strauss (1966)	65
2.8	Relation between effective migration velocity and particle diameter with tubular and chute electrodes in commercial sized plant, in Strauss (1966)	65
2.9	Effective migration velocities as a function of particle size for boiler flue dust, catalyst dust, cement dust and coal dust, Henrich (1961)	65
2.10	Collection efficiency against air velocity (2s = 25 cm), Dinelli et al. (1979)	68
2.11	Thickness of the collected dust layers as a function of the air velocity (2s = 25 cm; C = 500 mg m^{-3}; t = 90 min), Dinelli et al. (1979)	68
2.12	Comparison between hopper particle size distribution with and without re-entrainment, Oglesby et al. (1974)	86
2.13	Electrostatic precipitator system model, Nichols et al. (1970)	88
2.14	Comparison of results obtained from rigorous application of the model and estimation procedure, McDonald (1978 b)	93
2.15	Simplified flow diagram of precipitator model computer program, Gooch et al. (1977)	95

2.16	a, b) Experimentally measured and ideally calculated fractional collection efficiencies in the laboratory precipitator, Gooch et al. (1976 a, b)	98
3.1	Systems approach for variables which may affect separation	113
3.2	Inlet distribution (and outlet MMD) to ESP from coal fired power plant, Lee et al. (1975)	117
3.3	Relation between ESP efficiency and increase in additive (SO_3 or $(NH_4)_2 SO_4$) ion concentration in ash, Dalmon et al. (1971)	120
3.4	Inlet distribution to baghouse from electric arc furnace, Lee et al. (1975)	122
3.5	ESP elemental collection efficiencies of trace metals emitted from open heart furnace, Jacko et al. (1976)	124
3.6	Relation between ESP efficiency and atomic number, from the data of Jacko et al. (1976) and Vernigor (1965)	126
3.7	Particle size segregation of metals, vertical retort combustion stack, Jacko et al. (1975)	130
3.8	Segregation of solids from tars in aluminium production, from the data of Bakke (1975)	133

4.1	Schematic diagram of experimental facility	151
4.2	Schematic diagram of corona wire support system	155
4.3	Photograph of laboratory-scale ESP	158
4.4	Typical clean air voltage-current characteristic, at 21^{o}C and 25% relative humidity	159
4.5	Average velocity profiles at the ESP inlet	163
4.6	Average relative turbulence profiles at the ESP inlet	165
4.7	Schematic diagram of Tafa dust feeder	169
4.8	Schematic diagram of Wright dust feeder, Wright (1950)	172
5.1	Normalized concentration profiles of cupric oxide at the ESP inlet, at 2.8 ms^{-1}	189
5.2	Mechanical collection of the coarser oxides prior to the ESP inlet, as a function of air velocity	191
5.3	Reduction in MMD of cupric oxide at the ESP inlet, due to sedimentation	193
5.4	Mechanical collection of cupric oxide, in the ESP, as a function of air velocity and applied voltage	195
5.5	Relation between number of particles counted, weight percent and accuracy (Yamate et al., 1977)	201

5.6	a) Counting pattern used with optical microscope	203
	b) Chosen diameter for optical microscope counting and sizing	203
5.7	a, b) Typical optical microphotographs of a bulk sample of the coarser oxides, dispersed in N-heptane	205
5.8	Typical optical microphotograph of the coarser oxides, at the ESP inlet	225
5.9	Typical scanning electron microphotograph of a bulk sample of the coarser oxides	225
5.10	Size distribution parameters of CuO at various input voltages to the Tafa feeder	226
5.11	Size distributions of the coarser oxides, as determined by bulk sample analysis using the X-ray Sedigraph 5000D	230
5.12	Comparison between the size distributions of the coarser oxides derived from the optical microscope data and the X-ray Sedigraph 5000D	232
5.13	Size distributions of alumina obtained by the X-ray Sedigraph (bulk sample), the optical microscope and the Andersen MKIII cascade impactor, with the minicyclone off-line	234
5.14	Size distributions of alumina obtained by the optical microscope and the Andersen MKIII cascade impactor, with the minicyclone on-line	236

5.15	Typical optical microphotograph of alumina at the ESP inlet	238
5.16	a, b) Typical transmission electron microphotographs of alumina.	238
5.17	Average size distribution of the Noranda dust at the ESP inlet	241
5.18	Typical scanning electron microphotograph of the Noranda dust	243
5.19	Size distributions of bulk size fractions of the Noranda dust (X-ray Sedigraph)	246
5.20	Average elemental size distributions of the Noranda dust at the ESP inlet (Andersen MKIII cascade impactor)	250
5.21	Relation between capacitance and void fraction for the various dusts	255
5.22	Relation between dielectric constant and void fraction for the various dusts	258
5.23	a) Experimental apparatus for bulk resistivity measurements (Davis et al.,1979)	263
	b) Electric circuitry (")	263
	c) Bulk resistivity cell (")	263
5.24	Bulk resistivity of CuO as a function of applied field and relative humidity	266
5.25	Bulk resistivity of TiO_2, MgO, Al_2O_3 and Noranda dusts as a function of applied field and relative humidity	267

6.1	Variation of global collection efficiency of CuO with air velocity	293
6.2	Variation of re-entrainment of CuO with air velocity	296
6.3	Effect of air velocity on the non-cumulative collection efficiency of CuO along the ESP length, at high voltage	298
6.4	Effect of air velocity on the cumulative collection efficiency of CuO along the ESP length, at high voltage	299
6.5	Effect of air velocity on the non-cumulative collection efficiency of CuO along the ESP length, at low voltage	300
6.6	Effect of air velocity on the cumulative collection efficiency of CuO along the ESP length, at low voltage	301
6.7	Variation of the effective collection efficiency of CuO with particle size and air velocity, at high voltage	306
6.8	Variation of the effective collection efficiency of CuO with particle size and air velocity, at low voltage	307
6.9	Variation of the effective migration velocity of CuO with particle size and air velocity	309
6.10	Re-entrainment of CuO as a function of particle size and air velocity, at high voltage	310

6.11	Re-entrainment of CuO as a function of particle size and air velocity, at low voltage	311
6.12	Non-cumulative collection efficiency of MgO as a function of ESP length	316
6.13	Cumulative collection efficiency of MgO as a function of ESP length	317
6.14	Variation of the effective collection efficiency of MgO with particle size	319
6.15	Variation of the effective migration velocity of MgO with particle size	321
6.16	Cumulative collection efficiency of Al_2O_3 as a function of ESP length	325
6.17	Cumulative collection efficiencies of alumina as a function of ESP length, for various particle shapes (SRI simulations)	332
7.1	Variation of global collection efficiency of CuO and MgO with air velocity, in mixtures of CuO/MgO	341
7.2	Comparison between the global experimental and theoretical separation of the pair CuO/MgO with the experimental expected values, as a function of air velocity	342
7.3	Cumulative collection of CuO and MgO for different feed conditions, as function of ESP length	345

7.4	Photograph of precipitated dust layer for a mixture of CuO and MgO, showing species segregation with depth of layer	348
7.5	Effect of air velocity on the cumulative collection and separation of mixtures of CuO/MgO as function of ESP length	349
7.6	Variation of CuO concentration along the ESP length for mixtures of CuO/MgO, at 38 KV and various air velocities	351
7.7	Effect of electric field on the cumulative collection and separation of mixtures of CuO/MgO, at 5 ms^{-1} and various applied voltages	353
7.8	Variation of global collection of CuO with inlet concentration	355
7.9	Variation of global collection of MgO with applied voltage, at low applied voltage	357
7.10	Variation of global collection of MgO with corona power, at low corona powers	358
7.11	Effect of inlet concentration of CuO on collection and separation of mixtures of CuO/MgO	360
7.12	Relation between the experimental and estimated re-entrainment of CuO in mixtures with MgO, from multiple regression analysis	362
7.13	Cumulative collection and separation of mixtures of TiO_2/CuO as function of ESP length	366

7.14	Simulated effect of particle shape on the cumulative collection of TiO_2 as function of ESP length	368
7.15	Cumulative collection and separation of mixtures of TiO_2/MgO as function of ESP length	373
7.16	Variation of MgO and TiO_2 concentrations along the ESP length, for mixtures of MgO/TiO_2, at 38 KV and 2 ms^{-1}	375
7.17	Cumulative collection and separation of a mixture of CuO/TiO_2/MgO as function of ESP length, at 23.5 KV and 5 ms^{-1}	380
7.18	Cumulative collection and separation of mixtures of CuO/TiO_2/MgO as function of ESP length, at 29-29.5 KV, 5 ms^{-1} and high dust loadings	382
7.19	Cumulative collection and separation of mixtures of CuO/TiO_2/MgO as function of ESP length, at 30 KV, 5 ms^{-1} and low dust loadings	383
7.20	Variation of concentrations of CuO, MgO and TiO_2 along the ESP length, with mixtures of CuO/MgO/TiO_2 at 29-30 KV and 5 ms^{-1}	385
7.21	Cumulative collection and separation of a mixture of CuO/Al_2O_3 as function of ESP length, at high voltage and high velocity	390
7.22	Cumulative collection and separation of a mixture of CuO/Al_2O_3 as function of ESP length, at medium voltage and high velocity	391

7.23	Cumulative collection and separation of a mixture of CuO/Al_2O_3 as function of ESP length, at low voltage and high velocity	392
7.24	Cumulative collection and separation of a mixture of MgO/Al_2O_3 as function of ESP length, at high voltage and high velocity	394
7.25	Cumulative collection and separation of a mixture of MgO/Al_2O_3 as function of ESP length, at low voltage and high velocity	395
7.26	Cumulative collection and separation of a mixture of TiO_2/Al_2O_3 as function of ESP length, at high voltage and high velocity	397
7.27	Cumulative collection and separation of a mixture of TiO_2/Al_2O_3 as function of ESP length, at medium voltage and high velocity	398
7.28	Cumulative collection and separation of a mixture of TiO_2/Al_2O_3 as function of ESP length, at low voltage and high velocity	399

8.1	Overall individual size distributions of the Noranda dust at the ESP inlet (Andersen MKIII cascade impactor)	409
8.2	Elemental individual size distributions of the Noranda dust at the ESP inlet (Andersen MKIII cascade impactor)	411
8.3	Cumulative elemental collection and separation of the Noranda dust as function of ESP length, at high voltage and 5 ms^{-1}	418
8.4	Cumulative elemental collection and separation of the Noranda dust as function of ESP length, at medium voltage and 5 ms^{-1}	419
8.5	Cumulative elemental collection and separation of the Noranda dust as function of ESP length, at low voltage and 5 ms^{-1}	420
8.6	Simulated effect of dielectric constant of the Cu rich particles on the cumulative separation of the Noranda dust along the ESP length, at medium voltage and 5 ms^{-1}	422
8.7	Simulated effect of particle size distribution of the Cu rich particles on the cumulative separation of the Noranda dust along the ESP length, at medium voltage and 5 ms^{-1}	427
8.8	Relation between cumulative separation and recovery for the pair TiO_2/MgO	432
8.9	a, b) Relation between cumulative separation and recovery for the pairs MgO/Al_2O_3 (a) and TiO_2/Al_2O_3 (b)	434
8.10	Relation between cumulative separation and recovery for the Noranda dust	435

8.11	Theoretical relation between separation and recovery, according to the Deutsch Equation of collection efficiency	439
8.12	Separation nomograph	442
8.13	Comparison between theoretical and experimental results of separation versus recovery, for the Noranda dust, at high voltage and 5 ms^{-1}	444
8.14	Comparison between theoretical and experimental results of separation versus recovery for TiO_2/Al_2O_3, at 5 ms^{-1}	446
8.15	Comparison between theoretical and experimental results of separation versus recovery for TiO_2/MgO, at 5 ms^{-1}	448
B.1	Clean-plate voltage-current characteristics of laboratory-scale ESP	B2
B.2	Relation between total secondary current (i) from the power supply and along the ESP length ($i_1 + i_2$)	B3
B.3	Relation between current to the first plate (i_I) and current to the second plate (i_{II})	B4
B.4	Hysteresis of clean-plate voltage-current characteristics	B6
B.5	Velocity profiles at the ESP outlet, used to calibrate the Venturi meter	B9
B.6	Sampling location at the ESP inlet for velocity and turbulence measurements	B13
B.7	Velocity profiles at the ESP inlet, obtained with a pitot tube at an average velocity of 4.8 ms^{-1}	B14

B.8	Velocity profiles at the ESP inlet, obtained with a pitot tube at an average velocity of 2.8 ms^{-1}	B15
B.9	Velocity profiles at the ESP inlet, obtained with a hot-wire anemometer at an average velocity of 4.8 ms^{-1}	B16
B.10	Velocity profiles at the ESP inlet, obtained with a hot-wire anemometer at an average velocity of 1.1 ms^{-1}	B17
B.11	Relative turbulence intensities at the ESP inlet, at an average velocity of 4.8 ms^{-1}	B18
B.12	Relative turbulence intensities at the ESP inlet, at an average velocity of 1.1 ms^{-1}	B19
B.13	Calibration curve of Tafa feeder rotameter, at ~25°C and 1 atm	B22
B.14	Calibration curve of Tafa feeder, for CuO	B23
B.15	Calibration curve of Wright feeder rotameter at ~25°C and 1 atm	B24
C.1	Calibration curve of sampling rotameter at ~25°C and 1 atm	C2
C.2	Velocity profiles at the sampling station at the ESP outlet and location of dust sampling points	C3
C.3	Comparison between log-normal approximations and experimental number frequency data for CuO	C9
C.4	Comparison between different methods of converting from number to weight basis, on a cumulative scale (CuO)	C10

C.5	Binomial standard deviations of a typical cumulative CuO size distribution, by number	C12
C.6	Accuracy of converting a typical CuO size distribution from a number to a weight basis, according to the method of Yamate et al. (1977)	C14
C.7	Typical particle size distribution of CuO, after sedimentation prior to the ESP inlet	C17
C.8	Effect of dispersing medium in the size distribution of the Noranda dust, obtained with the X-ray Sedigraph 5000D	C20
C.9	Schematic diagram of minicyclone	C24
C.10	Fractional efficiency curves of the minicyclone, with alumina, at 15 ℓ min^{-1}	C27
C.11	Accuracy of converting optical microscope derived alumina size distributions, from a number to a weight basis, according to the method of Yamate et al. (1977)	C31
C.12	Sensitivity of the MMD of alumina to the proportion of total count (optical microscope data)	C32

LIST OF TABLES

Table		Page
2.1	Characteristic Dimensions for Corona Onset Calculations, Cooperman (1963)	15
2.2	ESP's Threshold Velocities for Reentrainment	80
3.1	Partial Composition of Samples from a Blast Furnace ESP, Oglesby et al. (1970)	127
3.2	Ratio of Concentrations of Fine-to-Coarse Fractions of Precipitated Al_2O_3, Bohm et al. (1976)	132
3.3	Composition of Copper Converter Flue Dust, Tayler (1976)	135
3.4	Partial Composition of Reactor and Converter Catches, Davis et al. (1979)	137
5.1	Pure Powders used in Experimental Work	180
5.2	Aerodynamic Cut-Diameters of Andersen MKIII Cascade Impactor, at 20°C and 21.2 ℓ min^{-1}	210
5.3	Estimated Parameters of Log-Normal Least Squares Fitting	227
5.4	Collection Efficiencies of CuO: Simulation Tests on Size Distribution Effect	228
5.5	Chemical Composition of Bahco Size Fractions (Comparative Elemental Peak Ratios by EDX), Davis et al. (1979)	244
5.6	Elemental Composition of Noranda Bulk Size Fractions	247

5.7	Chemical and X-ray Diffraction Data for Noranda Reactor Dust (Catch), Davis et al. (1979)	248
5.8	Dielectric Constants (Literature Values)	253-254
5.9	Estimated Dielectric Constants	259
5.10	Estimated Parameters of Surface Resistivity, for Use with Eq. 5.37	269
5.11	Composition of Noranda Dust at the ESP Inlet	276
6.1	Experimental Precipitation Conditions and Results for Cupric Oxide	291
6.2	Non-Cumulative Collection Efficiencies of CuO	297
6.3	Size Distributions of CuO as Function of ESP Length	304
6.4	Experimental Precipitation Conditions and Results for Magnesium Oxide	314
6.5	Non-Cumulative Collection Efficiencies of MgO	315
6.6	Size Distributions of MgO as Function of ESP Length	318
6.7	Experimental Precipitation Conditions and Results for Titanium Dioxide	323
6.8	Experimental Precipitation Conditions and Results for Alumina	323
6.9	Non-Cumulative Collection Efficiencies of Al_2O_3	326
6.10	Effect of Deviations from Spherical Shape in Increasing the Theoretical Migration Velocity	330

7.1	Experimental Precipitation Conditions and Global Results for Mixtures of CuO/MgO	339
7.2	Non-Cumulative Collection Efficiencies (CuO/MgO)	340
7.3	Experimental Global Collection Efficiencies of Sequential Feed Run	344
7.4	Variation of CuO Concentration in Precipitated Layer (CuO/MgO)	346
7.5	Experimental Precipitation Conditions and Global Results for Mixtures of TiO_2/CuO	364
7.6	Non-Cumulative Collection Efficiencies (TiO_2/CuO)	364
7.7	Variation of CuO Concentration in Precipitated Layer (TiO_2/CuO)	370
7.8	Experimental Precipitation Conditions and Global Results for Mixtures of MgO/TiO_2	371
7.9	Non-Cumulative Collection Efficiencies (MgO/TiO_2)	371
7.10	Variation of MgO Concentration in Precipitated Layer (TiO_2/MgO)	376
7.11	Experimental Precipitation Conditions and Global Results for Mixtures of CuO/MgO/TiO_2	377
7.12	Non-Cumulative Collection Efficiencies (CuO/MgO/TiO_2)	378
7.13	Variation of CuO and MgO Concentration in Precipitated Layer (TiO_2/CuO/MgO)	379
7.14	Experimental Conditions and Global Results for Al_2O_3/Coarser Oxides	387

7.15	Non-Cumulative Collection Efficiencies (Coarser Oxides/Al_2O_3)	388
8.1	Experimental Conditions and Global Results for the Noranda Dust	407
8.2	Non-Cumulative Collection Efficiencies (Noranda Dust)	408
8.3	Global Collection Efficiencies (Overall Noranda Dust)	412
8.4	SRI Elemental Collection Efficiencies	414
8.5	Size Distributions of Cu and (Pb + Zn + Cd), Undersize	416
8.6	Total Elemental Concentrations (TEC) from Cascade Impactor and Comparison with Feed Composition (Noranda Dust)	424
B.1	Venturi Discharge Coefficient	B11
B.2	Tafa Feeder Conditions for CuO	B20
C.1	Raw Data from Optical Microscope: Direct Conversion Method (Cupric Oxide Composite Sample)	C5
C.2	Logarithmic Likelihood Function for CuO	C6
C.3	Particle Size Statistical Data from Table C.1 (CuO)	C7
C.4	Generation of Number and Weight Distributions (CuO)	C11
C.5	Effect of Sedimentation in Distorting the Inlet Size Distribution (CuO)	C16

C.6	Optical Microscope Raw Data for Cupric Oxide	C22
C.7	Optical Microscope Raw Data for MgO and TiO_2	C23
C.8	Optical Microscope Raw Data for Alumina	C28
C.9	Cascade Impactor Raw Data for Alumina	C29
C.10	Cascade Impactor Raw Data for Overall Noranda Dust	C34
C.11	Cascade Impactor Raw Data for Elements of Noranda Dust	C35

CHAPTER 1

INTRODUCTION

Electrostatic precipitators (ESP's) are high efficiency gas-solid separation devices, used for air pollution control in many types of industries, from power plants to various manufacturing processes.

ESP's are also used for the recovery of valuable materials. These may have intrinsic value, such as precious metals, or more generally, they have process value. Precious metals and other process materials have been recovered in ESP's since 1910-1920 (White, 1963). Applications include the recovery of gold and silver from mints and of copper, lead and zinc from non-ferrous smelters. In some industries, the recovery of the flue dusts is an important economic factor. Such is the case for the collection of particulates emitted from recovery boilers in the pulp and paper (Kraft) industry, and from Portland cement kilns.

When the precipitated dust is recovered in bulk, in most cases the materials have to be subjected to further enrichment (or separation) by appropriate means. This is due to the fact that the precipitated dust is contaminated to such a degree that direct recycling to the process is not feasible. The enrichment steps usually involve hydrometallurgical or pyrometallurgical techniques.

In many cases these techniques are reliable and economical, but in some cases the purification processes are dif-

ficult and/or costly. An example is the reclamation of zinc from iron oxide rich fumes which are produced in the processing of galvanized scrap (Moore, 1978).

Economic benefit will result if the flue dusts can be physically benefitiated in some desired component(s), prior to being processed by extractive metallurgical techniques. This is the case for the recovery of metallurgical-grade alumina from coal fly ash (Eisele et al., 1979).

Although several cases have been reported in which segregation of different chemical species has occurred in industrial ESP's, the segregation mechanisms have never been fully investigated. The exploitation of solid-solid segregation in ESP's could be quite interesting in certain processing industries where, for example, a valuable particulate material could be at least partially separated from a detrimental or waste material in the process of removing both from a gas stream. The lack of information on the segregation mechanisms which occur in an ESP provided the incentive for the present study.

The objectives of the work were as follows:

1. To design and build a laboratory-scale ESP typical of industrial geometries; the ESP should permit ready access to the precipitated dust.
2. To study experimentally the effect of the ESP operating variables (applied voltage and air velocity) and of the dust variables (particle size distribution and electrical properties) on the solid-solid segregation of mixtures of pure compounds.

3. To study theoretically the effect of the above variables on the solid-solid segregation.
4. To identify the various segregation mechanisms.
5. To extend the results obtained with mixtures of pure compounds to a typical industrial flue dust.

Chapter 2 reviews the fundamental theory of electrostatic precipitation, and the computer model (Southern Research Institute (SRI), Alabama) used for simulation purposes. The SRI model was used as a systems approach to electrostatic precipitation theory, and as such it was used without empirical correction factors. The reader familiar with the theory of precipitation and the SRI model is requested to proceed to the next chapter. Chapter 3 is a literature review on solid-solid segregation in ESP's. The quantification of separation is also discussed in this chapter. Chapter 4 describes the laboratory-scale ESP and the dust feeders used. Chapter 5 describes the materials and experimental techniques used in this work. The experimental results on particle size distributions and electrical properties of the various dusts are also given in this chapter. Chapter 6 presents and discusses the experimental results and theoretical predictions of collection of pure compounds. Chapter 7 presents the experimental results and theoretical predictions on collection and separation of mixtures of pure compounds. Chapter 8 gives the corresponding information for a typical industrial dust, and discusses a simplified separation model based on the Deutsch Equation of collection efficiency.

Chapter 9 summarizes the conclusions of the work and gives suggestions for further research.

Each chapter has its own references and a single nomenclature appears on page 457.

Finally, since this is the first thesis done at McGill University in this area, every effort was made for completeness, both in the literature review and in the detailed explanation of the experimental techniques.

REFERENCES

Eisele, J.A. and Bauer, D.J. (1979): "Evaluation of Technology for the Recovery of Metallurgical-Grade Alumina from Coal Ash", IC 8791, Bureau of Mines Information Circular.

Moore, J.J. (1978): "Recycling of Non-ferrous Metals", Int. Metals Reviews, No. 5, Review 234, pp.241-264.

White, H.J. (1963): "Industrial Electrostatic Precipitation", Addison-Wesley Pub. Co., pp.10-18.

CHAPTER 2

FUNDAMENTALS OF ELECTROSTATIC PRECIPITATION

2.1 Introduction

The process of electrostatic precipitation can be divided into three main steps :

1. Generation of a corona and associated electric field.
2. Particle charging.
3. Particle collection.

In industrial electrostatic precipitators (ESP's) a fourth step, particle removal, is also of major importance.

The relevant characteristics of the theoretical treatment of electrostatic precipitation for a negative corona in air are reviewed next. Extensive use is made of the rationalized MKS system of units, as discussed by Hendricks(1973) and Sears et al.(1976).

2.2 Corona Generation and Space-Charge Effects

The first step in electrostatic precipitation is the establishment of a copious source of ions. Gases are non-conductors, although free electrons and ions are a natural result of atmospheric radiation. Davis et al.(1961) and Oglesby et al.(1970, 1978) state that about 20 electron-ion pairs per cm^3 per second are produced by atmospheric radiation. If an electric field is applied to a dielectric, there is a value of the field for which it becomes a conductor, which is the breakdown strength

of the dielectric. White (1963) defines corona as the localized breakdown of a gas, which does not propagate to form a streamer. A streamer is a luminous conducting filament of heavily ionized gas extending from the electrode surface. The breakdown strength of air, at standard conditions, is about 3×10^6 Vm^{-1}.

If a high-voltage is applied to a parallel-plate capacitor a uniform field results, and breakdown occurs at the breakdown strength of the dielectric. A corona is not possible in this situation, and breakdown occurs in the entire inter-electrode spacing, a condition termed sparkover. If one of the electrodes has a short radius of curvature, e.g., a fine wire, very high fields can exist in the immediate vicinity of the electrode. The naturally occurring electrons are accelerated in the high field region of the fine wire, and upon collision with neutral molecules, orbital electrons are released. These are called primary emission electrons. The electric field must be high enough to increase the kinetic energy of the impacting electrons to the point where the ionization potential is attained on impaction. For most atoms and molecules, Oglesby et al. (1970,1978) and White (1963) cite values within 10-25 eV for the ionization potential energy.

Davis et al. (1961) consider that the first corona point usually appears due to irregularities on the electrode surface, where the breakdown strength of the gas at that point was exceeded. The inelastic collisions of the high energy electrons produce not only the primary emission electrons but also the corresponding positive ions. Collisions of these ions with the cathode (corona wire) release further electrons, which

are the secondary emission electrons. These are also formed by photoelectric emission at the cathode, photoionization of the gas by UV radiation from the gas and by metastable gas atoms. The secondary electrons are in turn accelerated by the electric field, producing further positive space-charge (charge carried by positive ions) and primary emission electrons. This process of electron multiplication by an electric field is termed an electron avalanche, reviewed in detail by Davis et al. (1961), Oglesby et al. (1970,1978) and White (1963).

Increasing the applied voltage will only produce more localized regions at the cathode where breakdown occurs, until a critical voltage is reached at which the corona stabilizes. The stable corona is known as a glow discharge, which Oglesby et al. (1975) define as the equilibrium situation between the positive space-charge near the cathode, the negative space-charge (including the free electrons) in the interelectrode spacing and the applied field. The boundary of the corona glow region is then determined by the electric field strength necessary for impact ionization. The characteristics of the ionization zone depend primarily on the electric field near the wire, the gas composition and the nature of the wire.

Increasing the applied voltage over the value necessary for a stable corona will produce an increase in current, and a point is reached where the voltage is sufficient to sustain a spark across the interelectrode region. The increase in current is non-linear with the applied voltage, due to the increased gas conductivity at higher fields (non-ohmic behaviour). Although many industrial ESP's operate above sparkover, the useful operating

range of a corona is given approximately by the onset and sparkover voltages.

Outside the glow discharge region, the electric field is not sufficiently high to sustain the electron avalanche, and a quiescent zone without positive ions occurs. Here, the electrons are captured by electronegative neutral molecules, and negative ions are formed. These ions drift towards the passive (collection) electrode, and for clean air they comprise most of the negative space-charge, since the concentration of free electrons is usually very small. Oglesby et al. (1970) give a method for estimating the free electron contribution to the current, based on conservation of current.

Neglecting the free electron component of the current may introduce serious errors under certain conditions. White (1963) shows that at very high average fields (applied voltage divided by the wire-to-plate spacing) of the order of 7×10^5 Vm^{-1}, the free electron component of current cannot be ignored. Awad et al. (1975) and Penney et al. (1957) consider this situation to be near sparkover, while Penney et al. (1957) and Smith et al. (1978) show that short distances between the discharge and passive electrodes have the same effect. Recently, McDonald et al. (1980) showed that reduced air densities also give rise to an appreciable free electron component of current.

When dust particles are also present in the inter-electrode region, the current is carried by positive ions and some dust particles near the discharge electrode, and by negative ions, some free electrons and most of the dust particles outside

the corona glow region. Cobine (1956) empirically determined the size of the corona glow region to be of the same order of magnitude as the discharge wire radius, which is much smaller than the interelectrode spacing.

Bush et al. (1979), Cobine (1956) and Oglesby et al. (1978) cite that thermal ionization becomes important in ESP's operating above about 1088 K, although a lower critical limit of 800 K has been reported by Shale (1965). Below these temperatures, thermal ionization may be completely ignored.

The equation which relates the current to the applied potential is Ohm's Law, which in its general form is:

$$\bar{j} = -\rho b \bar{\nabla} V \qquad (2.1)$$

where $(\bar{j})$ is the current density vector, (ρ) is space-charge (charge per unit volume of gas), (b) is charge carrier mobility (velocity per unit electric field strength) and $(\bar{\nabla} V)$ is potential gradient. In scalar form, Eq. 2.1 is:

$$j = \rho b E \qquad (2.2)$$

where (E) is electric field strength.

In the general case where the charge carriers are free electrons, negative ions and charged dust particles, i.e. outside the corona glow region, the various space-charges and mobilities have to be taken simultaneously into account. Usually, the current carried by the electrons and the dust can

be ignored. Under this assumption, Oglesby et al. (1978) assign an equivalent mobility to the charge carriers. Then:

$$b_{eq} \simeq \rho_i b_i / \rho \qquad (2.3)$$

where the index (i) refers to negative ions. Neglecting the current carried by the charged dust particles is not the same as neglecting its space-charge contribution, because the ionic mobilities are much larger ($\sim$ 200 x) than those of the charged particles. Thus, in Eq. 2.3 the space-charge ρ is the sum of the ionic and dust space-charges, i.e.:

$$\rho \simeq \rho_i + \rho_d \qquad (2.4)$$

Mobilities of ions in air were measured and are tabulated in some references, among them Hewitt (1957), International Critical Tables (1933), Liu et al. (1967), McDonald et al. (1977), Robinson (1971), Shale (1965) and Smith et al. (1978).

The ratio of ionic space-charge to total space charge must be known to determine the equivalent mobility. This ratio is a function of ESP longitudinal direction, because the percent of space-charge removed is related to the percent dust removal. McDonald et al. (1978a) and Oglesby et al. (1978) give the following approximate expression for the equivalent mobility:

$$b_{eq} \simeq b_i \left(\frac{j}{j + \frac{b_i}{b_d} j_d} \right) \qquad (2.5)$$

where (j) and (j_d) are the average current densities at the plate due to ions and dust particles, respectively, and (b_i/b_d) is the ratio of ion-to-dust particle mobilities. This ratio varies with the size of the dust particles and electric field conditions. In Eq. 2.5, it is assumed that the average current density at the plates is the average ionic current density at the plates, a condition which is approximated in practice.

The motion of the ions in the interelectrode spacing causes a secondary flow (electric wind) to develop. Adam (1979), Robinson (1967a,1968a,1971), Ramadan et al. (1969), Stock et al. (1977) and Soo (1972) believe that the electric wind adds turbulence to the turbulence of the main gas flow, although measurements performed by Gensler (1968) and Gensler et al. (1968) show no difference in turbulence intensities with or without a negative corona. The electric wind results from momentum transfer of the ions to the gas molecules, which generates a flow normal to the main flow. Based on theoretical arguments, Robinson (1971) shows that the electric wind velocity should vary as the square root of the corona current. Another secondary flow, caused by the gas-dust particles coupling momentum may also exist in ESP's, and this is treated theoretically for a cylindrical geometry by Stock et al. (1977).

In considering the actual performance of ESP's, Cooperman (1971), Nichols et al. (1970), Oglesby et al. (1970, 1975) and Soo (1972) feel that the principal effect of the electric wind is an increase in the reentrainment of the precipitated dust, although particle transport to the collection

plates may actually be enhanced (Robinson (1971) and Strauss (1966)). Investigations on reentrainment due to electric wind were done by Lakey et al. (1955) and Spencer (1976); they concluded that large particles of high conductivity are affected to the greatest extent. The effect of particle size and conductivity on reentrainment is examined in Section 2.7.

It is usual to include the electric wind as one of the various causes of reentrainment, because it is difficult to isolate its effect from other non-ideal effects which are normally present. These include non-uniformity in main flow profile, gas bypassage (sneakage) through collection hoppers, sparking and high air velocities in dry dust collection.

2.3 Electric Field in Parallel-Type Precipitators

2.3.1 Corona-Onset Voltage and Field Intensity

When a high-voltage is applied to a pair of electrodes, one of which has a short radius of curvature, e.g. a fine wire, stable corona is established at a value of electric field intensity given by the semi-empirical relation (Peek, 1929):

$$E_o = 3\times10^6\ mD\left(1 + 0.03\sqrt{\frac{D}{a}}\right) \qquad (2.6)$$

where (m) is a wire roughness factor, equal to one for perfectly smooth wires and usually in the range 0.5-0.9, (D) is air density relative to 20°C and 1 atm, and (a) is corona wire radius. Because the field strength given by Eq. 2.6 is only valid near the corona electrode, the shape of the passive electrode is not important, and the same is true for the polarity of the discharge.

McDonald et al. (1977), Penney et al. (1960) and White (1963) assume the radius of the corona glow region to be the same for parallel-type and cylindrical geometries. Assuming that there is no space-charge distortion of the field in the corona glow region, Crawford (1976) and McDonald et al. (1977) give the following approximation for the field intensity at the boundary (E_i):

$$E_i = E_o \, a/r_i \qquad (2.7)$$

where (r_i) is the radius of the corona glow region.

From Eq. 2.6, smaller diameter wires require a larger electric field for corona onset, and for a very large radius, $E_o \rightarrow 3 \times 10^6$ Vm^{-1}, which is the breakdown strength of air at ambient conditions. In this case, the field is approximately uniform over the entire interelectrode spacing and sparkover of the gas gap occurs.

A theoretical expression for the corona onset voltage applicable to parallel-type ESP's is given by Cooperman (1960):

$$V_o = a \, E_o \ln(d/a) \qquad (2.8)$$

where $d = 4s/\pi$ for $s/c \leq 0.6$

and $d = \dfrac{c \exp(\pi s/2c)}{\pi}$ for $s \geq 2.0$.

Values of the geometrical factor (d) in the intermediate region of (s/c), where (s) is wire-to-plate spacing and (c) is one-half the wire-to-wire spacing, are given in Table 2.1.

TABLE 2.1

Characteristic Dimensions for Corona Onset Calculations
Cooperman (1963)

s/c	0.8	1.0	1.2	1.4	1.6	1.8
d/c	1.104	1.529	2.101	2.865	3.937	5.376

According to Cooperman (1960,1963), Eq. 2.8 is accurate to within 1%, and was experimentally verified by Robinson (1965) over a large range of electrode dimensions, in atmospheric air, for smooth discharge wires with neighbours on both sides, i.e. excluding the extremity wires. In an ESP, corona onset voltages are always somewhat lower than given by Eq. 2.8, because of wire roughness and the effect of the extremity wires.

As the applied voltage is increased above corona onset, increased currents occur, but both the experimental evidence of Colli et al. (1954) and the theoretical analysis of Loeb (1953) suggest that the product $E_i r_i$ (in Eq. 2.7) is established at corona onset and remains essentially unchanged over a wide range of applied voltages and currents above onset. An approximate expression for the space-charge density at the boundary of the corona glow region is given by McDonald et al. (1977) as:

$$\rho_{ri} = \frac{2cj}{\pi b_i E_i r_i} \qquad (2.9)$$

where (j) is the average current density at the plate and the other variables are defined as previously. The importance of Eq. 2.9 is in the estimation of the space-charge distribution in the interelectrode spacing (Section 2.3.3).

The operational range of applied voltages for an ESP is approximately given as between the sparkover and onset voltages. Robinson (1971), Spencer (1976a), Shale et al. (1968), Sproull et al. (1951) and White (1977a) show that the sparkover voltage is approximately inversely proportional to the absolute temperature. The data of Bush et al. (1979), Robinson (1971), Shale (1965) and Shale et al. (1968) show that corona onset voltage varies directly with density and inversely with temperature, and that the operational range increases with decreasing temperature. Density and temperature affect both onset and sparkover voltages through their action on the equivalent ion mobilities, which increase with decreasing gas density and increasing temperature and electric field. The first effect is due to an increase in the electron mean free path. The second effect is due to an increase in thermal ionization, which is negligible below about 800 K, and the electric field effect is due to an increase in secondary emission at the cathode.

Heinrich (1961) and Little (1956) show that small scale ESP's can operate at much higher voltages than the full-size units they are meant to simulate; one possible reason is given by Collins et al. (1971) as the capacitance difference of the electrode systems. With a low capacitance, by the time the pre-breakdown activity has built up sufficiently, the voltage

can fall below sparkover because current from the pre-breakdown pulses is quickly withdrawn. White (1963) previously applied this principle to the electrical sectionalization of a full-size ESP, where small sections are independently energized by small (low capacitance) power supplies.

2.3.2 Electrostatic Field

At applied voltages lower than the corona onset voltage, the electrostatic potential is described by Laplace's Equation:

$$\nabla^2 V = 0 \qquad (2.10)$$

The lack of axial symmetry of a parallel-type ESP, due to the presence of multiple corona-wires, considerably complicates the solution of Laplace's Equation. Analytical solutions are readily derived for cylindrical geometries, both with and without corona current, and these are available from Crawford (1976), Oglesby et al. (1970,1975,1978) and White (1963).

The solution of Laplace's Equation for parallel-type ESP's is based on conformal transformations (see Currie (1974)). Penney et al. (1960) used a conformal mapping technique which transforms an elliptical wire midway between two parallel planes (a close representation of a parallel-type ESP geometry) into two coaxial cylinders (a representation of cylindrical ESP geometry). The contributions of individual wires to the potential at any point in space were determined, and superimposition of

solutions for all the corona wires was possible, due to linearity of Laplace's Equation. It should be noted that Laplace's Equation is invariant with respect to a conformal transformation.

This technique is laborious, and a more expedient method was developed by Cooperman (in McDonald et al. (1977), Robinson (1971) and White (1963)). The transformal conformation used by Cooperman replaces a wire midway between two parallel plates with a wire parallel to a single plate, and the method of images is used to solve for the potential distribution. The result, after superimposition of potentials due to all corona wires, is a series solution containing as many terms as there are corona wires, given by:

$$V_e(x,y) = \frac{V}{\lambda} \sum_{n=-\infty}^{+\infty} \ln \frac{\cosh\{\pi(y-2nc)/2s\} - \cos(\pi x/2s)}{\cosh\{\pi(y-2nc)/2s\} + \cos(\pi x/2s)} \qquad .....(2.11)$$

where $V_e(x,y)$ is the electrostatic potential at the point in space defined by the coordinate pair (x,y), (V) is the applied voltage and (n) is the number of corona wires. The parameter (λ) is given by:

$$\lambda = \sum_{n=-\infty}^{+\infty} \ln \frac{\cosh(\pi nc/s) - \cos(\pi a/2s)}{\cosh(\pi nc/s) + \cos(\pi a/2s)} \qquad (2.12)$$

The coordinate system is centered in a discharge wire, and (x,y) are respectively the directions normal and parallel to the main gas flow direction. The series given by Eq. 2.11

converges rapidly, and only a few terms need to be evaluated. The electrostatic field at the plate, computed from Eq. 2.11 agrees well with the experimental data of Tassicker (in McDonald et al., 1977).

2.3.3 Corona Current and Space-Charge

In the presence of corona current, Laplace's Equation is substituted by the more general Poisson's Equation:

$$\nabla^2 V = -\rho/\varepsilon_o \qquad (2.13)$$

where (ε_o) is the permittivity of free space (8.85 pF m^{-1}). Due to the non-linearity of Poisson's Equation, even if an analytical solution could be obtained for the potential distribution due to one corona wire, superimposition of potentials would not be possible. Basically, the problem is to obtain a solution which obeys the fundamental laws of conduction in a gas. These are the generalized Ohm's Law (Eq. 2.1), Poisson's Equation (Eq. 2.13) and the Current Continuity Equation, which at steady-state is:

$$\bar{\nabla} \cdot \bar{j} = 0 \qquad (2.14)$$

In an attempt to solve this problem, Cooperman (1960) applied a perturbation technique, starting with a pure electrostatic field. The distribution of space-charge was estimated

by assuming a small current flow, and a new potential distribution was generated. The final value of space-charge was the one which caused a negligible change in the generated electric field. Assuming a uniform space-charge distribution, the contribution of the space-charge to the potential is given by:

$$V(x) = \frac{jc \ln(d/a)}{\pi\varepsilon_o bV}(s^2-x^2) \qquad (2.15)$$

The total potential at any point (x,y) is determined by superimposition of the electrostatic potential (Eq. 2.11) with the space-charge potential (Eq. 2.15). At the corona wire (x = a), the potential is the applied voltage, and the electrostatic component is the corona onset voltage. Then:

$$V_o = V_o + \frac{s^2 jc \ln(d/a)}{\pi\varepsilon_o Vb} \qquad (2.16)$$

which is an approximation to the voltage current characteristic of a parallel-type ESP, valid for small corona currents. The voltage-current characteristics generated by Eq. 2.16 are very sensitive to the value of corona onset voltage, which in turn is very sensitive to the wire roughness.

The presence of a space-charge component of the electric field increases the potential near the collection plates above its electrostatic value. This was shown by White (1963) who approximated the corona wires by a uniform current sheet electrode. Under this condition, Poisson's Equation becomes unidimensional, and integration gives:

$$E_p^2 = E_{ep}^2 + 2js/b\varepsilon_o \qquad (2.17)$$

where (E_p) and (E_{ep}) are respectively the total field and electrostatic component at the collection plates.

There are some factors which influence the current-voltage characteristics. White (1963) says that dust deposits on the electrodes may either reduce or increase the onset voltage, and shift the entire voltage-current curve to either lower or higher currents. Small deposits of dust on the discharge electrodes can produce localized high field regions, which tend to emit a corona at reduced voltages. This is equivalent to a decrease in the wire roughness in Eq. 2.6, and the effect is to shift the entire voltage-current characteristic to a lower voltage region. Heavy deposits of dust on the discharge electrodes tend to suppress corona, by increasing the effective wire diameter (Eq. 2.6) and by producing a voltage drop across the dust deposit. Deposits on the collection plates may also produce an appreciable voltage drop with serious consequences for the performance of ESP's. This phenomenon is examined in Section 2.6.

To avoid the shortcomings of an analytical solution such as that of Cooperman (1960,1963), Leutert et al. (1972) performed the numerical integration of Poisson's Equation, coupled with the Current Continuity Equation. The solution is based on the finite difference method, described in detail by Smith (1975). Major assumptions of the model are: the wires and immediate vicinity of the discharge region are only considered as ion sources, and thus the region of high electric fields near the wires is

ignored; the motion of all charge carriers can be described by an equivalent mobility.

Basically, derivatives at a point are approximated by difference quotients over a small interval. The analytical solution of a two-dimensional elliptic equation (Poisson's Equation) is a function of the space coordinates (x,y) which satisfy the differential equation at every point of the area enclosed by a boundary, and which satisfy certain conditions (boundary conditions) at the boundary.

Poisson's Equation can be discretized with central differences, giving:

$$V_o = \frac{1}{2(a_x^2 + a_y^2)} \{a_y^2(V_2 + V_4) + a_x^2(V_1 + V_3) + \frac{a_x^2 a_y^2 \rho_o}{\varepsilon_o}\} \quad .....(2.17)$$

The Current Continuity Equation can be combined with the general form of Ohm's Law and discretized with backward differences, giving, for a constant equivalent mobility:

$$\rho_o = -\frac{\varepsilon_o}{2a_x a_y}(a_y E_{ox} + a_x E_{oy}) + \{(\frac{\varepsilon_o}{2a_x a_y})^2 (a_y E_{ox} + a_x E_{oy})^2 + \frac{\varepsilon_o}{a_x a_y}(a_y E_{ox}\rho_2 + a_x E_{oy}\rho_3)\}^{\frac{1}{2}} \quad .....(2.18)$$

In Eqs. 2.17 and 2.18, the subscripts refer to points in the numerical mesh, as seen in Fig. 2.1, where (a_x, a_y) are the mesh intervals. The point labelled zero corresponds to every possible point in the total numerical grid, as seen in Fig. 2.2, although it corresponds to the discharge wire for the first set of calculations. Because of symmetry, only one-half of the wire-to-wire spacing needs to be considered, and the solution is assumed to apply to similar integration grids throughout the entire ESP length. Similar expressions to Eqs. 2.17 and 2.18, but which take into account the effect of non-constant mobility are given by McDonald et al. (1977).

The reason why central differences are applied to the potential distribution only, is because an initial estimate of a space-charge grid is not readily available. Although central differences are more accurate than backward differences, McDonald et al. (1977) overcome the problem by choosing a sufficiently small grid mesh. In the actual numerical procedure, described in more detail by McDonald et al. (1977), McDonald (1978a) and Oglesby et al. (1978), values must be assigned to the potential, electric field and space-charge to points that are exterior to the region of integration. Due to symmetry, these values are the same as those of symmetrically correspondent interior points.

Of special importance are two of the boundary conditions, namely that the potential is the applied voltage at point A (discharge wire) and that the computed current density at the plate is equal to the measured value. The current density is

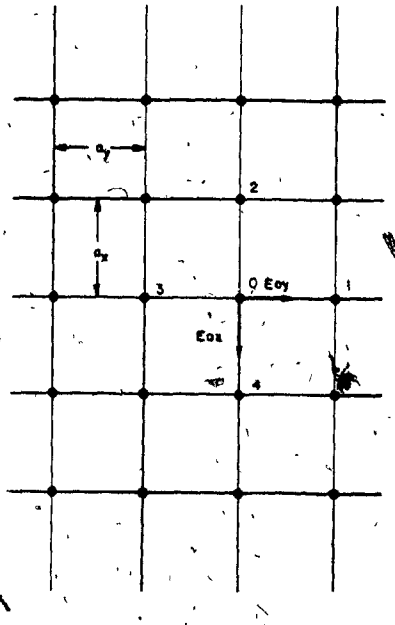


Figure 2.1 Partial grid showing nomenclature used in the numerical analysis of the electrical conditions, McDonald et al. (1977)

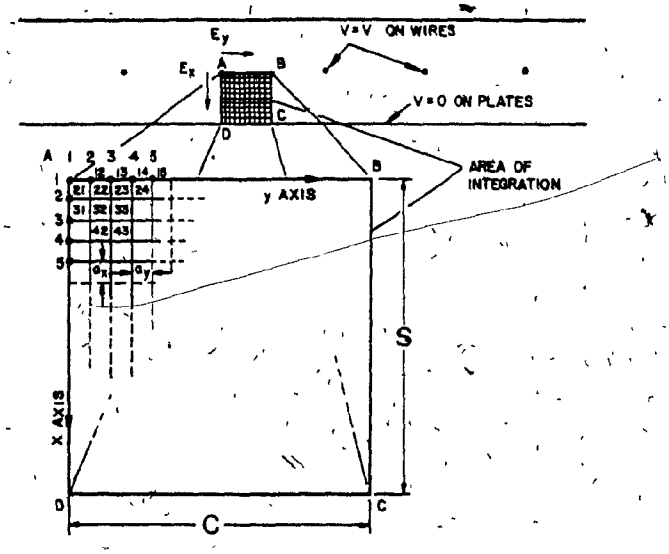


Figure 2.2 Nomenclature used in the numerical analysis of the electrical conditions in wire-duct precipitators, McDonald et al. (1977)

computed from Ohm's Law (Eq. 2.2) for points at the plate, and averaged over the number of grid points in the direction of gas flow. In the case where the voltage current characteristics are unknown, the boundary conditions have to be modified, and the applied voltage which produces a given current density at the plates becomes unknown. McDonald et al. (1977) and McDonald (1978a) describe in detail the modified method used to generate current-voltage characteristics.

The complete set of boundary conditions, for the case of known voltage current characteristics, is:

$$V = \text{applied voltage, at A} \qquad \text{(i)}$$

$$E_x = E_y = 0, \text{ at A and B} \qquad \text{(ii)}$$

$$E_x = 0, \text{ along AB} \qquad \text{(iii)}$$

$$E_y = 0, \text{ along AD, BC and CD} \qquad \text{(iv)}$$

$$V = 0, \text{ along CD} \qquad \text{(v)}$$

$$\frac{b_{eq}}{N} \sum_{i=1}^{N} \rho_{p_i} E_{p_i} = \left\{ \left(-\frac{\Delta V}{\Delta X}\right) \rho b \right\}_{\text{average at plate}} = \text{measured current density} \qquad \text{(vi)}$$

where the subscript i refers to (N) points at the plate in the direction of gas flow.

The numerical scheme is as follows: obtain an initial estimate of the potential grid, using Eq. 2.11, and of the space-charge at the wire, using Eq. 2.9. The values of space-charge

can then be determined along lines AB and AD, using backward differences, and then at the interior points. A new potential grid is generated and the method is repeated until convergence of the potential grid is obtained. The boundary condition on current density at the plate is then checked, and if necessary, a new initial estimate of space-charge at the wire is used, until convergence of both the potential grid and the calculated and measured average current densities at the plate occurs.

Because current-voltage curves are not generated by the process outlined, the value of the roughness factor in Eq. 2.9 is not critical. If the modified method of McDonald et al. (1977) is used to generate current-voltage curves, then the results are very sensitive to wire roughness factor, as it affects the space-charge distribution, which in turn will affect the potential distribution and the (unknown) applied voltage. The same high sensitivity to wire roughness also occurs when predicting ESP characteristics using Cooperman's low current solution (Eq. 2.16).

Probes for measuring potential distributions in parallel-type ESP's are described by Lagarias (1959), Penney et al. (1960) and Tassicker (1974). Fig. 2.3 shows comparisons of the experimental data of Penney et al. (1960) and Tassicker (in McDonald et al. (1977)), for negative corona in ambient air, with the finite difference method of Leutert et al. (1972), as implemented by McDonald et al. (1977). The agreement with experimental data is good, but of special importance is the

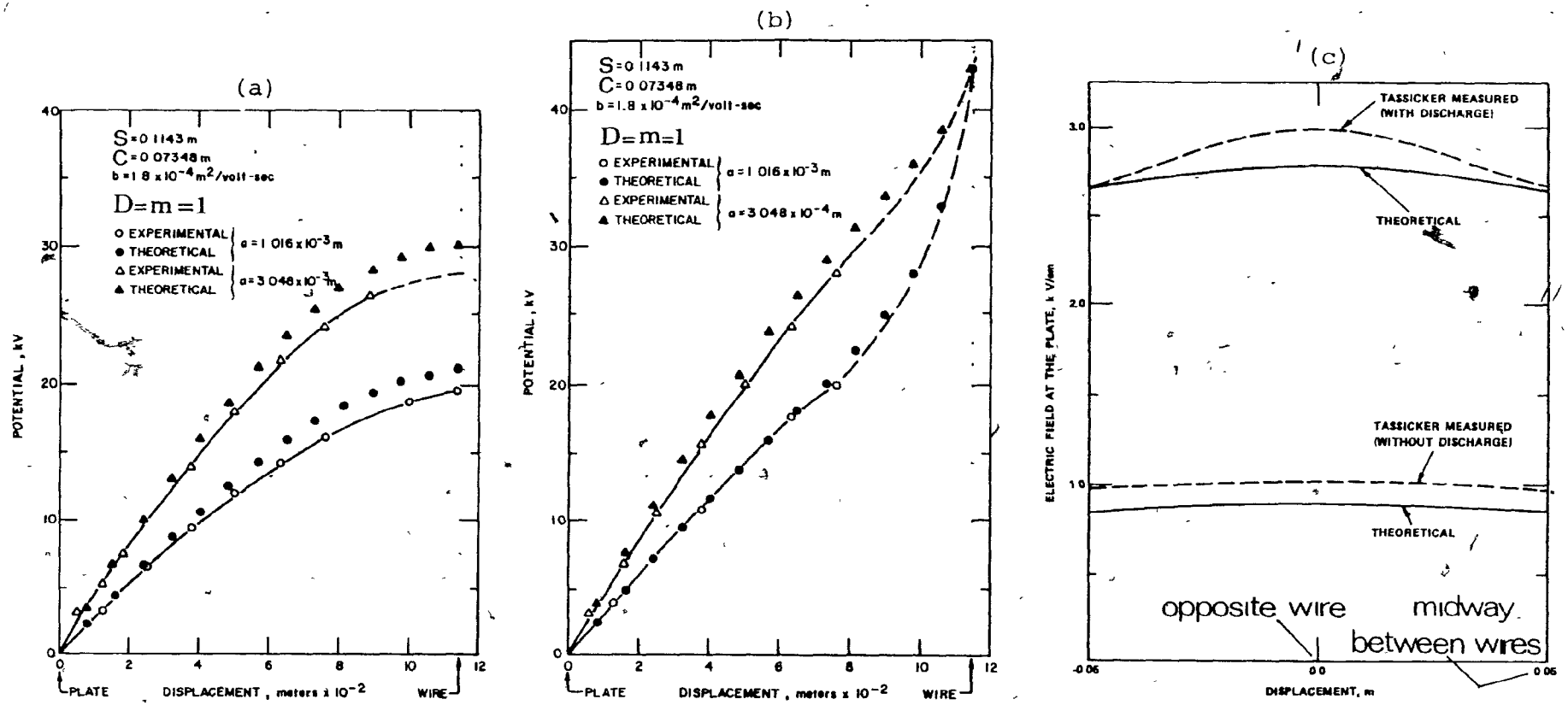


Figure 2.3

(a) Theoretical and experimental potential profiles along a line from a point midway between the wires to the plate, McDonald et al. (1977)

(b) Theoretical and experimental profiles along a line from the corona wire to the plate, McDonald et al. (1977)

(c) Theoretical and experimental electric field at the plate as a function of displacement, McDonald et al. (1977)

slope of the potential near the plate, which determines the electric field at the plate. A correct estimation of the electric field intensity at the plate is necessary, as theoretically the charged particles attain a terminal velocity towards the collection plates which is proportional to the electric field intensity at the plates (Section 2.5.2).

The simulated curves of Fig. 2.3 were obtained by assuming a constant equivalent mobility, irrespective of position within the ESP. The experimental conditions of Penney et al. and Tassicker are for clean laboratory air, and so the approximation is valid. In the general case where dust space-charge is present, the variation of the equivalent mobility with space coordinates can be taken into account in the flow direction only. Experimental values of equivalent mobility as function of position are also lacking.

Hewitt (1957), International Critical Tables (1933), Liu et al. (1967), McDonald et al. (1977), Robinson (1971), and Smith et al. (1978) report values of ionic mobilities in laboratory air at standard conditions ranging from $1.1\text{-}2.7\times10^{-4}$ $m^2V^{-1}s^{-1}$, and McDonald et al. (1977) suggest that values between $1.6\text{-}2.0\times10^{-4}$ $m^2V^{-1}s^{-1}$ are suitable for studies of both polarity coronas, i.e. the theoretical predictions are little affected in this range. For industrial ESP's, the problem is very complex, since the composition and heavy dust loads of the flue gases are expected to greatly affect the equivalent mobility. Reduced densities, due to the high temperatures (for hot-side ESP's) may also increase the equivalent mobility.

From the experimental data of Gallo et al. (1971), Jarzebski et al. (1974), Lagarias (1959), Lakey et al. (1955) and Penney et al. (1960), and the finite difference method of Leutert et al. (1972) and McDonald et al. (1977), some interesting conclusions can be drawn:

- Both current density and electric field at the plate show a maximum opposite the discharge wire.

- The current decreases with increasing wire radius and wire-to-plate spacing, for a fixed applied voltage.

- The wire-to-wire spacing has a very small effect on the voltage-current characteristics, over a wide range of values.

- For the same current density at the plate, the average field at the plate increases slowly as wire size increases but rapidly as plate-to-plate spacing increases. The wire-to-wire spacing has only a minor effect on the field at the plate, as it affects only the electrostatic component of the field.

Lagarias (1959) measured potential distributions in parallel-type ESP's in the presence of dust space-charge, and concluded that the electric field at the plate depends on dust loading only as it affects the current density at the plate.

The increase in field strength at the plate with duct width, for the same average interelectrode field, is due to an increase in the space-charge component of the field. This has recently been taken advantage of by some ESP's manufacturers (Pettersen, 1980), due to the great reduction in plate area which is allowable without degrading the ESP performance.

2.4 Particle Charging

The negative ions generated by the corona are responsible for charging the dust particles, although a small percentage of the particles may receive their charge from positive ions within the boundary glow region. The classical mechanisms of particle charging by ions in an electric field are reviewed by Crawford (1976), Oglesby et al. (1970, 1975, 1978), Robinson (1971) and White (1951,1963). These mechanisms are termed field and diffusion charging. Although both act simultaneously, the former is dominant for particles with diameter above about 1-2 μm, while the latter predominates for diameters below about 0.2 μm, and in the intermediate range both are important. For particles less than about 0.1 μm in diameter, with large Knudsen numbers (ratio of ion mean free path to particle radius $\gtrsim$ 0.2), special theories are required such as those developed by Gentry et al. (1967) and Parker (1975), but these are of little importance to ESP's.

2.4.1 Field Charging

The corona ions follow the electric field lines, in the direction of maximum potential gradient, except for collisions with gas molecules. According to White (1963), these path irregularities are of the order of the mean free path of the ions. The ion mean free path can be estimated by Langevin's Equation (in Liu et al. (1967,1968) or Loeb (1961)) to be of the order of 0.01-0.1 μm in air at standard conditions. Thus, ion-path irregularities have only to be considered for submicron

particles. When the ion reaches the dust particle, it is held at the surface by induced charges.

The following assumptions are made in the derivation of the classical field charging equations:

- the particles are spherical;
- there are no field interactions between charged particles;
- the particles are surrounded by a uniform ion concentration in a region of uniform electric field strength (far from the immediate vicinity of the particle); and
- the charge on the particles is evenly distributed over the entire surface.

The first assumption is rarely met in industrial dusts, and only probably for the smaller particles formed by condensation processes. Hignett (1967), Smith et al. (1961) and White (1963) state that the effect of non-sphericity on the charge acquired by a particle is to produce an increase in the charge due to the larger specific surface area. Carefully controlled measurements performed by Smith et al. (1961) indicate that this effect is unlikely to be of practical importance. The next two assumptions are probably closely approached in ESP's, due to the ratio of particles : ESP dimensions, as well as to the relatively low concentrations of particles. The last assumption is only met if the particles rotate in the turbulent air flow.

When an uncharged dielectric particle, i.e. with permittivity larger than ε_o, the vacuum permittivity, is placed in a uniform electric field, distortion of the electric field occurs in the vicinity of the particle, the degree of distortion increasing with particle permittivity. The permittivity of a medium (ε) is related to the vacuum permittivity by the relative dielectric constant (K):

$$\varepsilon = K\varepsilon_o \qquad (2.19)$$

The dielectric constant is strictly not a constant, since it varies with the frequency of the applied field, the temperature of the medium and possibly with particle size. For typical ESP conditions, with a DC field in the interelectrode spacing, variation with frequency is of no concern. Tassicker (1971,1975) measured the dielectric constant of samples of fly ash, as a function of temperature, and found that the dielectric constant increased with increasing temperature. The dielectric constant is actually a complex quantity, but the imaginary part is negligible at zero (or low) frequencies. Hendricks (1973), Botcher (1952), Pampuch (1976) and Waye (1967) relate the dielectric constant to the polarizability of the material and its ability to store energy. In the case of pure electronic polarization, the dielectric constant is the square of the index of refraction, but such cases are rare. When ionic and space-charge polarization exist, values of dielectric constant are larger.

Values of dielectric constants of solids are tabulated in several references, among them those of Fink (1975), Handbook of Chemistry and Physics (1976-77), International Critical Tables (1933), Kaye et al. (1973), Kingery et al. (1976), Pender et al. (1975), Samsonov (1973), Say (1973), Von Hippel (1954) and Waye (1967). The dielectric constant can also be experimentally measured, and methods are outlined by Botcher (1952), Tassicker (1971) and Waye (1967).

Besides its importance in particle charging, the dielectric constant is also important in determining the characteristic time constant of charge transfer from a charged dielectric. This situation occurs with the charged dust deposited on the collection plates and upon Tassicker (1975) it could be important in ESP's operating near sparkover.

A new ESP design based on the existence of a small but significant charge transfer time was developed by Penney et al. (1978).

The adhesive forces of the precipitated layer due to the corona current are also dependent on the permittivity of the dust medium, as theoretically derived by Penney et al. (1962) and Tassicker (1975). These are reviewed in more detail in Section 2.7.

The charging rate of a dust particle of diameter (D) and dielectric constant (K), placed in a uniform field of strength (E_o) is given by:

$$\frac{dQ}{dt} = (N_o e b_i Q_s / 4\epsilon_o)(1-Q/Q_s)^2 \qquad (2.20)$$

where (N_o) is free ion density, (e) is the elementary charge (1.602×10^{-19} coulomb), (Q) is particle charge after charging time (t), and (Q_s) is saturation charge, given by:

$$Q_s = 3\pi \left(\frac{K}{K+2}\right) \varepsilon_o E_{av} D^2 \qquad (2.21)$$

where (E_{av}) is the average field in the interelectrode spacing.

For an initially uncharged particle, Eq. 2.20 integrates into:

$$Q = Q_s \frac{t}{t+\tau} \qquad (2.22)$$

where (τ) is the charging time constant, i.e. the time to achieve 50% saturation charge, given by:

$$\tau = \frac{4\varepsilon_o}{N_o e b_i} \qquad (2.23)$$

Equation 2.21 is of fundamental importance in electrostatic precipitation studies which involve particles larger than about 2 μm in diameter, and it has been verified experimentally by a number of authors, among them Hewitt (1957) and White (1951, 1963). It shows that the charge is proportional to the area of the particle, to the electric field strength and to the factor $\left(\frac{K}{K+2}\right)$, which is equal to one for perfect conductors and to 1/3 for perfect insulators. From Eq. 2.22, 90% of the saturation charge is attained within about ten time constants. In full-size ESP's, operating at high fields and currents, coupled with a low

air velocity ($\sim$ 1 ms^{-1}), neglecting (τ) does not produce any appreciable error. According to Little (1956), Pui et al. (1977) and Robinson (1961,1972), neglecting the delay in particle charging for laboratory units of small size, operating at high air velocities and/or low fields and currents may introduce an appreciable error.

The charging time constant varies along the ESP length, because the free ion density decreases as charging progresses. If the dust loading at the ESP inlet is very large, corona quenching may occur, and charging by ion bombardment no longer obeys Eq. 2.22. Charging under corona quenching is discussed by Awad (1975) and Sproull (1963). Usually, the charging time constant will vary from a higher value at the inlet of the ESP to a lower value at the outlet.

Another factor which influences the charging time constant is the wave form of the high voltage rectifier system, and this is discussed by Oglesby et al. (1970) and White (1963).

2.4.2 Diffusion Charging

This mechanism of particle charging is related to the thermal (Brownian) motion of the ions, and as such exists without the application of an external field. The classical diffusion charging equation is derived on the assumption that ion diffusion to the particle surface does not depend on the application of an external field. Hewitt (1957), Liu et al. (1968,1978), Murphy et al. (1959), Penney et al. (1957) and Smith et al. (1978)

experimentally verified the important effect of the applied field, for the size range where diffusion charging is appreciable. Charging is enhanced because the electric field imparts momentum to the ions, which may then strike a particle against its self-field. The exterior electric field is attractive for the incoming ions on one side of the particle and repulsive on the opposite side. Since the attractive field increases more the ion concentration near the particle surface than the decrease on the opposite side due to the repulsive field, charging is enhanced. The first factor is thought to be important for charging by free electrons, due to their large mean free paths as compared to the ions, and so may be important at very high fields, near sparkover, for short interelectrode spacings and at reduced gas densities. The second factor is present even at moderate fields ($\sim 10^5$ Vm^{-1}) and is thought to be the dominant factor.

There are two main methods of considering the charging of particles by ion diffusion. Liu et al. (1977,1978) consider the charging as a diffusion process, in which ions move continuously towards the particle along a concentration gradient. On the other hand, Liu et al. (1967,1968), Murphy et al. (1959), Smith et al. (1975,1976) and White (1951,1963) consider charging as a probabilistic process governed by the Kinetic Theory of Gases. For the first approach to be valid, the ion density must be sufficiently large for the charging process to be considered continuous and this condition is not generally met in ESP's. For example, for a monodisperse distribution of 1 μm diameter particles

of unit density, assuming a free ion concentration of 10^{13} m^{-3} and a dust load of 1 gm^{-3} (which are common values for industrial ESP's), the ratio of ion to particle concentration is about five at the inlet. With a collection efficiency of 95%, this ratio increases to about one hundred. So, for typical conditions prevailing in ESP's, diffusion charging is a discontinuous phenomena, and theoretical treatments based on Kinetic Theory are more appropriate.

The assumptions used in deriving the classical diffusion charging equation are:

- the particles are spherical,
- the ions which reach the particle surface are retained by induced charges with 100% attachment efficiency, and
- the external field is only considered as a source of ions, and does not influence the charging process.

Under these assumptions, White (1963) derives the following equation:

$$\frac{dQ}{dt} = \frac{e\pi D^2 \hat{v} N_o}{4} \exp\left(-\frac{Qe}{2\pi\varepsilon_o DkT}\right) \qquad (2.24)$$

For an initially uncharged particle, Eq. 2.24 integrates into:

$$Q = (2\pi\varepsilon_o DkT/e)\ln(1 + D\hat{v}N_o e^2 t/8\varepsilon_o kT) \qquad (2.25)$$

where (k) is Boltzmann's constant (1.38×10^{-23} J K^{-1}) and ($\hat{v}$) is

ion mean thermal velocity, given by:

$$\hat{v} = \left(\frac{8kT}{\pi m}\right)^{1/2} \qquad (2.26)$$

where (m) is mass of a single ion. In electrostatic precipitators, the charging ions are usually considered to be O_2 ions.

From Eq. 2.25, there is no limiting charge for diffusion charging, and this is because there is no upper limit for the thermal velocities. The chance of finding an ion with a given velocity decreases as the velocity increases, but is never zero. The potential due to the particle charge (self-field) increases due to ion collisions, and the probability of finding an ion with sufficient energy to overcome the particle potential will decrease. Then, the diffusion charging rate decreases with time.

Equation 2.25 has been experimentally verified by a number of authors, among them Hewitt (1957), Liu et al. (1967) and White (1951,1963), for particles of submicron size and in the presence of low field strengths.

2.4.3 Combined Field and Diffusion Charging

At moderate or high field strengths, experimental values of charges acquired by fine particles (D < 1-2 μm) are larger than those predicted by the classical diffusion charging equation by a factor of two or three. This discrepancy can be observed in the data of Hewitt (1957), Liu et al. (1968,1978), Penney et al. (1957), Smith et al. (1978) and Van Bush et al. (1980), and it holds for particles down to about 0.1 μm diameter.

In an attempt to solve this problem, Liu et al. (1968) and Smith et al. (1975,1976) expressed the ion concentration near the particle surface as a function of the electric field near the particle surface. According to Liu et al. (1968), the particle surface is divided into two separate regions, with different charging regimes. Before saturation by field charging occurs, only field charging is present in the surface area of the particle for which it can occur, i.e. for an angle of approach of the incoming ions relative to the undisturbed electric field (θ) less than a critical value (θ_o) (Fig. 2.4). In the particle surface defined beyond this critical angle, diffusion charging is allowed at a rate defined by the classical diffusion equation.

Saturation by field charging occurs when the external field (distorted by the presence of the dielectric particle) equals the self-field from the particle. In the classical diffusion charging theory (Crawford, 1976; Oglesby et al., 1970, 1975,1978; Robinson, 1971; and White, 1951,1963), the ion concentration in the potential field due to the charged particle is equal to the free ion concentration (N_o) only at an infinite distance from the particle. According to Liu et al. (1968), after saturation charge the point at which the ion concentration equals the free ion concentration moves closer to the particle surface. To determine this critical distance, Liu et al. (1968) assumed that the conditions of ion and potential distribution at the particle surface along a zero angle of approach of the incoming ions with respect to the undistorted field were representative of the entire particle surface. This assumption is

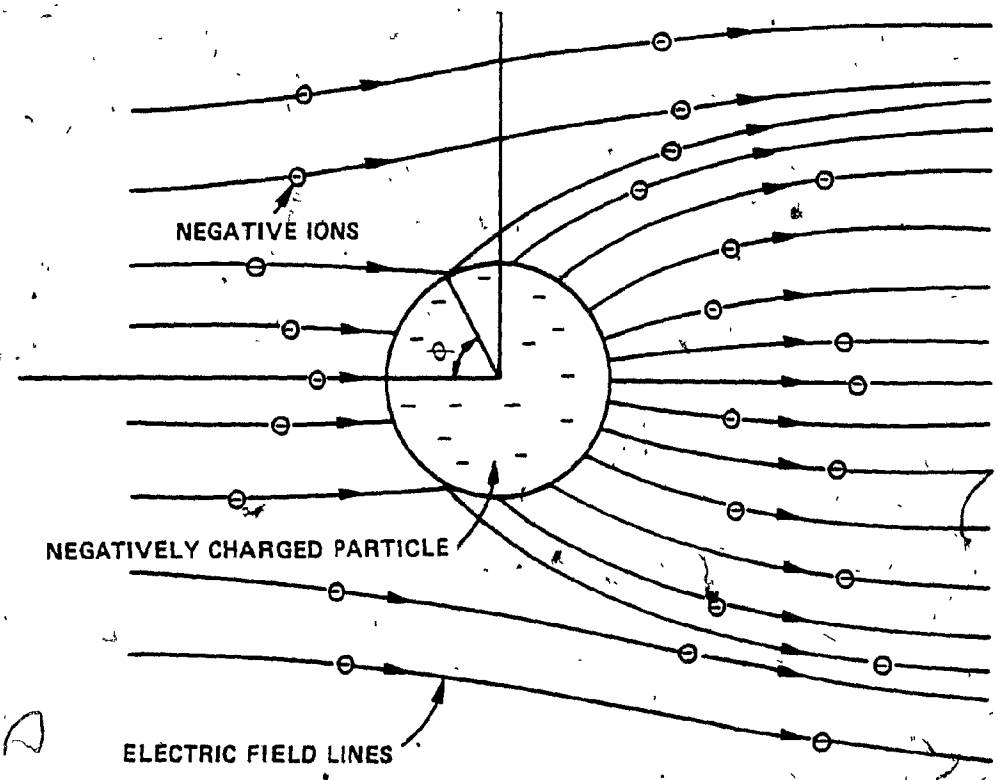


Figure 2.4 Electric field lines for partially charged particle in electric field, McDonald et al. (1978)

probably only approximated by conducting particles, where the particle surface is equipotential. The total charging rate is given by Liu et al. (1968) as:

$$\frac{dQ}{dt} = \frac{N_o e b_i Q_s}{4\varepsilon_o}\left(1 - \frac{Q}{Q_s}\right)^2 + \frac{e\hat{v}\pi D^2 N_o\left(1 + \frac{Q}{Q_s}\right)}{8} \exp\left(\frac{-Qe}{2\pi\varepsilon_o DkT}\right)$$

$$+ \frac{e\hat{v}\pi D^2 N_o}{4} \exp\{(V_s - V_o)/kT\} \qquad (2.27)$$

where (V_o) and (V_s) are respectively the undisturbed potential (at some distance (r_o) from the particle center) and the potential at the particle surface. The critical distance is determined from:

$$E_{av}\left\{1 + 2\,\frac{K-1}{K+2}\left(\frac{D}{2r_o}\right)^3\right\} = \frac{Q}{4\pi\varepsilon_o r_o^2} \qquad (2.28)$$

which is the condition of a vanishing radial electric field along a zero angle of approach of the incoming ions relative to the undisturbed (E_{av}) field. The vanishing of the radial field at the particle surface determines the critical angle for saturation charging (necessary for obtaining the ratio Q/Q_s in Eq. 2.27).

After the critical distance (r_o) is determined, the undisturbed potential is found by:

$$V_o = \frac{Q}{4\pi\varepsilon_o r_o} + E_{av}\left\{r_o - \left(\frac{D^3}{8r_o^2}\right)\left(\frac{K-1}{K+2}\right)\right\} \qquad (2.29)$$

which is simply the potential distribution at a distance (r_o) from a charged particle of diameter (D), with instantaneous

charge (Q), along a zero angle of approach of the incoming ions relative to the undistorted field. The potential at the particle surface (V_s) in Eq. 2.27 is also determined by Eq. 2.29, allowing $r_o = D/2$.

Equation 2.27 must be numerically integrated, and it agrees well with the experimental data of Hewitt (1957) and Smith et al. (1978) only if the assumption is made that average thermal ion velocities are of order 118 ms^{-1}, which corresponds to ion clusters of around 15 O_2 molecules, and if the ionic mobility is around $1.1x10^{-4}$ $m^2V^{-1}s^{-1}$, which is the experimental value determined by Liu et al. (1967). As pointed out by Smith et al. (1976), these values are unlikely to be representative of conditions encountered in ESP's. If higher values of mobilities and thermal velocities are used, then the integration of Eq. 2.27 produces charges which are much larger than those found experimentally.

Smith et al. (1975,1976) followed a somewhat similar approach to Liu et al. (1968), but with two important differences. The particle surface is divided into three main regions, with distinct charging mechanisms in each. These regions are chosen by mathematical necessity for solving the potential equations outside the particle surface. In the particle surface defined below the critical value for saturation charging, field charging is the only charging mechanism. Beyond this critical angle, defined by the vanishing of the radial field at the particle surface, and until an angle of approach of the incoming ions relative to the undistorted field equal to 90^o, both field and

diffusion charging occur. Here, the potential at the particle surface is also related to the undisturbed potential at some finite distance from the particle (r_o), but unlike Liu et al. (1968), Smith and McDonald do not consider any restriction on the angle of approach of the incoming ions, i.e. (r_o) is defined by the vanishing of the radial field at all angles, by:

$$E_{av}\{1 + 2\frac{K-1}{K+2}(\frac{D}{2r_o})^3\}\cos\theta = \frac{Q}{4\pi\varepsilon_o r_o^2} \qquad (2.29)$$

where (θ) is the angle of approach of the incoming ions relative to the undistorted field (Fig. 2.4).

In the third charging region, beyond $\theta = \pi/2$, the self-field from the particle and the external field are in the same direction, and there is no finite value (r_o) for which the radial field vanishes. Here, the effect of the applied field is ignored, and the classical diffusion charging equation applies. The total charging rate is given by:

$$\frac{dQ}{dt} = (\frac{Q_s e N_o b_i}{4\varepsilon_o})(1 - \frac{Q}{Q_s})^2 + \frac{e\pi D^2 N_o \hat{v}}{8}\int_{\theta_o}^{\pi/2} \exp\{\frac{Qe(r_o - D/2)}{2\pi\varepsilon_o D r_o kT} + \frac{\{3(D/2)r_o^2 - r_o^3(K+2) + (D^3/8)(K-1)\}}{kTr_o^2(K+2)} eE_{av}\cos\theta\}\sin\theta\, d\theta + \frac{D^2\hat{v}eN_o\pi}{8}\exp(\frac{-Qe}{2\pi\varepsilon_o DkT}) \qquad .....(2.30)$$

where (θ_o) is the limiting angle for field charging, given by:

$$\cos\theta_o = Q/Q_s \qquad (2.31)$$

Equation 2.30 must also be numerically integrated, and details are given in McDonald (1978a), Oglesby et al. (1978) and Smith et al. (1975,1976). The agreement of Eq. 2.30 with the experimental data of Hewitt (1957), McDonald et al. (1980a), Smith et al. (1978) and Van Bush et al. (1980) is good, using commonly accepted values of ion mobilities and thermal velocities.

Recently, Liu et al. (1977,1978) succeeded in solving numerically the diffusion equation in the presence of an electric field, where the assumptions of a steady-state continuous charging process were made. Despite the fact that the charging process under typical ESP conditions may not be considered a continuous process, the solutions of Liu et al. (1977,1978) agree well with the experimental data of Hewitt (1957) and Smith et al. (1978), using commonly accepted values of ion mobilities and thermal velocities. This solution has one serious drawback: it requires a large expenditure of computing time.

When the effect of electric field on the ion distribution is neglected, the appropriate equations are the classical field and diffusion charging equations, and the total charging rate is given by summing the charging rates given by Eqs. 2.20 and 2.24, which is an equation with no analytical solution.

2.4.4 Comparison with Experimental Data

Experimental results on particle charging are available from Hewitt (1957), Higneft (1967), Liu et al. (1967,1977), McDonald et al. (1980a), Penney et al. (1957), Smith et al. (1978), Van Bush et al. (1980) and White (1951,1963), among others.

General conclusions are as follows:

- charging of large particles ($D > 1$ μm) at moderate or high fields is well described by classical field charging theory;
- charging in the absence of an exterior electric field (or with a low field) is well described by classical diffusion theory;
- where both charging mechanisms occur, diffusion is enhanced by an external applied field. This is important for all particle sizes in the intermediate range ($0.2 < D \lesssim 1$-2 μm) or even for smaller particles ($D \sim 0.1$ μm) at high fields;
- highly abnormal charges may be encountered if the particles are charged near the corona wires, or if the free electron component of current is important;
- in the absence of abnormal charging conditions, and for turbulent gas flow, the average field in the interelectrode spacing is adequate in representing the charging field strength. The charging time is also adequately represented by the effective ESP length divided by the average gas velocity.

With the exception of the experimental data of McDonald et al. (1980a) and Van Bush et al. (1980), individual particle charges have always been determined in very small precipitators, typically with cylindrical geometry with internal diameters of only 5-7.6 cm. With such small dimensions and negative corona, the free electron component of current may be important, and

higher charges than those predicted by ionic theories are found. With positive corona under similar conditions, ionic theories agree well with experimental data.

Figure 2.5(a,b,c,d) shows the experimental data of Hewitt (1957), for positive corona, as compared with the theories of Liu et al. (1968) and Smith et al.(1975, 1976), taken from Smith et al.(1975). Also shown in this figure is the value of charge computed by simply adding the charges acquired by the separate mechanisms of field and diffusion charging, i.e. by:

$$Q = Q_s\left(\frac{t}{t+\tau}\right) + \frac{2\pi\varepsilon_o DkT}{e}\ln\left(1 + \frac{D\hat{V}N_o e^2 t}{8\varepsilon_o kT}\right) \qquad (2.32)$$

In Fig. 2.5, the ionic mobility was taken as 2.2×10^{-4} $m^2V^{-1}s^{-1}$, and slightly different results are obtained if other values of mobility are chosen.

The agreement between Eq. 2.32 and the experimental data may be fortuitous, but it also occurs with the data of McDonald et al. (1980a), Penney et al. (1978) and Smith et al. (1978), in the absence of a free electron component of current. As stated by McDonald (1978a), calculating the charge by the sum of field and diffusion charges gives reasonable estimates between about 0.09-1.4 μm diameter. As is seen in Fig. 2.5, the agreement is very good above about 0.5 μm diameter.

Smith et al. (1978) measured the charge acquired by small particles ($0.019 < D < 7$ μm) of different dielectric constants, and the agreement with Eq. 2.32 is also satisfactory.

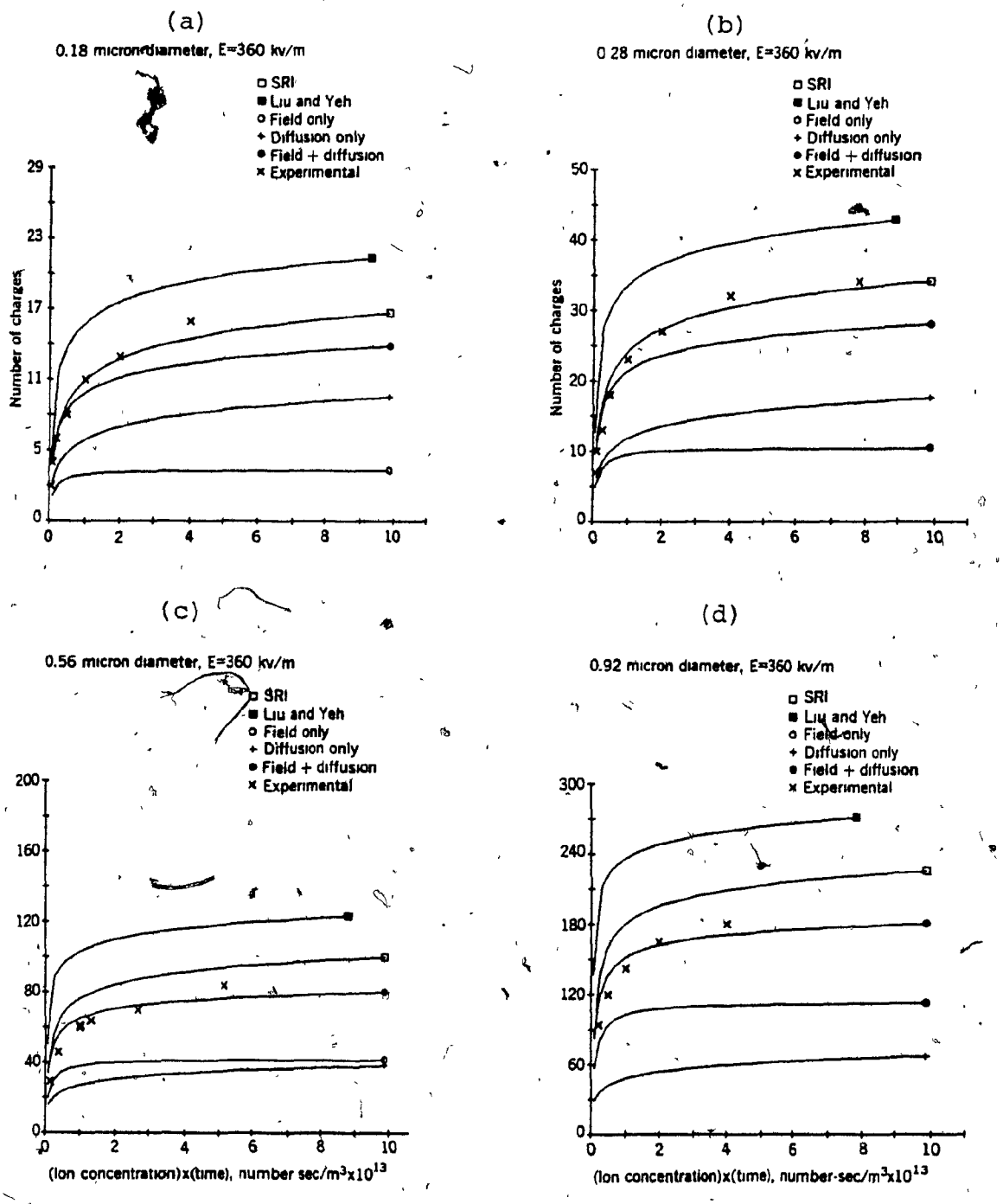


Figure 2.5, a, b, c, d

Comparison of charging theories with the experimental results of Hewitt (1957), in Smith et al. (1975)

Of special importance to precipitation is the measurement of charges acquired by particles under actual precipitating conditions, i.e. with particle chargers representative of industrial geometry (mainly the parallel-type ESP) and size (typically wire-to-plate spacings between 7.6-15.2 cm). Such results are given by McDonald et al. (1980a) for laboratory-scale ESP's with a wire-to-plate spacing of 12.7 cm, and by Van Bush et al. (1980) for a pilot-plant ESP. For the laboratory-scale ESP's, McDonald et al. (1980a) give results for particle diameters between about 0.6-3 μm, at both positive and negative coronas, at various field strengths and current densities and at ambient and above-ambient temperatures. The important conclusion was reached that both positive and negative coronas produce similar charges at ambient temperature, but negative coronas give much higher charges than positive coronas at higher temperatures. The effect is attributed to the increased free electron component of current at reduced densities. The good agreement obtained between both polarities at ambient temperature and the theory of Smith et al. (1975, 1976) is an indication that the electron component of current is negligible for plate-to-plate spacings which are typical of industrial geometries, at ambient temperature. Good agreement is also obtained with the Smith and McDonald ionic charging theory and the experimental results of positive corona, at elevated temperatures.

Figure 2.6 shows the comparison of some experimental values of charges with the theoretical values of Eq. 2.30 and Eq. 2.32. Both the experimental values and the theoretical values given by Eq. 2.30 are taken from McDonald et al. (1980a), for a laboratory-scale ESP operating at ambient temperature and negative corona, for dioctylphthalate (DOP) aerosol. For the use of Eq. 2.32, an ion mobility of 1.6×10^{-4} $m^2 V^{-1} s^{-1}$ and thermal velocity of 500 ms^{-1} were used. These are the values used by Smith et al. (1976) for comparison of their ionic charging theory with the data of Hewitt (1957). The relative dielectric constant for DOP is equal to 5.1 according to Hewitt (1957), Liu et al. (1968) and Smith et al. (1978), and it is equal to 7.2 according to Liu et al. (1967) and Murphy et al. (1959). For this difference in dielectric constant the effect is small, as can be seen from Fig. 2.6.

The theory of Smith et al. (1975,1976) gives slightly better prediction, on the average, than the simple solution of Eq. 2.32, but the difference is small, and probably within the measurement error of the charge. Similar agreement between experimental data and either Eq. 2.30 or 2.32 as seen in Fig. 2.6 is obtained with the data of McDonald et al. (1980a) for other electric field strengths ($2.7\text{-}3.0 \times 10^5$ Vm^{-1}) and product $N_o t$ ($0.5\text{-}1.1 \times 10^{14}$ $m^{-3} s$), with negative corona at ambient temperature.

The error bars in Fig. 2.6 are an indication of the experimental error involved. Liu et al. (1977,1978) and Smith et al. (1976) give an estimation of the experimental error

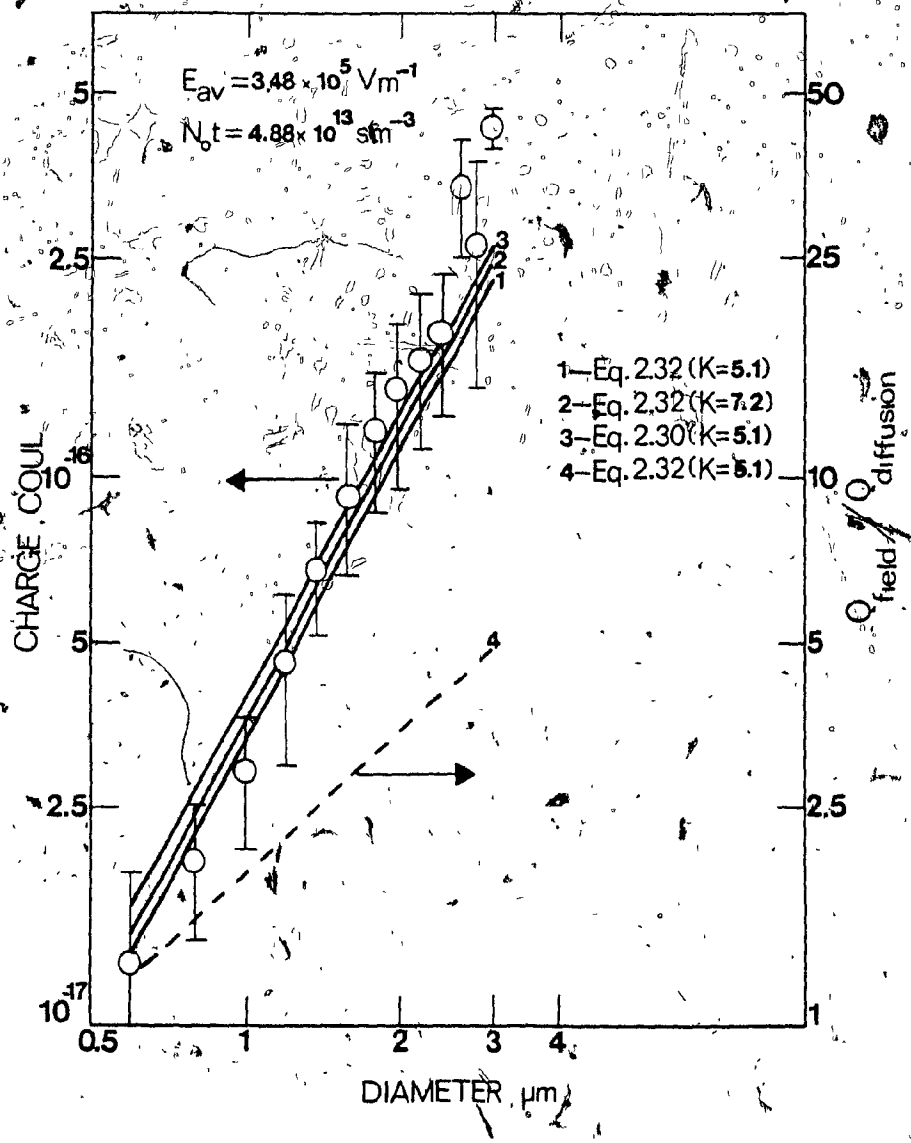


Figure 2.6 Comparison of charging theories (Eqs. 2.30 and 2.32) with the experimental data of McDonald et al. (1980 a)

involved in the data of Hewitt (1957) to be 15 to 20%. As a conclusion, it may then be said that existing theories of particle charging applicable to particle sizes normally encountered in ESP's ($0.1 < D < 100$ μm) predict charges which are within the uncertainty of the experimental data. For the present work, the simple approximate solution given by adding the classical field and diffusion charges (Eq. 2.32) was used.

2.5 Particle Collection

2.5.1 Introduction

The formation of a corona generates ions which charge the dust particles. If the charged particles are subjected to an electric field, a drift or migration towards the passive (collection) electrode occurs. Most industrial ESP's are single-stage units, where the electric field for charging is the same as the precipitating field. In two-stage units, used mainly for cleaning of ventilation air, the precipitating field is an electrostatic field maintained between a pair of non-discharging electrodes.

In industrial ESP's, the flow is always turbulent. There are two main schools of thought relative to the motion of fine particles in ESP's. According to Gensler (1968), Oglesby et al. (1970,1978), Robinson (1968a,1971) and White (1963), for particles with diameters less than about 10-20 μm, the turbulent motion of the gas stream predominates over the electric drift of the particle, i.e., the individual trajectories are highly random in both velocity and direction. Data for size

distributions of typical industrial dispersoids collected by ESP's is given by Reynolds et al. (1975) and by Theodore et al. (1976), and on the average, about 70-80% by weight is below 10-20 μm. Thus, for typical applications of precipitators, turbulence in the gas stream is probably predominant in determining particle motion. This was experimentally confirmed with 5-10 μm alumina particles by Gensler (1968), and with 55% by weight of fly ash particles below 10 μm by Robinson (1968a). The level of turbulence did have a significant effect on the characteristics of the particle trajectories, with decreasing turbulence decreasing the randomness of the particles' trajectories. By statistical analysis, Gensler concluded that, on the average, the particles took on a definite movement towards the collection plate when corona conditions were imposed, and that the velocity fluctuations of the particles were isotropic. The isotropicity was unaffected by corona conditions.

For particles larger than about 10-20 μm, the trajectories are probably deterministic, and an appropriate model of precipitator performance was developed by Reynolds et al. (1975) and Theodore et al. (1973). This model, known as the "Theodore Model", relies on statistical techniques to describe the average behaviour of many particles, i.e., only on the average are the trajectories deterministic. A completely deterministic model, which describes the trajectories of individual particles was developed by Stock et al. (1977) for cylindrical ESP's.

The prediction of particle collection in ESP's is difficult due to a number of reasons, among them:

- the effect of electric wind, briefly discussed in Section 2.2.1;
- the presence of particle concentration gradients, as observed by Dinneli et al. (1979), Gooch et al. (1976a,1976b), Pyle et al. (1980), Robinson (1968b) and Ross (1980). These concentration gradients are both in the longitudinal and traverse direction, relative to the main gas flow.
- the presence of various deleterious effects on ESP performance, such as poor gas flow distribution, particle reentrainment and back-corona. These are discussed by Burton et al. (1975), McDonald (1978a), Oglesby et al. (1970,1975,1978) and White (1963, 1977a,1977b).

Various attempts have been made to account for these phenomena, notably the works of Cooperman (1971), Feldman et al. (1977) and Robinson (1967b), but according to Oglesby et al. (1978), these theories have never been experimentally validated. For instance, Cooperman assumes that the dust concentration near the collection plates is larger than at the ESP core, and the experimental data of Dinneli et al. (1979) and Gooch et al. (1976a,1976b) confirm this hypothesis. On the other hand, Pyle (1980) measured particle diffusivities for particle diameters between 1-5 μm, which are about two to three orders of magnitude smaller than the values assumed by Cooperman (1971).

Pyle (1980) and Robinson (1968b) also found the effect of corona polarity to be of importance in determining the concentration profiles, and Gooch et al. (1976a, 1976b) found the plate-to-plate spacing, particle size and operating characteristics of voltage-current to be also important. White (1963, 1977c) gives a method of modelling the effect of non-uniform gas flow distribution, if experimental data exist on the velocity distribution at the ESP inlet, but the same cannot be said of reentrainment effects caused either by poor flow distribution, low particle adhesion to the collection plates or high air velocities. In such cases, either empirically determined correction factors or extremely simplified models, which may not be realistic, are used.

2.5.2 Theoretical Migration Velocity

This is the terminal velocity that charged particles attain towards the collection plates. To derive a theoretical expression for this velocity, the following assumptions are made:

- the fluid is quiescent;
- invariant particle charge;
- negligible added mass, rotation and history effects;
- negligible gravity and buoyancy effects;
- small $Re_p = \frac{\rho D W}{\mu}$, such that Stokes regime applies. Here, (Re_p) is Reynolds number of particle, (D) is particle diameter, (w) is particle velocity relative to the stationary fluid, and (ρ) and (μ) are the fluid density and viscosity.

- the particles are spherical.

With the above assumptions, the following equation is derived:

$$m \frac{dw}{dt} = QE - 3\pi\mu Dw/C \qquad (2.33)$$

where (m) is particle mass and (C) is Cunningham correction factor, which arises from the fact that small particles show molecular slip, i.e. the drag force is lower than given by Stokes' law. In Eq. 2.33, the inertia force ($m \frac{dw}{dt}$) and the drag force ($3\pi\mu Dw/C$) are balanced against the electrical force (QE). The derivation of Eq. 2.33 is given by Oglesby et al. (1970, 1978) and White (1963). According to Crawford (1976) and White (1963), the Cunningham factor should be used for particle diameters below 1 μm.

The Cunningham factor is given by McDonald (1978a) and by Theodore et al. (1976) as:

$$C = 1 + \frac{2\lambda}{D} \{1.26 + 0.4 \exp(-0.55 \frac{D}{\lambda})\} \qquad (2.34)$$

where (λ) is molecular mean free path, given by Smith et al. (1977) as:

$$\lambda = \frac{2\mu}{1.01 \times 10^7 P} \left(\frac{8.3 \times 10^7 T}{3 M_{air}}\right)^{1/2} \qquad (2.35)$$

where λ(m), μ(Kg $m^{-1}s^{-1}$), T(K), P(atm) and (M_{air}) is molecular weight of air.

Eq. 2.33 integrates into:

$$w = \frac{CQE}{3\pi\mu D}\left\{1 - \exp\left(-\frac{3\pi\mu D}{Cm} \cdot t\right)\right\} \qquad (2.36)$$

where the term $(\frac{Cm}{3\pi\mu D})$ is the time constant of the motion (τ_m). The velocity (w) reaches about 99% of its terminal value within five time constants, and this is usually a very short time as compared to the residence time of the particles in the gas stream. For instance, Oglesby et al. (1978) show that below D = 80 μm and for unit density spheres, the terminal velocity is reached in less than about 0.1 s. Oglesby et al. (1975) consider the inertia forces to be negligible for particles up to about 100 μm in diameter, and this is equivalent to dropping the exponential term in Eq. 2.36. Then:

$$w \simeq \frac{CQE}{3\pi\mu D} \qquad (2.37)$$

Strictly speaking, Stokes' law applies only for a zero particle Reynolds number, but Corn (1966), Theodore et al. (1976) and White (1963) consider that for practical purposes this range may be extended up to one or two, without any significant error. Lowe et al. (1953) compare the theoretical migration velocities at various field strengths, for different particle sizes, using both Stokes' law and experimental values of drag force. For $Re_p < 0.5$, Stokes' law is acceptable up to about 30 μm diameter at very high fields and up to about 50 μm at low fields.

This means that in general the consequences of using Stokes' law in electrostatic precipitation theory are slight, because:

- the majority of industrial dispersoids treated by ESP's have a large proportion of their mass below about 10-20 μm diameter;
- even for short ESP's operating at high air velocities, the theoretical collection efficiencies of particles with diameters above about 10 μm are very large, and almost unaffected whether the migration velocity is calculated based on Stokes' law or on a more appropriate expression for the drag force.

The assumption of invariant charge used for the derivation of Eq. 2.36 may be relaxed, by allowing field charging to be the only charging mechanism present, i.e., for size distributions with a negligible submicron size fraction. In this case, the charge (Q) in Eq. 2.33 is substituted by its value given by Eq. 2.22, and integration gives:

$$w = w_o \frac{t}{t + \tau} \qquad (2.38)$$

where (w_o) is the saturation migration velocity, given by:

$$w_o = \frac{CEQ_s}{3\pi\mu D} \qquad (2.39)$$

If the charging time constant may be ignored, $w = w_o$.

2.5.3 Collection Efficiency Equation

In Section 2.5.1, some of the problems facing the derivation of a realistic collection efficiency equation were discussed. Due to the complexity involved, Oglesby et al. (1970,1975,1978) and White (1963) made the following assumptions:

- turbulence causes the particles to be uniformly distributed in any cross-section;
- the gas velocity is uniform except for a boundary layer near the wall;
- particle motion in the laminar boundary-layer at the collection plates is governed by Stokesian flow;
- there are no multiparticle effects;
- the particles are all spheres of uniform size;
- the effect of collisions between ions and gas molecules (electric wind) can be ignored;
- there are no disturbing effects such as erosion or reentrainment, uneven gas flow or back corona.

The probability of particle collection is the probability that the particle enters the laminar layer near the wall, such that in an interval Δt, it travels $w\Delta t$ in the traverse direction and $v_{av}\Delta t$ in the longitudinal (gas flow) direction. The probability concept of particle collection was applied to ESP's by White (1963) and it is only meaningful when applied to a large number of particles, since the efficiency of collection for a single particle is either zero or 100%. The probability of collection is then the ratio of number of particles at the boundary-layer to overall number of particles. With the assumption of

uniform interelectrode concentration at any cross-section, the probability of collection is given by the ratio of boundary-layer thickness to the interelectrode spacing. Then:

$$\eta = 1 - \exp\left(-\frac{w_o L}{v_{av} s}\right) \qquad (2.40)$$

which is the Deutsch-Anderson collection equation. In Eq. 2.40, (η) is collection efficiency of ESP with length (L), (v_{av}) is the average gas velocity and (s) is wire-to-plate spacing.

The assumption of uniform dust concentration in any cross section may be relaxed, and Oglesby et al. (1970,1978) give a similar expression taking this factor into account. No experimental confirmation of the modified collection efficiency is available, however.

An implicit assumption for the derivation of Eq. 2.40 is that the charge on the particles does not vary during the collection process. This restricts the applicability of the Deutsch Equation, as such, to particles which enter the ESP with invariant charge, i.e., with saturation charge. Thus, the Deutsch Equation is strictly applicable only to particles which do not gain charge by ion diffusion, and for conditions where the charging time constant can be neglected. Because the charging rate by ion diffusion decreases rapidly with charging time, and as full-size ESP's usually operate at low velocities and high fields, these restrictions are of little significance for typical industrial precipitators. For smaller units, operating at high air velocities and/or low field strengths, considerable errors

might occur by the application of Eq. 2.40 where the theoretical migration velocity is based on saturation charge.

To avoid this shortcoming, Robinson (1961) rederived the Deutsch Equation allowing for the effect of charging time when field charging is the only charging mechanism present. Then:

$$\eta = 1 - \left(\frac{L+v_{av}\tau}{v_{av}\tau}\right)^{w_o\tau/s} \cdot \exp\left(-\frac{w_o L}{v_{av} s}\right) \qquad (2.41)$$

where (w_o) is given by Eq. 2.39, and (τ) is charging time constant, given by Eq. 2.23. Robinson's Equation reduces to the Deutsch Equation when $\tau \to 0$.

In the more general case, where both field and diffusion charging might be important, the Deutsch Equation can still be used provided it is applied to short precipitation segments, where the actual charge may be considered to be constant. This is the approach followed by Southern Research Institute (SRI) of Alabama, U.S.A., in their computer program of ESP performance. This is discussed in detail in Section 2.8, and it has the advantage of including the effect of charging time, irrespective of what particular charging theory is actually used.

Because the assumption was made that collection takes place only for particles which are near the laminar boundary layer at the plates, the appropriate electric field strength for particle collection is the electric field at the plate, which may be estimated by the methods outlined in Section 2.3.3.

The application of the previous equations of collection efficiency is restricted to a single particle size, because the

charge and hence the migration velocity is a function of particle size. Real dispersoids are rarely monodisperse, and this problem may be overcome by applying the collection equations to narrow size fractions, where a single mean size is attributed to each size interval. The global efficiency is then a weighted average of the fractional collection efficiencies (i.e., for each particle size), taking into account the complete size distribution.

If this theoretically derived collection efficiency is substituted into a Deutsch-type efficiency equation, then the parameter (w), backcalculated from the efficiency equation is called the precipitation rate parameter. The theoretical (w) for each particle size is called a (theoretical) fractional migration velocity. So, the prefix fractional relates to a particular particle size. This nomenclature will be further expanded in Section 2.8.

Because of the many simplifying assumptions underlying the Deutsch Equation (or a similar form), only in special situations is the collection efficiency described by such a simple relation. This happens in precipitators where good control is achieved over flow and electrical conditions, and where non-ideal effects such as particle reentrainment are absent. This was experimentally verified by Little (1956) for a pilot-plant ESP, and by Lakey et al. (1955), Pui et al. (1977), Robinson (1961) and White (1963) for laboratory-scale ESP's.

In general (and probably invariably in full-size ESP's), many non-ideal effects may occur, such as concentration gradients, charging near corona wires, non-uniform gas flow, particle reentrainment, anomalous electrical characteristics and great variability over short periods of time in inlet conditions of dust loading, gas temperature and gas flow rate. Then, it is common practice (especially for industrial units) to fit the experimentally measured collection efficiency to a Deutsch-type equation, and determine the parameter (w) from the fitting procedure. This gives rise to the so-called experimental precipitation rate parameter, which bears no connection to the theoretical migration velocity. The disadvantages of this method are that the physical principles of the collection mechanism are lost, and that the quantitative conclusions are specific to a certain ESP operating under a limited range of conditions.

The theoretical migration velocity is independent of the average gas velocity (neglecting the effect of charging time), but Oglesby et al. (1970,1974,1975,1978) and White (1963) report that the effective migration velocity and the precipitation rate parameter increase with average gas velocity, unless reentrainment occurs. Various hypotheses are put forward as to what is the cause, by Cooperman (1971), Oglesby et al. (1974,1975), Robinson (1971), Strauss (1966) and White (1977b), ranging from increased turbulence at higher velocities which brings the particles nearer the discharge wires, to the fact that the Deutsch Equation neglects

longitudinal and transverse diffusion. Oglesby et al. (1974, 1975) and White (1977b) attribute the effect to the polidispersity of real dispersoids, such that an increase in effective migration velocity is actually to be expected when applying the Deutsch Equation to a polydisperse system. An example is given by Oglesby et al. (1975).

One variable which was not considered in the theory is the mechanical collection of the ESP, i.e., the collection efficiency without corona power. Gravitational forces acting on the particles cause the larger and denser particles to collect at the ESP bottom (on collection hoppers), i.e., the ESP behaves as a settling chamber. Under these conditions, Potter (1978) expresses the total collection as:

$$\eta_t = \eta' + \eta'_m \qquad (2.42)$$

where (η'_m) is the mechanical contribution to the total collection (η_t). Lagarias (1963) and Potter (1978) give values for (η'_m) of the order of 20-60% in full-size ESP's.

An alternative for determining the electrical collection (η') in the presence of mechanical collection (η'_m) is to correct the inlet stream taking into account the mechanical collection. This was done by Brown et al. (1971) and Pui et al. (1977), where:

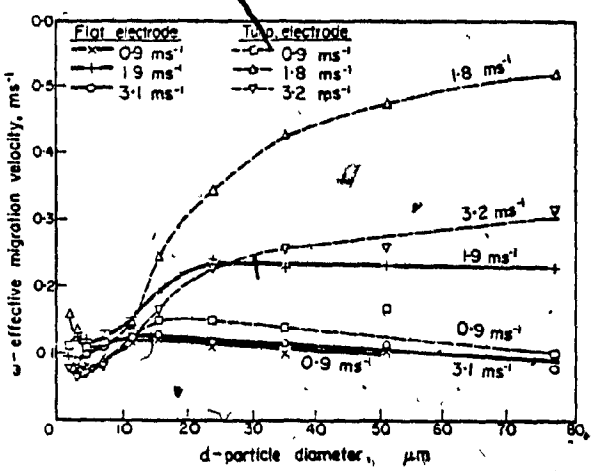
$$\eta = \frac{\eta'}{1 - \eta'_m} \geq \eta' \qquad (2.43)$$

It is interesting to see that the efficiency equations do not depend explicitly on particle concentration at the ESP inlet, and unless space-charge supression or excessive re-entrainment occur, ESP efficiency is essentially independent of inlet concentration over a wide range. This was shown by Dinneli et al. (1979) and White (1963).

It is important to examine some experimental data on collection efficiency (or related variables, as migration velocities) of ESP's. The majority of data pertaining to precipitators, which have been published, deal mainly with global efficiencies and their variation with operating precipitator parameters, such as specific collection area (ratio of total collection area of ESP to volumetric gas flow rate = $L/v_{av}s$) and corona power. Very little data are available on fractional migration velocities or on migration velocities as function of ESP length. Also, collection efficiencies as function of ESP length are rare in the literature.

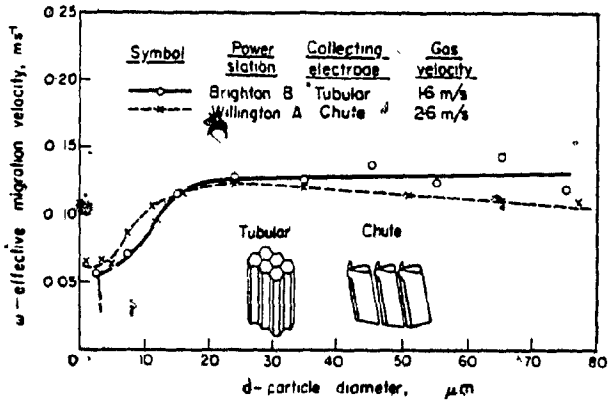
Figure 2.7, taken from Strauss(1966), shows migration vecities for a pilot-plant ESP connected to a pulverized fuel fired boiler. Figure 2.8, taken from the same author , shows similar results for two full-size ESP's operating at different power stations. Figure 2.9, from Heinrich (1961), is for full-size ESP's, connected to power boilers, cement kilns and catalyst cracking processes. Also shown in this figure is the theoretical saturation fractional migration velocity. The different trends displayed by the different curves is remarkable. In some, the

Figure 2.7

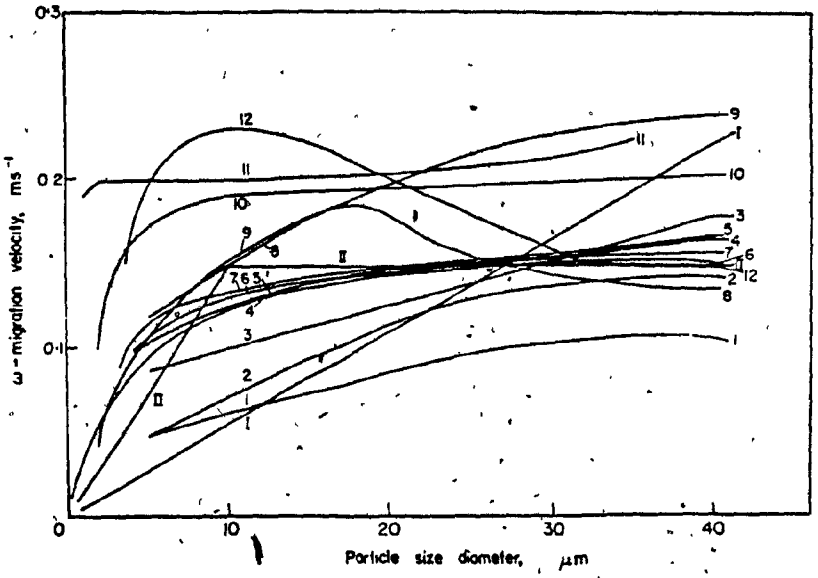


Relation between effective migration velocity and particle diameter for different gas velocities with flat and tulip electrodes in a pilot plant, in Strauss (1966)

Figure 2.8



Relation between effective migration velocity and particle diameter with tubular and chute electrodes in commercial sized plant, in Strauss (1966)



I Theoretical curve
II Assumed average curve for average conditions.

1, 2, 3 = boiler flue dust precipitator.
4 = catalyst dust precipitator.
5 = cement kiln dust precipitator.
6 = boiler flue dust precipitator.
7 = boiler flue dust precipitator.
8 = boiler flue dust precipitator (vertical).
9, 10 = boiler flue dust precipitator.
11 = coal dust precipitator.
12 = boiler flue dust precipitator (vertical).

Figure 2.9 Effective migration velocities as a function of particle size for boiler flue dust, catalyst dust, cement dust and coal dust, Henrich (1961)

migration velocity increases with particle size both above and below about 5 μm (Figs. 2.7 and 2.8), or it may remain constant or even decrease above about 10 μm, depending on the air velocity. In others (Fig. 2.9) the migration velocity increases continually with particle size, or it reaches a maximum at about 10 μm diameter and then either stays constant or decreases.

The experimental values of migration velocity tend to be larger than the theoretical values for fine particles, 15 μm being the critical size quoted by Strauss (1966), and smaller for the larger particles. The same phenomenon has been observed in laboratory-scale ESP's by Gooch et al. (1976a,1976b), and McDonald (1978a) quotes a critical diameter of about 5 μm below which migration velocities are larger than theory predicts. Field data obtained by McDonald et al. (1978) for ESP's treating fumes from copper and aluminium smelters show collection efficiencies larger than theoretical predictions below about 1 μm diameter, while above this size the reverse occurs.

The discrepancy between the experimental and theoretical migration velocities is attributed by Gooch et al. (1976a,1976b), Heinrich (1961), McDonald (1978a), McDonald et al. (1978), Robinson (1971) and Strauss (1966) to the fact that:

- diffusion is neglected in the Deutsch Equation, which should be more important for the finer particles;
- turbulence may cause the finer particles to be carried near the corona wires, with the consequence that the charging field may be much larger than the

average field in the interelectrode spacing (E_{av}). In this case, the charging field might be better approximated by the field intensity near the corona wires, given by Eq. 2.6 (Robinson, 1971); and

- non-ideal effects, as particle reentrainment, particle agglomeration and electric wind.

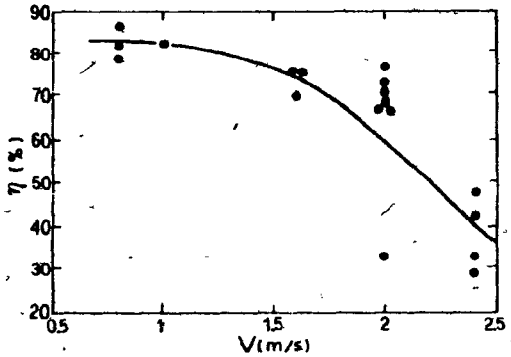
It is possible that in an actual situation of collection of dry particles by ESP's, all of these factors are involved to some degree, and no theory presently exists which adequately takes them into account.

Figure 2.10, from Dinneli et al. (1979), shows the experimental collection efficiencies as a function of air velocity, for a pilot plant ESP collecting a low resistivity fuel oil ash (MMD ≈ 50 μm). It is seen that there is a steep decrease in collection efficiency with air velocity, and very low collection efficiencies were obtained for velocities above 2 ms^{-1}.

Figure 2.11 shows collection profiles along the ESP length, as a function of air velocity, for the same dust-ESP system.

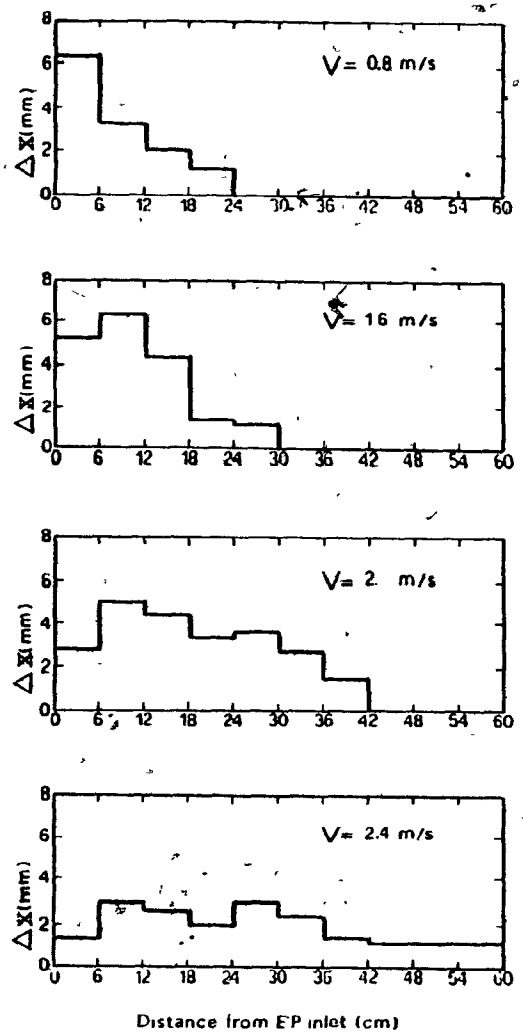
Since larger particles are preferentially collected near the ESP inlet and the airborne dust concentration decreases downstream, a decrease in migration velocity with ESP length should be expected. This has been reported by Dinneli et al. (1979) for dry collection up to 1 ms^{-1} and by Robinson (1971) for wet collection (oil mist) up to 8 ms^{-1}.

Figure 2.10



Collection efficiency against air velocity (2s = 25 cm), Dinelli et al. (1979)

Figure 2.11



Thickness of the collected dust layers as a function of the air velocity (2s = 25 cm; C = 500 mg m^{-3}; t = 90 min), Dinelli et al. (1979)

Recent studies by Ross (1980) show that the experimental migration velocity varies also with transverse position in the interelectrode spacing, from a minimum near the high tension electrode to a maximum near the collection plates, which is attributed by Ross (1980) to the existence of transverse concentration gradients.

2.6 Dust Resistivity

The dust layer precipitated on the ESP plates constitutes both a resistance path to the current flow and a capacitance due to its dielectric properties. The current flow establishes a potential drop across the dust layer, due to its finite conductivity. The bulk resistivity of a powdered material is (Lakey et al. (1955), Waye (1967)) the resistance of a unit volume of the material, including pore space, and has units Ohmm.

Sproull et al. (1951) derived a theoretical expression for the voltage drop across the dust layer, when electrical equilibrium is attained, as:

$$\Delta V = rj\Delta x\{1 - \frac{t'}{t}(1-e^{-t/t'})\} \qquad (2.44)$$

where (j) is current density at the plate, (Δx) is dust thickness, (t) is time and (t') is the relaxation time of charge transfer from a dielectric, given by:

$$t' = K\varepsilon_o r \qquad (2.45)$$

where (K) is relative dielectric constant and (r) is bulk resistivity. The exponential term in Eq. 2.44 is negligible for a period of time exceeding about five t', which occurs with dust resistivities below about 10^{11} Ohmm, for most materials ($K < 10$) in a very short time (< 1 min). Also, if $r < 10^{11}$ Ohmm and for exposure times (to the corona current) of the order of 2-3 min, Eq. 2.44 reduces to:

$$\Delta V = jr\Delta x \qquad (2.46)$$

Since the precipitated dust layer in (dry) ESP's is exposed to the corona current for periods of time well above 3 min, and as dust resistivities are usually below 10^{11} Ohm m, the use of Eq. 2.46 is justified under most cases.

Resistivity influences collection efficiency in that the dust layer may reduce the voltage available for charging, trigger back corona and lead to reentrainment. Katz (1980), McLean (1976), Penney (1951), Penney et al. (1978) and White (1974) state that for dust resistivities above about 10^{9} Ohmm, the voltage drop across the deposited layers is large, and very high localized fields can be produced in the air gaps between particles, with possible gas (or particle) breakdown, a condition termed backcorona, which seriously affects ESP performance. The voltage drop across the dust layer is subtracted from the applied voltage, and the voltage available for charging is reduced.

Under these high resistivities, the voltage available in the interelectrode spacing is usually not high enough to sustain sparking. The condition of back-corona produces positive ions (for a negative corona) which adversely affects the charging process. Bakke (1975), Bogatyrev (1974), Lakey et al. (1955) and White (1963) report a lower critical value for dust resistivity of about 10^8 Ohmm, above which back-corona is likely to occur, while Potter (1978) and Van Bush et al. (1980) found the critical value to be between 10^9 and 10^{10} Ohmm.

The lower side of bulk resistivities also causes problems in ESP's, namely low dust adhesion or even repulsion of the dust layer into the gas stream (Section 2.7). Bakke (1975), Dalmon et al. (1971) and Katz (1980) consider dusts with resistivities below about 10^5 Ohmm to be prone to reentrainment, while Bogatyrev (1974) cites the critical value of 10^2 Ohmm.

Back-corona occurs when the localized high fields in the air gaps or in the particles' contact spots exceed the breakdown strength of the medium. An estimation of the critical resistivity can be done by Cooperman's method (in Robinson (1971)), which states that breakdown occurs when the time constant of the dust (Eq. 2.45) exceeds the relaxation time of charge transfer of the surrounding gas, proportional to the ratio of the electric field at the plate to the average current density at the plate. A different estimation is obtained by McDonald et al. (1980b), who have derived a simplified expression for the localized electric field in the air gap between particles, taking into account both polarization and space-charge effects in the dust layer. The

localized fields can greatly exceed the average field in the layer (Eq. 2.46), depending on dielectric constant and dust resistivity.

The critical resistivity for back-corona onset can also be experimentally estimated, using Eq. 2.46 and resistivity cells.

The bulk resistivity is due to the contribution of conduction mechanisms throughout the interior of the particles (volume resistivity) and throughout the particle surface (surface resistivity). McLean (1976) expresses the resistivity (r) as a parallel association of volume (r_v) and surface (r_s) resistivities. Then:

$$r = \frac{r_v r_s}{r_v + r_s} \qquad (2.47)$$

Conduction mechanisms throughout the interior of the particles may be either electronic or ionic. For fly ash, Bickelhaupt (1974,1980) found conduction to be ionic. Surface conduction mechanisms are ionic, and occur because of chemical or physical adsorption of electrolytic films or of moisture. Bickelhaupt (1975) studied surface conduction mechanisms in fly ash, as a function of ash chemical composition.

There are many variables that affect resistivity, besides chemical composition. These were investigated by Bickelhaupt (1974,1975), Lakey et al. (1955), McLean (1976), McLean et al. (1974), Oglesby et al. (1970,1978), Potter (1978), Spencer (1976a), Sproull et al. (1951) and White (1963,1974),

and include mode of compaction, humidity, temperature, particle size, electric field, chemical composition of flue gases and time of application of the electric field.

The volume resistivity may be expressed as:

$$r_v = A_v \exp(E_a/kT) \qquad (2.48)$$

where (E_a) is activation energy, (k) is Boltzmann constant and (A_v) is a parameter depending on the compaction and intrinsic properties of the material. Both (E_a) and (A_v) are experimentally determined, by measuring the resistivity as a function of temperature, at high temperatures, i.e., where surface conduction is unimportant.

McLean (1976) expresses the surface resistivity as:

$$r_s = A_s \exp\{-pB\exp(C/T)\} \qquad (2.49)$$

where (A_s) depends on the compaction and intrinsic properties of the material, (B,C) are empirical constants and (p) is partial pressure of adsorbant at temperature (T). If the adsorption is of chemical nature, then the partial pressure (p) should be replaced by ($p-p_o$), where (p_o) represents the partial pressure of adsorbant after all the low-binding energy (physically adsorbed) components have been removed. For moisture adsorption without chemical reaction, Eq. 2.49 applies. Experimental determination of (A_s,B,C) is possible using two sets of resistivity measurements at low enough temperature such that volume conduc-

tion is unimportant. White (1974) gives the value of approximately 360K below which surface conduction becomes important.

Both Eqs. 2.48 and 2.49 were experimentally verified. Although limited data are available on the validation of Eq. 2.49, experimental results obtained by McLean (1976) for fly ash agree closely with it.

An alternate semi-empirical expression for the resistivity due to the simultaneous contribution of volume and surface conduction is given by Ditl et al. (1976), and agreement with experimental data for fly ash is also satisfactory. The application of Eq. 2.49 requires less experimental data than the method of Ditl et al. (1976), and is easier to implement.

In Eqs. 2.48 or 2.49, no mention is made to the effect of the applied electric field. This was studied by McLean et al. (1974), who concluded that most of the voltage drop in an individual particle (which is part of a bulk arrangement of particles) occurs through the particles' contact points with the neighbouring particles. At these contact spots, very high fields are produced due to the high current densities. These high electric fields modify the electrical characteristics of the contacts, and the overall conductivity of the layer increases. This phenomenon is similar to the non-ohmic behaviour of corona fields, and the effective resistivity is:

$$r_{eff} = r \exp(-ZE_{av}) \qquad (2.50)$$

where (Z) is an empirical constant independent of the average field throughout the dust layer (E_{av}) and (r) is given by Eq. 2.47. The phenomenon of decreased resistivity at high fields makes it possible for ESP's to operate without back-corona with high resistivity dusts, if these high resistivities were measured at low fields. This is discussed by Potter (1978).

Methods of measuring dust resistivities are given in ASME Power Test Code 28 (1965), Lakey et al. (1955), Nichols (1974), Nichols et al. (1975), Oglesby et al. (1970,1978), Penney (1951), Sproull et al. (1951) and White (1956,1963,1974).

In order for resistivity measurements to be meaningful, the following should be specified:

- particle size distribution;
- mode of compaction (applied pressure, bulk density);
- chemical composition of particles and gas;
- temperature;
- humidity;
- applied field and current density; and
- time of exposure of the dust sample to the high voltage.

Of these factors, size distribution and mode of compaction are probably the least important. Other conditions being equal, Bickelhaupt (1974), McLean (1976), Spencer (1976a) and White (1956) found surface resistivity to decrease with particle size. This is attributed by McLean (1976) and White (1956) to the increase in the number of parallel paths for charge transfer (resistivity is proportional to the number of series paths per

unit depth and inversely proportional to the number of parallel paths per unit area), and by Bickelhaupt (1974) and Nichols (1974) to an increase in specific surface, which increases the adsorption capability of the layer.

Lakey et al. (1955) and McLean (1976) found that both volume and surface resistivities decrease with increase in bulk density, but the surface resistivity is less sensitive to pressure effects. Both particle size and pressure affect the measured resistivity by a factor of two to three.

Resistivity increases with the time of application of the high voltage (in measuring cells) relative to its value measured immediately after the applied voltage transients have subsided. McLean et al. (1974) found a multiplication factor of two to three, for a period of one minute. This is attributed to polarization effects at the electrodes, or to current absorption phenomena.

Chemical composition of both particles and gas (in the surface conduction mode), temperature, humidity and the applied field may produce variations in the measured resistivity by orders of magnitude, and so these should be clearly stated together with the measured resistivity value.

2.7 Dust Adhesion and Reentrainment

The term adhesion is considered here as referring to both interparticle as well as to particle-to-wall adhesion.

The various forces which act in an electrostatically deposited dust layer have been identified by Tassicker (1975)

as London-Van der Waal, triboelectric, capillary (surface tension), surface dipole (contact potential) and electric field-corona. A review of the theory of adhesion forces is given by Corn (1966), which states that "...it is not yet possible to accurately predict the forces of adhesion between a specified population of particles and a substrate." This difficulty arises from the numerous variables involved, such as particle size, porosity and compaction, dielectric constant, humidity, adsorbed surface dipolar molecules, work function interfaces [1], electric field and current density, particle shape and microscopic surface texture of particle and substrate. The importance of dust adhesion in ESP's is due to the highly deleterious effect of reentrainment in the collection efficiency, as well as to the difficulty in removing tenaciously adhering deposits.

Lakey et al. (1955), Oglesby et al. (1970,1974,1978), Penney (1975), Robinson (1967b,1971), Seman et al. (1967) and White (1963) attribute reentrainment to direct gas scouring at the plates and to impaction of airborne particles on previously precipitated dust. Other forms of dust reentrainment include dust pick-up from collection hoppers and rapping reentrainment. This last form of reentrainment occurs during the rapping periods, i.e., when clearing the collection plates by hammering or vibration, and was studied by Spencer (1976b,1976c).

The original studies on dust reentrainment of Bagnold (1954) were related to wind blown sand; a threshold wind velocity

---

[1] Work-function is the energy required to remove one electron at the Fermi level (energy of the free electron gas at 0 K), out of the solid to infinity (Inculet (1973)).

for reentrainment exists which, for particle diameters above about 100 μm, is proportional to the square root of the product of specific gravity and particle size. Below about 50-100 μm diameter, the threshold velocity for reentrainment increases with decreasing particle size. Bagnold's results were extended by Chepil (1945), who also found that different threshold velocities were obtained from a loose layer of particles as compared to a thin layer of particles coating a surface. Bagnold and Chepil concluded that the smaller particles are more difficult to reentrain because they are embedded in a laminar sublayer, where turbulent eddies from the air flow do not penetrate. Chepil (1945) further concluded that turbulent eddies are more responsible in lifting and transporting particles than the average forward air velocity.

The reentrainment of small particles ($5 < D < 30$ μm) from flat surfaces was studied both from a theoretical and experimental point of view by Punjrath et al. (1972), who concluded that initiation of particle movement occurs when the local aerodynamic drag force exceeds the friction force of the system particle-substrate, and propagation of movement downstream from the point of initiation is caused by momentum transferred from initially moving particles. Higher turbulence intensities also resulted in higher reentrainment levels, in agreement with Chepil (1945).

Studies of reentrainment in turbulent pipe flow have been conducted by Beal (1978), Sehmel (1971) and Wasan et al. (1973). The conclusions were reached that larger particles are

more easy to reentrain since they project further into the gas stream, that reentrainment increases with the thickness of the deposited layer and that surface roughness also affects reentrainment. Specifically, Wasan et al. (1973) were interested in losses occurring in long sampling lines, and they found that electrostatic charge increases the rate of deposition of particles smaller than about 3 μm diameter, while reentrainment decreases the rate of deposition above this size of particles. Sehmel (1971) found reentrainment to occur for particles as small as 2 μm diameter, but to be increasingly important for particles above 14 μm diameter.

Chepil (1945) found that the movement of difficultly erosive particles below about 50 μm diameter was enhanced by the bombarding effect of coarser fractions in saltation.[1]

It is difficult to estimate how these conclusions apply to conditions prevailing in an ESP. Threshold velocities for reentrainment in ESP's have been reported by Bogatyrev (1974), Hesketh (1973), Hignett (1967) and Strauss (1966), and these are given in Table 2.2.

Reentrainment caused by impaction of airborne particles in ESP's has been reported by Penney (1975), Seman et al. (1967) and Robinson (1971). The severity of the reentrainment increases

---

1 According to Corn (1966), saltation is a condition of minimum fluid velocity required to carry solids without allowing them to settle in a horizontal pipe.

TABLE 2.2

ESP's Threshold Velocities for Reentrainment

Material	Threshold Velocity (m/s)	D (μm)	Source
Carbon Black	0.6	< 100	Hesketh (1973), Strauss (1966)
CuO	∿1	N/A	Bogatyrev (1974)
Cu_2S	∿1	N/A	Bogatyrev (1974)
Fly Ash (non-carbonaceous)	1.8	< 74	Hignett (1967)
Fly Ash	2.4	< 100	Hesketh (1973), Strauss (1966)
Cement Dust	3.1-3.6	< 100	Hesketh (1973), Strauss (1966)

with increased impaction velocity and increased particle size of impacting particles. Due to this impact reentrainment, the collection of fine particles may be seriously impared by the presence of larger particles.

Of particular importance to ESP's is the electric force caused by the corona current flowing through a finite conductivity dust. The various expressions available in the literature for this force can be represented by the general equation:

$$F = \frac{\varepsilon_o}{2}\{(\lambda_1)(\lambda_2 jr)^{\lambda_3} - E_{ex}^2\} \qquad (2.51)$$

where (F) is the net attractive force per unit area, and (E_{ex}) is the field exterior to the dust layer, expressed by Oglesby et al. (1978) as:

$$E_{ex} = \frac{V-\Delta V}{s-\Delta x} \qquad (2.52)$$

where (ΔV) is the voltage drop across the layer thickness (Δx), with an applied voltage (V). For thin dust deposits, (E_{ex}) is simply the average field in the interelectrode spacing.

In Eq. 2.51, ($\lambda_1, \lambda_2, \lambda_3$) are all constants. According to Penney et al. (1962), $\lambda_1 = \lambda_2 = K$ (relative dielectric constant of the dust layer); according to Tassicker (1975), $\lambda_1 = K$ and (λ_2) depends on particle elasticity, varying from one to twenty; Lowe et al. (1953) and McLean (1977) state that $\lambda_2 = 1$ and (λ_1) has to be empirically determined. These different

formulations arise from the assumptions under which Eq. 2.52 is derived. If the high electric fields established in the contact points of the particles in the dust layer are neglected, then according to Lowe et al. (1953), Penney et al. (1962) and Tassicker (1977), $\lambda_3 = 2$. If the electric field in the contact spots is considered, then the dependence of the adhesion force on the field established in the layer becomes approximately linear, i.e., $\lambda_3 \simeq 1$.

Due to the various approximations involved, Eq. 2.51 is probably only qualitatively correct. It shows that the force due to the corona current is attractive for high fields established in the dust layers. As the current density and dielectric constant vary over a much more limited range than the dust resistivity, it is this last variable which determines to a great extent whether the corona forces are attractive or repulsive. This may partially explain the data on Table 2.2, as carbon black and the copper compounds have much lower resistivities than those of non-carbonaceous fly-ash or cement dust. Typical orders of magnitude, taken from Bogatyrev (1974) and Strauss (1966) are 10^{-5} Ohmm for carbon black, 10^3-10^4 Ohmm for Cu_2S and CuO and 10^8 Ohm m(or more) for non-carbanaceous fly-ash and cement dust.

Dust deposits in discharge electrodes are usually much more difficult to remove than those at the collection plates, and from Eq. 2.51, Oglesby et al. (1978) conclude that this is due to the much larger current densities. From geometrical arguments, it can be readily seen that the ratio of current density at the wires to current density at the plates is directly

proportional to wire-to-wire spacing and inversely proportional to wire diameter.

In ESP's, the main factors which are then thought to influence dust reentrainment are the intrinsic adhesion of the dust particles, average gas velocity, turbulence, particle size, corona current, resistivity and dielectric constant of the dust.

Bogatyrev (1974) found the effect of corona current in increasing reentrainment to be small when compared to gas velocity and intrinsic dust adhesion. Lakey et al. (1955) found this effect to be important for the larger particles of low resistivity. Spencer (1976a) also found the reentrainment due to corona current to be important for larger particles ($D > 25$ μm) and unimportant for smaller sizes ($D < 7$ μm). This effect was reduced at higher humidities. The effect of humidity on particle adhesion is reported by Corn (1966) and Niedra et al. (1965), and usually an increased humidity increases interparticle forces. To counteract this is the effect of increased humidity in decreasing bulk resistivity (in the surface conduction mode), and this may be the predominant effect.

Without corona current (as when the corona power is off), the force expressed by Eq. 2.51 ceases. Penney (1975) and Penney et al. (1962) consider the dust particles to be held at the plate by a permanent dipole effect due to differences in contact potentials at the particles' surfaces. Niedra et al. (1965) extend this concept to coulomb-type forces due to multipole characteristics of the particles' surfaces, while Dalmon et al.

(1971) consider that mechanical (intrinsic) forces are responsible. These last authors found that the mechanical forces were of the order of the electrical forces for a high resistivity fly ash ($r \approx 10^{11}$-10^{12} Ohmm) of mean mass diameter 10 μm, but that they were dominant for a low resistivity fly ash ($r \approx 10^{5}$ Ohmm) of mean mass diameter 50 μm.

Reentrainment can be detected in a number of ways. Oglesby et al. (1978) and White (1963) suggest:

- plotting the nepperian logarithm of the penetration ($1-\eta$) as a function of inverse gas velocity;
- plotting the precipitation rate parameter as a function of gas velocity;
- measuring the size distributions at the inlet and outlet of the ESP;
- measuring the particle charge at the outlet of the ESP.

The first two methods require information at non-reentraining velocities, and are only strictly applicable to monodisperse dusts. This is because they are based on the assumption of invariant precipitation rate parameter with gas velocity. The measurement of size distribution is always applicable, and according to Oglesby et al. (1974) and White (1963), the detection of a significant proportion of large particles is a sure sign of reentrainment. That large particles of low resistivity are more prone to reentrainment has been theoretically derived by Lowe et al. (1953) and experimentally verified by Lakey et al. (1955) and Spencer (1976a). White

(1963) also reports experimental data showing the effect of increased particle size in increasing reentrainment.

If reentrainment is occurring, the larger particles present at the outlet may be agglomerates of finer particles. Spencer (1976b,1976c) shows this to occur with rapping reentrainment, or it may occur when fines are impacted by larger particles.

Figure 2.12, taken from Oglesby et al. (1974), shows how reentrainment may distort the size distribution of dust collected along the ESP length. The data is from a pilot-plant ESP operating under severe reentrainment losses.

With severe reentrainment, the proportion of positively charged particles at the ESP outlet increases, but White (1963) points out that the detection of reentrainment by charge measurement may not be generally applicable.

Due to the complexity of the reentrainment phenomena, no reliable analytical method has been developed with predictive capabilities, and usually reliance is made upon very simple models which may not represent the physical process, e.g., considering reentrainment size independent, or upon empirical corrections to the theoretical fractional efficiencies (or migration velocities). The use of a precipitation rate parameter is an example of an empirical correction to the Deutsch Equation.

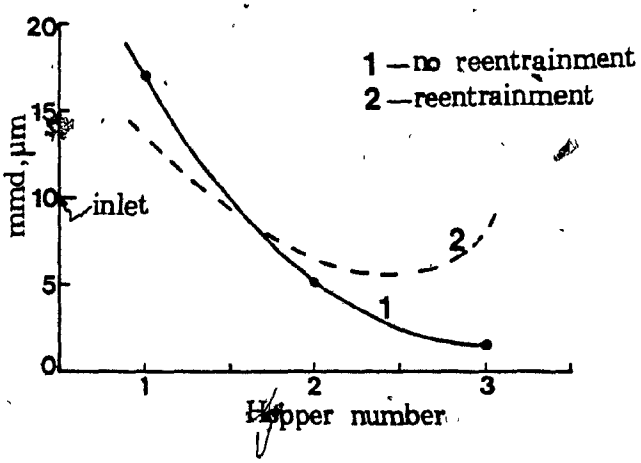


Figure 2.12 Comparison between hopper particle size distribution with and without re-entrainment, Oglesby et al. (1974)

2.8 The SRI Electrostatic Precipitator Performance Computer Model

2.8.1 General Description

The electrostatic precipitator is a complex system, in which the various subsystems (corona generation, electric field, particle charging and collection, dust properties, non-ideal effects) are closely interrelated. The systems analysis of ESP's presented here was first worked out by Nichols et al. (1970) and Oglesby et al. (1970), at Southern Research Institute (SRI), Alabama. The complexity of the complete description of the electrostatic precipitation process can be appreciated in Fig. 2.13, taken from Nichols and Oglesby (1970), and it shows the high degree of interaction which is possible. The difficulties in simulating such a system are enormous, and Nichols and Oglesby took the approach of considering only the subsystems for which theoretical relations which had been experimentally validated were available. Unfortunately, at the time, a reliable theory of electric fields in parallel-type ESP's with the presence of space-charge was not yet available, and the model included the theoretical relationships derived for cylindrical (tubular) ESP's. Also, no corrections were included in the original model to account for non-ideal effects, which may either increase or decrease the collection as compared to theoretical predictions, and field charging was the only charging mechanism considered.

Experimental validation of the model was performed by comparing the global collection efficiencies predicted and experimentally determined for five full-size ESP's collecting fly ash from utility boilers. The agreement was very good

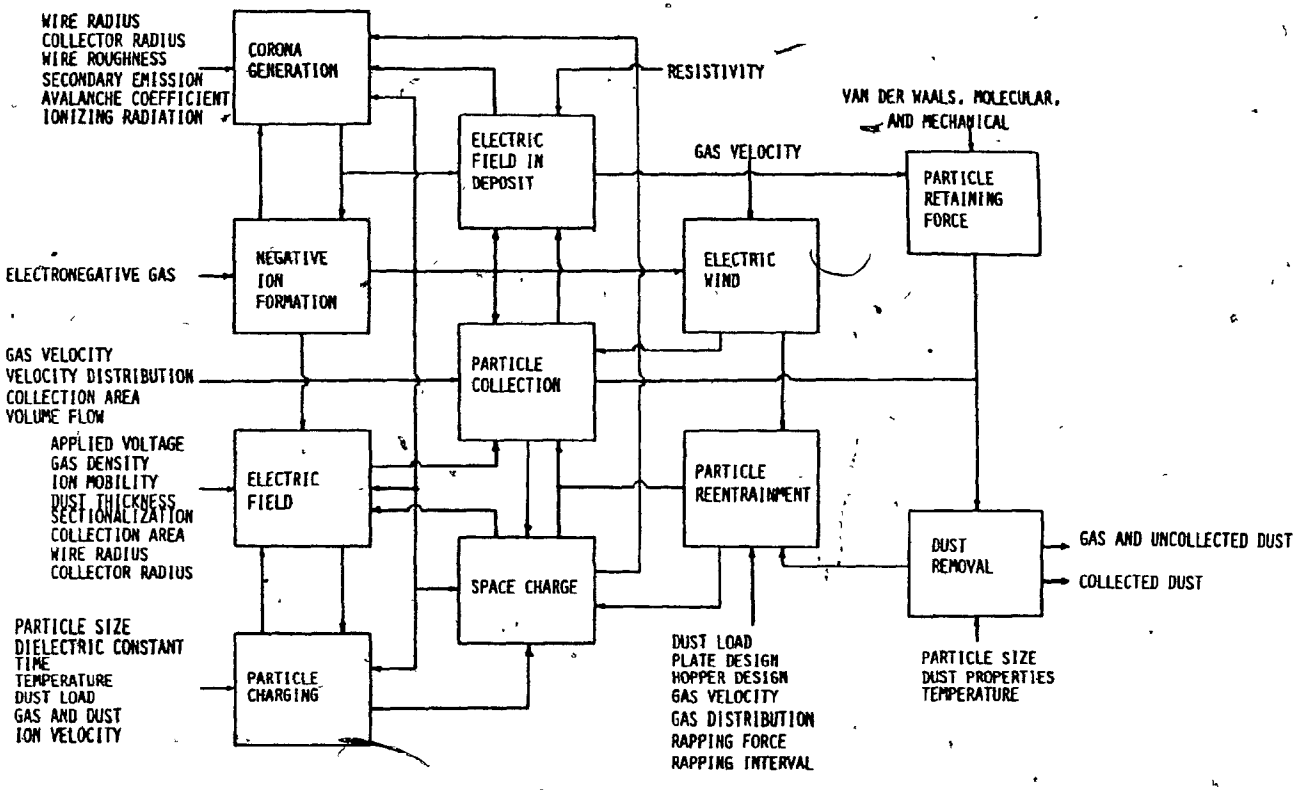


Figure 2.13 Electrostatic precipitator system model, Nichols et al. (1970)

(within 2.5%) when reentrainment was absent. The presence of reentrainment produced collection efficiencies well below those that were theoretically projected.

Gooch et al. (1975,1976a,1976b,1977) and McDonald (1978a,1978b) extended the model to include reliable theories for electric fields in parallel-type ESP's and particle charging, and corrections for non-ideal effects, as gas sneakage through collection hoppers or electrified regions and reentrainment due to rapping and other causes. For a detailed discussion of the SRI computer model, the reader is referred to McDonald (1978a, 1978b).

The main characteristics of the model are as follows:

- The electric field at the plate, which influences the migration velocity of the charged particles is estimated by two methods: if the current-voltage characteristics are known, the numerical technique of Leutert et al. (1972) is used; if the current-voltage characteristics are unknown, then the numerical technique of McDonald et al. (1977) is used. These were discussed in Section 2.3.3.
- The particle charges are estimated either by the theory of Smith et al. (1975,1976) or by the simpler analytical solution of summing the charges acquired by field and diffusion charging. The relative merits of the two estimations were discussed in Section 2.4.4.

- The collection efficiency is estimated by the use of the Deutsch Equation. Since this equation is only valid for single sized particles of constant charge (Sections 2.5.2 and 2.5.3), this problem is overcome by applying the Deutsch Equation to small length increments and to representative mean sizes of size classes in the particle size distribution histogram. The global efficiency is then calculated by weight averaging the fractional efficiencies over the entire size distribution. In other words, the ESP is treated as a series of smaller units (in length) where the Deutsch Equation can be applied.
- Provisions are included in the model to correct for non-ideal effects, such as gas sneakage, non-uniform velocity distribution, reentrainment and particle charging near corona wires or particle concentration gradients.

A note of caution should be given here. The theoretical corrections due to gas sneakage and no-rap reentrainment are considered to be independent of particle size or location within the ESP, and it is doubtful that such a condition exists in practice, as stated by McDonald (1978a). These corrections tend to lower the predicted collection. The empirical corrections included in the model were determined in full-size ESP's, and they might not apply to smaller units. These include corrections for non-uniform velocity distribution and rapping re-

entrainment, which tend to lower the collection efficiency, and corrections attributed to particle charging near corona wires and particle concentration gradients, which tend to increase the efficiency for particles smaller than about 5 μm.

Specifically, the collection efficiency for the i^{th} particle size in the j^{th} length increment is given by:

$$\eta_{ij} = 1 - \exp\left(-\frac{w_{ij}L_j}{v_{av}s}\right) \qquad (2.53)$$

The fractional efficiency for the i^{th} particle size averaged over all the ESP length, which is named an <u>effective efficiency</u>, is given by:

$$\eta_{iL} = \sum_j \eta_{ij}N_{ij}/N_{il} \qquad (2.54)$$

where (N_{ij}) is the number concentration of particles of size (i) entering length increment (j), and (N_{il}) is the inlet number concentration for size (i) particles. The <u>global collection efficiency</u> is then:

$$\eta = \sum_i \eta_{iL}M_i \qquad (2.55)$$

where (M_i) is the percentage by weight of the i^{th} particle size in the inlet histogram.

For the calculation of the electric field at the plate, in the case of known current-voltage characteristics, an equivalent mobility is estimated in each incremental length

of precipitation, using Eq. 2.5, where the ratio of ionic to dust mobilities is taken to be 200. The equivalent mobility is used in one boundary condition of the numerical integration of Leutert et al. (1972), as was seen in Section 2.3.3. The computer model also considers an approximation to the calculation of the electric field at the plate, where it is equal to the average field in the interelectrode spacing scaled down by the factor 1.75. This scaling factor was experimentally determined with full-size ESP's collecting fly ash, and as such the approximate method should be avoided for other applications or for smaller ESP's.

For the calculation of particle charges, the choice of using either Eq. 2.30 or 2.32 is primarily dictated by the inlet size distribution. As is seen in Section 2.4.4, there is good general agreement between the simpler approximation of Eq. 2.32 and the experimental data for particle diameters larger than about 0.5 μm, whereas the agreement is better for smaller sizes if Eq. 2.30 is used. Thus, if the inlet size distribution has only a small percentage (by weight) below about 0.5 μm diameter, the use of Eq. 2.32 should give good estimates of particle charges. If, on the other hand, the size distribution is essentially below 0.5 μm, then the more refined theory of Smith et al. (1975,1976) should be used. Figure 2.14, from McDonald (1978b) shows the comparison of using the numerical technique of Leutert et al. (1972) and the charging equation of Smith et al. (1975,1976) against the simpler approximation of estimating the field at the plate and using Eq. 2.32 for particle charging.

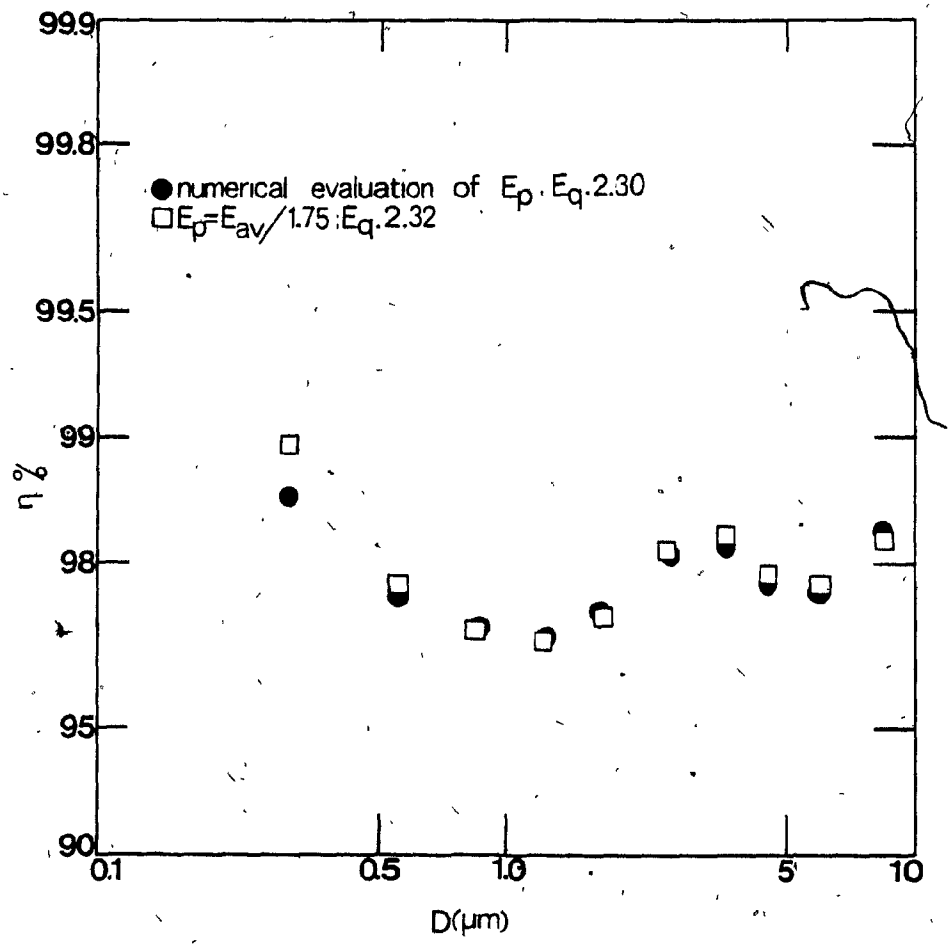


Figure 2.14 Comparison of results obtained from rigorous application of the model and estimation procedure, McDonald (1978 b)

Since the estimated field, in this particular case, was on the average only 2% lower than the more rigorous calculation, the difference attributable to the different charging equations is also very small. The advantage in using the simpler Eq. 2.32 is in the saved computer time.

The fractional migration velocity is calculated using Eq. 2.37 in each incremental length of ESP. For each particle size, an effective efficiency is calculated by Eq. 2.54, and if a migration velocity is then back-calculated from the Deutsch Equation, it is termed an effective migration velocity. The global efficiency is calculated by Eq. 2.55, and back-calculation of a migration velocity from Deutsch Equation produces the precipitation rate parameter. It is important to distinguish between these variables, to better understand the output from the computer model (Appendix A).

Figure 2.15, from Gooch et al. (1977) shows a simplified flow diagram of the computer program, which is given in detail by McDonald (1978a). Basically, the program is structured under three major loops, the outermost converging on the global efficiency. The next loop runs over each length increment, while the inner loop runs over each particle size. Details of the convergence criteria, including those for the numerical integration of the electric field equations are given by McDonald (1978a).

Also shown in Fig. 2.15 is the part of the simulation which runs over the theoretical and empirical corrections used to account for non-ideal effects. These should be used with great care, as outlined before. In the present study the non-

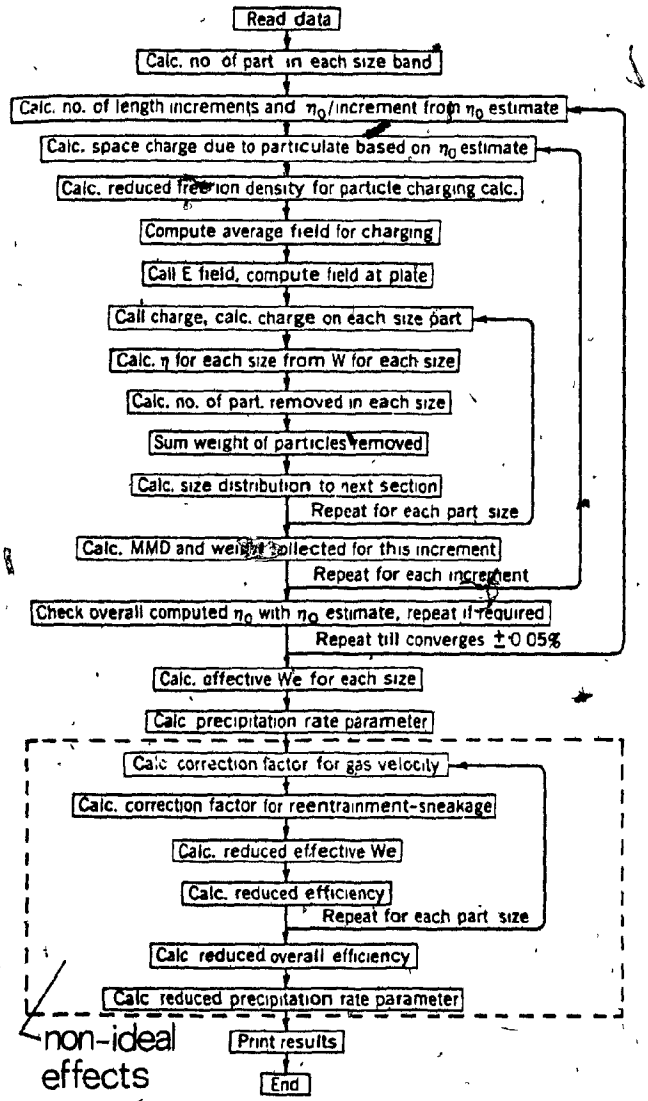


Figure 2.15 Simplified flow diagram of precipitator model computer program, Gooch et al. (1977)

ideal effects were all eliminated or bypassed, and the collection efficiencies (or migration velocities) thus calculated are based on strictly theoretical principles. The theoretical corrections for reentrainment, for example, are based on the assumption that a fixed fraction of the precipitated dust is reentrained, irrespective of position within the ESP length, within each stage (electrically sectionalized) of the ESP. Then, for a single stage, the corrected <u>effective migration velocity</u> (w^*_{iL}) is given by:

$$w^*_{iL} = w_{iL} \cdot \frac{\ln\{1-\eta_{iL}(1-R)\}}{\ln(1-\eta_{iL})} \qquad (2.56)$$

and the corrected effective efficiency (η_i^*) is simply given by:

$$\eta^*_{iL} = \eta_{iL}(1-R) \qquad (2.57)$$

where (iL) refers to the i^{th} particle size averaged over the entire ESP length. In Eqs. 2.56 and 2.57, (R) represents the fraction of dust reentrained, independent of particle size.

Appendix A shows typical input-output data for the estimation of ideal migration velocities and collection efficiencies for a parallel-type ESP of laboratory-size, using the SRI computer program. The example refers to the collection of a coarse oxide (CuO) with a size distribution which is input as a log-normal distribution.

2.8.2 Experimental Verification

In order to experimentally validate their model, SRI conducted a series of tests in a small laboratory-scale, parallel-type ESP. Conditions were such that reentrainment was absent, while a small percentage of gas sneakage was present.

Figures 2.16 a) and b), from Gooch et al. (1976a,b) show that the agreement of the experimental data (for particle sizes between 0.55-2.5 μm diameter) with the model predictions is good for the short wire-to-plate spacing of 6.35 cm, at a current density of around 5.4×10^{-4} Am^{-2}, and it deteriorates at both higher and lower current densities. When the wire-to-plate spacing is increased to 9.5 cm, the agreement worsens, and the experimental results are larger than the theoretical predictions, except at the low current density of 1.1×10^{-4} Am^{-2}.

McDonald (1978b) also shows experimental results and model predictions for a wire-to-plate spacing of 12.7 cm, average air velocity of 0.976 ms^{-1} and average current density at the plates of 2.58×10^{-4} Am^{-2}, and the trends are similar to those in Figs. 2.16 a) and b).

The lower experimental results are attributed to the effects of irregular corona current and gas sneakage, while the higher experimental values are attributed to the presence of transverse concentration gradients and particle charging near corona wires. The qualitative agreement is in all cases very good. Experimental investigation by Gooch et al. (1976a,b)

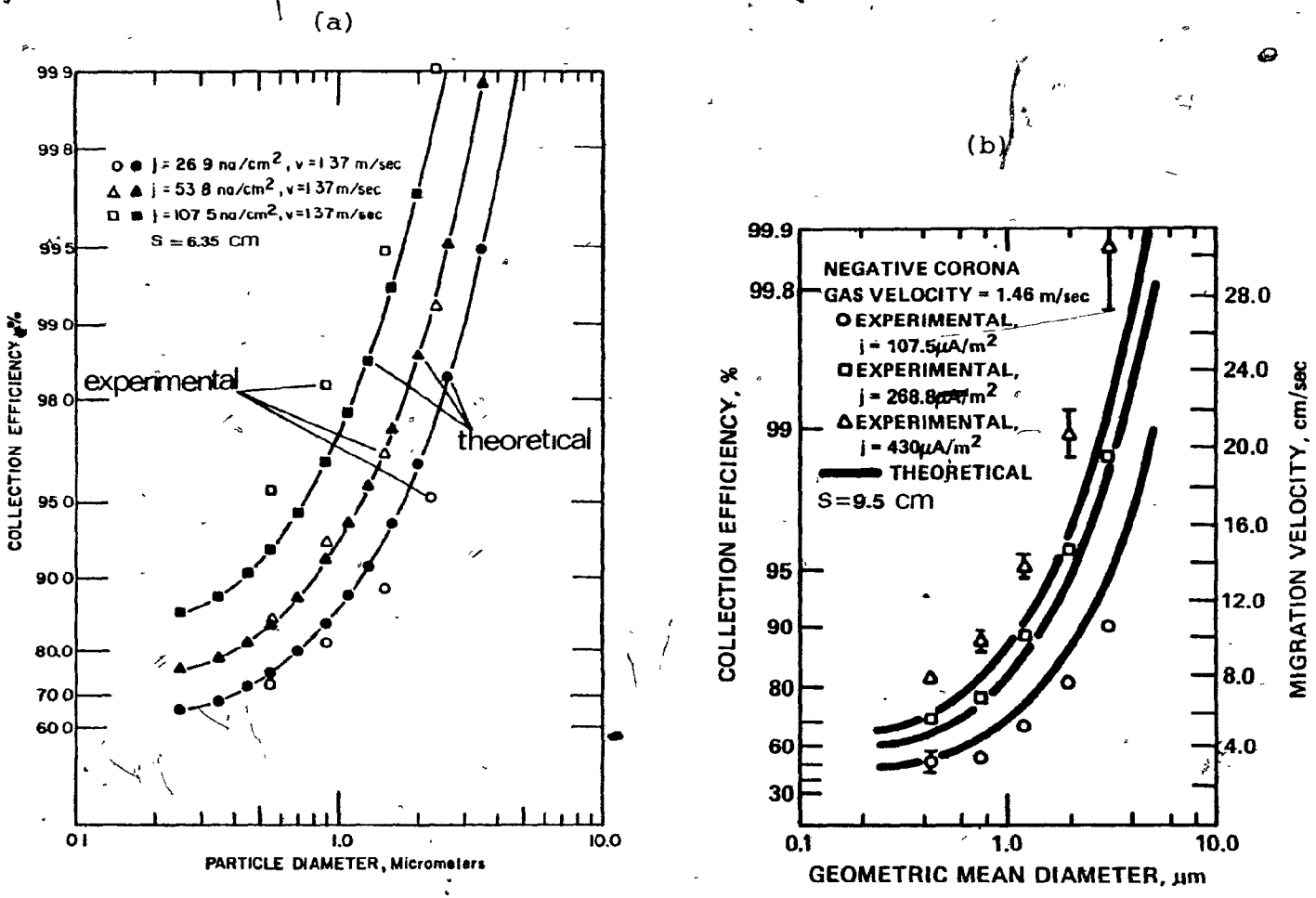


Figure 2.16 a, b Experimentally measured and ideally calculated fractional collection efficiencies in the laboratory precipitator, Gooch et al. (1976 a, b)

demonstrated the existence of transverse concentration gradients for the wire-to-plate spacing of 9.5 cm, but not for the smaller spacing.

The theoretical predictions of the model have also been compared with full-size and pilot-plant experimental data. Gooch et al. (1976a,1976b,1977) and McDonald (1978b) show data for both hot-side and cold-side ESP's collecting flyash, and the theoretical agreement is in general fair, but it can be greatly improved by using correction factors built in the model. McDonald et al. (1978c) show data for three full-size ESP's operating in non-ferrous industries of copper and lead, and in general the predicted values are less than the measured values of collection efficiency in the fine range of particle sizes (below about 1-2 μm), while the reverse occurs in the coarser range of sizes.

As general conclusions, it may be said that the SRI computer model serves as a basis for comparing experimental data, which agrees well with the model predictions in the absence of reentrainment and other non-ideal effects. In well controlled laboratory-scale ESP's, in the absence of reentrainment or gas sneakage, some unmodelled effects might be present, which tend to increase the collection of the fine particles. These include particle charging near the corona wires and particle concentration gradients. At low current densities, the reverse might also occur.

One variable which is not included in the theoretical approach to the space-charge and electric field

calculations is the dust bulk resistivity. This is only considered in the model to prevent specifying higher current densities than those which cause electrical breakdown in the dust layer. In other words, the effect of the precipitated dust layer on current density distribution and electric field at the plate is ignored. The extent to which this unmodelled effect is important is not known.

Although the SRI computer model is not the final answer to predict the performance of ESP's, it is probably one of the most important developments in the recent theory of electrostatic precipitation, since it considers some of the important interactions occurring in such a complex system, and presents a workable model which might be implemented as more information becomes available.

REFERENCES

Adam, B. (1979): 4th Int. Symposium on Plasma Chemistry, Conf. Proceedings, S. Veprek and J. Hertz (eds.), August 27-September 1, pp.616-621.

ASME Power Test Code 28 (1965): "Determining the Properties of Fine Particulate Matter", pp.10, 15-17, 34-37.

Awad, M.B. and Castle, G.S.P. (1975): "The Efficiency of Electrostatic Precipitators under Conditions of Corona Quenching", JAPCA, 25, No. 2, February, pp.172-176.

Bagnold, R.A. (1954): "The Physics of Blown Sands and Desert Dunes", Methuen and Co., London.

Bakke, E. (1975): "Wet Electrostatic Precipitators for Control of Submicron Particles", JAPCA, 25, No. 2, February, pp.163-167.

Beal, S.K. (1978): "Correlations for the Sticking Probability and Erosion of Particles", J. Aerosol Sci., 9, Pergamon Press, pp.455-461.

Bickelhaupt, R. (1974): "Electrical Volume Conduction in Fly Ash", JAPCA, 24, No. 3, March, pp.251-255.

_____ (1975): "Surface Resistivity and the Chemical Composition of Fly Ash", JAPCA, 25, No. 2, February, pp.148-152.

_____ (1980): "An Interpretation of the Deteriorative Performance of Hot-Side Precipitators", JAPCA, 30, No. 8, August, pp.882-888.

Bogatyrev, M. (1974): "The Influence of Dust Resistivity on the Effectiveness of Collecting it in Electrofilters" (in Russian), Tsvetnye Metally, 5, pp.79-81.

Botcher, C.J.F. (1952): "Theory of Electric Polarization", Elsevier Pub. Co., pp.415-420.

Brown, R.F. and Walker, A.B. (1971): "Feasibility Demonstration of Electrostatic Precipitation at 1700°F", JAPCA, 21, No. 10, October, pp.617-620.

Burton, C.L. and Smith, D.A. (1975): "Precipitator Gas Flow Distribution", JAPCA, 25, No. 2, February, pp.139-143.

Bush, J.R., Feldman, P.L. and Robinson, M. (1979): "High Temperature, High Pressure Electrostatic Precipitation", JAPCA, 29, No. 4, April, pp.365-371.

Chepil, W.S. (1945): "Dynamics of Wind Erosion: II. Initiation of Soil Movement", Soil Science, 60, pp.397-411.

Cobine, J.D. (1956): "Theory and Engineering Application: Gaseous Conductors", Dover Pub. Inc.

Colli, L., Facchini, U., Gatti, E. and Persano, A. (1954): "Dynamics of Corona Discharge between Cylindrical Electrodes", J. Applied Physics, 25, No. 4, April, pp.429-435.

Collins, W.E. and Penney, G.W. (1971): "Effect of Capacitance on Electrostatic Precipitator Operating Voltage", IEEE Trans., IGA-7, No. 3, June, pp.427-432.

Cooperman, P. (1960): "A Theory for Space-Charge-Limited Currents with Application to Electrical Precipitation", AIEE Trans., 79, March, pp.47-50.

_____ (1963): "Dust Space-Charge in Electrical Precipitation", IEEE Trans., Comm. and Electronics, 66, July, pp.324-326.

_____ (1971): "A New Theory of Precipitator Efficiency", Atmospheric Environment, Pergamon Press, 5, pp.541-551.

Corn, M. (1966): "Aerosol Science", Academic Press, C.N. Davies (ed.), pp.359-392.

Crawford, M. (1976): "Air Pollution Control Theory", McGraw-Hill, pp.298-361.

Currie, L.G. (1974): "Fundamental Mechanics of Fluids", McGraw-Hill.

Dalmon, J. and Tidy, D. (1971): "The Cohesive Properties of Fly Ash in Electrostatic Precipitation", Atmospheric Environment, Pergamon Press, 6, pp.81-92.

Davis, R. and Cook, R.W.E. (1961): "The Surge Corona Discharge", IEE Proceed., 108, pp.230-239.

Dinneli, G., Borgatti, C. and Rea, M. (1979): "Electrostatic Precipitation Tests with Fuel Oil Ash", JAPCA, 29, No. 3, March, pp.242-248.

Ditl, P. and Coughlin, R.W. (1976): "Improving Efficiency of Electrostatic Precipitation by Physicochemical Modification of the Electrical Resistivity of Flyash", AIChE J., 22, No. 4, July, pp.730-736.

Feldman, P.L., Kuman, K.S. and Cooperman, G.D. (1977): "Turbulent Diffusion in Electrostatic Precipitators", AIChE Air Symposium Series, 73, pp.120-130.

Fink (1975): "Electronics Engineers' Handbook", McGraw-Hill, 1st Ed.

Gallo, C.F. and Lama, W.L. (1971): "The Lateral Distribution of Current from Wire-to-Plane Coronas", IEEE Trans., IGA-7, No. 3, May/June, pp.420-426.

Gensler, W.G. (1968): "A Study of Individual Particle Trajectories in Electrostatic Precipitation", Ph.D. Thesis, Carnegie-Mellon University, pp.130-131.

_____ and Penney, G.W. (1968): "An Experimental Method of Particle Trajectory Analysis in Electrostatic Precipitation", IEEE 3rd Conf. Record, IGA-ES-THU-3, pp.41-56.

Gentry, J. and Brock, J.R. (1967): "Unipolar Diffusion Charging of Small Aerosol Particles", J. Chem. Physics, 47, No. 1, July, pp.64-69.

Gooch, J.P. and Francis, N.L. (1975): "A Theoretically Based Mathematical Model for Calculation of Electrostatic Precipitator Performance", JAPCA, 25, No. 2, February, pp.108-113.

_____ and McDonald, J.R. (1976a): "Conference on Particle Collection Problems in Converting to Low Sulfur Coals", SRI/EPA Contract 68-02-2114, EPA-600/7-76-016, pp.68-106.

_____ and McDonald, J.R. (1976b): "Symposium on Particulate Control in Energy Processes", SRI/EPA Contract 68-02-1318, EPA-600/7-76-010, pp.217-265.

_____ and McDonald, J.R. (1977): "Mathematical Modelling of Fine Particle Collection by Electrostatic Precipitation", AIChE Air Symposium Series, 73, No. 165, pp.146-159.

"Handbook of Chemistry and Physics" (1976-77), CRC Press, 57th ed., pp.E-58-60.

Heinrich, D.O. (1961): "Study on Electro-Precipitator Performance in Relation to Particle Size Distribution, Level of Collection Efficiency and Power Input", Trans. Inst. Chem. Eng., 39, pp.145-163.

Hendricks, C.D. (1973): "Electrostatics and Its Applications", John Wiley & Sons, Wiley-Interscience Pub., A.D. Moore (ed.).

Hesketh, H.E. (1973): "Understanding and Controlling Air Pollution", Ann Arbor Science Pub., Inc.

Hewitt, G.W. (1957): "The Charging of Small Particles for Electrostatic Precipitation", AIEE Trans., 76, part I, pp. 300-306.

Hignett, E.T. (1967): "Particle Charge Magnitudes in Electrostatic Precipitation", Proc. IEE, 114, No. 9, September, pp.1325-1328.

Inculet, I.I. (1973): "Electrostatics and Its Application", John Wiley & Sons, Wiley-Interscience Pub., A.D. Moore (ed.).

"International Critical Tables of Numerical Data, Physics, Chemistry and Technology", (1933), McGraw-Hill, pp. 74-105, 110-117.

Jarzebski, S. and Chojnowski, M. (1974): "Influence of Shapes of Corona Electrodes on Density of Emission Currents in Electrostatic Dust Collectors", Atmospheric Environment, 8, Pergamon Press, pp.29-40.

Katz, J. (1980): "Factors Affecting Resistivity in Electrostatic Precipitation", JAPCA, 30, No. 1, January, pp.195-201.

Kaye, G.W.C. and Laby, T.H. (1973): "Tables of Physical and Chemical Constants", Longman, 14th ed., pp.109-114.

Kingery, W.D., Bowen, H.K. and Uhlmann, D.R. (1976): "Introduction to Ceramics", John Wiley & Sons, 2nd ed.

Lagarias, J.S. (1959): "Field-Strength Measurements in Parallel-Plate Precipitators", AIEE Trans., 78, September, pp.427-433.

_____ (1963): "Predicting Performance of Electrostatic Precipitators", JAPCA, 13, No. 12, December, pp.595-598.

Lakey, J.R.A. and Bostock, W. (1955): "Researches into Factors Affecting Electro-Precipitation", Trans. Inst. Chem. Eng., 33, pp.252-263.

Leutert, G. and Bohlen, B. (1972): "The Spatial Trend of Electric Field Strength and Space-Charge Density in Plate-Type Electrostatic Precipitators" (in German), Staub-Reinhault, Luft, 32, No. 7, pp.297-301.

Little, A. (1956): "Practical Aspects of Electrostatic Precipitator Operation-Experiments on a Pilot Plant", Trans. Inst. Chem. Eng., 34, pp.259-268.

Liu, B.Y.H., Whitby, K.T. and Yu, H.H.S. (1967): "Diffusion Charging of Aerosol Particles at Low Pressures", J. Applied Physics, 38, No. 4, pp.1592-1597.

_____ and Yeh, H.C. (1968): "On the Theory of Charging of Aerosol Particles in an Electric Field", J. Applied Physics, 39, No. 3, pp.1396-1402.

_____ and Kapadia, A. (1977): "Electrical Charging of Aerosol Particles at Low Pressures - Part II", Progress Report, ERDA Contract E(11-1)-1248, Particle Technology Laboratory Publication 338, University of Minnesota.

_____ and Kapadia, A. (1978): "Combined Field and Diffusion Charging of Aerosol Particles in the Continuum Regime", J. Aerosol Science, 9, Pergamon Press, pp.227-242.

Loeb, L.B. (1953): "Current Increase at Constant Amplification Factor in Steady Corona with Coaxial Cylindrical Geometry", Physical Review, 90, No. 1, April, pp.144-145.

_____ (1961): "The Kinetic Theory of Gases", Dover Pub. Inc., N.Y., 3rd ed., pp.552.

Lowe, H.J. and Lucas, D.H. (1953): "The Physics of Electrostatic Precipitation", British J. Applied Physics, Sup. 2, pp.540-546.

McDonald, J.R. (1978a): "A Mathematical Model of Electrostatic Precipitation, Revision 1, Volume I - Modelling and Programming", Contract SRI/EPA 68-02-2114, EPA-600/7-78-111a.

_____ (1978b): "A Mathematical Model of Electrostatic Precipitation, Revision 1, Volume II - User Manual", Contract SRI/EPA 68-02-2114, EPA-600/7-78-111b.

_____ and Sparks, L.E. (1978): "A Precipitator Performance Model: Application to the Non-Ferrous Metals Industry", Southern Research Institute, Alabama, unpublished.

_____, Anderson, M.H., Mosley, R.B. and Sparks, L.E. (1980a): "Charge Measurements on Individual Particles Exiting Laboratory Precipitators with Positive and Negative Corona at Various Temperatures", J. Applied Physics, 51, No. 7, July, pp.3632-3643.

_____, Mosley, R.B. and Sparks, L.E. (1980b): "An Approach for Describing Electrical Characteristics of Precipitated Dust Layers", JAPCA, 30, No. 4, April, pp.372-376.

McLean, K.J. and Huey, R.M. (1974): "Influence of Electric Field on the Resistivity of a Particulate Layer", Proc. IEE, 121, No. 1, pp.76-80.

McLean, K.J. (1976): "Factors Affecting the Resistivity of a Particulate Layer in Electrostatic Precipitators", JAPCA, 26, No. 9, pp.866-870.

_____ (1977): "Cohesion of Precipitated Dust Layer in Electrostatic Precipitators", JAPCA, 27, No. 11, November, pp.1100-1103.

Murphy, A.T., Adler, F.T. and Penney, G.W. (1959): "A Theoretical Analysis of the Effects of an Electric Field on the Charging of Fine Particles", AIEE Trans., 78, part I, September, pp.318-326.

Nichols, G.B. and Oglesby, S. (1970): "Electrostatic Precipitator Systems Analysis", AIChE Annual Meeting, Southern Research Institute, unpublished.

Nichols, G.B. (1974): "Techniques for Measuring Fly Ash Resistivity", Environmental Protection Technology Series, SRI contract 68-02-1303, PB 244 140, NTIS, U.S. Department of Commerce.

_____ and Spencer, H.W. (1975): "Test Methods and Apparatus for Conducting Resistivity Measurements", Contract SRI/EPA 68-02-1083, Final Report to EPA, SRI-EAS-75-090, 3121-IIIF.

Niedra, J.M. and Penney, G.W. (1965): "Orientation and the Adhesion of Particles", IEEE, Int. Conv. Record, 13, part 7, pp.88-94.

Oglesby, S. and Nichols, G.B. (1970): "A Manual of Electrostatic Precipitator Technology, Part I - Fundamentals", Southern Research Institute.

_____ (1974): "Electrostatic Precipitator Technology for Source Emission Control", AIChE Symposium Series, 70, No. 137, pp.351-356.

_____ (1975): "Gas Cleaning for Air Quality Control", Marchello, M. and Kelly, J.J. (eds.), Marcel Dekker, pp.167-255.

_____ (1978): "Electrostatic Precipitation", Marcel Dekker, Inc., Pollution Eng. and Technology.

Parker, L.W. (1975): "Field Charging Theory for Electrostatic Precipitation of Ultrafine Particles", APCA 68th Annual Meeting, #75-02.2, Massachusetts, June 15/20.

Pampuch, R. (1976): "Ceramic Materials - An Introduction to their Properties", Elsevier Sci. Pub. Co.

Peek, F.W. (1929): "Dielectric Phenomena in High Voltage Engineering", McGraw-Hill, 3rd ed.

Pender, H. and McIlwain, K. (1975): "Electrical Engineers' Handbook", Wiley Handbook Series, 4th ed.

Penney, G.W. (1951): "Electrostatic Precipitation of High Resistivity Dust", AIEE Trans., 70, pp.1192-1196.

_____ (1975): "Adhesive Behaviour of Dust in Electrostatic Precipitation", JAPCA, 25, No. 2, February, pp.113-117.

_____ and Lynch, R.D. (1957): "Measurements of Charge Imparted to Fine Particles by a Corona Discharge", AIEE Communication & Electronics, 76, July, pp.294-299.

_____ and Matick, R.E. (1960): "Potentials in D-C Corona Fields", AIEE Trans., 79, May, pp.91-99.

_____ and Klinger, E.H. (1962): "Contact Potentials and the Adhesion of Dust", AIEE Trans., part I, 81, July, pp.200-204.

_____ and Gelfand, P.C. (1978): "The Trielectrode Electrostatic Precipitator for Collecting High Resistivity Dust", JAPCA, 28, No. 1, January, pp.53-55.

Pettersen, H.H. (1980): "New Trends in Electrostatic Precipitation: Wide Duct Spacing, Precharging, Pulse Energization", IEEE Cement Industry Technical Conference, Toronto, May.

Potter, E.C. (1978): "Electrostatic Precipitator Technology: A Different Viewpoint", JAPCA, 28, No. 1, January, pp.40-45.

Pui, D.Y.H. and Liu, B.Y.H. (1977): "Electrical Charging of Small Particles at Low Pressures - Part I", Progress Report, ERDA Contract E(11-1)-1248, Particle Technology Laboratory Publication 338, University of Minnesota.

Punjrath, J.S. and Heldman, D.R. (1972): "Mechanisms of Small Particle Reentrainment from Flat Surfaces", J. Aerosol Science, 3, Pergamon Press, pp.429-440.

Pyle, B.E., Pontius, D.H., Snyder, T.R. and Sparks, L.E. (1980): "Particle Trajectory Studies in a Scale Model Electrostatic Precipitator", APCA 73rd Annual Meeting, #80-49.2, Montreal, June 22-27.

Ramadan, D.E. and Soo, S.L. (1969): "Electrohydrodynamic Secondary Flow", Physics of Fluids, 12, pp.1943-1945.

Reynolds, J.P., Theodore, L. and Marino, J. (1975): "Calculating Collection Efficiencies for Electrostatic Precipitators", JAPCA, 25, No. 6, June, pp.610-616.

Robinson, M. (1961): "A Miniature Electrostatic Precipitator for Sampling Aerosols", An. Chemistry, 33, No. 1, pp.109-113.

_____ (1965): "Corona-Starting Voltages for Parallel Wire-Plate Electrodes", IEEE, Int. Conv. Record, 13, part 7, pp.73-77.

_____ (1967a): "Electric Wind Turbulence in Electrostatic Precipitation", JAPCA, 17, No. 9, September, pp.605-606.

_____ (1967b): "A Modified Deutsch Efficiency Equation for Electrostatic Precipitation", Atmospheric Environment, 1, Pergamon Press, pp.193-204.

_____ (1968a): "Turbulent Gas Flow and Electrostatic Precipitation", JAPCA, 18, No. 4, April, pp.235-239.

_____ (1968b): "The Effect of Polarity on Particle Concentration Profiles in Electrostatic Precipitators", JAPCA, 18, No. 10, October, pp.688-690.

_____ (1971): "Air Pollution Control - Part I", John Wiley & Sons, W. Strauss (ed.), pp.227-334.

_____ (1972): "A Note on the Significance of Particle Charging Time in Electrostatic Precipitation", Atmospheric Environment, 6, Pergamon Press, pp.61-63.

Ross, J.N. (1980): "Studies of an Electrostatic Precipitator using Laser Doppler Anemometry", Optica Acta, 27, No. 1, pp.19-23.

Samsonov, G.V. (1973): "The Oxide Handbook", IFI Plenum

Say, M.G. (1973): "Electrical Engineers' Reference Book", Butterworths, 13th ed.

Sears, F.W. and Zemansky, M.W. (1976): "University Physics, Part II - Electricity and Magnetism", Reading, Mass., Addison-Wesley Pub. Co., 5th ed.

Sehmel, G.A. (1971): "Complexities of Particle Deposition and Reentrainment in Turbulent Pipe Flow", J. Aerosol Science, 2, Pergamon Press, pp.63-72.

Seman, G.W. and Penney, G.W. (1967): "Photographic Records of Particle Trajectories During Electrostatic Precipitation", IEEE Trans., PAS-86, No. 3, pp.69-72.

Shale, C.C. (1965): "The Physical Phenomena Underlying the Negative and Positive Coronas in Air at High Temperatures and Pressures", IEEE, Int. Conv. Record, 13, part 7, pp.77-87.

_____ and Holden, J.H. (1968): "The Role of Wire Size in Negative Electrical Discharge at High Temperature", IEEE 3rd Conf. Record, IGA-ES-THU-5, pp.59-66.

Smith, G.D. (1975): "Numerical Solution of Partial Differential Equations", Oxford University Press.

Smith, P.L. and Penney, G.W. (1961): "The Charging of Non-spherical Particles in a Corona Discharge", AIEE Trans., Comm. & Electronics, 80, part 1, July, pp.340-346.

Smith, W.B. and McDonald, J.R. (1975): "Calculation of the Charging Rate of Fine Particles by Unipolar Ions", JAPCA, 25, No. 2, February, pp.168-172.

_____ (1976): "Development of a Theory for the Charging of Particles by Unipolar Ions", J. Aerosol Science, 7, Pergamon Press, pp.155-166.

_____, Cushing, K. and McCain, J.D. (1977): "Procedures Manual for Electrostatic Precipitator Evaluation", EPA-600/7-77-059.

_____, Felix, L.G., Hussey, D.H., Pontius, D.H. and Sparks, L.E.: "Experimental Investigation of Fine Particle Charging by Unipolar Ions - A Review", J. Aerosol Science, 9, Pergamon Press, pp.101-124.

Soo, S.L. (1972): "A Critical Review on Electrostatic Precipitators", AIChE Symposium Series, 68, No. 126, pp.185-193.

Spencer, H.W. (1976a): "Electrostatic Precipitators: Relationship between Resistivity, Particle Size and Sparkover", Contract SRI/EPA 68-02-1303, EPA-600/2-76-144.

_____ (1976b): "Conference on Particulate Collection Problems in Converting to Low Sulfur Coals", SRI/EPA-600/7-76-016, pp.123-148.

_____ (1976c): "Symposium on Particulate Control in Energy Processes", SRI/EPA Contract 68-02-1318, EPA-600/7-76-010, pp.317-341.

Sproull, W.T. and Nakada, Y. (1951): "Operation of Cottrell Precipitators: Effects of Moisture and Temperature", Ind. Eng. Chem., 43, No. 6, June, pp.1350-1358.

_____ (1963): "Corona Quenching: Its Significance in Electrical Precipitation", JAPCA, 13, No. 12, December, pp.617-621.

Stock, D.E. and Crowe, C.T. (1977): "The Effect of Electrodynamic Secondary Flow on the Performance of Electrostatic Precipitators", AIChE Symposium Series, 73, No. 165, pp.254-265.

Strauss, W. (1966): "Industrial Gas Cleaning", Pergamon Press, 1st ed., pp.336-396.

Tassicker, O.J. (1971): "The Temperature and Frequency Dependence of the Dielectric Constant of Power Station Fly Ash", Staub-Reinhault, Luft, 31 (in German), pp.331-335.

_____ (1974): "Boundary Problem for Measurement of Current Density and Electric Field Strength with Special Reference to Ionized Gases", Proc. IEE, 121, No. 3, March, pp.213-220.

_____ (1975): "Some Aspects of Electrostatic Precipitator Research in Australia", JAPCA, 25, No. 2, February, pp.122-127.

Theodore, L., Reynolds, J.P. and Navarrete, R.L. (1973): "Results of a New Technique for Calculating Collection Efficiencies in Electrostatic Precipitators", APCA 66th Annual Meeting, #73-292, Chicago, June.

_____ and Buonicore, A.J. (1976): "Industrial Air Pollution Control Equipment for Particulates", CRC Press, pp.37-61, 139-190.

Vann Bush, P., Pontius, D.H., Smith, W.B. and Sparks, L.E. (1980): "Field Evaluation of the SRI/EPA Precharger-Collector System", APCA 73rd Annual Meeting, #80-32.6, June 22-27, Montreal.

Von Hippel, A.R. (1954): "Dielectric Materials and Applications", International Press Books in Science and Engineering.

Wasan, D.T., Sood, S.K., Davies, R. and Lieberman, A. (1973): "Aerosol Transport: Particle Charge and Reentrainment Effects", J. Coll. and Int. Science, 43, No. 1, April, pp.144-149.

Waye, B.E. (1967): "Introduction to Technical Ceramics", McLaren & Sons, Ltd., London.

White, H.J. (1951): "Particle Charging in Electrostatic Precipitation", AIEE Trans., 70, pp.1186-1191.

_____ (1956): "Chemical and Physical Particle Conductivity Factors in Electrical Precipitation", Chem. Eng. Prog., 52, No. 6, June, pp.244-248.

_____ (1963): "Industrial Electrostatic Precipitation", Reading, Mass., Addison-Wesley Pub. Co.

_____ (1974): "Resistivity Problems in Electrostatic Precipitation", JAPCA, 24, No. 4, April, pp.314-338.

_____ (1977a): "Electrostatic Precipitation of Fly Ash", JAPCA, 27, No. 3, March, pp.206-217.

_____ (1977b): "Electrostatic Precipitation of Fly Ash", JAPCA, No. 4, April, pp.308-318.

_____ (1977c): "Electrostatic Precipitation of Fly Ash", JAPCA, No. 1, January, pp.15-21.

CHAPTER 3

LITERATURE REVIEW ON SELECTIVE PRECIPITATION

3.1 Variables Affecting Solid-Solid Segregation in ESP's

The variables which may possibly affect the segregation of solid species in electrostatic precipitators are of two types: those which affect the behaviour of the particles prior to precipitation, and those which affect it after dust collection at the plates.

Figure 3.1 shows the interactive nature of the relevant variables which may affect the segregation process. Although the complexity of the interactions is enormous, it may be said that all variables which selectively affect either the charge or the reentrainment of the dust particles will produce some degree of solid-solid segregation.

The segregation of solids in ESP's is the enrichment of some component(s) (relative to the other component(s) present in the flue gas), in the dust collected by the precipitator. Since a necessary condition is the existence of different solid species in the flue dust, two important particle variables to be considered are dielectric constant and particle size. The range of dielectric constants for materials present in flue systems may be from about two to one hundred or more, but the effect of dielectric constant (K) on the charge acquired by the particles is felt through the factor $(\frac{K}{K+2})$, and hence it is greatly reduced. It may become important under certain condi-

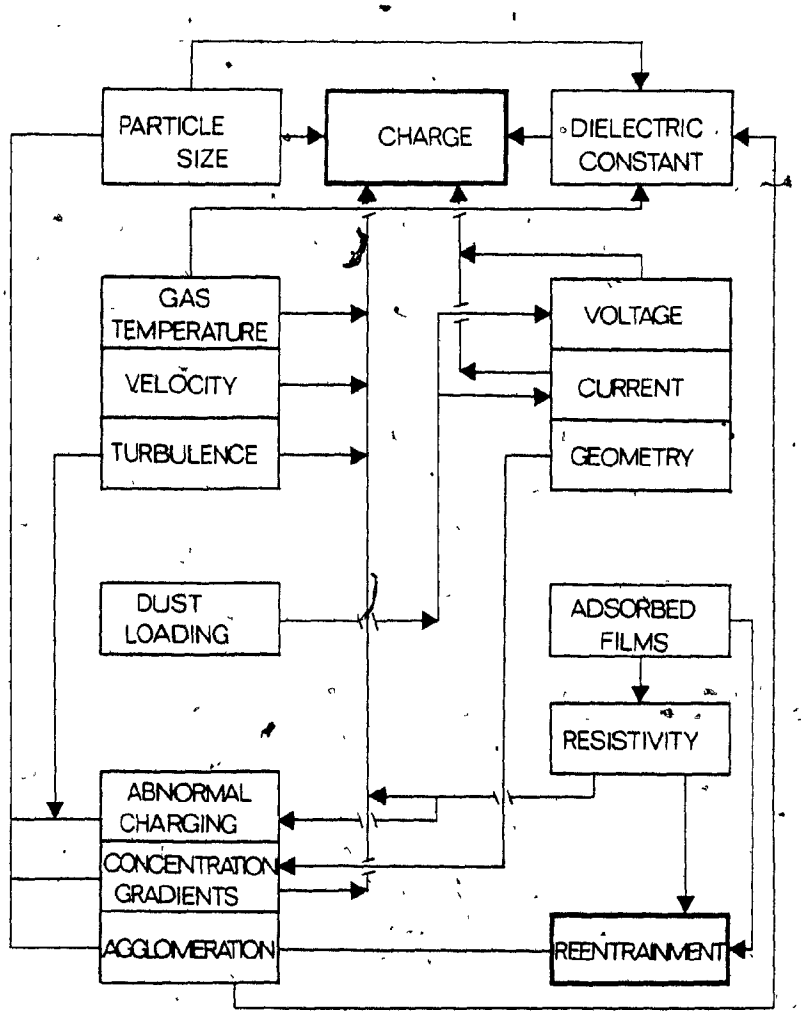


Figure 3.1 Systems approach for variables which may affect separation

tions, and in this case higher permittivity materials will be preferentially collected.

Since particle sizes available in flue dusts at the inlet of ESP's may cover a range from about 0.1-100 μm in diameter, it is likely that segregation by size may occur if different species are preferentially concentrated in different particle sizes. If the particles are larger than 1-2 μm in diameter, ion bombardment is the dominant charging mechanism, and the charge acquired by the particles is proportional to the square of particle diameter. The particle migration velocity is then approximately proportional to particle diameter, and larger particles should be preferentially collected.

When diffusion charging is the dominant mechanism, the migration velocity increases with decreasing particle size. In the intermediate range of particle diameters ($0.2 < D < 1\text{-}2$ μm) where both charging mechanisms are important, a minimum in migration velocity should be expected at a specific particle size, depending on particular conditions of temperature, pressure and electric field. This has been experimentally verified by McCain et al. (1975) and White (1977a).

Reentrainment of the collected particles depends on both the mechanical (intrinsic) and corona forces of adhesion. The interparticle forces are greatly affected by moisture or adsorbed films, while the corona forces are largely controlled by the bulk resistivity of the precipitated dust.

In order to understand the extent to which particle size, dielectric constant and adhesion are responsible for observed solid-solid segregation in ESP's, the major instances of observed segregation are now examined.

3.2 Observed Solid-Solid Segregation in ESP's

3.2.1 Power Plants

The ESP's collecting fly ash from industrial power generation stations account for about 60% of total ESP installed capacity (Pettersen, 1980). This includes collection of fly ash from both coal and oil fired industrial boilers, but by far the major application is in coal fired boilers.

The recent trend towards research on the environmental impact of trace metals has produced some information relevant to the segregation of solids from power plant ESP's.

Typical bulk analyses of fly ash from coal fired boilers collected in ESP's are given by Bickelhaupt (1974,1975), Eisele et al. (1979), Furr et al. (1977), Lee et al. (1973,1975), Oglesby et al. (1970), Smith et al. (1979) and White (1977b), and for samples collected downstream of ESP's by Lee et al. (1973,1975) and Ondov et al. (1978). Although wide variations are observed with samples provenient from different coals, typical major elements are Al, Fe and Si, while typical minor elements are Ti, Mg, Mn, S, Ni, Cu, unburned C and the alkalines Na and K.

The alumina content of fly ash ($\sim$ 15-30% Al_2O_3) is considered by Eisele et al. (1979) as a possible alternative for

the extraction of metallurgical-grade alumina, and by Mehrotra et al. (1979) as a source of aluminium and titanium.

The bitumen residue of the Athabasca tar sands is being considered as an alternate fuel for industrial boilers. The elements Ni, V and Ti are concentrated in the ash produced by the combustion of the bitumen fraction, as discussed by Sirianni et al. (1972), Stemerowicz et al. (1975) and Vezina et al. (1965).

Cheng et al. (1976) show that there are important differences between the particulates emitted from fuel oil or coal fired boilers. On a bulk composition, the element V seems to be a major component of fuel oil ash. High contents of V ($\sim$ 10%) are reported by Dinneli et al. (1979) for fuel oil ash.

The microscopic characterization and the mechanisms of formation of particulates from power plants have been the object of studies by Carpenter et al. (1980), Cheng et al. (1976), Fisher et al. (1976), Parungo et al. (1978) and Smith et al. (1979). These studies show that the more volatile components are concentrated in the submicron range, where there is a large uniformity of elemental composition from particle to particle. The more refractory elements are concentrated on the coarser fractions, with a larger heterogeneity of elemental composition.

The size-composition dependence of fly ash is quantitatively reported by Lee et al. (1973,1975), Parungo et al. (1978) and Smith et al. (1979). Figure 3.2, from the data of Lee et al. (1975) shows that large differences can occur for particle size distributions of various metallic components of

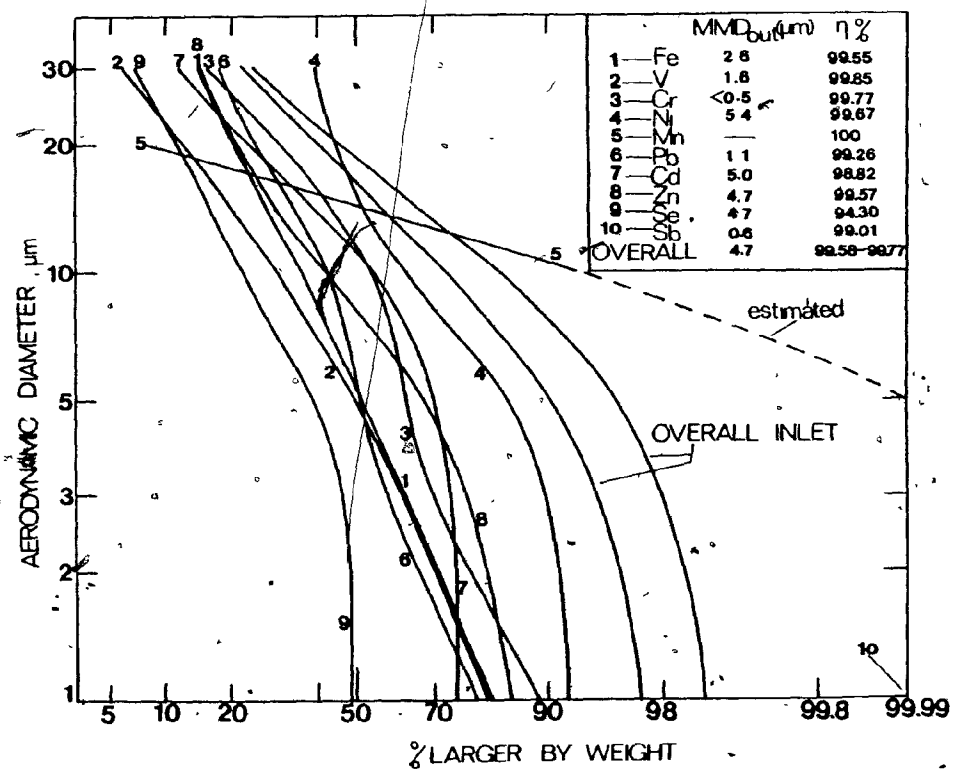


Figure 3.2 Inlet distribution (and outlet MMD) to ESP from coal fired power plant, Lee et al. (1975)

coal ash at the inlet of an ESP. Also shown in this figure are the mean mass aerodynamic diameters of the various elemental distributions at the outlet of the ESP, as well as the elemental collection efficiencies. By comparing the inlet and outlet distributions, all except Se (and possibly Sb) show a substantial reduction of mean size when passing through the ESP. The element Se shows both a substantial increase in mean size and a lower collection efficiency than the other elements. No explanation is given by Lee et al. (1975) for this phenomenon. Neglecting this element, there is a slight increase in collection efficiency with particle size, but the correlation is very poor. This could be due to the experimental error in distinguishing between efficiencies which vary by less than 1%, or due to the fact that factors other than differences in particle size are contributing to the observed differences in elemental efficiencies.

It is important to notice the very high overall efficiency, (≈ 99.7%) reported by Lee et al. (1975) for this particular ESP. In this case, the elemental efficiencies are also very high, and the segregation based on the overall ESP length is very poor. On the other hand, the particles emitted may be enriched in one (or more) components, and this may be an important consideration for environmental impact. For recovery purposes, though, the observed segregation based on global ESP length is of no practical significance. This is not to say that segregation along the ESP length did not occur to any significant extent, but unfortunately these data are not available.

Dalmon et al. (1971) conducted experiments on the collection efficiency of a low resistivity ($\sim 10^5$ Ohmm) coal fly ash, as a function of additive (SO_3 and $(NH_4)_2\ SO_4$) concentration in the ash, in a tubular-type laboratory ESP. The particular ash used by Dalmon et al. (1971) had a very high carbon content ($\sim$ 33%) and low overall collection efficiencies resulted due to the poor collection of the carbon fraction. Figure 3.3 shows the pronounced effect of additive addition in increasing the collection efficiency of the carbon fraction, while only slightly increasing that of the ash fraction. According to Dalmon et al. (1971), the additives increased interparticle adhesion, thereby preventing reentrainment of the carbon (lower resistivity) fraction. In this particular case, a substantial segregation between the carbon and ash fractions is observed for the untreated ash; this decreases drastically when the reentrainment of the carbon fraction is prevented. Since the resistivity of the additive $(NH_4)_2SO_4$ in powder form is larger than that of the bulk ash ($\sim 10^5$ Ohmm), it is possible that the resistivity of the carbon fraction might have increased substantially with the additive addition, thereby also contributing to a decrease in reentrainment.

3.2.2 Iron and Steel Industry

ESP's used for the control of air pollution in the ferrous industries account for about 10% of total ESP installed capacity (Pettersen, 1980). Information relative to the bulk size distributions and chemical composition for the various

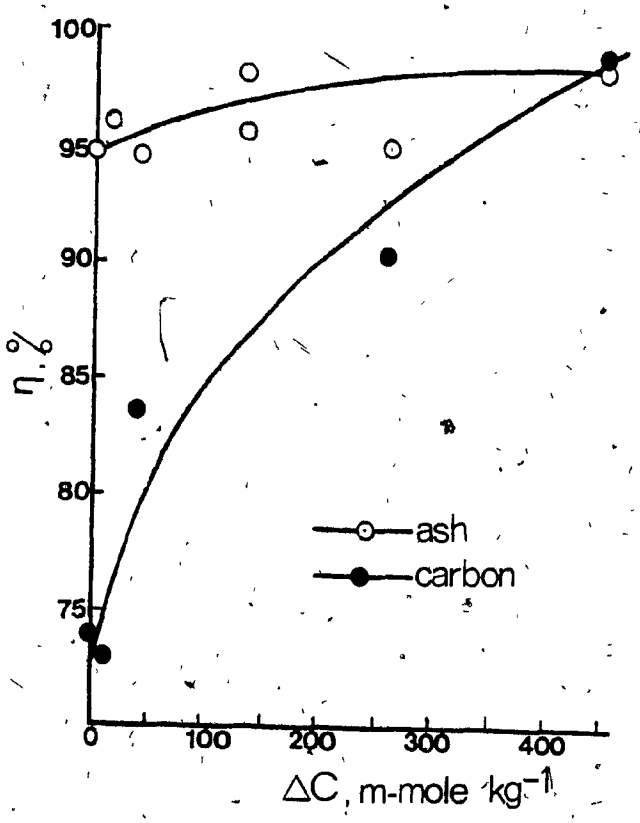


Figure 3.3 Relation between ESP efficiency and increase in additive (SO_3 or $(NH_4)_2 SO_4$) ion concentration in ash, Dalmon et al. (1971)

effluents of this industry is given by Oglesby et al. (1970) and Steiner (1976). Basically, the gaseous effluents are very rich in iron oxides, with other metallic elements being Al, Cr, Zn, Pb, Mg and Mn. Although the iron content of the dusts collected in ESP's is high, recycling these dusts to the blast furnaces (used to produce pig iron from the smelting of iron ore with charcoal, coke or raw coal) may be objectionable, due to the presence of impurities. Oglesby et al. (1970) give the case of dust collected from ESP's downstream of blast and open hearth furnaces (used to produce steel from solid pig iron provenient from the blast furnace), which is not recycled to the blast furnace due to contamination by Pb and Zn. The particulates collected in ESP's from open hearth furnaces are very rich in iron oxides, typically between 60-96%, which is equivalent to a good iron ore, and thus a loss is incurred by not recycling the precipitated dust. This corresponds to about 6-11 Kg/ton (steel) for open hearth emissions and 14-150 Kg/ton (pig iron) for blast furnace emissions. Two other types of furnaces used in making steel from cast iron or steel scrap, the basic oxygen type and the electric arc type, also emit sizable amounts of iron rich particulates, respectively about 7-30 Kg/ton (steel) and 5-25 Kg/ton (steel).

The size composition dependence of emissions from the iron and steel industries is reported by Lee et al. (1975) for an electric arc furnace, and is given in Fig. 3.4. Comparison of these data with those from a coal fired power plant (Fig. 3.2) shows a substantial difference in elemental distribution

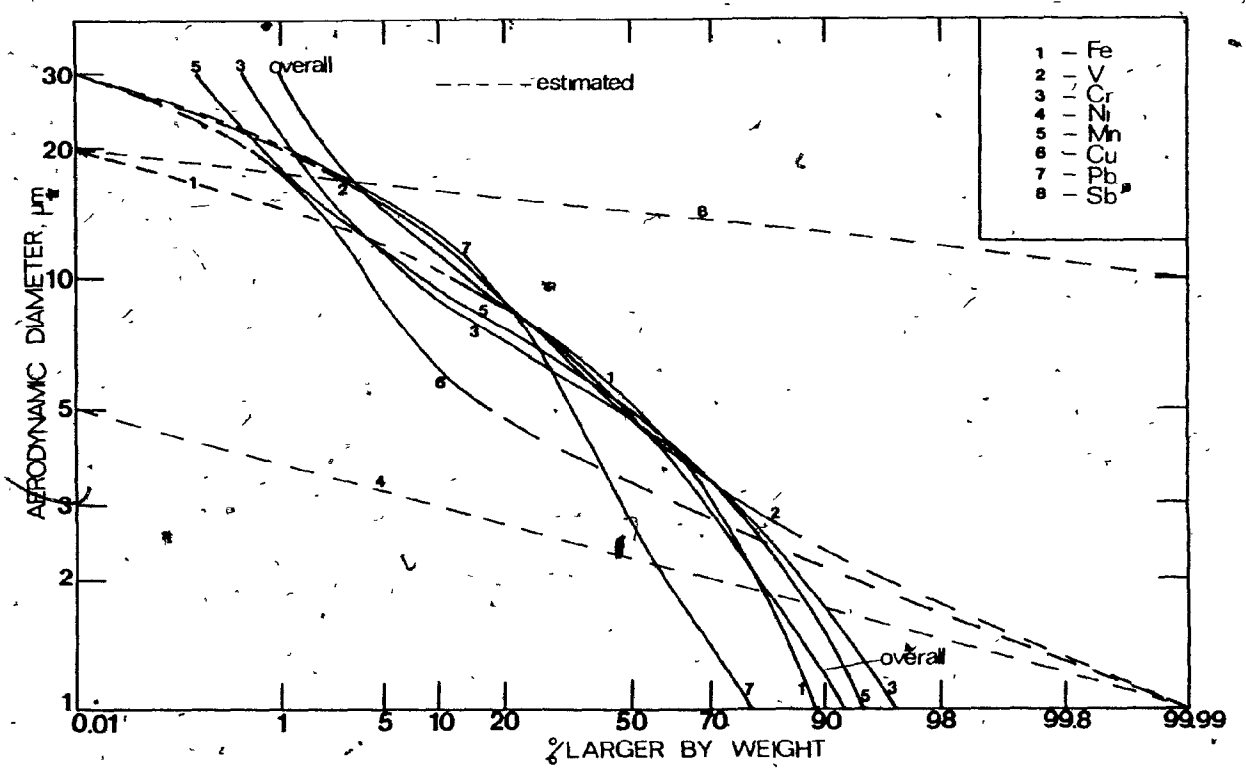


Figure 3.4 – Inlet distribution to baghouse from electric arc furnace, Lee et al. (1975)

with respect to particle size. With the exception of Sb and Ni, the other metals are much more uniformly distributed with respect to size in the emissions from the electric arc furnace. Segregation by an ESP due to size differences is more likely to occur for the power plant emissions. Since the electric arc furnace was equipped with a baghouse, no information is available for elemental efficiencies from an ESP.

Maczek et al. (1980) report the recovery of Zn and Pb (as oxides) by an ESP from dust collected by baghouses installed in electric-arc steelmaking furnaces. A typical enrichment in concentration of 2.5 in (Zn + Pb) was achieved; enrichment is the ratio of concentration of (Zn + Pb) collected in the ESP to the concentration of these metals in the electric furnace dust. It is not known whether any appreciable segregation occurred in the ESP for these two metals.

More complete information is available for ESP's collecting particulate emissions from open hearth and blast furnaces. Jacko et al. (1976) measured both global and elemental efficiencies for a number of trace metals emitted from an open hearth furnace, as a function of particle size; the results relevant to metal segregation by the ESP are shown in Fig. 3.5. It is interesting to note a minimum in collection efficiency around 5-7 μm diameter, with magnitude depending on the particular element. The presence of a minimum in collection efficiency near 5 μm diameter is thought to be peculiar to ESP's, and is attributed by Jacko et al. (1976) to agglomeration of the charged particles leaving the ESP. As discussed in Chapter 2, other

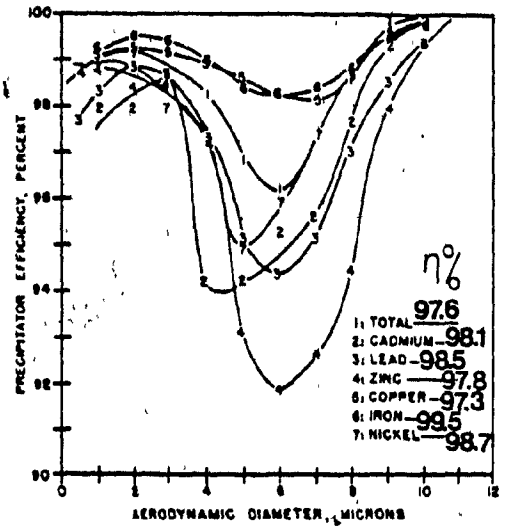


Figure 3.5 ESP elemental collection efficiencies of trace metals emitted from open hearth furnace, Jacko et al. (1976)

causes might produce the observed minima.

The variation in collection efficiencies for the various metals analysed is larger than in the power plant case (Fig. 3.2, excluding the peculiar behaviour of Se), but the observed metal segregation in the collected dust is small and probably without practical significance. On the other hand, the emission factors (from the ESP) for the various metals are quite different, which may be of environmental concern. Jacko et al. (1976) do not provide data on the elemental particle size distributions.

Vernigor (1965) studied the preferential deposition of constituents of blast furnace dust in electrostatic precipitators, considering the size range of 9-15 μm for the precipitated dust and lower than 9 μm for dust escaping collection. Figure 3.6 shows the collection efficiencies of the respective components, as a function of atomic number of the metal (or metalloid), which is the independent variable correlated by Vernigor. Also shown are the data for metals of Jacko et al. (1976). The inclusion of Al among the metalloids weakens the correlation proposed by Vernigor and no correlation is observed for the data of Jacko et al. (1976). Also, Vernigor made no attempt to correlate the observed behaviour with the fundamental theory of electrostatic precipitation. Chemical analysis of the collected dust and of the dust at the ESP outlet revealed that Fe and Cu were concentrated in the collected dust, while Ca, Mg, S, P and Zn were concentrated at the outlet. Little or no change was observed for Si, Al and Mn.

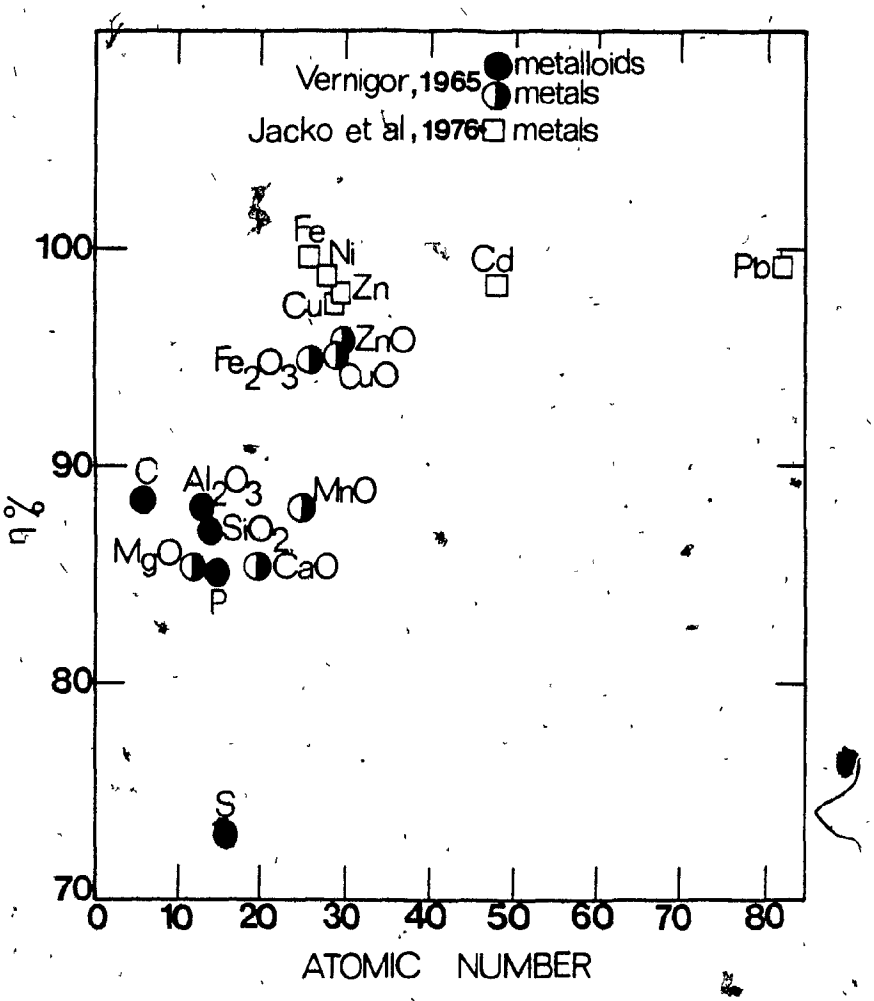


Figure 3.6 Relation between ESP efficiency and atomic number, from the data of Jacko et al. (1976) and Vernigor (1965)

Oglesby et al. (1970) report the following dust analysis for a blast furnace electrostatic precipitator:

TABLE 3.1

Oglesby et al. (1970)

Partial Composition of Samples from a Blast Furnace ESP, %

Material	Before the ESP	In the ESP	After the ESP
Fe_2O_3	14.40	19.30	8.64
Al_2O_3	6.91	15.58	6.70
MnO	2.16	1.10	1.49
CaO	6.36	7.12	4.68
MgO	8.04	9.90	9.28
ZnO	1.20	0.90	1.20
K_2O	20.90	2.70	22.40
Na_2O	9.25	1.55	9.75

These results show that Fe_2O_3 and Al_2O_3 concentrate in the ESP catch, while the alkalis K_2O and Na_2O concentrate in the outlet stream. Smaller effects are observed for the other components. Except for the elements Fe and Zn, there is no correlation between the trends presented in Table 3.1 and the experimental results of Vernigor (1965).

3.2.3 Cement Industry

The ESP's controlling atmospheric emissions from cement plants correspond to about 10% of total ESP installed capacity (Pettersen, 1980). Recovery of dust from cement kilns

is important because it contains a large amount of materials of the same composition as the kiln feed, which according to Oglesby et al. (1970) is about 41% CaO, 19% SiO_2, 10% Fe_2O_3, 10% (K_2O + MgO + Na_2O) and the balance are volatiles or combustibles. Due to a limitation in the alkali content in the kiln, the total amount of dust collected in the ESP cannot be recycled to the kiln, because raw materials usually fed to the kiln contain more alkali than is allowed in the finished clinker. These alkalis vaporize in the kiln but condense downstream in the colder ESP.

Oglesby et al. (1970) report that there is a fractionating effect of the ESP, which tends to concentrate the alkali-bearing constituents downstream from the other cement constituents. This effect permits a higher recycling to the kiln of the dust collected in the ESP, while maintaining an acceptable level of alkalis at the kiln feed.

Because the mechanism of vaporization followed by condensation usually forms very fine particles, and as the alkalis are more volatile than the other components, it is probable that size segregation is the main mechanism of preferential dust collection by ESP's operating in cement kilns. No quantitative data could be found to substantiate this hypothesis.

3.2.4 Pulp and Paper Industry

The ESP's collecting emissions from this industry correspond to about 7% of total ESP installed capacity (Pettersen,

1980). The recycling of dust collected in ESP's downstream of the recovery boiler (Kraft process) is an important economic factor in the pulp and paper industry (Oglesby et al., 1970). The recovered dust is returned to the process without further purification, and no segregation is reported for this industry.

3.2.5 Non-Ferrous Metals Industry

The ESP's installed for emission control in non-ferrous industries represent about 7% of total ESP installed capacity (Pettersen, 1980). The importance of materials recovery and a review of extraction techniques of aluminium, copper, zinc, lead, tin, precious metals, titanium and refractory metals is given by Moore (1978).

3.2.5.1 Zinc and Lead Smelters

The emissions from these industries are not well described in the literature. Data from Eatough et al. (1979), Jacko et al. (1975) and Oglesby et al. (1970) indicate emissions rich in Pb and Zn, with minor metallic elements Fe, Cd, Cu, Au and Ag, and various other trace elements. A typical trace metal segregation by size is given by Jacko et al. (1975) for particulate emissions from a zinc production facility, and is shown in Fig. 3.7, demonstrating that in this particular case the more volatile elements Pb, Zn and Cd are concentrated in the finer fraction while the more refractory Cu is evenly distributed with particle size. No information could be found on component segregation in ESP's controlling emissions from zinc or lead smelters.

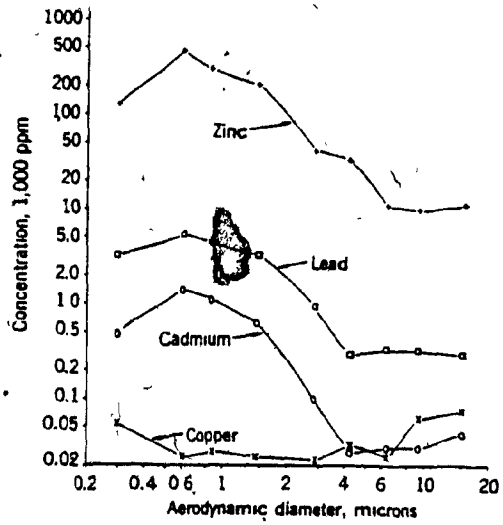


Figure 3.7 Particle size segregation of metals, vertical retort combustion stack, Jacko et al. (1975)

3.2.5.2 Aluminium Production

Some limited information is available on emission characterization and segregation observed in ESP's collecting fumes from aluminium potlines. Hanna et al. (1972) report that emissions from Soderberg reduction cells show segregation of particulate fluorides, which are concentrated in the larger particles. Specifically, the mean mass diameters of the overall emission and the particulate fluorides were 5.5 and 13 μm respectively. A similar size segregation was explored by Bohm et al. (1976) to purify the alumina used as feed in the reduction cells, using ESP's. The impurities are mainly Fe, Ti, P, V, Zn and Ga, which cannot be recycled to the reduction cells, which concentrate on the finer fraction of the emitted alumina.

The selective precipitation of the alumina fractions allows a better recovery of Al_2O_3 (used as feed to the reduction cells) and both solid and gaseous fluorides, the latter being adsorbed by the alumina in appropriate units (the recovery of fluorides is important from the point of view of pollution control). The finer alumina fraction, which is collected in the ESP's downstream of the coarser fraction, and which is enriched in the contaminants may then be disposed of, without affecting the contaminant level in the reduction cells.

Table 3.2, from Bohm et al. (1976) shows the ratio of concentrations for the listed impurities of the removed (fine fraction) to recycled (coarse fraction) of the precipitated alumina.

TABLE 3.2

Bohm et al. (1976)

Ratio of Concentrations of Fine-to-Coarse Fractions of Precipitated Al_2O_3

Fe	Si	Ti	P	V	Zn	Ga
2.1	1.1	3.4	2.2	3.2	0.9	1.3

With the exception of Zn, all the impurities are concentrated in the finer fraction. Unfortunately, no information is given on the elemental size distributions at the ESP inlet, nor on the size distributions of typical coarse and fine fractions.

Bakke (1975) reports different collection efficiencies from hydrocarbons and solid particles emitted from Soderberg potlines, in an irrigated ESP. Figure 3.8, taken from Bakke's data, shows the difference in ESP collection efficiencies between the tar and solid fractions, at different values of specific collection area (ratio of collection area to actual volumetric flow of gas through the ESP). It can be seen that a significant segregation occurs at high gas velocities (low values of SCA); this is reduced as the gas velocity decreases. Since both collection efficiencies of tars and solid particles increase with a decrease in air velocity, the segregation increased with a decrease in collection efficiencies.

Bakke (1975) attributes the segregation to two simultaneous contributions: the very low dielectric constant ($\sim$ 2) and the small size of the tar particles ($\sim$ 0.1 μm), as compared

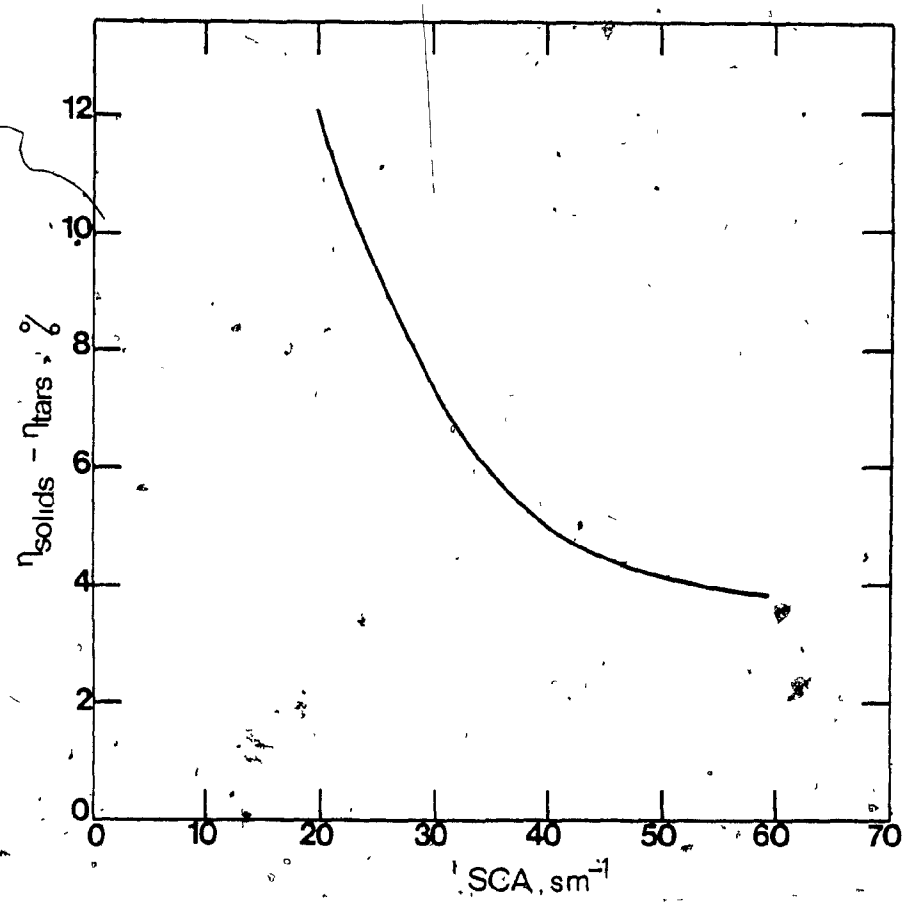


Figure 3.8 Segregation of solids from tars in aluminium production, from the data of Bakke (1975)

to the solid particles.

3.2.5.3 Copper Smelters

Information on the chemical composition of emissions from copper smelters is available in Davis et al. (1979), Eatough et al. (1980), Oglesby et al. (1970) and Tayler (1976). In general, these emissions are rich in Fe, Cu, Zn, Pb and Cd, with various other minor constituents, like As, Bi, Ag and Au.

The analysis of size and composition of a copper reverberatory furnace and converter flue dusts, both before and after collection by ESP's was obtained by Tayler (1976). This author fractionated collected samples into two size classes: those below 1 μm diameter and those larger than this size. Chemical analysis showed that these size fractions corresponded to different chemical compositions, the coarser fraction consisting of the more refractory elements, while the more volatile elements were concentrated in the submicron fraction. Tayler (1976) attributed the existence of chemical-size segregation to different mechanisms of particle formation. The coarser fraction was most probably caused by disruption of the melt by gas bubbles or mechanical stirring, while the finer fraction was probably formed by condensation in the gas stream.

Table 3.3 shows the main composition of the converter flue dusts, with simultaneous sampling at inlet and outlet of the ESP.

TABLE 3.3

Tayler (1976)

Composition of Copper Converter Flue Dust

Size (μm)	Percent by Weight					
	As	Bi	Cu	Fe	Pb	Zn
> 1						
Before ESP	8.8	1.6	12.6	6.3	13.5	2.3
After ESP	11.5	2.9	4.5	0.8	38.6	5.8
< 1						
Before ESP	27.8	3.3	0.7	0.2	31.7	4.0
After ESP	20.5	4.4	0.9	0.7	41.4	4.6
Both Size Fractions						
Before ESP	22.0	2.8	4.4	2.1	26.1	3.5
After ESP	16.1	3.7	2.7	0.7	40.0	5.1

The results for the reverberatory furnace flue dust are similar, but because sampling was not simultaneously performed at the inlet and outlet of the ESP, the values are not strictly comparable. Apart from the size segregation mentioned before, the dust at the ESP outlet is enriched in Bi, Pb and Zn. From the data in Table 3.3, the fraction above 1 μm corresponds to 30% of the collected dust prior to the ESP, and to 49% after the ESP. Tayler (1976) suggested that agglomeration of the fine dust occurred within the ESP..

Very similar results on size-composition fractionation were obtained by Davis et al. (1979) for flue dusts from copper converter and reactor systems, but these authors also analysed the dust precipitated along the ESP's lengths. The analysis

included size fractionation of samples collected before, in and after the ESP's; chemical and morphological characterization of the different size fractions; and electrical bulk resistivity determination for the different size fractions.

With respect to possible segregation observed in the ESP's, the following important conclusions can be made:

- No major bulk resistivity variation with particle size was observed, and measurements of resistivity did not correlate with major elemental composition.
- Segregation of solid species was observed in both converter and reactor ESP's. This is shown in Table 3.4, where it is clear that Pb, Zn and Cd show an increase in concentration from inlet to outlet of the ESP, while Cu shows a decrease (all analyses reported in Table 3.4 are coincidental for each ESP).
- Experimental runs performed with a pilot-plant ESP showed no correlation between global efficiency and chemical composition of the precipitated dust.
- Qualitative and semi-quantitative techniques applied to samples collected at the ESP inlet revealed no substantial difference between the different size fractions for each particular system.
- Semi-quantitative techniques applied to samples collected in the ESP's hoppers revealed that the reactor catch fine fraction was enriched in Pb and Zn and had a lower content in Cu than the coarser fraction. Similar effects were obtained for the

converter catch.

TABLE 3.4

Davis et al. (1979)

Partial Composition of Reactor and Converter Catches

	Reactor	Pb	Zn	Cu	Cd
Gas Flow ↓	Hopper A	17.96	4.14	23.12	4.76
	Hopper B	24.08	6.14	13.28	6.14
	Hopper C	30.18	6.84	6.12	7.98
	Converter				
Gas Flow ↓	Hopper A	18.3	5.7	26.3	0.64
	Hopper B	31.1	10.9	10.9	1.10
	Hopper C	35.5	10.8	8.7	1.28

Due to the unavailability of elemental particle size distributions at the inlet of the ESP's and elemental collection efficiencies from both the data of Davis et al. (1979) and Tayler (1976), it is difficult to access the mechanism under which metal segregation did occur. Since bulk resistivities were all above about 10^8 Ohmm and no correlation with chemical composition was observed by Davis et al. (1979), segregation by selective reentrainment is not probable. On the other hand, semi-quantitative analyses of size fractionated samples of the reactor and converter catches, reported by Davis et al. (1979), seem to indicate that Cu is concentrated in the coarser fractions, while Pb and Zn are concentrated in the fines. These results are in good agreement with those of Tayler (1976), who also showed

quantitatively that Cu is concentrated in the coarser fractions at the inlet of the examined ESP's.

The enrichment of Cu in the first hoppers and further decrease in Cu concentration in the direction of gas flow, as shown in Table 3.4, together with the above discussion, seems to point to preferential collection for the coarser fractions, i.e., elemental segregation produced by size segregation. The possible effect of dielectric constant is not known.

3.2.6 Municipal Incinerators

Incinerated sewage sludge can be a valuable resource for metals such as Cu, Al and Zn, and even in some cases Ag and Au, as reported by Gabler (1979). Due to the increased trend in the use of ESP's to control emissions from municipal incinerators (Oglesby et al., 1970), it is possible that data will be obtained on segregation in this application in the future. At the moment, however, no such information is available.

3.2.7 Petroleum Industry

ESP's are widely used to recover catalysts from discharge streams of catalyst regenerators, produced by attrition of the catalyst (Oglesby et al., 1979). No segregation is reported in this application.

3.3 Quantitative Definition of Segregation (Separation)

The observed segregations are apparent in Section 3.2, because different concentrations of the constituents of a flue

dust are reported prior to, in and after ESP's, because different collection efficiencies are measured for different components or because different elements are segregated in the direction of gas flow for the dust catch of the ESP.

Whatever the causes might be for the observed segregation, it is important that this segregation be quantified by a precise number (or set of numbers), so that different processes and/or operating parameters may be compared.

Economic factors usually influence the choice of a segregation process, but they are not a measure of the physical excellence of the segregation; they will not be considered here.

There is no uniform consensus on how to express the effectiveness of a segregation process. Gaudin (1939) states that in the non-ferrous metals industry, recovery (R) of metal is the most important criterion, with grade of concentrate (R_1) next and ratio of concentration (R_2) third. In iron beneficiation, ratio of concentration is typically more important, with grade of concentrate next and recovery third. In coal washing, the yield (reciprocal of the ratio of concentration) is the most important criterion. For any component present in the feed (F) with mass fraction (f), in the concentrate (C) with mass fraction (c) and in the tailings (T = F - C) with mass fraction ($t = \frac{Ff-Cc}{T}$), the following applies:

$$R = Cc/Ff \qquad (3.1)$$

$$R_1 = c/f \qquad (3.2)$$

$$R_2 = F/C \qquad (3.3)$$

where only two of the relations are independent, since $R_1 = RR_2$. Usually, any two of the above relations are employed together in expressing the effectiveness of the segregation process. The disadvantage of this method is in trying to compare the effectiveness of segregation in two processes (or tests) where both recovery and grade (for example) are not simultaneously larger (or smaller).

The selectivity index (SI) is one method that overcomes this problem. It is defined as the geometric mean of the relative recoveries and relative rejections (recoveries in the tailings) of two metals, minerals or groups of metals or minerals. Thus,

$$SI = \sqrt{\frac{R_i(1-R_j)}{R_j(1-R_i)}} \qquad (3.4)$$

where (i,j) are the two components under consideration. For zero segregation, SI = 1, while for complete segregation SI $\to \infty$.

Schultz (1970) reviewed the available concepts on effectiveness of segregation. The basic requirements for the expression of a separation efficiency are that it:

1) be a function of feed and products amounts and concentrations;

2) be applicable to any physical separation, including multicomponent systems;

3) be a single number between zero (no separation) up to 100% (complete separation);

4) be independent of the physical process;

5) be the same whether it is calculated as the separation of (i) from (j) or of (j) from (i), in a binary system; and

6) be physically meaningful.

The selectivity index proposed by Gaudin (1939) is not a true separation efficiency, since the ideal separation is not finite, and hence comparison of the observed separation with the ideal separation cannot be performed on a precise basis. According to Schulz (1970), the only measure of the effectiveness of a segregation process which obeys all six criteria listed above is the separation efficiency (E_s), defined as:

$$E_{s_{ij}} = R_i - R_j \qquad (3.5)$$

This definition is recommended by Akhtar (1974), for simple separation operations.

The criteria (1,3,4 and 5) are automatically obeyed. To adapt Eq. 3.5 to multicomponent systems, two different approaches are possible. In the first case, components (i) and (j) are considered the only components in the feed, i.e., $E_{s_{ij}}$ will express the separation of (i) from (j) in the presence of

each other and of unspecified materials. In the second approach, component (i) is considered as the valuable component (not necessarily an economic consideration), and the separation will be between (i) and the waste component (j), i.e.:

$$E_{s_{ij}} = R_i - \frac{C}{F}\left(\frac{\Sigma c_j}{\Sigma f_j}\right)_{j \neq i} \qquad (3.6)$$

which may be written as:

$$E_{s_{ij}} = R_i - \frac{\sum_{j \neq i} R_j f_j}{1 - f_i} \qquad (3.7)$$

The second term in the rhs of Eqs. 3.6 and 3.7 represents the weighted average recovery of the waste products ($j \neq i$) in the concentrate.

Condition no. 6, of physical meaningfulness, can be shown to apply to both Eqs. 3.5 and 3.6 (or 3.7), in that ($E_{s_{ij}}$) represents the proportion of feed material that undergoes complete (100%) separation. The same does not apply to a multi-component system if only one waste component ($j = 1$) is considered at a time.

With respect to the application to ESP's, the recovery of component (i) is simply its collection efficiency, and the recovery of the waste components ($j \neq i$) is the weighted average of their collection efficiencies. If then (E_{c_i}) represents the cumulative collection efficiency (with ESP length) of component (i), then:

$$E_{s_{ij}} = E_{c_i} - \frac{\sum_{j \neq i} E_{c_j} f_j}{1 - f_i} \qquad (3.8)$$

The cumulative collection efficiency of component (i) up to length (L_k) is related to the non-cumulative collection efficiency of component (i), $(\eta_{c_i})_{\Delta L_k}$ in the length interval $\Delta L_k = L_k - L_{k-1}$ by:

$$(\eta_{c_i})_{\Delta L_k} \sim (E_{c_i})_{L_k} - (E_{c_i})_{L_{k-1}} \qquad (3.9)$$

where the index (k) runs from one to the number of length increments into which the ESP has been divided. Non-cumulative separation efficiencies may be calculated, based on non-cumulative collections, by:

$$\eta_{s_{ij}} = \eta_{c_i} - \frac{\sum_{j \neq i} \eta_{c_j} f_j}{1 - f_i} \qquad (3.10)$$

for any particular length increment in the ESP.

In Eqs. 3.9 and 3.10, the non-cumulative collection efficiencies are based on 100% at the inlet of the ESP, and as such do not represent the true collection efficiencies of the length increments.

3.4 Conclusions

Solid-solid segregation has been observed in some situations where ESP's are used. The advantageous use of the observed segregation has been reported by Oglesby et al. (1970) for the cement industry and by Bohm (1976) for the aluminium

reduction industry. Elemental efficiencies of trace metals have been measured by Lee et al. (1975) for power plant ESP's, and correlation with elemental size distributions is poor. Dalmon et al. (1971) observed fly ash segregation due to selective reentrainment of the carbon fraction.

Elemental ESP efficiencies have been measured in the iron and steel industries by Jacko et al. (1976) and Vernigor (1965). This last author proposed a correlation of component efficiency with elemental atomic number, but the data of Jacko et al. (1976) do not support such a conclusion. The data reported by Oglesby et al. (1970) are also in general disagreement with the data of Vernigor (1965).

Component segregation in the aluminium industry is reported by Bakke (1975) and Bohm et al. (1976) for emissions from Soderberg cells. Data of Hanna et al. (1972) support the hypothesis that the observed segregation is caused by size-composition differentiation. Bakke (1975) also attributed the observed segregation between tars and solids to a large difference in relative dielectric constants. This author showed that increased velocities increased the observed segregation.

Component segregation in copper smelter flue dusts collected by ESP's is reported by Davis et al. (1979) and Tayler (1976), who consider as most likely hypothesis the preferential size collection by the ESP of materials which exhibit a different size-composition relationship.

The observation of a differential size-composition relationship is probably due to different mechanisms of formation. This was studied for power plants flue dusts by Carpenter et al. (1980), Cheng et al. (1976), Fisher et al. (1976), Parungo et al. (1978) and Smith et al. (1979), and for copper smelters by Davis et al. (1979) and Eatough et al. (1980). These last authors also characterized particulate emissions from lead smelters.

To the author's knowledge, no systematic laboratory study has been performed on the variables which may affect the selective collection of solid species by precipitators.

Finally, a definition of separation efficiency proposed by Schulz (1970) was presented and chosen as the basic quantitative measure of segregation for the present work. It represents the fraction of inlet dust which undergoes a complete separation.

REFERENCES

Akthar, S. (1974): "Mathematical Representation of Separation Operations and Separation Efficiency", Trans. AIME, Society of Mining Engineers, 255, March, pp.22-26.

Bakke, E. (1975): "Wet Electrostatic Precipitators for Control of Submicron Particles", JAPCA, 25, No. 2, February, pp.163-167.

Bickelhaupt, R. (1974): "Electrical Volume Conduction in Fly Ash", JAPCA, 24, No. 3, March, pp.251-255.

_____ (1975): "Surface Resistivity and the Chemical Composition of Fly Ash", JAPCA, 25, No. 2, February, pp.148-152.

Bohm, E.; Reh, L., Sparwald, V. and Winkhaus, G. (1976): "Removal of Impurities in Aluminum Smelter Dry Gas Cleaning using the Vaw/Lurgi Process", Light Metals, 2, pp.509-524.

Carpenter, R.L.; Clark, R.D. and Su, Y.F. (1980): "Fly Ash from Electrostatic Precipitators: Characterization of Large Spheres", JAPCA, 30, No. 6, June, pp.679-681.

Cheng, R.J.; Mohnen, V.A.; Shen, T.T.; Current, M. and Hudson, J.B. (1976): "Characterization of Particulates from Power Plants", JAPCA, 26, No. 8, August, pp.787-790.

Dalmon, J. and Tidy, D. (1971): "The Cohesive Properties of Fly Ash in Electrostatic Precipitation", Atmospheric Environment, 6, Pergamon Press, pp.81-92.

Davis, H.J.; Kerbyson, J.D. and Nethersole, D.C. (1979): "Study of Factors Affecting the Electrostatic Precipitation Efficiency of Particulates in Nonferrous Smelter Gases", Contract ØSS77-00216, prepared by Centre de Recherche Noranda for Environment Canada, July.

Dinneli, G.; Borgatti, C. and Rea, M. (1979): "Electrostatic Precipitation Tests with Fuel Oil Ash", JAPCA, 29, No. 3, March, pp.243-248.

Eatough, D.J.; Eatough, N.L.; Hill, M.W.; Mangelson, N.F.; Ryder, J.; Lee, D.H.; Meisenheimer, R.G. and Fisher, J.W. (1979): "The Chemical Composition of Smelter Flue Dusts", Atmospheric Environment, 13, Pergamon Press, pp.489-506.

Eisele, J.A. and Bauer, D.J. (1979): "Evaluation of Technology for the Recovery of Metallurgical-Grade Alumina from Coal Ash", IC-8791, Bureau of Mines Information Circular, U.S. Dept. of the Interior.

Fisher, G.L.; Chang, D.P.Y. and Brummer, M. (1976): "Fly Ash Collected from Electrostatic Precipitators: Microcrystalline Structures and the Mystery of the Spheres", Science, 192, No. 4239; May, pp.553-555.

Furr, A.K.; Parkinson, T.F.; Hinrichs, R.A.; Van Campen, D.R.; Bache, C.A.; Gutenman, W.H.; St. John, L.E. Jr.; Pakkala, I.S. and Lisk, D.J. (1977): "A National Survey of Elements and Radioactivity in Fly Ashes", Env. Science & Technology, 11, No. 13, December, pp.1194-1201.

Gabler, R.C. Jr. (1979): "Incinerated Municipal Sewage Sludge as a Potential Secondary Resource for Metals and Phosphorus", RI 8390, Bureau of Mines Report of Investigations, U.S. Dept. of the Interior.

Gaudin, A.M. (1939): "Principles of Mineral Dressing", McGraw-Hill Book Co., Inc., New York and London, pp.231-238.

Hanna, T.R. and Pilat, M.J. (1972): "Size Distribution of Particulates Emitted from a Horizontal Spike Soderberg Aluminum Reduction Cell", JAPCA, 22, No. 7, July, pp.533-536.

Jacko, R.B.; Neuendorf, D.W. and Yost, K.J. (1975): "Trace-Metal Samples Collected in the Front and Back Halves of the EPA Stack Sampling Train", JAPCA, 25, No. 10, October, pp.1058-1059.

_____; Neuendorf, D.W. and Faure, F. (1976): "Fractional Collection Efficiency of Electrostatic Precipitator for Open Hearth Furnace Trace Metal Emissions", Env. Science and Technology, 10, No. 10, October, pp.1002-1005.

Lee, R.E. Jr. and von Lehmden, D.J. (1973): "Trace Metal Pollution in the Environment", JAPCA, 23, No. 10, October, pp.853-857.

_____; Crist, H.L.; Riley, A.E. and MacLeod, K.E. (1975): "Concentration and Size of Trace Metal Emissions from a Power Plant, a Steel Plant and a Cotton Gin", Env. Science and Technology, 9, No. 7, July, pp.643-647.

Maczek, H. and Kola, R. (1980): "Recovery of Zinc and Lead from Electric-Furnace Steelmaking Dust at Berzelius", J. of Metals, January, pp.53-58.

McCain, J.D.; Gooch, J.P. and Smith, W.B. (1975): "Results of Field Measurements of Industrial Particulate Sources and Electrostatic Precipitator Performance", JAPCA, 25, No. 2, February, pp.117-121.

Mehrotra, A.K.; Bishnoi, P.R. and Svrcek, W.Y. (1979): "Metal Recovery from Coal Ash Via Chlorination - A Thermodynamic Study", CJChE, 57, April, pp.225-232.

Moore, J.J. (1978): "Recycling of Nonferrous Metals", Int. Metals Reviews, No. 5, review 234, pp.241-264.

Oglesby, S. and Nichols, G.B. (1970): "A Manual of Electrostatic Precipitation Technology, part II. Application Areas", Southern Research Institute, NTIS PB-196 381.

Ondov, J.M.; Ragaini, R.C. and Biermann, A.H. (1978): "Elemental Particle Size Emissions from Coal-Fired Power Plants: Use of an Inertial Cascade Impactor", Atmospheric Environment, 12, Pergamon Press, pp.1175-1185.

Parungo, F.; Ackerman, E.; Proulx, H. and Pueschel, R. (1978): "Nucleation Properties of Fly Ash in a Coal-Fired Power-Plant Plume", Atmospheric Environment, 12, Pergamon Press, pp.929-935.

Pettersen, H.H. (1980): "New Trends in Electrostatic Precipitation: Wide Duct Spacing, Precharging, Pulse Energization", IEEE Cement Industry Technical Conference, Toronto, May.

Schulz, N.F. (1970): "Separation Efficiency", Trans. AIME, Society of Mining Engineers, 247, March, pp.81-87.

Sirianni, G.V. and Viens, G.E. (1972): Pyrometallurgical Recovery of Nickel and Vanadium from Athabascan Tar Sands Fly Ash", Dept. of Energy, Mines and Resources (Ottawa), Mines Branch Investigation Report IR 72-23, June 7.

Smith, D.R.; Campbell, J.A. and Nielson, K.K. (1979): "Characterization and Formation of Submicron Particles in Coal-Fired Plants", Atmospheric Environment, 13, Pergamon Press, pp.607-617.

Steiner, B.A. (1976): "Air Pollution Control in the Iron and Steel Industry", Int. Metals Reviews, No. 209, September, pp.171-192.

Stemerowicz, A.; Bruce, R.W.; Sirianni, G.V. and Viens, G.E. (1975): "The Recovery of Vanadium and Nickel from Athabasca Tar Sands Fly Ash", CIM Annual Western Meeting, Edmonton, Alberta, Mineral Sciences Laboratory Report MRP/MSL/75/230 (OP+J), Canada Centre for Mineral and Energy Technology".

Tayler, P.L. (1976): "Characterization of Copper Smelter Flue Dust", APCA 69th Annual Meeting, Portland, Oregon, #76-24.3, June 27-July 1.

Vernigor, P.I. (1965): "Deposition of Constituents of Blast Furnace Dust in Electrostatic Precipitators", Stal (in English), No. 11, pp.937-938.

Vezina, J.A. and Gow, W.A. (1965): "The Preparation of Commercial-Grade Vanadium Pentoxide from Boiler Ely Ash", Mines Branch Technical Bulletin TB-63, Department of Mines and Technical Surveys, Ottawa.

White, H.J. (1977a): "Electrostatic Precipitation of Fly Ash", JAPCA, 27, No. 3, March, pp.206-217.

____ (1977b): "Electrostatic Precipitation of Fly Ash", JAPCA, 27, No. 2, February, pp.114-120.

CHAPTER 4

EXPERIMENTAL EQUIPMENT

4.1 General Description

A single-stage, single gas passage laboratory-scale wire and plate ESP was designed and built for the purpose of experimentally studying the selective collection of solid species by electrostatic precipitation.

Figure 4.1 is a schematic diagram of the experimental facility. The air is drawn in from the laboratory. Its flow rate is controlled by a gate valve in the blower intake line, and measured by a Venturi meter. The blower is a Canada Fans (size 6 CI, SS wheel) with a 3 HP, 1750 rmp motor. The blower itself operates at 3590 rpm delivering 0.32 Nm^3s^{-1} against 20 cm (w.g.). The Venturi meter was designed according to ASME specifications, with the difference that it was fabricated from sheet metal instead of machined. Details of the Venturi meter calibration can be found in Appendix B.

From the Venturi meter, the air passes through a flexible hose which minimizes the propagation of vibrations from the blower to the ESP. The transition from the piping system to the ESP is made through a divergent channel provided with adjustable guiding vanes for flow straightening. These are rectangular since the flue transition is only diverging in one direction. All system piping is made of alu-

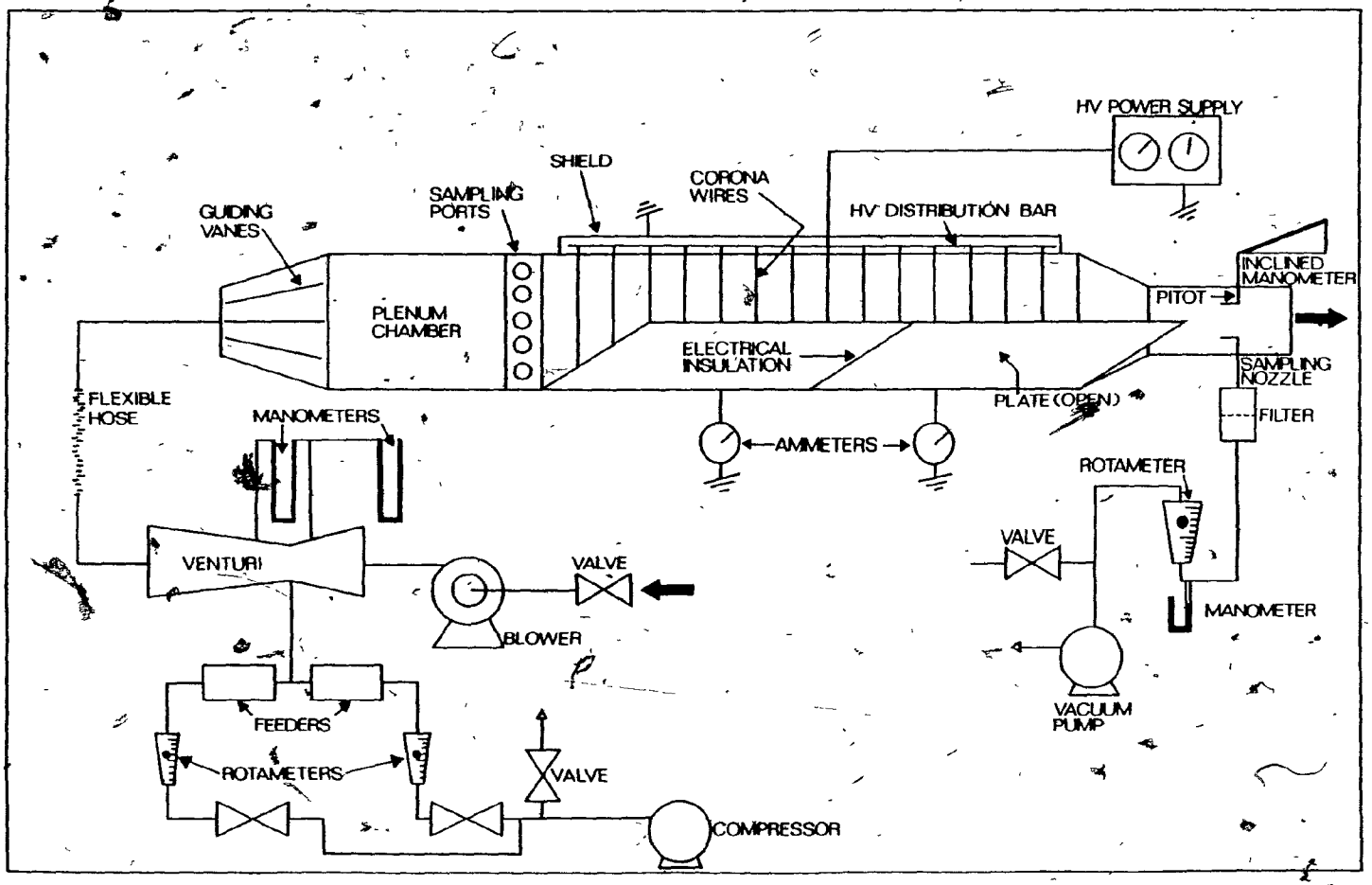


Figure 4.1 Schematic diagram of experimental facility

minium having an inside diameter of 15.4cm. The diverging section is 46 cm long, with a 15° included angle and is also made of aluminium. From the diverging section the air enters an aluminium plenum chamber 1.22m long, used to allow for some flow development prior to the ESP inlet.

A 36 long plexiglas section containing a series of sampling ports is located in the ESP before the first discharge electrode. The ports can be used for dust sampling as well as air velocity and turbulence measurements. The plexiglass allows visual observation and isolates the ESP electrically from the duct work.

The ESP itself consists of two stainless steel plates in series, on each side. The first plates are 1.25 m long and the second plates are 1.28 m long, giving a total ESP length of 2.53 m. The plate-to-plate spacing is 16.2 cm, which is also approximately the width of both the diverging section and the plenum chamber. The 15 corona wires are made of stainless steel and are spaced 15.2 cm apart. Although plate-to-plate spacings in full-size ESP's may be as large as 30 cm or more, the plate-to-plate spacing used is characteristic of ESP's collecting fumes from copper converters (White, 1963). The lower value chosen has the advantages of lower capacity requirements for the air blower and probably a smaller effect of transverse dust concentration gradients (Gooch et al., 1976 a, b).

The corona wires are straight and cylindrical with a diameter of 1.57 mm. Although other wire geometries may be superior from the point of view of electrical characteristics (Jarzebski et al., 1974 and Pyle et al., 1980), the cylindrical geometry is widely used and is amenable to a more rigorous mathematical treatment. The wires and collection plates are 38.5 cm high, which gives a total collection area of 1.95 m^2 and a total discharge wire length of 5.78 m.

The fact that the wire-to-wire and the plate-to-plate spacings have similar values is not critical, and other wire-to-wire spacings could be chosen which would produce similar electrical characteristics.

The ESP is energized by a single DC power supply (Del Electronics Corp, model 40 TC 5-1, Mount Vernon, N.Y.) with continuously variable output secondary voltage from 0-40 KV and a maximum rated secondary current of 5 mA. The power supply is protected from current transients with a fixed overload relay at 120% of rated current. The secondary voltage-current values are indicated at the power supply control board, with meters of precision ± 0.8 KV and ± 0.1 mA.

To energize the ESP, the power supply is connected to an aluminium high voltage distribution bar, 1.27 cm in diameter, which is in turn connected with small steel springs to the corona wires. The wires pass through small holes in the plexiglas top of the ESP, and are rigidly held at the ESP

plexiglass bottom by welded washers. The small steel springs are used to allow some movement of the corona wires without deforming them. This is advantageous in preventing wire damage when cleaning the ESP. To prevent gas sneakage through the electrified region above the discharge wires, the small steel springs are encapsulated in silicone sealed plexiglas cylinders. Figure 4.2 is a schematic diagram of the discharge wire support system.

The welded washers which hold the discharge wires to the ESP bottom are coated with anticorona lacquer (TV Corona Dope, GC Electronics, Illinois) to prevent sparking; an additional layer of plexiglass electrically insulates the discharge wires from the grounded supporting table.

The ESP was designed so that the collection plates could be opened on hinges fastened to the supporting table. This design eliminates the collection hoppers and with them the non-ideal effects due to gas sneakage and dust reentrainment from the hoppers. The plates are closed with 12 "C" clamps on each side, evenly spaced, and sealed with a 7 cm width flexible tape to prevent air leakage.

The plate height and length are similar to one of the laboratory-scale ESP's used by Gooch et al (1976, a, b) at Southern Research Institute, Alabama, USA. They found good agreement between the measured and theoretical values of electric field intensity and potential distribution for

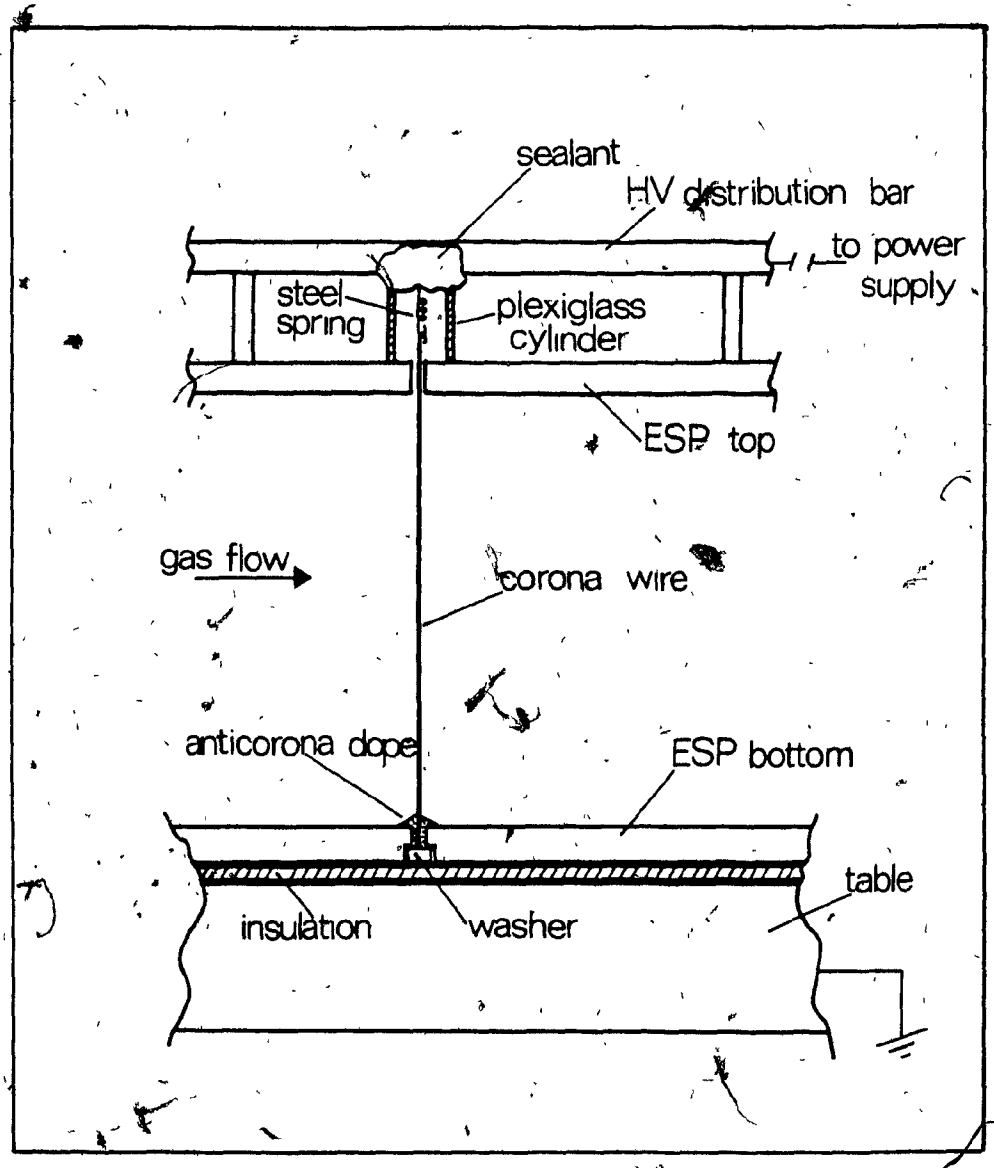


Figure 4.2 Schematic diagram of corona wire support system

such a small scale; this indicates that the electric field distribution is not noticeably distorted by end effects. This was further confirmed by McDonald (1978).

The plates are cleaned by brushing the precipitated dust into an appropriate receiver. Since the ESP is not provided with a rapping system, reentrainment due to rapping is avoided. The collection plates are flat; although other geometries of collection plates are used in industrial ESP's with the objective of reducing dust reentrainment, flat plates have better electrical characteristics and are amenable to a more precise mathematical treatment.

In order to observe any significant change in current density along the ESP length, the collection plates are grounded through two separate milliammeters. The first ammeter reads current from a single 1.25 m long plate with a precision of ± 0.02 mA while the second receives current from the corresponding plate at the other side of the ESP plus the two 1.28 m long plates, with a precision of ± 0.05 mA. This arrangement allows the measurement of current along the ESP length while simultaneously giving a value of the total current which can be compared with the secondary current from the power supply control board.

At the end of the ESP an aluminium converging section 31 cm long provides the transition between the rectangular cross-section ESP to a circular cross-section outlet

aluminium piping of 15.4cm i.d.. A straight section 85 cm in length is located before the sampling port, and additional piping vents the air to the outside atmosphere. Figure 4.3 is a photograph of the interior of the laboratory-scale ESP.

4.2 Electrical Characteristics

The electrical characteristics of the ESP were experimentally determined using laboratory air at room temperature, pressure and humidity. Preliminary investigations showed that the voltage-current curves were a function of gas flow rate. This was due to the effect of increased static pressure in the ESP at the higher flow rates, which tended to buldge the collection plates. The increased plate-to-plate spacing reduced the current for the same applied voltage. The problem was solved by stiffening the plates with steel angles welded parallel to the ESP height.

Figure 4.4 shows a typical characteristic curve obtained at 21°C and 25% relative humidity, where (V) is the applied voltage and (i) is the secondary current read at the power supply control board. Slightly different curves were generated at different relative humidities, which were measured by a sling psychrometer.

The non-ohmic behaviour characteristic of gas discharges can be seen from the curvature of the voltage-current curves. The total current obtained from the milliammeters receiving current from the electrically insulated plates

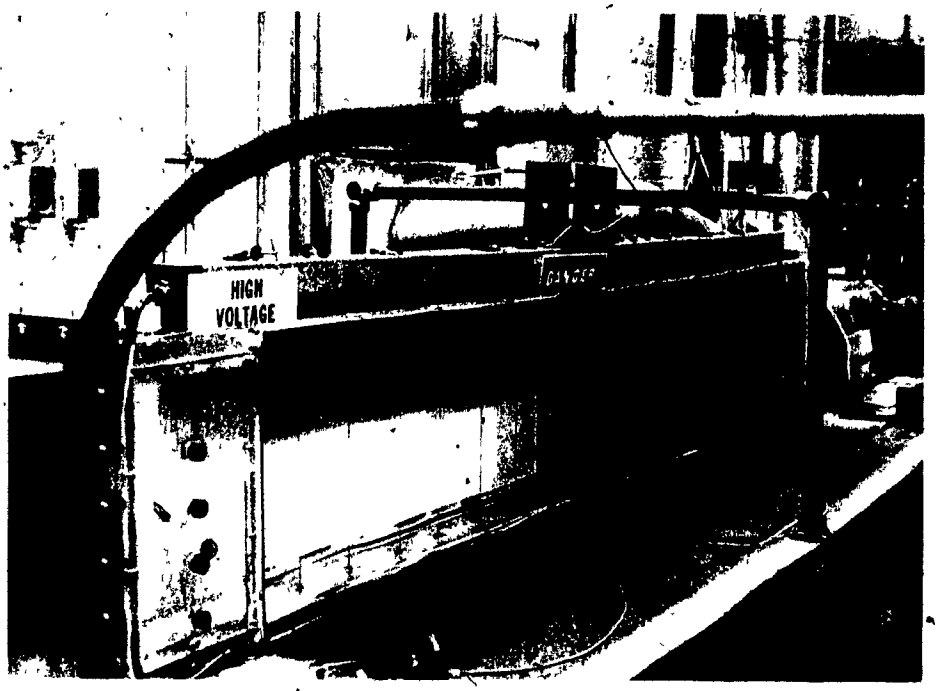


Figure 4.3 Photograph of laboratory-scale ESP

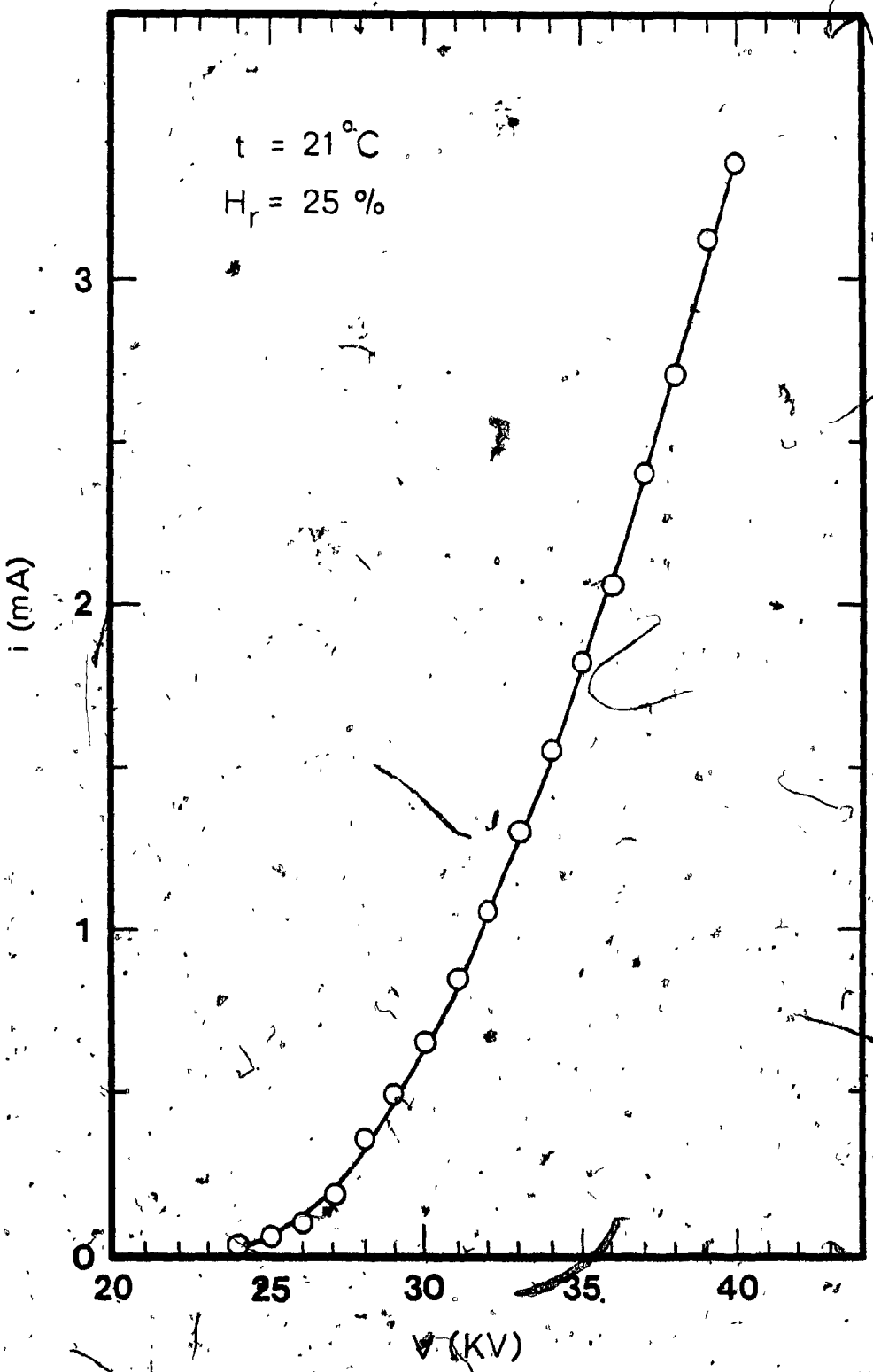


Figure 4.4 Typical clean air voltage-current characteristic, at 21°C and 25% relative humidity

agreed well with the secondary current read at the power supply control board. Also, the current did not vary along the ESP length, as expected with laboratory air, clean plates and a single power supply.

A slight hysteresis effect was observed such that lower currents were obtained if the voltage-current curves were determined by stepping-down the applied voltage. The detailed experimental data obtained are shown in Appendix B, Figures B.1-B.4.

4.3 Gas Flow Characteristics

Air flow rates through the ESP were measured using a Venturi meter of ASME design. The Venturi meter was calibrated by traversing with a pitot tube-inclined micromanometer assembly at the outlet of the ESP. Details of the Venturi calibration can be found in Appendix B, Section B2, Figure B.5.

The calibrated Venturi meter gives information on the total volumetric gas flow through the ESP, but it says nothing about the quality of the gas flow at the ESP itself. It is known (White, 1963, Burton et al, 1975) that a poor velocity distribution at the ESP inlet can be responsible for the lowering of the collection efficiency, due to the non-uniformity of the flow by itself and to the increased reentrainment of the precipitated dust. In order to minimize

the possible deleterious effect of poor gas flow distribution, the expansion from the piping system to the ESP inlet was provided with adjustable guiding vanes. A plenum chamber was also installed upstream of the ESP, to allow for some flow development.

One indication of gas flow quality is the standard deviation of the velocity distribution, normalized to the average air velocity. This may be written as:

$$s^*_v = \sqrt{\frac{\Sigma (v-v_{av})^2}{N-1}} / v_{av} \qquad (4.1)$$

where (s^*v) is the normalized standard deviation, (v) the point velocities and (N) the number of sampled points.

Velocity profiles were determined at the ESP inlet by using both a standard pitot tube-micromanometer assembly and a hot-wire anemometer. The hot-wire anemometer was calibrated using the pitot tube, according to the manufacturer's guidelines (Thermo Systems Inc., 1968), at the center of the channel flow at the ESP inlet.

Preliminary velocity distributions were determined by using the pitot-tube at some sampling points at the inlet of the ESP, without guiding vanes at the inlet expansion and without the plenum chamber. A large improvement in the quality of flow was obtained by including the plenum chamber. Further improvements were obtained by trial-and-error adjus-

tment of the guiding vanes located at the inlet expansion.

More complete velocity profiles were then determined by both pitot and hot-wire traverses at the ESP inlet. Figure 4.5 shows the average velocity profiles obtained with both the pitot tube and the hot-wire anemometer at the ESP inlet, for an average air velocity of 4.8 ms^{-1} as determined from the Venturi meter calibration. The hot-wire results are lower on the average by about 3-4% as compared to the pitot results. This is probably due to the accuracy of the linearization process used in the calibration of the hot-wire anemometer (± 5-6% from 1-3ms^{-1}, < 5% above 3ms^{-1}) and to the fluctuations of the micromanometer readings from the pitot tube.

Also shown are the average velocity profiles obtained with the hot-wire anemometer at an average air velocity of 1.1 ms^{-1}. The coordinate system of Figure 4.5 is centered at the center point of the channel flow at the ESP inlet. This is shown in Appendix B, Figure B.6, and the complete velocity profiles are given in Figures B.7 through B.10.

The standard deviations of the velocity distributions, normalized to the average air velocity were determined to be 4.8% from the pitot tube and 5.8% from the hot-wire measurements, both at the high air flow rate. At the lower flow rate, this value increased to 13.8% using the hot-wire data. Since a value of 10% is considered very good and ac-

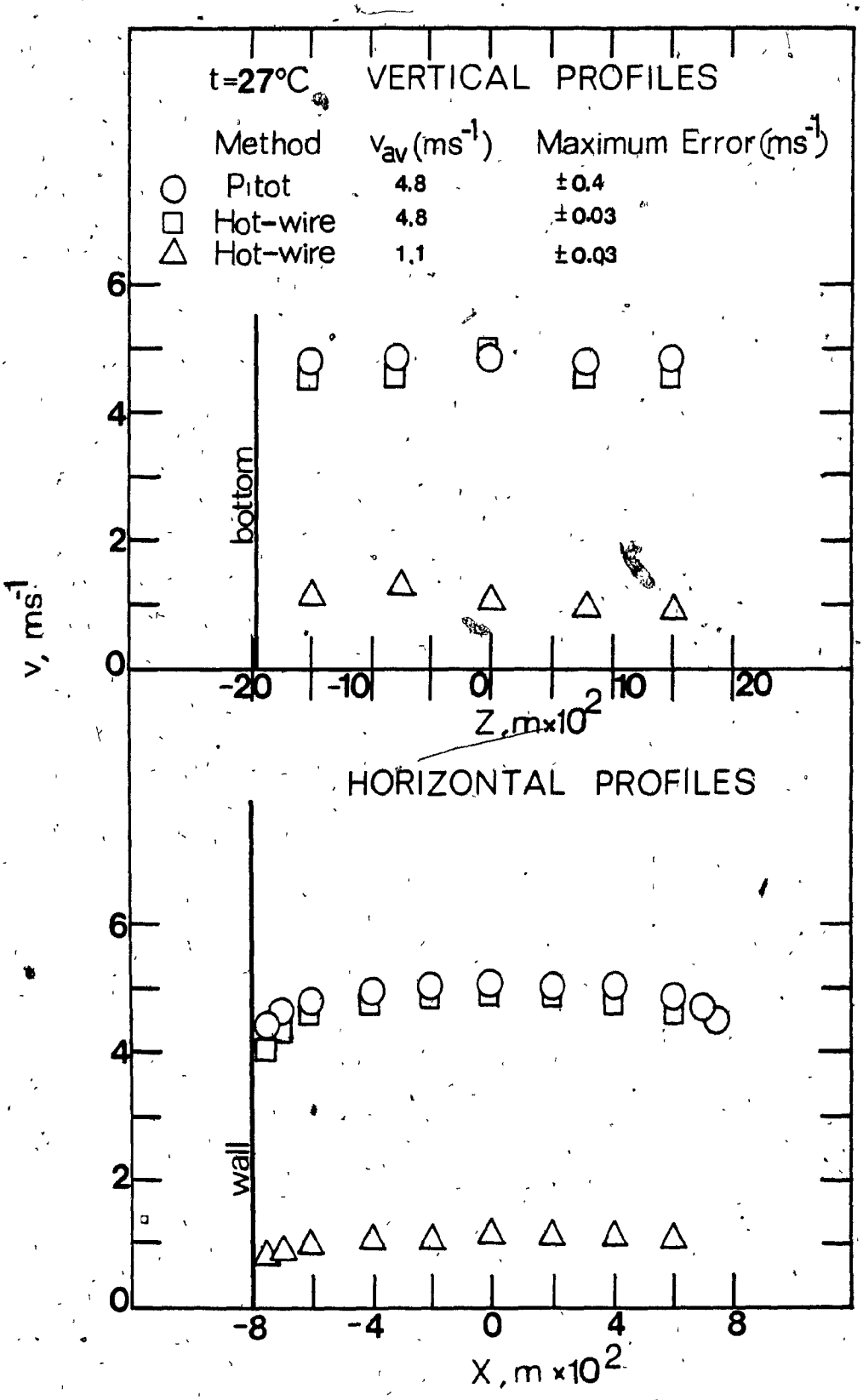


Figure 4.5 Average velocity profiles at the ESP inlet

ceptable values are as high as 25% (Burton et al., 1975; White, 1963), the experimental values obtained were considered satisfactory and no further improvements were attempted.

Turbulence intensities were also measured at the ESP inlet, using the hot-wire anemometer, and the average relative intensities are shown in Figure 4.6. The intensity of turbulence is the energy amplitude of the velocity fluctuations, and was calculated by assuming a unidimensional main flow with isotropic fluctuations of velocity. Then:

$$\tau = \sqrt{\overline{v'^2}}/v = \sqrt{\overline{V'^2}}/V \qquad (4.2)$$

where the rms fluctuations and time averaged voltage values, respectively $\sqrt{V'^2}$ and (V) are direct output data from the hot-wire anemometer readout. In equation 4.2, (τ) is the relative turbulence intensity, $\sqrt{v'^2}$ is the rms fluctuation of velocity and (v) is the time averaged point velocity.

Comparing the velocity and the turbulence profiles, the first are more symmetric,especially in the vertical direction. This may be due to incomplete development of the flow, since the ratio of length to equivalent diameter of the plenum chamber is only about 11. The detailed turbulence profiles can be found in Appendix B, Figures B.11 and B.12.

The turbulence intensities are high, but not uncommon (Gensler, 1968). Such high values of turbulence are

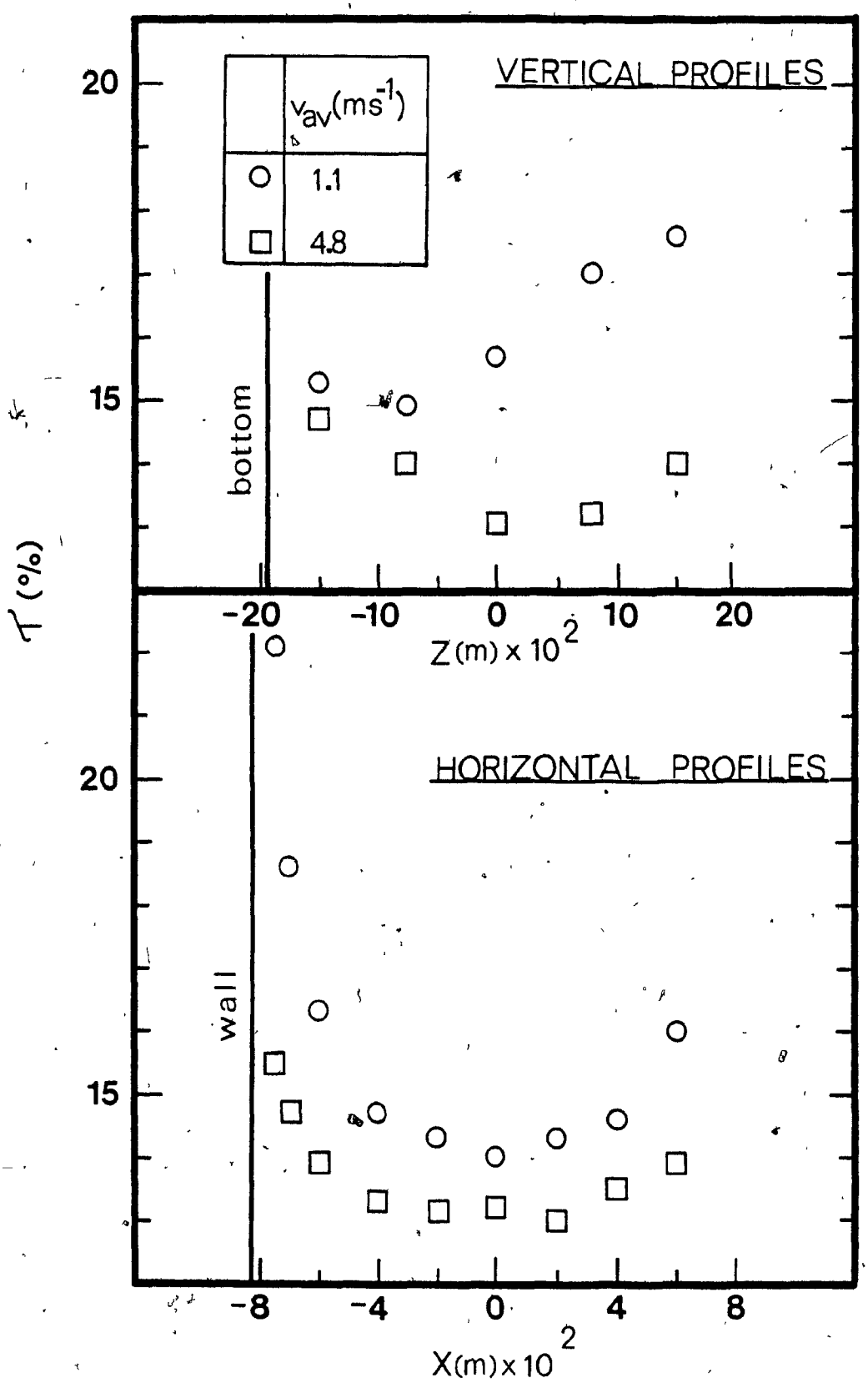


Figure 4.6 Average relative turbulence profiles at the ESP inlet

probably due to the expansion prior to the plenum chamber.

4.4 Particle Generation and Feeding

4.4.1 General Considerations

The generation of solid particles may be broadly classified into dry powder dispersion, atomization of solutions or suspensions and in-situ generation. The first two methods are described by Grassel (1976), Guichard (1976), Liu (1974), Moreno et al. (1976) and Raabe (1976), while in-situ generation of submicron particles (e.g., the use of furnaces and plasmas to produce oxides or other salts) is described by Veale (1972).

One thing is apparent from the reviewed literature, and that is the general difficulty of generating and feeding fine particles (i.e., those below about 5 μm in diameter). For coarser particles, other types of feeders may be used. These are described generically by Thomson (1978), on an industrial scale, although the same principles may apply to smaller-scale feeders.

The atomization of solutions or suspensions has the great disadvantage of very small generation rates; Veale (1972) quotes a rate of about 0.5g per month! The in-situ generation by use of appropriate equipment (high intensity arcs, plasmas and furnaces) with mechanisms of submicron particle formation such as evaporation-condensation (with or without chemical reactions), nucleation, precipitation and thermal decomposition requires

specialized and expensive equipment and considerable operating experience.

The generation of solid particles by dry dispersion of a bulk quantity of the powder was considered to be the best alternative. Several characteristics are desired for a feeding system using the dry dispersion approach. These are:

1) Generation of sufficient amounts of dust such that gravimetric determinations on the sampling filters and on the ESP plates may be performed with sufficient accuracy. There is no specific limit, since an increased experimental time will compensate for a smaller feed rate. It is nevertheless desirable to keep the sampling times within reasonable limits.
2) Uniform generation rates and particle size distributions throughout the entire experimental runs.
3) Minimum effect of static charge due to the dust dispersion and feeding process.
4) Good dispersion characteristics, such that most (or preferably all) of the dust enters the ESP as individual particles.

The extent to which these criteria were met was a strong function of both the type of feeder and the dust to be dispersed. In this research, the particular dusts were ulti-

mately chosen for their important size and/or electrical characteristics. Considerable time and effort was then spent on identifying and obtaining suitable feeders for this work. These are described next.

4.4.2 The Tafa Dust Feeder

A Tafa vibrating dust feeder (Tafa Metallisation Inc., model 104B, N.H.) was used to feed cupric oxide at the Venturi meter throat. This feeder operates by transporting powder up an inclined vibrating ramp at the edge of a dust hopper (Figure 4.7). The feed rates are controlled by the input voltage to the vibrating ramp, and the dust is pneumatically conveyed from a discharge hole at the end of the inclined ramp. It was found that this feeder only operated well with free-flowing powders, such as with the cupric oxide used in this work. All the four criteria required for the feeding were then met.

The Tafa feeder calibration curve for cupric oxide is given in Appendix B, Figure B.14. Smaller feed rates than those shown in Figure B.14 were obtained by partially plugging the discharge hole at the edge of the vibrating ramp.

The operation of the Tafa feeder for non-free-flowing dusts was quite erratic and unsatisfactory.

4.4.3 The Vibrating Screw Feeder

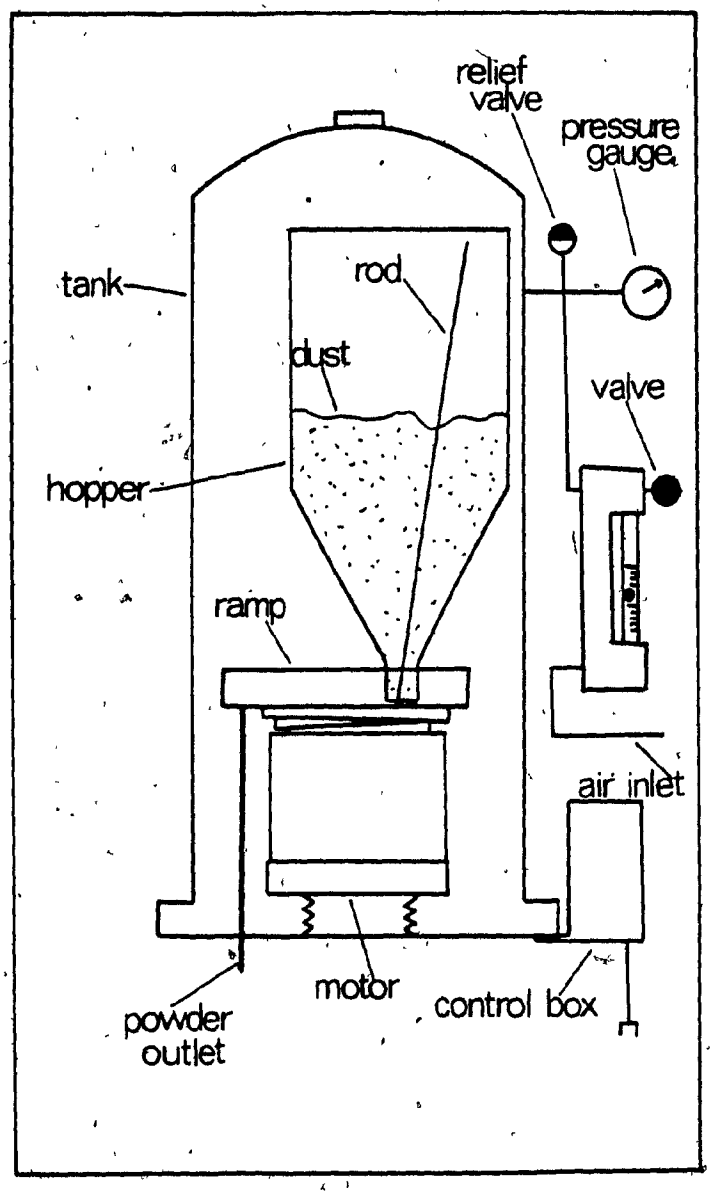


Figure 4.7 Schematic diagram of Tafa dust feeder

A screw feeder was designed and built to feed non-free flowing dusts with particle sizes predominantly larger than 5 μm in diameter, such as the oxides of magnesium and titanium used in this work. The feeder consists of a brass dust reservoir, a screw connected to a variable speed motor and a conveying line. A small vibrator at the base of the dust reservoir prevents bridging of the dust and allows for a more uniform feed rate. The dusts were injected upstream from the Venturi throat.

The dust feed rates from the screw feeder are varied by controlling the screw rotational speed or by changing the screw itself. The feed rates obtained were less uniform than those with the Tafa feeder with cupric oxide, but still adequate as a source of test dust.

Dry compressed air was used as the carrier medium with both the Tafa and screw feeders. Both feeders were grounded and copper conveying lines were used to reduce static charge build-up. Preliminary runs with pure electrostatic fields (i.e., at applied voltages below corona-onset voltage) revealed that the feeders did not impart any significant charge to the dust particles. Samples taken from the outlet of both the Tafa and screw feeders revealed that the feeders did not alter the particle size distributions of the powders used in this work. The relevant data are presented in Chapter 5 and Appendix C.

4.4.4 The Wright Dust Feeder

Both the Tafa and screw feeders were highly unsatisfactory for the feeding of particles predominantly smaller than about 5 μm in diameter, due to very poor dust dispersion characteristics. The tendency of a bulk sample of small particles to agglomerate makes it difficult to redisperse them.

A Wright dust feeder (L. Adams, Minerva Road, London, England) was used to feed both fine alumina and an industrial dust (Chapter 5, Section 5.1) at the Venturi throat. This feeder works by allowing dust to be ground from a packed plug by a scraping blade, at a rate controlled by a constant speed motor and variable gearing mechanism, as shown in Figure 4.8. The dust feed rate is controlled by changing the gearing ratio, the packed plug surface area or bulk density. This last method should be avoided, since a dust which is packed too loosely will produce non-uniform feed rates, while on packing too tightly prevents the scraping blade to operate correctly and feeding may stop.

The Wright dust feeder was operated with 15 $lmin^{-1}$ of dry compressed air, and both feeder and copper conveying lines were grounded to prevent static charge build-up. Preliminary runs with pure electrostatic fields did not reveal any appreciable static charge.

Careful packing of the dust is necessary to pre-

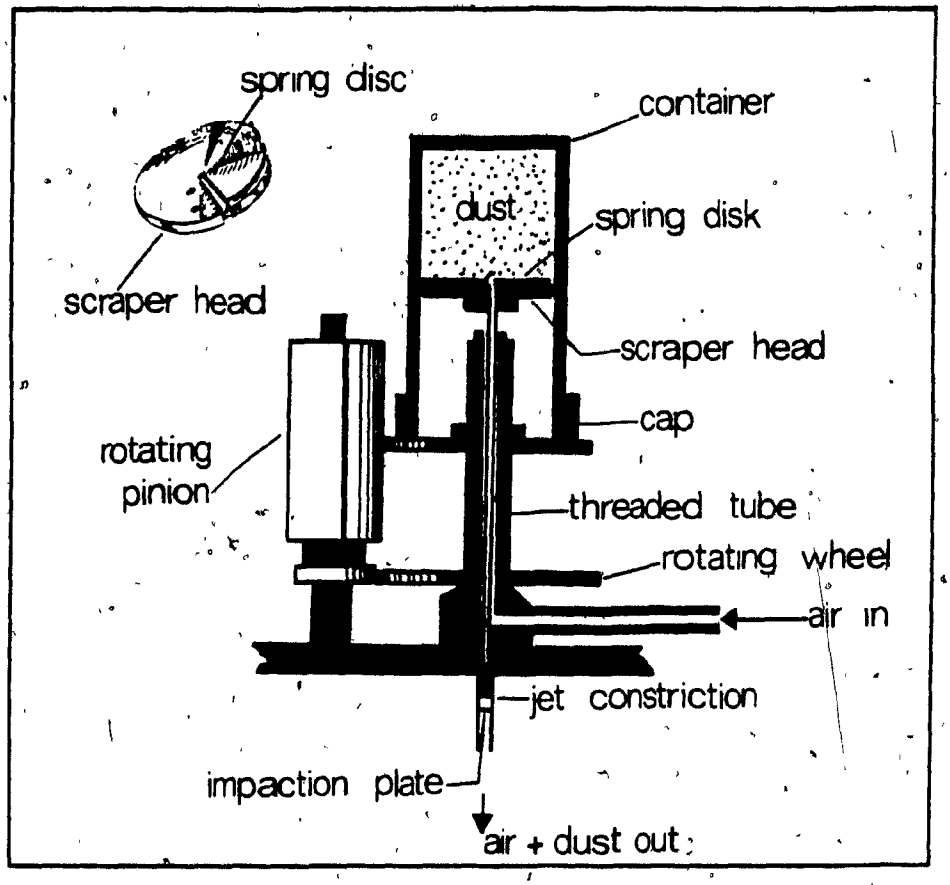


Figure 4.8 Schematic diagram of Wright dust feeder, Wright (1950)

vent excessive dust lamination, and the operating instructions of the feeder should be carefully followed (Adams, 1964). The dust can be packed in two reservoirs. For the present study, the larger reservoir (~ 40 cm^3 of effective volume) was used, since this gives higher flow rates. The optimum packing pressures were found by trial and error to be around 5880 KPa for the fine alumina and 2450 KPa for the industrial dust. The dusts were slowly packed in a hydraulic press.

The air flow rate through the Wright feeder was measured by a rotameter whose calibration curve is given in Appendix B, Figure B.15. The dust scraped off the packed plug is pneumatically conveyed towards an impingement plate which breaks the agglomerates (Figure 4.8).

The uniformity of feed rates was determined by weighing the dust container prior to and after feeding the fine alumina for a known amount of time, and it was found to be 8.5 ± 1.8 g hr^{-1} at the 95% confidence level, for five different feed cycles (a feed cycle comprised drying the alumina overnight at 105°C, packing it at a pressure of 6000 KPa and feeding it with the Wright feeder for one hour). The observed ± 21% variation in feed rates agrees well with the value reported by Wright (1950) for coal dust and sampling times of 1/2 hour.

Visual observation of alumina samples taken isoki-

netically at the ESP inlet showed incomplete dispersion from the Wright feeder. This is further discussed in Chapter 5.

4.4.5 The Fluidized Bed Feeder (FBF)

A FBF similar in design to that of Willeke et al, (1974) but operated with continuous feeding was built and tested under various operating conditions, bed and feed materials, with the purpose of producing submicron particles. The bed was difficult to operate over long periods of time (> 1/2 hr) due to dust accumulation on the bed material or on the bed walls. This occured even with a grounded brass bed and nickel spheres as the bed material , probably due to triboelectric effects (Guichard, 1975). Both TiO_2 (Titanox 2077, Canadian Titanium Pigments, Montreal) and Al_2O_3 (0.3 µm Polishing Alumina, Micrometallurgical Ltd., Toronto) of primary particles below 0.4 µm were tested as feed materials to the FBF. The smaller size distributions at the bed outlet were obtained with low dust feed outputs, typically below 1-1.5g hr^{-1}. Dispersion from the bed was not complete, and very similar results were obtained with the two feed materials.

The particle size distributions obtained from the Wright feeder using the fine alumina were coarser than those obtained at the best operating conditions of the FBF, respectively about 4 and 2.5 µm for the mean mass diameters. A substantial reduction in particle size from the Wright feeder

was achieved by using a minicyclone (Chapter 5 and Appendix C). The particle size distribution of alumina at the ESP inlet was then similar to that obtained at the best operating conditions of the FBF. Since larger and easier to control feed rates could be obtained with the Wright feeder-minicyclone system than with the FBF, the former was preferred.

It should be stressed that both methods failed to produce essentially submicron particles (by weight) at reasonable mass flow rates.

4.5 Safety Precautions

Due to the high voltages of the power supply that energizes the ESP, special attention had to be taken to insure proper and safe operation of the equipment. The ESP and power supply shared a common ground with the building transformer which supplied the primary current to the high-voltage power supply. All ground connections were made via 8 gage stranded copper wire to a common copper bus bar, which then was connected to the ground at the building transformer. The high-voltage aluminium distribution bar was covered with a plexiglas shield, which was in turn covered with grounded sheet metal.

All sampling probes were grounded. The power supply itself is protected from overload currents above 120% of the maximum rated current.

During each experiment, the current measured at the ESP plates was compared to that measured at the power supply. Any difference between the two indicated an uncontrolled current leak through faulty insulation and the experiment was discontinued until the problem was rectified. Common problem points were between the grounded sheet metal at the high-voltage distribution bar and the "C" clamps closing the ESP plates.

REFERENCES

Adams, L. (1964): "The Wright Dust Feeder Mechanism - Instructions for Use", Minerva Road, Chase Estate, London N.W. 10, Issue No. 2, September.

Burton, C.L. and Smith, D.A. (1975): "Precipitator Gas Flow Distribution", JAPCA, 25, No. 2, February, pp.139-143.

Gensler, W.G. (1968): "A Study of Individual Particle Trajectories in Electrostatic Precipitation", Ph.D. Thesis, Carnegie-Mellon University, pp.101,107 and 115.

Gooch, J.P. and McDonald, J.R. (1976a): "Conference on Particle Collection Problems in Converting to Low Sulfur Coals", SRI/EPA Contract 68-02-2114, EPA-600/7-76-016, pp.68-106.

_____ (1976b): "Symposium on Particulate Control in Energy Processes", SRI/EPA Contract 68-02-1318, EPA-600/7-76-010, pp.217-265.

Grassel, E.E. (1976): "Aerosol Generation for Industrial Research and Product Testing", in "Fine Particles", B.Y.H. Liu (ed.), Academic Press, pp.145-172.

Guichard, J.C. (1973): "La Triboelectrisation des Aérosols de Particules Métalliques Générés par un Lit Fluidisé à deux Constituants", Staub-Reinhalt Luft, 33, No. 4, April, pp.169-174 (in French).

_____ (1976): "Aerosol Generation using Fluidized Beds", in "Fine Particles", B.Y.H. Liu (ed.), Academic Press, pp.173-192.

Jarzebski, S. and Chojnowski, M. (1974): "Influence of Shapes of Corona Electrodes on Density of Emission Currents in Electrostatic Dust Collectors", Atmospheric Environment, 8, Pergamon Press, pp.29-40.

Liu, B.Y.H. (1974): "Laboratory Generation of Particulates with Emphasis on Submicron Aerosols", JAPCA, 24, No. 12, December, pp.1170-1172.

McDonald, J.R. (1978): Personal communication, April 12, Southern Research Institute, Alabama.

Moreno, F. and Blann, D. (1976): "Large Flow Rate Redispersion Aerosol Generator", in "Fine Particles", B.Y.H. Liu (ed.), Academic Press, pp.195-218.

Pyle, B.E., Pontius, D.H., Snyder, T.R. and Sparks, L.E. (1980): "Particle Trajectory Studies in a Scale-Model Electrostatic Precipitator", APCA 73rd Annual Meeting, #80-49.2, Montreal, June 22-27.

Raabe, O.G. (1976): "The Generation of Aerosols of Fine Particles", in "Fine Particles", B.Y.H. Liu (ed.), Academic Press, pp.57-110.

Thermo-Systems Inc. (1968): "Hot-Film and Hot-Wire Anemometry: Theory and Application", Bulletin TB5, Thermo-Systems Inc., 2500 Cleveland Avenue North, St. Paul, Minnesota 55113.

Thomson, F.M. (1978): "Smoothing the Flow of Materials through the Plant: Feeders", Chemical Engineering, October, pp.77-87.

Veale, C.R. (1972): "Fine Powders: Preparation, Properties and Uses", Halsted Press Division, John Wiley and Sons, Inc., N.Y.

Willeke, K., Lo, C.S.K. and Whitby, K.T. (1974): "Dispersion Characteristics of a Fluidized Bed", J. Aerosol Science, 5, Pergamon Press, pp.449-455.

Wright, B.M. (1950): "A New Dust-Feed Mechanism", J. of Scientific Instrum., 27, pp.12-15.

CHAPTER 5

CHARACTERIZATION OF POWDERS AND EXPERIMENTAL TECHNIQUES

5.1 Choice of Powders

Powders of pure chemical compounds were chosen as the primary materials for the present work, as this allows for an easier characterization of the powder variables which may affect the precipitation process.

The choice of the pure experimental powders was based on the following criteria:

1) The size distribution at the ESP inlet should be representative of those occurring at the inlet of industrial ESP's.
2) There should be an appreciable difference in electrical properties and/or size distribution between the different powders, since these are the dust properties which may affect the precipitation process.
3) The different chemical species should be amenable to an accurate chemical analysis, when present as a mixture at the ESP inlet.
4) The different powders should be commercially available and inexpensive.
5) The different chemical species should occur in typical industrial dusts collected by full-size ESP's.

6) If possible, the individual particles of the different powders should be distinguishable under an optical microscope.

The pure chemical species used in this work are listed in Table 5.1.

TABLE 5.1

Pure Powders used in Experimental Work

Material	Designation	Colour	Source
CuO	Cupric Oxide	Black	Fisher Scientific Co., Montreal
MgO	Heavy Magnesium Oxide	White	Anachemia Ltd., Montreal
TiO_2	Tam Ceramic Rutile	Brown	Canadian Titanium Pigments Ltd., Montreal
Al_2O_3	0.3 μm Polishing Alumina	White	Micro Metallurgical Ltd., Toronto

Cupric oxide was chosen for its low resistivity (Section 5.6); magnesium and titanium oxides were chosen respectively for their low and high dielectric constants, together with high resistivities (Sections 5.5 and 5.6); alumina was chosen for its small particle size and high resistivity.

The oxides of copper, magnesium and titanium were sieved through a 270 mesh (53 μm) sieve, using a Tyler sieve shaker. During the sieving process, some agglomeration of very fine particles occurred for both the oxides of titanium and magnesium. With magnesium oxide, agglomeration was severe, and

several different lots of powder were tried. The powder finally used was a composite of two different lots (Nos. 81001 and 470626) which were relatively easy to sieve.

Since industrial particulate matter is generally composed of different chemical species belonging to the same individual particles, it was also desired to extend the experimental work to a typical industrial dust. The chosen industrial dust was a composite catch from an ESP collecting dust from a copper reactor at the Noranda smelter, Noranda, Quebec. This dust is very fine, with appreciable contents of lead, zinc, cadmium and copper.

5.2 Dust Sampling

5.2.1 General Considerations

The dust was sampled at both the inlet and outlet of the ESP, with different aims. At the outlet, sampling was always done simultaneously with each experimental run, to acquire information on both dust loading and chemical composition in the exit air. This information was combined with data on the precipitated dust weight and chemical composition and allowed the inlet dust loading and chemical composition to be calculated, and the elemental and global collection efficiencies to be evaluated.

If desired, information could also be obtained on the particle size distribution of the exit dust. Dust collected on the sampling filter at the ESP outlet used for size distribution

analysis was simply shaken off the filter for subsequent redispersion. This is discussed in Section 5.3.2.1.

Sampling at the ESP inlet was not performed to determine global or elemental collection efficiencies. The presence of relatively low air velocities and particle concentration gradients due to sedimentation implied that a complete traverse both in the horizontal and vertical direction would have to be made for each experimental run, to correctly estimate the average dust concentration. This proved to be highly impractical and was not routinely performed. Higher air velocities were obtained at the ESP outlet, and simpler horizontal traverses proved to give reliable dust concentration measurements.

With the larger particles of the oxides of copper, magnesium and titanium, sampling at the ESP inlet was done to determine the degree of dispersion obtained from the powder feeders and examine the presence of dust concentration gradients. With the finer particles of alumina or the Noranda dust, sampling at the ESP inlet was performed to acquire estimates on the global and elemental particle size distributions, and also on the degree of dispersion obtained from the powder feeder.

It is necessary that a representative sample be extracted from the air stream. All sampling done in this work was within the isokinetic guidelines of Oglesby et al. (1978), Orr et al. (1976), Selden (1977) and Smith et al. (1977,1978).

The method proposed by Selden(1977) was used to estimate the sampling errors; these were found to be ±2%

for all conditions used in the present work.

5.2.2 Sampling Trains

5.2.2.1 Outlet Sampling Train

The sampling train at the ESP outlet consisted of an appropriate sampling nozzle (Nutech Corp., Durham, N.C.), a filter holder and appropriate filters (Schleicher and Schuell on-line filter holder), a mercury manometer and rotameter for pressure (vacuum) and flow measurements and a vacuum pump (Gast Manufacturing Corp.) provided with a bleed valve for flow control. The vacuum pump was located downstream of the rotameter as recommended by Smith et al. (1977) to prevent errors due to possible leakage.

Isokinetic conditions were maintained at the sampling points by controlling the flow with the bleed valve and by using one of two nozzles of 6.35 and 9.55 mm i.d., depending on flow rate. The nozzles are tapered for minimum flow disturbance and had one single 90° long-radius bend; the probes were kept as short as possible (25 cm) to minimize dust deposition. It has been shown by Elder et al. (1981) and Jacko et al. (1975) that dust deposition in typical industrial sampling trains (goose-neck nozzles with probes 1.3 m long) may be significant, due both to the nozzle shape and probe length and to condensation and thermophoretic phenomena, which are common when sampling hot and moist industrial flue gases.

Preliminary experiments performed with the oxides of copper, magnesium and titanium showed negligible nozzle or probe

deposition, as determined by washing the probe with acetone and weighing the solid residue after evaporation.

The filter holder accommodated 47 mm diameter filters, and was provided with a domed inlet for uniform dust distribution. Some dust deposited on the upstream half of the filter holder and on the sealing O-ring. The domed inlet was disassembled for cleaning, and the dust deposited here and on the sealing O-ring was carefully brushed off onto the sampling filter, using a small brush.

Two types of filters were used, depending on the particle size distribution at the ESP inlet. For size distributions with a small mass fraction below about 0.8 μm in diameter, nitrocellulose membrane filters (Schleicher and Schuell) of 0.8 μm pore size were used. This involved all the experimental runs with the pure powders listed in Table 5.1. For size distributions with a large submicron mass, two glass microfiber filters in series (Whatman GF/A) were used. These filters have a collection efficiency of 99.8% for particles above 0.3 μm diameter, at 5 cm s^{-1} face velocity, and were used in the experimental runs with the industrial (Noranda) dust.

The use of membrane filters is preferred when microscopic examination or chemical analysis of the collected dust are to be performed. This is because membrane filters retain the particles on the surface of the filter, while glass fibre filters are bed filters, and also because the chemical composition of glass fiber filters may introduce unwanted contamination.

This problem is discussed in Section 5.7. Smaller pore size membrane filters could not be used due to an excessive pressure drop and insufficient pumping capacity. It is possible that 0.8 μm pore size membrane filters could be used to efficiently capture particles as small as 0.3 μm in diameter (Gelman-Sciences, Laboratory Catalog, 1979-1980, pp. 31), but this was not tried.

Both glass fiber and membrane filters are affected by ambient moisture. To avoid weighing errors due to this variable, the filters were dessicated overnight under vacuum, both prior to and after each experimental run. A sensitive Mettler H20T electrobalance with precision ± 0.01 mg up to 160 g was used for weighing.

To determine the precision to which the filters may be weighed, these were dessicated overnight and weighed, allowed to return to equilibrium with ambient humidity, dessicated once more overnight and reweighed. Both types of filter weights were reproducible to ± 0.02 mg.

The sampling rotameter calibration curve is shown in Appendix C, Fig. C.1. The mercury manometer provided pressure (vacuum) readings at the rotameter conditions, which were used to set the correct flow rate. The flow was manually controlled by a bleed valve upstream from the vacuum pump and if required, adjusted during an experimental run.

The accuracy of the outlet sampling train was verified during preliminary experiments using cupric oxide and the Tafa vibrating feeder, with the ESP energized at high voltages (~ 38 KV) at various air flow rates. Sampling performed immediately

downstream of the ESP outlet contraction with horizontal traverses showed good agreement between the measured feed rates from the powder feeder and the calculated values based on the dust sampled at the outlet of the precipitator and collected in the ESP system, for average air velocities at the ESP inlet up to $2ms^{-1}$. The dust collected in the ESP system comprised the precipitated dust and the dust which sedimented in the piping system and plenum chamber. Sampling was performed at eight centroids of equal area(Smith et al., 1977).

With larger air velocities, the calculated feed rates based on the collection and sampling systems were always larger than the measured feed rates from the powder feeder. The discrepancy increased with air velocity up to a maximum of about 43% at an average inlet velocity of 5.3 m s^{-1}.

Vertical sampling traverses performed at the ESP outlet, at an average air velocity through the ESP of 5.3 m s^{-1}, energized at high voltage ($\sim$ 38 KV) indicated lower dust loadings (about 35%) than expected. The larger dust loadings of the horizontal traverses and the lower dust loadings of the vertical traverses were probably caused by particle concentration gradients due to the effect of the electric field.

This problem was corrected by placing a short converging nozzle immediately downstream of the outlet contraction, which smoothly reduced the outlet diameter from 15.4 to 10.2 cm, followed by a straight 85 cm long aluminium pipe of 15.4 cm i.d. (a longer pipe could not be used due to space limitations). The

sampling station was relocated at the end of this straight section. The velocity profiles, as measured by a pitot-micromanometer assembly, are shown in Appendix C, Fig. C.2.

Horizontal and vertical sampling traverses performed at the modified outlet sampling station, with an average air velocity at the ESP inlet of 5 m s^{-1}, energized at high voltages (∿ 38 KV), showed very good agreement (± 3%) between the measured dust flow rates from the Tafa feeder and the calculated values based on the dust collected in the ESP and sampled at the ESP outlet, indicating representative dust concentration profiles. Turbulence created by the sudden expansion immediately downstream of the converging nozzle and the presence of the straight section prior to the sampling port were probably responsible for a better mixing of the dust particles prior to the sampling station. No significant dust deposition was observed downstream of the converging nozzle.

5.2.2.2 Inlet Sampling Trains

The inlet sampling train used for the determination of dust concentration gradients or the degree of dust dispersion was the same as the outlet sampling train, since the corresponding measurements were not taken simultaneously.

The inlet sampling train used for the determination of the global and elemental particle size distributions of the fine alumina and industrial dusts consisted of a 7.49 mm i.d. nozzle, made of stainless steel with a tapered inlet and a single 90° long-radius bend, an Anderson MKIII inertial cascade impactor

(Anderson 2000 Inc., Atlanta, Georgia), a manometer and dry test meter for pressure and flow measurements and a vacuum pump (Gast Manufacturing Corp.) provided with a bleed valve for flow control. The gas flow measured at the test meter conditions was corrected to the sampling nozzle conditions of near atmospheric pressure, using the ideal gas law. The sampling point was the center point of the flow channel at the ESP inlet.

Blank tests were performed to check whether the sampling results would be influenced by the background dust concentration; this was found to be negligible for conditions typical of the experiments.

5.2.3 Dust Concentration Gradients at the ESP Inlet and Sedimentation Effects

Cupric oxide was sampled at various positions at the ESP inlet, to determine the uniformity of dust concentration profiles. The experiments were performed with cupric oxide because this material had the highest density (6.4 g cm^{-3}) and would thus give the greatest non-uniformities.

The average velocity through the ESP was 2.8 m s^{-1}, and a sampling nozzle of 9.55 mm i.d. was used. The velocity profiles are given in Appendix B, Fig. B.8.

Sampling times were kept to 10 min per sampling point, and one replicate was performed for one sampling point. The measured local concentrations, determined by dividing the weight sampled at each location by the volume of sampling air are shown in Fig. 5.1, normalized to the concentration at the center point

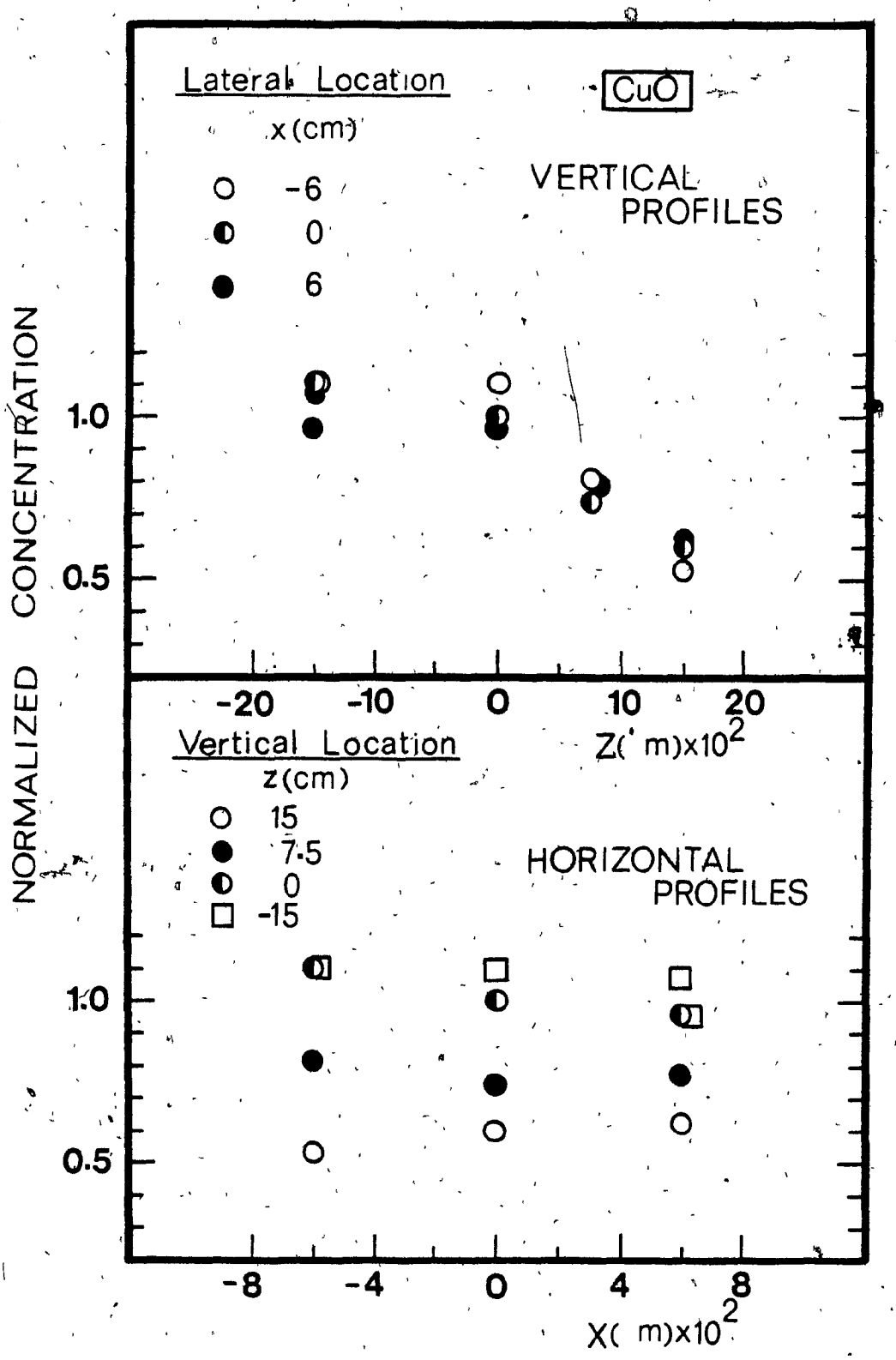


Figure 5.1 Normalized concentration profiles of cupric oxide at the ESP inlet, at 2.8 ms^{-1}

of the channel flow at the ESP inlet. The good uniformity of the horizontal profiles as compared to the gradients observed in the vertical direction is probably due to sedimentation of the cupric oxide particles. This might have been aggravated by the lower velocities present near the ESP top.

The dust collected on the filters was examined under an optical microscope after redispersion, and it was found that the larger particles were predominantly present near the center and bottom of the ESP inlet, confirming the assumption of sedimentation. No such variation in particle size was observed with lateral position.

This vertical stratification may also occur in full-size ESP's and is unavoidable in practice. In this case, it may be compounded by dust reentrainment from the collection hoppers (Oglesby et al., 1978).

The sedimentation occurring prior to the ESP inlet is important as it may change the particle size distribution which actually enters the ESP. Figure 5.2 shows the effect of average air velocity on the sedimentation of the coarser oxides occurring prior to the ESP inlet. The degree of sedimentation is here expressed as the fraction of dust collected in the flue duct and plenum chamber prior to the ESP inlet. The sedimentation occurring for the fine alumina and industrial dust was negligible, due to their small particle size and to the high test velocities through the ESP (5 m s^{-1}) which were used with these powders. In general, cupric oxide is affected more by sedimentation than the oxides of magnesium or titanium, probably because of its higher density.

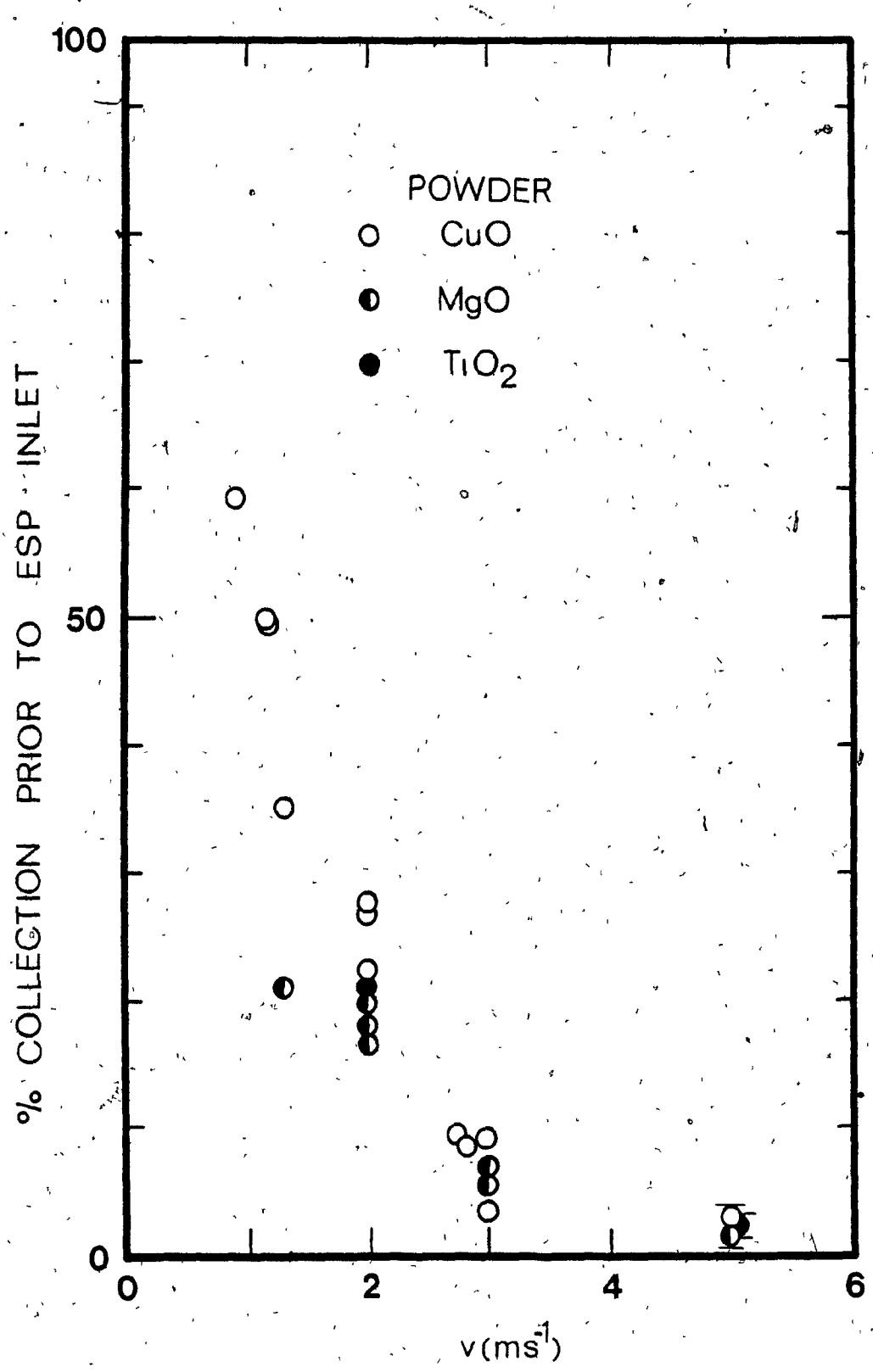


Figure 5.2 Mechanical collection of the coarser oxides prior to the ESP inlet, as a function of air velocity

To determine the effect of the sedimented dust on the inlet size distribution, a series of particle size distribution measurements were made on the powders collected in the plenum chamber, at various air velocities. The size distributions were determined by optical microscopy, as discussed in the next section. The mass of particles in each size band of the sedimented dust was subtracted from the mass of particles in the corresponding size bands of the dust before sedimentation occurred. An example is given in Appendix C, Section C.4. Figure 5.3 shows the results obtained with cupric oxide, normalized to the undisturbed value of geometric mean mass diameter (MMD).

The data in Fig. 5.3 indicate that corrections to the size distribution at the ESP inlet may be important below an average ESP velocity of about 3 ms^{-1}. Since these data were used in the SRI computer model (discussed in Chapter 2 and Appendix A), it was necessary to establish the possible error in the simulation results due to an error in the input size distribution. To estimate this error, simulations were performed using as input data both the corrected and uncorrected size distributions at the ESP inlet, at various conditions of applied field and air velocity. The simulated collection efficiencies for the corrected and uncorrected size distributions did not vary by more than 2% over all the experimental conditions tested (applied voltages between 24 and 40 KV and air velocities between 0.9 and 3 ms^{-1}).

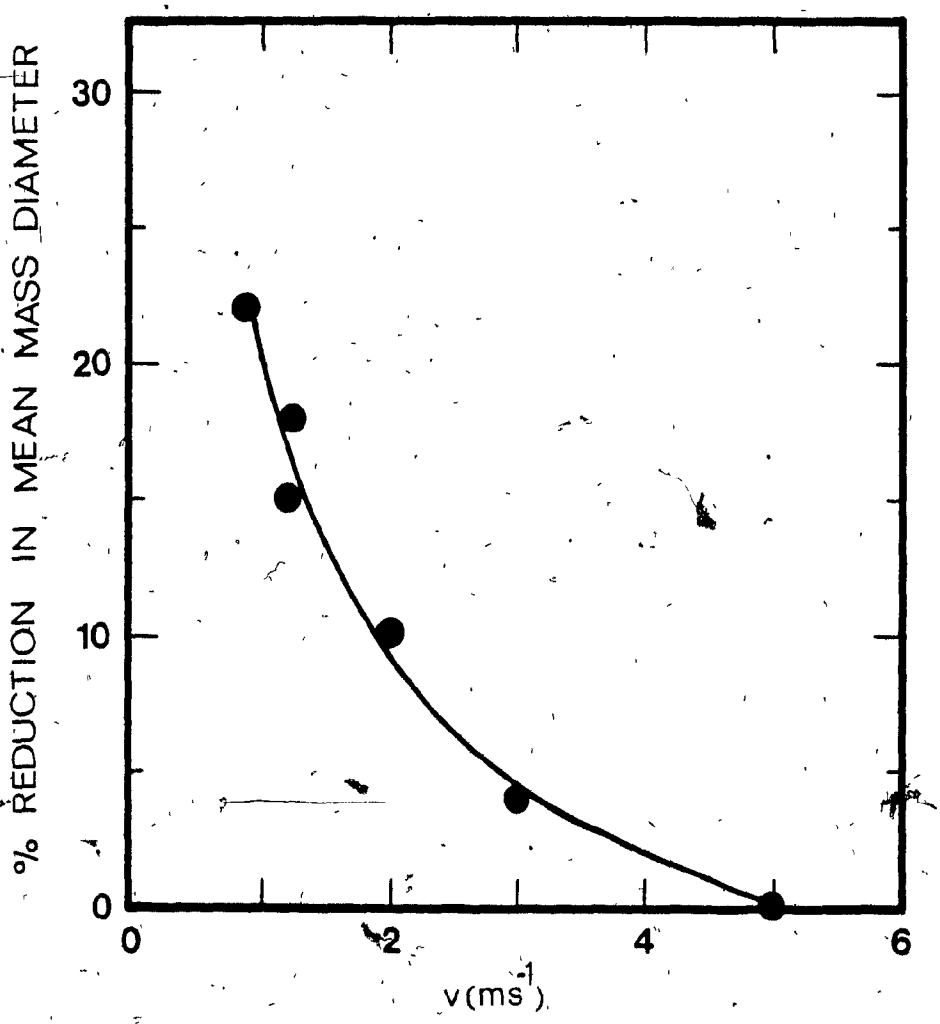


Figure 5.3 Reduction in MMD of cupric oxide at the ESP inlet, due to sedimentation

In this work, the corrected particle size distributions were always used both as input data for the SRI computer model and to determine the fractional collection efficiencies and migration velocities (Chapter 6).

Sedimentation of dust also occurred in the ESP itself, but here the observed values were highly dependent on the applied electric field. Figure 5.4 shows the mechanical collection of the ESP, at various air velocities and applied voltages, using cupric oxide as feed to the ESP. The mechanical collection was calculated by the ratio of dust weight deposited on the ESP bottom to the dust weight that actually entered the ESP.

For a zero applied field, sedimentation is very important even at average air velocities of 3 ms^{-1}. At the very low applied voltages of ~ 25 KV (near the corona onset voltage of 21 KV), sedimentation is only slightly decreased. As the applied voltage increases to the very high value of 38-40 KV, sedimentation is drastically reduced.

The competing effects of the electric field, which tends to pull the particles to the collection plates, and gravity, which tends to pull the particles to the ESP bottom are apparent in the data of Fig. 5.4. Thus, sedimentation data obtained at zero applied field is of little value for the particular ESP used, and no such data were taken for the other powders. The effect of the applied field in disturbing the mechanical collection should be much less severe for a full-size ESP, due to its much greater plate height.

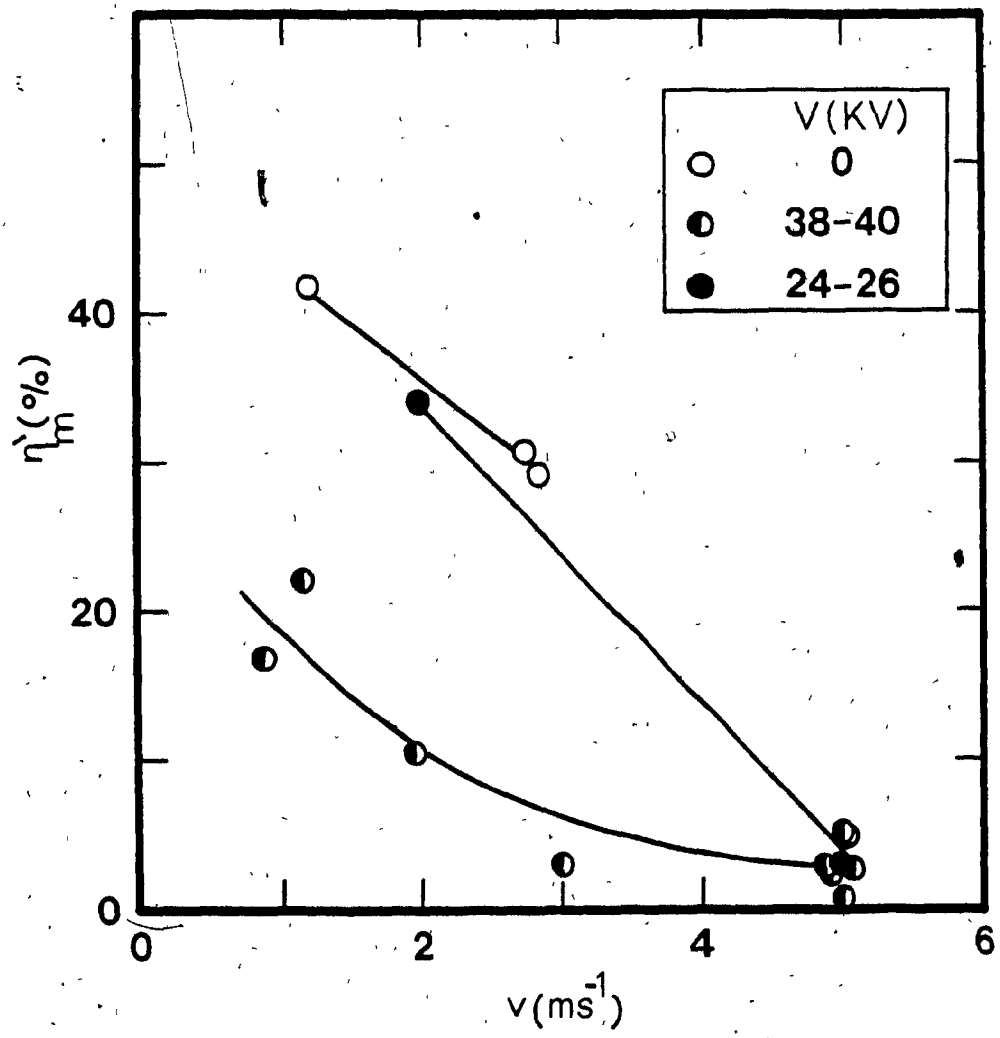


Figure 5.4 Mechanical collection of cupric oxide, in the ESP, as a function of air velocity and applied voltage

5.3 Size Analysers and Analysis

5.3.1 General Considerations

Knowledge of the particle size distribution of the various powders at the ESP inlet was necessary to determine the fractional collection efficiencies or as input size distributions for the SRI computer model (Chapter 2, Section 2.8 and Appendix A).

If adequate dispersion of the dust particles is accomplished by the powder feeder, the appropriate size distribution at the ESP inlet can be estimated by measuring the size distribution of a bulk quantity of the dust.

If, on the other hand, the powder feeder is incapable of providing adequate dispersion of the dust particles, agglomerates and single particles will be present at the ESP inlet. Particle size distributions determined from a bulk sample may be totally unrepresentative of the true size distribution at the ESP inlet, and means must be provided for in-situ determination of size distributions.

The presence of a few agglomerates may also have a very pronounced effect in distorting the particle size distribution of the dispersed particles, depending on the range of particle sizes. A small proportion of agglomerates might have only a slight effect on the size distribution of relatively coarse particles, while completely altering the size distribution (by weight) of very fine particles. This is aggravated by the fact that agglomeration is usually much more severe for the finer particles.

A representative sample must be taken, whether the sample is withdrawn from a gas stream or from a bulk quantity of the powder. This was done by sampling isokinetically and by averaging over a number of samples and establishing the appropriate confidence limits.

The dust particles were collected on sampling filters for microscopic observation with three purposes: to determine the degree of dispersion of the particles at the ESP inlet; to determine the size distribution at the ESP outlet by redispersing the sampled particles; and to estimate the size distribution of the fine alumina at the ESP inlet.

For the determination of the degree of dispersion at the ESP inlet, very small samples (i.e., very short sampling times) are required, to avoid superposition of particles on the filter surface.

If the collected sample is used for actual size distribution measurements, longer sampling times are preferred, to avoid sizing an unrepresentative sample due, for instance, to powder feeder fluctuations. In this case, the effect of particle superposition cannot be ignored and further redispersion is necessary. This limits the method to powders which are well dispersed by the feeders.

For the present work, only the coarser oxides of copper, magnesium and titanium were sized using redispersion of collected dust (whether sampled from the air stream or from a bulk quantity of the material), since these were the only dusts which were readily dispersed by the corresponding powder feeders.

5.3.2 Particle Size Analysers

5.3.2.1 The Optical Microscope

The subject of particle size analysers is treated by Allen (1968), Davies (1973), Lapple (1968), McCain et al. (1974), McCrone et al. (1967), Orr (1978) and Stockham et al. (1977). From a review of the possible methods of size analysers available, the optical microscope was chosen as the basic tool. It is applicable to a broad range of particle sizes (down to about the wavelength of light, or ~ 0.5 μm), can provide information on the presence of agglomerates, can allow for independent observation of differently coloured particles and requires only very small sample sizes, of the order of a few hundred particles. However, its use is time consuming, produces fatigue and may be prone to a systematic error in either over or undersizing particles. The optical microscope used was a Reichert-Zetopan, provided with 12.5 X eyepieces and a series of objectives up to 63 X and a 0.80 numerical aperture. With the largest magnification objective, the resolving power of the microscope was about 0.3 μm (Yamate et al., 1977). The microscope has a mechanical stage movable manually by micrometers in two perpendicular directions. An eyepiece containing a linear graduated scale provided the base measurement used for particle sizing. A Polaroid camera was attached to the microscope axis to provide microphotographs at a maximum possible magnification of 630 X.

The eyepiece was calibrated with a Reichert microscope slide with a known scale of 2 mm in 200 equal divisions, at the actual magnification used for the measurements. Due to the small

size of the large majority of the particles (below 10 μm), the maximum magnification was always used. Calibration of the eye-piece scale showed that the smaller divisions corresponded to 1.6 μm, with a maximum sizing field of view of 160 μm.

The following three steps must be successfully completed to obtain a suitable sample for microscopic particle sizing:

1) Provide adequate dispersion on the microscope slide so that individual particles and not agglomerates are counted and sized.
2) Provide sufficiently high particle concentrations on the slide so that a statistically valid number of particles is counted.
3) Provide uniform coverage of the slide such that a representative sample is counted and sized.

A number of dispersants and dispersing techniques were tested. Good dispersion was obtained for the coarser oxides (CuO, MgO, TiO_2) using n-heptane or sodium hexametaphosphate (Calgon) in water at 0.05% concentration. A 0.5% solution of Calgon in water worked for the Noranda dust while no entirely satisfactory dispersant was found for the fine alumina. Ultrasonic vibration was not useful in any case; a gentle shearing action improved dispersion of the fine dusts but had little effect on the coarser oxides.

N-heptane was the preferred dispersant for the coarser oxides since its slow evaporation in the absence of a slide cover avoided the migration of fine particles to the edges of the slide. Fast evaporation produces a rapidly moving interface which

enhances particle transport, collision and agglomeration. The technique involved placing one or two drops of the suspension on the slide and gently tilting the slide to distribute this uniformly over the surface.

Proper concentrations of particles in the dispersant were also determined experimentally. Too high a concentration leads to agglomeration and too low a concentration greatly increases measurement time and may yield unrepresentative samples.

The number of particles to be counted in any size range, to achieve a desired accuracy (binomial standard deviation) is:

$$\sigma(S_i) = \left\{\frac{S_i(1-S_i)}{N}\right\}^{\frac{1}{2}} \qquad (5.1)$$

which is valid for $5 \lesssim S_iN < N-5$ (Raabe, 1971), where $\sigma(S_i)$ is the standard deviation of the observed cumulative frequency by number (S_i) below a specific size, and (N) is total number of counts.

Figure 5.5, taken from the tabular data of Yamate et al. (1977), can be used to determine the number of particles which should be counted to obtain a given accuracy when a weight based distribution is to be computed from a number based distribution. In general, if a size distribution is not too broad, a total count of 400-600 particles with a minimum count of 5 particles for any size range is considered adequate. A minimum of 500 particles were sized and counted for all the coarser oxides used in this work. The expected standard error in the arithmetic mean

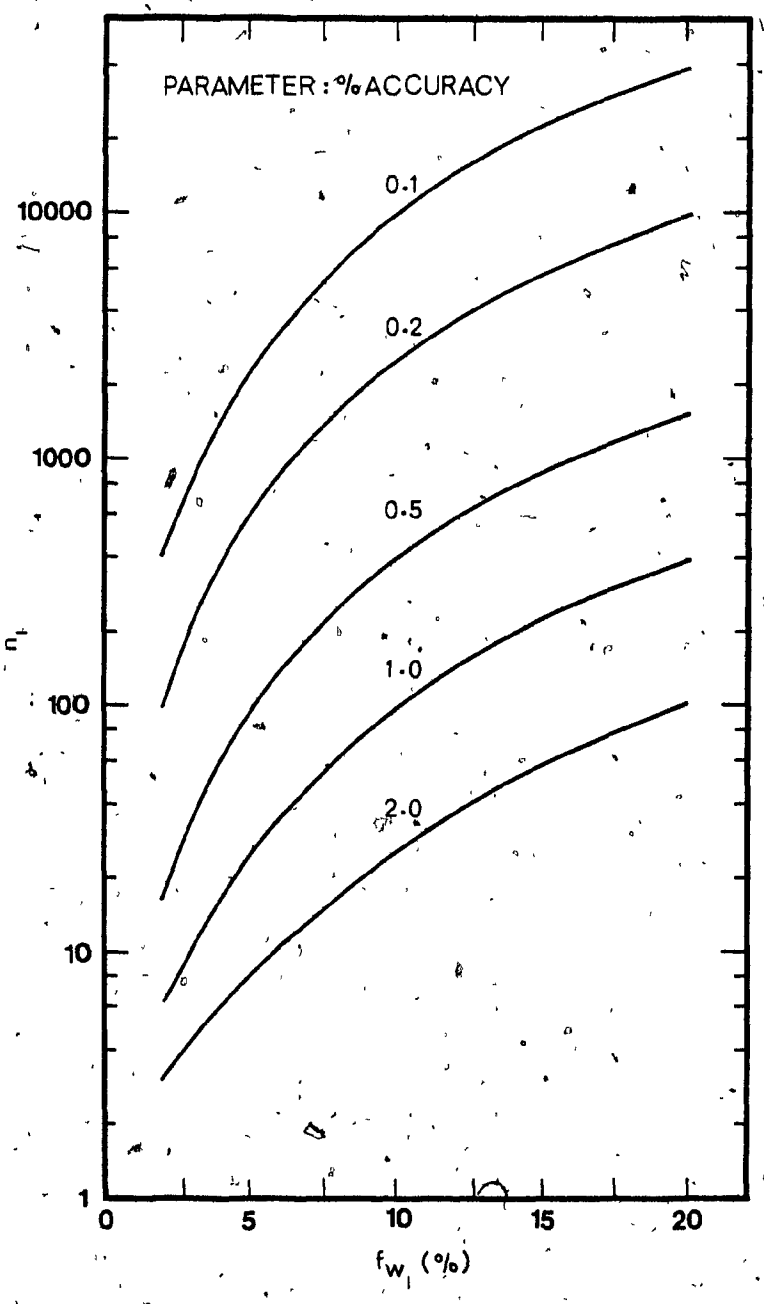


Figure 5.5 Relation between number of particles counted, weight percent and accuracy (Yamate et al., 1977)

number diameter is given by $\frac{1}{\sqrt{N}}$, where (N) is the total count. Thus, a maximum standard error of 4.5% is expected for the arithmetic mean number diameters.

A much larger count was made to estimate the size distribution of the fine alumina at the ESP inlet, due to the large proportion of very fine particles. An example of the application of Eq. 5.1 and Fig. 5.5 is given in Appendix C, Section C.3.

To ensure a representative sample of particles, the mechanical stage micrometers followed a search pattern similar to that shown schematically in Fig. 5.6a, until all the sample within the region of influence of the stage micrometers was covered. Particles overlapping one end of the ocular scale were neglected, and particles overlapping the other end were counted to minimize the risk of counting a particle twice.

Figure 5.6b shows the particle diameter which was chosen for the measurements. The diameter of a particle in a single direction is meaningless when applied to a single particle (unless spherical), but it is of value when applied to a large number of particles in random orientation. One of such diameters is Feret's diameter, which is the length between tangents on opposite sides of the particle, normal to the fixed direction of scan. It approaches the projected area diameter (diameter of a circle of the same area as the projected area of the particle) as the number of counts increases (Stockham et al., 1977).

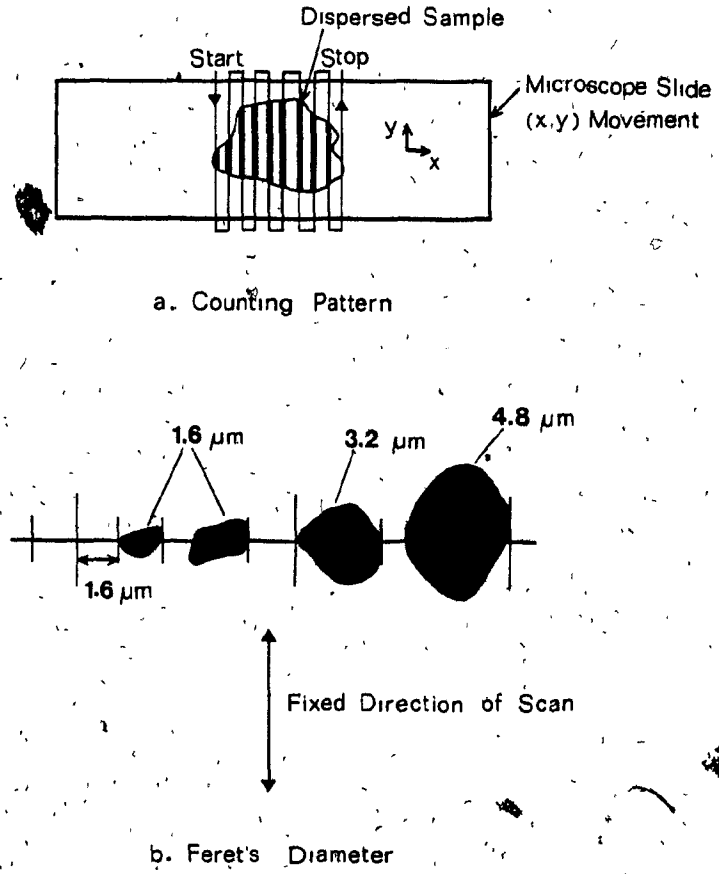


Figure 5.6

a) Counting pattern used with optical microscope

b) Chosen diameter for optical microscope counting and sizing

Although various other particle dimensions can be measured under the optical microscope, Feret's diameter is probably the easiest to measure. For spherical particles, microscope based diameters are essentially Stokesian diameters (diameter of sphere of the same density and terminal velocity of particle), but deviations occur due to non-sphericity. In general, conversion of diameters measured on different basis cannot be theoretically performed. Particles which have Feret's diameters that are not integer multiples of the minimum eyepiece division were assigned the closest multiple of minimum eyepiece divisions.

The sizing of the particles was performed by writing down the number of particles observed in each size range, and integer multiples of 1.6 μm were used as the different size ranges. The occurrence of particles above about 30 μm in diameter was rare for all distributions measured. Sporadically, large isolated particles of 40-50 μm could be seen, but since a single 50 μm particle has the same weight as one thousand 5 μm particles (of the same shape), these isolated occurrences were ignored; otherwise, severe distortion of the size distribution would occur. The statistical treatment of the experimental data is given in Section 5.3.3, where methods to account for the larger particles are considered.

Figures 5.7a,b are microphotographs of a bulk sample of the mixed oxides of copper, magnesium and titanium, dispersed in n-heptane, at two different magnifications. It is seen that

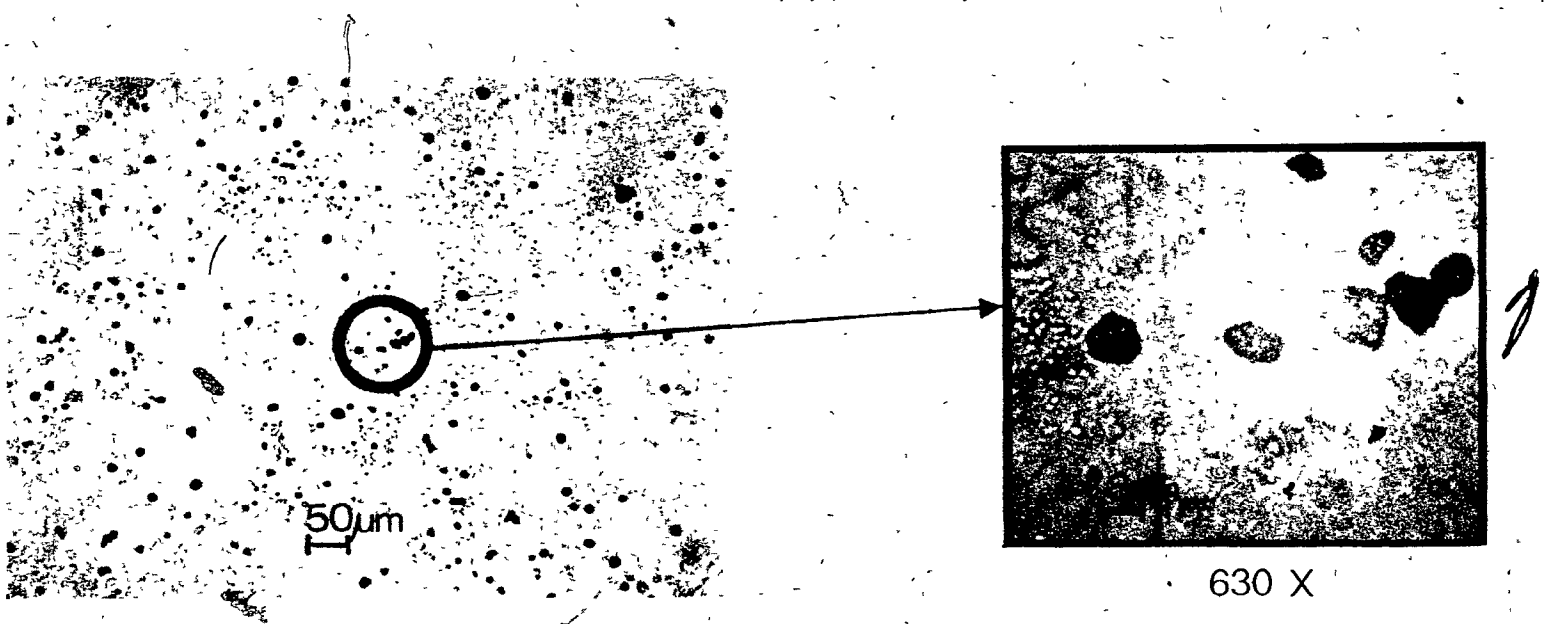


Figure 5.7 a, b Typical optical microphotographs of a bulk sample of the coarser oxides, dispersed in N-heptane

individual particles are easily resolved at the higher magnifications used for the size distribution measurements; the use of low magnifications should be avoided, otherwise the results may be biased towards the larger sizes. It should be pointed out that no particle size distributions were measured when the three coarser oxides were simultaneously present at the ESP inlet, and as such it was not necessary to distinguish the various particles.

The optical microscope was only routinely used to determine the size distributions of the coarser oxides. For the fine alumina, evidence of agglomeration from the powder feeder (Section 5.4.2) and the small particle sizes involved dictated the use of in-situ measurement techniques. The optical microscope was nevertheless used to confirm the existence of agglomerates and to provide an estimation of the particle size distribution of the fine alumina at the ESP inlet, as discussed in Section 5.4.2.

The optical microscope was not used for sizing the industrial dust, since the presence of agglomerates and the required information on elemental size distributions would probably be highly unreliable, at best. In-situ methods were used, as described in Section 5.4.3.

5.3.2.2 The X-Ray Sedimentometer

A Sedigraph 5000 D Particle Size Analyser (Micromeritics Instrument Corporation, Norcross, Georgia) was used to independently check the optical microscope results. It measures Stokes' diameters by sedimentation. A dilute suspension

of the particles dispersed in an appropriate liquid medium is circulated through a cell with glass windows. The instrument determines the concentration of particles remaining in the sedimentation cell by means of a finely collimated beam of X-rays, after the circulation pump is stopped. The weight concentration of particles is linearly related to the logarithm of the transmittance, by Beer's law (Micromeritics Instrument Corporation Instruction Manual, Sedigraph 5000 D Particle Size Analyzer). The instrument provides information on the cumulative weight percent undersize of a particular Stokes diameter, up to a maximum particle size specified by the user. The X-ray Sedigraph can measure particle sizes from about 0.1 to 100 μm in diameter, and the reproducibility of the results was always within ± 1%.

The choice of the dispersing medium may have a strong effect on the results obtained. All dusts used in this work were tested for bulk size distribution measurements using the X-ray Sedigraph. Similar size distributions were obtained for the oxides of copper, magnesium, titanium and aluminium, using either Calgon at 0.05 or 0.5% in water. Completely different results were obtained for the Noranda dust using the dispersing mediums, dispersion being much better with the more concentrated solution of Calgon, as revealed by the much smaller sizes obtained for the same weight percent of particles. Ultrasonic vibration did not improve the dispersion of any of the powders. These observations agree with the dispersion tests performed on the optical microscope and discussed before.

A numerical example on the use of the X-ray Sedigraph is given in Appendix C, Section C.5.

5.3.2.3 The Andersen Cascade Impactor

An Andersen MK III inertial cascade impactor was used as part of an inlet sampling train, to obtain information on the particle size distribution of alumina and industrial dust. This is a size fractionating device, working on the principle of inertial impaction described by Marple et al. (1976), Newton et al. (1977) and Ranz et al. (1952). It is composed of a series of nine perforated stainless steel plates (stages) mounted on a main frame. The stages are arranged in order of geometrically decreasing hole sizes, with the holes in adjacent stages off-center. A sample of the airborne dust is aspirated at a known flow rate through an appropriate sampling nozzle, and the different particles are size classified by inertial impaction. The first stage is only a jet stage and the last stage is only a collection stage. Glass fiber collection substrates were used to reduce taring weights and the probability of dust bounce-off and reentrainment; these non-ideal phenomena have been shown by Ondov et al. (1978) and Rao et al. (1977) to alter the theoretical impactor cut-points (particle diameter at each impactor stage for which the collection efficiency is 50%). The glass fiber substrates and backfilter (Reeve Angel 934-AH), used to capture very small particles which escaped impaction on the substrates or (large) particles which may have been blown-off or reentrained, were dessicated overnight under vacuum, prior to weighing both

before and after an experimental run. Due to the very small masses collected, an appreciable error may occur due to the loss of glass fibers during handling. To reduce this effect, the substrates were first shaken by hand, then mounted in the impactor, shaken once more, mounted and shaken for a third time, prior to the initial dessication. A precision of ± 0.02 mg was obtained with both substrates and backfilter.

To avoid reentrainment, the sampling flow rate was kept at approximately 14 ℓ min^{-1}. No evidence of reentrainment was detected, as deduced from the absence of an appreciable weight proportion collected in the backfilter and from the absence of particle streaks on the glass fiber substrates.

The cascade impactor cut-points were calculated by the following equation:

$$D_2 = D_1 \left(\frac{\rho_1 v_1 C_1}{\rho_2 v_2 C_2}\right)^{\frac{1}{2}} \qquad (5.2)$$

where (D,ρ,C,v) are respectively the values of impactor cut-point (D), particle density (ρ), Cunningham correction factor (C) and jet velocity (v) at known (1) and unknown (2) conditions.

Since the Cunningham factor involves the particle diameter (Eq. 2.34, Chapter 2), the above relation has to be solved by trial and error. Known values of (D,ρ,v) are necessary. This information is provided by the impactor manufacturer, and is given in Table 5.2 for a flow rate of 21.2 ℓ min^{-1} and spheres of unit density.

An alternate method involves the use of the impactor design data, as outlined by Smith et al. (1977,1978), and gave essentially the same results.

TABLE 5.2

Aerodynamic Cut-Diameters of Andersen MK III Cascade Impactor, at 20°C and 21.2 ℓ min^{-1}

Stage No.	1	2	3	4	5	6	7	8
D (μm)	10.9	6.8	4.6	3.2	2.0	1.0	0.61	0.41

5.3.3 Particle Size Statistics

The statistical treatment of experimental data related to particle size distribution analysis is treated in a variety of texts, among them Allen (1968), Corn et al. (1976), Crawford (1976), Herdan et al. (1960), Lapple (1968), Licht (1980), McDonald (1980) and Raabe (1971).

The collection efficiencies for the present work were determined on a weight basis, and so the relevant particle size distributions must also be expressed on a weight basis. Particle size distribution data obtained by the Andersen cascade impactor are already on a weight basis, and no further conversion was necessary other than the determination of the actual impactor cut-points. On the other hand, data derived from the optical microscope are on a number basis, and further conversion to a weight basis was mandatory.

A particle size distribution determined on any basis (including number and weight) can be expressed either in a differential or cumulative form, using the discrete raw data or a continuous approximation to them.

The number frequency histogram is the discrete distribution of the observed number of particles in each particular size range. The number frequency distribution usually refers to the continuous approximation of the histogram and is called a probability density function.

The cumulative distribution may be obtained from either the discrete or continuous frequency functions, and it represents the proportion of the number (or weight) of the particles which is below (or above) a certain particle size.

The advantages of expressing the results on a cumulative rather than a differential basis are the following:

1. When converting number to weight distributions, a false plurimodal weight distribution (i.e., with more than one peak) may occur using the differential number histogram.
2. The cumulative plots are usually better than the differential plots at showing which function best describes the observed distribution.
3. When determining the appropriate mathematical function which describes the number distribution, the fitting techniques are more correctly applied to cumulative distributions. This is because the

particle sizes in each size band on a differential distribution are compressed to the mean size of the size bands. These values do not correspond to the true observed particle sizes.

A disadvantage of cumulative plots is that fine detail is lost, and that systematic errors tend to be transported along the distribution. Although plurimodality is more dramatically shown in differential distributions, the presence of points of inflection on a cumulative distribution indicates the same phenomenon. In the present work, plurimodality was not observed.

The most direct way to convert number into weight distributions is to weigh the observed number frequencies by the corresponding cubed diameters. If (n_i) particles from a total number (N) were counted in the size range represented by the mean diameter (D_i), then the number fraction of particles of size (D_i) is given by:

$$f_{n_i} = n_i D_i / \sum_{i=1}^{m} n_i D_i \qquad (5.3)$$

where the summation is carried over all particle size ranges (m). Likewise, the weight fraction of particles of size (D_i) is given by:

$$f_{w_i} = n_i D_i^3 / \sum_{i=1}^{m} n_i D_i^3 \qquad (5.4)$$

The arithmetic mean number diameter (MND_a) is given by:

$$MND_a = \sum_{i=1}^{m} n_i D_i / \sum_{i=1}^{m} n_i = \frac{1}{N} \sum_{i=1}^{m} n_i D_i \qquad (5.5)$$

and the arithmetic mean mass diameter (MMD_a) is given by:

$$MMD_a = \sum_{i=1}^{m} n_i D_i^4 / \sum_{i=1}^{m} n_i D_i^3 \qquad (5.6)$$

which is the average size based on a unit weight of the particles, not to be confused with the diameter of the particle of average weight (Licht, 1980).

To convert Eq. 5.3 into Eq. 5.4, the assumption has to be made that all particles have the same tridimensionally symmetric shape and density. The disadvantages of using the direct conversion of number to weight basis are the following:

1) The weighted proportions are too sensitive to experimental errors, since these are raised to higher powers, with the consequence that false plurimodality may occur. This is especially severe for the larger particles of low frequency of occurrence.
2) No mathematical representation of the distribution is obtained, and thus the entire distribution must be explicitly given.

These difficulties may be overcome by using a mathematical representation of the distribution, which contains two or three parameters. The calculations can be extended to particle sizes not actually counted due to their low frequency of occurrence and the effect of experimental errors in the extremes of

the distribution can be minimized. The problem is then to identify the distribution which best fits the data and to determine the best estimates for the values of the parameters. The log-normal distribution was found to give the best overall fit for the powders used in this work, and the following discussion is centered on this particular distribution function. [1]

The log-normal number distribution is a normal (Gaussian) distribution of the logarithms of the particle sizes, expressed by the number frequency function:

$$f_n(\ln D) = \frac{1}{\sqrt{2\pi}\,\ln \sigma_g} \exp\left\{-\frac{(\ln D - \ln MND)^2}{2(\ln \sigma_g)^2}\right\} \quad (5.7)$$

where $f_n(\ln D)$ is the fraction of particles by number between $\{\ln D, \ln D + \frac{dD}{D}\}$, where (dD) is a differential particle size, (σ_g) is the geometric standard deviation (dimensionless) and (MND) is the geometric mean number diameter, defined as:

$$MND = \prod_i D_i^{n_i/N} \quad (5.8)$$

Equation 5.8 can be converted into:

---

1 Although some other types of functions give a slightly better fit of some of the observed distributions (e.g., the "upper-limit" log-normal function for the case of cupric oxide (Licht, (1980)), the difference is very small and of no practical significance, as shown in Table 5.4 (Section 5.4.1).

$$\ln \text{MND} = \frac{1}{N} \sum_i n_i \ln D_i \qquad (5.9)$$

i.e., the logarithm of the geometric mean diameter is the arithmetic mean of the logarithms of the diameters. The geometric mean is of particular interest for a log-normal distribution, since it coincides with the mode (value of diameter for which the greatest frequency of particles is observed) and with the median (value of diameter for which the cumulative distribution is equal to 1/2).

Equation 5.7 can be normalized by:

$$t = \frac{\ln D - \ln \text{MND}}{\ln \sigma_g} \qquad (5.10)$$

and the cumulative fraction (by number) undersize t = T is given by:

$$S(T) = \frac{1}{\sqrt{2\pi}} \int_{-\infty}^{T} \exp(-\frac{t^2}{2}) dt \qquad (5.11)$$

The cumulative fraction oversize t = T is likewise given by:

$$G(T) = \frac{1}{\sqrt{2\pi}} \int_{T}^{\infty} \exp(-\frac{t^2}{2}) dt \qquad (5.12)$$

One method of estimating the values of MND and σ_g used by McDonald (1978) is to evaluate the variable (T) for all measured values S(T), and compare the obtained values with the observed particle diameters, at corresponding values of S(T), using a least squares regression analysis. From Eq. 5.10, the set of

points (t,ln D) will lie on a straight line of slope $(\frac{1}{\ln \sigma_g})$ and intercept $(-\frac{\ln MND}{\ln \sigma_g})$, and the coefficient of determination obtained is an indication of how well the log-normal function describes the observed data. Initial estimates of (MND) and (σ_g) are not required, since these are obtained from the regression equation coefficients.

To use the method, the variable (T) is approximated by the following function (Abramowitz et al., 1964):

$$T = \phi - \left\{ \frac{a_o + a_1\phi + a_2\phi^2}{1 + b_1\phi + b_2\phi^2 + b_3\phi^3} \right\} \qquad (5.13)$$

where the function (ϕ) is given by:

$$\phi = \sqrt{\ln \frac{1}{S^2(T)}}, \quad 0 < S(T) \leq 0.5 \qquad (5.14)$$

and by:

$$\phi = \sqrt{\ln \frac{1}{G^2(T)}}, \quad 0.5 < S(T) \leq 1 \qquad (5.15)$$

The values of the constants in Eq. 5.13 are given by:

$$a_o = 2.515517 \qquad (5.16a)$$

$$a_1 = 0.802853 \qquad (5.16b)$$

$$a_2 = 0.010328 \qquad (5.16c)$$

$$b_1 = 1.432788 \qquad (5.16d)$$

$$b_2 = 0.189269 \qquad (5.16e)$$

$$b_3 = 0.001308 \qquad (5.16f)$$

with an error in (T) less than 0.00045. Due to symmetry of the normalized distribution, $T(S) = -T(G)$, and $S(-\infty) = 0$, $S(0) = 0.5$ and $S(+\infty) = 1$. From the regression analysis, $T = A + B \ln D$, where (A,B) are the regression equation coefficients. Comparison with Eq. 5.10 gives:

$$MND = \exp(-\frac{A}{B}) \tag{5.17}$$

and

$$\sigma_g = \exp(\frac{1}{B}) \tag{5.18}$$

A different normalization can also be made. If

$$t = \frac{\ln D - \ln MND}{\sqrt{2} \ln \sigma_g} \tag{5.19}$$

then Eq. 5.11 becomes:

$$S(T) = \frac{1}{2}\{1 + \text{erf } T\} \tag{5.20}$$

where the error-function can be found in statistical tables (Maisel, 1971). A least squares fitting of the estimated values of (T) versus the corresponding values of (ln D) for the same S(T), will give the following estimates of the parameters of the distribution:

$$MND = \exp\left(-\frac{A}{B}\right) \tag{5.21}$$

$$\sigma_g = \exp\left(\frac{1}{\sqrt{2}\,B}\right) \tag{5.22}$$

where (A) and (B) are the new regression equation coefficients. The polynomial approximation was preferred to the error function evaluation using statistical tables, to avoid the inaccuracies of interpolation of the tabulated values.

A better statistical approach to estimate the parameters of a log-normal distribution is the use of the maximum likelihood method (Raabe,1971).

The probability of observing (n_i) particles in the size interval (D_i,D_{i-1}) is given by:

$$P_i = \left\{ \int_{\ln D_{i-1}}^{\ln D_i} f_n(\ln D)\, d \ln D \right\}^{n_i} \tag{5.23}$$

where $f_n(\ln D)$ is given by Eq. 5.7. Where there are (m) size classes, the total probability of the distribution of data is:

$$P = \prod_{i=1}^{m} P_i \tag{5.24}$$

Equation 5.24 is referred to as the likelihood function. More convenient for a log-normal distribution is the logarithmic likelihood function, given by:

$$L = \ln P = \sum_{i=1}^{m} n_i \ln \int_{\ln D_{i-1}}^{\ln D_i} f_n(\ln D) d \ln D \qquad .....(5.25)$$

Raabe (1971) uses a second-order Taylor expansion for (L), such that its maximum value may be determined with successive estimates of the parameters of the distribution. Initial estimates are required, and can be determined by the least square fitting methods described before. Raabe's method is appropriate for a digital computer and difficult to use otherwise. The maximum likelihood method can nevertheless be easily applied by using a trial and error solution on the normalized distribution, given by Eq. 5.11. The method is as follows:

1) Estimate the mean and standard deviation of the number distribution, i.e., $\ln \overline{MND}$ and $\ln \sigma_g$. This can be done by a least squares fitting technique.

2) Determine the value of the variable $t = t_i$ for every particle size D_i from i = 1,m. This is given by Eq. 5.10.

3) Determine the value of the logarithmic likelihood function, given by:

$$L = \sum_{n_i=1}^{m} n_i \ln S(t_i) \qquad (5.26)$$

4) Repeat with new estimates, until the maximum value of (L) is achieved, at the desired accuracy.

Both the least squares fitting and the maximum likelihood methods are applicable to cumulative distributions, and as such do not suffer from the inherent problem of assigning all particle sizes within a specific size range to the mean value of the size interval. Also, if the distribution can be adequately described as log-normal, then an entire distribution can be generated, including sizes which were not counted but which are known to exist and which may significantly contribute to the size distribution on a weight basis.

Once estimates of the parameters of the distribution by number are known, the log-normal distribution by number can be generated using either the error function tables or polynomial approximations. Since these do not involve graphical or numerical interpolation, they were preferred. The variable (t), given by Eq. 5.10 can be calculated for each size range, using the estimates of MND and σ_g. The following polynomial approximation was used to compute the integral given by Eq. 5.11 (Abramowitz et al., 1964):

$$R = \frac{1}{\sqrt{2\pi}} e^{-\frac{t^2}{2}} (b_1 p + b_2 p^2 + b_3 p^3 + b_4 p^4 + b_5 p^5) + \varepsilon(t) \quad \ldots.(5.27)$$

where:

$$b_1 = 0.319381530 \quad (5.28a)$$

$$b_2 = -0.356563782 \quad (5.28b)$$

$$b_3 = 1.781477937 \quad (5.28c)$$

$$b_4 = -1.821255978 \quad (5.28d)$$

$$b_5 = 1.330274429 \quad (5.28e)$$

with the residual $\varepsilon(t) < 7.5 \times 10^{-8}$. The variable (p) is given by:

$$p = \frac{1}{1 + |t|r} \tag{5.29}$$

where (r) is given by:

$$r = 0.2316419 \tag{5.30}$$

The value of S(t) is given by:

$$S(t) = 1 - R, \; t \geq 0 \tag{5.31}$$

or by:

$$S(t) = R, \; t < 0 \tag{5.32}$$

When the number of size classes is small (six or less), it is probably better to use a direct transformation of number to weight basis, without trying to fit the observed distribution to any particular function. This is because of the reduced number of degrees of freedom available (three or less).

Once appropriate estimates of the parameters of the number log-normal distribution are obtained, the transformation to a weight basis is straightforward, using the following relation:

$$MMD = MND \exp\{3(\ln \sigma_g)^2\} \tag{5.33}$$

where (MMD) is the geometric mean mass diameter. The size distribution on a weight basis is also log-normal with the same geometric standard deviation. The factor (3) in the exponential arises from the assumption of tridimensionally symmetric particles. Hesketh (1977) recommends the use of a lower factor (2.66), which may be experimentally found by determining the number of particles in a known weight. In this work, the factor (3) was always used.

The generation of the size distribution on a weight basis can be performed in the same way as the generation of the size distribution on a number basis, with the MND substituted by the MMD.

The log-normal distributions also allow for easy conversion between the geometric and arithmetic means and standard deviations, if required.

One important attribute of the log-normal distributions is the convenience of their graphical representation. When cumulative distributions are plotted on log-probability paper (i.e., the x-axis is a logarithmic scale and the y-axis is a probit scale) a straight-line results, with the geometric mean of the distribution corresponding to the 50% cumulative value and the geometric standard deviation corresponding to the following relations:

$$\sigma_g = \frac{D_{84.1}}{D_{50.0}} = \frac{D_{50.0}}{D_{15.9}} = \sqrt{\frac{D_{84.1}}{D_{15.9}}} \qquad (5.34)$$

where the D_j's are the particle diameters corresponding to the cumulative value (j) of the distribution. The number and weight based size distributions are parallel lines, displaced only by the corresponding values of geometric means.

The data obtained from the optical microscope for the coarser oxides of copper, magnesium and titanium was treated in the various ways described in this section, from the direct conversion to the least squares and maximum likelihood estimation of the distribution parameters. The relevant results are given in Section 5.4.1.

A comparative calculation example is given for one of the experimental powders in Appendix C, Section C.3.

5.4 Size Distributions at the ESP Inlet

5.4.1 Cupric Oxide, Magnesium Oxide and Titanium Dioxide

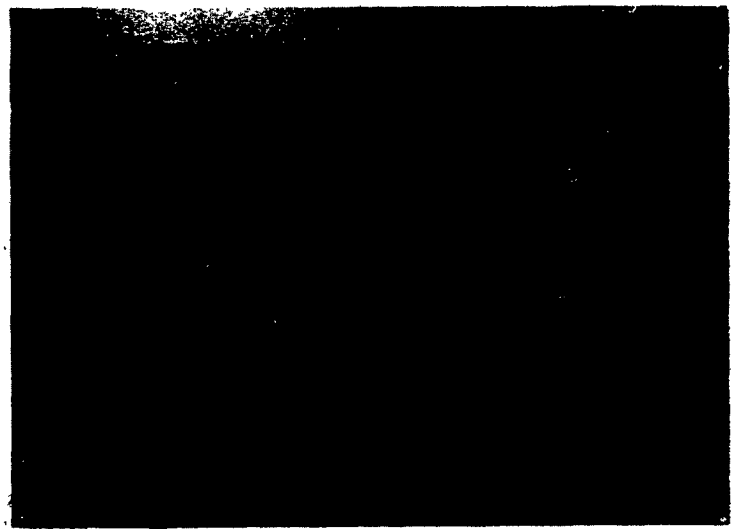
To determine the degree of dispersion of these powders, sampling was performed at the ESP inlet, using 0.8 μm pore size membrane filters.

The filters were rendered transparent by placing two drops of a 1:1 solution of dimethyl phthalate in diethyl oxalate on the backside of the filter, to minimize particle disturbance. Figure 5.8 is a microphotograph of particles of CuO, MgO and TiO_2 sampled at the ESP inlet. Cupric oxide was fed using the Tafa vibrating feeder, and both magnesium and titanium oxides were fed using the screw feeder. Despite the very short sampling time (a few seconds), some particle superposition can be seen. Dispersion from the feeders is good for all three oxides.

Figure 5.8 also shows that the TiO_2 and CuO particles deviate more from spherical shape than the MgO particles. The CuO particles are readily identified due to their black colour; the TiO_2 and MgO particles were identified by comparing micro-photographs of the single components.

Figure 5.9 is a typical electron microphotograph of these oxides, taken with a Jeol CX-100 scanning-transmission electron microscope. A small amount of the powders was placed in water and ultrasonically vibrated for 20 min before a drop was placed on a carbon-coated copper grid. The different particles were identified by energy dispersive analysis of X-rays (EDX). It shows that the TiO_2 particles are more angular than either the CuO or MgO particles.

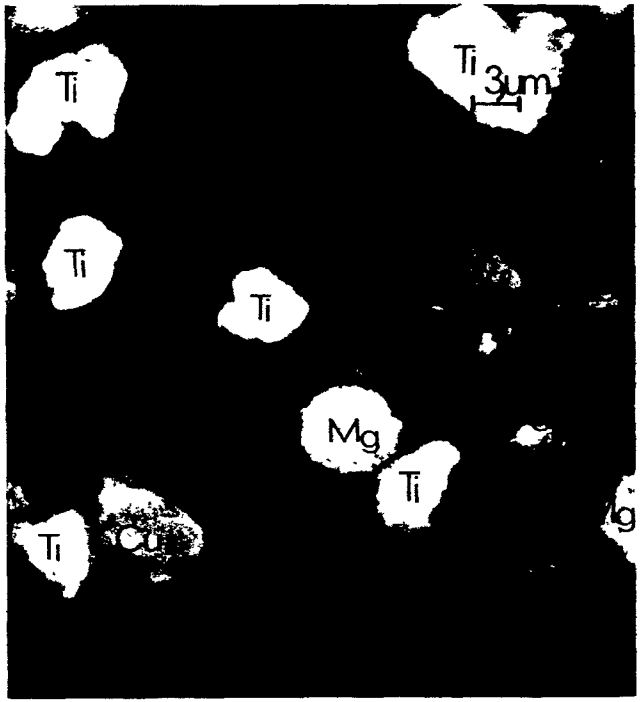
To determine if the powder feeders introduced significant changes in the size distributions of these oxides, size distribution measurements were made on dust collected both from the powder feeder bins and at the outlet of the conveying lines of the feeders. Particular attention was paid to the Tafa vibrating feeder, where measurements were made for different input voltages to the vibrating ramp. Figure 5.10 shows the observed geometric means and standard deviation for the number and weight based distributions, obtained by performing a least squares approximation of a log-normal distribution to the observed distribution. There is no significant difference in the various samples, and it was concluded that the Tafa vibrating feeder did not alter the size distribution of cupric oxide. The data were used to determine the reproducibility of the size measurements



400 X

a)

Figure 5.8 Typical optical microphotograph of the coarser oxides at the ESP inlet



2000 X

b)

Figure 5.9 Typical scanning electron microphotograph of a bulk sample of the coarser oxides

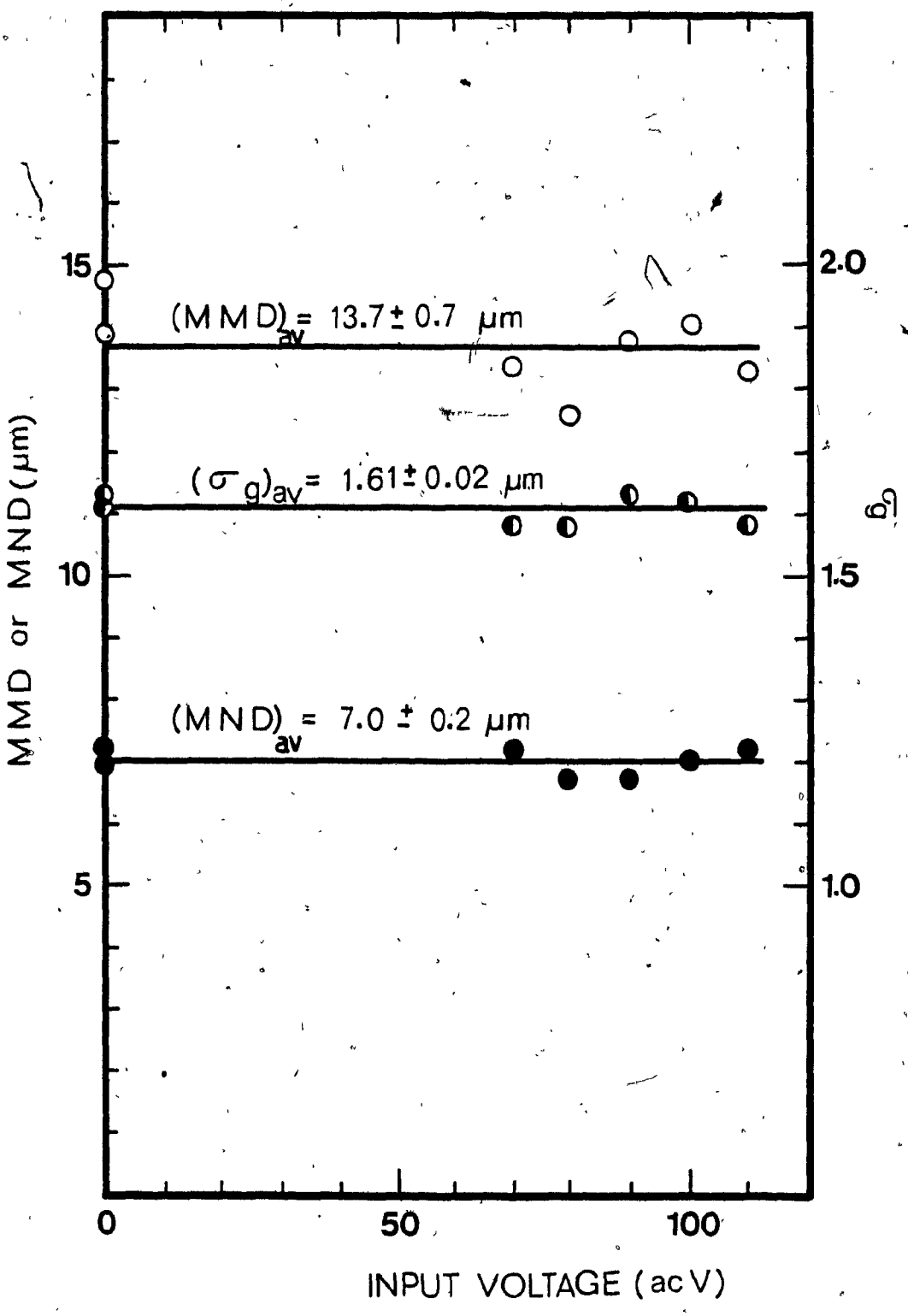


Figure 5.10 Size distribution parameters of CuO at various input voltages to the Tafa feeder

using the optical microscope. The average values and their 95% confidence limits are shown in Fig. 5.10, where it is seen that the precision of the estimation of the geometric mean number diameter and standard deviation are respectively ± 3% and ± 1%. A poorer precision (± 5%) is obtained for the geometric mean mass diameter. The raw data and computations are given in Appendix C, Section C.6, Table C.6.

The screw feeder used to feed the oxides of magnesium and titanium also did not alter the size distributions of these dusts. This test was performed only at one intermediate feed rate.

The raw data and computations are given in Appendix C, Section C.6, Table C.7.

The estimated parameters of the log-normal approximations to the observed composite distributions using the least squares method are given in Table 5.3, together with the determination coefficients (r^2). The composite distributions were obtained by adding the observed frequencies in each size class (Appendix C, Tables C.7 and C.8).

TABLE 5.3

Estimated Parameters of Log-Normal Least Squares Fitting

Powder	MMD (μm)	σ_g	r^2
CuO	13.6	1.59	0.98
MgO	14.6	1.79	0.98
TiO_2	15.0	1.74	0.99

It is important to notice that the various distributions on a weight basis have similar values of geometric means, although the CuO distribution is narrower.

The extent to which the various approximations represent with sufficient accuracy the observed distributions was tested by using the SRI computer program under simulated typical experimental conditions of high velocity (5 ms^{-1} through the ESP) and both high and low applied fields. A high velocity was chosen, since a poorer charging environment magnifies the effect of differences in the size distributions which are input to the computer program. Table 5.4 shows the global collection efficiencies corresponding to the various size distributions on a weight basis which were used as approximations to the observed composite distribution of cupric oxide.

TABLE 5.4

Collection Efficiencies of CuO: Simulation Tests on Size Distribution Effect

	Approximation Method				
		Log-Normal		"Upper-Limit" Log-Normal	
Applied Voltage (KV)	Direct	Least-Squares	Maximum Likelihood	Least-Squares	Maximum Likelihood
38	98.7	98.9	99.0	98.7	N/A
24	68.1	69.7	71.8	69.5	N/A

The simulation results of Table 5.4 show that little difference exists between the different methods of approximating the observed distributions (the maximum likelihood "upper-limit" log-normal approximation was not considered, since it is expected to give the same results as the least squares approximation). Similar differences were obtained with magnesium oxide, and smaller differences with titanium dioxide. Since the least squares log-normal approximation is very convenient to use, it was chosen to approximate the observed distributions for CuO, MgO and TiO_2.

The composite values given in Table 5.3 were used as input to the SRI computer program and for computing the fractional collection efficiencies.

The X-ray sedimentometer described in Section 5.3.2.2 was used as an independent check on the particle size distributions obtained with the optical microscope. It was important to determine the size distributions on a weight basis directly, since transformation of number to weight basis was necessary when counting and sizing with the optical microscope.

Figure 5.11 shows the size distributions of the three oxides, as measured by the X-ray Sedigraph 5000 D. It shows that the particle size distributions of these oxides are similar, and that the median values are somewhat lower than estimated by using the number data from the optical microscope. Also, the weight fraction of submicron particles is negligible.

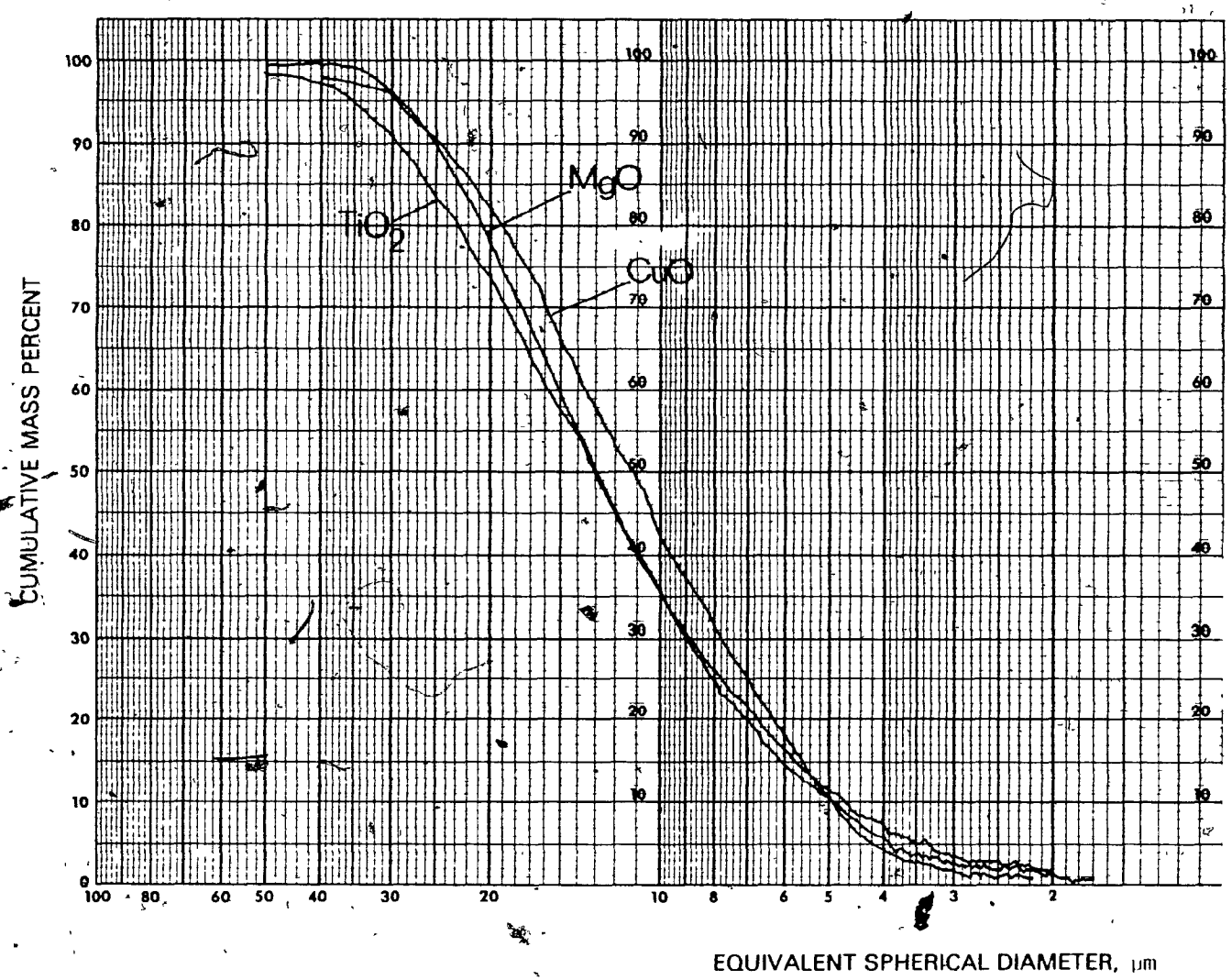


Figure 5.11 Size distributions of the coarser oxides, as determined by bulk sample analysis using the X-ray Sedigraph 5000D

The fact that the distributions are somewhat different from the estimated using the microscope data is not surprising, but the fact that the medians are consistently smaller may either be due to a systematic error of oversizing with the optical microscope or the fact that the particles are not spherical. The tendency of particles to assume their most stable position when deposited on a substrate reveals their greatest dimensions to examination, and this may bias the optical microscope results (Orr, 1978).

The distributions obtained on the Sedigraph and the optical microscope are plotted on log-probability paper in Fig. 5.12, for comparison. The optical microscope curves refer to the least-squares approximation of the observed distributions by log-normal distributions, using the composite values from Table 5.3. The distributions obtained with the Sedigraph are only shown for comparison and were not used in any other way.

5.4.2 Aluminium Oxide (Alumina)

The main purpose of using the fine alumina listed in Table 5.1 was to produce an aerosol of predominantly submicron particles at the ESP inlet. The combination of this alumina with any of the coarser oxides described above allowed the effect of particle size on the observed segregation to be experimentally studied and theoretically verified.

The Wright dust feeder was used to feed the alumina to the Venturi throat; sampling at the ESP inlet using 0.8 μm pore

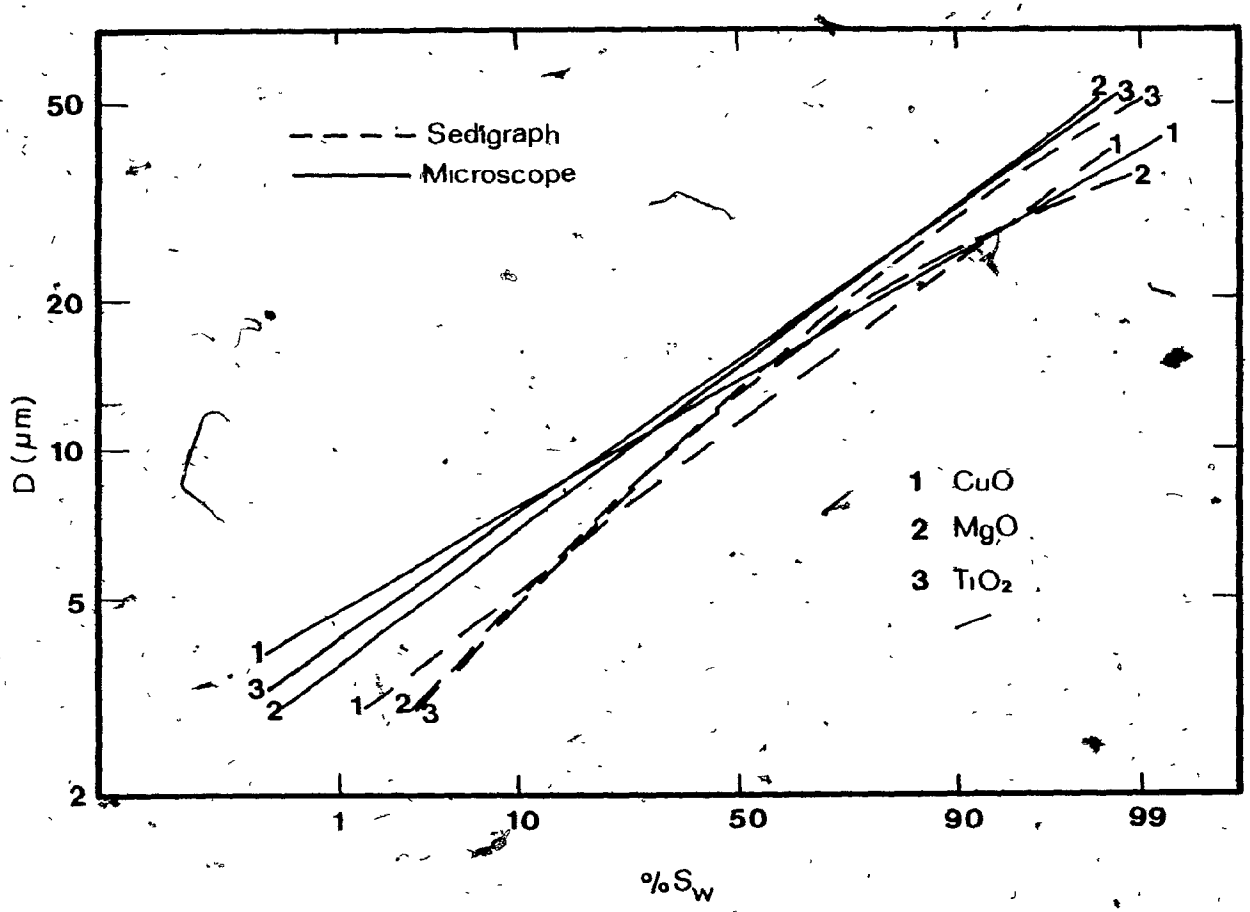


Figure 5.12 Comparison between the size distributions of the coarser oxides derived from the optical microscope data and the X-ray Sedigraph 5000D

nitrocellulose membrane filters showed strong agglomeration of the alumina particles, indicating incomplete dust dispersion.

Measurements of the particle size distribution of the alumina at the ESP inlet were made using both the optical microscope and the Andersen MKIII inertial cascade impactor. For optical microscope measurements, the particles were counted and sized as collected on membrane filters, i.e., without further redispersion. Very short sampling times were used to minimize particle superposition, and a large count was made due to the large fraction of micron and submicron particles.

The experimental results obtained with these methods are shown in Fig. 5.13, where the size distribution of a bulk sample of alumina as determined using the X-ray Sedigraph is also shown for comparison. The raw data and computations are given in Appendix C, Section C.7, Tables C.8 and C.9.

Figure 5.13 shows fair agreement between the size distributions measured by the different methods, although the distribution from the impactor is broader, showing more finer and coarser particles. The Sedigraph results, although not strictly comparable, show that most of the mass of alumina is present in agglomerates, with a negligible submicron mass. This is in qualitative agreement with the other measuring methods.

A comparison of SRI simulations for the alumina (with the size distributions given in Fig. 5.13) and for the coarser oxides suggested that some separation due to the difference in particle sizes would theoretically be observed but that separation could be enhanced by further size reduction of the

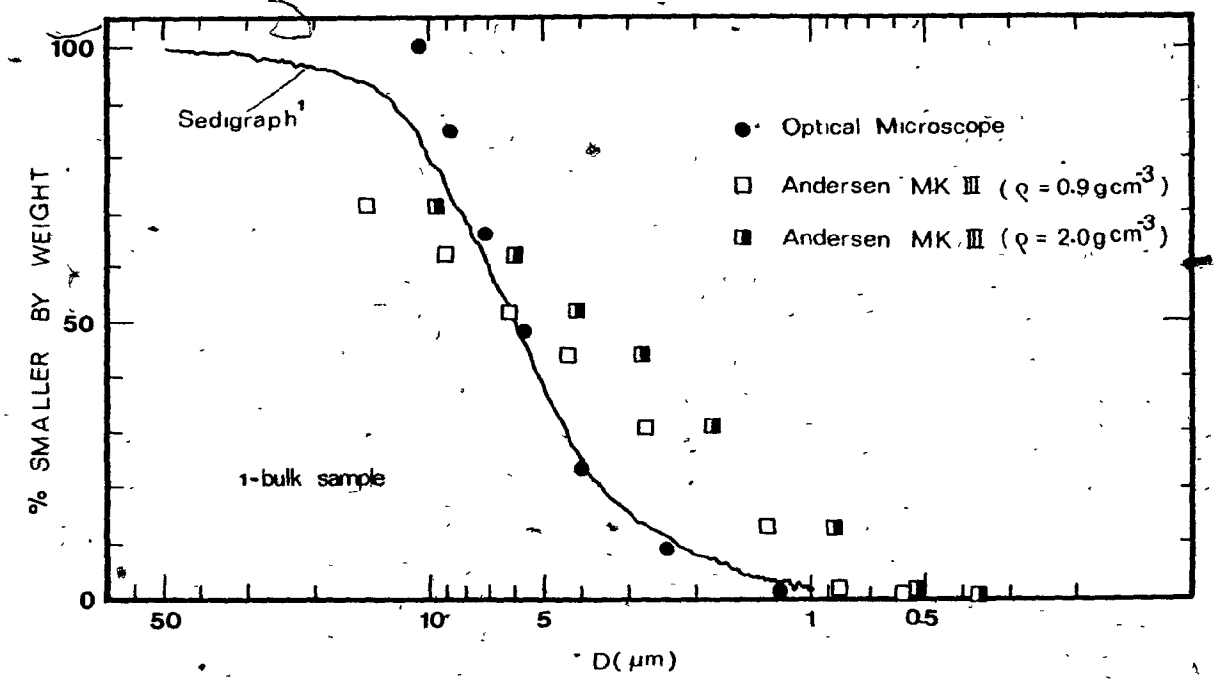


Figure 5.13 Size distributions of alumina obtained by the X-ray Sedigraph (bulk sample), the optical microscope and the Andersen MKIII cascade impactor, with the minicyclone off-line

alumina feed to the ESP.

A minicyclone of standard design (Crawford, 1976) was built and installed between the Wright feeder and the dust injection port at the Venturi throat, to achieve this reduction. Details of the cyclone design and performance are given in Appendix C, Section C.7, Figs. C.9 and C.10.

Size distribution measurements of the alumina at the ESP inlet were obtained using the optical microscope and the Andersen impactor. The experimental results are shown in Fig. 5.14. The raw data and computations are given in Appendix C, Section C.7, Tables C.8 and C.9.

A much poorer agreement was obtained between the cascade impactor and the optical microscope data with the cyclone on-line. The impactor was always operated at about 14 ℓ min^{-1} and no evidence of reentrainment existed. The optical microscope data show only a slight decrease in median size, which is in strong contrast to the impactor data. Preliminary experiments performed with the ESP energized at 26 KV and with an average air velocity of 5 ms^{-1} showed a decrease in global collection efficiency from 36 to 22% when the minicyclone was on-line. This is consistent with a decrease in the mean size of the particles at the ESP inlet, in qualitative agreement with the cascade impactor data. The reason why the optical microscope data failed to reveal any significant change in the size distribution with or without the minicyclone was probably due to the high sensitivity of the weight based distribution to the presence of a few agglomerates, since most of the particles by number were

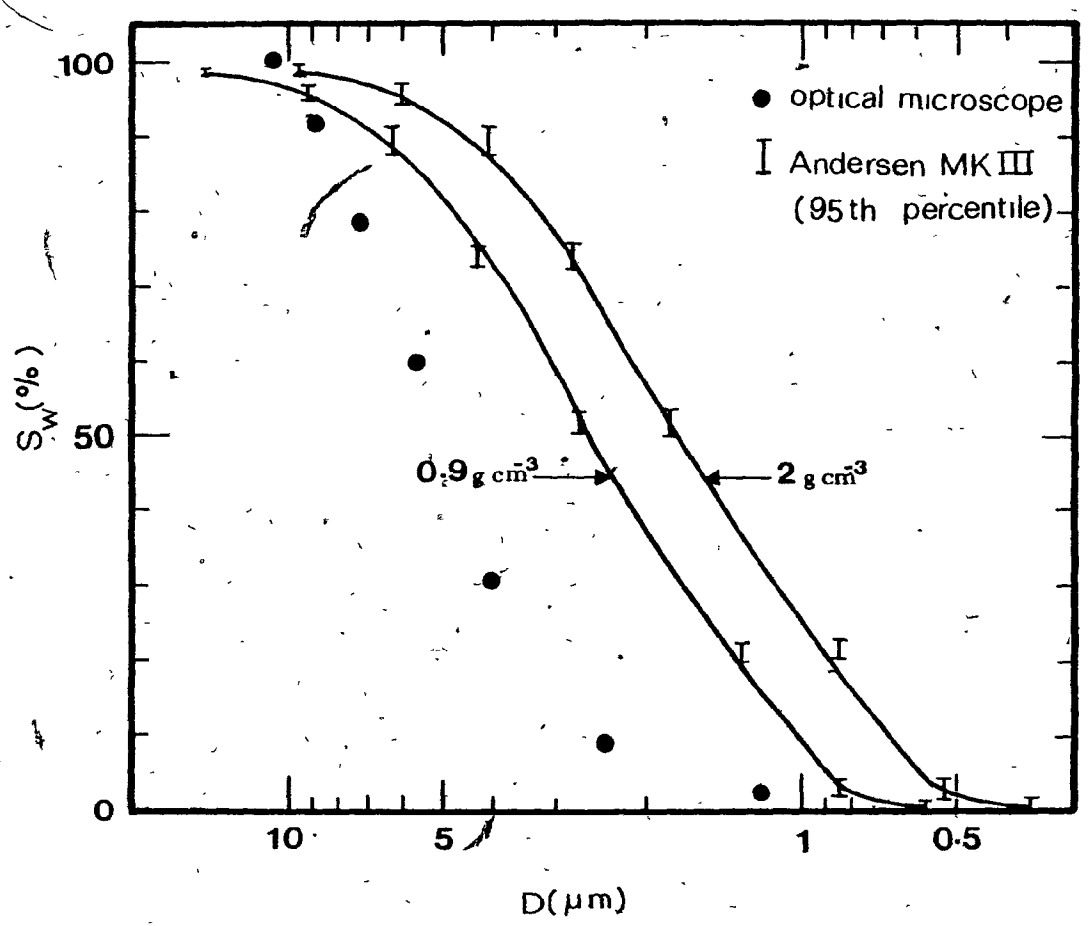


Figure 5.14 Size distributions of alumina obtained by the optical microscope and the Andersen MKIII cascade impactor, with the minicyclone on-line

of micron or submicron size. This is quantitatively discussed in Appendix C, Section C.7. For these reasons, the cascade impactor data were considered to be more reliable and were used as the input size distribution to the SRI computer program.

As shown in Figs. 5.13 and 5.14, the impactor distributions depend on the density assigned to the alumina particles. Figure 5.15 is a typical microphotograph of alumina at the ESP inlet, with the minicyclone on-line; various agglomerates ranging in size from 2 to 4 μm can be seen. Figure 5.16 shows typical transmission electron photographs of the fine alumina, after ultrasonic dispersion in water for 20 min, taken with a Jeol CX-100 scanning-transmission electron microscope. The high degree of agglomeration as well as the presence of large voids is apparent in Fig. 5.16b. The agglomerates are composed by two crystallographic forms of alumina, due to the process of formation of the alumina crystals (Flock, 1978 and Waye, 1967). The smaller crystals are cubic γ-Al_2O_3 formed by calcining aluminium hydroxide at about 800 K. The larger crystals are hexagonal α-Al_2O_3, formed by extending the calcination temperatures to above about 1200 K. The proportion of the two phases depends mainly on the final calcination temperature, and the primary crystals may be sintered through solid bridges. This confers great stability to the agglomerates (Hench et al., 1980), and may be one possible cause for the poor dispersion obtained using the Wright feeder.

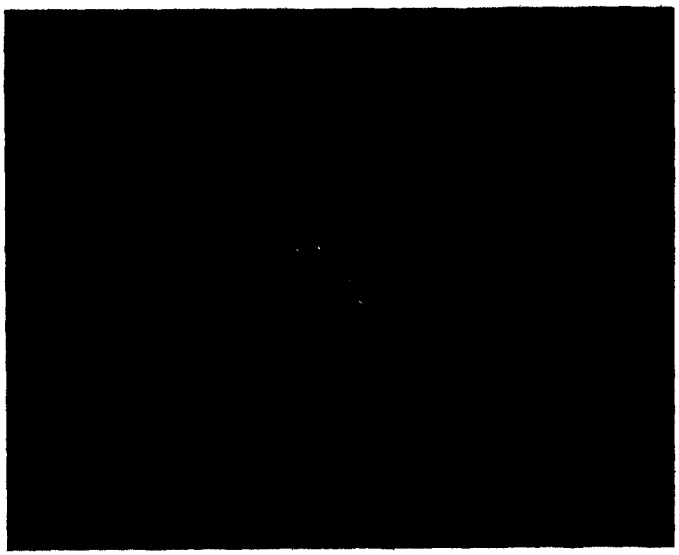


Figure 5.15 Typical optical microphotograph of alumina at the ESP inlet

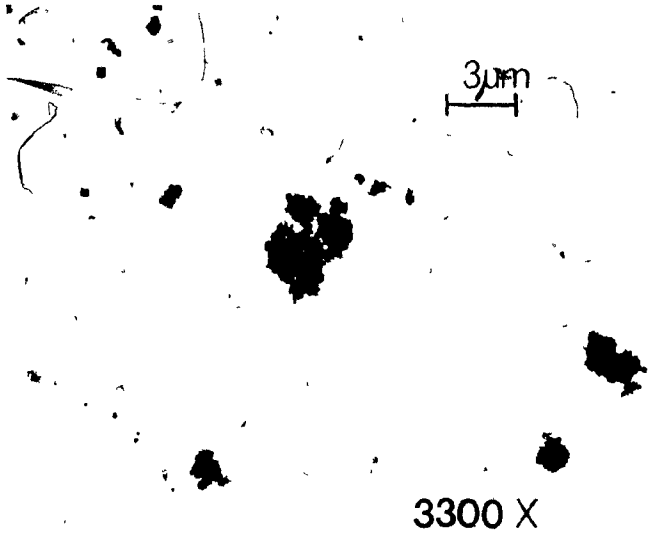


Figure 5.16a Typical transmission electron microphotograph of alumina



Figure 5.16b Typical transmission electron microphotograph of alumina

The high degree of agglomeration of the alumina particles poses a problem on what density to assign to the agglomerates. The lower limit of 0.9 g cm^{-3} corresponds to the bulk density of the packed plug in the Wright feeder, with the operating compaction pressure of 5880 KPa. This density value includes the voids between agglomerates and it is probable that the density of the agglomerates was underestimated. On the other hand, assigning the true density of alumina (3.9 g cm^{-3}) to the alumina agglomerates will also be grossly in error. The density of the agglomerates was estimated using pressure-density data provided by Niesz et al. (1978) for a similar type of alumina. The value of 50% relative density (i.e., 2 g cm^{-3}) was considered as a reasonable estimate on the upper limit of density for the alumina agglomerates. This corresponds to a packing pressure of 6.4×10^5 KPa, which is the maximum value reported. The corresponding cascade impactor data is shown in Figs. 5.13 and 5.14. The effect of uncertainties in the density of the agglomerates on the simulation results is discussed in Chapters 6 and 7.

5.4.3 The Industrial (Noranda) Dust

The Wright feeder was also used to feed the industrial (Noranda) dust to the ESP, but without the minicyclone since the entire size spectrum was desired. Size distributions were obtained by isokinetic sampling at the ESP inlet using the Andersen MKIII inertial cascade impactor.

The dust was dried overnight at 105°C before packing in the Wright feeder, at a pressure of 2450 KPa, or less than half that used for the alumina dust. The packing pressures which produced uniform feed rates over long periods of time (> 2 hr) were found for each dust by trial and error. With the industrial dust, plugging occurred at the jet constriction above the impingement plate, probably due to the presence of large particles. This problem was solved by removing the jet constriction. It is not known how this affected the size distribution at the outlet of the Wright feeder, although it is probable that deagglomeration might be superior with the jet constriction in place.

Figure 5.17 shows the size distribution of the industrial dust as determined with the Andersen MKIII inertial cascade impactor. The raw data and calculations are given in Appendix C, Section C.7, Table C.10. The bulk density of the Noranda dust packed at 2450 KPa was 1.3 ± 0.1 g cm^{-3} (one standard deviation, 3 samples). The true density was measured by a gas pycnometer (Micromeritics Model 1302, Norcross, Georgia) to be 3.2 ± 0.1 g cm^{-3} (one standard deviation, 3 samples). These two values of densities were used to compute the effective impactor cut-points shown in Fig. 5.17, and they should represent the limits of low density corresponding to the presence of agglomerates and high density corresponding to individual particles, ignoring density differences from particle to particle. Also shown for comparison are the distributions obtained by the X-ray Sedigraph

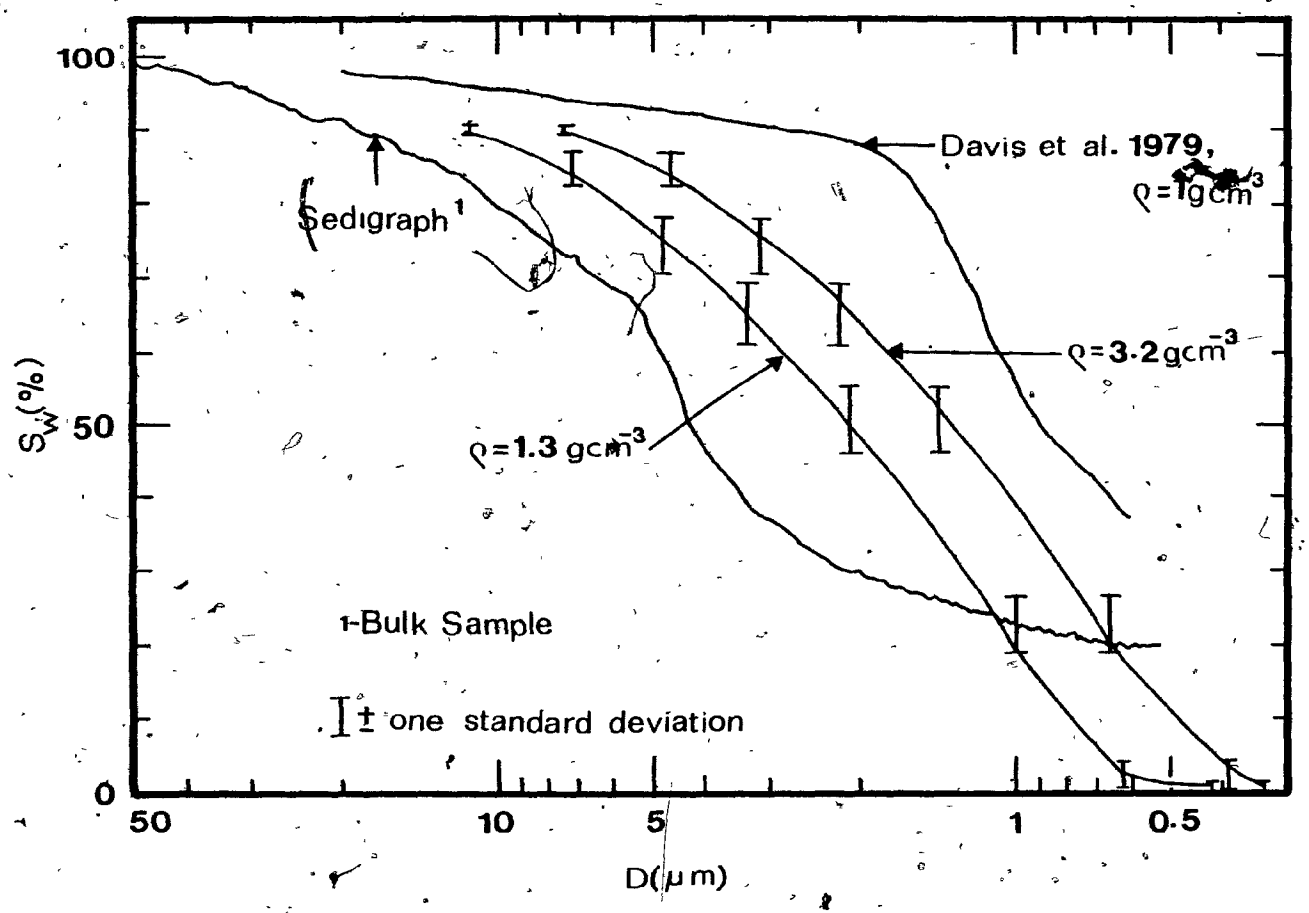


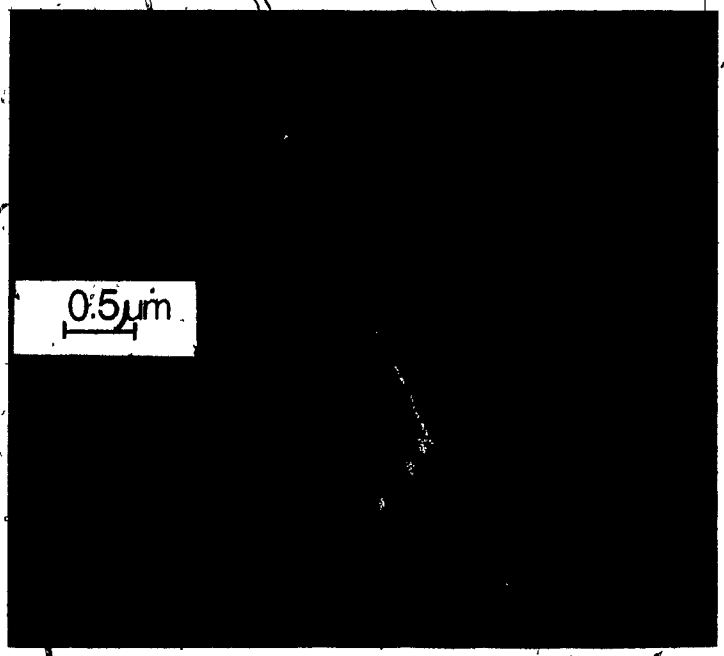
Figure 5.17 Average size distribution of the Noranda dust at the ESP inlet

and by Davis et al. (1979) for the aerodynamic (unit density) size distribution of the inlet dust to the copper reactor ESP at the Noranda smelter using an Andersen MKIII cascade impactor. The Sedigraph results were a strong function of the dispersing medium (Appendix C, Section C.5), but show an important weight fraction (> 20%) of submicron particles, in qualitative agreement with the impactor data. The fact that the size distribution obtained by Davis et al. (1979) is highly displaced towards the finer particles is probably due to two factors:

1) The Noranda dust used in the present work was a composite catch from the ESP installed downstream from the copper reactor, and as such it is expected to be coarser than at the reactor ESP inlet.
2) The Wright feeder probably did not disperse the agglomerates completely.

These two effects act in the same direction and displace the size distribution towards coarser sizes.

Figure 5.18 is a typical scanning electron microphotograph of the Noranda dust, after ultrasonic dispersion in water for 20 min, taken with a Jeol CX 100 scanning-transmission electron microscope. The five elements Pb, Zn, Cu, Cd and S were identified in both coarser and finer particles, using energy dispersive analysis of X-rays (EDX). The EDX method is only semiquantitative, since the peak heights are not only a function of the elemental concentration but also of the atomic number. The ratio of peak heights observed for particle (A) for Cu versus Pb (about 16:3) is an indication that these particles have a higher copper content.



20000 X

A - Main elements Cu S
Minor elements Pb Zn Cd

B - Pb Zn Cd Cu S As

Figure 5.18 Typical scanning electron microphotograph of the Noranda dust

On the other hand, the corresponding ratio of peak heights observed for particle (B) (about 3:8) does not necessarily mean that these particles have a higher content in Pb, since the atomic number of Pb is also much larger than that of Cu.

Table 5.5, from Davis et al. (1979) shows the comparative elemental peak ratios obtained by EDX for a reactor composite precipitator catch (similar to the dust used in this work), made on two size fractions obtained by a Bahco centrifugal microparticle classifier.

TABLE 5.5

Chemical Composition of Bahco Size Fractions

(Comparative Elemental Peak Ratios by EDX)

Elements Identified	Size Range (μm) 2.6 < D < 7.8	D > 26
Si	-	1.8
Fe	0.5	8.1
Cu	4.0	19.0
Zn	13.4	4.0
Pb	6.0	2.7
As	10.0	8.0
Cd	13.4	14.0

Special attention is given to the elements Cu, Zn, Pb and Cd, since these were the elements studied in this project. The results in Table 5.5 agree qualitatively with the observations made earlier on the elemental peak ratios observed for particles of type (A) and (B) (Fig. 5.18).

A bulk sample of the industrial dust was separated into two size fractions using the Wright feeder-minicyclone system operated at 15 ℓ min^{-1}. The finer fraction which escaped collection by the minicyclone was captured using a sampling bottle similar to the one used for the calibration of the Tafa vibrating feeder (Appendix B, Section B.3); it is possible that some fine dust escaped collection by the sampling bottle. The cyclone efficiency was estimated from the elemental mass balances on the cyclone catch and overflow to be around 50%. The elemental compositions were determined by atomic absorption spectroscopy (AAS) and are given in Table 5.6. The different results are replicates of the AAS analysis, performed as explained in Section 5.7.

The size distributions of the different size fractions were estimated using the X-ray Sedigraph and the results are given in Fig. 5.19. The fact that the cyclone overflow shows less fine particles below about 0.8 μm than both the feed or cyclone catch is probably due to fine particle losses from the sampling bottle. The densities of the different size fractions were measured by a gas pycnometer to be respectively 3.22 ± 0.06, 3.07 ± 0.15 and 3.05 ± 0.10 g cm^{-3} for the feed, catch and overflow, indicating no significant difference in density (the values are the average ± one standard deviation, 3 samples each).

The chemical composition of a similar dust as analysed by the Noranda Research Center (Davis et al., 1979) is given in Table 5.7.

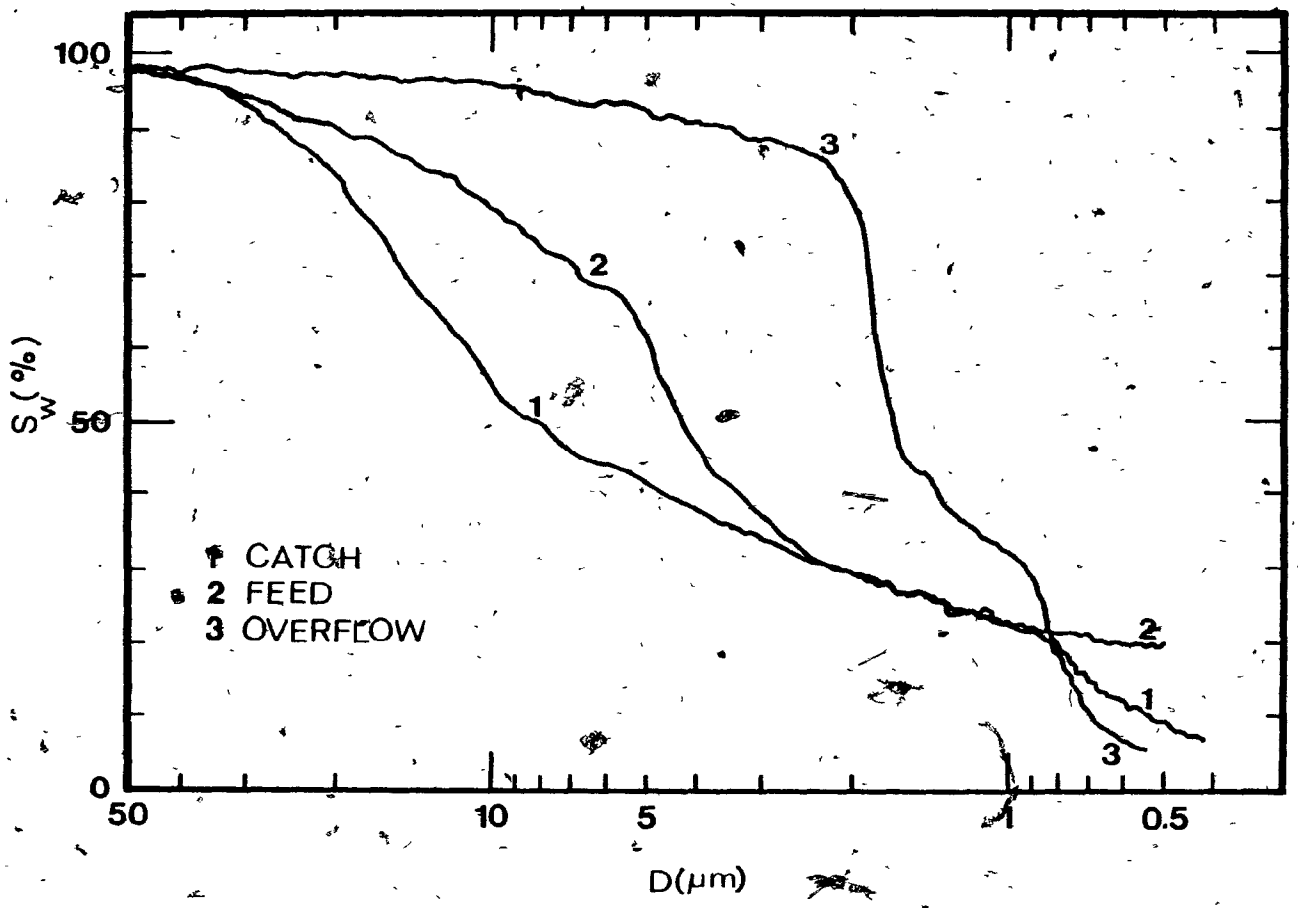


Figure 5.19 Size distributions of bulk size fractions of the Noranda dust (X-ray Sedigraph)

TABLE 5.6

Elemental Composition of Noranda Bulk Size Fractions (%)

Cu	Pb	Zn	Cd	HCl Insolubles
Feed				
6.7	32.9	10.2	11.3	3.6
6.8	27.1	10.0	12.1	3.6
6.7	25.4	11.9	11.6	5.4
6.9	26.9	9.9	11.0	3.9
7.3	25.4	9.7	11.5	N/A
7.1	28.0	10.7	12.7	3.2
6.9 ± 0.2 (1)	27.6 ± 2.9	10.4 ± 0.9	11.7 ± 0.6	3.9 ± 1.1
Cyclone Catch				
10.2	23.5	9.9	10.4	7.5
11.6	23.7	9.2	9.8	N/A
10.9	23.6	9.6	10.1	7.5
Cyclone Overflow				
1.3	31.7	11.3	13.4	0.1
1.9	30.7	10.4	12.5	N/A
1.6	31.2	10.9	13.0	0.1

(1) Average ± 95% confidence limit.

TABLE 5.7

(Davis et al., 1979)

Chemical and X-ray Diffraction Data for Noranda Reactor Dust (Catch)

Chemical Analysis

Cu	Pb	Zn	Cd	Bi	As	Fe	SO_4^{2-}	S^{2-}	C
3.66	35.4	12.6	4.7	0.76	3.86	2.5	21.9	8.9	-
9.68	24.0	8.4	12.3	1.53	2.93	-	23.2	2.56	1.33

Laboratory and Species Identified

XRD: $PbSO_4$, ZnO, $CdSO_4.H_2O$, PbS_2O_3, $2\ ZnCO_3.3\ Zn(OH)_2$, $Cu_{1.5}ZnSO_4(OH)_3$, Fe_3O_4

Species after Dissolving Pb and Other Sulphates

Major: Lead Orthoarsenate Hydroxide:

$3(3\ PbO.As_2O_5).Pb(OH)_2$

Minor: Lead Orthoarsenate:

$3PbO.As_2O_5$, and Fe_2O_3

From the chemical and XRD data provided by Davis et al. (1979), it is apparent that this type of dust is very complex. Of importance is the fact that Pb, Zn, Cd and Cu are present in proportions which are in agreement with the data given in Table 5.6. The large variability of elemental composition seen in Table 5.7 is probably due to process variations, since the two samples were collected on different dates.

It is also apparent from the information of Table 5.6 and Fig. 5.19 that the coarser fraction is richer in copper, while the finer fraction is richer in lead, zinc and cadmium, in agreement with the semiquantitative data of Davis.et al. (1979) given in Table 5.5 and the earlier observations made on Fig. 5.18. The X-ray Sedigraph data and elemental composition of the different bulk size fractions is of little quantitative value for purposes of input data to the SRI computer model. For this, elemental size distributions at the ESP inlet are needed.

This information was provided by chemical analysis of the dust collected on the cascade impactor stages, using AAS. The details are given in Section 5.7 and Fig. 5.20 gives the corresponding elemental distributions at the ESP inlet; the corresponding global size distribution was presented earlier (Fig. 5.17).

Only one density (3.2 g cm^{-3}) was considered when plotting the elemental distributions. This value assumes that no agglomerates leave the Wright feeder and that there are no particle density differences. In the presence of agglomerates the curves will be shifted towards coarser sizes, as seen in

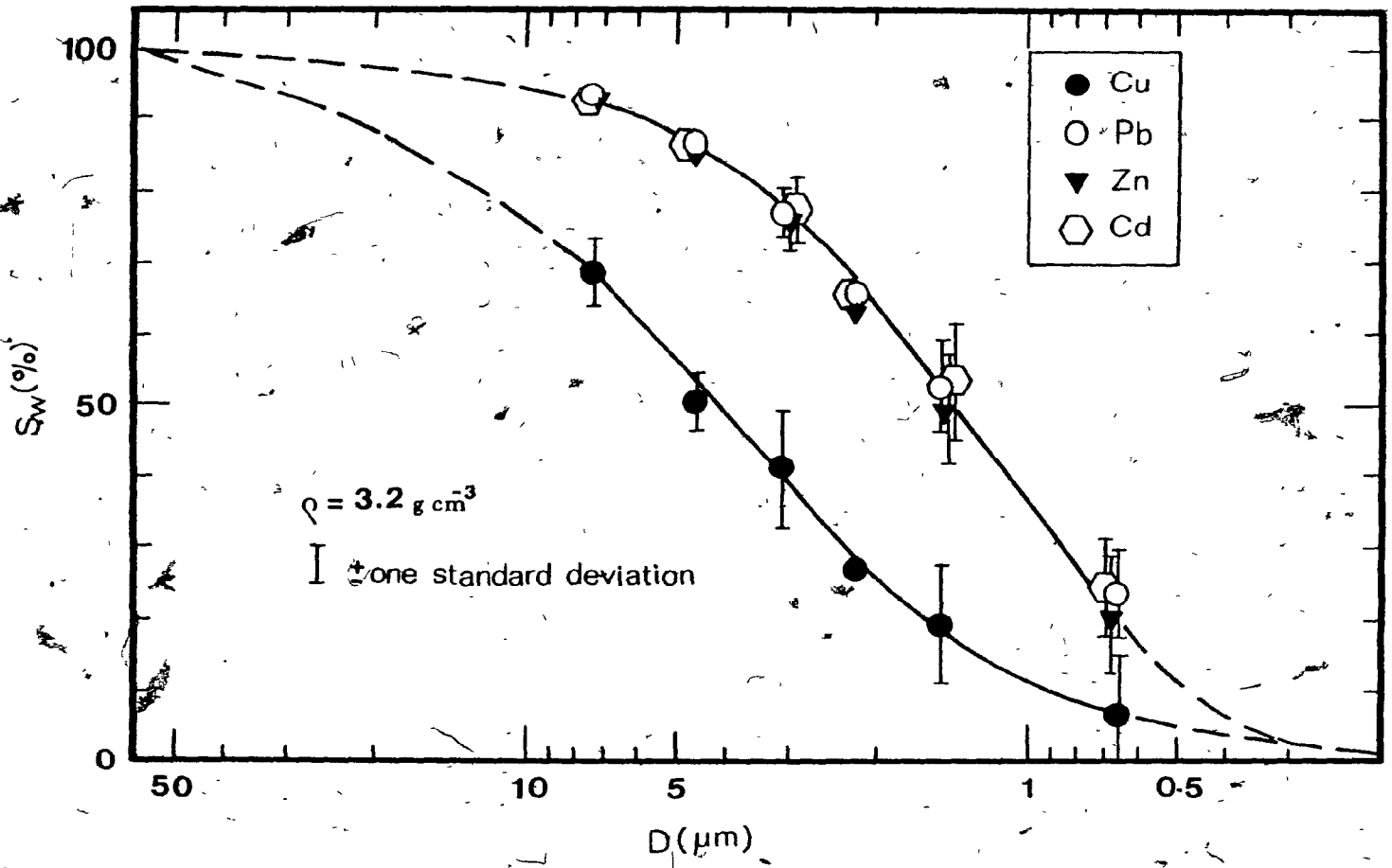


Figure 5.20 Average elemental size distribution of the Noranda dust at the ESP inlet (Andersen MKIII cascade impactor)

Fig. 5.17, but the difference between the elemental distributions will remain. The two distributions would collapse only if the density attributed to the lead, zinc and cadmium rich particles was about eight times the density attributed to the copper rich particles, which is extremely unlikely. It was concluded that the copper rich particles correspond to a coarser size distribution than the lead, zinc and cadmium rich particles. No apparent difference was observed between the elemental distributions of the lead, zinc and cadmium rich particles.

The data given in Fig. 5.20 should not be interpreted as considering that the element Cu is physically separated in distinct particles from the other elements. Figure 5.20 only gives an estimate on the elemental distribution of Cu, Pb, Zn and Cd with respect to particle size, irrespective whether the particles are formed of one or more of these elements. The different particle sizes probably show all of the above elements, but in different proportions, as suggested by the earlier discussion of Fig. 5.18 and Table 5.5.

The weight collected in each substrate for each of the four elements, from which Fig. 5.20 was obtained, is given in Appendix C, Table C.11.

5.5 Dielectric Constant

Knowledge of the relative dielectric constant (K) of the dust particles is important, since this variable affects the charge acquired by the different particles through the factor $(\frac{K}{K+2})$. The dielectric constant was used as input to the SRI

computer model, and it was first estimated for the pure powders listed in Table 5.1 from literature values. Table 5.8 gives the literature values that were found for each of the pure powders (no information could be obtained for the industrial (Noranda) dust). For the case of rutile (tetragonal crystals), the mean value of dielectric constant is given, since these crystals are anisotropic with different values of dielectric constant for different crystallographic orientation with respect to the applied field (Waye, 1967).

The values given in Table 5.8 are at ambient temperature, for a wide range of frequencies. As seen before (Chapter 2, Section 2.4.1), the effect of frequency can be neglected at ambient temperature. From the data of Table 5.8, it can be seen that widely different values may occur for different crystallographic structures of the same chemical species, and even for the same crystallographic structure (case of the rutiles). Fortunately, the effect of the dielectric constant is reduced due to the factor $\frac{K}{K+2}$ which enters the field charging equations, such that uncertainties in the dielectric constant have less serious effects than their absolute values suggest.

An estimation of the dielectric constant of the particles was made by measuring the capacitance of a small cylindrical condenser of electrode area and spacing of 20.4 cm^2 and 5.0 mm respectively, filled with the dusts packed at different bulk densities. The powders were contained by a plexiglass cylindrical section placed between the two 0.64 cm thick copper electrodes.

TABLE 5.8

Dielectric Constants (20-25°C)

Material	Dielectric Constant	Reference
TiO_2		
Brown Rutile	114	Handbook of Chemistry & Physics (1976)
Brown Rutile	111-145	International Critical Tables (1933)
Translucent Rutile	31,73-83	International Critical Tables (1933)
TiO_2	14-110	Handbook of Chemistry & Physics (1976)
TiO_2	80-100	Pender et al. (1975)
TiO_2	114	Samsonov (1973)
TiO_2	114	Kingery et al. (1976)
TiO_2	86	Kaye et al. (1973)
Rutile	100-110	Waye (1967)
Rutile	40-90	Say (1973)
Rutile	40-115	Samsonov (1973)
Ceramic Rutile	12-80	Kaye et al. (1973)
TiO_2	100	Fink et al. (1978)
MgO		
MgO (Magnesia)	10.4	Hove et al. (1965)
MgO	2.2-3.5	Fink (1975), Pender et al. (1975)
MgO	3.1-3.6	Samsonov (1973)
MgO (Periclase)	9.65	Kingery et al. (1976)
MgO (Periclase)	9.7	Kaye et al. (1973)
MgO	8.2	Fink et al. (1978)
CuO		
CuO	18.1	Handbook of Chemistry & Physics (1976) International Critical Tables (1933)
CuO	10.7-18	Samsonov

.....(cont'd.)

TABLE 5.8 (cont'd.)

Material	Dielectric Constant	Reference
Al_2O_3		
Al_2O_3	8.1-10.0	Eink et al. (1978)
Saphire	10.1	Kaye et al. (1973)
Ceramics	8.5-10.8	Kaye et al. (1973)
Al_2O_3	4.5-8.4	Handbook of Chemistry & Physics (1976)
Al_2O_3	12.5	International Critical Tables (1933)
Al_2O_3	9.3	Kingery et al. (1976)
Al_2O_3	10.5-12.3	Samsonov (1973)
Al_2O_3	10.5	Hove et al. (1965)

The capacitance was measured with a Doric C-Meter model 130 A, with a precision of ± 0.1 pF and accuracy ± 1 pF. This capacity meter operates by determining the RC time constant of the test capacitor and a standard resistor, using a small DC voltage applied to the test specimen.

The dusts were dried overnight at 105°C to reduce the effect of moisture, which was not studied as a parameter.

Figure 5.21 gives the experimental results obtained for the powders used in this work, including the two size fractions of the Noranda dust obtained by bulk fractionation using the minicyclone (Table 5.6 and Fig. 5.19). Also shown are some measurements performed on different rutiles other than the one used in this work (ceramic rutile). The different rutiles were obtained from Canadian Titanium Pigments Ltd., Montreal, with MMD's (determined using the X-ray Sedigraph) ranging from 0.4 μm

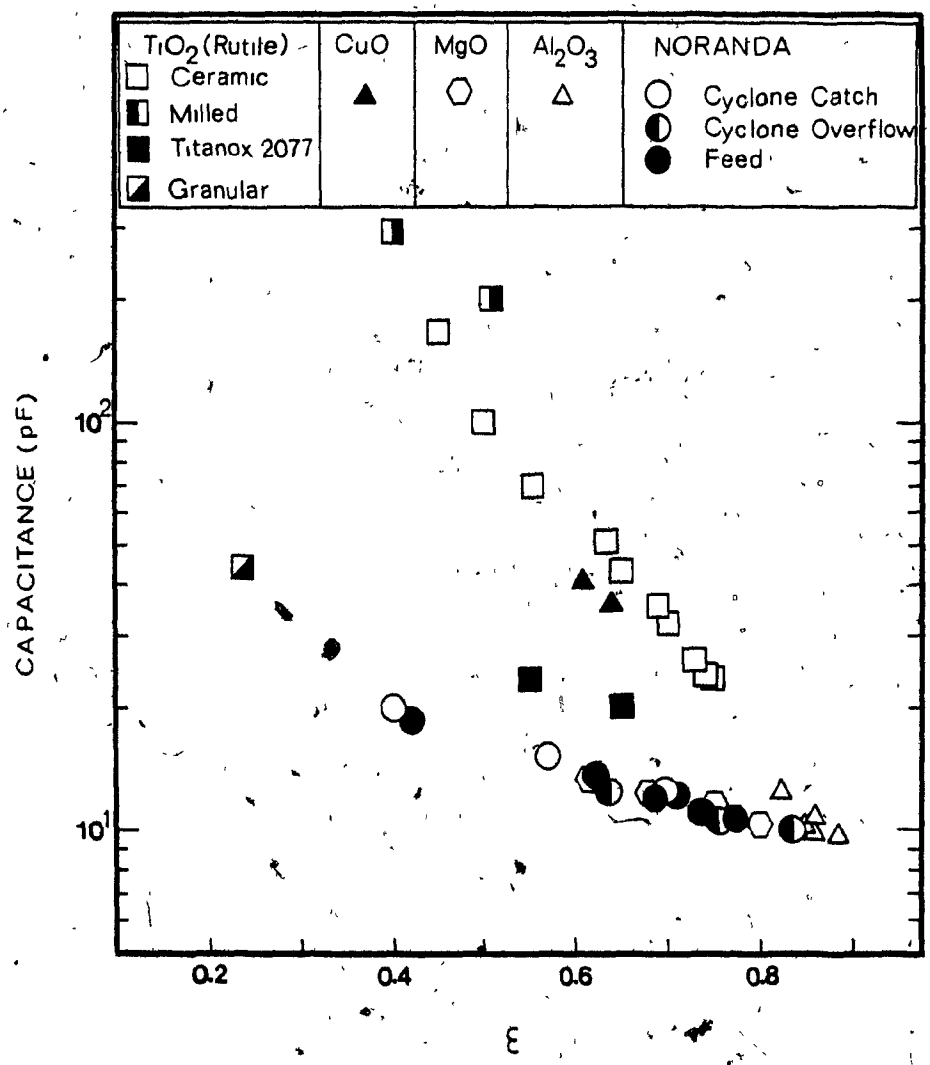


Figure 5.21 Relation between capacitance and void fraction for the various dusts

for Titanox 2077 (a white paint pigment) to above 50 μm for granular rutile (black). Both ceramic and milled rutiles are brown, with mean mass diameters around 10 μm. The void fractions were calculated from the measured bulk densities of the materials and the respective theoretical values.

Some interesting conclusions arise from the data of Fig. 5.21:

- Very different values of capacitance were obtained with the different rutiles, with no apparent correlation with mean particle size. This is in qualitative agreement with the wide range of values reported in the literature (Table 5.8).
- Of the materials used in this work, TiO_2 and CuO have the highest capacitances at the same void fraction, while MgO and the Noranda dust have the lowest values.
- There seems to be no appreciable difference between the capacitance of the different sized Noranda fractions, and no apparent correlation with particle size or chemical composition.
- The measured capacitances are a function of the void fraction.

To estimate the relative dielectric constant from the data of Fig. 5.21, it is necessary to take the void fraction into account. An extrapolation of the data to zero void fraction could be seriously in error, due to the lack of experimental data at low void fractions. The relative dielectric constant of the mixture of particles and air is given by Pampuch (1976) as:

$$K' = C/C_o \qquad (5.35)$$

where (C) and (C_o) are respectively the measured capacitances with and without the compacted dust. The value of (C_o) was determined to be 8 ± 0.1 pF. Botcher (1952) developed a theoretical expression for the dielectric constant of a composite of particles and air (K') as a function of the true dielectric constant of the material that forms the particles (K) and the void fraction (ε) as:

$$K = \frac{3K'(1-\varepsilon) + 2K'(K'-1)}{3K'(1-\varepsilon) - (K'-1)} \qquad (5.36)$$

This relation has been experimentally verified by Botcher (1952) for NaCl and by Hove et al. (1965) for Al_2O_3, and is recommended by Hove et al. (1965) and Tassicker (1971). Figure 5.22 shows the results obtained by the application of Eq. 5.36 to the data of Fig. 5.21, for the powders used in this work.

Except for the fine alumina, the good uniformity of results is an indication that Eq. 5.36 is probably applicable. The high scatter obtained for the alumina particles could be due to poor compaction of the dust in the condenser. Since the measured values represent the dielectric constant of the material forming the particles for a zero void fraction, care must be taken in interpreting its meaning, since surface effects may be present on individual particles at the ESP inlet which may alter its value from the measured one. Botcher (1952) also states that the

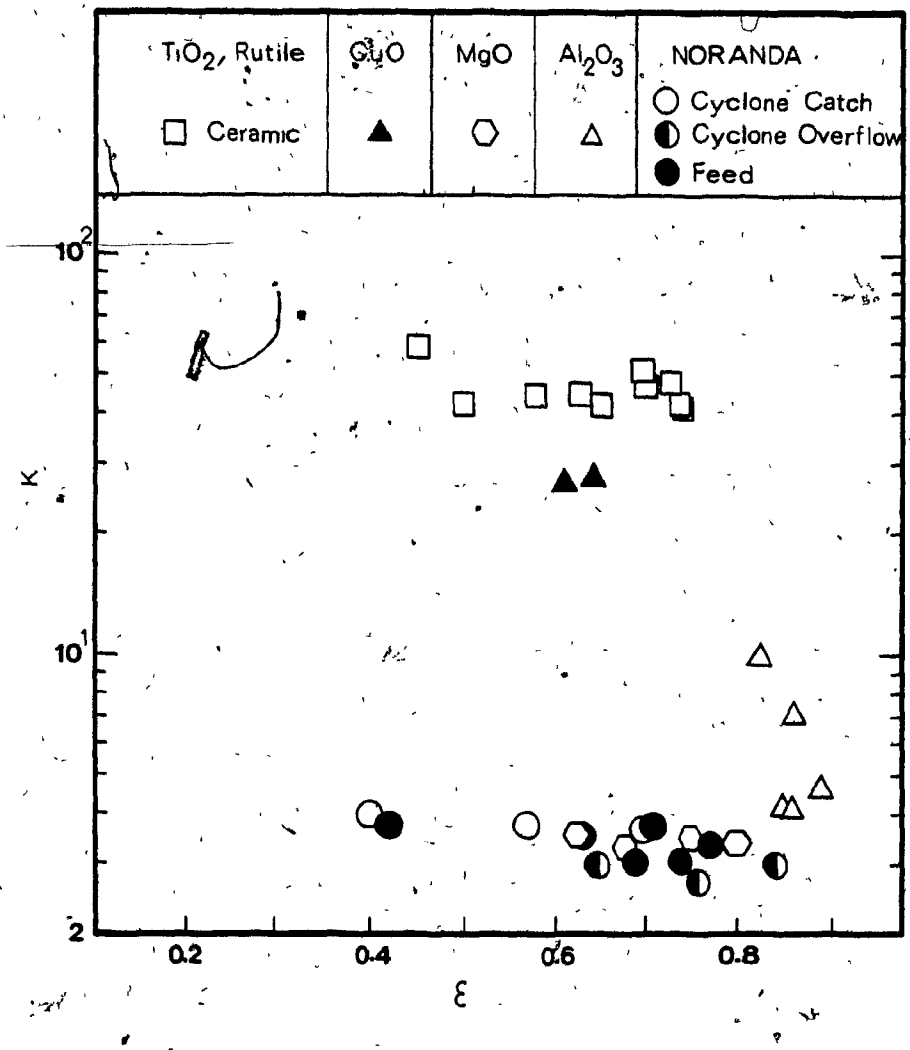


Figure 5.22 Relation between dielectric constant and void fraction for the various dusts

condenser size may have an effect on the obtained values. Also, for the Noranda dust, the particles have different composition depending on particle size, such that the meaning of the measured value of dielectric constant is unclear. For all these reasons, the measured values should only be regarded as a first approximation to the true dielectric constant of the individual particles at the ESP inlet.

Table 5.9 gives the measured average values (± one standard deviation) for the different dusts.

TABLE 5.9

Estimated Dielectric Constants

Material		Dielectric Constant
CuO		27.0 ± 1.0
MgO		3.4 ± 0.1
TiO_2		46.0 ± 6.0
Al_2O_3		5.9 ± 2.5
Noranda	Feed	3.4 ± 0.3
	Cyclone Catch	3.8 ± 0.2
	Cyclone Overflow	2.9 ± 0.1

Comparison of the measured values with those given in the literature (Table 5.8) shows good agreement for all dusts except CuO. Because of the low resistivity of CuO (Section 5.6), its capacitance could only be measured after coating the electrode surfaces in contact with the powder with a plastic

film; otherwise the capacitor would leak. Even so, it could not be shown conclusively that no leakage occurred. Simulations performed at various conditions of air velocity (up to 5 ms^{-1}) and applied field (24-40 KV) showed negligible difference in predicted collection efficiency (less than 2%) whether the experimental value of K = 27 or the literature value of K = 18.1 was used. Similar tests performed for TiO_2, using a recommended value of K = 114 (Hare, 1980) and the experimental value of K = 46 yielded theoretical collection efficiencies within 1% for all conditions tested.

The experimental values listed in Table 5.9 were used for all the computer simulations for the pure powders. For the case of the Noranda dust, estimated values of dielectric constant corresponding to the elemental distributions of Fig. 5.20 are needed. For the lead, zinc and cadmium rich particles, a value of K = 2.9 was used. This corresponds to the cyclone overflow, which is essentially copper free. For the copper rich particles, a value of K = 10 was used. This corresponds approximately to the value reported for $CuSO_4$ (Fink et al., 1978). The cyclone catch, although much richer in copper than the cyclone overflow (Table 5.6), contains also appreciable amounts of Pb, Zn and Cd, and its dielectric constant may not be representative of the dielectric constant of the copper rich particles.

5.6 Bulk Electrical Resistivity

The experimental runs, with the ESP, were performed at ambient temperature and the effective resistivity of the precipitated dust layer is the surface resistivity (Chapter 2, Section 2.6).

Although literature values of surface resistivity are available for some powders, great care must be exercised in using those values since a wide variation may occur due to measurement methods and surface effects. The only reliable values are those measured under conditions similar to those prevailing at the ESP (White, 1978). For the case of air as the flue gas, the humidity and electric field conditions may have an important effect on the effective value of the bulk resistivity of the precipitated dust layer. According to McLean (1976) and McLean et al. (1974), the surface resistivity may be expressed as:

$$r_{eff} = A_s \exp\{- pB \exp(\frac{C}{T})\} \cdot \exp(-ZE_{av}) \qquad (5.37)$$

where (A_s) depends on the intrinsic properties of the material and mode of compaction, (p) is partial pressure of water vapor at temperature (T), (B,C) are empirical constants and (Z) is independent of the average field. The average electric field through the dust layer (E_{av}) is computed from:

$$E_{av} = \frac{\Delta V}{\Delta x} = jr_{eff} \qquad (5.38)$$

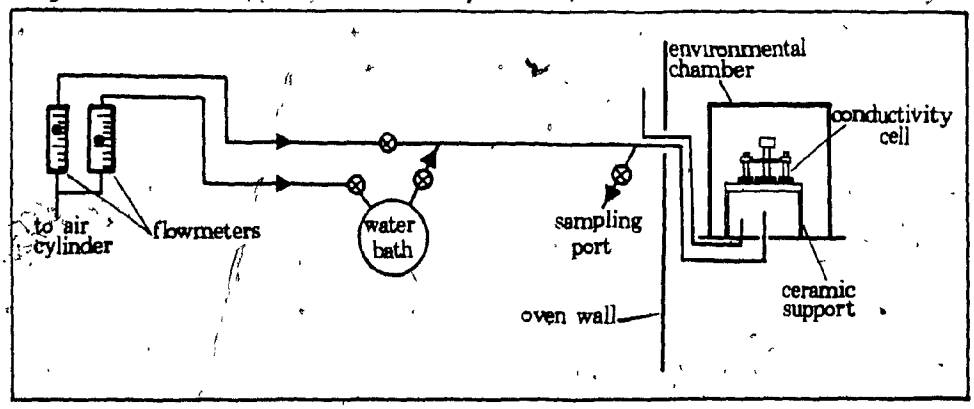
where (ΔV) is the applied voltage across the dust layer of thickness (Δx), such that an average current density (j) will occur. For a precipitated dust layer, (j) refers to the average current density at the collection plates. Equations 5.37 and 5.38 may be combined to solve for (r_{eff}) by trial and error.

The bulk resistivities of the various dusts were measured in an ASME bulk resistivity cell (ASME Power Test Code 28, 1965) available at the Noranda Research Center, Pointe Claire, Quebec. Figure 5.23a (Davis et al., 1979) is a schematic diagram of the apparatus, which includes provisions for humidifying and heating the dust specimen; Fig. 5.23b (Davis et al., 1979) is a schematic diagram of the electrical circuitry and Fig. 5.23c (Davis et al., 1979) shows the high voltage conductivity cell in detail.

The method of operation was as follows (ASME Power Test Code 28, 1965):

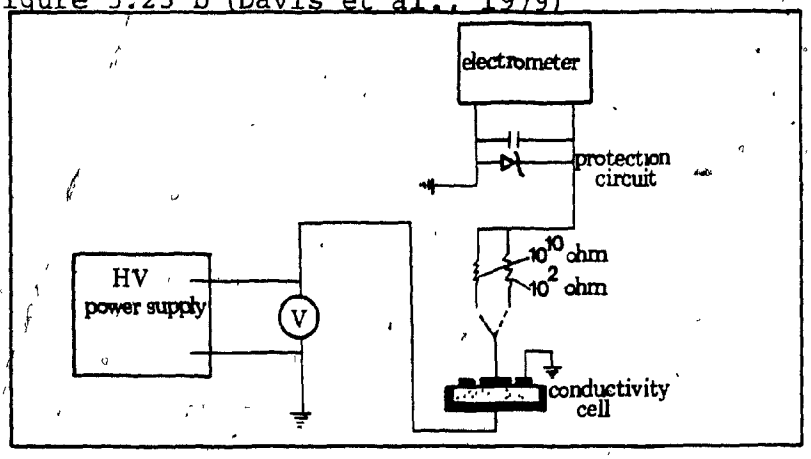
1) The dust was placed in the conductivity cell 5mm deep with a spatula and levelled by drawing a straight edge blade across the top of the cup.
2) The disk electrode of 5.07 cm^2 area was gently lowered onto the surface of the dust, exerting a fixed pressure of 980 Pa, and mounted in the electric oven to establish the desired temperature and humidity. The temperature was set by a thermostatically controlled forced-convection oven and the humidity by circulating pre-conditioned air through the specimen. The dust cup is made of

Figure 5.23 a(Davis et al., 1979)



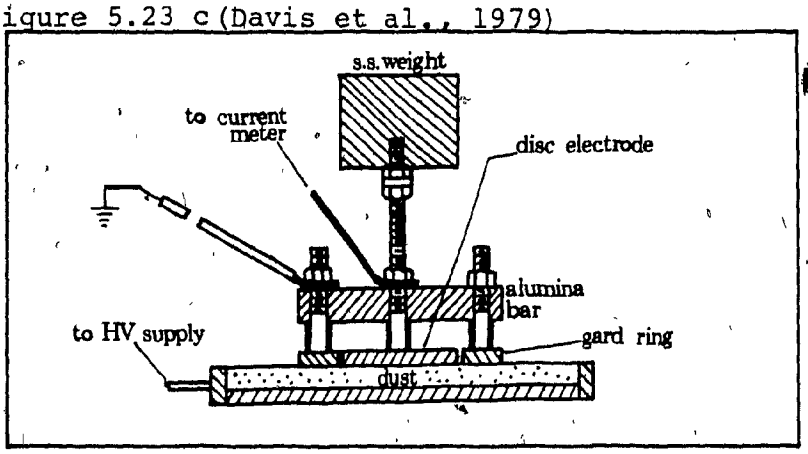
Experimental apparatus for bulk resistivity measurements

Figure 5.23 b (Davis et al., 1979)



Electric circuitry

Figure 5.23 c(Davis et al., 1979)



Bulk resistivity cell

porous sintered stainless steel and the humidifying air was injected directly beneath, to provide intimate contact between the humidifying air and the dust sample.

The pre-conditioned air was prepared by bubbling extra dry air through a water bath and mixing with extra dry air at controlled rates. Both rates were measured with calibrated rotameters. The moisture content of the resulting air was measured at the oven inlet by gravimetric determination, using tubes filled with magnesium perchlorate and immersed in ice. The relative humidities of the pre-conditioned air were reproducible to within ± 2% (absolute value).

The flow rate of the test atmosphere was controlled to allow about 8-10 volume changes per hour inside the environmental chamber, i.e., 1.1-1.4 ℓ min^{-1}.

3) An increasing DC positive voltage was applied to the test specimen with a CRI AC-DC power supply (Canadian Research Institute, model E-19647, Ontario) up to a maximum of 10 KV, and the current measured at each voltage with a Keithley electrometer, model 610B. The input to the electrometer was protected from surge currents with a 10 V zener diode (Fig. 5.23b). The measurements were taken approximately one minute after the application of the voltage to the test specimen.

4) The effective resistivity was calculated from the voltage-current measurements using Eq. 5.38.

Although all the measurements were taken with a sample thickness of 5 mm, Davis et al. (1979) obtained similar results using either 5 or 3 mm thick samples.

The conditions for equilibrium of temperature and moisture content of the sample with that of the controlled atmosphere were determined by the requirement that the resistivity measurements be reproducible within 10% when determined by two successive measurements made 15 min apart. It was found that about 6-8 hr per sample were required to fulfil this requirement at ambient temperature, and about 4 hr at 60-70°C. Shorter times (1-2 hr) are usually considered sufficient at higher temperatures.

Figures 5.24 and 5.25 show the experimental results obtained for the different powders, at ambient temperatures (21-24°C). Also shown are experimental data for CuO and MgO at a higher temperature.

Most of the results were obtained with the same undisturbed sample of dust, i.e., breakdown was not reached and so the dusts did not require remixing. This procedure eliminates the variable of dust compaction, and some replicates were performed with both alumina and the Noranda dusts to obtain information on the possible effect of this variable. From the replicate points in Fig. 5.25, it is seen that the results were reproducible within a factor of three. Figure 5.24 also shows the results obtained with a different sample of CuO, where the humidity was slightly different from previous conditions, and order of magni-

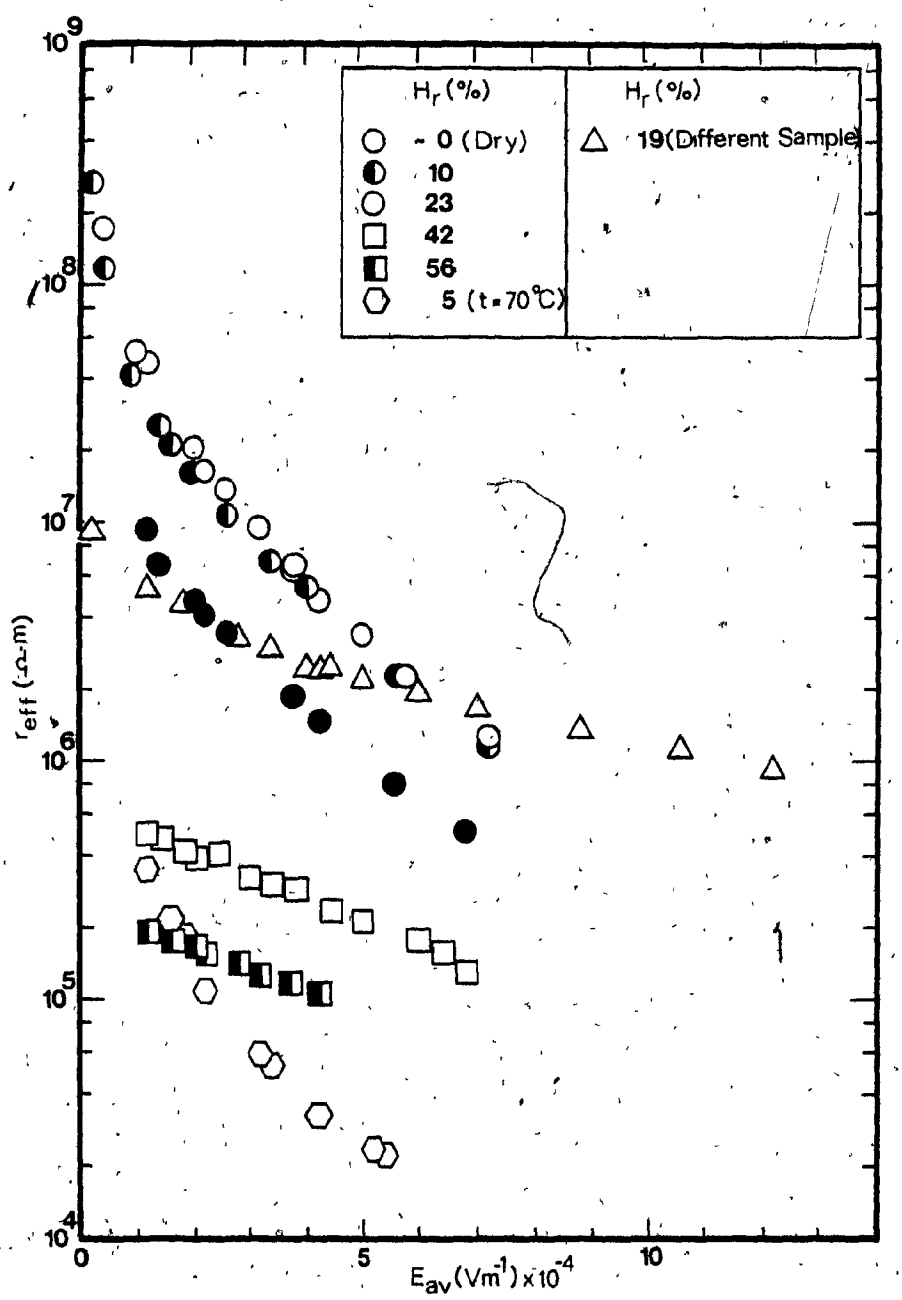


Figure 5.24 Bulk resistivity of CuO as a function of applied field and relative humidity

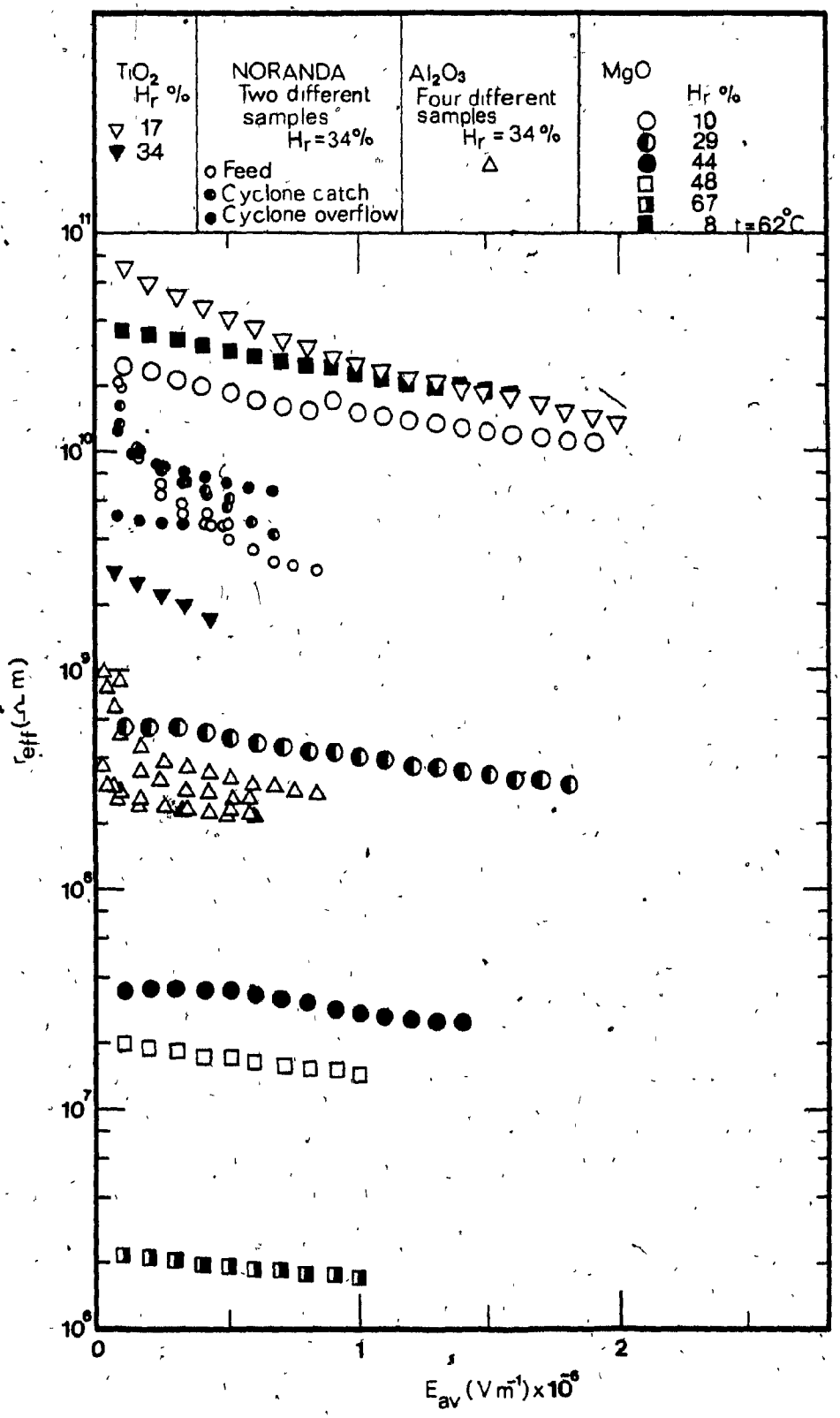


Figure 5.25 Bulk resistivity of TiO_2, MgO, Al_2O_3 and Noranda dusts as a function of applied field and relative humidity

tude agreement was obtained.

The experimental data of Figs. 5.24 and 5.25 show that the resistivity of cupric oxide is the lowest of all dusts, at comparable values of relative humidity. Similarly, the resistivities of the Noranda dusts are the highest. The effect of increased applied field and humidity is to lower the effective resistivity for all dusts tested at different humidities (CuO, MgO, TiO_2) but the humidity effect is the strongest. Also, there seems to be no significant difference between the resistivities of the different Noranda size fractions, and as such no correlation with particle size or chemical composition. These results agree qualitatively with those of Davis et al. (1979) for the resistivity of Bahco fractionated samples of the copper reactor ESP catch.

The experiments performed at a higher temperature with both CuO and MgO provided information necessary for the fitting of the experimental data to the surface resistivity model of McLean (1976). For cupric oxide, the observed resistivities at 70°C were smaller than at ambient temperature (24°C) at the same partial pressure of water vapor (12.5 mm Hg), and McLean's model could only be used neglecting the temperature influence. The reason that the observed resistivities were smaller at a higher temperature is probably due to the increased effect of volume conduction. This hypothesis could not be tested due to the difficulty in attaining temperatures above ambient but less than about 60-70°C with the available forced-convection oven.

For magnesium oxide, the observed resistivities at 62°C were larger than at ambient temperature (21°C) at the same partial pressure of water vapor (12.5 mm Hg), an indication that volume conduction was still unimportant.

Table 5.10 gives the estimated values of the parameters of Eq. 5.37 for the oxides of copper and magnesium. For cupric oxide, the parameters were estimated by least-squares fitting of the resistivity data at ambient temperature, assuming C = 0 (in Eq. 5.37), since the resistivity values obtained at a higher temperature showed the effect of volume conduction. For magnesium oxide, the parameters (A_s, B, C) were estimated as suggested by McLean (1976).

The parameter (Z) was estimated by averaging the different values obtained by least-squares fitting of the resistivity data at different values of applied field (E_{av}) for each partial pressure of water vapor.

TABLE 5.10

Estimated Parameters of Surface Resistivity (Eq. 5.37)

Material	A_s (Ohm m)	B ($mm\ Hg^{-1}$)	C (K)	Z (mV^{-1})
CuO	1.6×10^{8}	0.51	(0)	$\sim 4.9 \times 10^{-5}$
MgO	2.0×10^{11}	2.83×10^{-8}	5117	$\sim 3.7 \times 10^{-7}$

Although the parameter (Z) was actually a function of (p,T), decreasing with increasing partial pressure of water vapor and decreasing temperature, the assumption of constant (Z) corresponds to a constant slope for each dust on Figs. 5.24 and 5.25 and was considered a reasonable approximation in view of uncertainties introduced by other variables, e.g., the compaction mode.

In Table 5.10, the value of (B) estimated for CuO is much larger than that for MgO, due to the fact that the temperature effect was neglected, i.e., C = 0.

Equation 5.37 was used with the data of Table 5.10 to estimate the resistivities of CuO and MgO at the various precipitating conditions of humidity and average current density at the plates. These data are not available for the other dusts, where measurements were limited to one or two relative humidities. It will be seen in the next chapters that this lack of information was not critical for a correct interpretation of the precipitation phenomena, and that an order of magnitude estimate of the resistivity would be sufficient.

Equation 5.37 (with the data of Table 5.10) agrees within a factor of three with the experimental values of resistivity for both CuO and MgO at all relative humidities and current densities at which the experimental resistivities were measured.

5.7 Chemical Analyses

Chemical analyses of the dusts collected in the ESP and on the sampling trains at both inlet and outlet of the ESP were performed by atomic absorption spectroscopy (AAS). Basically, an atomic absorption spectrophotometer consists of (Robinson, 1975):

- a light source which emits the spectrum of the element of interest, usually a hollow cathode lamp;
- an absorption cell in which the atoms of the sample to be analysed are formed by thermal dissociation, usually in a flame;
- a monochromator with exit slit for selection of the appropriate absorption line;
- a detector permitting measurement of the intensity of radiation; and
- an amplifier with display instrument for the readout of the absorption values.

Dusts must first be solubilized in specific mediums, diluted to appropriate levels and aspirated into the flame of the AA spectrophotometer for analysis.

The absorbance is directly proportional to the concentration, for low concentrations (Beer's law). At some higher value of concentration, the absorbance increases less than proportionately with concentration, and the construction of calibration curves becomes necessary. The upper limit of concentration for which Beer's law is applicable depends on both the element to be analysed and on the particular spectrophotometer.

Two different AA spectrophotometers were used, depending on the element to be analised. A Perkin-Elmer 403 dual-beam AA spectrophotometer was used for the analysis of copper, magnesium, lead, zinc and cadmium, using an air-acetylene flame. A Pye-Unicam SP 190 single-beam AA spectrophotometer was used for the analysis of aluminium, with a nitrous oxide-acetylene flame. The element titanium was not analysed by AAS but rather determined by difference, due to the possibility of various interferences which could decrease the accuracy of the results.

The analyses were always performed at dilution levels at which Beer's law was applicable. The maximum recommended concentrations for the various elements at which Beer's law was applicable were read from the respective AA spectrophotometer application manuals, and experimentally verified.

One problem is to obtain a representative sample of the dust to be analysed. With the exception of the cascade impactor substrates and the outlet sampling filter, it was not practical to dissolve the entire sample and replicates were performed to establish the confidence limits to which the analyses could be performed (see for example Table 5.6).

When cupric and magnesium oxides were present in mixtures with alumina or titanium dioxide, the elements Cu and Mg were analysed by AAS and the compounds Al_2O_3 or TiO_2 were determined by difference.

Experiments with mixtures of CuO and MgO revealed that essentially the same results were obtained by either analysing for both Cu and Mg, or only for one element and determining the other by difference.

The oxides of Cu and Mg were solubilized with a 5% volume H_2SO_4 and 1% volume HNO_3 weak acid solution (Young, 1971). The solutions were filtered to remove possible undissolved material (for example, in mixtures with TiO_2 or Al_2O_3) and diluted with deionized water to appropriate levels. The standards were prepared by dissolving a known amount of the pure powder and diluting to the appropriate levels.

For the analysis of alumina by AAS, the reactive γ-Al_2O_3 is readily dissolved in concentrated HF (49%) at room temperature, but the stable α-Al_2O_3 is resistant to chemical attack. Usually, α-Al_2O_3 can be brought into solution only after fusion with a flux such as potassium bissulfite (Heslop et al., 1963); however, this depends on the reactivity of the particular α-alumina (Gitzen, 1970).

The alumina used in this work could only be partially solubilized after 15 hrs of attack by concentrated HF, at room temperature.

The alumina standards were prepared from partial dissolution of the feed to the minicyclone and corresponded to a certain fixed content of α and γ phases.

To determine whether this phase content was representative of samples collected along the ESP length, one experimental

run was performed at an intermediate voltage (30 KV) and high air velocity (5 ms^{-1}). A total of eight samples from the cyclone feed (2), cyclone catch (2) and collected along the ESP length (4) were analysed for alumina solubility by gravimetric determination of the insoluble α-Al_2O_3. All samples except one cyclone feed and one cyclone catch were submitted to continuous agitation (using Teflon coated magnetic stirrers) during the solubilization period. The partially solubilized samples were then filtered through 0.15 μm membrane filters and dried before weighing. No appreciable difference was observed between the phase contents of the different samples, as inferred from the proportion of soluble (probably γ-Al_2O_3) and insoluble (α-Al_2O_3) weights with respect to the total sample weight. The experimentally determined insoluble content of 81.5 ± 0.7% (average ± one standard deviation) agrees well with the nominal content of 80 to 90% in α-Al_2O_3 specified for this type of alumina (Niesz et al., 1978). The results from the gravimetric analysis were confirmed by AAS of the solubilized alumina; a linear relation was obtained between the total sample weight (α+γ phases) and the measured absorbance.

Operation of the AA spectrophotometer with a N_2O-C_2H_2 flame was less convenient than with an air-C_2H_2 flame, due to the safety precautions required (explosions of mixtures of N_2O-air may occur) and the build up of carbon on the tip of the burner head, which had to be removed before a measurement was taken. Due to these reasons, with mixtures of CuO/Al_2O_3 or MgO/Al_2O_3, the elements (Cu) and (Mg) were determined by AAS,

while Al_2O_3 was found by difference. With mixtures of Al_2O_3/TiO_2 the element (Al) was directly determined by AAS.

The determination of the elements (Mg) and (Al) by AAS is subject to some interferences (Kirkbright et al., 1974 and Rubeska et al., 1969). For the determination of (Mg) in the presence of (Al), the final solutions were made to 500 µg ml^{-1} in $SrCl_2$, while for the determination of (Al) the final solutions were made to 2000 µg ml^{-1} in KCl. The possible interferences were effectively removed as checked by analysis of known mixtures of the respective compounds.

Since TiO_2 was always determined by difference, it was necessary to check whether its impurities affected the measurements. From data provided by Canadian Titanium Pigments Ltd., Montreal (Product Data Sheet CP-5, Ceramic Rutile), a typical composition is 96% TiO_2 with a total of 3% in ZrO_2, SiO_2, Fe_2O_3, Cr_2O_3 and V_2O_5. It was experimentally verified that the analysis of Cu, Mg and Al in the presence of TiO_2 was not altered by these impurities.

The Noranda dust was dissolved using conc. HCl, which dissolved about 96% of the dust, leaving 4% of insoluble black and white residue, consisting probably of sulfides, silica and unburned carbon. Complete dissolution is possible (Davis et al., 1979), but the simpler use of conc. HCl was preferred due to the small amount of insoluble residue and to the simplicity of the operation. The insoluble residue was filtered for each sample to be analysed by AAS.

For the analysis of the dust collected in the cascade impactor and the outlet sampling filter, contamination occurred due to acid extraction of the elements Pb, Zn, Cd and Cu from the glass fibers. A series of blank tests were performed to determine the extent of the contamination for appropriate correction. Table 5.11 gives the average results (± one standard deviation) of the composition of the Noranda dust fed to the ESP inlet, as determined from AAS analysis of bulk feed samples (Table 5.6), from the impactor substrates and from the dust collected in the ESP and at the outlet sampling filter (elemental mass balances).

TABLE 5.11

Composition of Noranda Dust at the ESP Inlet (%)

	Cu	Pb	Zn	Cd
Feed (6 samples)	6.9±0.2	27.6±2.8	10.4±0.8	11.7±0.6
Cascade Impactor[1] (3 samples)	3.4±2.3	28.9±2.2	10.8±1.3	12.6±1.8
Elemental Mass Balances[1] (3 samples)	7.5±1.2	26.0±3.7	9.8±0.4	10.9±1.4

[1] Averaged with respect to sampling time.

The good agreement of the different measurements is an indication of the feasibility of performing AAS analysis on the impactor substrates. The largest error (with respect to either feed or elemental mass balances) occurs in the detection

of Cu, and this was probably due to a preferential loss of Cu rich particles to the walls of the cascade impactor. This is discussed in Chapter 8.

5.8 Particle Collection Experiments

The following is a sequential description of a typical experimental run involving both sampling at the inlet and outlet of the ESP, to determine both experimental and theoretical collection and separation efficiencies:

1) Desicate overnight the impactor substrates, backfilter and outlet sampling filter, and weigh to ± 0.02 mg. Mount on the respective holders and connect the holders to the sampling nozzles. Place the inlet sampling nozzle at the midpoint of the channel flow at the ESP inlet, and the outlet sampling nozzle at the first sampling point of the outlet sampling station (Fig . C.2, Appendix C).
2) Prepare particle feeder(s).
3) Open ESP outlet valve.
4) Turn blower on and allow about 1/2 hr for the temperature at the ESP inlet to stabilize. Read the temperature. Adjust the flow rate of air through the ESP using the blower inlet valve and Eq. B.4 (Appendix B), using the pressure drop across the Venturi meter.

5) Calculate the correct sampling velocities for both the inlet and outlet sampling trains. Calculate the correct sampling flow rates from the sampling nozzle diameters.

6) Set the desired flow rate of air at atmospheric conditions for the sampling train at the ESP outlet (Fig. C.1, Appendix C), read the pressure at the rotameter and correct the flow rate according to the standard rotameter equation:

$$Q\rho_{air} = Kh\sqrt{\rho}_{air} \qquad (5.39)$$

where (Q) is volumetric flow rate, (ρ_{air}) is air density, (K) is rotameter constant (determined from the calibration curve) and (h) is float height.

Set the flow rate of air to the approximate desired level (at atmospheric conditions) for the sampling train at the ESP inlet, as measured by a dry test meter; read the pressure at the test meter and correct the flow by using the ideal gas law:

$$Q_{atm} \simeq Q\left(\frac{P}{P_{atm}}\right) \qquad (5.40)$$

where (Q_{atm}) is the desired flow rate at the nozzle condition of near atmospheric pressure (P_{atm}), (Q)

is the metered flow rate at the test meter pressure (P) and where the effect of temperature was neglected.

The sampling flows are adjusted by using the bleed valves upstream of the vacuum pumps.

7) Read ambient humidity and temperature with a wet-dry bulb psychrometer.

8) Turn on the HV supply, increasing the voltage to the desired level. Read both the total current from the power supply and the current to the plates, using the appropriate ammeters. If these values do not check, turn the power supply off and correct the fault (Chapter 4, Section 4.5).

9) Start flow of compressed air to the powder feeder and turn the powder feeder(s) on. Simultaneously start counting the elapsed time.

10) After the appropriate elapsed time, change outlet sampling filter location to the next sampling point, allowing an equal time per sampling point (minimum of 3 min). Immediately readjust the outlet sampling flow rate to keep isokinetic conditions.

11) Read the temperature, humidity, applied voltage and currents at regular intervals to check for any appreciable difference during the experiment.

12) At the end of the experiment, turn powder feeder(s) and compressed air off. Turn (sampling) vacuum pumps off.

13) Turn off the blower while slowly decreasing the applied voltage. This prevents loss of particles from the collection plates since the adhesion forces due to the corona current cease to exist without corona. Turn the power supply off and close the ESP outlet valve.

14) Place filter holder with filter, impactor substrates and backfilter on desicator, overnight, carefully brushing-off onto the appropriate substrates any dust that might remain on the cascade impactor entrance cone and cross pieces.

15) Open the ESP plates by removing the "C" clamps and the sealing tape.

16) Carefully brush the dust precipitated on the plates to small pre-weighed plastic bags. Divide the ESP into equal length intervals and collect separately the dust from each size increment. Weigh each sample to ± 0.01 g.

17) Brush off the dust collected on the ESP bottom to a pre-weighed plastic bag. Weigh to within ± 0.01 g.

18) Brush off the dust collected on the plenum chamber and the piping system prior to the ESP inlet to a pre-weighed plastic bag. Weigh to within ± 0.01 g.

19) With a small vacuum cleaner and pre-weighed vacuum filter, thoroughly remove the small amount of dust that remains after the brushing operation. Weigh the vacuum cleaner filter to within ± 0.01 g and add the sample weight to the corresponding brushed weights.

20) Wash the ESP plates with ethanol, close the plates and seal them with flexible tape. The ESP is now prepared for the next run.

21) After desication , weigh the impactor substrates, backfilter and outlet sampling filter to within ± 0.02 mg, carefully brushing off onto the sampling filter any dust that might remain on the filter holder. Carefully place the substrates, backfilter and outlet sampling filter on appropriate containers used for the dissolution of the samples whenever AAS analysis is required.

22) Compute the global (electrical, i.e., at the plates and mechanical) collection based on the outlet filter and dust collected both at the plates (along the ESP length) and on the ESP bottom.

23) If required, perform AAS analysis on the various samples collected along the ESP length, at the ESP bottom, on the outlet sampling filter and on the cascade impactor substrates and backfilter.

24) Compute the elemental (or component) collection efficiencies from the global collection efficiency and the AAS analysis, as a function of ESP length.

25) Compute the segregation between the different elements (or components).

26) If required, measure the size distribution of samples collected on the ESP plates or at the outlet sampling filter.

27) Estimate the size distribution at the ESP inlet, from the cascade impactor bulk data.

28) Estimate the elemental size distributions at the ESP inlet from the above information and the AAS analysis of the impactor substrates and backfilter.

29) Use the experimental data on size distribution, electrical properties and average operating conditions corresponding to each experimental run as input to the SRI computer model.

30) Compare the experimental results of collection and separation efficiencies with those obtained from the simulation.

The detailed information on the operating conditions of each experimental run and both the experimental and simulation results obtained are given in the next three chapters.

REFERENCES

Abramowitz, M. and Stegun, I.A. (1964): "Handbook of Mathematical Functions", National Bureau of Standards, pp.931-933.

Allen, T. (1968): "Particle Size Measurement", Chapman and Hall, Ltd., London.

ASME Power Test Code 28 (1965): "Determining the Properties of Fine Particulate Matter", pp.15-17.

Botcher, C.J.F. (1952): "Theory of Electric Polarization", Elsevier Pub. Co., pp.415-420.

Crawford, M. (1976): "Air Pollution Control Theory", McGraw-Hill, pp.129-140.

Davies, R. (1973): "Rapid Response Instrumentation for Particle Size Analyses - A Review", American Laboratory, December, pp.17-55.

Davis, H.J.; Kerbyson, J.D. and Nethersole, D.C. (1979): "Study of Factors Affecting the Electrostatic Precipitation Efficiency of Particulates in Non-Ferrous Smelter Gases", prepared by Centre de Recherche Noranda, Quebec, for Environment Canada, July.

Elder, J.C., Tillerg, M.I. and Ettinger, H.J. (1981): "Evaluation of EPA Method 5 Probe Deposition and Filter Media Efficiency", JAPCA, 31, No. 1, January, pp.66-68.

Flock, W.M. (1978): "Bayer-Processed Aluminas" in "Ceramic Processing before Firing", Onoda and Hench (eds.), John Wiley & Sons Ltd., pp.85-100.

Fink, (1975): "Electronic Engineers' Handbook", McGraw-Hill, 1st ed.

_____ and Beaty (1978): "Standard Handbook for Electrical Engineers", McGraw-Hill, 11th ed.

Gitzen, W.H. (1970): "Alumina as a Ceramic Material", The American Ceramic Society, pp.103.

"Handbook of Chemistry & Physics" (1976-1977), CRC Press, 57th ed., pp.E 58-60.

Hare, A.L. (1980): "Personal Communication" - Tioxide International Ltd., Billingham, Cleveland, England, September 18.

Hench, L.L. and Jenkins, E.J. (1978): "Characterization of Agglomerates with Transmission Electron Microscopy", in "Ceramic Processing before Firing", Onoda and Hench (eds.), John Wiley & Sons Ltd., pp.75-84.

Herdan, G.; Smith, M.L.; Hardwick, W.H. and Connor, P. (1960): "Small Particle Statistics", Butterworths, London.

Hesketh, H.E. (1977): "Fine Particles in Gaseous Media", Ann Arbor Science Pub. Inc., pp.2.

Hove, J.E. and Riley, W.C. (1965): "Modern Ceramics: Some Principles and Concepts", John Wiley & Sons, Inc., pp.228-229.

"International Critical Tables of Numerical Data, Physics, Chemistry and Technology" (1933), McGraw-Hill, pp.74-105.

Kaye, G.W.C. and Laby, T.H. (1973): "Tables of Physical and Chemical Constants", Longman, 14th ed., pp.109-114.

Kingery, W.D.; Bowen, H.K. and Uhlmann, D.R. (1976): "Introduction to Ceramics", John Wiley & Sons, 2nd ed.

Kirkbright and Sargent (1974): "Atomic Absorption and Fluorescence Spectroscopy", Academic Press.

Lapple, C.E. (1968): "Particle-Size Analysis and Analysers", Chem. Engineering, May, pp.149-156.

Licht, W. (1980): "Air Pollution Control Engineering", M. Dekker Inc., 1980, pp.49-54.

Maisel, L. (1971): "Probability, Statistics and Random Processes", Simon & Schuster, Tech. Outlines, N.Y.

Marple, V.A. and Willeke, K. (1976): "Inertial Impactors: Theory, Design and Use", in "Fine Particles: Aerosol Generation, Measurement, Sampling and Analysis", B.Y.H. Liu (ed.), Ac. Press, pp.412-446.

McCain, J.D.; Cushing, K.M. and Smith, W.B. (1974): "Methods for Determining Particulate Mass and Size Properties: Laboratory and Field Measurements", JAPCA, 24, No. 12, December, pp.1172-1176.

McCrone, W.C.; Draftz, R.G. and Delly, J.G. (1967): "The Particle Atlas - Vols. I/II", Ann Arbor Science Pub., Inc., Michigan.

McDonald, J.R. (1978): "A Mathematical Model of Electrostatic Precipitation, Revision 1, Vol. I - Modelling and Programming", Contract SRI/EPA 68-D2-2114, EPA-600-7-78-111a, pp.132-134.

McLean, K.J. (1976): "Factors Affecting the Resistivity of a Particulate Layer in Electrostatic Precipitators", JAPCA, 26, No. 9, pp.866-870.

_____ and Huey, R.M. (1974): "Influence of Electric Field on the Resistivity of a Particulate Layer", Proc. IEE, 121, No. 1, pp.76-80.

Newton, G.J.; Raabe, O.G. and Mokler, B.V. (1977): "Cascade Impactor Design and Performance", J. Aerosol Science, 8, Perg. Press, pp.339-347.

Nichols, G.B. (1974): "Techniques for Measuring Fly Ash Resistivity", Environmental Protection Technology Series, EPA-650/2-74-079, National Technical Information Service, U.S. Dept. of Commerce, pp.21.

Niesz, D.E. and Bennett, R.B. (1978): "Structure and Properties of Agglomerates", in "Ceramic Processing before Firing", Onoda and Hench (eds.), John Wiley & Sons Ltd., pp.61-73.

Oglesby, S. Jr. and Nichols, G.B. (1978): "Electrostatic Precipitation", Marcel Dekker, pp.330-344.

Ondov, J.M.; Ragaini, R.C. and Biermann, A.H. (1978): "Elemental Particle-Size Emissions from Coal-Fired Power Plants: Use of an Inertial Cascade Impactor", Atm. Environment, 12, Perg. Press, pp.1175-1185.

Orr, C. Jr. (1978): "Physical Characterization Techniques for Particles", in "Ceramic Processing before Firing", Onoda and Hench (eds.), John Wiley & Sons, Ltd., pp.39-59.

_____ and Keng, E.Y.H. (1976): "Sampling and Particle-Size Measurement" in "Handbook on Aerosols", R. Dennis (ed.), Technical Inf. Center, Office of Public Affairs, U.S. Energy R & D Administration, pp.93-117.

Pampuch, R. (1976): "Ceramic Materials: An Introduction to their Properties", Elsevier Sci. Pub. Co.

Pender, H. and McIlwain, K. (1975): "Electrical Engineers' Handbook", Wiley Handbook Series, 4th ed.

Raabe, O.G. (1971): "Particle Size Analysis Utilizing Grouped Data and the Log-Normal Distribution", J. Aerosol Science, 2, Perg. Press, pp.289-303.

Ranz, W.E. and Wong, J.B. (1952): "Impaction of Dust and Smoke Particles on Surface and Body Collectors", Ind. & Eng. Chemistry, 44, No. 6, June, pp.1371-1380.

Rao, A.K. and Whitby, K.T. (1977): "Non-ideal Collection Characteristics of Single Stage and Cascade Impactors", Am. Ind. Hyg. Assoc. J., 38, No. 4, April, pp.174-179.

Robinson, J.W. (1975): "Atomic Absorption Spectroscopy", 2nd ed., M. Dekker, N.Y.

Rubeska and Molden (1969): "Atomic Absorption Spectrophotometry", CRC Press, International Series of Physical Analysis.

Samsonov, G.V. (ed.) (1973): "The Oxide Handbook", IFI Plenum.

Say, M.G. (1973): "Electrical Engineers' Reference Book", Butterworths, 13th ed.

Selden, M.G. Jr. (1977): "Estimate of Errors in Anisokinetic Sampling of Particulate Matter", JAPCA, 27, No. 3, March, pp.235-236.

Smith, W.B.; Cushing, K.M. and McCain, J.D. (1977): "Procedures Manual for Electrostatic Precipitator Evaluation", SRI/EPA Contract 68-02-2131, EPA-600/7-77-059, June.

_____; Cavanaugh, P.R. and Wilson, R.R. (1978): "Technical Manual: A Survey of Equipment and Methods for Particulate Sampling in Industrial Process Streams", SRI/EPA Contract 68-02-2131, EPA-600/7-78-043, March.

Stockham, J.D. and Fochtman, E.G. (eds.) (1977): "Particle Size Analysis", Ann Arbor Science.

Tassicker, O.J. (1971): "The Temperature and Frequency Dependence of the Dielectric Constant of Power Station Fly-Ash", Staub-Reinhalt, Luft, 31, (in German), pp.331-335.

Waye, B.E. (1967): "Introduction to Technical Ceramics", MacLaren & Sons Ltd., London.

White, H.J. (1978): personal communication, May 30.

Yamate, G. and Stockham, J.D. (1977): "Sizing Particles using the Microscope" in "Particle Size Analysis", Stockham and Fochtman (eds.), Ann Arbor Science, pp.23-33.

Young, R.S. (1971): "Chemical Analysis in Extractive Metallurgy", Griffin, London.

CHAPTER 6

PRECIPITATION OF PURE COMPOUNDS EXPERIMENTAL RESULTS, THEORETICAL PREDICTIONS AND DISCUSSION

6.1 Introduction

The following chapter presents the experimental results and theoretical predictions of the experiments carried out with pure compounds. If no interaction exists between different materials in an ESP, it is reasonable to believe that chemical segregation could be predicted on the basis of the collection efficiencies of the pure components. Initial experiments with pure compounds were carried out to test this hypothesis.

The experimental results on collection efficiency of pure compounds are presented globally, as a function of ESP length and/or particle size.

Global efficiencies were determined from the dust loading at the ESP outlet and from the mass collected in the precipitator.

Efficiencies as function of the ESP length were determined by dividing the plates into eight sections of equal length (approximately 31.6 cm each). The dust collected from each section (or group of sections) was weighed separately. Occasionally, size distributions from the first, fourth and eighth sections were determined by optical microscopy.

Efficiencies as function of particle size were determined from the global efficiencies and the size distributions at the inlet and outlet of the ESP.

The experimental data were compared with predictions of the Southern Research Institute (SRI) electrostatic precipitator performance computer model and correlated with Eq. 2.41 (Chapter 2), which is:

$$E_c = 1 - \left(\frac{L + v\tau}{v\tau}\right)^{w\tau/s} \cdot \exp\left(-\frac{wL}{vs}\right) \qquad (6.1)$$

where (E_c) is the cumulative collection efficiency up to length (L), (v) is the average air velocity through the ESP, (τ) is the charging time constant, (w) is the migration velocity and (s) the wire-to-plate spacing.

Equation 6.1 was used to correlate data along the ESP length whenever a significant deviation from theoretical predictions was observed, since it is an explicit function in this variable. In its present form, the SRI computer model requires a major modification to accomodate the application of corrections along the ESP length; this was not attempted.

The ideal collection efficiencies determined using both the SRI model or Eq. 6.1 (with the same value of average electric field at the plates) are identical for all practical purposes.

The effect of sedimentation prior to the ESP inlet is to reduce both the mass of dust entering the ESP and the mean mass diameter and geometric standard deviation of the size distribution. The sedimentation occurring in the ESP itself further compounds this effect, which for cupric oxide became appreciable at average air velocities through the ESP below about

3 ms^{-1}. For these reasons, the definition of electrical collection efficiency in the presence of mechanical collection described by Eq. 2.53 of Chapter 2 was used. Efficiencies were thus determined by:

$$\eta = \frac{\eta'}{1 - \eta'_m} \qquad (6.2)$$

where (η') and (η'_m) are respectively the fractions of inlet dust precipitated and sedimented.

Particle size distributions at the ESP inlet, which were used as input data to the SRI computer model (and/or Eq. 6.1) were corrected for sedimentation occurring both in the plenum chamber and on the ESP bottom (an example of the calculations involved is given in Section C.4, Appendix C).

From theory of sedimentation in turbulent flows (Crawford, 1976), a reduction in both MMD and σ_g should be expected due to sedimentation, and this was observed in all cases.

6.2 Precipitation of Cupric Oxide

6.2.1 Global Collection Efficiencies

Table 6.1 lists the experimental conditions and global results of the experiments carried out with cupric oxide. The values of bulk effective resistivity were calculated according to Eq. 5.37 and the values listed in Table 5.10 (Chapter 5), taking into account the prevailing experimental conditions of relative humidity and average current density at the ESP plates

TABLE 6.1

Experimental Precipitation Conditions and Results for Cupric Oxide

Run No.	MMD_{in} (μm)	$\sigma_{g_{in}}$	v (ms^{-1})	C_i (mgm^{-3})	V (KV)	$jx10^4$ (Am^{-2})	$rx10^{-5}$ (Ohmm)	MMD_{out} (μm)	$\sigma_{g_{out}}$	η' (%)	η'_m (%)	η (%)
1	9.9	1.41	0.9	131	39.0	17.2	20	7.0	1.69	82.8	16.7	99.4
2	11.2	1.48	1.2	135	40.0	18.3	14	-	-	76.5	22.1	98.3
3	12.0	1.48	2.0	177	38.2	15.7	29	12.5	1.89	56.4	10.4	63.0
4	13.2	1.58	3.0	153	38.6	14.3	9	13.4	1.63	22.5	2.83	23.2
5	13.6	1.59	5.0	94	38.0	13.2	23	13.8	1.64	16.2	5.16	17.1
6	13.6	1.59	5.0	93	38.0	12.1	2	-	-	16.4	2.74	16.9
7	13.6	1.59	5.0	99	38.0	12.2	8	-	-	20.2	2.57	20.7
8	13.6	1.59	5.0	99	38.3	13.1	8	-	-	21.8	2.79	22.4
9	13.6	1.59	5.0	98	38.0	13.1	13	-	-	18.5	4.95	19.5
10	13.6	1.59	5.0	101	37.7	12.1	2	-	-	21.0	0.54	21.1
11	10.6	1.45	2.0	208	23.5	1.31	4	9.8	1.58	44.8	36.2	70.2
12	13.6	1.59	5.0	65	26.5	1.10	11	14.0	1.58	21.1	3.25	21.9

(no appreciable variation of current density was observed along the ESP plates). The experimental runs were between 24 and 32 min long, the temperature was between 292 and 304 K and the relative humidity between 19 and 47%.

Figure 6.1 shows the observed global collection efficiencies as a function of the average air velocity through the ESP. Also shown are the theoretical predictions of the SRI computer model. A marked decrease in collection efficiency with increasing air velocity is observed for cupric oxide and the experimental values are lower than the theoretical values, the difference increasing with air velocity. A similar trend has been reported for a low resistivity (10^3-3×10^4 Ohmm) fuel oil ash and is shown in Fig. 2.10 of Chapter 2.

The probable reason for the non-ideal behaviour of cupric oxide in the ESP is reentrainment of the particles onto the gas stream once they have been precipitated. This reentrainment is probably caused by the low dust resistivity and high air velocities, as discussed in Chapter 2, Section 2.7.

The net force of attraction of the precipitated dust layer to the collection plates due to the corona current was estimated by Eq. 2.51 of Chapter 2, which is:

$$F = \frac{\varepsilon_o}{2}\{\lambda_1(\lambda_2 jr)^{\lambda_3} - E_{ex}^2\} \qquad (6.3)$$

where (ε_o) is permittivity of vacuum (8.85×10^{-12} Fm^{-1}), (j) is average current density at the plates, (λ_1, λ_2, λ_3) are appropri-

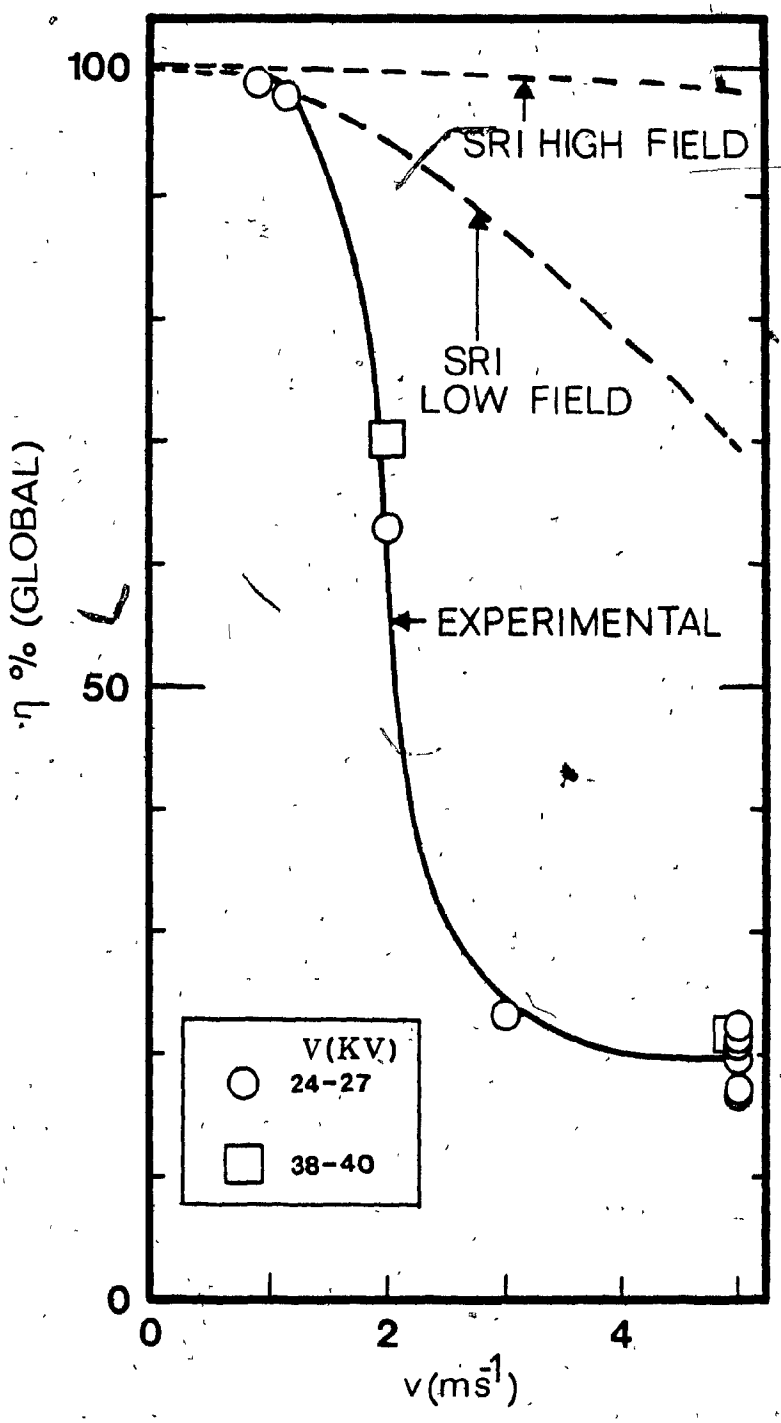


Figure 6.1 Variation of global collection efficiency of CuO with air velocity

ate parameters and (E_{ex}) is the average electric field intensity outside the dust layer. As discussed in Chapter 2, Section 2.7, one possibility is $\lambda_1 = \lambda_2 = K$ and $\lambda_3 = 2$, where (K) is the relative dielectric constant of the dust layer. For thin deposits, Eq. 6.3 reduces to:

$$F \simeq \frac{\varepsilon_o}{2}\{(jrK)^2 - (\frac{V}{s})^2\} \qquad (6.4)$$

where (V) is the applied voltage and (s) is the wire-to-plate spacing.

The degree of reentrainment (R) was determined using Eq. 2.57 of Chapter 2, with the assumption that reentrainment is the only cause for deviation from ideal collection. This equation is

$$R = 1 - \eta_{exp}/\eta \qquad (6.5)$$

where (η) and (η_{exp}) are respectively the theoretical and experimental collection efficiencies.

A multiple linear regression (performed on the Music/Statpak system of McGill University) of reentrainment versus air velocity and the net force of attraction showed a strong correlation with air velocity and a weak correlation with force of attraction. Due to the low resistivities, the forces of attraction were always negative (repulsive) and primarily determined by the applied voltage. Since the applied voltage varied little from run to run at both high and low field conditions,

neither did the net force of attraction. Reentrainment increased with increasing air velocity and increasing repulsive force.

Figure 6.2 shows the reentrainment as a function of the air velocity; it increases almost linearly from about 1.2 to 3 ms^{-1} and then levels off.

The precision of the measurements was estimated from runs 5-10, which were taken as replicates despite unavoidable slight changes in voltage, humidity or current density. The results show that small changes in the operating variables do not significantly affect the measured collection efficiency. The observed standard deviation represents about 11% of the average global collection efficiency, which was 19.6%.

No significant difference was found between experimental times of 24 or 32 min. The inlet concentrations were very small (about one order of magnitude smaller than in a typical industrial case), and the precipitated layers were very thin; they were visually estimated to be less than 1 mm thick.

6.2.2 Collection Efficiencies as Function of ESP Length

Table 6.2 gives the experimentally determined non-cumulative collection efficiencies as a function of incremental length. The cumulative efficiencies are found by adding the corresponding non-cumulative values. For runs No. 7 and 8 only the global efficiency is available.

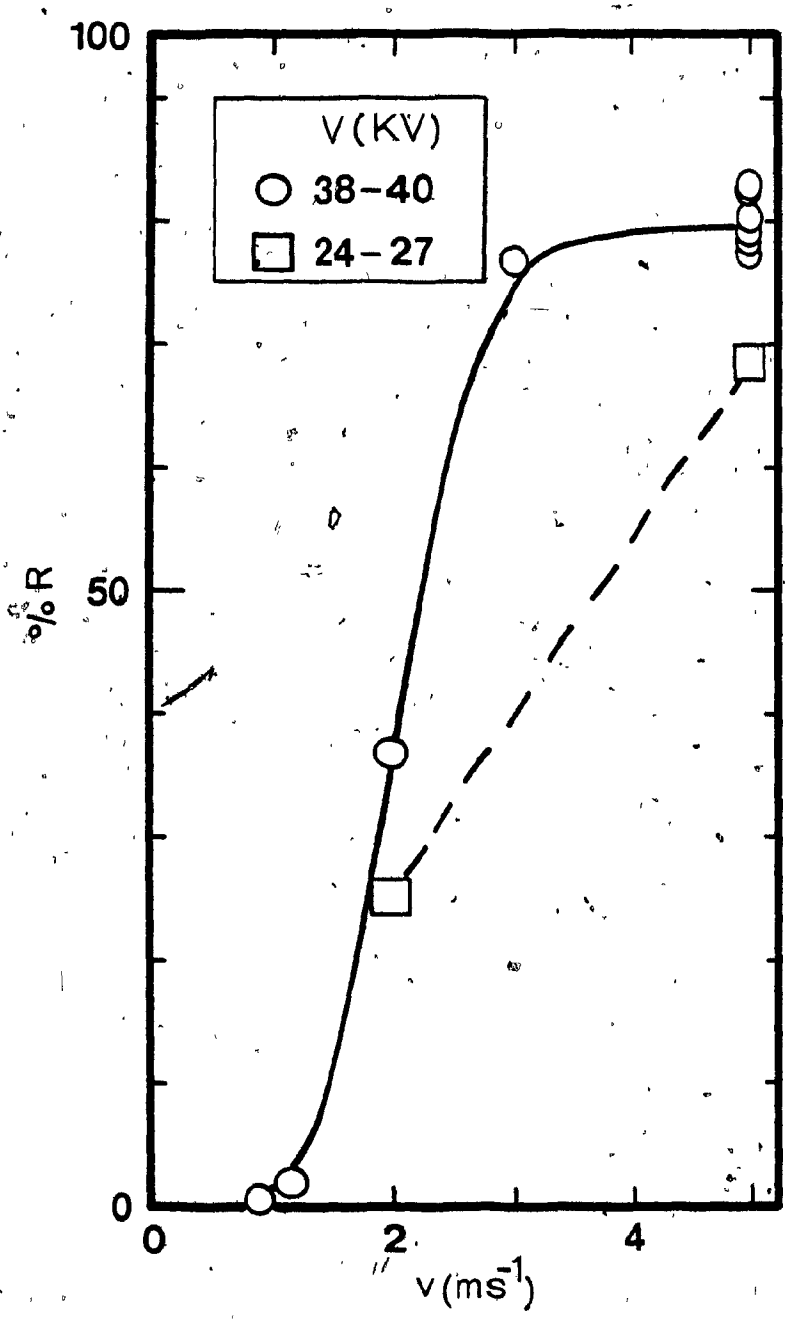


Figure 6.2 Variation of re-entrainment of CuO with air velocity

TABLE 6.2

Non-Cumulative Collection Efficiencies (%), CuO

Run No.	Increment No. 1	2	3	4	5	6	7	8
1	50.9	26.1	8.25	6.50	4.13	2.25	0.88	0.38
2	37.0	26.0	9.78	7.28	5.38	5.63	3.86	3.32
3	8.38	17.1	10.9	6.41	3.56	4.00	3.45	9.17
4	2.04	2.56	2.57	2.94	2.36	2.14	1.89	6.65
5	0.99	1.25	1.61	1.78	1.33	1.75	1.77	6.61
6	0.90	1.71	1.84	2.26	1.44	1.80	1.47	5.42
7								(20.7) (1)
8								(22.4) (1)
9	1.42	1.63	1.72	1.96	1.45	1.92	1.74	7.63
10	1.35	1.54	1.83	2.35	1.79	2.17	2.08	7.98
11	6.30	8.42	11.1	12.1	7.97	7.63	6.52	10.2
12	2.38	3.79	3.29	2.89	2.01	2.72	2.08	2.72

(1) Global Collection Efficiency

Figure 6.3 shows the non-cumulative collection efficiencies along the ESP length, at high applied fields and different values of air velocity. Figure 6.4 shows the corresponding cumulative data. Figures 6.5 and 6.6 show the corresponding data for the two experimental runs performed at low applied fields.

Also shown in these figures are the theoretical predictions of the SRI computer model and the curves obtained by fitting Eq. 6.1 to the experimental data. Two methods were used to empirically modify Eq. 6.1. The first method involved deter-

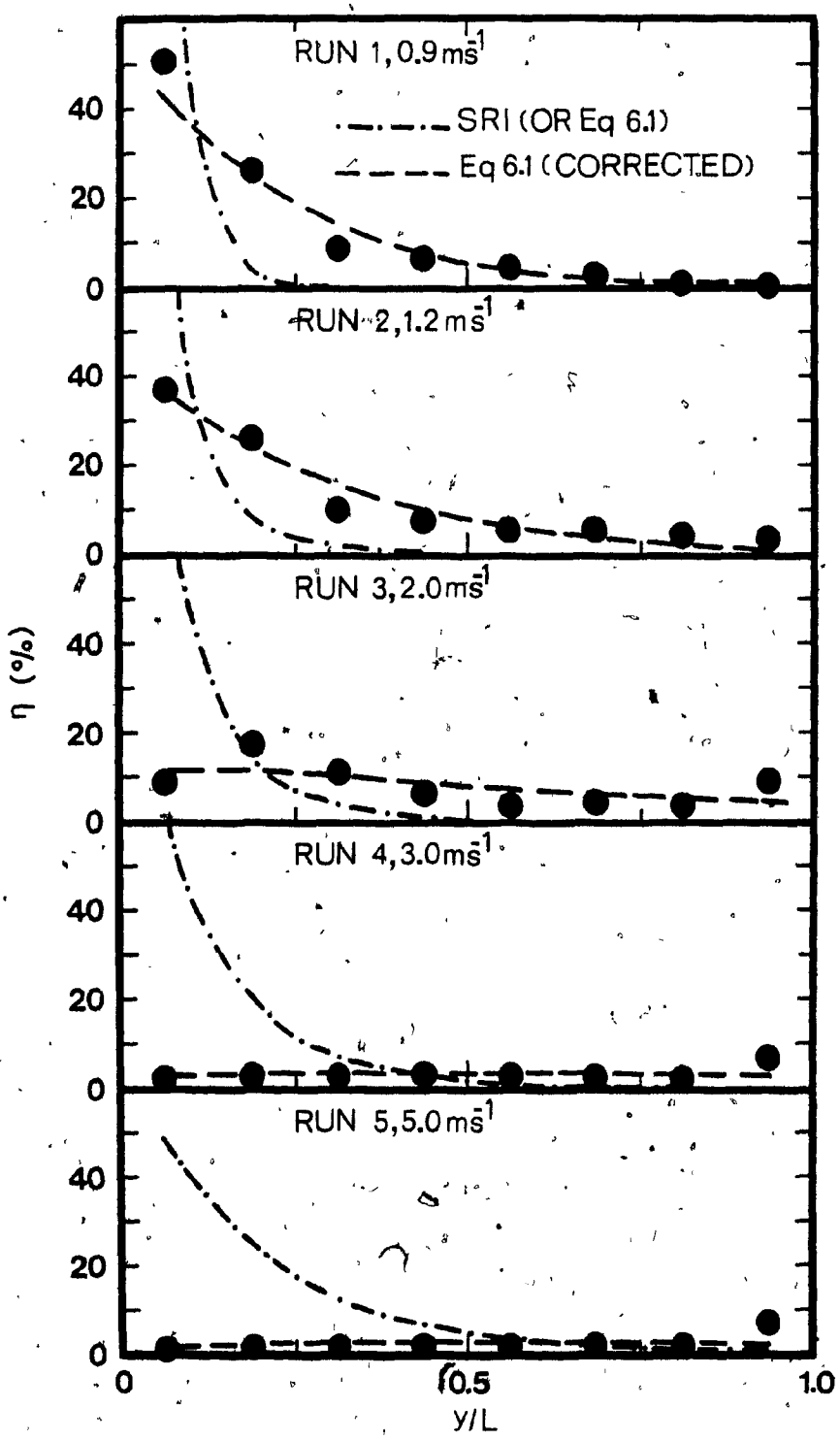


Figure 6.3 Effect of air velocity on the non-cumulative collection efficiency of CuO along the ESP length, at high voltage

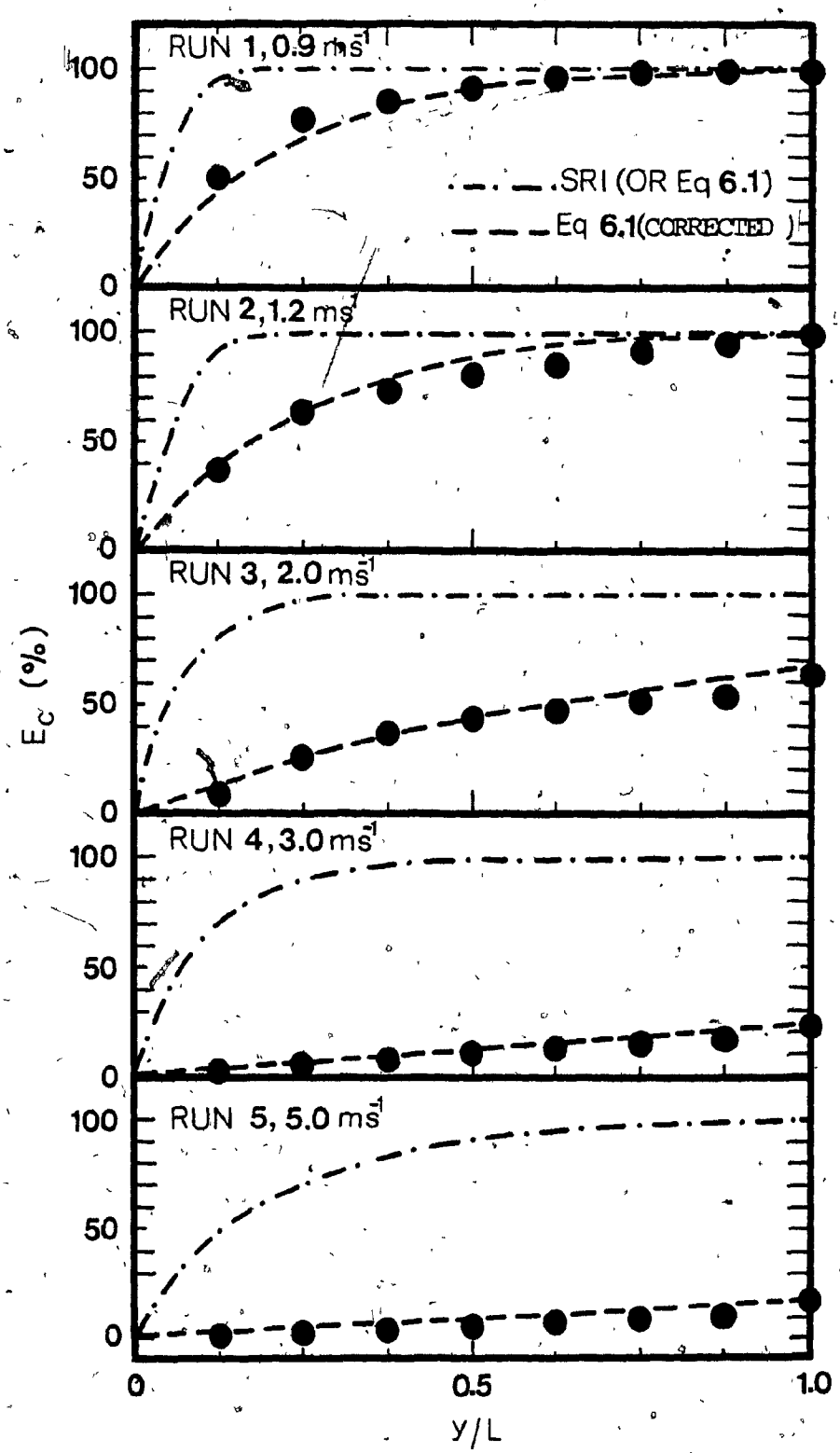


Figure 6.4 Effect of air velocity on the cumulative collection efficiency of CuO along the ESP length, at high voltage

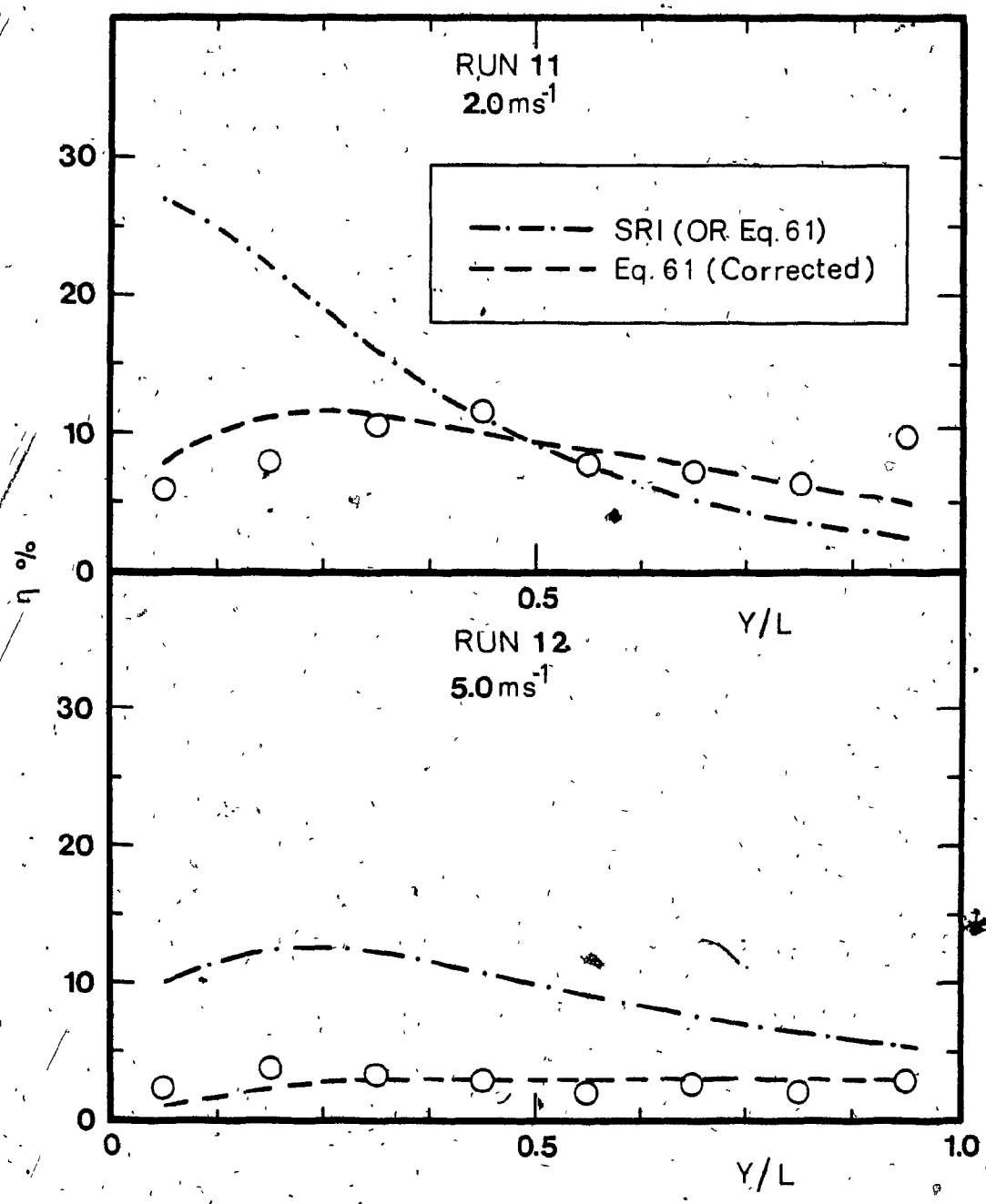


Figure 6.5 Effect of air velocity on the non-cumulative collection efficiency of CuO along the ESP length, at low voltage

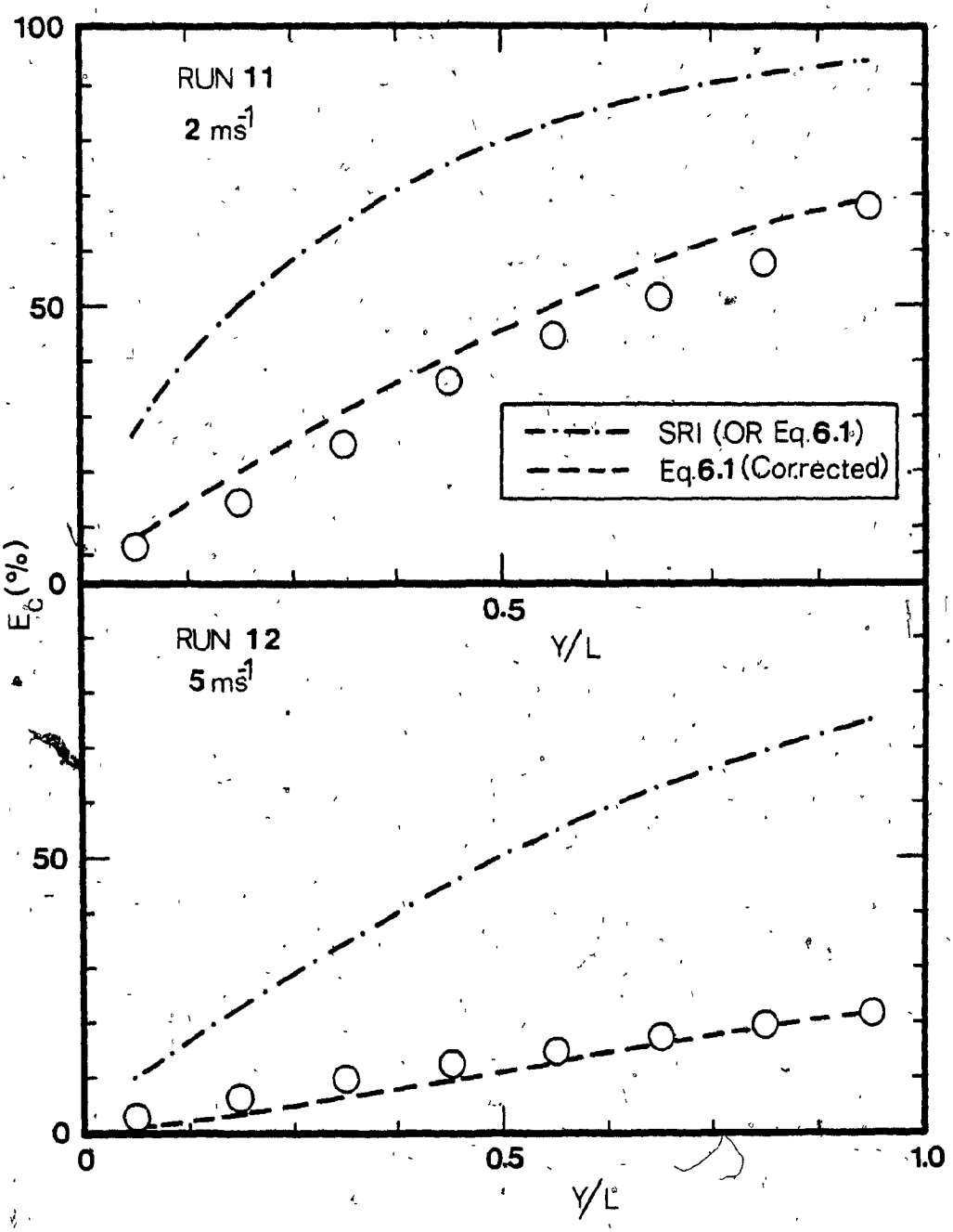


Figure 6.6 Effect of air velocity on the cumulative collection efficiency of CuO along the ESP length, at low voltage

mining the experimental precipitation rate parameter (experimental effective migration velocity for the entire size distribution, w_{exp}) using Eq. 6.1 in the rearranged form:

$$w_{exp} = \frac{\ln(1-E_{c_{exp}})}{\frac{\tau}{s}\ln(\frac{L+v\tau}{v\tau}) - \frac{L}{vs}} \qquad (6.6)$$

where $(E_c)_{exp}$ is the experimental value of global collection efficiency (Table 6.2). The empirically corrected values of (cumulative) collection efficiency were then determined for each incremental length, using Eq. 6.1 and the empirically determined w_{exp}.

The second method involved determining the experimental effective fractional migration velocity (i.e., for each particle size and the global ESP length), using Eq. 6.6 and the experimental effective fractional collection efficiencies. These were determined using the global collection efficiencies and the size distributions at both the inlet and outlet of the ESP (Tables 6.1 and 6.2). The computed fractional efficiencies are given in Section 6.2.3.

No significant difference was observed between the two methods of fitting the experimental data, but this conclusion might not be generally true. The simpler method of empirically correcting Eq. 6.1 without measuring the inlet and outlet size distributions may give a poor fit along the ESP length in the case of a broad size distribution if the coarser and finer particles exhibit widely differing collection efficiencies.

Figures 6.3 and 6.5 show that the precipitated dust becomes more uniformly distributed along the ESP length with increasing air velocity; similar trends are presented in Fig. 2.11 of Chapter 2 for a low resistivity fuel oil ash. The theoretical predictions of the SRI computer model are well above the experimental results, the difference increasing with increasing air velocity. The agreement between the empirically corrected Eq. 6.1 and the experimental data is good in all cases.

Unfortunately, the correction method requires information on global efficiencies and particle size distributions, and as such has no predictive capabilities.

Table 6.3 gives the measured parameters of the size distributions of the dust collected in the first, fourth and eighth length increments, for the experimental runs listed. Also shown are the theoretical predictions of the MMD of the SRI computer model and the empirically corrected values from Eq. 6.1. These were determined by empirically correcting Eq. 6.1 using particle size distribution data.

The results of Table 6.3 show that the MMD of cupric oxide decreases downstream (i.e., expected behaviour) only at low air velocities. At velocities above 1.2 ms^{-1} there is no variation or even an increase in MMD. This phenomenon is attributed to reentrainment of CuO; similar behaviour has been reported (Fig. 2.12 of Chapter 2). The SRI predictions show a substantial decrease in MMD with ESP length, in strong disagreement with the experimental data. The empirically corrected values (from Eq. 6.1) are in good qualitative agreement with

TABLE 6.3

Size Distributions as Function of ESP Length, CuO

Run No.	Increment No.	MND (μm)	σ_g	MMD (μm) Experimental	SRI	Eq. 6.1 (1)
1	1	7.5	1.47	11.7	9.9	10.2
	4	4.3	1.61	8.5	4.2	9.6
	8	2.8	1.71	6.8	2.4	8.4
2	1	7.5	1.50	12.3	10.7	-
	4	5.7	1.54	10.0	4.8	-
	8	4.8	1.61	9.5	2.8	-
3	1	6.0	1.50	9.8	11.3	11.9
	4	5.4	1.60	10.5	6.7	12.0
	8	5.3	1.75	13.6	4.4	12.0
4	1	5.8	1.49	9.3	13.1	12.6
	4	5.3	1.54	9.3	7.1	12.7
	8	5.5	1.63	11.3	5.5	12.8
11	1	6.2	1.51	10.3	12.6	12.5
	4	5.7	1.57	10.5	10.5	12.2
	8	5.3	1.55	9.4	8.3	11.7

(1) Empirically corrected using size distribution information.

the measured values; quantitatively, the agreement is reasonable. It should be noted that the theoretical predictions of MMD of Eq. 6.1 (i.e., non-corrected values) are very similar to the SRI predictions.

6.2.3 Collection Efficiencies as Function of Particle Size

The effective fractional collection efficiencies were determined using the size distributions at both inlet and outlet of the ESP and the global collection efficiencies (Table 6.1), and are shown in Figs. 6.7 and 6.8 at high and low electric fields respectively.

The curves at high fields are all similar, showing a decrease in collection efficiency with increasing air velocity and a maximum with particle size at about 10-15 μm diameter. The curves at low fields show two distinct behaviours, and only the results at 2 ms^{-1} are similar to those at high fields. A study of the sensitivity of the fractional efficiencies to small changes in the geometric MMD and σ_g of the measured distributions revealed that the shape of the curves is very sensitive to small changes in σ_g. For example, an increase of only 5% in the observed σ_g of the outlet distribution for run No. 12 would produce a downward sloping curve similar to all the others. This change affects mainly the extremes of the distributions, i.e., both finer and coarser particles, while only slightly changing the fractional efficiencies for the mid-range of the distributions ($5 < D < 25$ μm). Since most of the mass is contained in this mid-range of particle sizes, the uncertainties in the shape of the curves have no appreciable effect on a global weight basis.

As seen from Figs. 6.7 and 6.8, fractional efficiencies for both very fine or very large particles could not in general be determined: this would lead to negative efficiencies. The

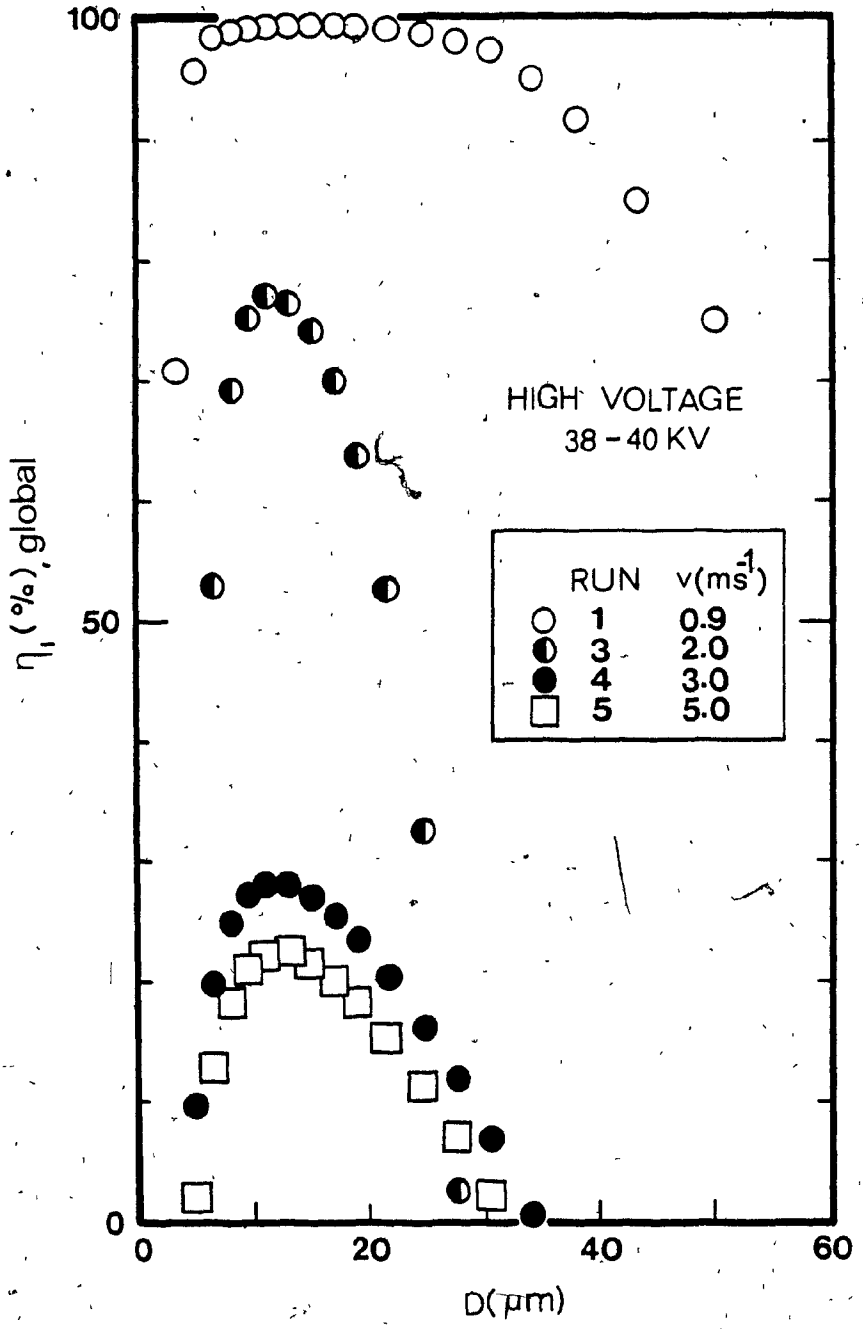


Figure 6.7 Variation of the effective collection efficiency of CuO with particle size and air velocity, at high voltage

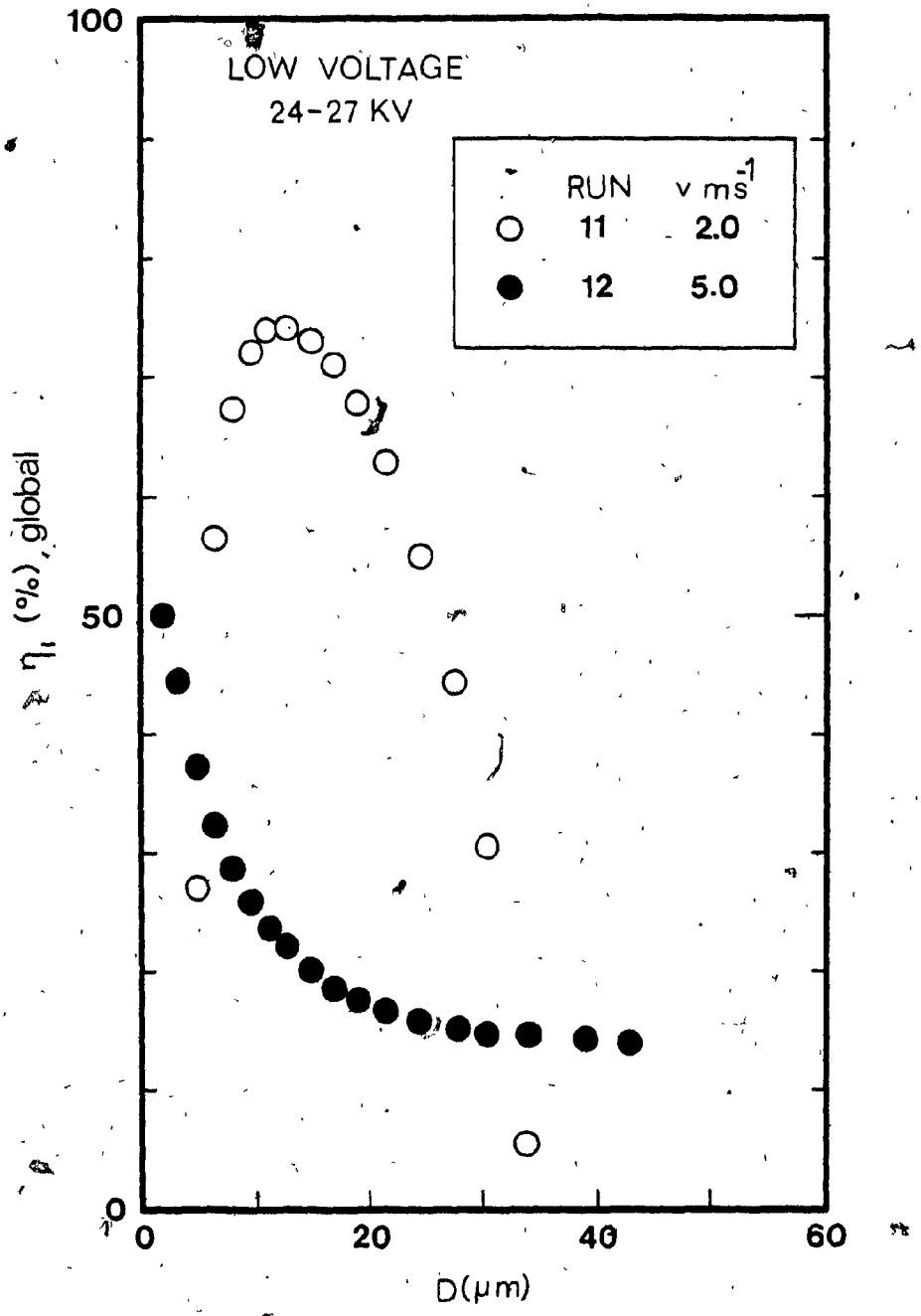


Figure 6.8 Variation of the effective collection efficiency of CuO with particle size and air velocity, at low voltage.

fractional efficiencies of these particle sizes were thus arbitrarily set to zero. The effect of the uncertainties involved (when using Eq. 6.1 with particle size distribution information) is small, since the weight contained in these particles was always less than 4% of the total weight of the inlet distributions.

Figure 6.9 shows the experimental fractional effective migration velocities, determined using Eq. 6.6 as applied to each experimental run. Again, all curves except that at low field and 5 ms^{-1} show a similar shape. The occurrence of a maximum in migration velocity at about 10-20 μm diameter has been reported in the literature, as may be seen in Figs. 2.7, 2.8 and 2.9 of Chapter 2. To the author's knowledge, the behaviour exhibited at low field and 5 ms^{-1} has not been reported; it is possible that it is an artifact of experimental error in measuring the outlet size distribution, together with a high sensitivity to the value of geometric standard deviation.

Figures 6.10 and 6.11 show the estimated percent fractional reentrainment, obtained by applying Eq. 6.5 to each particle size. The curves at high field and the curve at low field and 2 ms^{-1} show a minimum in reentrainment at about 10-15 μm diameter. The high reentrainment of the coarser particles is probably due to the fact that the larger particles may protrude above a laminar sublayer at the plates, where they will be more easily reentrained by the action of turbulent eddies. Also, the larger particles may experience larger repulsive forces due to the corona current. The increased reentrainment observed

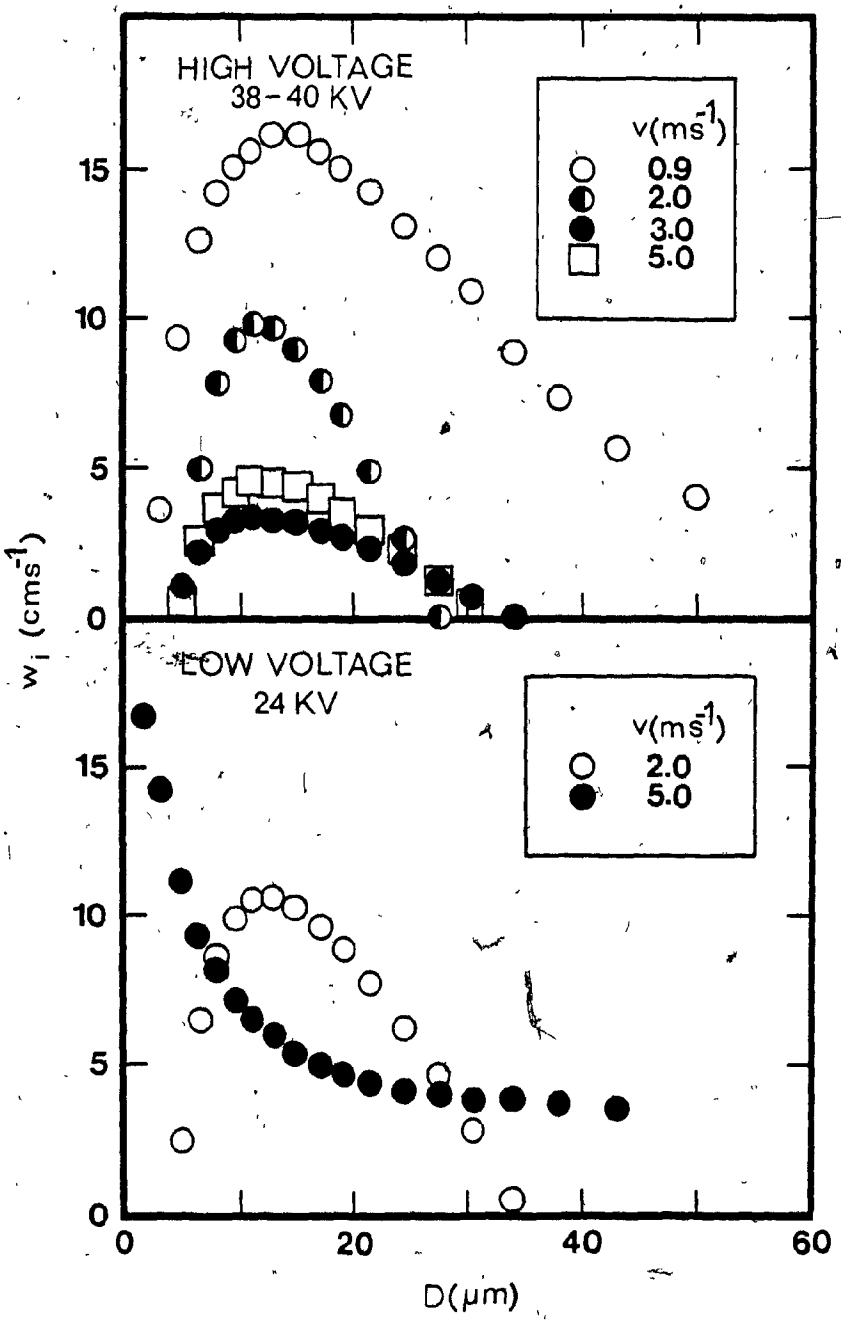


Figure 6.9 Variation of the effective migration velocity of CuO with particle size and air velocity

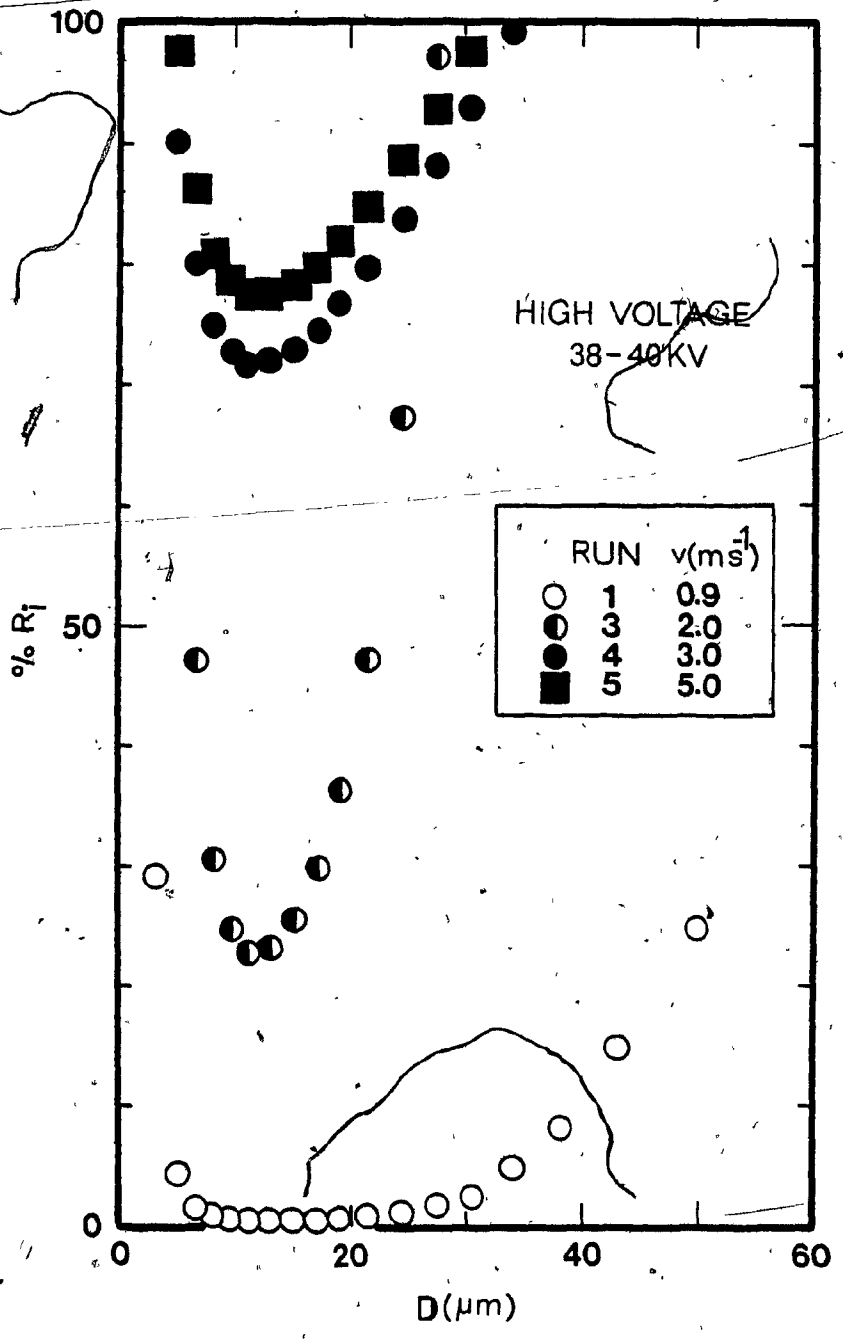


Figure 6.10 Re-entrainment of CuO as a function of particle size and air velocity, at high voltage

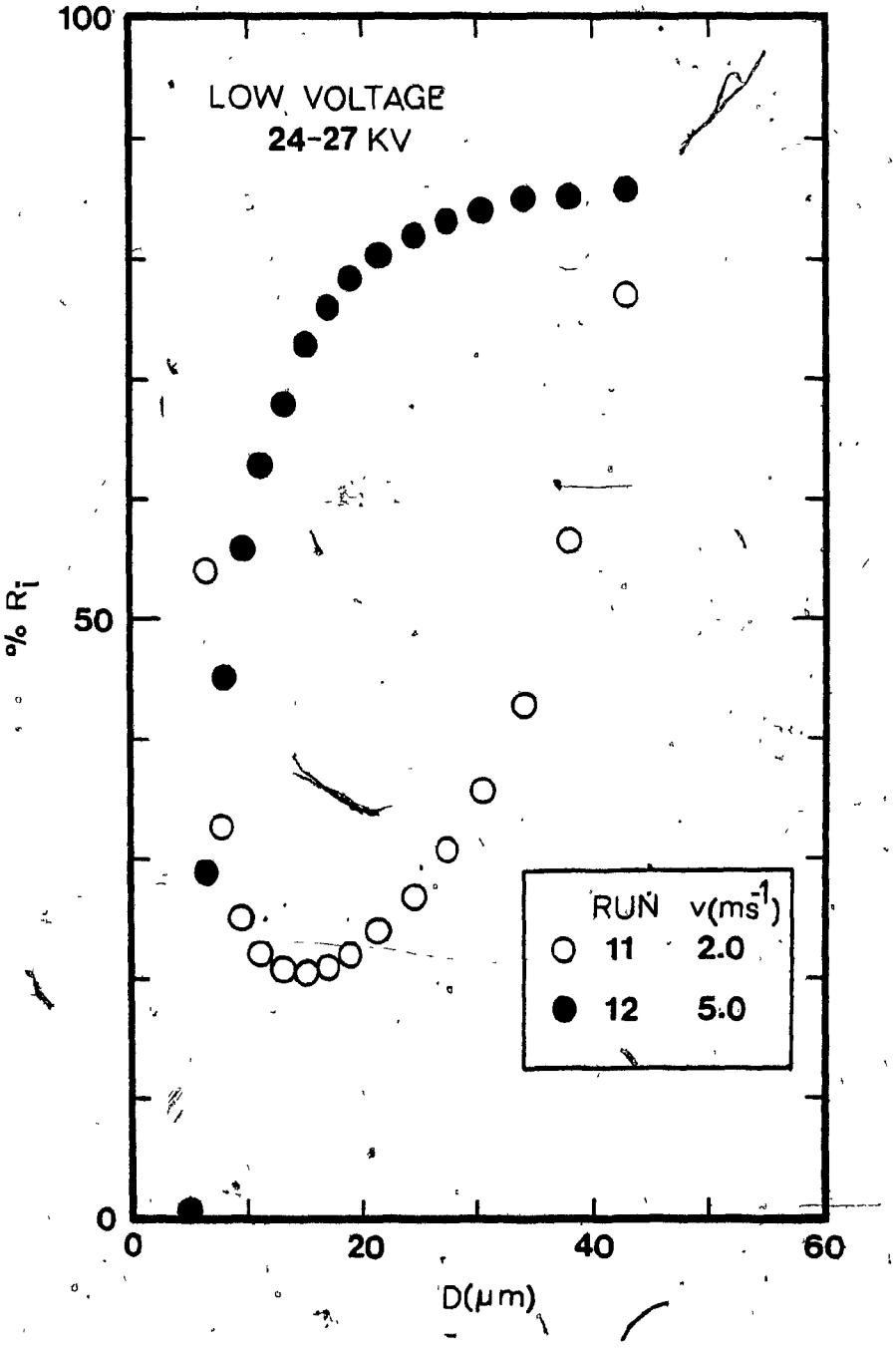


Figure 6.11 Re-entrainment of CuO as a function of particle size and air velocity, at low voltage

(in almost all cases) for the finer particles may be due to impact by airborne particles or to agglomeration of the fine particles once precipitated; these agglomerates will be re-entrained as if they were larger particles. For a more complete discussion of the reentrainment phenomenon, the reader is referred to Chapter 2, Section 2.7.

The curve at low field and 5 ms^{-1} shows a continuous increase in reentrainment with particle size, in conflict with all the other results. Due to the high sensitivity of the fractional efficiencies of both coarser and finer particles to small variations in the geometric standard deviation of the measured size distributions, the curves shown in Figs. 6.7-6.11 should be treated with caution; more experiments are needed to understand this complex phenomenon and to resolve the apparent conflict of the experimental data. These experiments were not performed due to the following reasons:

- The extremes of the size distributions, which are most affected by variations in the measured parameters of the distribution, contain only a small fraction (typically 5-10%) of the total weight of the distribution.
- The reentrainment of cupric oxide is highly affected by the presence of other components, as it will be seen in Chapter 7. The reentrainment data obtained for the pure CuO are then of little value for the relevant case of segregation in ESP's, which is the main topic of this research.

6.3 Precipitation of Magnesium Oxide

6.3.1 Global Collection Efficiencies

Table 6.4 lists the experimental conditions and global results of the experiments carried out with magnesium oxide. The values of bulk effective resistivity were calculated according to Eq. 5.37 and the values listed in Table 5.10 (Chapter 5), as was done for CuO. The experimental runs varied from 24 to 32 min, the temperature from 300 to 302 K and relative humidities from 36 to 52%. Table 6.4 also lists the theoretical global efficiencies predicted by the SRI computer model, and comparison with the experimental results suggests a near ideal behaviour for the magnesium oxide dust.

The net force of attraction of the precipitated dust layer to the collection plates due to the corona current was again estimated using Eq. 6.4, and negative values similar to those computed for cupric oxide were obtained. For the case of cupric oxide, the critical values of resistivity for which the force given by Eq. 6.4 becomes positive are on the average about 20 and 150 times larger than the experimental values, at high and low fields respectively; this ratio decreases to about 5 or 6 for magnesium oxide. The uncertainties involved in determining the effective resistivity (different techniques may yield results which differ by a factor of ten (Nichols, 1974)), as well as the approximate nature of Eq. 6.4 do not allow any definite conclusions to be drawn as to whether the forces are in fact positive or negative, especially for magnesium oxide.

TABLE 6.4

Experimental Precipitation Conditions and Results for Magnesium Oxide

Run No.	MMD_{in} (μm)	$\sigma_{g_{in}}$	v (ms^{-1})	C_i (mgm^{-3})	V (KV)	$jx10^4$ (Am^{-2})	$rx10^{-7}$ (Ohm-m)	MMD_{out} (μm)	$\sigma_{g_{out}}$	η' (%)	η'_{in} (%)	η (%)	η_{SRI} (%)
13	13.0	1.72	2.0	238	38.0	12.6	1	6.4	1.75	97.1	2.77	99.8	99.5
14	14.0	1.77	3.0	176	38.9	13.1	3	-	-	90.1	4.79	94.7	98.2
15	14.6	1.79	5.0	76	26.3	1.15	17	12.8	1.80	58.3	3.06	60.2	64.2

Comparison of the theoretical and experimental values of global collection efficiency for magnesium oxide shows that reentrainment is either absent or small. The agreement is best at the lowest velocity of 2 ms^{-1}.

6.3.2 Collection Efficiencies as Function of ESP Length

Table 6.5 gives the experimentally determined non-cumulative collection efficiencies for each increment of length.

TABLE 6.5

Non-Cumulative Collection Efficiencies (%), MgO

Run No.	Increment No. 1	2	3	4	5	6	7	8
13	69.2	25.9	3.32	0.63	0.32	0.31	0.10	0.06
14	43.3	36.4	6.47	3.02	1.58	1.44	1.44	1.01
15	3.16	7.83	7.10	9.13	13.0	7.53	5.68	6.79

Figure 6.12 shows the values listed in Table 6.5, while Fig. 6.13 shows the corresponding cumulative data. Also shown in these figures are the theoretical predictions of the SRI computer model; the agreement is seen to be very good at 2 ms^{-1} and high applied voltage and deteriorates only slightly as the air velocity is increased and the voltage reduced.

No empirical corrections using Eq. 6.1 were performed for the case of magnesium oxide, since the theoretical predictions of the SRI computer model were close to the experimental results.

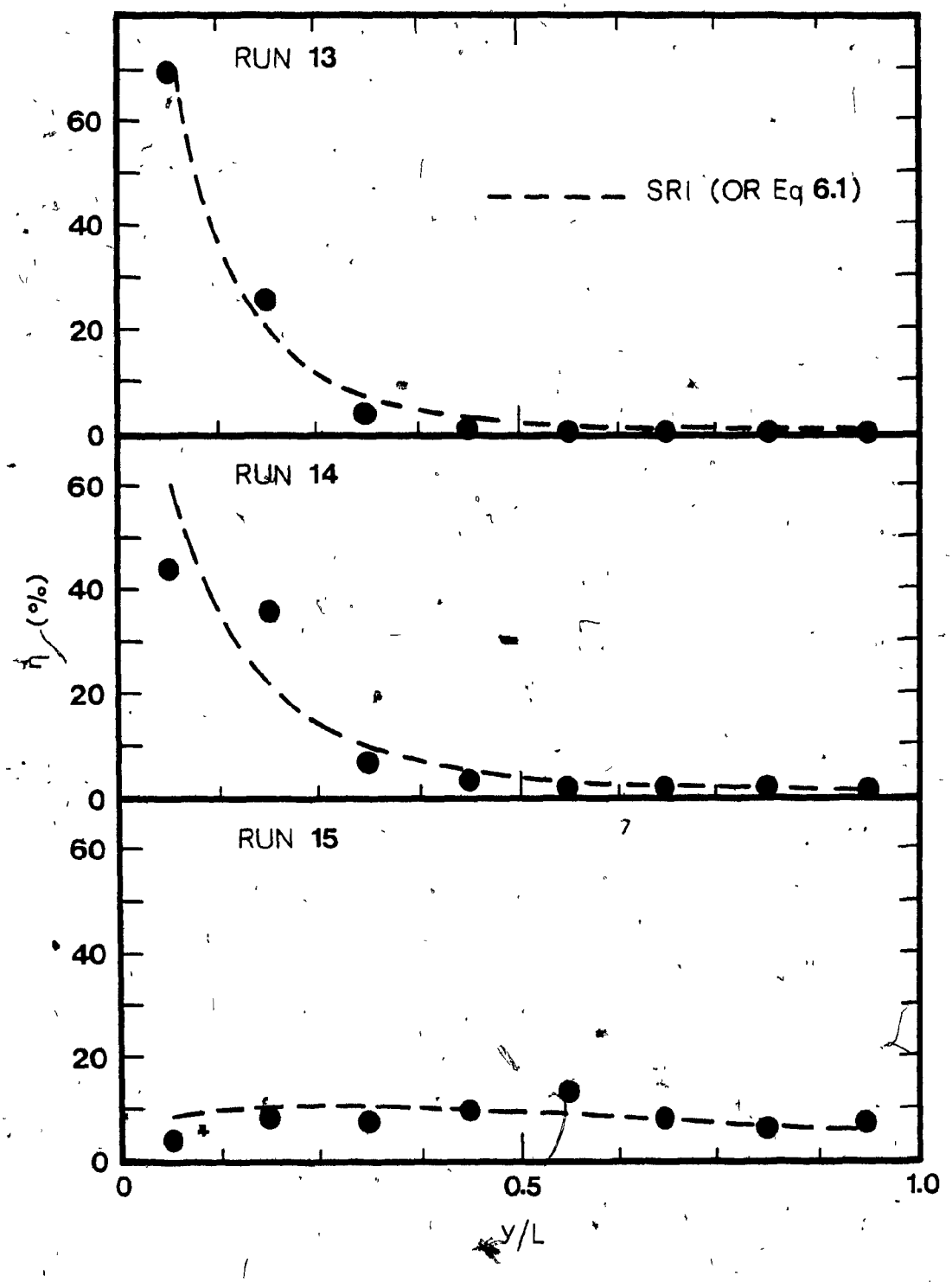


Figure 6.12 Non-cumulative collection efficiency of MgO as a function of ESP length

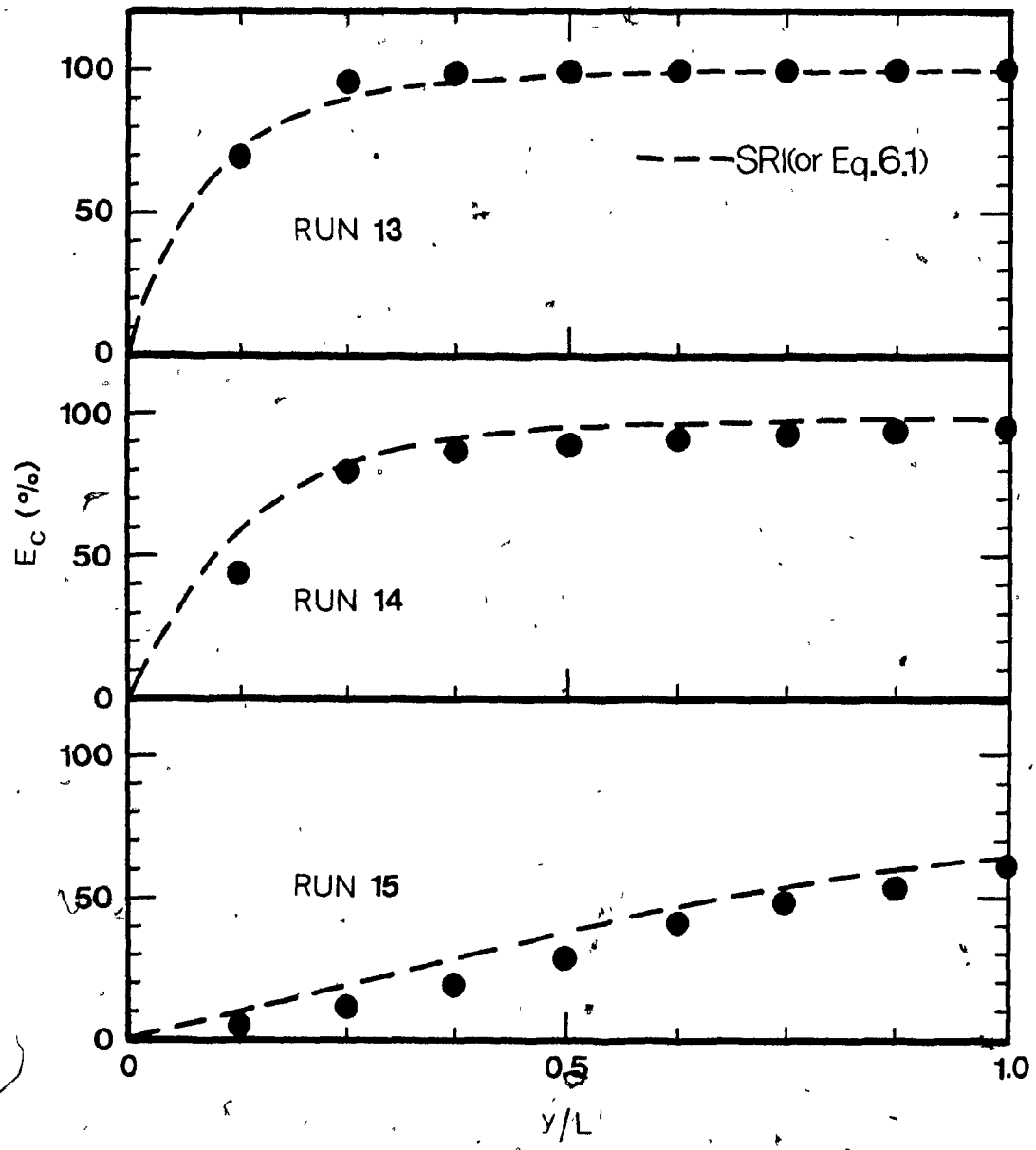


Figure 6.13 Cumulative collection efficiency of MgO as a function of ESP length

Table 6.6 gives the measured parameters of the size distributions of the dust collected in the first, fourth and eighth length increments, for the experimental run performed at 38 KV and 2 ms^{-1}. Also shown are the theoretical predictions using the SRI computer model. No experimental data is available for runs No. 14 or 15.

TABLE 6.6

Size Distributions as Function of ESP Length, MgO

Run No.	Increment No.	MND (μm)	σ_g	MMD (μm)	
				Experimental	SRI
13	1	5.4	1.88	17.8	15.9
	4	3.9	1.65	8.3	8.5
	8	2.9	1.65	6.2	5.6

The results of Table 6.6 show that the MMD of magnesium oxide decreases downstream, in good agreement with the predictions of the SRI model.

6.3.3 Collection Efficiencies as Function of Particle Size

The effective fractional collection efficiencies were determined using the size distributions at both inlet and outlet of the ESP and the global collection efficiencies (Table 6.4), and are shown in Fig. 6.14. Also shown are the SRI predictions.

The two experimental curves are similar, showing an increase in collection efficiency with increasing particle size.

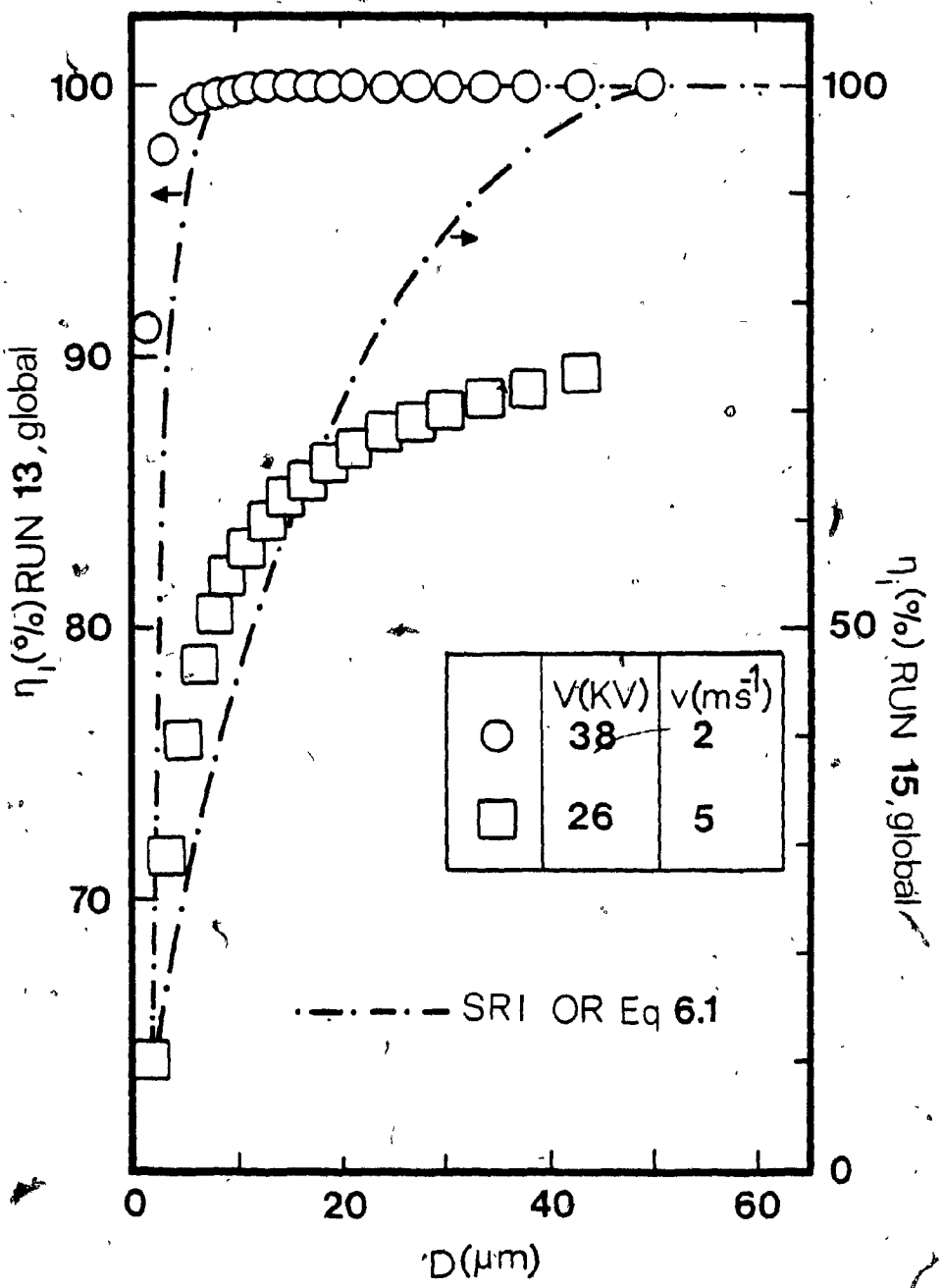


Figure 6.14 Variation of the effective collection efficiency of MgO with particle size

Comparison with theory reveals that the finer particles (below about 10-15 μm) show a higher collection than the theoretical predictions, and the reverse occurs for the coarser particles. The higher collection of the finer particles may be due to abnormal charging near the corona wires, as has been suggested by Robinson (1971), among others (Section 2.5.3, Chapter 2), while the poorer collection of the coarser particles may be due to reentrainment. The two effects act in opposing directions and the net result is a global collection in good agreement with theoretical predictions.

Figure 6.15 shows the experimental fractional effective migration velocities, determined using Eq. 6.6 as applied to each particle size. The experimental migration velocities are larger below about 10-15 μm diameter than the theoretical predictions. These curves are similar to some experimental data presented in Fig. 2.9 of Chapter 2, where the higher collection of the finer particles was attributed to turbulence causing the particles to be carried near the corona wires, where they will acquire a higher charge; the lower collection of the larger particles was attributed to particle reentrainment or to concentration gradients (Chapter 2, Section 2.5.3).

As in the case of CuO, the extremes of the curves of Figs. 6.14 and 6.15 are sensitive to the measured particle size distributions and should be treated with caution.

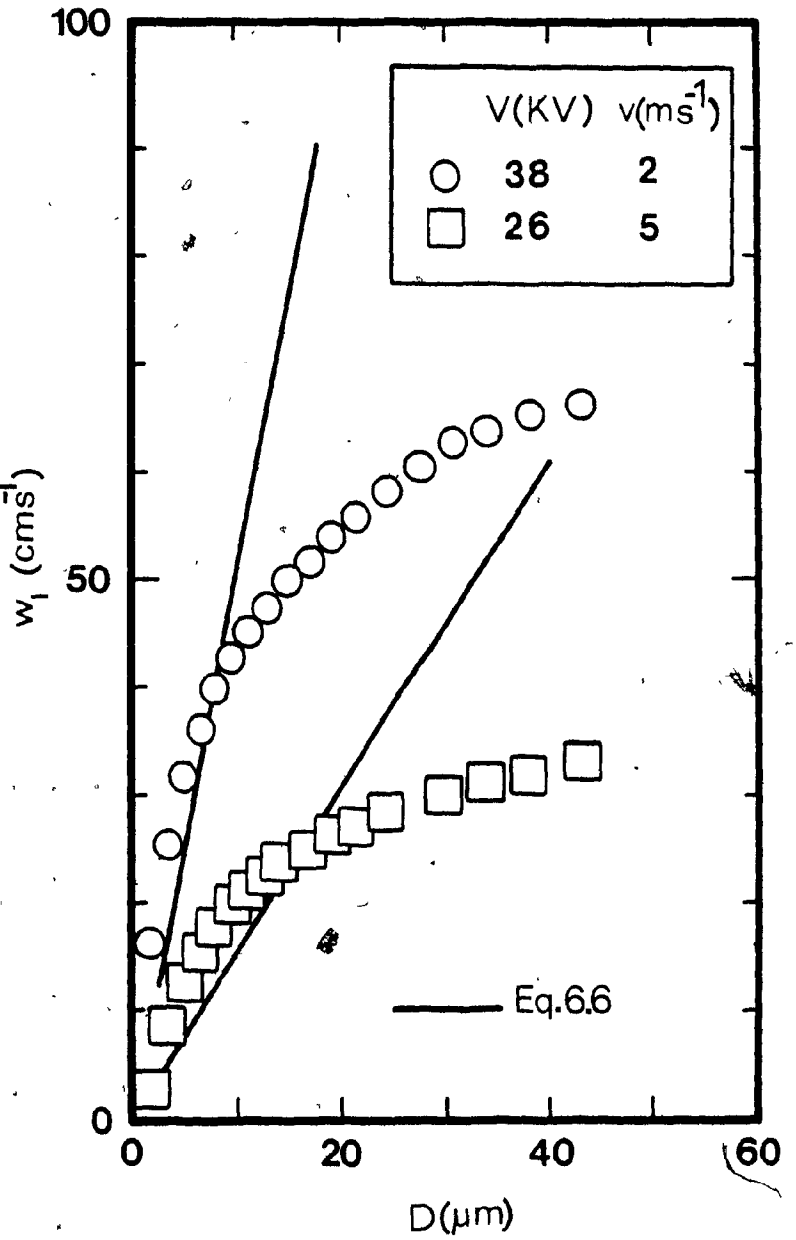


Figure 6.15 Variation of the effective migration velocity of MgO with particle size

6.4 Precipitation of Titanium Dioxide

6.4.1 Global Collection Efficiency

Only one experimental run was performed with pure TiO_2, with the experimental conditions and global experimental results listed in Table 6.7. Measurements along the ESP length or as function of particle size were not performed. Very good agreement was obtained with the global efficiency computed using the SRI model. The high resistivity of titanium dioxide (estimated from Fig. 5.25, Chapter 5) is a strong deterrent to reentrainment, and a positive net force of attraction due to the corona current is predicted by Eq. 6.4. The experimental run was 32 min long, the temperature 302 K and the relative humidity 44%.

6.5 Precipitation of Alumina

6.5.1 Global Collection Efficiencies

Table 6.8 lists the experimental conditions and global results of the experiments carried out with aluminium oxide. The resistivity values were estimated from Fig.5.25 of Chapter 5. The experimental runs varied from 96 to 144 min, the temperature from 296 to 302 K and the relative humidity from 37 to 51%.

Table 6.8 also shows the theoretical(SRI) global efficiencies using as input size distribution two estimates based on the Andersen MKIII cascade impactor data (Fig. 5.14 of Chapter 5). The uncertainty in the size distribution results from the uncertainty in estimating the density of the alumina agglomerates, as discussed in Section 5.4.2 of Chapter 5.

TABLE 6.7

Experimental Precipitation Conditions and Results for Titanium Dioxide

Run No.	MMD_{in} (μm)	σ_g	v (ms^{-1})	C_i (mgm^{-3})	V (KV)	$jx10^4$ (Am^{-2})	r (Ohmm)	η' (%)	η'_m (%)	η (%)	η_{SRI} (%)
16	13.6	1.66	2.0	133	37.6	12.6	10^8-10^9	98.0	1.93	99.9+	99.96

TABLE 6.8

Experimental Precipitation Conditions and Global Results for Alumina

Run No.	v (ms^{-1})	C_i (mgm^{-3})	V (KV)	$jx10^4$ (Am^{-2})	r (Ohmm)	η' (%)	η'_m (%)	η (%)	η_{SRI} (%)	
									$\rho = 0.9$ g cm^{-3}	$\rho = 2.0$ g cm^{-3}
17	5.0	2.82	25.7	1.03	10^8-10^9	23.0	1.31	23.3	25.5	19.5
18	5.0	2.62	30.0	2.90	10^7-10^8	48.2	2.12	49.2	41.0	32.4

Comparison of the experimental efficiencies with the theoretical predictions show that the experimental values are larger for the particle size distribution corresponding to a density of 2 g cm^{-3}. The lower limit of 0.9 g cm^{-3} corresponds to the bulk density of alumina, packed in the Wright feeder at about 6000 KPa. Since the alumina agglomerates should have a density larger than this value (2 g cm^{-3} being a reasonable estimate), it was concluded that the alumina is collected to a greater extent than theoretically predicted. The good agreement at low field for a density of 0.9 g cm^{-3} is probably fortuitous; it will be seen in Chapter 7 that the collection of alumina is underpredicted at high fields (applied voltage of 38 KV), irrespective of the density attributed to the alumina agglomerates.

The higher collection might be due to several factors, which are discussed in Section 6.5.3.

6.5.2 Collection Efficiency as Function of ESP Length

Table 6.9 gives the experimentally determined non-cumulative collection efficiencies as a function of each two increments of length, for the only run (with pure alumina) for which the measurements were taken.

Larger increments were used because of the small weights of dust used in these runs. Figure 6.16 shows the corresponding cumulative data. Also shown are the theoretical (SRI) predic-

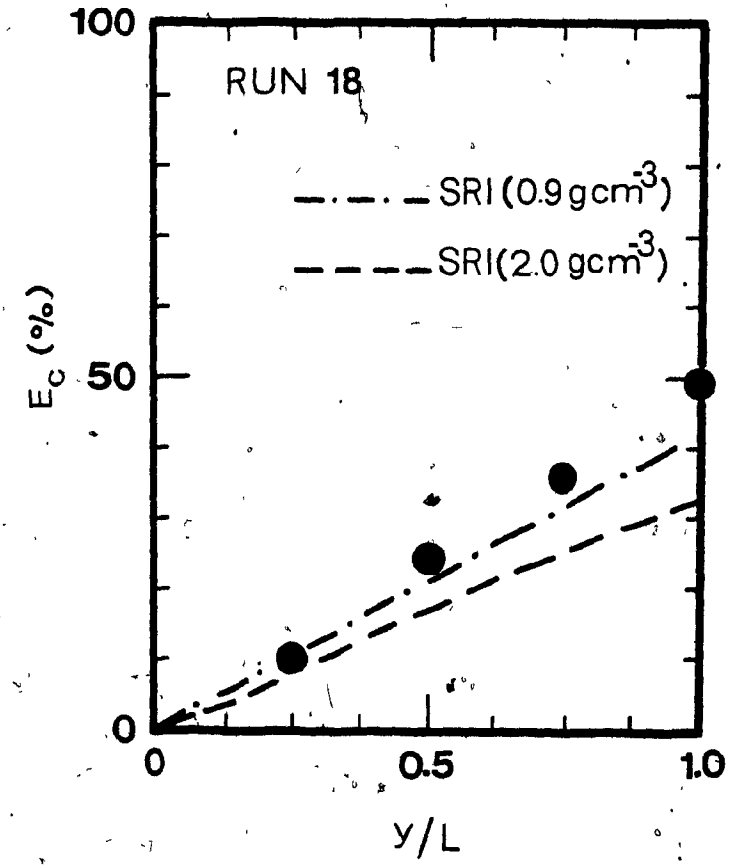


Figure 6.16 Cumulative collection efficiency of Al_2O_3 as a function of ESP length

TABLE 6.9

Non-Cumulative Collection Efficiencies (%), Al_2O_3

Run No.	Increment No. 1+2	3+4	5+6	7+8
18	10.2	14.3	13.5	11.3

tions, for both estimates of the particle size distribution of alumina. No experimental data were obtained for the particle size distributions at the ESP outlet, and so the estimation of fractional efficiencies or migration velocities was not possible.

6.5.3 Uncertainties in the SRI Simulation

The discrepancies observed between the collection of alumina and the theoretical predictions may be due to several causes, among them: abnormal charging near corona wires; uncertainties in the dielectric constant; and particle shape not being spherical. Each of these is examined next.

6.5.3.1 Abnormal Charging near Corona Wires

The contribution of high electric field strengths to the total charge may be important (Oglesby et al., 1970; Smith et al., 1961). The maximum effect of increased charge due to the particles passing near the corona wires was estimated by assuming that the charging field equals the field at the boundary of the corona glow region (which is approximately equal to the

corona onset field). Using Eqs. 2.6 and 2.7 of Chapter 2 and an empirical expression for the radius of the corona glow region (Crawford, 1976), the field intensity at this boundary was estimated to be 6×10^6 Vm^{-1}, at 25°C and 1 atm, for smooth discharge-wires. The SRI model was used with the charging field set at 6×10^6 Vm^{-1}, leaving all the other variables unchanged. The calculated global collection efficiencies of 41.6 and 74.4%, respectively, at low and medium applied voltage (Runs 17 and 18), for the finer particle size distribution estimate ($\rho = 2$ g cm^{-3}), are much larger than the experimental efficiencies. This shows that a charging field larger than the average field in the interelectrode spacing may be the cause of the observed collection efficiencies, but no definite conclusions can be reached. The use of the corona onset field for particle charging near corona wires has been suggested by others (Robinson, 1971).

6.5.3.2 Dielectric Constant

The effect of uncertainties in dielectric constant was simulated by setting the dielectric constant of alumina equal to 12.5; this is the highest value reported in the literature for alumina (Table 5.8, Chapter 5). The SRI model was used with this value of dielectric constant, leaving all the other variables unchanged. The calculated global collection efficiencies of 21.5 and 35.4% respectively at low and medium applied voltage are lower than the experimental efficiencies. The effect of uncertainties in the dielectric constant is thus small, and it was

concluded that it cannot explain the observed collection efficiencies.

6.5.3.3 Particle Shape

It is usually accepted that deviations from spherical shape are of secondary importance in electrostatic precipitation (Smith et al., 1961). According to White (1963), the results for spherical particles apply in order of magnitude to equivalent non-spherical particles; this seems to be adequate for many purposes.

The possible effect of deviations of the alumina agglomerates from spherical shape (and the increased specific surface area) are difficult to estimate, since the agglomerates do not have a precise geometric shape. Smith et al. (1961) have done precise measurements on the charge acquired by large metallic non-spherical particles (diameter of equivalent volume sphere of 3-5 mm) in a corona discharge. From data provided by these authors, the highest ratios of saturation charge per unit surface area of a non-spherical particle to the theoretical value for a sphere were obtained with cylindrical particles. The charge/area ratio does not depend on particle size, although it depends on particle shape and orientation. On the average, the maximum charge/area ratio for a cylindrical particle was 21% larger than for a sphere. However, the actual charge on the cylindrical particle is larger than that of a spherical particle of the same volume, due to the larger surface area of the former.

To estimate the possible effect of different particle shapes on the SRI predictions, the SRI model was used with simulated increased migration velocities corresponding to three different non-spherical shapes: a sphere with a sharp projection (surface area increased by 10%); a right cylinder of length-to-diameter ratio equal to 2.67; and a right cylinder of length-to-diameter ratio equal to 0.25. These shapes were chosen from the ones used by Smith et al. (1961) to represent a near spherical particle with a protruding edge, an elongated particle and a disk-like particle. Smith et al. (1961) state that the non-spherical particles tend to orient themselves in the electric field to acquire the maximum charge; this corresponds to having the long axis of a cylinder parallel to the charging field. Likewise, the cylindrical particles will tend to line up with the long axis parallel to the precipitating field. The different particle shapes and their preferred orientation with respect to the surrounding gas affects the viscous resistance to motion through the fluid. The possible changes in terminal velocity were estimated for the cylindrical particles using the following correlations (Clift et al., 1978):

$$\Delta_1 = \frac{1}{\chi\sqrt{\psi}} \exp\left\{\frac{0.622(\chi-1)}{\sqrt{\psi}\,\chi^{0.345}}\right\} \qquad (6.7)$$

$$\Delta_2 = \frac{1}{\chi\sqrt{\psi}} \exp\{0.576\sqrt{\psi\chi}(\chi-1)\} \qquad (6.8)$$

where (Δ) is the ratio of drag on particle to that on the equivalent volume sphere, in Stokes flow; (χ) is the ratio of the diameter of equivalent volume sphere to the diameter of projected area equivalent sphere; (ψ) is the ratio of surface area of equivalent volume sphere to that of the cylindrical particle (sphericity). Equation 6.7 is applicable to motion parallel to the axis (case of the elongated cylinder), while Eq. 6.8 is applicable to motion normal to the cylinder axis (case of the disk). The value of the shape factor χ also depends on the direction of motion relative to the cylinder axis.

Table 6.10 gives the computed values of increased charge and modified terminal velocity, normalized to the case of a sphere.

TABLE 6.10

Effect of Deviations from Spherical Shape in Increasing the Theoretical Migration Velocity

	Sphere with Projection	Cylinder ($\frac{L}{D}$ = 2.67)	Disk ($\frac{L}{D}$ = 0.25)
Ratio of Charge/Area[1]	1.13	1.21	1.21
Ratio of Drag (Δ)	1[2]	0.999	1.093
λ[3]	1.24	1.51	1.78

(1) Smith et al. (1961)
(2) Assumed
(3) Migration Velocity Enhancement Factor

In Stokes flow, the ratio of drag (Δ) is the inverse of the ratio of terminal velocities for the same external force

(Clift et al., 1978). Since the external force varies with the particle charge, the ratios of migration velocity at steady-state were computed from:

$$\lambda = A^{-1}(Q/A)/(Q/A)_{sphere}{}^{x(A/A_{sphere})} \qquad (6.9)$$

where Q/A is the ratio of charge -to-area.

The theoretical migration velocities for spheres were then multiplied by the corresponding value of (λ) listed in Table 6.10.

Figure 6.17 shows the results obtained with the SRI model using the modified migration velocities; comparison is made with the range of experimental data available for the fine alumina (Chapters 6 and 7). It can be seen that the non-spherical shapes produce a significant increase in collection efficiency. However, the alumina agglomerates do not have any of the simulated shapes (Chapter 5, Figs. 5.15 and 5.16a), and Smith et al. (1961) do not give experimental data for highly irregular shapes or agglomerates. Also, the values of charge/area ratio given by Smith et al. (1961) and listed in Table 6.10 assume that the particles have attained their saturation charge; this is not the case near the ESP inlet.

Due to the above considerations, no definite conclusions can be reached. However, it can be said that deviations from sphericity will probably increase the collection efficiency above that of spheres of equal weight; the SRI model seems very sensitive to this effect.

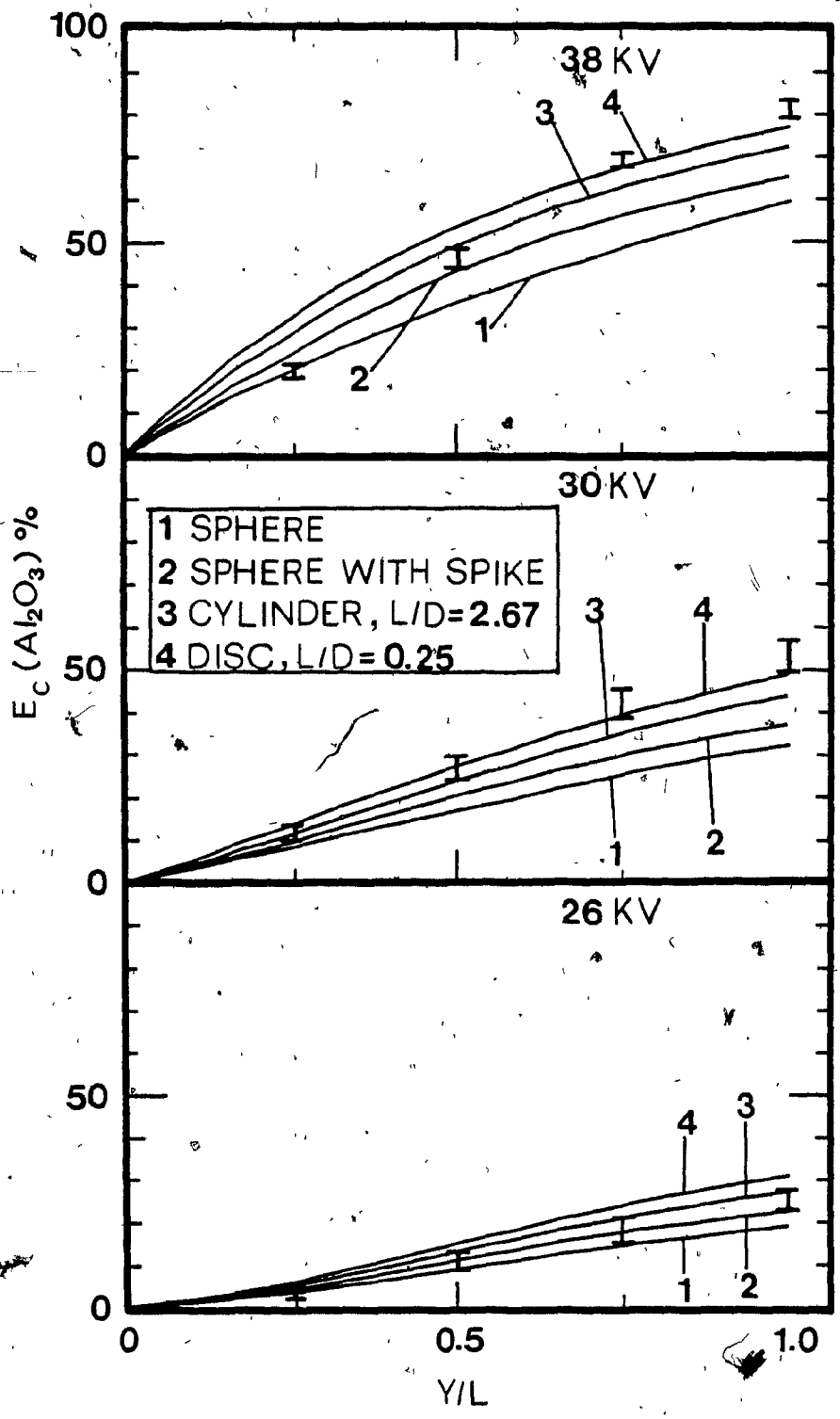


Figure 6.17 Cumulative collection efficiencies of alumina as a function of ESP length, for various particle shapes (SRI simulations)

6.6 Conclusions

The behaviour of the oxides of copper, magnesium, titanium and aluminium when fed alone to the ESP was experimentally studied. The experimental data were compared with theoretical predictions using the SRI computer model of ESP performance. Specifically, it was observed that:

1. Poor predictions were obtained for the precipitation of CuO, due to reentrainment. The low bulk resistivity of CuO is considered the single major cause of reentrainment.
   Reentrainment was found to be a complex function of air velocity, particle size and applied voltage. It increased with air velocity and applied voltage and (in general) both above and below particle diameters of about 10 to 15 μm.
2. Good predictions were obtained for the global precipitation of MgO and TiO_2. These materials have higher resistivities than CuO, and reentrainment on a global weight basis was not detected to any appreciable extent. However, the collection efficiencies for the fine MgO particles (below about 10-15 μm in diameter) were larger than theoretical predictions; this could be due to abnormal charging near the corona wires. The collection efficiencies for the coarser particles were smaller than theoretical predictions; this could be due to reentrainment.

3. Alumina showed higher collection efficiencies than theoretical predictions. The presence of agglomerates at the inlet of the ESP produces an uncertainty on the size distribution of the alumina particles, but this does not seem to affect the above conclusion. The higher collection may be due to abnormal charging near the corona wires or to deviations from spherical shape. It is possible that these two effects co-exist for alumina. Further experimental work is necessary to establish the exact cause of the higher collection observed for fine particles.
4. Separation due to size and/or resistivity differences (i.e., reentrainment) may be expected based on the precipitation of pure compounds. This is discussed in the next two chapters.

REFERENCES

Clift, R.; Grace, J.R. and Weber, M.E. (1978): "Bubbles, Drops and Particles", Academic Press, pp.69-81.

Crawford, M. (1976): "Air Pollution Control Theory", McGraw-Hill, pp.323.

Nichols, G.B. (1974): "Techniques of Measuring Fly Ash Resistivity", Environmental Protection Technology Series, EPA-650/2-74-079, August, NTIS, U.S. Dept. of Commerce, pp.34-38.

Oglesby, S. Jr. and Nichols, G.B. (1970): "A Manual of Electrostatic Precipitator Technology - Part I: Fundamentals", Southern Research Institute, pp.88.

Robinson, M. (1971): "Air Pollution Control, Part I", John Wiley & Sons, W. Strauss (ed.), pp.265.

Smith, P.L. and Penney, G.W. (1961): "The Charging of Non-spherical Particles in a Corona Discharge", AIEE Trans., Comm. & Electronics, 80, part 1, July, pp.340-346.

White, H.J. (1963): "Industrial Electrostatic Precipitation", Addison Wesley Pub. Co., pp.136-137.

CHAPTER 7

BEHAVIOUR OF MIXTURES OF PURE COMPOUNDS EXPERIMENTAL RESULTS, THEORETICAL PREDICTIONS AND DISCUSSION

7.1 Introduction

This chapter gives the experimental results and theoretical predictions on collection and separation efficiencies of mixtures of pure compounds. Collection and separation efficiencies are reported as cumulative values with ESP length. The advantage of this is that the ESP length necessary to achieve a specified separation and collection duty can easily be visualized and the comparison of experimental results is simplified. The non-cumulative values of collection efficiencies are also given in tabular form. The actual measured concentrations of the dust precipitated along the ESP length can be computed, if desired, from the following equation:

$$C_{p_j} = \frac{\eta_j (1-\eta'_m)_j (C_{ri})_j}{\sum_{j=1}^{k} \eta_j (1-\eta'_m)_j (C_{ri})_j} \qquad (7.1)$$

where (C_{p_j}) is weight concentration of component (j) in the precipitated dust for a particular length increment, (η_j) is the collection efficiency for the same length increment, $(C_{ri})_j$ is the weight concentration at the ESP inlet, $(\eta'_m)_j$ is the fraction of inlet dust that sedimented on the ESP bottom and (k) is the total number of components forming the mixture at the ESP inlet.

Separation efficiencies ($E_{s_{ij}}$) between components (i) and (j) were computed from:

$$E_{s_{ij}} = E_{c_i} - E_{c_j} \qquad (7.2)$$

where (E_{c_i}) refers to the cumulative collection efficiency of component (i). As discussed in Chapter 3, Section 3.4, $E_{s_{ij}}$ will take values from zero to one only in the case of a binary mixture. For a multicomponent mixture, Eq. 7.2 represents the difference in collection efficiencies between the two components in the presence of each other and of unspecified components, but it is not a true separation efficiency. To distinguish it from a true separation efficiency the symbol $E'_{s_{ij}}$ is used.

For graphical representation, the arbitrary criteria was adopted that for the use of Eq. 7.2 component (i) would be theoretically easier to collect than component (j). This may lead to negative separation efficiencies. The theoretical order of collection efficiencies is as follows: $E_{TiO_2} > E_{CuO} > E_{MgO} > E_{Al_2O_3}$, at the same experimental conditions.

7.2 Mixtures of CuO/MgO

7.2.1 Interaction Effect

The single component experiments with pure CuO and MgO shown in Chapter 6 suggest that a chemical segregation of the two species should be possible at high applied voltages ($\sim$ 38 KV) and air velocities above about 2 ms^{-1}, or at low applied voltages ($\sim$ 24 KV) and high air velocities (5 ms^{-1}).

It was shown that at high applied voltages, most of the MgO is captured, in agreement with theoretical (SRI) predictions, but the CuO escapes collection due to particle reentrainment. This would provide an example of a segregation mechanism other than particle size, since both materials tested have similar size distributions (Chapter 5, Section 5.4.1).

Table 7.1 lists the experimental conditions and global results of the experiments carried out with mixtures of CuO and MgO.

The experimental runs were 24 min long, the temperature varied from 299 to 303 K and the relative humidity from 26 to 45%. Table 7.2 lists the non-cumulative collection efficiencies.

Figure 7.1 shows the global collection efficiencies for both compounds at high voltage (~ 38 KV), as a function of air velocity. It can be seen that the collection efficiency of CuO is actually larger than that of MgO, except at 5 ms^{-1}. Figure 7.2 shows the expected separation efficiencies based on the behaviour of the single compounds (Chapter 6) and the experimentally observed values, at similar experimental conditions. Also shown in these two figures are the theoretical predictions of the SRI computer model.

The disagreement between the experimentally expected and observed separations shows that there is a very strong interaction between the two materials. The presence of MgO prevents the strong reentrainment which CuO exhibits when fed alone to the ESP. This is confirmed by the good agreement between the SRI predictions for the collection of CuO and the

Table 7.1

Experimental Precipitation Conditions and Global Results for Mixtures of CuO/MgO

Run No.	v(ms^{-1})	V(KV)	j x10^{4} (Am^{-2})	C_i (mg m^{-3})	Material	C_{ri} (%)	MMD(μm)	σ_g	r(Ohmm)	η'(%)	η_m'(%)	η(%)
19	1.3	38.0	12.4	467	CuO	64.0	11.2	1.48	$1x10^{6}$	94.2	5.73	99.9
					MgO	36.0	12.7	1.67	$2x10^{8}$	98.0	1.[illegible]4	99.9
20	2.0	38.8	12.4	669	CuO	48.8	12.0	1.48	$2x10^{5}$	96.5	3.38	99.9
					MgO	51.2	13.0	1.72	$4x10^{7}$	97.5	2.14	99.6
21	3.0	38.0	13.1	297	CuO	60.7	13.2	1.58	$3x10^{5}$	97.1	2.71	99.8
					MgO	39.3	14.0	1.77	$3x10^{7}$	96.3	3.03	99.3
22	5.0	38.0	13.0	158	CuO	61.8	13.6	1.59	$1x10^{6}$	90.9	2.79	93.5
					MgO	38.2	14.6	1.79	$3x10^{8}$	92.9	2.43	95.2
23	5.0	24.3	1.16	266	CuO	90.5	13.6	1.59	$2x10^{6}$	21.1	1.86	21.5
					MgO	9.5	14.6	1.79	$9x10^{8}$	48.9	0.76	49.3
24	5.0	23.8	1.10	155	CuO	41.0	13.6	1.59	$8x10^{5}$	45.7	4.14	47.6
					MgO	59.0	14.6	1.79	$7x10^{7}$	38.4	2.13	39.2
25	5.0	24.3	1.15	58	CuO	29.2	13.6	1.59	$3x10^{6}$	46.1	1.64	48.0
					MgO	70.8	14.6	1.79	$4x10^{8}$	43.4	2.97	44.7
26	5.0	23.3	1.10	330	CuO	44.7	13.6	1.59	$9x10^{5}$	45.4	2.01	46.3
					MgO	55.3	14.6	1.79	$9x10^{7}$	35.4	0.97	35.8
27	4.9	32.0	5.44	222	CuO	67.1	13.6	1.59	$1x10^{6}$	69.8	1.86	71.1
					MgO	32.9	14.6	1.79	$3x10^{8}$	88.9	1.46	90.2

Table 7.2

Non-Cumulative Collection Efficiencies (CuO/MgO), %

Run No.	Material	Increment No. 1	2	3	4	5	6	7	8	
19	CuO	-	-	-	-	-	-	-	99.9	(1)
	MgO	-	-	-	-	-	-	-	99.9	(1)
20	CuO	60.2	38.5		1.23	←	0.01	→		
	MgO	62.5	35.5		1.57	←	0.07	→		
21	CuO	40.3	42.2	11.7	3.09	←	2.31	→	0.31	
	MgO	39.8	42.7	12.2	2.70	←	1.70	→	0.16	
22	CuO	17.9	35.0	21.9	10.0	3.24	2.32	1.61	1.52	
	MgO	17.8	40.6	21.6	8.4	3.24	1.91	1.10	0.60	
23	CuO	2.21	3.18	2.36	2.39	2.23	3.04	4.43	1.68	
	MgO	1.95	6.96	2.04	6.03	4.33	9.34	1.61	2.55	
24	CuO	7.98	4.54	5.33	8.63	2.61	8.78	7.18	2.59	
	MgO	2.72	1.71	3.09	7.66	2.26	10.8	8.58	2.37	
25	CuO	5.70	5.54	4.32	7.78	8.31	6.65	2.67	6.99	
	MgO	1.80	2.12	1.70	7.56	10.4	7.03	3.34	10.8	
26	CuO	←	27.4	→		←	19.0	→		
	MgO	←	15.3	→		←	20.5	→		
27	CuO	←	53.3	→		←	17.8	→		
	MgO	←	69.1	→		←	21.1	→		

(1) Global Collection Efficiency

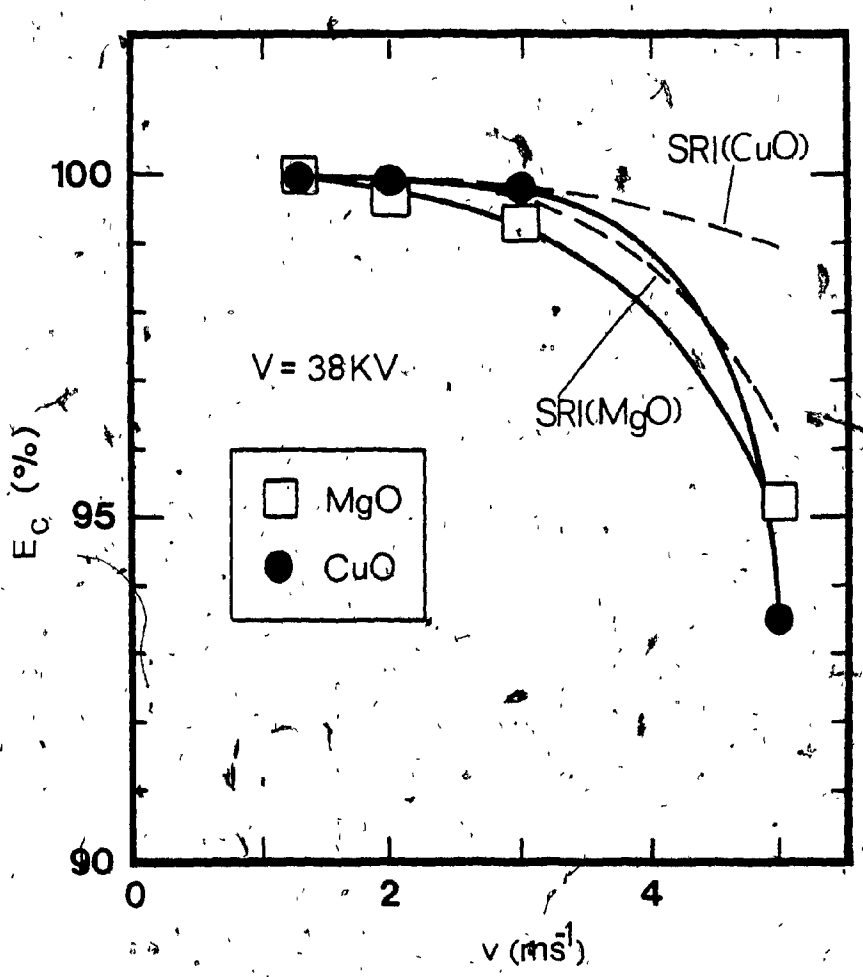


Figure 7.1. Variation of global collection efficiency of CuO and MgO with air velocity, in mixtures of CuO/MgO

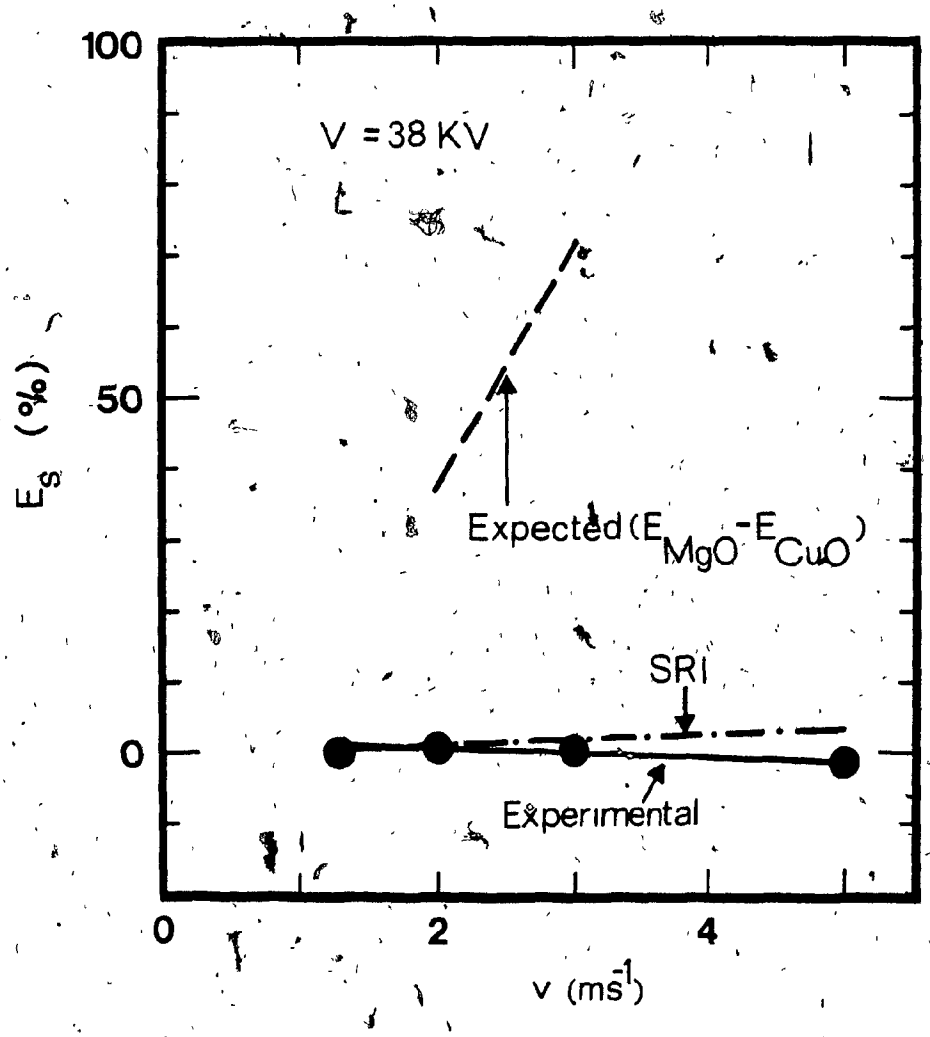


Figure 7.2 Comparison between the global experimental and theoretical separation of the pair CuO/MgO with the experimental expected values, as a function of air velocity

experimental results, up to an air velocity of 3 ms^{-1}. At 5 ms^{-1}, the collection efficiency of CuO drops sharply and becomes lower than that of MgO, an indication that reentrainment might have occurred to some degree.

The interaction between the two compounds may be explained as follows: during the first period of simultaneously feeding CuO and MgO (i.e., when the plates are clean) CuO is easily captured but equally easily reentrained as was demonstrated in the pure component runs (Chapter 6). However, a fine layer of MgO, which is captured but not reentrained, is soon built up and then the reentrainment of CuO is dramatically reduced. This is due to the higher resistivity of MgO which prevents the discharge of the CuO particles and their repulsion into the gas stream. It is possible that increased interparticle forces also reduced reentrainment.

Further confirmation of the interaction between MgO and CuO was given in an experimental run where first pure MgO and then pure CuO were fed to the precipitator sequentially in time. Specifically, MgO was fed for 8 min at 283 mg m^{-3} and CuO for the next 16 min at 243 mg m^{-3}, with the ESP energized at 37.5 KV and with an average air velocity of 3 ms^{-1}. The resistivities of CuO and MgO were estimated to be respectively 10^6 and 2×10^8 Ohm m. Table 7.3 lists the experimental global results obtained. The collection efficiency of MgO remained about the same as expected, while the collection efficiency of CuO was improved from 23% (no prior injection of MgO) to 94%.

TABLE 7.3

Experimental Global Collection Efficiencies of Sequential Feed Run

Material	n' (%)	n'_m (%)	n (%)
CuO	90.6	3.20	93.6
MgO	96.1	2.74	98.8

This improvement was, however, a function of dust layer thickness and some reentrainment of CuO was observed visually (by the presence of black dust at the bottom of the outlet contraction) after a run time of about 18 minutes.

Figure 7.3 shows the cumulative collection efficiencies for both components, for the conditions of separate feed (Chapter 6), simultaneous feed (Table 7.1) and sequential feed (Table 7.3), at 38 KV and 3 ms^{-1}. It can be seen that the collection efficiency of MgO does not vary appreciably, but that of CuO varies drastically depending on the feeding conditions.

The existence of this interaction mechanism was further corroborated by analysing the precipitated dust layer both near the plate surface and farther from it. In every run where CuO was collected in the presence of MgO and where this analysis was performed, the dust sublayer adjacent to the plate was found to be deficient in CuO while that in the outer sublayer was enriched in CuO. Table 7.4 lists the experimental values obtained for the CuO concentration, with the location (increment number) at which the measurements were taken.

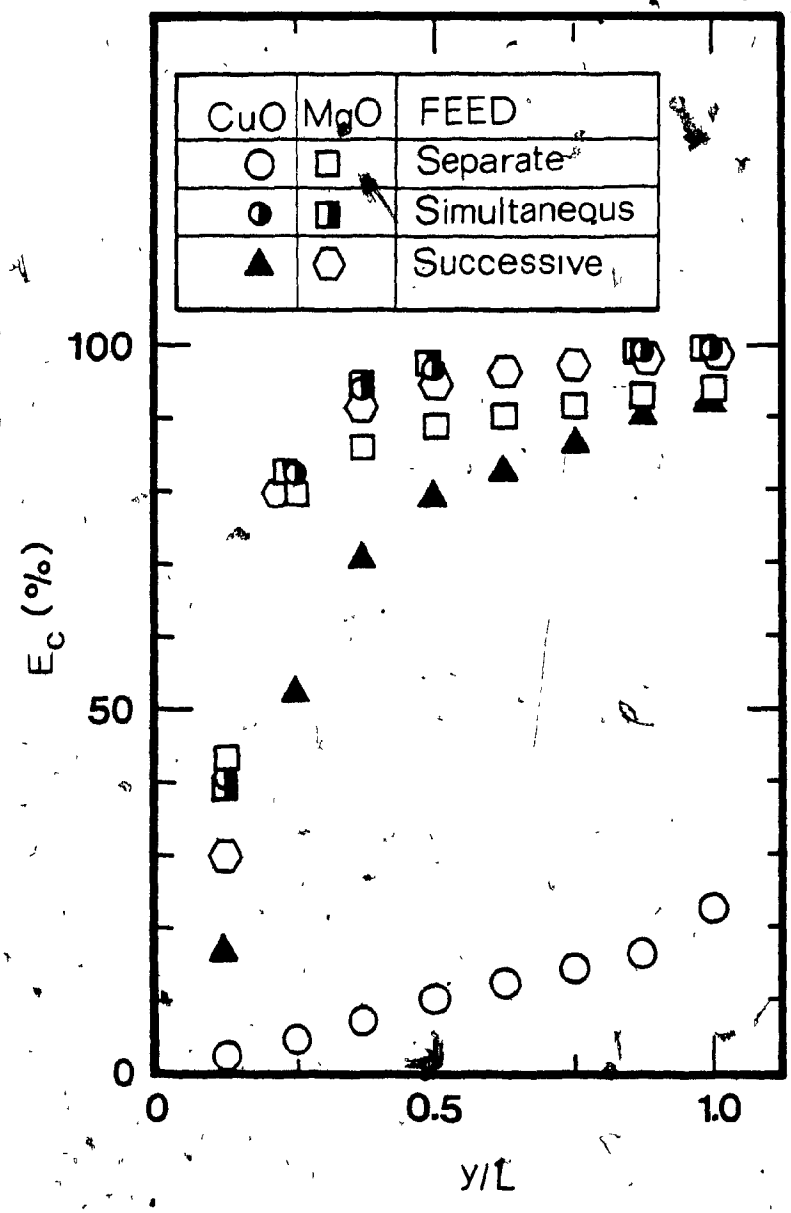


Figure 7.3 Cumulative collection of CuO and MgO for different feed conditions, as function of ESP length

TABLE 7.4

Variation of CuO Concentration in Precipitated Layer (CuO/MgO)

Run No.	Sub-layer Adjacent to Plate	Sub-layer Far from Plate	Overall Layer	Increment Number	Overall Increment
26	15.1	52.5	48.1	5-8 (190 cm from inlet)	42.5
27	30.8	64.1	62.0	1-4 (63 cm from inlet)	61.1
Sequential Feed	3.3	N/A	42.4	1 (16 cm from inlet)	48.1

Since the division of the dust layer into these two sublayers was arbitrary (a sharp scoop was used to remove an outer sublayer) the actual concentration differences reported in Table 7.4 should be regarded only as qualitative. Since each row of data in Table 7.4 represents a different operating condition and/or ESP location, the differences in absolute values between rows is not important. The results obtained for the sequential feed are as expected and these measurements were only performed to test the technique. Finally, there is good agreement between the overall layer composition and the composition of the length increment from which the layer was taken. The observed variations are due to the fact that the scooped layer represents only a small fraction of the length increment; variations in composition may thus be expected within each length increment. Figure 7.4 is a photograph of the scooped precipitated dust layer for run no. 26, clearly showing that the surface near the plate is richer in MgO, i.e., whiter.

7.2.2 Effect of Air Velocity

The effect of air velocity on the separation of CuO from MgO was studied at high electric fields (applied voltage of approximately 38 KV). The global collection and separation efficiencies are shown in Figs. 7.1 and 7.2 and were previously discussed. Figure 7.5 shows the cumulative collection and separation efficiencies for runs no. 19-22 (Table 7.1), as well as the theoretical (SRI) predictions. The theoretical collection curves for CuO are not shown but are similar to those of MgO,



Figure 7.4 Photograph of precipitated dust layer for a mixture of CuO and MgO, showing species segregation with depth of layer

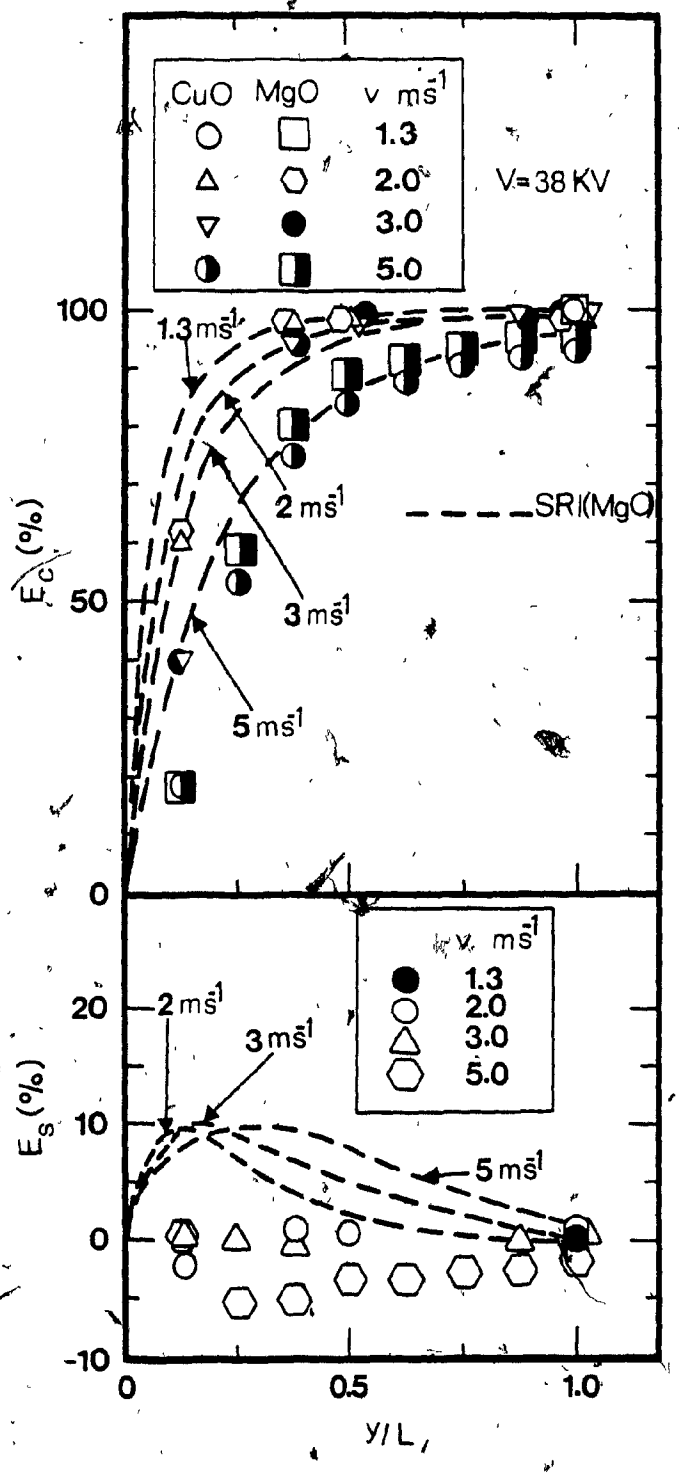


Figure 7.5 Effect of air velocity on the cumulative collection and separation of mixtures of CuO/MgO as function of ESP length

displaced towards higher collection efficiencies by the corresponding values shown in the separation graph. It can be seen that MgO is collected approximately according to theory, at all air velocities. This is in close agreement with the results obtained with pure MgO (Chapter 6). On the other hand, CuO is slightly better caught than MgO at velocities up to 3 ms^{-1}, but at the higher velocity of 5 ms^{-1}, MgO is preferentially caught. The separation efficiency was quite poor, showing a maximum of about (-6%) at the higher velocity. It is probable that separation increased with air velocity due to increased CuO reentrainment.

Figure 7.6 shows the CuO concentration as measured along the ESP length, normalized to the inlet CuO concentration, for the experimental runs for which the measurements were performed (no. 20-22, Table 7.1). Also shown are the theoretical (SRI) predictions. It can be seen that reasonable agreement was only obtained at the lower air velocity of 2 ms^{-1}, where both theory and experimental data show a decrease in relative CuO concentration with ESP length. This is a consequence of CuO being preferentially collected near the ESP inlet. As the air velocity is increased to 3 or 5 ms^{-1}, the experimental data show an increase in CuO concentration with ESP length, in disagreement with the theoretical predictions. This is probably due to the reentrainment of cupric oxide, which could then be occurring at velocities as low as 3 ms^{-1} (in the presence of MgO). However, the reentrainment of CuO in the presence of MgO is much smaller than in the case of pure CuO, and much poorer separation

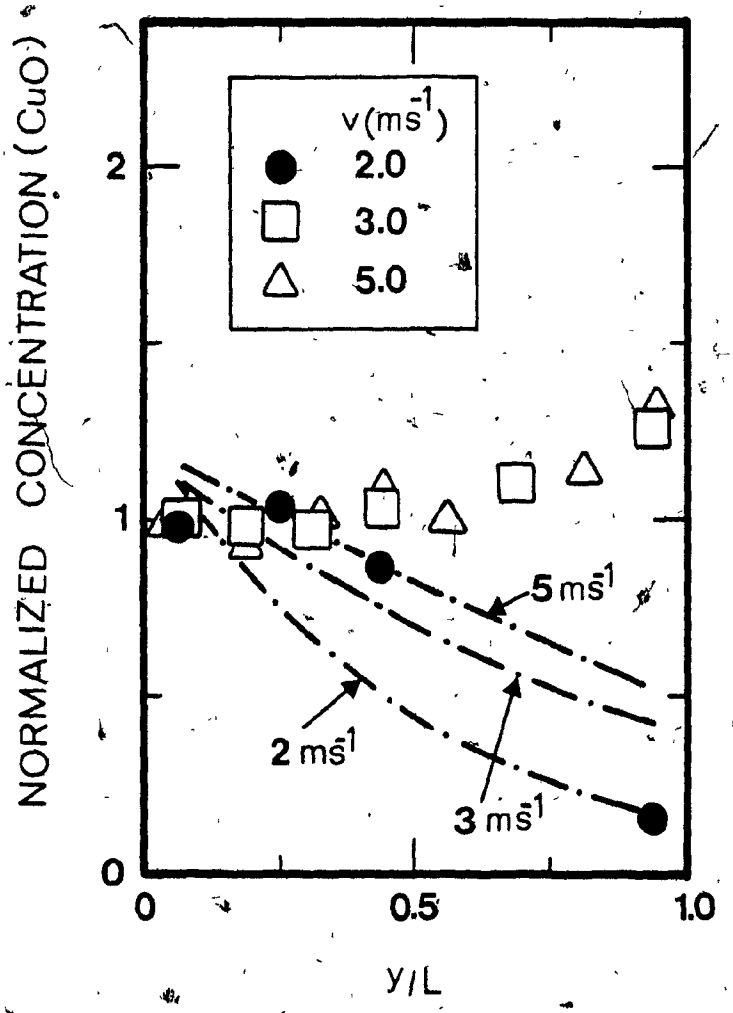


Figure 7.6 Variation of CuO concentration along the ESP length for mixtures of CuO/MgO at 38 KV and various air velocities

efficiencies were obtained than those predicted from the pure compound experiments (Chapter 6).

7.2.3 Effect of Electric Field

Figure 7.7 shows the effect of electric field on the cumulative collection and separation efficiencies of mixtures of CuO/MgO, at an air velocity of 4.9-5 ms^{-1} (runs 22, 23 and 27). Also shown are the theoretical (SRI) predictions. The theoretical curves for CuO are not shown, but are similar to the MgO curves, displaced towards higher efficiencies by the corresponding values shown in the separation graph. It can be seen that the collection of MgO agrees well with theoretical predictions at both 38 and 32 KV, but that lower efficiencies were obtained at 24 KV. The separation graph shows that MgO was preferentially collected at all voltages, and that separations close to 20 to 30% (absolute) were obtained at the lower voltages, indicating severe CuO reentrainment. This means that, in this case, the collection of MgO did not effectively prevent the reentrainment of CuO. This is especially true at the lower voltage ($\sim$ 24 KV), where the collection efficiency of CuO was similar to the one obtained in the pure component run. The values of relative CuO concentration at the ESP inlet given in Table 7.1 show that, for these particular runs, the inlet stream was very rich in CuO, especially at the lower voltage of 24 KV. It is then possible that the concentration of CuO at the ESP inlet plays an important role in determining the degree of reentrainment, and thus its segregation from other components

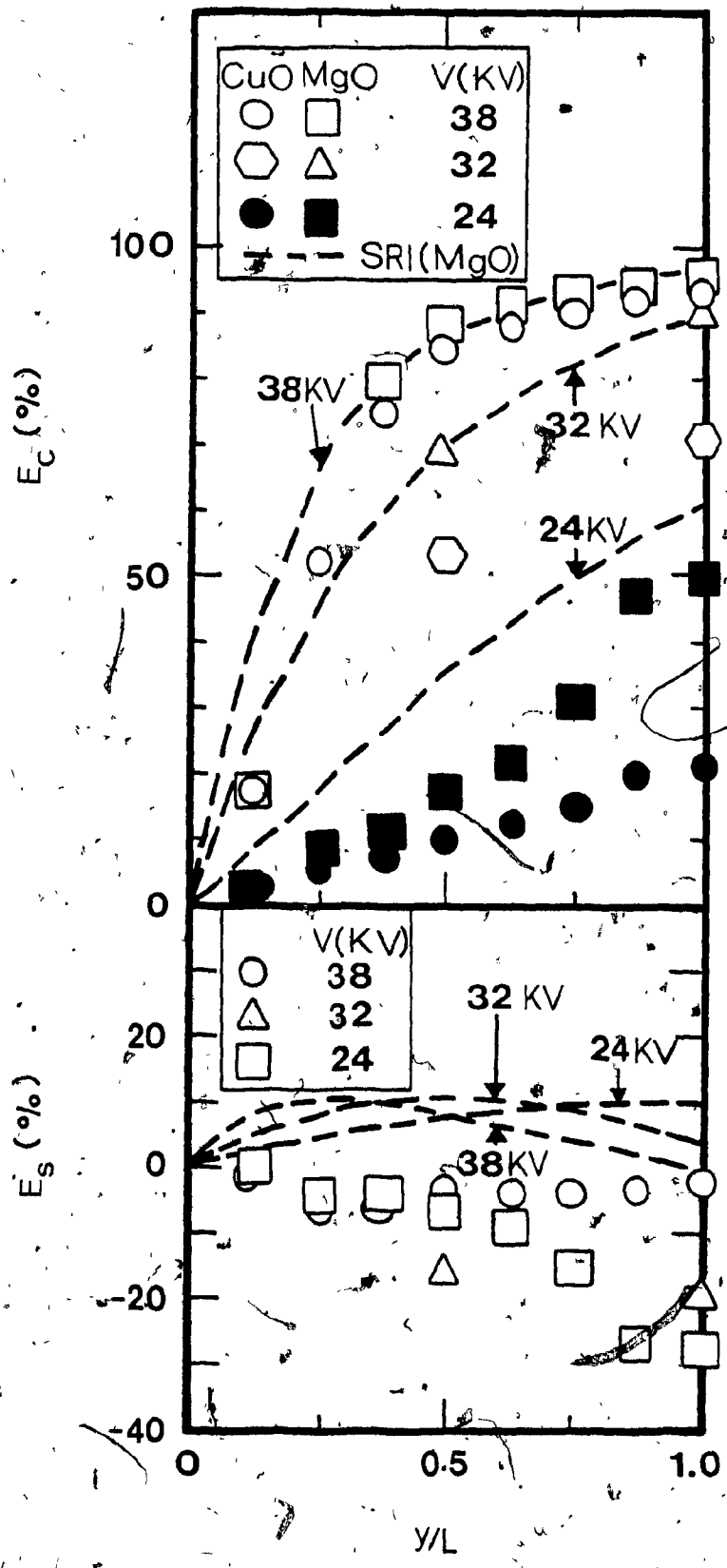


Figure 7.7 Effect of electric field on the cumulative collection and separation of mixtures of CuO/MgO, at 5ms^{-1} and various applied voltages

which do not reentrain. This is discussed next.

7.2.4 Effect of Relative Concentration

A series of runs with CuO/MgO was performed at low electric fields and high air velocity (no. 23-26, Table 7.1) to investigate the effect of CuO concentration. These test conditions were chosen since they produced the highest separation (Fig. 7.7).

A multiple linear regression of the collection efficiency of CuO as a function of applied voltage, total dust loading and percent inlet CuO concentration (performed on the MUSIC/STATPAK system of McGill University) showed that the efficiency of CuO was most strongly correlated with CuO concentration. This is shown in Fig. 7.8, where the collection efficiency of CuO when fed alone to the ESP under similar conditions of applied voltage and air velocity was also included. Figure 7.8 also shows the range of theoretical collection efficiencies predicted by the SRI model. It is seen that all experimental values lie below the theoretical predictions (which do not depend, for all practical purposes, on the CuO concentration), indicating that reentrainment occurs to some degree. As the inlet stream gets richer in CuO, the efficiency drops and approaches that of pure CuO (where reentrainment is maximum, other variables being held constant).

A similar treatment for MgO showed that the collection efficiency of MgO was most strongly correlated with applied voltage. This is shown in Fig. 7.9, where the collection efficien-

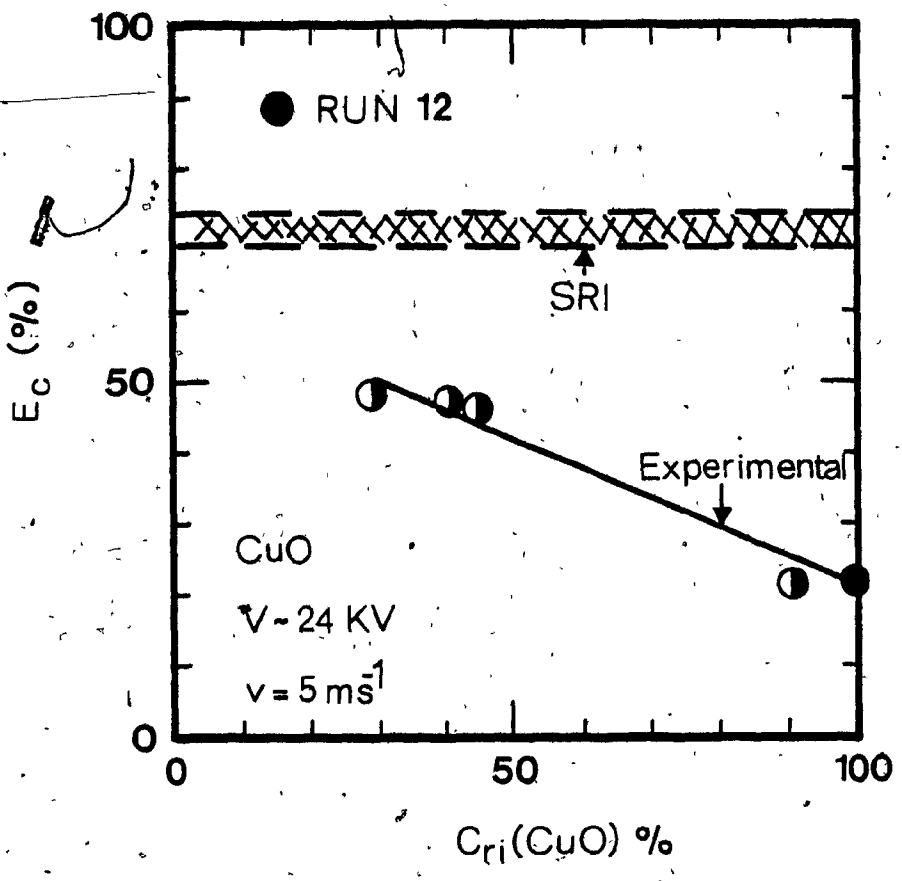


Figure 7.8 Variation of global collection of CuO with inlet concentration

cies of MgO when fed alone to the ESP and with TiO_2 and Al_2O_3 under similar conditions of applied voltage and air velocity were also included. Also shown for comparison are the theoretical predictions of the SRI model. It can be seen that the experimental values are all below the theoretical predictions (for this range of applied voltages, the theoretical predictions are practically independent of the applied voltage). The scatter of the data for the case of runs 31 and 41 suggests that some other variable other than applied voltage might also be important. In an attempt to determine this variable, the corona power (voltage x current) was calculated for all low voltage-high velocity runs in which MgO was present. The results are shown in Fig. 7.10, where it can be seen that the scatter was significantly reduced. It is possible that the low collection efficiencies experienced by MgO at the lower corona powers were due to irregularities in the corona current distribution. Magnesium oxide could be affected by the irregular corona current due to its difficulty in charging,i.e., due to its low dielectric constant. A similar behaviour has been observed by Gooch et al. (1976a,b) at low current densities, for dyoctylphthalate aerosol (also a low dielectric constant material), as discussed in Chapter 2, Section 2.8.2.

It would be expected that the corona irregularities disappear at higher corona powers; this is in agreement with the fact that the global collection of MgO agrees well with SRI predictions at corona powers above about 6 W.

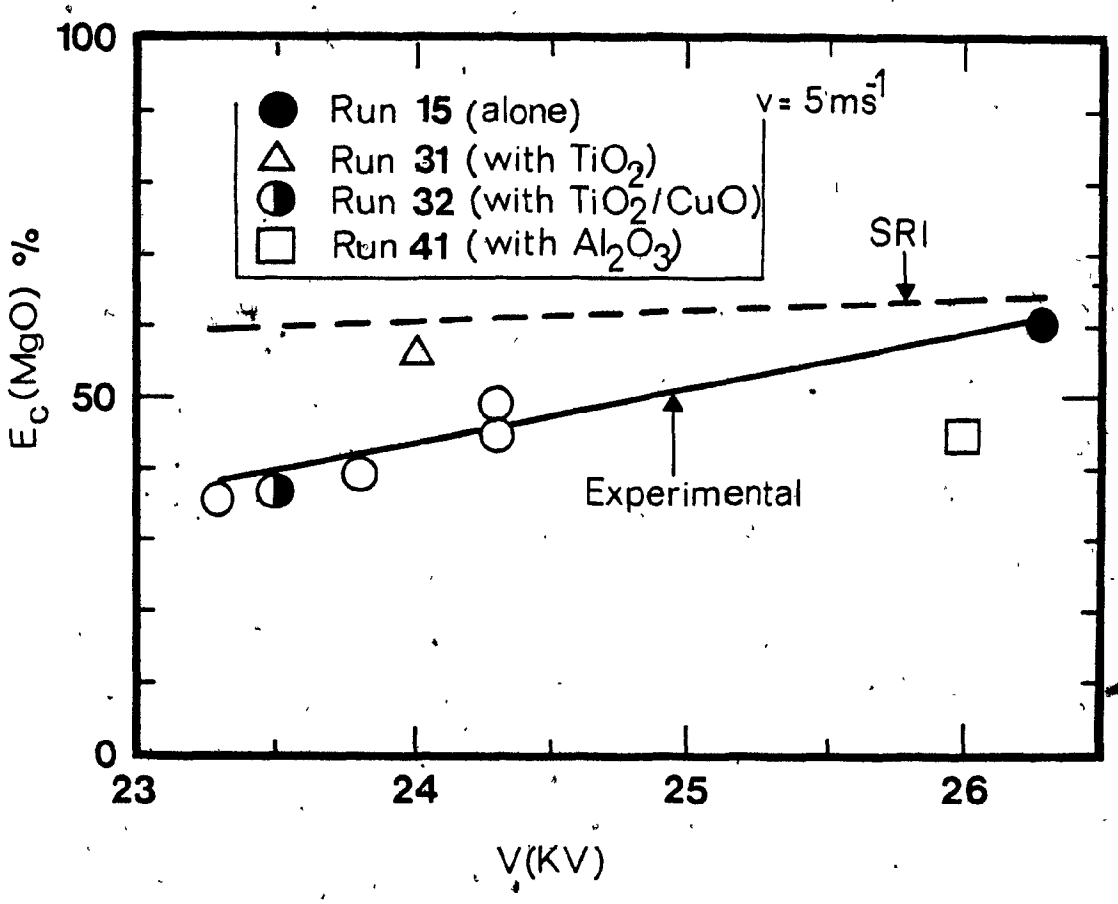


Figure 7.9 Variation of global collection of MgO with applied voltage, at low applied voltage

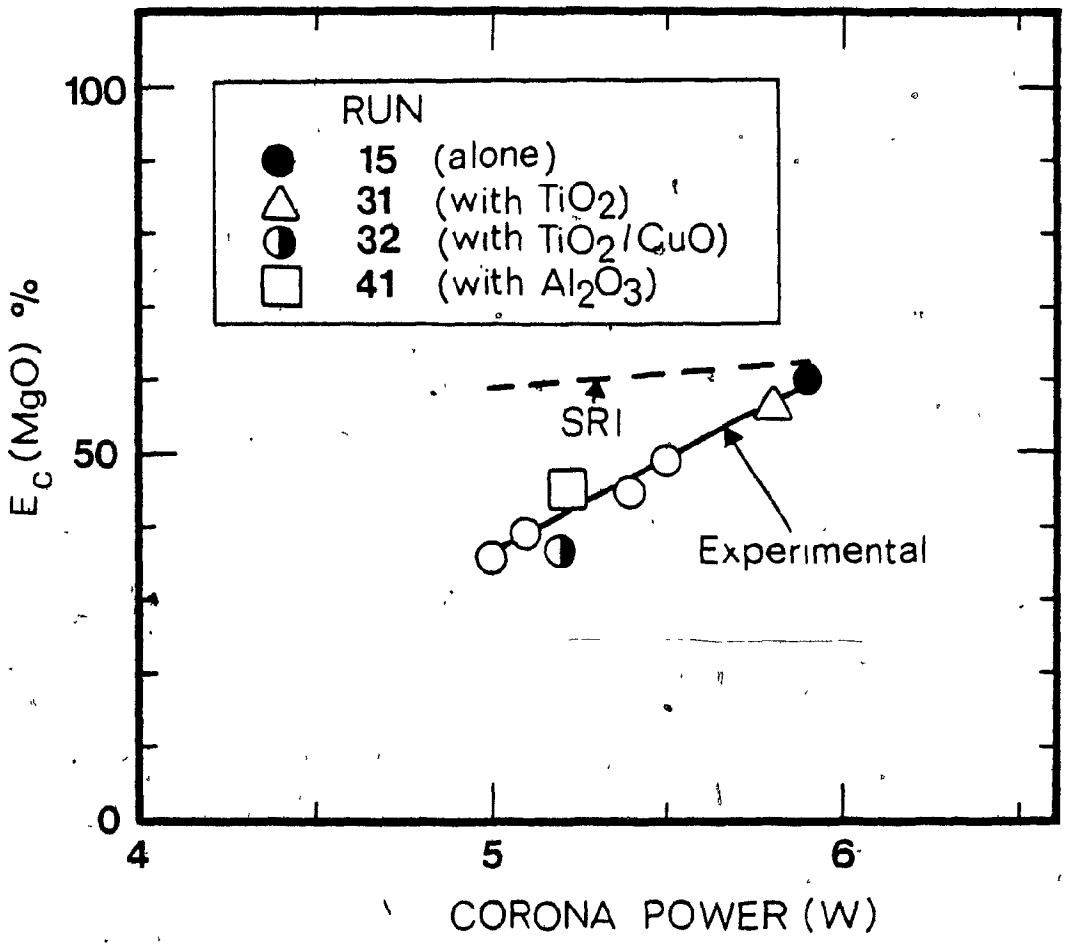


Figure 7.10 Variation of global collection of MgO with corona power, at low corona powers

A test performed on the effect of particle inertia in decreasing the collection efficiency of magnesium oxide at 5 ms^{-1}, near the ESP inlet (using Eq. 2.36 of Chapter 2), showed a negligible effect.

Figure 7.11 shows the effect of CuO concentration on the cumulative collection and separation efficiencies, as a function of ESP length. Also shown is the theoretical separation predicted from the SRI model. The collection efficiency of MgO varies somewhat depending mainly on the applied voltage, but the collection efficiency of CuO decreases drastically at high CuO concentrations. Further, while at the high CuO concentration the efficiency of MgO is larger, the reverse occurs at low CuO concentrations. This is due to the sharp reduction in CuO reentrainment at low CuO concentrations.

While at low CuO concentrations (moderate reentrainment) the separation efficiency is below about 10% (for the entire ESP), at high CuO concentrations (high reentrainment) the separation efficiency is around 30% (absolute), increasing (in absolute value) with increasing ESP length. Thus, reentrainment may increase the separation between chemical species, because it is selective.

The agreement between the SRI predictions and the observed separations is reasonable, for moderate CuO reentrainment.

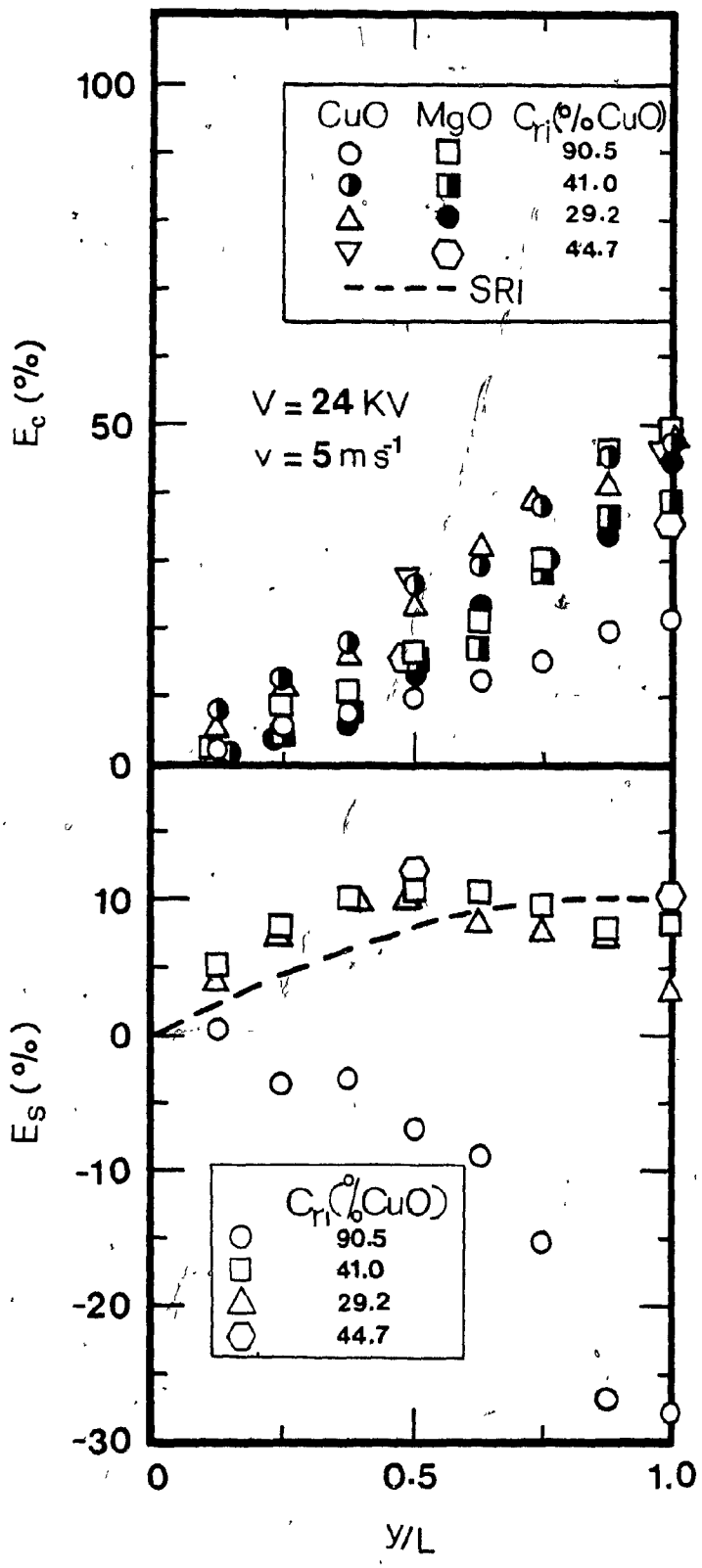


Figure 7.11 Effect of inlet concentration of CuO on collection and separation of mixtures of CuO/MgO

7.2.5 Reentrainment of CuO in Mixtures with MgO

A multiple linear regression of percent reentrainment of CuO as a function of air velocity, applied voltage and percent inlet CuO concentration for runs no. 19-27 (Table 7.1) showed that reentrainment increased with air velocity and inlet CuO concentration but decreased with applied voltage. Also, reentrainment was highly correlated with applied voltage and inlet CuO concentration but poorly correlated with air velocity. The poor correlation with air velocity is due to the fact that this variable only varied at high applied voltages, where reentrainment was very small. The high correlation observed with inlet CuO concentration is in agreement with the discussion in Section 7.2.4 on the effect of the inlet CuO concentration on its collection efficiency. The high correlation obtained with applied voltage is probably due to the fact that the reentrainment of CuO is in great part controlled by the collection of the higher resistivity MgO; since this increases with the applied voltage, the reentrainment of CuO should decrease with increasing applied voltage.

Figure 7.12 shows the observed versus estimated percent reentrainment of CuO, based on the results of the multiple regression analysis. The regression equation is also given.

7.2.6 Conclusions

1. Cupric oxide is preferentially collected unless reentrainment occurs.
2. Higher separations are obtained if the charging

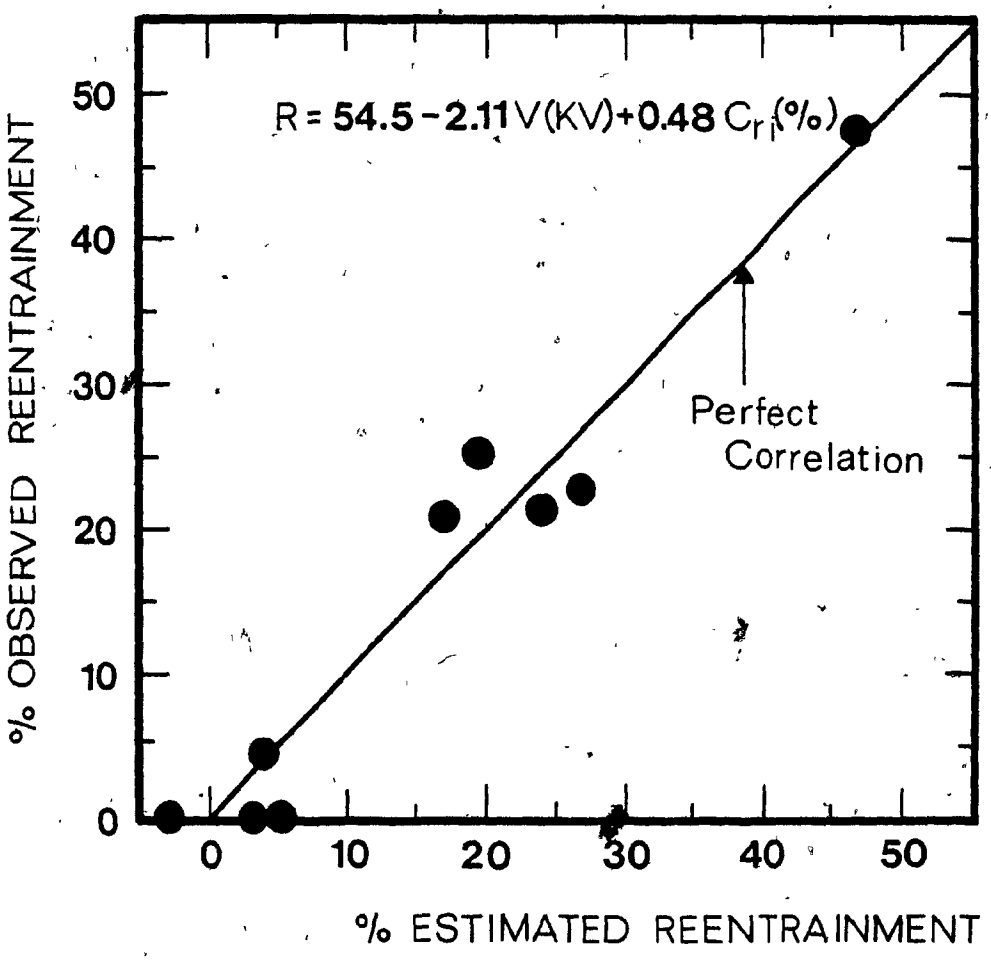


Figure 7.12 Relation between the experimental and estimated re-entrainment of CuO in mixtures with MgO, from multiple regression analysis

environment is poor, i.e., with high air velocities and/or low electric fields.

3. The overall separation efficiency of CuO and MgO is low except in the industrially insignificant case where the concentration of CuO is very high. The effect of electric field on separation is greater than that due to gas velocity.
4. Since CuO in the presence of MgO can only be strongly reentrained at high CuO concentrations, it is probable that a separation mechanism based on reentrainment can only be effective if the reentraining species is more difficult to charge (i.e., has a lower dielectric constant) than the higher resistivity species. This was not the case for the pair CuO/MgO.

7.3 Mixtures of TiO_2/CuO

In this case the reentraining species is also that which is more difficult to charge, since it has a lower dielectric constant. However, the effect due to the dielectric constant should be small since both materials have high dielectric constants.

Table 7.5 lists the experimental conditions and global results of the experiments carried out with mixtures of CuO and TiO_2. The resistivity of TiO_2 was estimated from Fig. 5.25 of Chapter 5. The temperature varied from 296 to 299 K, the experimental runs were 24 min long and the relative humidity varied from 18 to 22%.

TABLE 7.5

Experimental Precipitation Conditions and Global Results for Mixtures of TiO_2/CuO

Run No.	v (ms^{-1})	V (KV)	$jx10^4$ (Am^{-2})	C_i ($mg\ m^{-3}$)	Material	C_{ri} (%)	MMD (μm)	σ_g	r (Ohm m)	η' (%)	η'_m (%)	η (%)
28	4.9	36.3	13.4	273	CuO	31.0	13.6	1.59	$5x10^6$	85.1	3.02	87.8
					TiO_2	69.0	15.0	1.74	10^9-10^{10}	95.7	1.36	97.0
29	5.0	22.2	1.29	542	CuO	30.7	13.6	1.59	$2x10^7$	26.5	4.81	27.8
					TiO_2	69.3	15.0	1.74	10^9-10^{10}	70.5	2.13	72.0

TABLE 7.6

Non-Cumulative Collection Efficiencies (TiO_2/CuO)

Run No.	Material	Increment No. 1	2	3	4	5	6	7	8
28	CuO	1.66 13.2	15.9 12.9	9.73 8.07	11.4	4.18	←	10.7	→
	TiO_2	14.5 25.7	19.2 12.0	7.65 5.31	6.40	2.31	←	3.96	→
29	CuO	1.96	5.14	3.99	3.53	3.38	2.69	3.42	3.71
	TiO_2	18.8	19.7	9.51	6.56	5.19	3.65	4.26	4.42

Table 7.6 lists the corresponding non-cumulative collection efficiencies. In the case of run no. 28, the first three length increments were further sub-divided since TiO_2 was highly collected in the first meter of the ESP ($\sim$ 84% collection efficiency). This was evidenced by the distinct brown colour of TiO_2 in the dust precipitated near the ESP inlet. The experimental runs were performed at high velocity and at both high and low electric fields since the electric field effect was shown for mixtures of CuO/MgO to be more important than the effect of air velocity. The use of high air velocities also reduces sedimentation, which is especially large for CuO at reduced velocities.

Figure 7.13 shows the cumulative collection and separation efficiencies for mixtures of CuO/TiO_2, at an air velocity of 4.9-5 ms^{-1} for two different electric fields. Also shown are the SRI predictions. The collection of TiO_2 agrees well with theoretical predictions at the higher field, but it deviates from theory at the lower field, showing higher collection than predicted near the ESP inlet; this could be due to the non-spherical shape of the TiO_2 particles (Chapter 5, Figs. 5.8 and 5.9). An estimation of the possible effect due to enhanced charging of non-spherical particles was performed using the data of Smith et al. (1961), as discussed in Chapter 6, Section 6.5.3.3. Figure 7.14 shows the observed range of collection efficiencies for TiO_2, at 5 ms^{-1} and at high, medium and low applied voltages (the experimental data includes runs 28, 29, 31-36 and 42-44). Also shown are typical SRI predic-

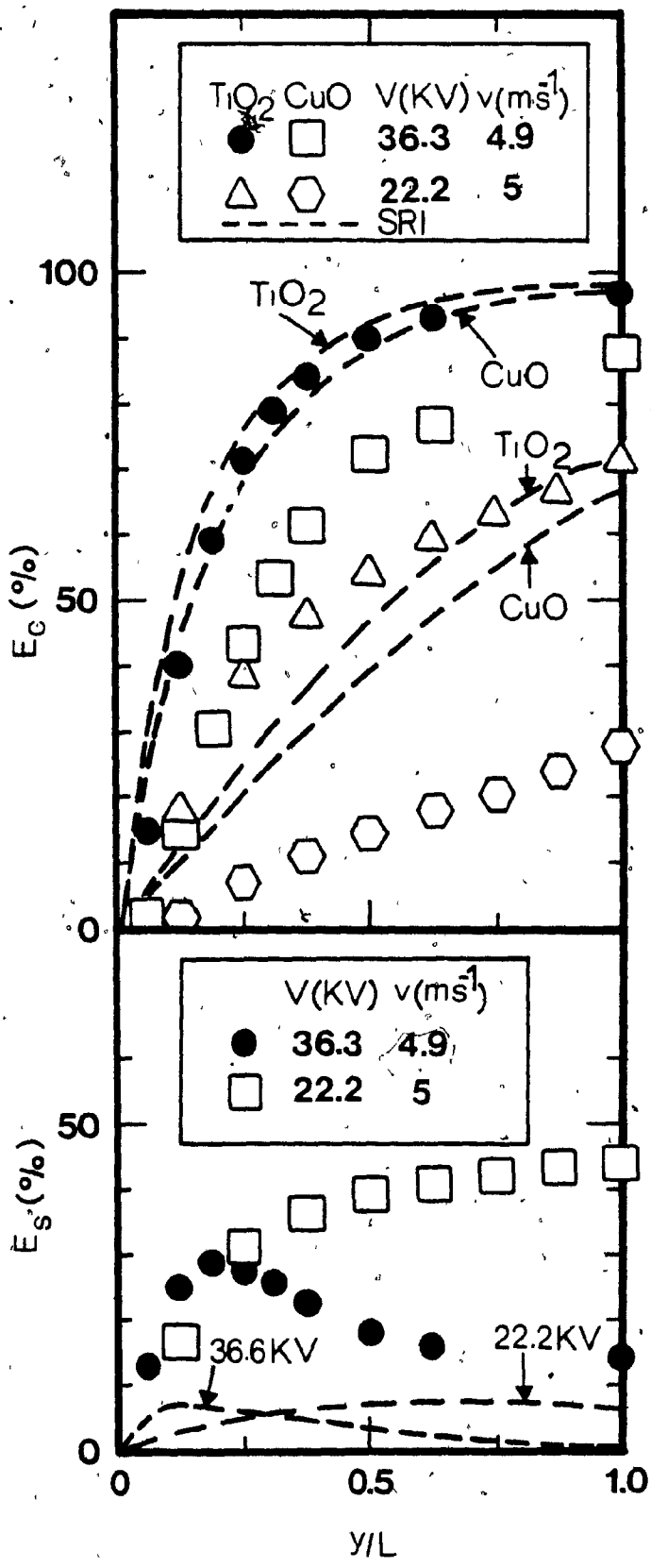


Figure 7.13 Cumulative collection and separation of mixtures of TiO_2/CuO as function of ESP length

tions, considering the particles to be spherical and cylindrical (length-to-diameter ratio of 2.67). A cylindrical shape was chosen to estimate the higher collections that may occur due to a strong deviation from a spherical shape. The migration velocity enhancement factor is given in Table 6.10 to be equal to 1.51.

Figure 7.14 shows that, in general, a better agreement is obtained if the TiO_2 particles are considered as spheres. However, better agreement is obtained near the ESP inlet, at low applied voltage, if the particles are considered as cylindrical. It is plausible that a better overall agreement may be obtained for all applied voltages if the particles are considered to have a geometrical shape which does not deviate as much from a sphere as a cylinder does. Unfortunately, the lack of experimental data on the charging of typical non-spherical particles and the difficulties in characterizing the shape of an irregular particle do not allow any definite conclusions to be reached.

The collection of CuO is always below theoretical predictions and the discrepancy increases with decreasing electric field. Due to the high resistivity of TiO_2 and the low CuO concentrations at the ESP inlet, it would be expected that the reentrainment of CuO would be effectively reduced. The reentrainment of CuO was highly reduced (as compared with the pure component runs) only at the high applied voltage. At the low electric field the reduction was less important. Also, with respect to the runs performed with mixtures of CuO/MgO discussed in Section 7.2, MgO seems to be more effective in reducing the reentrainment

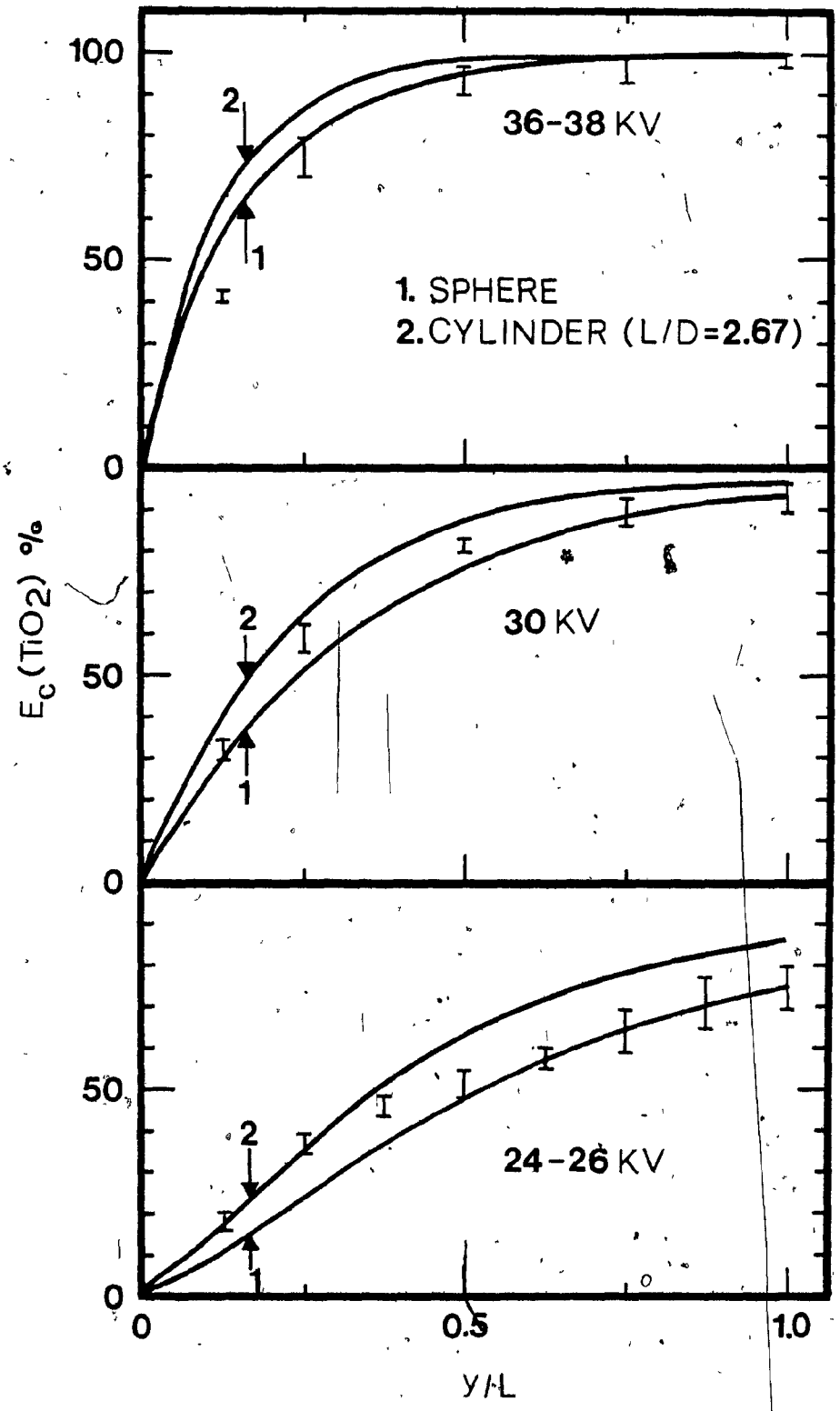


Figure 7.14 Simulated effect of particle shape on the cumulative collection of TiO_2 as function of ESP length

of CuO, despite having a lower resistivity than TiO_2. It is possible that interparticle forces also play an important role in determining the reentrainment of a low resistivity species, i.e., bulk resistivity is not the only factor involved. These phenomena need further investigation.

TiO_2 seems unaffected by the possible non-uniformity in corona current at the low applied voltage, in contrast with the behaviour of MgO. This may be due to the ease of charging of the TiO_2 particles due to their high dielectric constant, or to the possible effect of deviations from a spherical particle shape. Figure 7.13 also shows that there is qualitative agreement (i.e., in the shape of the curve) between the SRI predictions of separation efficiency and the experimental results. The observed global separations are much larger than predicted, mainly due to the effect of CuO reentrainment.

It is encouraging to see in Fig. 7.13 that separations up to 44% are possible with a short ESP. Although the dielectric constant of TiO_2 is very large, this example serves the purpose of experimentally verifying that high separations can be achieved where the material which is poorly charged reentrains to some significant extent. The global separation (i.e., for the entire ESP length) is seen to increase as the charging environment becomes less favorable in agreement with theoretical predictions.

The precipitated dust layer was analysed for CuO content both near the plate surface and farther from it, and qualitative agreement was obtained with the previous results on the pair CuO/MgO (Table 7.4). Table 7.7 shows the experimental results

obtained for the pair CuO/TiO_2.

TABLE 7.7

Variation of CuO Concentration in Precipitated Layer

(TiO_2/CuO), %

Run No.	Sub-Layer Adjacent to Plate	Increment No.	Overall Increment
28	29.9	4 (85 cm from inlet)	40.1
29	9.2	3 (79 cm from inlet)	15.3

It can be seen from Table 7.7 that in both runs the sub-layer adjacent to the plate is depleted in CuO, as would be expected in the case of CuO reentrainment.

7.4 Mixtures of TiO_2/MgO

Reentrainment is small or negligible for both MgO and TiO_2, under the experimental conditions reported in this work. Segregation of these compounds (of similar size distribution) must then be primarily based on differences in dielectric constant. The dielectric constant affects the degree of charging, and so will affect the degree of collection. Theoretically, the degree of charging should be about 52% larger for TiO_2 than for MgO.

Table 7.8 lists the experimental conditions and global results of the experiments carried out with mixtures of MgO/TiO_2. Table 7.9 lists the corresponding non-cumulative collection

TABLE 7.8

Experimental Precipitation Conditions and Global Results for Mixtures of MgO/TiO_2

Run No.	v (ms^{-1})	V (KV)	$jx10^4$ (Am^{-2})	C_i ($mg\ m^{-3}$)	Material	C_{ri} (%)	MMD (μm)	σ_g	r (Ohm m)	η' (%)	η'_m (%)	η (%)
30	2.0	38.0	13.2	307	MgO	43.1	13.0	1.72	$2x10^8$	97.0	3.03	99.9
					TiO_2	56.9	13.6	1.66	$\sim10^9$	97.3	2.75	99.9+
31	5.0	24.0	1.23	112	MgO	43.7	14.6	1.79	$5x10^8$	49.3	5.19	56.2
					TiO_2	56.3	15.0	1.74	$\sim10^9$	76.8	4.04	79.4

TABLE 7.9

Non-Cumulative Collection Efficiencies (MgO/TiO_2)

Run No.	Material	Increment No.							
		1	2	3	4	5	6	7	8
30	MgO	66.9	30.0	2.50	←	←	0.63	→	→
	TiO_2	74.1	23.1	2.36	←	←	0.47	→	→
31	MgO	2.92	5.11	4.38	6.56	8.75	12.4	11.7	4.38
	TiO_2	15.8	21.0	9.46	7.36	6.31	8.94	7.89	2.63

efficiencies. For this particular case, the experimental conditions were chosen to be at the extremes of high field-low velocity characteristic of industrial practice and low field-high velocity; this last condition was chosen for the high separations which were obtained with the pairs CuO/MgO and CuO/TiO_2 under similar conditions. The temperature varied from 297 to 300 K, the experimental runs were 24 min long and the relative humidity varied from 30 to 33%.

Figure 7.15 shows the cumulative collection and separation efficiencies of mixtures of MgO/TiO_2. Also shown are the theoretical predictions of the SRI computer model. Although the agreement between the experimental results as a function of ESP length and the theoretical predictions is not remarkable, the agreement based on the entire ESP length is good. The qualitative agreement is also good. At low velocity and high field, separation is very poor and is a maximum near the ESP inlet. At low electric field and high velocity, the separation is greatly improved. However, the agreement with theoretical predictions is worse at low field and high velocity. The larger deviations from theoretical predictions are observed for MgO, probably due to its sensitivity to low corona powers (Section 7.2.4).

By comparing Figure 7.15 with Figure 7.13, it can be seen that the agreement between the experimental results and the theoretical predictions is much better for the pair MgO/TiO_2 than for the pair CuO/TiO_2, where reentrainment greatly increases the separation predicted on theoretical grounds.

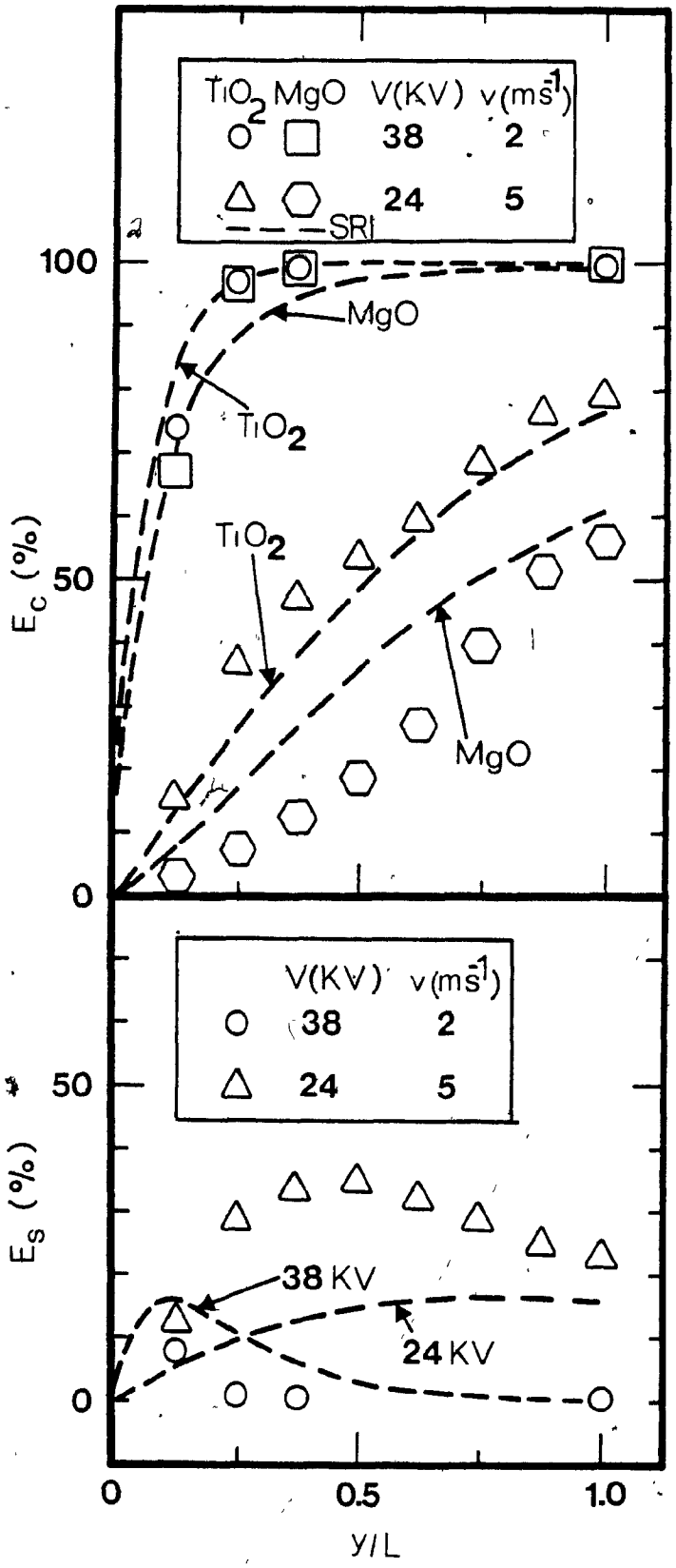


Figure 7.15 Cumulative collection and separation of mixtures of TiO_2/MgO as function of ESP length

Figure 7.16 shows the measured concentrations of MgO and TiO_2 along the ESP length for the high-voltage run. The analysis was performed at various intermediate points along each length increment to obtain a more complete profile of the concentration distribution. The results are normalized to the respective concentrations at the ESP inlet. Also shown are the theoretical (SRI) predictions.

It can be seen that the precipitated dust is very rich in TiO_2 near the ESP inlet. There is qualitative agreement between the SRI predictions and the experimental results, but quantitatively the agreement is only good up to the second length increment. In this particular case, the discrepancies observed after the second length increment are of little consequence since most of the precipitated dust ($\sim$ 97%) was collected in the first two length increments.

The precipitated dust layer was analysed for MgO content both near the plate surface and farther from it for the high voltage-low velocity run. The results are shown in Table 7.10, where it can be seen that no significant difference was observed. This is in agreement with the fact that neither of these compounds reentrained appreciably.

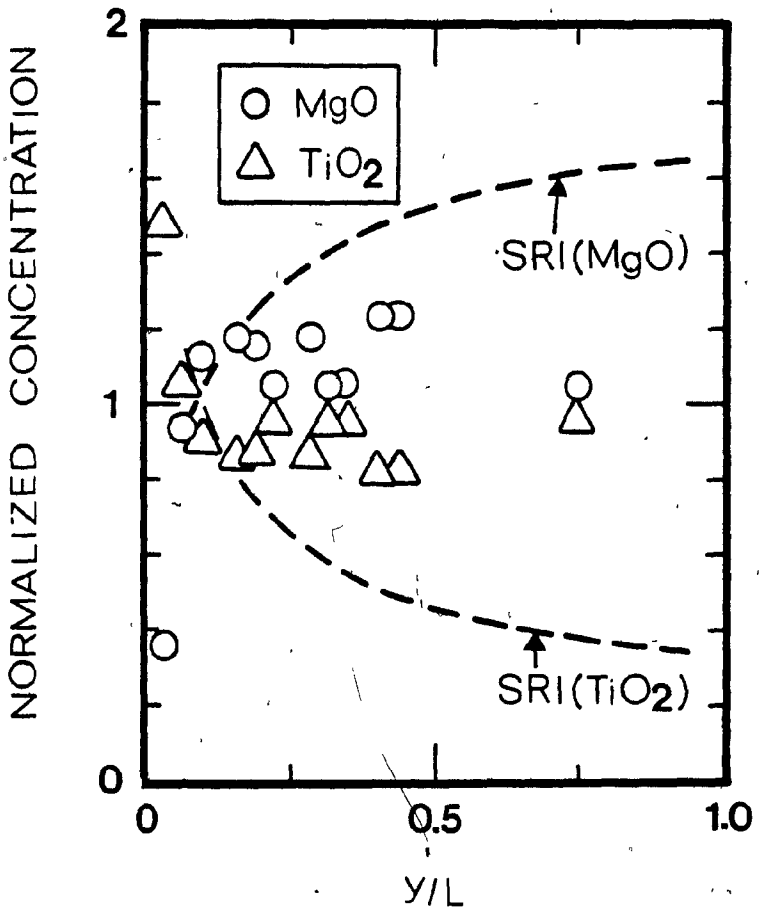


Figure 7.16 Variation of MgO and TiO_2 concentrations along the ESP length, for mixtures of MgO/ TiO_2, at 38 KV and 2 ms^{-1}

TABLE 7.10

Variation of MgO Concentration in Precipitated Layer

(TiO_2/MgO), %

Run No.	Sub-Layer Adjacent to Plate	Increment No.	Overall Increment
30	49.0	2 (47 cm from inlet)	48.8

7.5 Mixtures of $CuO/MgO/TiO_2$

A series of experimental runs was performed with mixtures of the three coarser oxides to determine if the behaviour was different from that of the binary mixtures.

Table 7.11 lists the experimental conditions and global results of the experiments carried out with mixtures of $CuO/MgO/TiO_2$. Table 7.12 lists the corresponding non-cumulative efficiencies. The temperature varied from 294 to 301 K, the experimental runs were 24 min long (except for run no. 34 which was only 8 min) and the relative humidity varied from 32 to 41%. Runs no. 33-36 were performed to investigate the effect of inlet dust loading and time on the performance of the ESP. The high values of $C_i \sim 1$ gm^{-3} correspond to typical industrial dust loadings, although much larger values ($C_i \sim 10$ gm^{-3} or more) are also common. Outlet sampling for run 34 was limited to the center of the flow channel since the run was only 8 min long. Runs no. 35 and 36 are considered replicates despite small variations in the current density and relative humidity.

TABLE 7.11

Experimental Precipitation Conditions and Global Results for Mixtures of $CuO/MgO/TiO_2$

Run No.	v (ms^{-1})	V (KV)	j$\times10^4$ (Am^{-2})	C_i ($mg\ m^{-3}$)	Material	C_{ri} (%)	MMD (μm)	σ_g	r (Ohm m)	η' (%)	η'_m (%)	η (%)
32	5.0	23.5	1.13	156	CuO	38.4	13.6	1.59	1×10^6	38.9	2.48	39.9
					MgO	27.5	14.6	1.79	1×10^8	36.0	2.48	36.9
					TiO_2	34.1	15.0	1.74	$\sim10^9$	66.9	2.00	68.3
33	5.0	29.0	3.50	954	CuO	36.7	13.6	1.59	2×10^6	80.9	2.81	83.3
					MgO	16.4	14.6	1.79	3×10^8	81.6	1.68	83.0
					TiO_2	46.9	15.0	1.74	$\sim10^9$	93.5	1.63	95.0
34	5.0	29.5	3.80	1300	CuO	41.3	13.6	1.59	3×10^6	79.1	3.04	81.5
					MgO	15.5	14.6	1.79	1×10^8	80.7	1.87	82.2
					TiO_2	43.2	15.0	1.74	$\sim10^9$	92.1	1.79	93.7
35	5.0	30.0	3.70	67	CuO	37.3	13.6	1.59	4×10^5	70.7	6.07	75.3
					MgO	18.1	14.6	1.79	7×10^7	77.9	3.14	80.4
					TiO_2	44.6	15.0	1.74	$\sim10^9$	86.4	3.53	89.6
36	5.0	30.0	3.63	62	CuO	38.1	13.6	1.59	8×10^5	68.8	5.89	73.1
					MgO	18.3	14.6	1.79	2×10^8	78.6	3.16	81.2
					TiO_2	43.6	15.0	1.74	$\sim10^9$	86.9	3.66	90.2

TABLE 7.12

Non-Cumulative Collection Efficiencies ($CuO/MgO/TiO_2$)

Run No.	Material	Increment No. 1	2	3	4	5	6	7	8
32	CuO	3.64	7.17	3.35	3.38	6.84	3.53	5.97	5.97
	MgO	2.03	5.49	2.24	2.34	7.72	3.46	7.06	6.61
	TiO_2	17.2	20.4	6.07	4.28	7.58	3.10	5.42	4.20
33	CuO	12.2	16.0	← 31.9 →		← 14.5 →		← 8.67 →	
	MgO	8.96	17.8	33.1		15.7		7.51	
	TiO_2	30.8	26.4	24.2		9.97		3.60	
34	CuO	13.2	14.4	← 29.9 →		← 16.0 →		← 8.08 →	
	MgO	8.57	18.1	30.2		17.5		7.94	
	TiO_2	30.0	28.1	24.1		8.10		3.53	
35	CuO	9.43	16.2	← 25.4 →		← 15.4 →		← 8.44 →	
	MgO	7.91	16.7	32.2		16.6		7.01	
	TiO_2	34.2	27.8	18.7		5.78		3.15	
36	CuO	8.25	14.9	← 26.0 →		← 15.8 →		← 8.15 →	
	MgO	6.33	16.3	32.6		18.6		7.29	
	TiO_2	33.9	27.0	19.0		7.27		3.07	

Figure 7.17 shows the cumulative collection and separation efficiencies for a mixture of CuO/MgO/TiO_2 at low voltage and high velocity. Also shown are the theoretical (SRI) predictions. The results are in good qualitative and quantitative agreement with those obtained under similar conditions for the pairs CuO/MgO (Fig. 7.11), and TiO_2/MgO (Fig. 7.15). Good quantitative agreement is not obtained for the pair TiO_2/CuO (Fig. 7.13), again due to the reduced re-entrainment of CuO in the presence of MgO, for the case of the three component run.

The precipitated dust layer was analysed for both CuO and MgO both near the plate surface and farther from it. Table 7.13 shows the experimental results obtained for run no. 32.

TABLE 7.13

Variation of CuO and MgO Concentration in Precipitated Layer (TiO_2/CuO/MgO), %

Run No.	Material	Sub-Layer Adjacent to Plate	Increment No.	Overall Increment
32	CuO	2.3	1 (16 cm from inlet)	17.8
	MgO	5.1	1	7.1

From the results of Table 7.13, it is seen that the sub-layer adjacent to the collection plate is depleted in CuO, in agreement with the results of the binary mixtures. Although the value obtained for the MgO concentration near the plate is

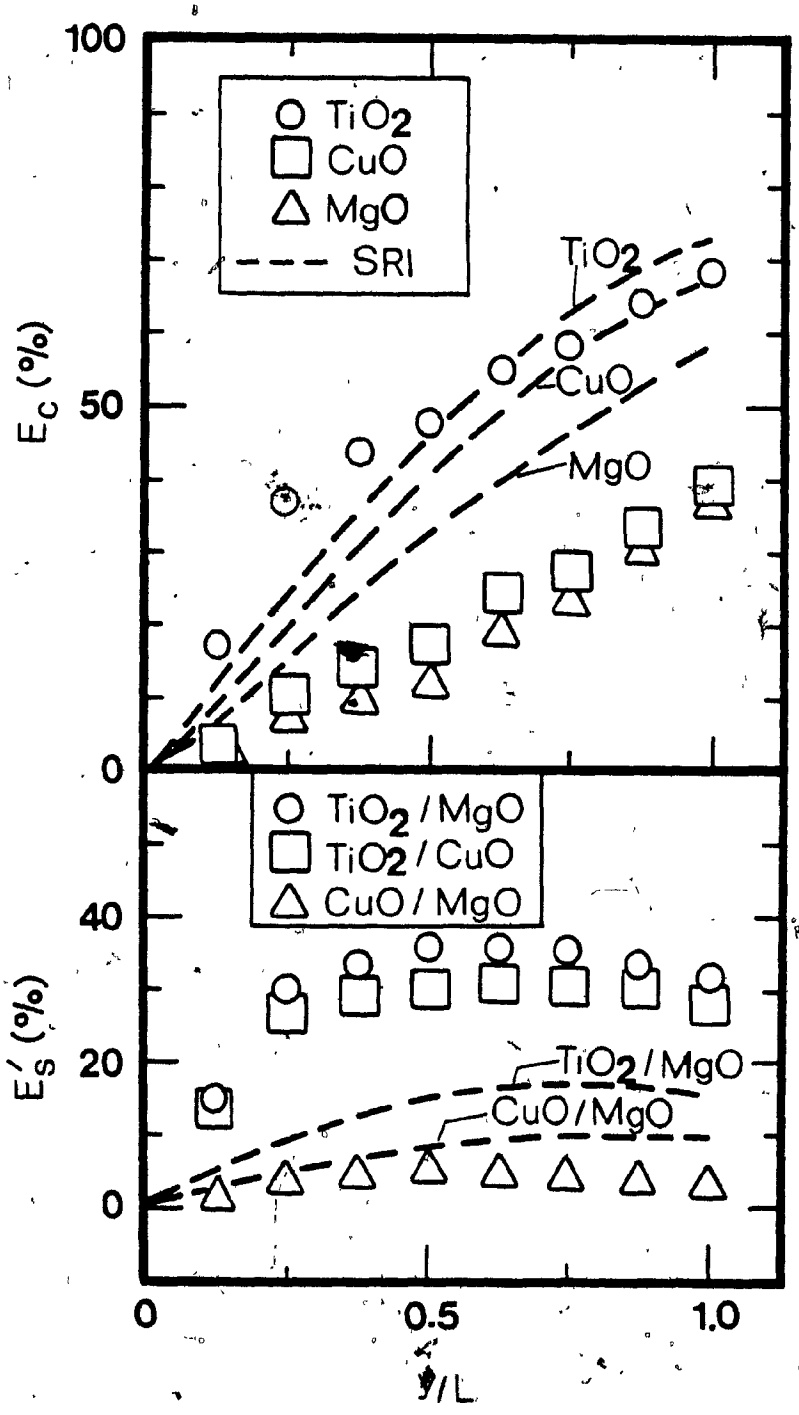


Figure 7.17 Cumulative collection and separation of a mixture of $CuO/TiO_2/MgO$ as function of ESP length, at 23.5 KV and 5 ms^{-1}

also smaller than for the overall increment, the difference is small and could be caused by local concentration variations.

Figures 7.18 and 7.19 show the cumulative collection and separation efficiencies for mixtures of $CuO/MgO/TiO_2$ at medium field and high velocity.

From Figures 7.18 and 7.19, it can be seen that there is no appreciable difference in behaviour either with respect to inlet dust loading or experimental time, although CuO is slightly better collected at the higher dust loadings.

Both TiO_2 and MgO precipitate in reasonable agreement with theoretical predictions. However, near the ESP inlet, the collection of MgO is overpredicted. This was also observed at low applied voltages, where the discrepancy was attributed to possible corona irregularities near corona-onset. Since it is unlikely that these irregularities are present at an applied voltage of 30 KV, there is probably another cause for the observed behaviour at the higher voltages. It is possible that some reentrainment of the coarser particles occurs, in agreement with the fractional efficiency curves discussed in Chapter 6, Section 6.3.3. This would mainly reduce the dust weight near the ESP inlet, i.e., where the coarser particles would (theoretically) precipitate.

Figures 7.18 and 7.19 also show that the best qualitative and quantitative agreement in both collection and separation efficiencies is obtained with the pair TiO_2/MgO. The separation efficiency data may be sensitive to small deviations of the experimental collection efficiencies from the theoretical predictions.

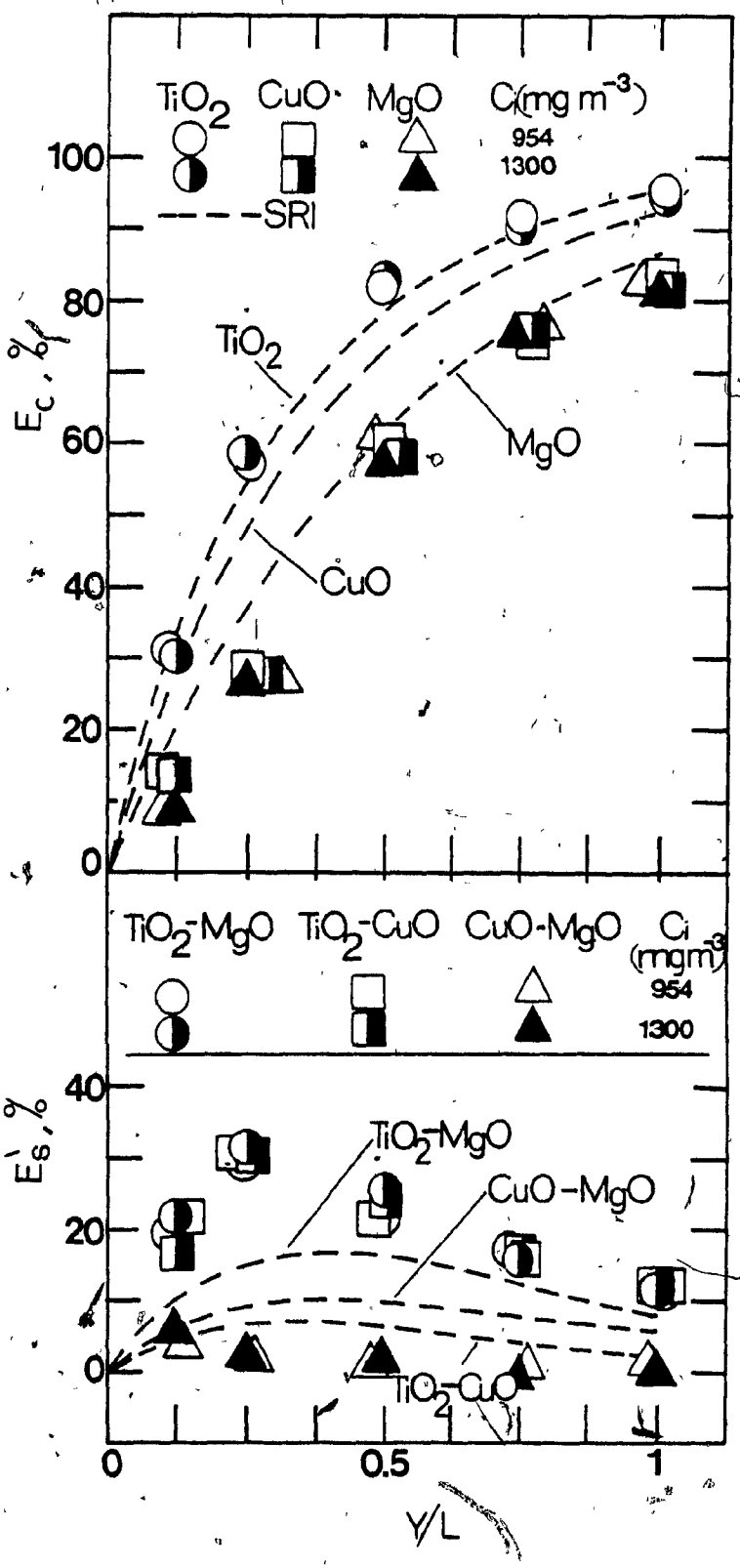


Figure 7.18 Cumulative collection and separation of mixtures of $CuO/TiO_2/MgO$ as function of ESP length, at 29-29.5 KV, 5 ms^{-1} and high dust loadings

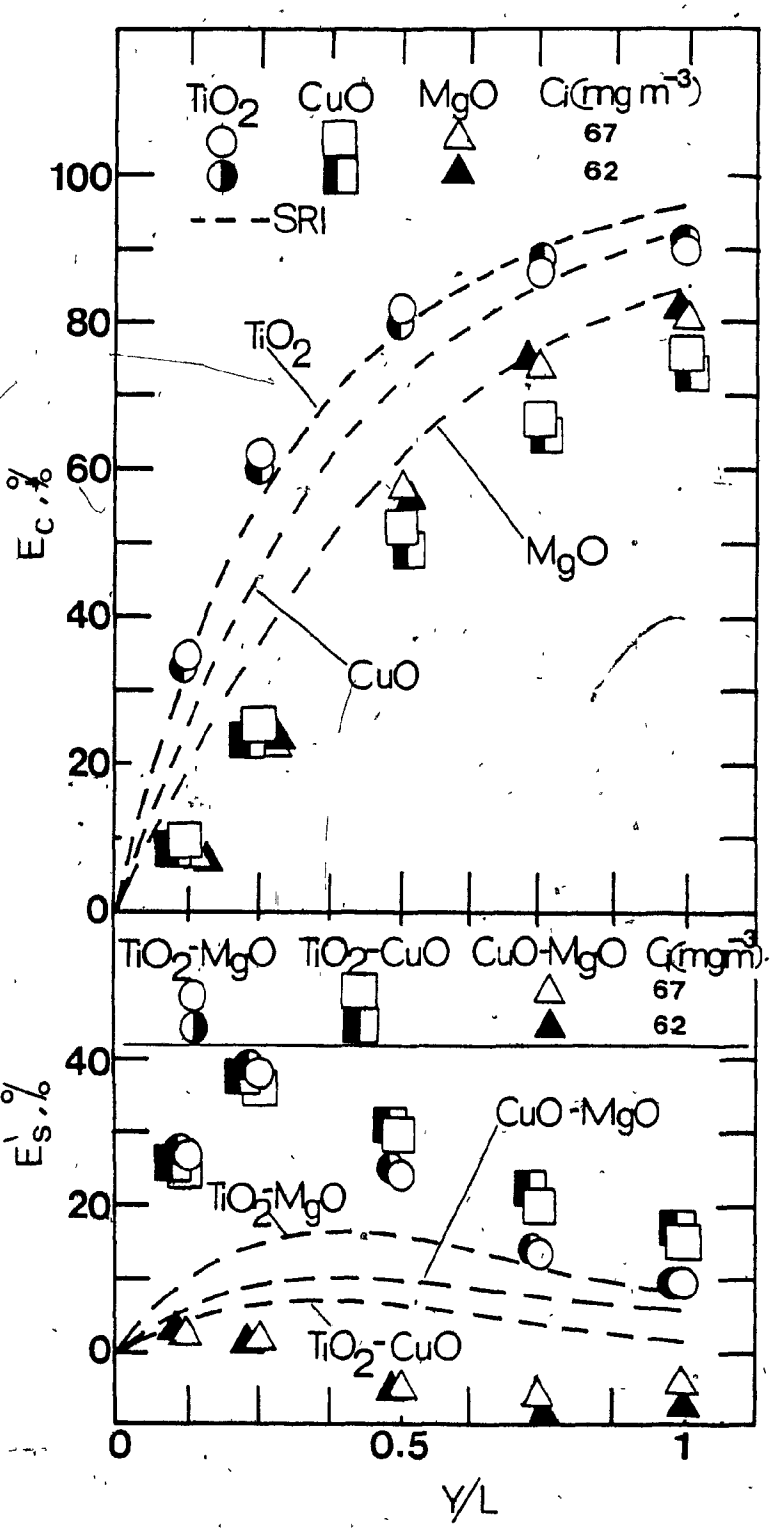


Figure 7.19 Cumulative collection and separation of mixtures of $CuO/TiO_2/MgO$ as function of ESP length, at 30 KV, 5 ms^{-1} and low dust loadings

If the deviations observed for both components are in the same direction, then a compensating effect occurs; the agreement between the observed and theoretical separation efficiencies may be good even though there might be a poor agreement between the observed and theoretical collection efficiencies. On the other hand, if the deviations observed for both components are in opposite directions, then there is a cumulative effect; the agreement between the observed and theoretical separation efficiencies may be poor even though there is a reasonable agreement between the observed and theoretical collection efficiencies. This last case occurs for the pair TiO_2/MgO.

Figure 7.20 shows the measured concentrations of the three components along the ESP length at medium applied voltage; there is no appreciable difference between the results of the various experimental runs. The results were normalized to the respective inlet percent concentrations and are shown as the average values ± one standard deviation. The results clearly show that the precipitated dust is highly enriched in TiO_2 near the ESP inlet and that it becomes enriched in the other components further downstream.

7.6 Mixtures of the Coarser Oxides with Alumina

The main purpose of the experiments carried out with mixtures of alumina and the coarser oxides was to investigate the effect of size distribution on the segregation in the ESP. Table 7.14 lists the experimental conditions and global results

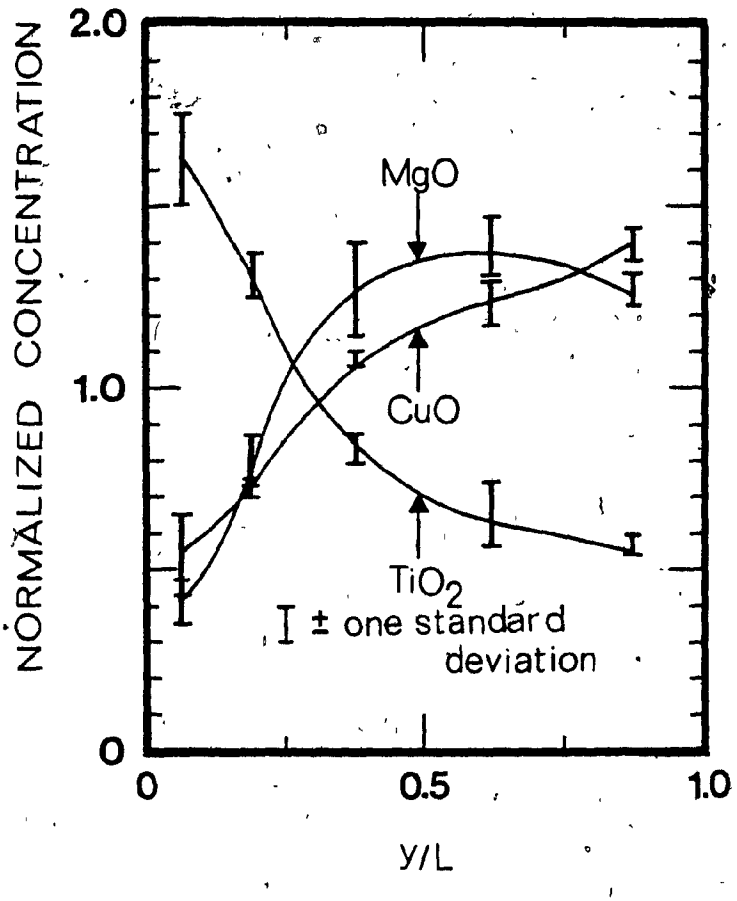


Figure 7.20 Variation of concentrations of CuO, MgO and TiO_2 along the ESP length, with mixtures of $CuO/MgO/TiO_2$ at 29-30 KV and 5 ms^{-1}

of the experiments carried out with alumina and the coarser oxides of copper, magnesium and titanium. Table 7.15 lists the corresponding non-cumulative collection efficiencies. The experimental runs were 144 min long, the temperature varied from 295 to 304 K and the relative humidity from 39 to 51%. Long experimental runs were necessary to increase the accuracy of the measurements due to the very small dust loadings at the ESP inlet.

All the experimental runs were performed at 5 ms^{-1}, due to the decreased sedimentation and to the better separations that were obtained with the coarser oxides at high velocities.

The size distribution of alumina differs greatly from the size distributions of the coarser oxides. The values of MMD and σ_g for alumina listed in Table 7.14 are only shown for comparison with the corresponding values of the coarser oxides. The size distribution of alumina used as input data to the SRI computer model is shown in Fig. 5.14 (Chapter 5) (a least-squares fitting using a log-normal approximation indicates that the size distribution of alumina derived from the Andersen impactor data is approximately log-normal).

7.6.1 Mixtures of CuO/Al_2O_3

To achieve a high separation between CuO and Al_2O_3, it is necessary that CuO does not reentrain to any appreciable extent. In an attempt to reduce the reentrainment of cupric oxide, small concentrations of CuO at the ESP inlet were used.

TABLE 7.14

Experimental Conditions and Global Results for Al_2O_3/Coarser Oxides

Run No.	v (ms^{-1})	V (VK)	$jx10^4$ (Am^{-2})	C_i ($mg\ m^{-3}$)	Material	C_{r_i} (%)	MMD (μm)	σ_g	r (Ohm m)	η' (%)	η'_m (%)	η (%)
37	4.9	37.8	11.9	4.24	CuO	31.9	13.6	1.59	$9x10^4$	89.9	3.92	93.6
					Al_2O_3	68.1	1.8-2.8(1)	2.02(1)	$\sim 10^8$	80.5	1.31	81.5
38	5.0	29.8	3.28	2.93	CuO	17.2	13.6	1.59	$3x10^4$	66.2	4.41	69.2
					Al_2O_3	82.8	1.8-2.8	2.02	$\sim 10^8$	52.3	2.14	53.4
39	5.0	26.0	1.03	3.53	CuO	16.9	13.6	1.59	$1x10^5$	25.6	3.00	26.4
					Al_2O_3	83.1	1.8-2.8	2.02	$\sim 10^8$	22.9	2.01	23.3
40	5.0	38.0	11.5	6.40	MgO	64.2	14.6	1.79	$7x10^7$	87.3	1.90	89.0
					Al_2O_3	35.8	1.8-2.8	2.02	$\sim 10^8$	78.8	1.22	79.8
41	5.0	26.0	1.03	5.21	MgO	54.8	14.6	1.79	$7x10^7$	42.9	3.90	44.6
					Al_2O_3	45.2	1.8-2.8	2.02	$\sim 10^8$	24.8	2.36	25.4
42	5.0	38.0	13.0	20.0	TiO_2	86.8	15.0	1.74	10^8-10^9	97.0	2.95	99.9
					Al_2O_3	13.2	1.8-2.8	2.02	$\sim 10^8$	80.6	3.16	83.3
43	5.0	30.0	4.00	13.6	TiO_2	82.6	15.0	1.74	10^8-10^9	92.5	3.37	95.8
					Al_2O_3	17.4	1.8-2.8	2.02	$\sim 10^8$	54.9	4.08	57.2
44	5.0	25.0	1.08	8.51	TiO_2	68.2	15.0	1.74	10^8-10^9	66.9	5.30	70.6
					Al_2O_3	31.8	1.8-2.8	2.02	$\sim 10^8$	26.7	2.64	27.4

(1) Least-squares log-normal approximation, depending on which density is attributed to the alumina agglomerates; MMD = 1.8 μm for $\rho = 2\ g\ cm^{-3}$ and MMD = 2.8 μm for $\rho = 0.9\ g\ cm^{-3}$. The geometric standard deviation is the same for both cases.

TABLE 7.15

Non-Cumulative Collection Efficiencies

(Coarser Oxides/Al_2O_3), %

Run No.	Material	Increment No. 1	2	3	4	5 ↔ 6	7 ↔ 8
37	CuO	⟵ 44.9 ⟶		⟵ 36.2 ⟶		7.58	4.96
	Al_2O_3	⟵ 18.6 ⟶		⟵ 27.1 ⟶		25.3	10.5
38	CuO	⟵ 16.9 ⟶		⟵ 27.7 ⟶		15.4	9.23
	Al_2O_3	⟵ 11.6 ⟶		⟵ 15.9 ⟶		14.4	11.6
39	CuO	⟵ 3.10⟶		⟵ 9.30⟶		6.20	7.75
	Al_2O_3	⟵ 3.11⟶		⟵ 6.84⟶		6.53	6.84
40	MgO	⟵ 52.9 ⟶		⟵ 28.9 ⟶		4.70	2.49
	Al_2O_3	⟵ 18.5 ⟶		⟵ 25.1 ⟶		24.1	12.1
41	MgO	⟵ 4.67⟶		⟵ 14.6 ⟶		14.0	11.4
	Al_2O_3	⟵ 2.91⟶		⟵ 5.81⟶		6.54	10.2
42	TiO_2	43.5	36.6	17.4		1.32	1.09
	Al_2O_3	3.26	18.0	27.0		22.4	12.6
43	TiO_2	29.3	28.5	25.0		9.92	3.08
	Al_2O_3	3.27	10.5	16.0		15.7	11.8
44	TiO_2	15.6	18.6	13.4		12.1	10.9
	Al_2O_3	0.68	3.72	8.46		7.78	6.77

To achieve uniform small feed rates of CuO, the dust discharge hole from the Tafa feeder was reduced in diameter from 6.35 to 1.27 mm, and the Tafa feeder was operated with an input voltage of ~ 50 V AC.

Figures 7.21-7.23 show the cumulative collection and separation efficiencies obtained with mixtures of CuO/Al_2O_3, at three different applied voltages. Also shown are the theoretical (SRI) predictions. It can be seen that higher collection efficiencies are theoretically predicted for CuO than were experimentally observed. The discrepancy increases with decreasing applied field, due to an increase in CuO reentrainment. The reentrainment of CuO is appreciable at medium field and severe at low field, probably because of the reduced collection efficiency of the high resistivity component (alumina). The collection efficiency of alumina is larger than theoretical predictions at all values of applied voltage, for the finer estimate of particle size distribution (ρ = 2 g cm^{-3}). For the coarser estimate of size distribution (ρ = 0.9 g cm^{-3}), the experimental collection efficiency is larger than theoretical predictions at both medium and high applied voltages. Good agreement is obtained at the lower voltage, but this is thought to be fortuitous (Chapter 6, Section 6.5.1).

The experimental values of separation efficiency are lower than theoretical predictions, the discrepancy increasing with decreasing voltage. Although some of the difference may be

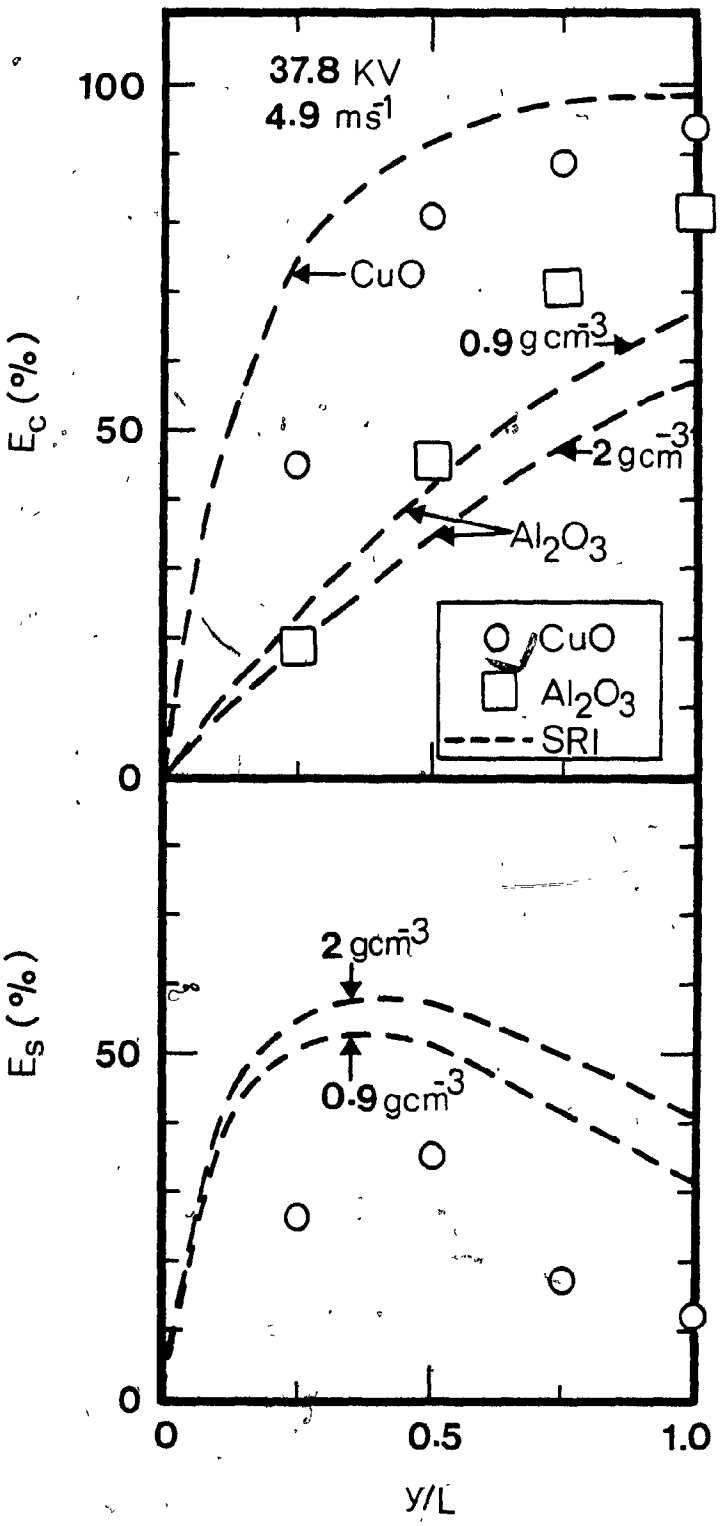


Figure 7.21 Cumulative collection and separation of a mixture of CuO/Al_2O_3 as function of ESP length, at high voltage and high velocity

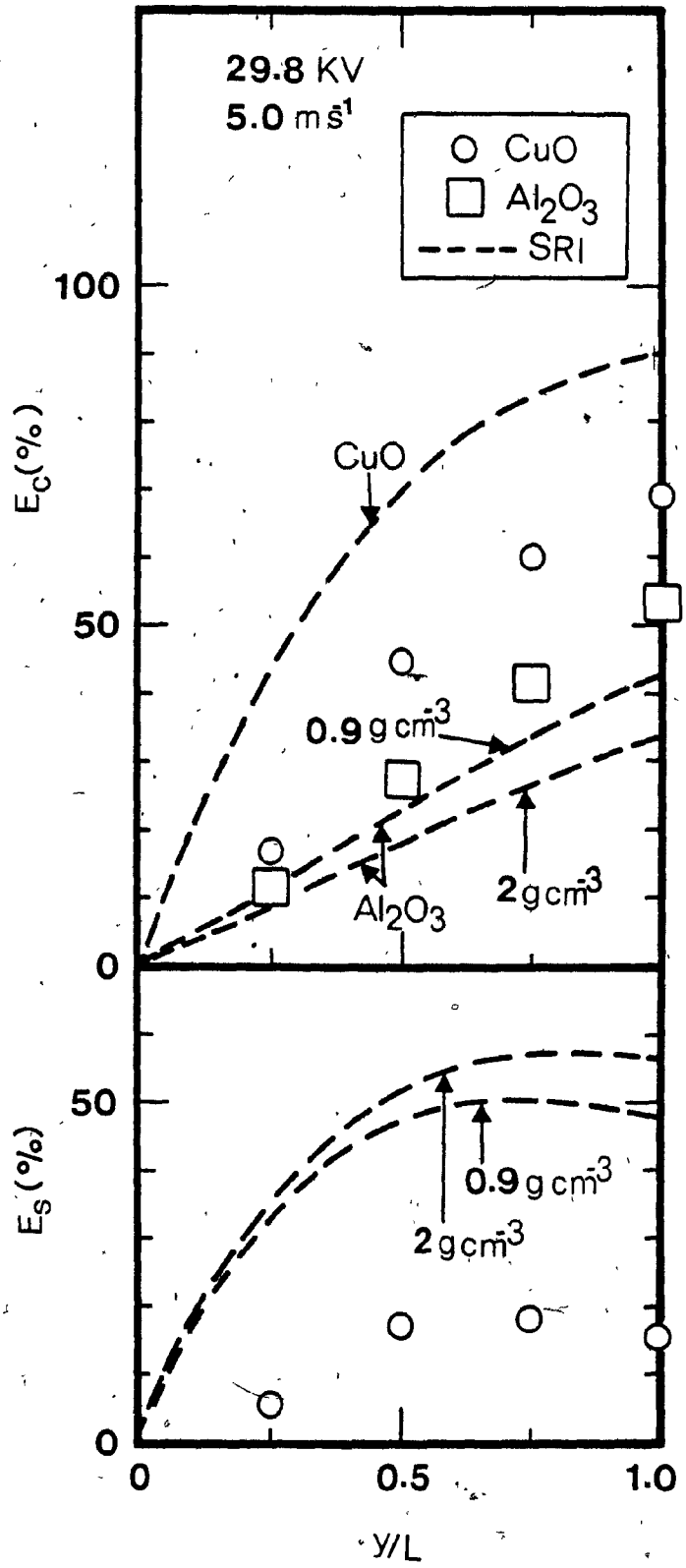


Figure 7.22 Cumulative collection and separation of a mixture of CuO/Al_2O_3 as function of ESP length, at medium voltage and high velocity

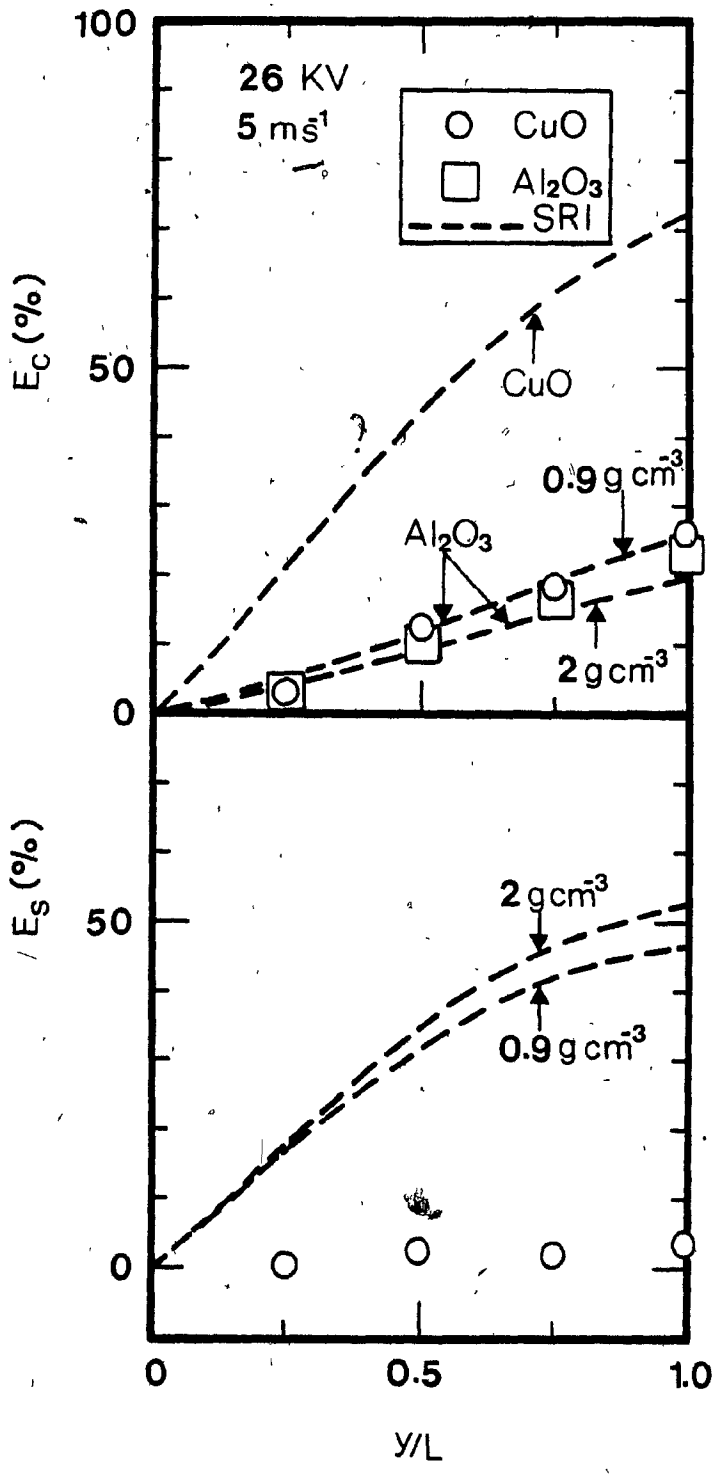


Figure 7.23 Cumulative collection and separation of a mixture of CuO/Al_2O_3 as function of ESP length, at low voltage and high velocity

attributed to the higher collection of alumina (as compared to SRI predictions), the major contribution to the observed differences is the lower collection of CuO. Despite the low relative concentrations of CuO at the ESP inlet, reentrainment was appreciable at both medium and low applied fields. Since the dust loading was very small, the plates were relatively "clean" even after 144 min of precipitation, especially at the lower voltages; thus the increased reentrainment of CuO under these conditions.

Figures 7.21-7.23 also show that high separations (up to ∿ 58%) were theoretically expected. The maximum experimental separation of 35% was obtained at high applied voltage, under conditions of moderate reentrainment. However, there is qualitative agreement between the experimental separations and theoretical predictions at both high and medium fields, i.e., unless reentrainment is very severe.

7.6.2 Mixtures of MgO/Al_2O_3

In this case, neither component reentrains to any appreciable extent. Figures 7.24 and 7.25 show the cumulative collection and separation efficiencies for mixtures of MgO/Al_2O_3, at both high and low applied fields. Reasonable qualitative and quantitative agreement is obtained between the SRI predictions and the experimental results, especially at the high applied voltage. A maximum separation of ∿ 40% was achieved in a very short ESP length, against theoretical predictions of 45 to 50%. The location of this maximum (with ESP length) also seems to be well predicted by the SRI model.

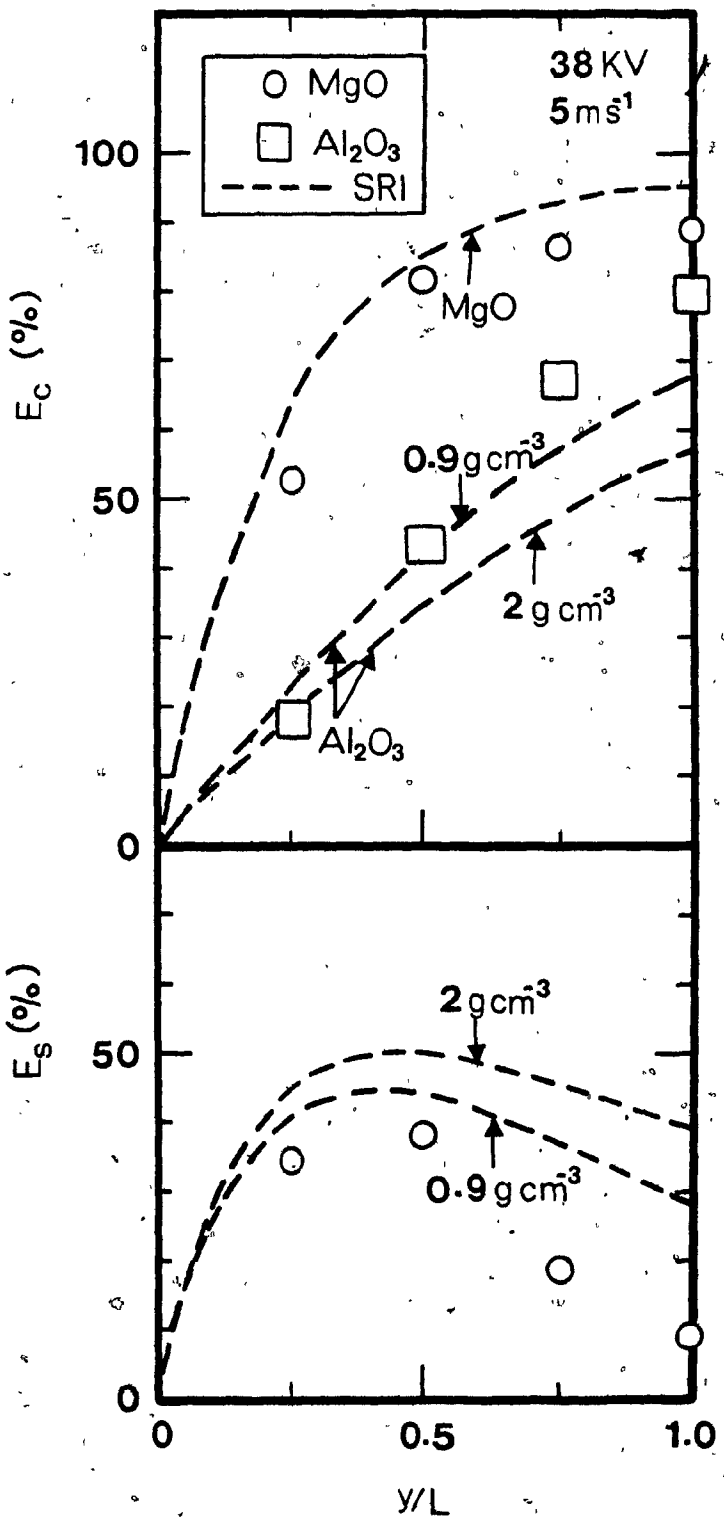


Figure 7.24 Cumulative collection and separation of a mixture of MgO/Al_2O_3 as function of ESP length, at high voltage and high velocity

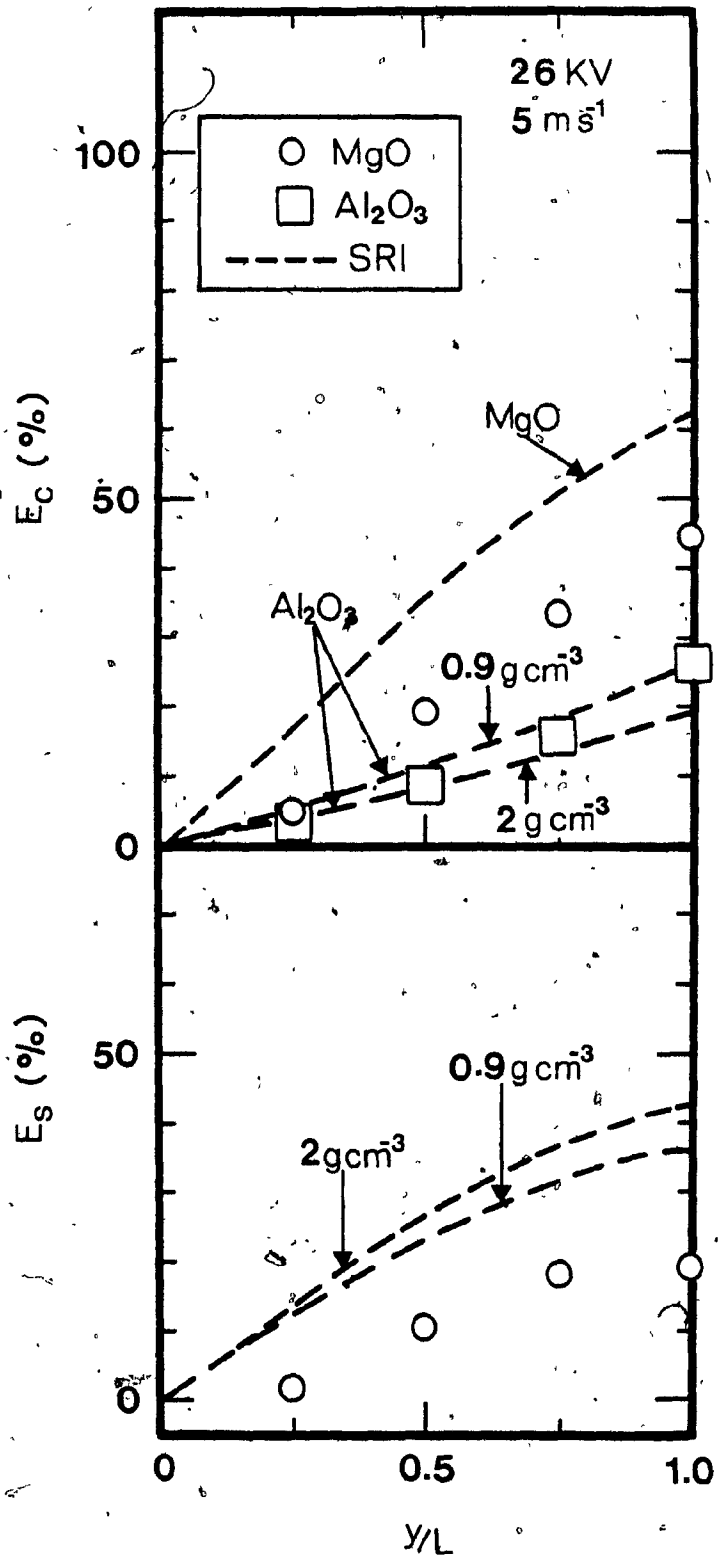


Figure 7.25 Cumulative collection and separation of a mixture of MgO/Al_2O_3 as function of ESP length, at low voltage and high velocity

At the low applied voltage, the collection efficiency of MgO is appreciably lower than theoretical predictions. As seen in Section 7.2.4, Figs. 7.9 and 7.10, it is possible that the lower collection of MgO is due to irregularities of the corona at low levels of corona power. A maximum separation of ∿ 20% was achieved, against theoretical predictions of 36 to 42%. The theoretical separations approach the experimental values if a low density of 0.9 g cm^{-3} is assigned to the alumina agglomerates.

7.6.3 Mixtures of TiO_2/Al_2O_3

In this case, neither component reentrains and the dielectric constant of TiO_2 is very large.

Figures 7.26-7.28 show the cumulative collection and separation efficiencies of mixtures of TiO_2/Al_2O_3, at high, medium and low applied fields. There is good qualitative and quantitative agreement between the experimental data and SRI predictions. As with MgO, the theoretical separations approach the experimental values for the coarser estimate of size distribution of alumina. High separation efficiencies (∿ 40-60%) are theoretically predicted and experimentally obtained.

The maximum in theoretical separation moves downstream in the ESP as either the applied field is reduced or the air velocity increased, i.e., for a poorer charging and precipitating environment. This can be seen, for example, in Figs. 7.5 and 7.7, or by comparing Figs. 7.26-7.28. However, the value of the maximum separation does not seem to vary much. This is in

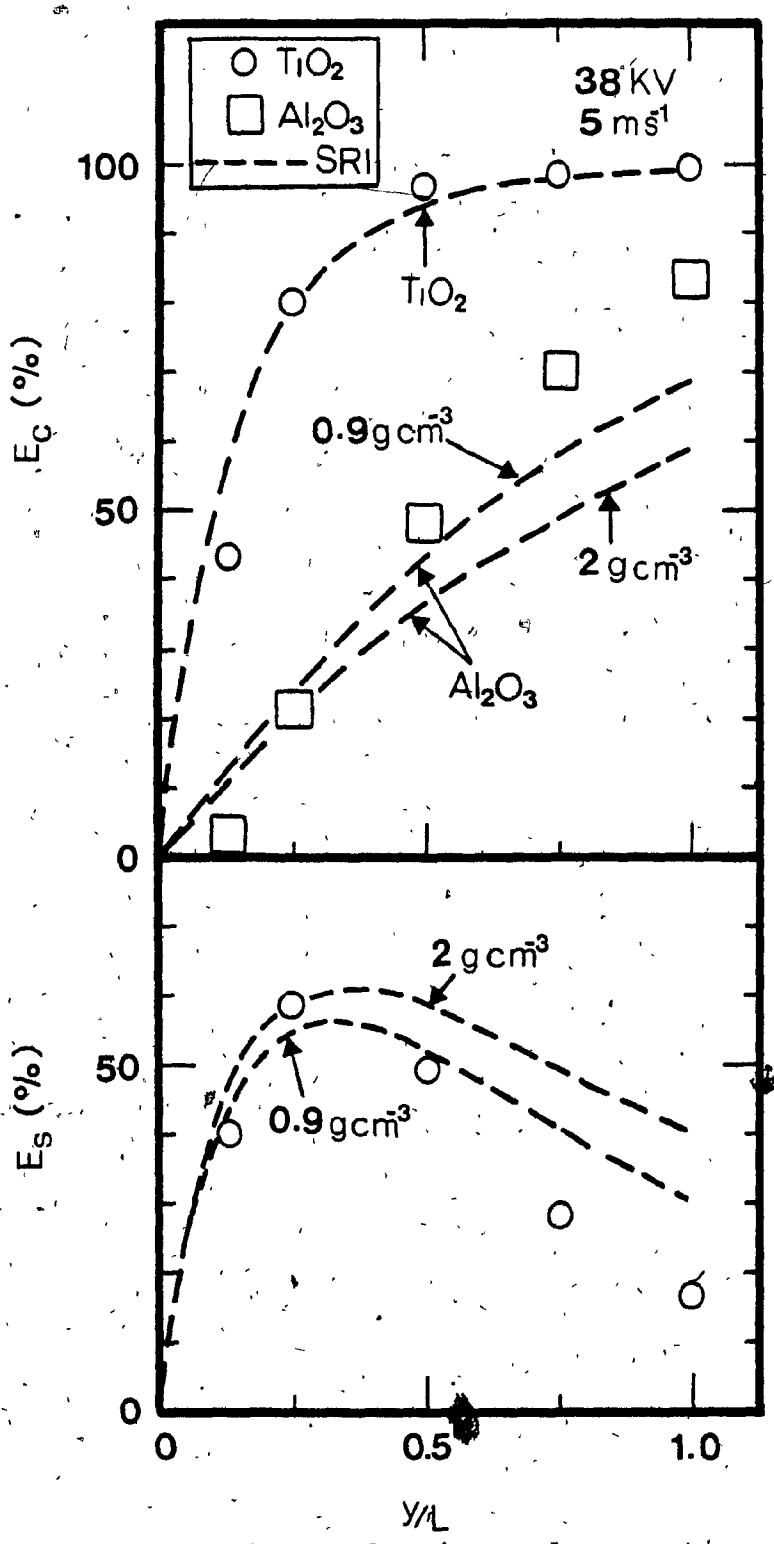


Figure 7.26 Cumulative collection and separation of a mixture of TiO_2/Al_2O_3 as function of ESP length, at high voltage and high velocity

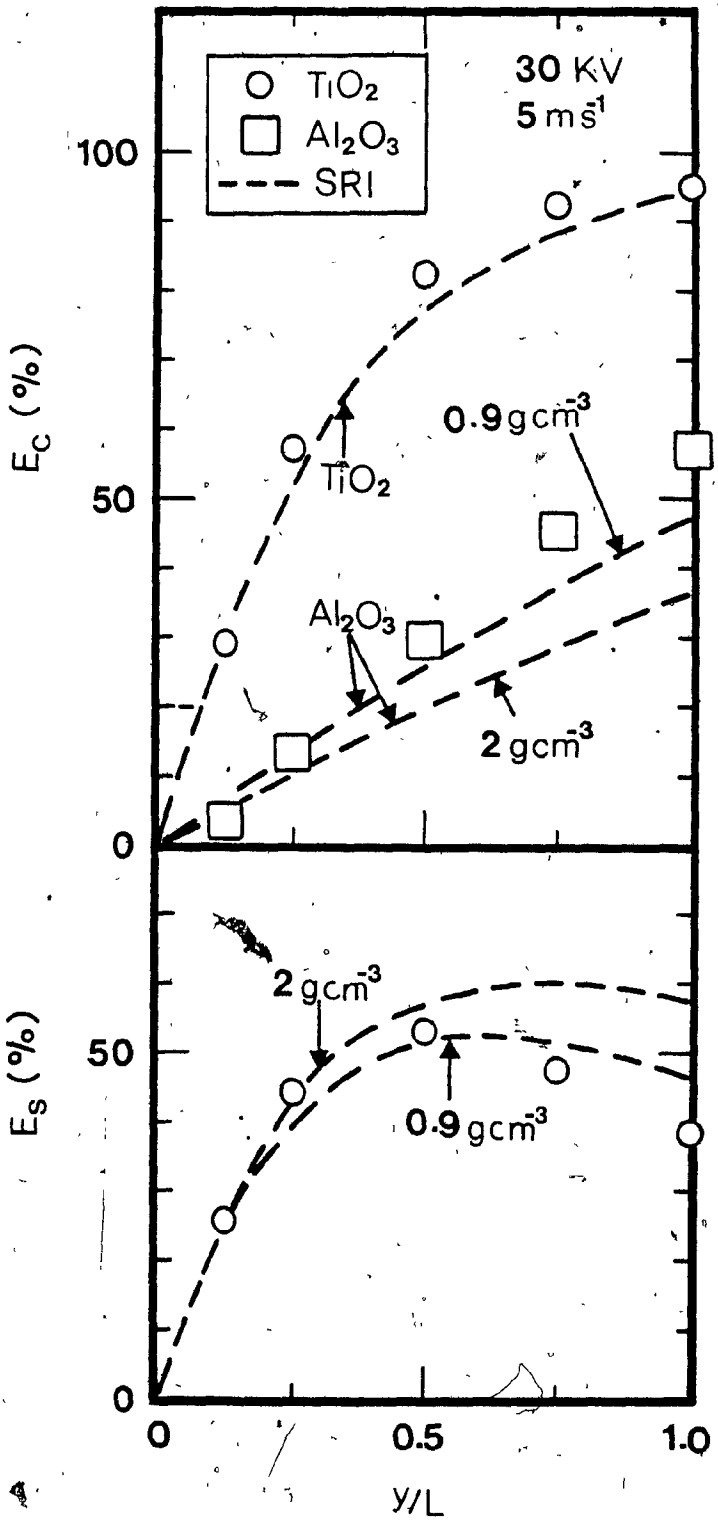


Figure 7.27 Cumulative collection and separation of a mixture of TiO_2/Al_2O_3 as function of ESP length, at medium voltage and high velocity

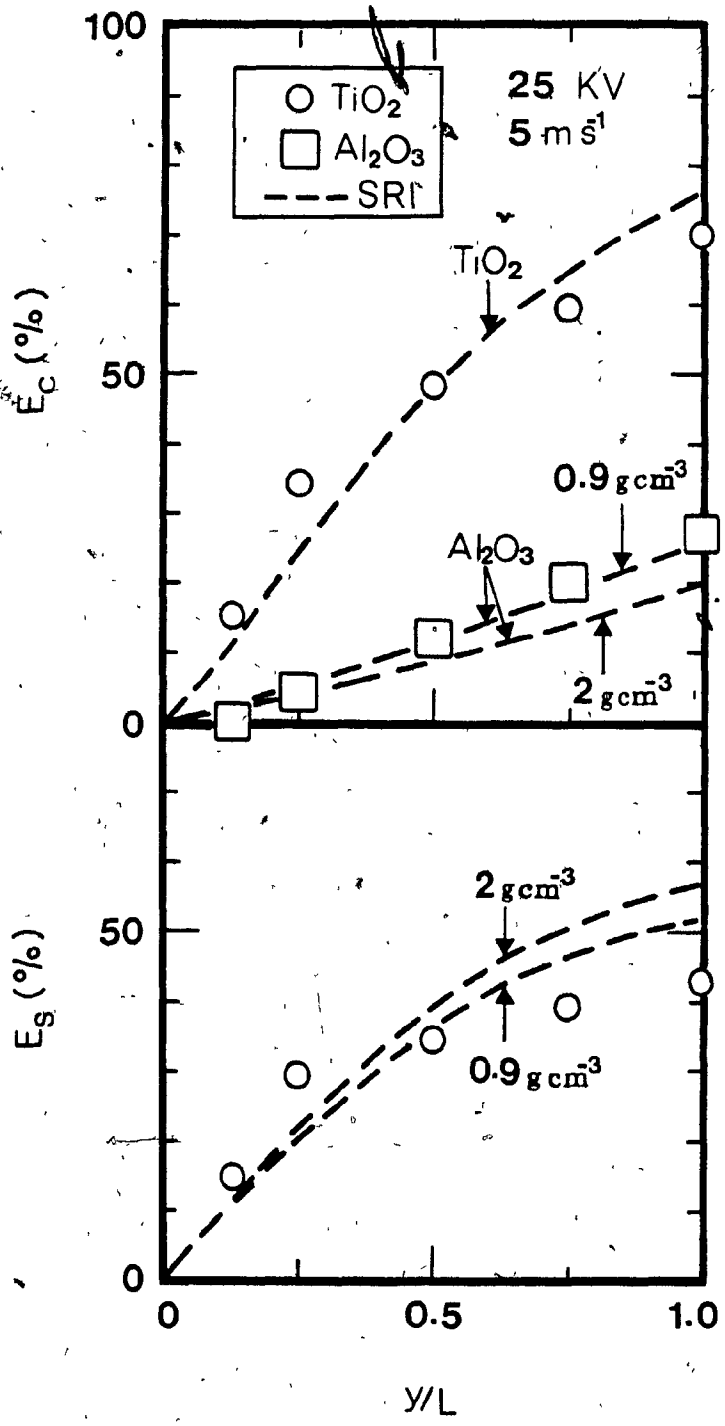


Figure 7.28 Cumulative collection and separation of a mixture of TiO_2/Al_2O_3 as function of ESP length, at low voltage and high velocity

agreement with the SRI predictions. There is not a very good agreement between the global separation and theoretical predictions. This is due to the higher collection of the fine alumina.

7.7 Conclusions

The following conclusions can be made on the segregation of mixtures of pure chemical species:

1) Size distribution is the dust variable which mostly affects the segregation process. High degrees of segregation may be expected with large differences in size distribution. This was observed with the pairs TiO_2/Al_2O_3, MgO/Al_2O_3 and to a certain extent with CuO/Al_2O_3, in the absence of severe CuO reentrainment.

2) Reentrainment may either increase or decrease the separation efficiency over that theoretically predicted, depending on which species reentrains. Since reentrainment is most likely to occur with coarser particles, it can be said that, in general, reentrainment will be deleterious to a segregation based on size differences. This was experimentally verified with the pair CuO/Al_2O_3. However, reentrainment of fine particles may also be important (Chapter 6, Section 6.2.3), and an experimental study on an individual basis is required.

3) In the absence of appreciable difference in size distributions, segregation of pure compounds in an ESP may still occur due to selective reentrainment and/or differences in dielectric constant. Reentrainment increases separation over theoretical predictions if the reentraining species is more difficult to charge, i.e., if it has a lower dielectric constant. This was observed with the pair TiO_2/CuO.

On the other hand, reentrainment is unfavorable for the segregation process if the reentraining species is more easily charged. This was observed with the pair CuO/MgO. However, high separations were achieved for severe CuO reentrainment.

4) Large differences in dielectric constant can produce segregation, in the absence of particle reentrainment and differences in particle size distribution. This was observed with the pair TiO_2/MgO. However, the possibility of some reentrainment of the coarser MgO particles cannot be ruled out at high velocities (5 ms^{-1}).

5) In general, global separation is enhanced at low electric fields and high air velocities (poor charging and precipitating environment). Because industrial ESP's usually operate at low air velocities and high electric fields, it is quite possible that the higher degrees of global segregation

reported here have not been observed in industrial practice.

6) The maximum in segregation moves downstream as the charging environment weakens. A maximum in segregation may occur near the ESP inlet. This was observed at high fields, and the effect becomes more marked the lower the air velocity. This segregation may well occur in industrial practice, but it is only appreciable if there is a large difference in size distributions.

7) There is good qualitative agreement between the SRI predictions and the experimental separation efficiencies, in the absence of severe reentrainment.

8) There is a fair to good quantitative agreement between the SRI predictions and the experimental separation efficiencies, in the absence of reentrainment. This limited agreement is possibly due to the presence of non-ideal effects, such as abnormal charging of fine particles near corona wires, the effect of corona irregularities at low corona powers and the effect of particle shape and agglomeration. These phenomena need further investigation.

9) The separation of pure solid species in an ESP can be predicted from the experimental behaviour of the single components, unless any of the species reentrains. In this case, an experimental study on an individual basis is required.

REFERENCES

Gooch, J.P. and McDonald, J.R. (1976a): "Conference on Particle Collection Problems in Converting to Low Sulfur Coals", SRI/EPA Contract 68-02-2114, EPA-600/7-76-016, pp.68-106.

_____: "Symposium on Particulate Control in Energy Processes", SRI/EPA Contract 68-02-1318, EPA-600/7-76-010, pp.217-265.

Smith, P.L. and Penney, G.W. (1961): "The Charging of Non-spherical Particles in a Corona Discharge", AIEE Trans., Comm. & Electronics, 80, part 1, July, pp.340-346.

CHAPTER 8

PART I

PRECIPITATION OF THE INDUSTRIAL COPPER REACTOR (NORANDA) DUST EXPERIMENTAL RESULTS, THEORETICAL PREDICTIONS AND DISCUSSION

8.1 Introduction

Three experimental runs were performed with the industrial (Noranda) dust to acquire some information on the precipitation and segregation of the elements Cu, Pb, Zn and Cd. These comprise about 55-57% by weight of the Noranda dust (Tables 5.6 and 5.7, Chapter 5).

The main purpose of the experiments was to test the contribution of the segregation mechanisms that were observed with mixtures of pure compounds (Chapter 7). However, it was not intended to fully investigate the precipitation characteristics of the Noranda dust; this would require a large number of experiments and was outside the scope of this research.

The size distributions measured with the Andersen cascade impactor (Chapter 5, Section 5.4.3) can be considered in two ways: as different size distributions for each experimental run; or as different measurements (replicates) of the same size distribution. The first approach assumes that the Wright dust feeder can produce different size distributions of the same dust, due to some uncontrolled variation in the operating variables. The second approach assumes that no such variation in size distribution can occur unless there is a measured change in the operating variables.

It is difficult to be certain which approach is correct, since some uncontrolled factors might be present (e.g., ambient humidity during the packing process). Data obtained with the fine alumina (Fig. 5.14, Chapter 5) seem to indicate that the second approach was applicable in that case since the size distributions were very reproducible. However, as it will be seen below, this was not the case with the Noranda dust.

The size distributions obtained with the cascade impactor were used as input data to the SRI computer model. Since it is not known whether they represent replicates of the same feed to the ESP or different distributions, it was decided to simulate the consequences of both assumptions.

The measured distributions for each experimental run are referred to as <u>individual</u> distributions; the <u>overall individual</u> distributions refer to the overall dust; while the <u>elemental individual</u> distributions refer to a particular element (Cu, Pb, Zn or Cd), or group of elements (Pb + Zn + Cd).

The <u>average</u> distributions refer to the mean distribution obtained by considering the three individual distributions as replicates. To obtain the <u>overall average</u> distribution, the overall individual distributions were weight averaged with respect to impactor sampling time. This is shown in Fig. 5.17, Chapter 5. To obtain the <u>elemental average</u> distributions, the elemental individual distributions were weight averaged also with respect to impactor sampling time. The results are shown in Fig. 5.20, Chapter 5.

8.2 Precipitation of the Overall Dust

Table 8.1 lists the experimental conditions and global results of the experiments carried out with the Noranda dust. Table 8.2 lists the corresponding non-cumulative collection efficiencies. The resistivity values were estimated from Fig. 5.25 of Chapter 5. The experimental runs varied from 72 min (run 45) to 144 min (runs 46 and 47), the temperature from 295 to 300 K and the relative humidity from 23 to 30%. A high velocity of 5 ms^{-1} was chosen due to the higher separations obtained with mixtures of pure compounds at high velocities (Chapter 7). The three runs were performed at high, medium and low applied voltage, since it was found that this variable greatly influenced the collection and segregation (as a function of ESP length) for mixtures of pure compounds.

Sampling with the cascade impactor at the ESP inlet was performed for the duration of the experimental runs; the raw data are given in Appendix C, Table C.10. Figure 8.1 shows the corresponding overall individual size distributions. It can be seen that very similar distributions were obtained for runs 46 and 47, and a somewhat finer distribution was obtained for run 45. Since this run was the shortest, it is possible that the difference is due to experimental inaccuracy due to the very small weights collected on the substrates. However, even smaller weights were collected with the impactor for the fine alumina dust (Table C.9, Appendix C) and the size distributions were reproducible. The difference in size distributions might then be due to some other cause, such as the effect of ambient

TABLE 8.1

Experimental Conditions and Global Results for the Noranda Dust

Run No.	v (ms^{-1})	V (KV)	$jx10^4$ (Am^{-2})	C_i ($mg\ m^{-3}$)	Material	C_{ri} (%)	d_{MMD}[1] (μm)	σ_g[1]	r (Ohm m)	η' (%)	η'_m (%)	η (%)
45	5.0	38.0	12.6	6.49	Overall Dust	100	1.22	3.36	10^9-10^{10}	69.3	1.14	70.1
					Cu	9.1	3.03	5.08	-	85.0	2.50	87.2
					Pb	21.6	1.08	3.10	-	65.1	1.06	65.8
					Zn	9.9	1.10	3.12	-	71.3	1.15	72.1
					Cd	9.1	1.00	3.02	-	61.3	1.25	62.0
46	5.0	30.0	4.0	7.84	Overall Dust	100	1.49	3.23	10^9-10^{10}	48.6	0.99	49.1
					Cu	7.1	4.06	2.86	-	75.3	2.67	77.4
					Pb	25.6	1.46	2.90	-	43.6	0.74	43.9
					Zn	9.4	1.57	2.90	-	43.4	1.01	43.8
					Cd	10.8	1.43	2.98	-	42.1	0.88	42.5
47	5.0	24.0	1.29	8.37	Overall Dust	100	1.56	3.08	10^9-10^{10}	37.7	0.89	38.0
					Cu	7.0	4.66	3.19	-	63.3	2.53	64.9
					Pb	28.7	1.43	2.85	-	30.6	0.93	30.8
					Zn	10.1	1.61	2.71	-	31.7	0.44	31.9
					Cd	11.8	1.46	2.95	-	30.6	0.75	30.8

[1]Based on least-squares log-normal approximation. For the global distribution, the weight of particles below 0.66 μm in diameter was ignored in the fitting procedure; all distributions are approximately log-normal, down to a particle diameter of 0.66 μm.

TABLE 8.2

Non-Cumulative Collection Efficiencies.

(Noranda Dust), %

Run No.	Material	Increment No.			
		1+2	3+4	5+6	7+8
45	Overall Dust	34.9	21.0	7.63	6.47
	Cu	51.3	25.6	6.41	3.85
	Pb	31.0	19.8	8.02	6.95
	Zn	40.7	18.6	6.98	5.81
	Cd	34.2	11.4	8.86	7.59
46	Overall Dust	18.8	15.5	7.84	6.84
	Cu	31.5	26.7	11.0	8.22
	Pb	16.2	13.8	7.45	6.52
	Zn	17.4	13.3	7.14	6.12
	Cd	15.9	12.8	7.08	6.64
47	Overall Dust	15.6	12.2	5.90	4.34
	Cu	25.3	23.4	9.74	6.49
	Pb	12.6	9.81	4.83	3.58
	Zn	13.3	10.2	4.87	3.54
	Cd	13.2	9.40	4.89	3.38

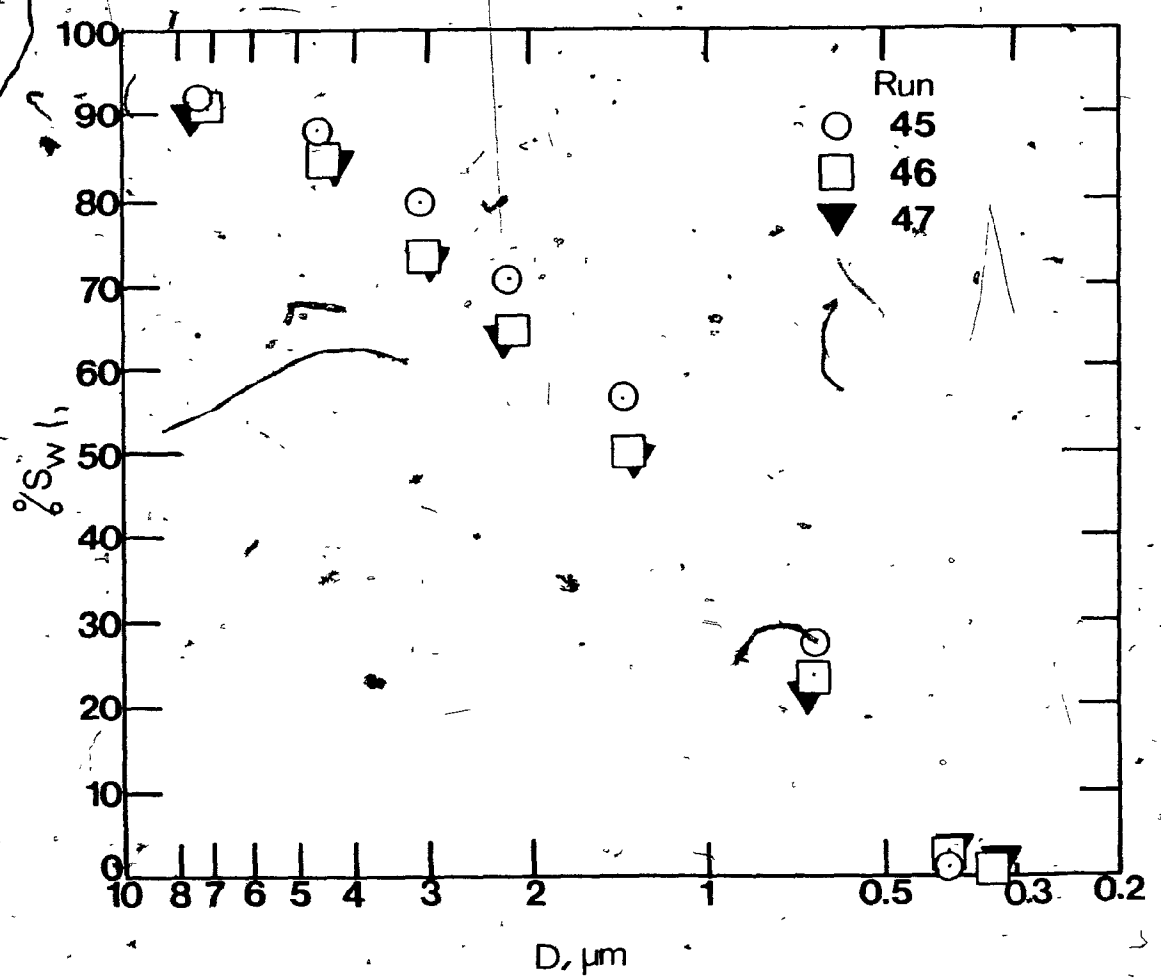


Figure 8.1 Overall individual size distributions of the Noranda dust at the ESP inlet (Andersen MKIII cascade impactor)

humidity on the packing of the Wright feeder.

Noranda dust was considered to consist of two separate components: copper rich particles and lead, zinc and cadmium rich particles (Chapter 5, Section 5.4.3). Figure 8.2 shows the elemental individual distributions. It can be seen that there is no appreciable difference between the size distributions of the Pb, Zn and Cd rich particles, for each particular run; the size distributions for run 45 are somewhat finer than for the other two runs, in agreement with the overall distributions (Fig. 8.1). However, there is a substantial difference between the size distributions of Cu in relation to those of Pb, Zn and Cd, irrespective of the experimental run.

SRI simulations of the collection of the overall dust were performed by simulating separately the collection of the Cu rich particles and of the Pb + Zn + Cd rich particles. The simulations were performed with both the elemental individual distributions (Table 8.5) and the corresponding average distributions (Table 8.5), considering the Pb, Zn and Cd rich particles as indistinguishable (Section 8.3.1).

The Cu rich particles were arbitrarily assigned the relative dielectric constant of $CuSO_4$ ($\sim$ 10), as an approximation to the chemical form of Cu in this dust (Sections 5.4.3 and 5.5, Chapter 5). The Pb + Zn + Cd rich particles were assigned the experimentally estimated relative dielectric constant of 2.9 (Section 5.5, Chapter 5).

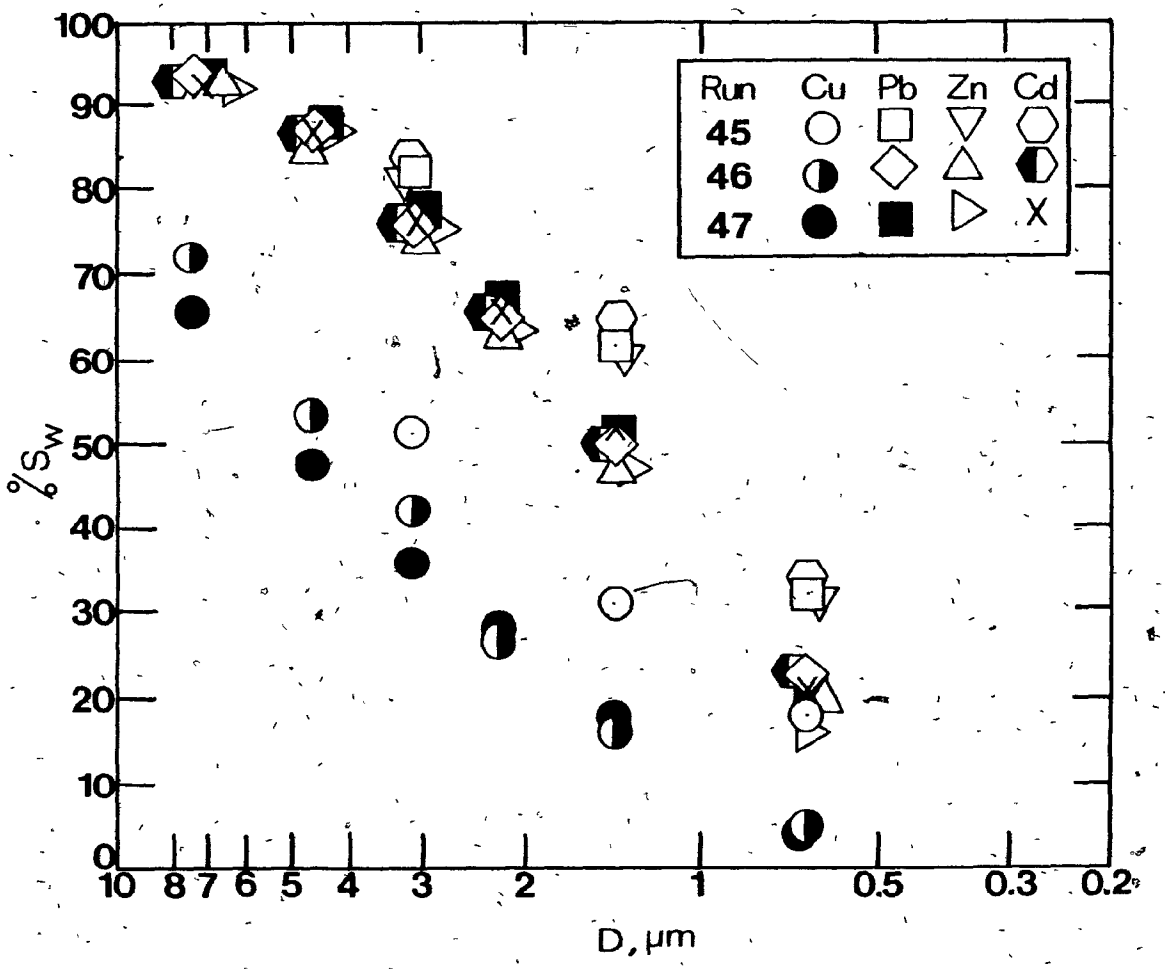


Figure 8.2 Elemental individual size distributions of the Noranda dust at the ESP inlet (Andersen MKIII cascade impactor)

Simulations using the elemental average distributions (Table 8.5) were also performed with both estimates of the Andersen cascade impactor, which depend on the density assigned to the dust particles; this was discussed in Section 5.4.3 of Chapter 5. Finally, the SRI results for the two components (Cu, Pb + Zn + Cd) were weight averaged according to the mean composition of the overall dust (Table 5.6, Chapter 5). The averaging process was carried out by assuming all the four elements to be present as sulphates, and correcting the concentrations to a total of 100%. The result was 16.5% $CuSO_4$ and 83.5% (Pb + Zn + Cd) SO_4. Table 8.3 gives the experimental global collection efficiencies as well as the SRI predictions, using the various size distributions referred to above.

TABLE 8.3

Global Collection Efficiencies

(Overall Noranda Dust), %

Run No.	Experimental	SRI		
		Individual Distributions[1]	Average Distributions[1]	
		(ρ=3.2 g cm^{-3})	(ρ=3.2 g cm^{-3})	(ρ=1.3 g cm^{-3})
45	70.0	53.4	55.2	63.5
46	49.0	38.4	37.6	44.4
47	38.0	23.7	23.8	28.0

[1] Table 8.5

It can be seen that the experimental values are larger than the theoretical predictions, and that there is no appreciable difference between the SRI results using the different distributions (for the same particle density). Also, better agreement is obtained by using the coarser estimates of size distributions, corresponding to the bulk density of the Noranda dust packed in the Wright feeder at 2450 KPa (1.3 g cm^{-3}). These results are in agreement with those obtained with the fine alumina (Chapters 6 and 7). It is possible that the higher collection is due to abnormal charging near the corona wires or to particle shape or agglomeration. However, no definite conclusions can be reached.

Considering the different elements as sulphates should introduce little error in the estimation of the SRI collection efficiencies of the overall dust; a total of 97.3-114.3% is obtained by using the average ± one standard deviation values of elemental feed composition given in Table 5.6, if the four elements are considered to be sulphates. Further evidence that sulphate is the major chemical form can be seen in Table 5.7, Chapter 5, for a similar dust.

8.3 Segregation of Copper from Lead, Zinc and Cadmium

8.3.1 Global Elemental Collection

Inspection of the global elemental collection efficiencies given in Table 8.1 reveals that Cu was preferentially collected with respect to Pb, Zn or Cd. Also, there seems to be no appreciable difference between the collections of Pb, Zn and Cd

for runs 46 and 47. The largest differences in the collection efficiencies of these three elements occurring at 38 KV could be due to experimental inaccuracy, since these differences were not observed at either medium or low voltages; or could be due to the effect of the applied voltage or to some uncontrolled factor. SRI simulations were performed to test the possible theoretical effect of the applied voltage. Both the elemental individual (Fig. 8.2) and elemental average distributions (Fig. 5.20, Chapter 5) were used in the simulations. The same value of dielectric constant (2.9) was attributed to the Pb, Zn and Cd rich particles. Table 8.4 gives the predictions for the three experimental runs.

TABLE 8.4

SRI Elemental Collection Efficiencies, %

Run No.	Element	Average Distributions[1] (ρ=3.2 g cm^{-3})	Individual Distributions[2] (ρ=3.2 g cm^{-3})
45	Pb	50.1	49.5
	Zn	51.5	49.9
	Cd	50.1	47.9
46	Pb	32.0	32.7
	Zn	33.5	34.0
	Cd	32.4	32.7
47	Pb	18.7	18.8
	Zn	19.9	20.0
	Cd	19.1	19.6

[1] Fig. 5.20, Chapter 5
[2] Fig. 8.2, Chapter 8

It can be seen that theory predicts little difference between the elemental collection efficiencies of Pb, Zn and Cd under similar conditions. This is true regardless of the various size distributions, and is consistent with the experimental data of runs 46 and 47.

The larger differences in elemental efficiencies for Pb, Zn and Cd observed at 38 KV were thus probably due to experimental inaccuracy caused by the lower amounts of the elements sampled for run 45, since it was the shortest and most efficient run. In view of the above considerations, it was concluded that the elements Pb, Zn and Cd do not segregate to any appreciable extent. In any case, little error is made by considering that these elements are indistinguishable. The weighed average experimental collection efficiencies of the three elements were determined by averaging the elemental efficiencies over the feed composition (Table 8.1). The maximum difference between the computed values and the respective elemental collection efficiencies is only 5.6% (absolute), occurring for Zn in run 45.

The appropriate size distribution for each experimental run which represents the three indistinguishable components is then the average of the corresponding elemental distributions, weighed with respect to elemental composition of the dust sampled with the cascade impactor. If it is assumed that the different elemental individual distributions are replicates, then further averaging with respect to sampling time produces an average size distribution of Pb + Zn + Cd representative of the three experi-

mental runs, a similar time averaging process was performed for the Cu rich particles, and the various size distributions are given in Table 8.5.

SRI simulations of the precipitation of the Cu rich particles and of the Pb + Zn + Cd rich particles were performed by using the various size distributions of Table 8.5. This is discussed next.

TABLE 8.5

Size Distributions of Cu and (Pb + Zn + Cd), % Undersize

	Copper			
D (μm)	Run:45	46	47	Average
60[1]	100	100	100	100
7.4	-	72.00	65.70	68.85
4.6	-	53.41	47.49	50.45
3.1	51.16	41.88	35.36	41.13
2.2	-	26.59	27.44	27.02
1.4	30.75	15.76	17.41	19.42
0.66	17.83	4.24	3.96	6.85
0.15	0	0	0	0
	Lead + Zinc + Cadmium			
60[1]	100	100	100	100
7.4	-	93.13	92.79	92.96
4.6	-	86.20	87.10	86.65
3.1	81.98	75.29	76.67	77.18
2.2	-	64.46	66.20	65.33
1.4	61.91	49.08	50.62	52.26
0.66	32.24	22.12	19.99	23.29
0.15	0	0	0	0

[1]From data of X-ray Sedigraph (Fig. 5.17, Chapter 5).

8.3.2 Elemental Collection and Separation as Function of ESP Length

Table 8.2 lists the non-cumulative elemental collection efficiencies as a function of incremental length. The corresponding cumulative values are shown in Figs. 8.3-8.5 at high, medium and low applied voltage.

It can be seen that the experimental elemental collection efficiencies are always larger than the predicted (SRI) values, in agreement with the overall dust collection. Also, the agreement is better for the coarser estimates of elemental particle size distributions, corresponding to a particle density of 1.3 g cm^{-3}.

On the other hand, the qualitative and quantitative agreement between the experimental and theoretical separation efficiencies is good. This is due to a compensating effect, since the deviations of experimental collection efficiencies from theoretical predictions are in the same direction for both components. Also, a better agreement is obtained using the individual distributions than the average distributions; this is especially true for run 45, where the individual distributions vary the most from the average distributions. There is little difference between the predicted separations based either on the coarser or on the finer estimates of particle size distributions, despite an appreciable variation in collection efficiencies. This is due to the same compensating effect described above. Finally, there is a shift in the location of the maximum separation towards the ESP outlet when the applied voltage is reduced. This is also predicted by the SRI model. Slightly

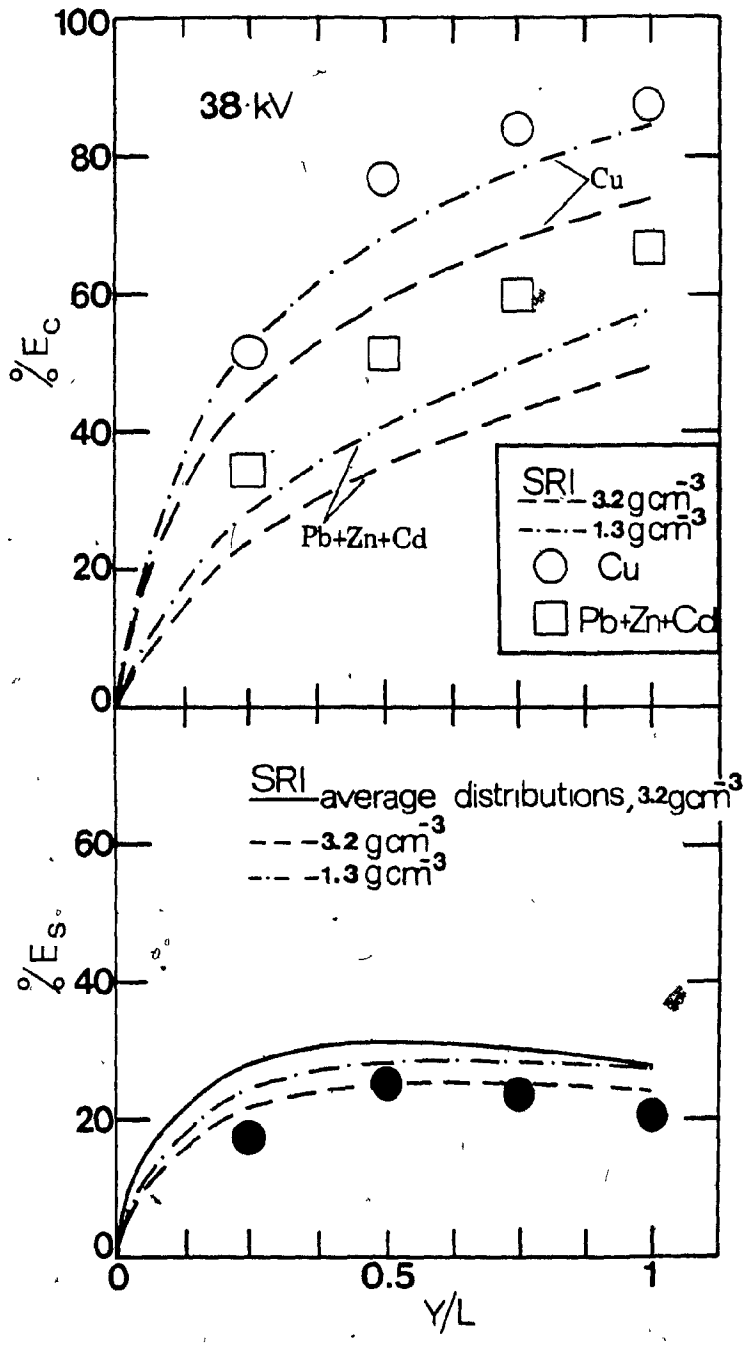


Figure 8.3 Cumulative elemental collection and separation of the Noranda dust as function of ESP length, at high voltage and 5 ms^{-1}

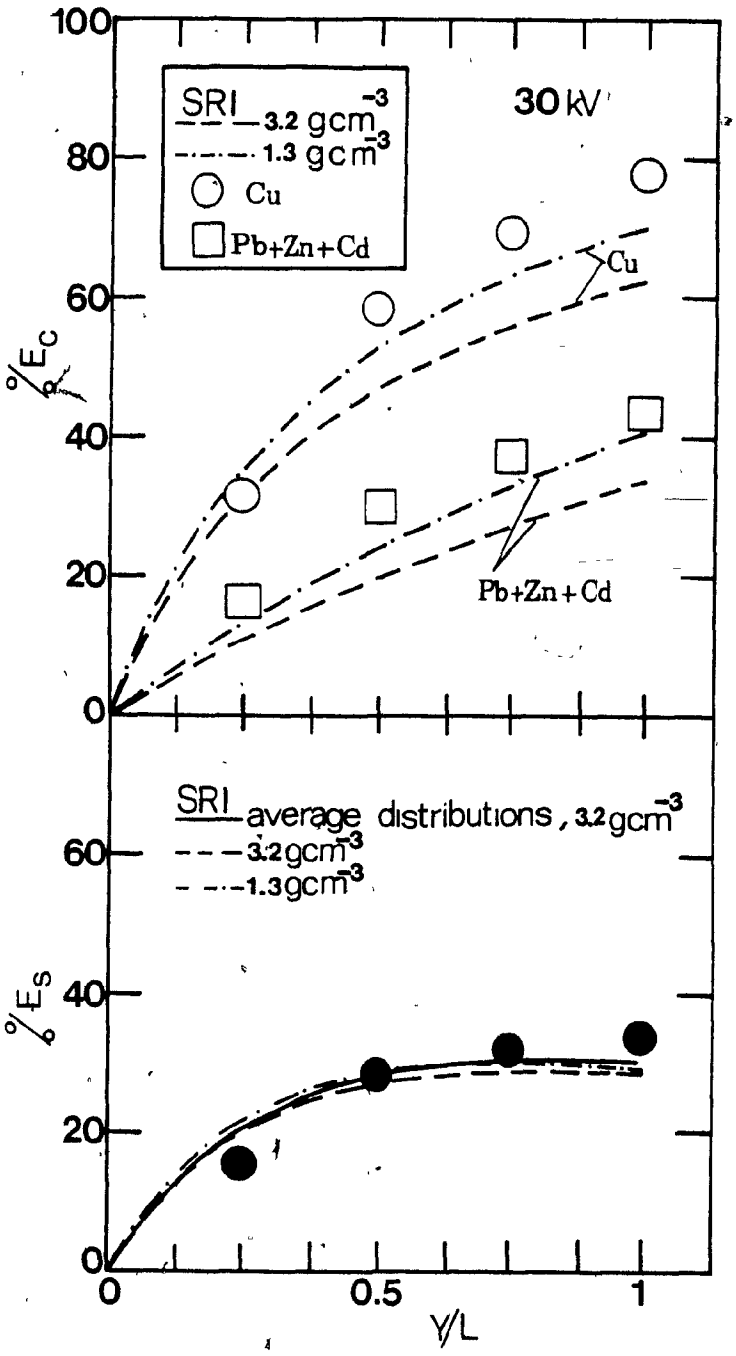


Figure 8.4 Cumulative elemental collection and separation of the Noranda dust as function of ESP length, at medium voltage and 5 ms^{-1}

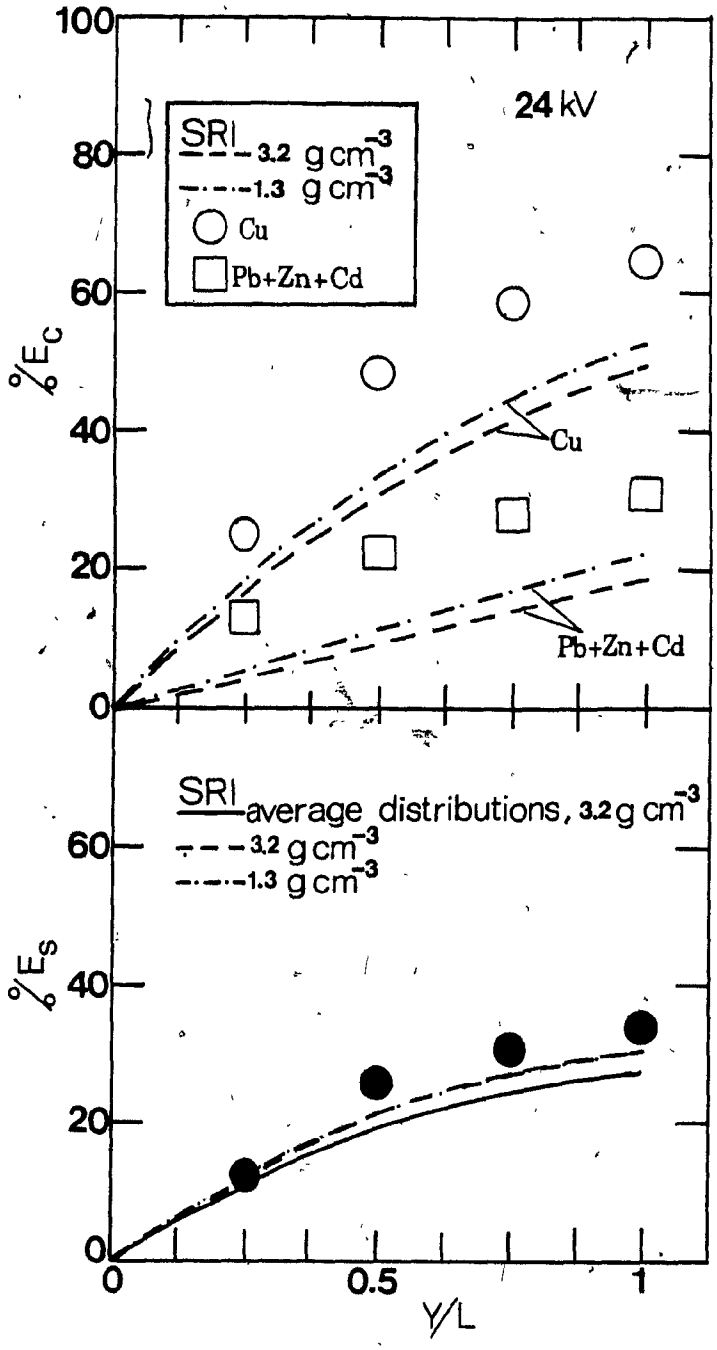


Figure 8.5 Cumulative elemental collection and separation of the Noranda dust as function of ESP length, at low voltage and 5 ms^{-1}

lower maximum separations were obtained at high voltage than at medium or low voltage. This agrees with the SRI predictions if the individual distributions are used as input data to the SRI computer program.

Despite the good agreement obtained with the SRI predictions and the experimental results of separation efficiency, there are some uncertainties in the input data to the SRI model. The effect of these uncertainties in the predicted separations is examined next.

8.4 Uncertainties in the SRI Simulation

8.4.1 Dielectric Constant

The dielectric constant of the Cu rich particles is not known, and it could be either larger or smaller than the estimated value (10). To estimate the possible effect of uncertainties in dielectric constant on the theoretical predictions, SRI simulations were performed for run 46 (as an example) using various dielectric constants for the Cu rich particles and the experimental value of 2.9 for the Pb + Zn + Cd rich particles. Figure 8.6 shows the effect on separation of varying the dielectric constant of the Cu rich particles from 2.9 to 100. It can be seen that the major difference occurs when the dielectric constant increases from 2.9 to 10, which corresponds to an increase in charge of 41%. Only a slight difference is observed when the dielectric constant increases from 10 to 100, which corresponds to an increase in charge of 18%. It can also be seen that a

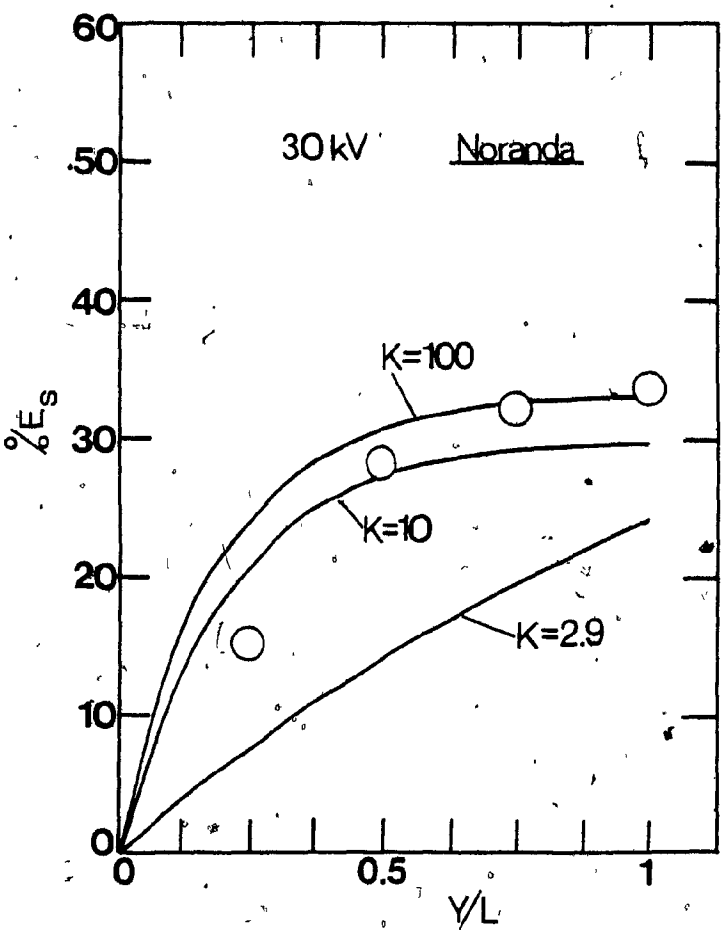


Figure 8.6 Simulated effect of dielectric constant of the Cu rich particles on the cumulative separation of the Noranda dust along the ESP length, at medium voltage and 5 ms^{-1}

separation of about 25% would be theoretically expected for the global ESP length caused by size differences alone, i.e., when $K_{Cu} = K_{Pb+Zn+Cd} = 2.9$.

Although the experimental data of Fig. 8.6 suggest that the dielectric constant of the Cu rich particles is larger than that of the Pb + Zn + Cd rich particles, the effect of uncertainties in the dielectric constant of the Cu rich particles is small; it is unlikely that the dielectric constant of the Cu rich particles is much lower than that of $CuSO_4$ ($\sim$ 10) or CuO ($\sim$ 10-18).

8.4.2 Particle Size Distribution

It was shown in Table 5.11 (Chapter 5) that the concentration of Cu from AAS analysis of the dust collected on the cascade impactor substrates was lower than expected from the composition of the Noranda dust. Also, the elemental mass balances for runs 45-47 confirmed that there was no substantial deposition of Cu rich particles prior to the ESP inlet. Table 8.6 gives the total elemental concentrations (TEC) of the dust collected in the cascade impactor. Also shown are the range of ratios of elemental concentrations obtained by dividing the TEC values by the maximum and minimum values of elemental concentrations experimentally obtained for the Noranda feed (Table 5.6, Chapter 5).

It can be seen that there is good agreement between the elemental concentrations of Pb, Zn and Cd with the expected values from the feed composition; on the other hand, the concentration

TABLE 8.6

Total Elemental Concentrations (TEC) from Cascade Impactor and Comparison with Feed Composition (Noranda Dust)

Run	Element	TEC (Impactor) %	Range of TEC (Impactor) / TEC (Feed)
45	Cu	6.40	0.88-0.96
	Pb	30.78	0.94-1.21
	Zn	12.41	1.04-1.28
	Cd	14.83	1.17-1.35
46	Cu	2.97	0.41-0.44
	Pb	30.25	0.92-1.19
	Zn	10.99	0.92-1.13
	Cd	12.41	0.98-1.13
47	Cu	2.20	0.30-0.33
	Pb	26.71	0.81-1.05
	Zn	9.79	0.82-1.01
	Cd	11.56	0.91-1.05
Average[1]	Cu	3.35	0.49
	Pb	28.94	1.05
	Zn	10.79	1.04
	Cd	12.55	1.07

[1]Taking into account the sampling time.

of Cu is always lower in the cascade impactor samples. On the average, the concentration of Cu is 51% lower than expected.

Ondov et al. (1978) have studied the elemental composition of samples collected by inertial cascade impactors. The ratio of elemental concentration of cascade impactor and total filter samples varied from 0.47 to 0.71, with an average (39 elements) of 0.60, for collection of dry particles with aerodynamic diameters essentially larger than 2 μm. On the other hand, for collection of wet particles with aerodynamic diameters essentially smaller than 2 μm; agreement between the two samples

was within ± 20% for the majority of the elements. They concluded that wall losses were responsible for the lower elemental concentrations of the coarser particles. Also, wall losses increased with sampling time, probably due to stage overloading.

The results of Table 8.6 suggest that wall losses might have been responsible for the lower collection of the copper rich particles. The aerodynamic mean mass diameters were calculated from the values listed in Table 8.1 to be between 1.8 and 2.9 μm for the Pb, Zn and Cd rich particles, and between 5.5 and 8.3 μm for the Cu rich particles. Also, the losses were more severe for the longer runs (46 and 47); however, it is doubtful that stage overloading did occur, in view of the very small weights collected per substrate. From Table 8.1, it can be seen that the MMD of the Cu rich particles was the largest for run 47; it is thus possible that the larger particle sizes of these particles produced increased wall losses. This poses a problem on the representativity of the size distribution of the Cu rich particles derived from the cascade impactor data. This would be especially true for runs 46 and 47, since in run 45, most of the Cu was detected (Table 8.6).

To estimate the effect of an error in the measured size distribution of the Cu rich particles, SRI simulations were made of run 46 (as an example) using a perturbation on the MMD of the Cu rich particles. The MMD of the Cu rich particles was arbitrarily varied from 3 to 5 μm, while keeping the geometric standard deviation equal to 3 (≈ measured value); the lower limit corresponds to the MMD of the Cu rich particles for run 45, where

most of the Cu was detected. The geometric standard deviation was also allowed to vary from 3 (∿ measured value) up to a maximum of 5 (which approximately corresponds to the value measured in run 45), while keeping the MMD equal to 4 μm (∿ measured value). The simulation results on the predicted separation are shown in Fig. 8.7.

It can be seen that the variation in the MMD has a much more pronounced effect than a corresponding variation in the geometric standard deviation. Since the larger particles are more susceptible to wall losses in the cascade impactor (Ondov et al., 1978), it is probable that curve no. 3 reflects a more realistic assumption than curve no. 1 (Fig. 8.7). However, no definite conclusions can be reached since the extent to which the particle size distribution of the Cu rich particles is affected by wall losses is not known. For this, it would be necessary to study the elemental size distributions of the particles that are lost to the impactor walls, using, for example, an electron microscope. The electron microscope would also be used to measure the size of the particles collected on the impactor substrates; the weight proportion of each element collected on the impactor walls could thus be assigned to the correct impactor substrate and the corrected elemental size distributions could then be constructed. This was not done for the present work.

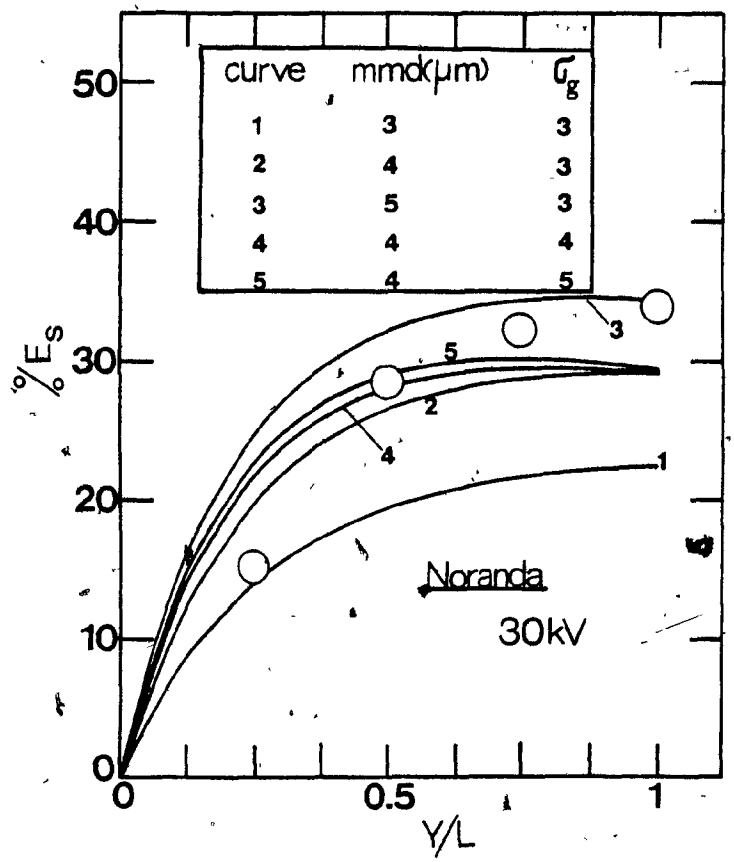


Figure 8.7 Simulated effect of particle size distribution of the Cu rich particles on the cumulative separation of the Noranda dust along the ESP length, at medium voltage and 5 ms^{-1}

8.5 Conclusions

The Noranda dust shows segregation of Cu rich particles from Pb + Zn + Cd rich particles. The dust collected in the ESP is richer in Cu than the feed, and maximum separation efficiencies of around 30% were obtained at 5 ms^{-1}. The agreement between the theoretical (SRI) predictions and the observed separations is good, using the elemental size distributions derived from the cascade impactor data and assigning the dielectric constant of $CuSO_4$ to the Cu rich particles. However, the simulation results are sensitive to uncertainties in the dielectric constant and the MMD of the copper rich particles.

The observed separation is probably caused by a combination of differences in dielectric constant and MMD of the Cu rich particles from the Pb + Cd + Zn rich particles. Differences in size distribution are thought to be the major cause of separation, since separations of up to 25% are theoretically predicted without differences in dielectric constant. The theoretical effect of differences in dielectric constant contributes only about 5-6% to the global separation but it is important near the ESP inlet.

Further experimental work is needed to establish to what extent wall losses in the cascade impactor may disrupt the measured size distribution of the Cu rich particles, and as such, affect the predicted separations.

REFERENCES

Ondov, J.M.; Ragaini, R.C. and Biermann, A.H. (1978): "Elemental Particle-Size Emissions from Coal-Fired Power Plants: Use of an Inertial Cascade Impactor", Atmospheric Environment, 12, Perg. Press, pp.1175-1185.

PART II

SEPARATION AND RECOVERY (COLLECTION)

8.6 Experimental Results

The experimental data obtained on the separation of mixtures of single components (CuO, MgO, TiO_2 and Al_2O_3) and of elements from an industrial dust (Cu from Pb, Zn and Cd) suggest that the experimental conditions of applied voltage and air velocity may greatly affect the degree of separation obtained in the global ESP length. These operating variables also affect the shape of the separation curve as a function of the ESP length; as the charging (and precipitating) environment become poorer, there is a shift in the maximum of separation from near the ESP inlet towards the ESP outlet; eventually, no maximum is observed within the available ESP length. However, the absolute value of the maximum separation does not seem to vary appreciably for the same pair of components. These observations are in agreement with SRI predictions. An exception is CuO, since its collection efficiency is also a function of the inlet conditions (relative concentration in the feed) and of the precipitation of the high resistivity component(s).

Since each separation efficiency for a fixed pair of components and global ESP length was obtained with different recoveries (collection efficiencies), it was decided to plot the observed separation efficiencies versus the observed recoveries, irrespective of ESP length. The "recovered" component was arbitrarily chosen to be the one which showed the largest global collection efficiency.

Figure 8.8 shows the experimental values of separation efficiency versus recovery for the pair TiO_2/MgO, for all the experimental runs in which these two components were present as a mixture (with or without other components) at the ESP inlet. Although there is some scatter in the data, there seems to be a unique curve that describes the observed behaviour. Figure 8.8 also shows the theoretical (SRI) predictions, which also follow a unique curve [1]. It can be seen that the majority of points show higher separations than predicted for the same recovery. All the experimental runs were performed at 5 ms^{-1}, except run 30 which was performed at 2 ms^{-1}. It was shown in Chapters 6 and 7 that reentrainment of the coarser MgO particles might occur at 5 ms^{-1}; this would increase the separation above theoretical predictions. Reentrainment of MgO is unlikely to have occurred at 2 ms^{-1}, and thus the lower separation observed at this velocity. As explained in Chapter 7, the discrepancies between the experimental separations and the theoretical predictions are due to the respectively lower and higher collection of MgO and TiO_2 near the ESP inlet (± 5-10% for each component) and to the decreased global collection of MgO at low corona powers. These phenomena tend to increase the separation above theoretical predictions, for the same recovery of TiO_2.

Figure 8.8 also shows that there is a smooth reduction in separation efficiency for recoveries greater than the recovery at which the maximum separation occurs, i.e., above

[1] Although there are some differences in the SRI predictions at different voltages and air velocities, these are of the order of ± 1-2% and insignificant for practical purposes (Section 8.7.1).

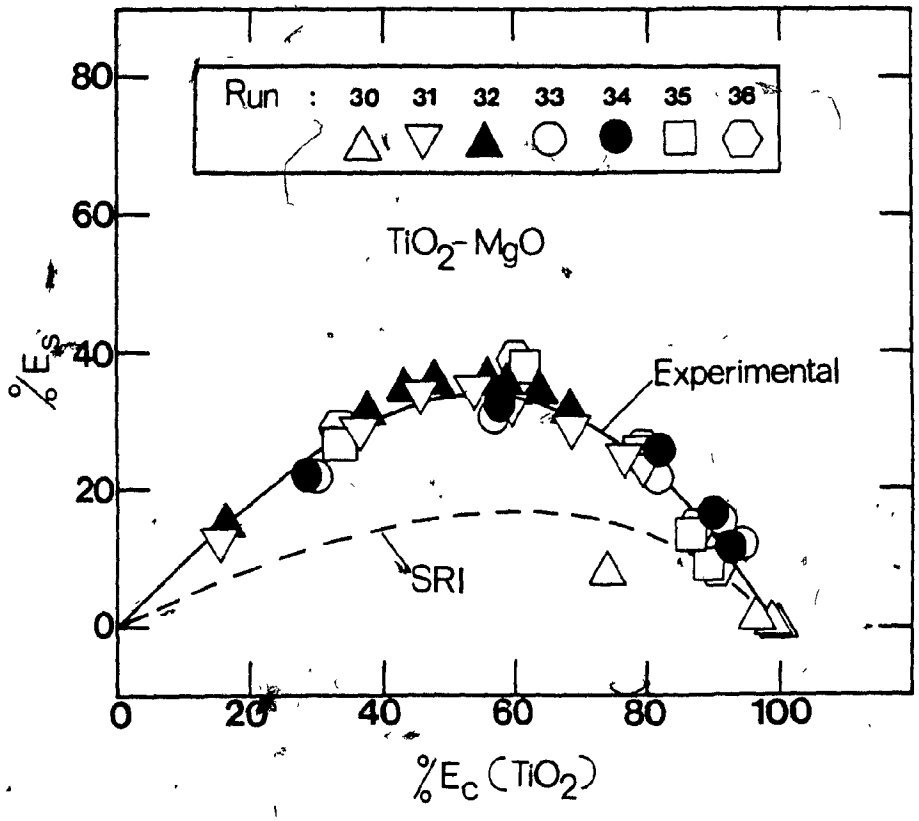


Figure 8.8 Relation between cumulative separation and recovery for the pair TiO_2/MgO

about 60% collection efficiency of TiO_2.

Figures 8.9a and b show the corresponding data and SRI predictions for the pairs MgO/Al_2O_3 and TiO_2/Al_2O_3. The qualitative agreement is very good and the quantitative agreement is reasonable. It can be seen that a sharp drop in separation is observed for recoveries in either MgO or TiO_2 above about 80%. Figures 8.9a and b also show that a better agreement is obtained with the experimental data if the coarser size distribution estimate of alumina is used, i.e., for ρ = 0.9 g cm^{-3}.

Figure 8.10 shows the corresponding data obtained with the Noranda dust. The SRI simulations were performed with both the elemental individual distributions (for each experimental run) and with the average distributions (Table 8.5).

It can be seen that the individual distributions produce simulation results which are closer to the experimental values than the average distributions do. This is especially true for the high voltage run (38 KV), where the individual distributions deviate the most from the average elemental distributions. Except for the high voltage run, the experimental data also seem to follow a unique curve; the agreement between the theoretical predictions based on the average elemental size distributions and the experimental data is reasonable.

One implication of the experimental data (and SRI predictions) of Figs. 8.8-8.10 is that the maximum separation between two components is achieved at approximately the same degree of recovery, irrespective of the operating conditions of the ESP.

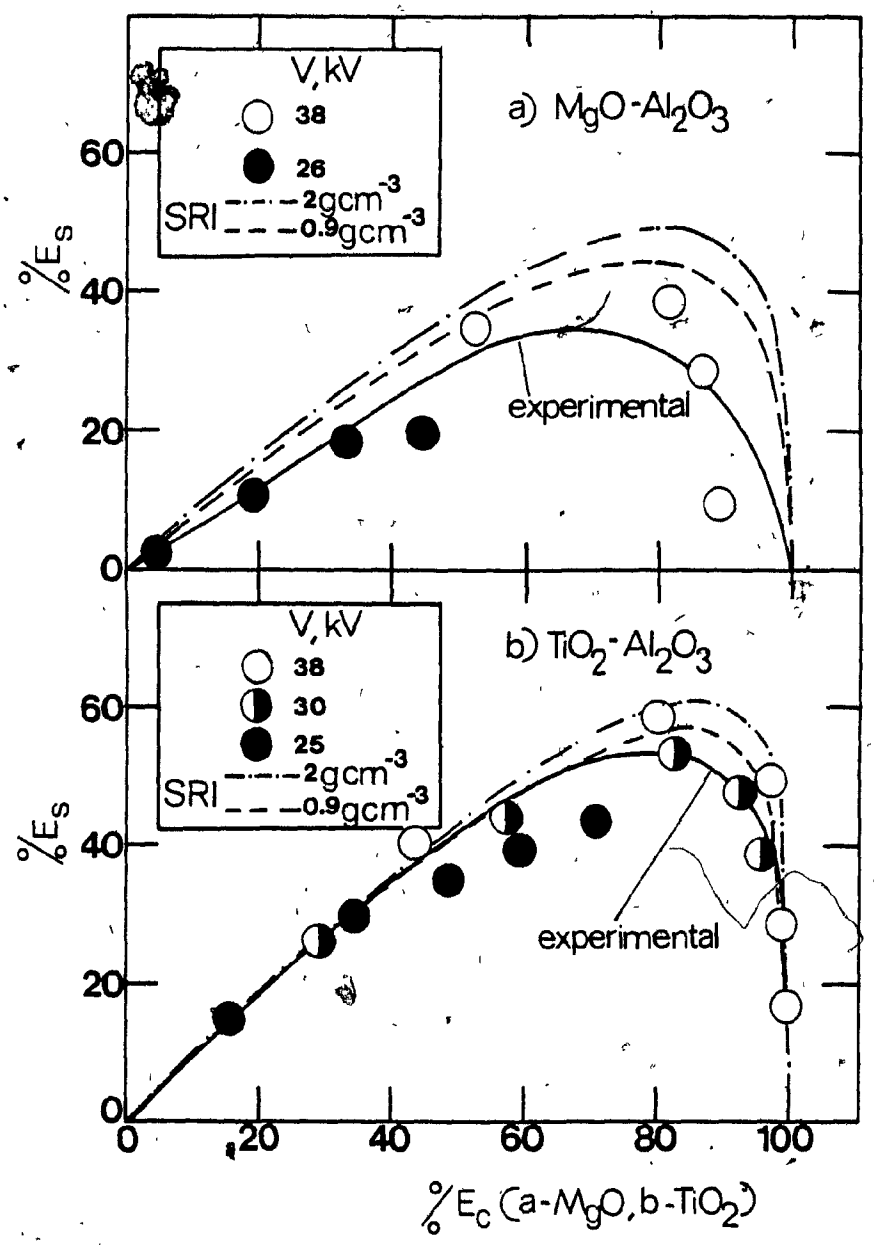


Figure 8.9 a and b) Relation between cumulative separation and recovery for the pairs MgO/Al_2O_3 (a) and TiO_2/Al_2O_3 (b)

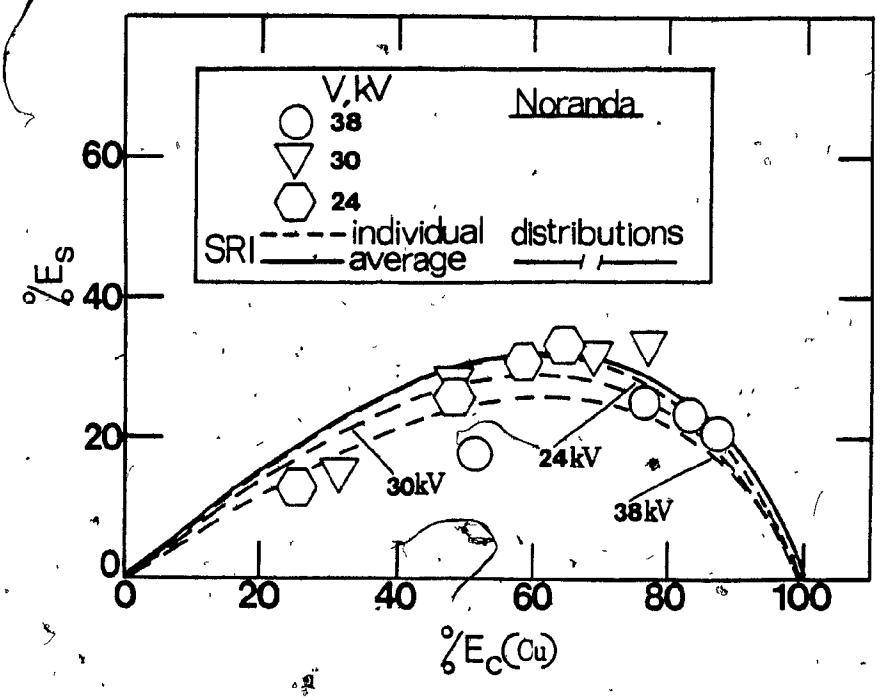


Figure 8.10 Relation between cumulative separation and recovery for the Noranda dust.

However, as seen above, the physical size of the ESP required to achieve a specified recovery (and thus a specified separation) depends strongly on the ESP operating conditions of electric field and air velocity.

It can also be concluded that poor global separations may be expected under typical industrial operating conditions, i.e., for recoveries above about 95%.

The unique relationship obtained with the SRI model and the corresponding experimental data suggest that this behaviour might be analytically derived from fundamental theory of electrostatic precipitation. This is discussed next.

8.7 Theoretical Considerations

8.7.1 Separation Nomograph

A unique relationship between separation and recovery can be directly derived from the Deutsch Equation of collection efficiency (Eq. 2.40, Chapter 2). If the assumption is made that the Deutsch Equation applies, then the separation between components (i,j) is given by:

$$E_{s_{ij}} = (1-E_{c_i})\{(1-E_{c_i})^{\frac{w_j-w_i}{w_i}} - 1\} \qquad (8.I)$$

where (E_s) is the separation efficiency, (E_c) is the collection efficiency and (w) is the theoretical migration velocity. Equation (8.1) shows that the separation is only a function of the recovery of one component and the ratio of theoretical migration velocities. Thus, a plot of $E_{s_{ij}}$ against E_{c_i} depends

only on the ratio of theoretical migration velocities. For particles with diameters above about 1 μm and under typical electric fields, field-charging is predominant over diffusion charging. Under such conditions, the ratio of theoretical migration velocities may be approximated by:

$$\frac{w_i}{w_j} \simeq \left(\frac{C_i Q_{s_i}}{C_j Q_{s_j}}\right)\left(\frac{D_j}{D_i}\right) \qquad (8.2)$$

where (C) is Cunningham correction factor, (Q_s) is saturation charge and (D) is particle diameter. The Cunningham correction factor (Eq. 2.34) is well approximated by:

$$C \simeq 1 + 2.52\,\frac{\lambda}{D} \qquad (8.3)$$

where (λ) is the molecular mean free path.

Using Eq. 8.3 and the theoretical expression for the saturation charge (Eq. 2.21), the following relation is derived:

$$\frac{w_i}{w_j} \simeq \frac{K_i(K_j+2)}{K_j(K_i+2)} \cdot \frac{D_i + 2.52\lambda}{D_j + 2.52\lambda} \qquad (8.4)$$

where (K) is the relative dielectric constant.

Since the molecular mean free path (λ) is constant at a fixed pressure and temperature, the ratio $\frac{w_i}{w_j}$ is approximately constant for a specified set of components, provided the pressure and temperature do not vary appreciably. The molecular mean free path at ambient temperature and pressure is approximately equal to 0.06 μm (Eq. 2.35, Chapter 2) and above about

1 μm in particle diameter, Eq. 8.4 may be approximated by:

$$\frac{w_i}{w_j} \approx \frac{K_i(K_j+2)}{K_j(K_i+2)} \cdot \frac{D_i}{D_j} \qquad (8.5)$$

This is equivalent at neglecting the effect of the Cunningham factor.

A plot of $E_{s_{ij}}$ as a function of E_{c_i} (Eq. 8.1) for a fixed pair of components should then yield a unique curve. Some perturbation may occur due to the fact that the ratio of theoretical migration velocities varies slightly along the ESP length (due to particle size variations) and due to the possible selective contribution of diffusion charging; this occurs when one component is predominantly formed by coarse particles and the other by submicron particles. However, for the cases tested in this work the difference is very small (typically less than 2%, as evidenced by the SRI simulations). It should be noted that other exponentially decaying equations of collection efficiency (e.g., Eq. 2.41, Chapter 2) also yield a unique relation such as Eq. 8.1. This behaviour is thus not restricted to the Deutsch Equation.

Figure 8.11 shows a plot of $E_{s_{ij}}$ as a function of E_{c_i} for various values of the parameter w_j/w_i. The shape of the curves is similar to the ones determined experimentally or from the SRI simulations, as can be seen from Figs. 8.8-8.10.

In the case where one or both of the components is essentially below about 0.5 μm in diameter, the contribution of diffusion charging may become important or even dominant; under such circumstances no simple relation such as Eq. 8.4

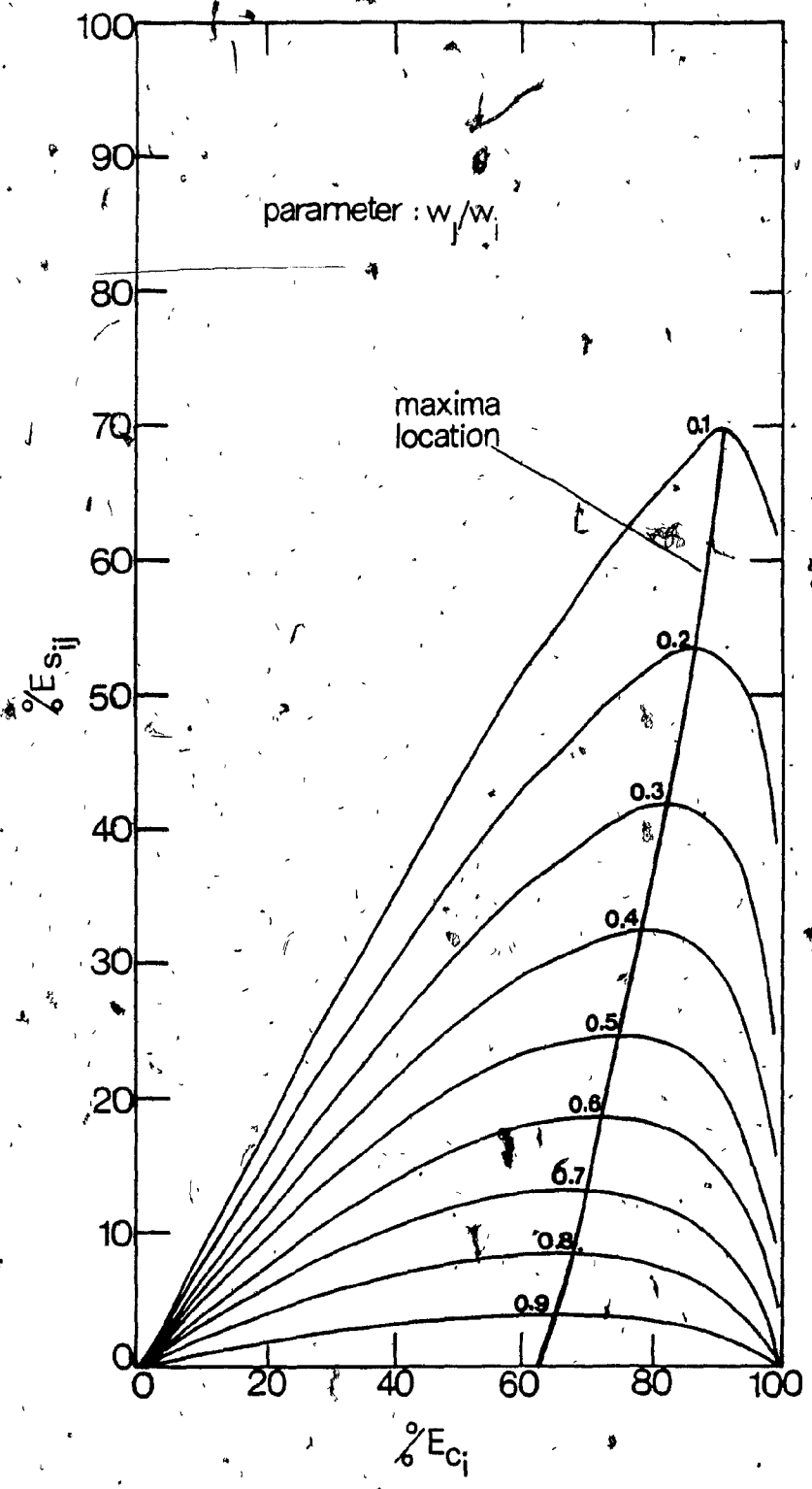


Figure 8.11 Theoretical relation between separation and recovery, according to the Deutsch Equation of collection efficiency

(or 8.5) could be derived.

The elemental concentration of the precipitated dust can be computed from:

$$C_{p_i} = \frac{C_{ri}\eta_i}{C_{ri}\eta_i + (1-C_{ri})\eta_j} = \frac{C_{ri}\frac{\partial E_{c_i}}{\partial L}}{C_{ri}\frac{\partial E_{c_i}}{\partial L} + (1-C_{ri})\frac{\partial E_{c_j}}{\partial L}} \quad \ldots\ldots(8.6)$$

where (η) is the non-cumulative collection efficiency for a particular length increment, (E_c) is the respective cumulative collection and (C_{ri}) is the fraction of component (i) at the ESP inlet. Equation 8.6 assumes that the mechanical collection of the ESP is the same for either component. Substituting the Deutsch Equation in Eq. 8.6 and developing, it becomes:

$$C_{p_i} = \frac{1}{1 + \left(\frac{1-C_{ri}}{C_{ri}}\right)\left(\frac{w_j}{w_i}\right)(1-E_{c_i})^{w_j/w_i - 1}} \quad (8.7)$$

which shows that for a specified feed, the concentration of the precipitated dust is also a unique function of the recovery of one component and the ratio of theoretical migration velocities. The recovery (E_{c_i}*) for which the separation is a maximum ($\frac{\partial E_{s_{ij}}}{\partial E_{c_i}} = 0$) is given by:

$$E_{c_i}^* = 1 - \left(\frac{w_i}{w_j}\right)^{\frac{w_i}{w_j - w_i}} \quad (8.8)$$

which tends to ($1 - \frac{1}{e}$) as $w_j \to w_i$. This means that theoretically a recovery of at least 63.2% is necessary to achieve the maximum separation. This can also be seen from Fig. 8.11. The maximum

separation is given by:

$$(E_{s_{ij}})_{max} = \left(\frac{w_i}{w_j}\right)^{\frac{w_j}{w_j-w_i}} - \left(\frac{w_i}{w_j}\right)^{\frac{w_i}{w_j-w_i}} \qquad (8.9)$$

The maximum theoretical separation occurs when the relative concentration of the precipitated dust equals the relative concentration in the feed, i.e., for $C_{ri} = C_{p_i}$. This can be shown by combining Eqs. 8.1 and 8.7 and finding $\frac{\partial E_{s_{ij}}}{\partial C_{p_i}} = 0$, or by direct substitution of Eq. 8.8 in Eq. 8.7.

The most relevant expressions derived above can be conveniently combined in a separation nomograph. Since elemental concentrations of the precipitated dust are convenient to measure experimentally, this variable was chosen as the abcissa of the nomograph. Figure 8.12 shows the nomograph, which has as parameters both the ratio of theoretical migration velocities and the recovery. The abcissa was normalized to reflect a 1:1 ratio of concentrations at the ESP inlet. Thus, the maximum separation will occur when $C_{p_i}^* = C_{ri} = 1/2$. This procedure eliminates the feed composition as a variable.

To use the nomograph, the actual measured concentration (C_{p_i}) is first converted to the normalized concentration ($C_{p_i}^*$) by the use of the following relation:

$$C_{p_i}^* = \frac{C_{p_i}\left(\frac{1-C_{ri}}{C_{ri}}\right)}{(1-C_{p_i}) + C_{p_i}\left(\frac{1-C_{ri}}{C_{ri}}\right)} \qquad (8.10)$$

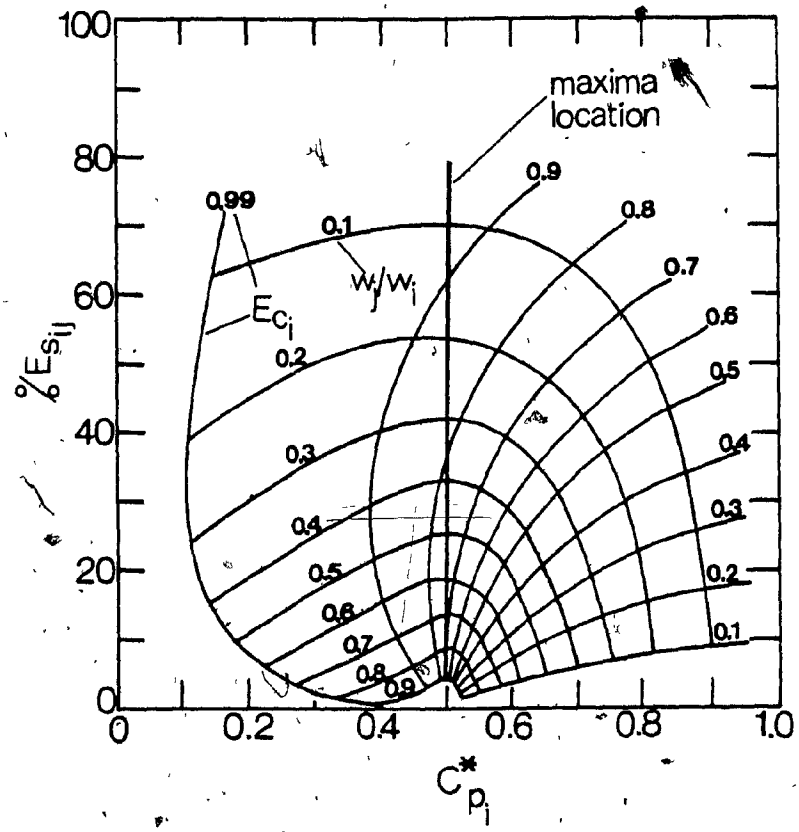


Figure 8.12 Separation nomograph

The separation efficiency and the corresponding recovery can be directly read from the graph, provided an estimate of the ratio of migration velocities is available.

The nomograph does not give any information on the ESP length necessary to achieve a specified recovery (or separation). For this, it is necessary to simulate the ESP under the actual operating conditions, using, for example, the SRI computer model. The advantage of the nomograph is that the theoretical separation can be approximately estimated without performing any computer simulations; experimental information on the concentration of the component of interest in the precipitated dust (or on elemental collection efficiencies) is, however, necessary.

8.7.2 Comparison with SRI Results and Experimental Data

One problem in the application of either Fig. 8.11 or 8.12 is the determination of the ratio of theoretical migration velocities. For a typical polydisperse aerosol there is no single particle diameter that describes the observed behaviour of the entire size distribution. However, if the size distributions are not too broad, the MMD may be a reasonable approximation of the entire size distribution (on a weight basis). To test this hypothesis, a typical experimental run with the Noranda dust was chosen (run 45, at an applied voltage of 38 KV). Figure 8.13 shows the experimental results obtained on a plot of separation versus recovery. Also shown are the SRI predictions (solid line) and the predictions based on Eq. 8.1. For the latter, two

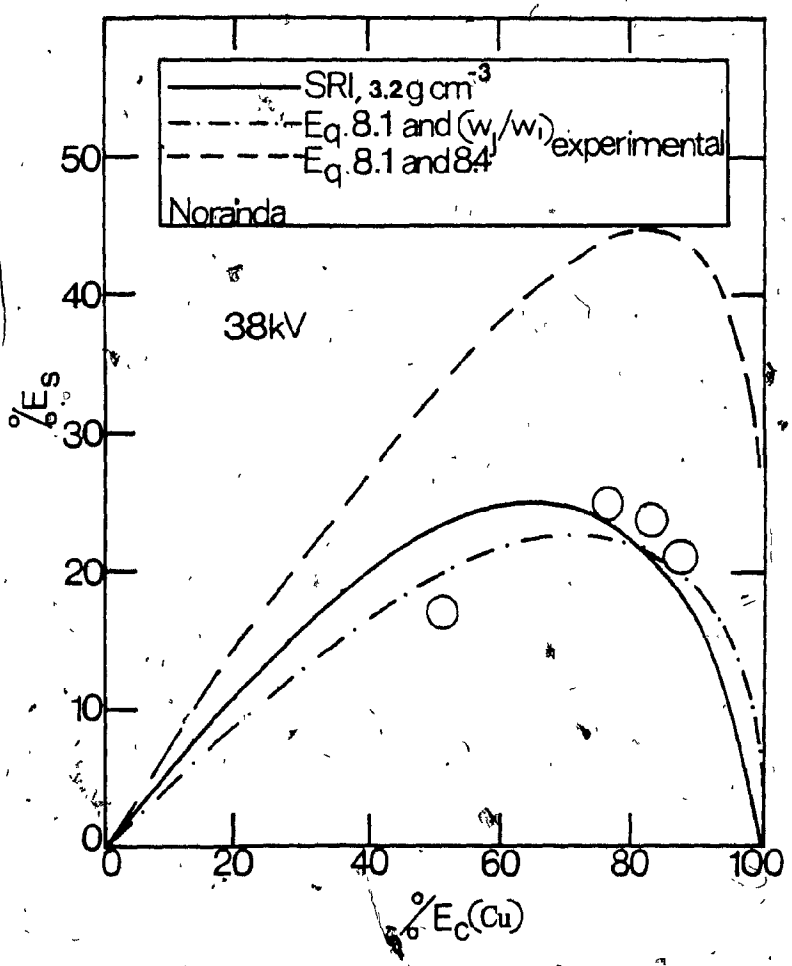


Figure 8.13 Comparison between theoretical and experimental results of separation versus recovery, for the Noranda dust, at high voltage and 5 ms^{-1}

estimates of the ratio of migration velocities were used; the first estimate is based on Eq. 8.4 and the second estimate is based on calculating the experimental effective migration velocities (i.e., for the global ESP length) for the components in question, using the data of Table 8.1 and the Deutsch Equation. These estimates yield the values of 0.27 and 0.53, respectively, for the ratio of migration velocity of the Pb + Zn + Cd/rich particles to that of the Cu rich particles.

It can be seen that the use of Eq. 8.4 with the MMD's highly overpredicts the separation with respect either to the experimental data or to the SRI results. A much better agreement is obtained if the experimental ratio of effective migration velocities is used. This means that for this particular case the use of Eq. 8.4 is not adequate. Inspection of the standard deviations of the elemental size distributions (Table 8.1) indicates that these are relatively broad. The behaviour of the components might thus not be adequately described by their MMD's. From the SRI results, a ratio of 0.49 is obtained for the effective migration velocities; this compares well with the experimental value of 0.53, and thus the good agreement obtained with these two curves.

When the size distributions are narrow, approximate results may be obtained by using Eqs. 8.1 and 8.4 with the particle diameters substituted by the MMD's. An example is given in Fig. 8.14 for the pair TiO_2/Al_2O_3, where it can be seen that the use of Eqs. 8.1 and 8.4 agrees well with the SRI predictions.

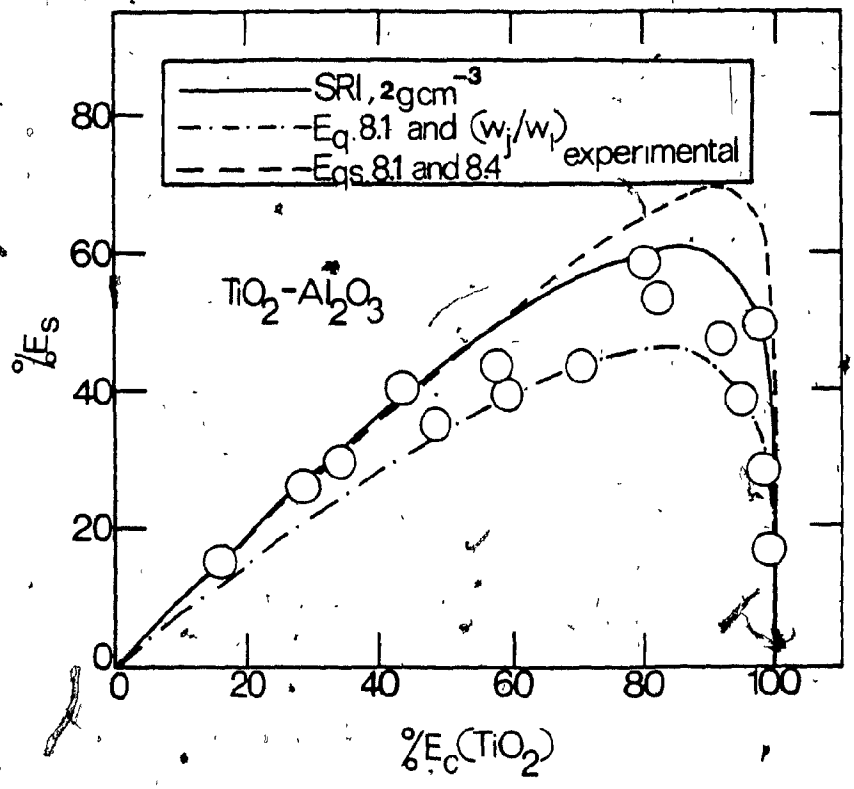


Figure 8.14 Comparison between theoretical and experimental results of separation versus recovery for TiO_2/Al_2O_3, at 5 ms^{-1}

It is also seen that the experimental data lie between the SRI predictions and those of Eq. 8.1 using the experimentally determined ratio of effective migration velocities ($\frac{w_j}{w_i} = 0.26$, on the average).

The SRI predictions and Eqs. 8.1 and 8.4 agree even more closely as the size distribution narrows; this is the case for TiO_2/MgO, as shown in Fig. 8.15. In this case, however, neither method predicts the observed behaviour. The reasons for the discrepancies between theory and the observed results were discussed before (Chapter 7 and Section 8.6). The poor agreement between the experimental data and Eq. 8.1 using the experimental value of the ratio $\frac{w_j}{w_i}$ (0.60, on the average) is due to the fact that the experimental migration velocities are calculated on a global basis (i.e., for the entire ESP), and appreciable deviations from theoretical predictions are apparent at the beginning of the ESP.

The separation nomograph (Fig. 8.12) can be used in one of two ways:

- To predict separations from experimental elemental concentrations of the precipitated dust; or
- To predict separations from experimental elemental (component) recoveries.

The limitations on the use of Fig. 8.12 are the same as for the use of Eqs. 8.1 and 8.4: reliable predictions will be obtained only when the materials follow the Deutsch Equation of collection efficiency (or some closely related form), and for narrow size distributions. In the case of broad distributions,

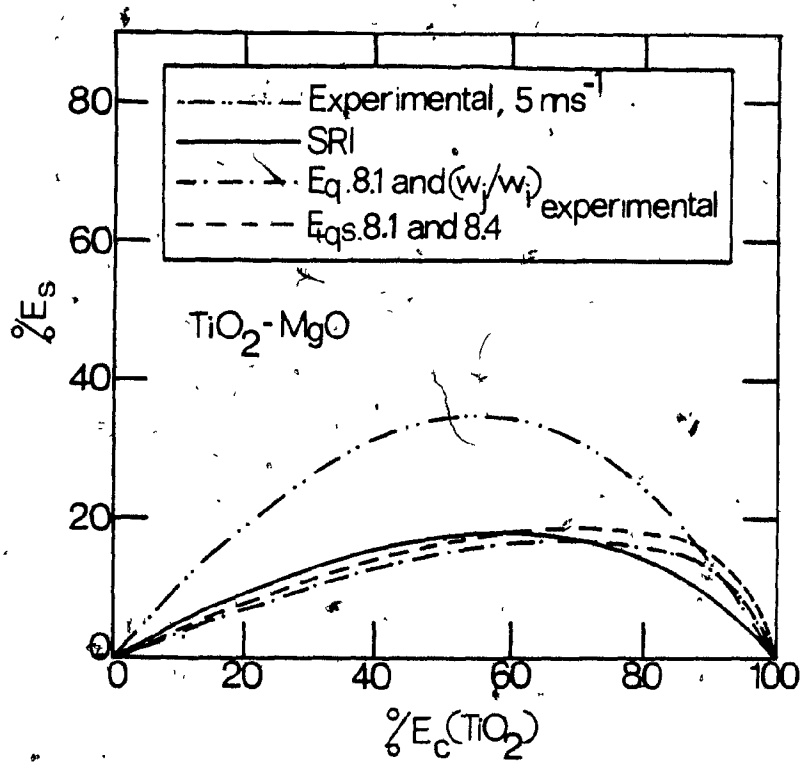


Figure 8.15 Comparison between theoretical and experimental results of separation versus recovery for TiO_2/MgO, at 5 ms^{-1}

it is recommended that the experimental ratio of effective migration velocities be employed.

To use the nomograph with experimental values of relative concentration (C_{p_i}), the following steps are necessary:

1) Normalize the measured values of C_{p_i} along the ESP length using Eq. 8.10.
2) For narrow distributions, estimate the ratio of migration velocities using Eq. 8.4 (or 8.5); for broad distributions ($\sigma_g \gtrsim 2$), determine the experimental ratio of effective migration velocities from the effective elemental (component) collection efficiencies and the Deutsch Equation.
3) Enter the values of C_{p_i}* and w_j/w_i on Fig. 8.12 and read the corresponding separation efficiencies.

If information is available on the effective elemental collection efficiencies, the effective (global) separation can be directly read from Fig. 8.12. However, the separation along the ESP length cannot be inferred from Fig. 8.12. For this, information on the concentration along the ESP length is necessary.

8.8 Conclusions

It has been shown theoretically that powders which precipitate according to the Deutsch Equation (or some other similar form) exhibit a single separation versus recovery curve, irrespective of the operating characteristics or physical size of the ESP. This behaviour is also predicted from the SRI model, which uses the Deutsch Equation in small incremental lengths of

precipitation.

The majority of the experimental data also show this unique behaviour. An exception occurs with CuO, due to its strong reentrainment, which is a function of the feed conditions and the precipitation of high resistivity components.

A separation nomograph was developed which allows for the estimation of separation efficiencies from experimental values of elemental concentrations in the precipitated dust, together with an estimation of the ratio of migration velocities. Essentially the same results are obtained either with the separation nomograph or the SRI model if a correct estimation of the ratio of migration velocities is used.

It is expected that the predictions from the separation nomograph be reasonable for powders which precipitate according to the Deutsch Equation. Serious deviations from experimental results may occur in the event that:

- the Deutsch Equation (or some similar form) is not followed;
- the ratio of migration velocities varies along the ESP length; or
- the ratio of migration velocities is poorly estimated.

Due to these uncertainties, it is recommended that the separation nomograph be used with caution. Its advantage is in minimizing the amount of computations required to estimate separation efficiencies in ESP's.

CHAPTER 9

CONCLUSIONS AND RECOMMENDATIONS

9.1 Conclusions

The separation of mixtures of pure compounds (CuO, MgO, TiO_2 and Al_2O_3) and of components from a typical industrial dust (Noranda copper reactor ESP catch) by electrostatic precipitation has been studied in a laboratory-scale ESP.

1. The dust properties which affect the solid-solid separation are particle size distribution, electrical resistivity and dielectric constant. Both differences in particle size distribution and dielectric constant affect the separation through differences in particle charging; these effects can be approximately predicted from existing theories of precipitation (e.g., the SRI computer model of electrostatic precipitator performance). The effect of particle size is more important than the effect of dielectric constant. The electrical resistivity affects the separation through dust re-entrainment; this effect is important for low resistivity dusts (effective bulk resistivity $\gtrsim 10^5$-10^7 Ohm m) and cannot be adequately predicted from existing theories.

While differences in particle size and dielectric constant tend to increase separation, dust re-entrainment may either enhance or decrease the separation, depending on which species re-entrains. Since coarser particles are more prone to re-entrainment, this phenomenon will generally reduce the separation based on size distribution differences.

The inlet dust loading had no appreciable effect on collection or separation in the range investigated in this work (~50 - 1300 mg m^{-3}).

2. The ESP operating variables which affect the separation are the air velocity, applied voltage and corona current. The applied voltage had the greatest effect in the separation obtained within the available ESP length.

A maximum in separation may occur near the ESP inlet, especially at low air velocities and high applied voltages. The maximum in separation moves downstream as the charging and precipitating environment weaken, i.e., for increased air velocities and decreased applied voltages. Thus, global separations are enhanced at low electric fields and high air velocities.

3. The separation of mixtures of pure compounds can be predicted from the behaviour of the individual species when fed separately to the ESP, only in the absence of appreciable re-entrainment.

4. The industrial dust used in this work exhibited chemical segregation with particle size, i.e., different elements were concentrated in different particle sizes. Specifically, it was found that Cu was concentrated in the coarser particles while Pb, Zn and Cd were concentrated in the finer particles.

The separation of the Cu rich particles from the Pb + Zn + Cd rich particles was primarily due to particle size differences, although some contribution of different dielectric constants is probable.

Simulation of the separation with the SRI model, assuming that the Cu rich particles are physically separated from the Pb + Zn + Cd rich particles, agrees well with the experimental results on separation.

5. An apparently unique relationship between separation and collection (recovery) was experimentally obtained for specific pairs of components which do not re-entrain appreciably. A similar behaviour is predicted from the Deutsch Equation of collection efficiency and the SRI model. A simple nomograph was developed based on the Deutsch Equation, to estimate separation efficiencies from elemental (component) concentrations in the precipitated dust; it gives essentially the same results as the SRI model if appropriate estimates of ratios of migration velocities for the different components are used.

9.2 Contributions to Knowledge

1. Design and construction of a laboratory-scale ESP of the wire-duct type which allows the study of collection and separation along the ESP length.

2. Experimental determination of the effects of particle size distribution, electrical resistivity (re-entrainment), dielectric constant, applied electric field and air velocity on the collection of typical pure compounds as a function of the ESP length.

3. Experimental determination of the effects of the above variables on the collection and separation of mixtures of the pure compounds, as a function of the ESP length.

4. Extension of the work on separation to a typical industrial dust.

5. Determination of conditions under which the SRI computer model of ESP performance is applicable, for dry collection and separation in a laboratory-scale ESP, neglecting the empirical correction factors originally built into the model.

6. Contribution to a better understanding of the re-entrainment of low resistivity dusts and of their interaction with high resistivity dusts.

7. Experimental and theoretical demonstration that separation shows a near unique relation with recovery, for a fixed pair of components which do not re-entrain appreciably.

8. Development of a separation nomograph which can provide reasonable estimates of separation efficiencies in ESP's under conditions of near-ideal collection.

9.3 Recommendations for Future Research

The results of this work suggest several areas where more research would be useful. These include collection of dry particulates and separation of components of typical industrial dusts. They are:

1. Re-entrainment of low resistivity dusts: a thorough experimental study is needed to understand the re-entrainment phenomena and the interaction with high resistivity dusts. The work should be performed with more than a single re-entraining species; some modelling could then be possible.

2. Abnormal collection of fine particles: this includes the effect of charging near corona wires, concentration gradients, particle diffusion, particle shape and agglomeration. In line with this, more research is needed to produce reliable dry dust feeders in the micron and sub-micron range of particle size.

3. Collection and separation of the Noranda dust: due to the limited number of experiments performed in this work, more experiments on collection and separation should be carried out with the Noranda dust, at various precipitator conditions.

4. Separation and recovery relationship: experiments should be performed to confirm the apparently unique relationship obtained between separation and recovery. These could be done on a global length basis, to reduce the experimental time needed to acquire the necessary information.

5. Separation of other industrial dusts: an assessment should be made of the various industries where separation by ESP's could be performed. This requires a thorough study of the characteristics of the particulates emitted from the various sources; much of this information can be found in relevant literature. Further experimental work should then be conducted on the dusts which show promising separation characteristics. Comparison of these dust characteristics with the separation results could provide useful guidelines for optimization of separation.

6. Cascade impactor performance evaluation: corroboration of the elemental fractionation obtained using cascade impactors should be provided by other means, e.g., electron microscope and EDX analysis of the dust collected on the substrates and impactor walls.

NOMENCLATURE

a	corona wire radius (m)
a_x	mesh interval in X direction (m)
a_y	mesh interval in Y direction (m)
A	intercept of regression equation of least-squares log-normal fit
A_s	parameter of surface resistivity (Ohm m)
A_v	parameter of volume resistivity (Ohm m)
b	mobility ($m^2V^{-1}s^{-1}$)
b_d	particle mobility ($m^2V^{-1}s^{-1}$)
b_{eq}	equivalent mobility ($m^2V^{-1}s^{-1}$)
B	empirical constant of surface resistivity model ($mm\ Hg^{-1}$), slope of regression equation of least-squares log-normal fit
c	one half the wire-to-wire spacing (m), concentration in concentrate
C	empirical constant of surface resistivity model (K), Cunningham correction factor, concentrate weight (Kg)
C_i	inlet dust loading ($mg\ m^{-3}$)
C_p	concentration in precipitated dust
C_p^*	concentration in precipitated dust normalized to concentration in feed
C_{ri}	inlet relative concentration
d	characteristic dimension (m)
D	particle diameter (μm), air density relative to 20^oC and 1 atm
e	electronic charge (1.602×10^{-19} coul), neperian base
E	electric field strenght (Vm^{-1})
E_{av}	average electric field in interelectrode spacing (Vm^{-1}), average electric field through precipitated dust layer (Vm^{-1})
E_c	cumulative collection efficiency by weight
E_c^*	value of E_c for maximum separation efficiency

$(E_c)_{exp}$	experimental value of E_c
E_{ep}	average electrostatic field at the plate(Vm^{-1})
E_{ex}	electric field exterior to dust layer(Vm^{-1})
E_i	electric field at the boundary of the corona glow region(Vm^{-1})
E_o	corona onset field(Vm^{-1})
E_p	average electric field at the plate(Vm^{-1})
E_s	separation efficiency by weight
E_s^*	maximum value of E_s
E_s'	difference in cumulative collection efficiencies
f	concentration in feed
f_n	number fraction of particles of a particular size
f_w	weight fraction of particles of a particular size
F	feed weight(Kg), net force of attraction of dust layer due to corona current(Nm^{-2})
G	cumulative fraction oversize
h	rotameter scale height
H_r	relative humidity
i	total secondary current from high-voltage power supply(mA), component in mixture, index that runs over all particle sizes
j	current density(Am^{-2}), component in mixture
j_d	average current density due to dust particles (Am^{-2})
j_i	average current density due to ions(Am^{-2})
k	Boltzmann's constant($1.38 \times 10^{-23} JK^{-1}$), number of components in mixtures at the ESP inlet, number of length increments of the ESP
K	relative dielectric constant
K'	relative dielectric constant of a composite of particles and air

L	ESP length(m), logarithmic likelihood function
m	discharge wire roughness, ionic mass(Kg), particle mass(Kg)
M_{air}	average molecular weight of air(28.9 Kg Kg-mol^{-1})
M_i	fraction by weight of ith particle size in inlet histogram
MMD	geometric mean mass diameter(μm)
MMD_a	arithmetic mean mass diameter(μm)
MND	geometric mean number diameter(μm)
MND_a	arithmetic mean number diameter(μm)
n	number of discharge wires
n_i	number of particles in particular size class
N	number of points in direction of gas flow for numerical integration of electric field, ion density(m^{-3}), total particle count, number of points in channel flow for which velocity or turbulence measurements are performed
N_{il}	number concentration of ith particles entering the ESP(m^{-3})
N_{ij}	number concentration of ith particles entering the jth length increment(m^{-3})
N_o	free ion density(m^{-3})
p	variable in polynomial approximation to normal integral, partial pressure of water vapor(mm Hg)
p_o	residual partial pressure of chemically bound component(mm Hg)
P	total pressure(atm), probability of observing a specific number of particles in a size interval
P_i	value of P(probability) for a specific size interval
Q	volumetric flow rate(am^3s^{-1}), particle charge(coul)
Q_s	particle saturation charge(coul)
r	constant, bulk electrical resistivity of precipitated dust layer(Ohm m)
r_{eff}	effective bulk electrical resistivity of precipitated dust layer(Ohm m)
r_i	radius of corona glow region(m)

r_o	distance from particle center at which the ion concentration(N) equals the free ion concentration(N_o)
r_s	surface bulk resistivity of precipitated dust layer (Ohm m)
r_v	volume bulk resistivity of precipitated dust layer (Ohm m)
R	fraction of dust reentrained, polynomial approximation to normal integral, recovery
R_1	grade of concentrate
R_2	ratio of concentration
Re_p	particle Reynold's number($\rho_{air} Dw/\mu$)
s	wire-to-plate spacing(m)
s_v^*	normalized standard deviation of velocity distribution
S	cumulative fraction undersize
SI	selectivity index
t	time(s), normalization variable of log-normal distribution, concentration in tailing
t^-	relaxation time of charge transfer from a dielectric(s)
T	absolute temperature(K), weight of tailing(Kg), particular value of t
v	jet velocity of cascade impactor stages(ms^{-1}), time averaged point velocity(ms^{-1})
$\hat{v}$	ion mean thermal velocity(ms^{-1})
v_{av}	average air velocity(ms^{-1})
$\sqrt{\overline{v^{-2}}}$	rms velocity from hot-wire anemometer(ms^{-1})
V	voltage(V), applied voltage(KV), point voltage from hot-wire anemometer(V)
V_e	electrostatic potential(V)
V_s	potential due to charged particle in external field, at the particle surface(V)
V_o	corona onset voltage(KV), potential due to charged particle in external field in region where the ion density(N) equals the free ion density(N_o)
$\sqrt{\overline{v^{-2}}}$	rms voltage from hot-wire anemometer(V)

X	coordinate transverse to gas flow relative to center point of inlet channel (m)
Y	coordinate parallel to gas flow relative to center point of inlet channel (m)
Z	empirical constant of effective resistivity model (mV^{-1}), vertical coordinate relative to center point of inlet channel (m)
Δ	ratio of drag on particle to that on equivalent volume sphere (Stokes' flow)
ΔV	voltage drop across dust layer (V)
Δx	dust layer thikness (mm)
θ	angle of approach of ions relative to undistorted exterior field (radians)
θ_o	maximum value of for ion bombardment (radians)
η	electrical non-cumulative collection efficiency by weight corrected with respect to mechanical collection, value of E_c for global ESP length
η'	non-cumulative fraction of precipitated dust
η_i'	fraction of inlet weight of component i collected in a particular length increment
η_{exp}	experimental value of η
η_{ij}	collection efficiency of the ith particle size in the jth length increment
η_{iL}	value of η_{ij} averaged over the entire ESP length (effective fractional collection efficiency)
η_{iL}^*	value of η_{iL} corrected for reentrainment
η_m'	fraction of inlet dust that sedimented
$\eta_{s_{ij}}$	separation efficiency of component i from j based on non-cumulative collection efficiencies
η_t	total collection efficiency ($\eta_m' + \eta'$)
ϵ	permittivity (Fm^{-1}), residue of polynomial approximation to normal integral, void fraction

ε_o	permittivity of vaccum(8.85×10^{-12} Fm^{-1})
$\bar{\nabla}$	nabla operator
∇^2	Laplacian operator
λ	parameter, molecular mean free path(m), migration velocity enhancement factor
μ	gas viscosity(Kg m^{-1} s^{-1})
ρ	particle density(gcm^{-3}), space charge(coul m^{-3})
ρ_{air}	air density($g\ cm^{-3}$)
ρ_d	dust space charge(coul m^{-3})
ρ_i	ionic space charge(coul m^{-3})
ρ_{ri}	ionic space charge at the boundary of the corona glow region(coul m^{-3})
$\sigma(S_i)$	binomial standard deviation of cumulative number undersize S_i
σ_g	geometric standard deviation of particle size distribution
τ	relative turbulence intensity, charging time constant(s)
τ_m	time constant of motion(s)
w	particle migration velocity(ms^{-1}), index that indicates weight
w_{exp}	experimental value of w (ms^{-1})
w_{ij}	migration velocity of ith particle size in jth length increment (ms^{-1})
w_{iL}	value of w_{ij} averaged over the entire ESP length (effective fractional migration velocity)
w^*_{iL}	value of w_{iL} corrected for dust reentrainment
w_o	saturation migration velocity(ms^{-1})
χ	ratio of diameter of equivalent volume sphere to the diameter of projected area equivalent sphere
ψ	ratio of surface area of equivalent volume sphere to that of particle(sphericity)
ϕ	appropriate function for least-squares log-normal fit

APPENDIX

Input/Output Data for the SRI Computer Model

For a complete description of the I/Ø data and format characteristics available in the computer model, the reader is referred to McDonald (1978 a, b). Here, only the more important I/Ø data are discussed. Pages A14 through A16 are an example of I/Ø data from the SRI computer program, as it was used in this study. The following is a brief description of the input variables, taken from McDonald et al. (1978 a, b):

NENDPT is the number of discrete points on a cumulative percent versus particle diameter curve.

NDATA is an indicator which tells the program to look for a certain type of data set. When NDATA = 1, a complete data set is input. This indicator is useful when constructing shortened data sets, i.e., when analysing the effect of some of the variables while all the others remain unchanged.

The statement of the second card is only used for identification purposes, and the values or variables are not used in the actual computation.

NEST is an indicator which can have the values 1 and 2. If NEST = 1, the program will evaluate the electric field at the plate using numerical integration of the appropriate equations. If NEST = 2, the program evaluates the electric field at the plate by scaling down the average electric field by the factor 1.75. In this study, NEST = 1.

NDIST is an indicator which can have the values of 1 or 2. If NDIST = 1, the user supplies the inlet particle size distribution. If NDIST = 2, the user supplies the parameters which describe a log-normal distribution, and the program calculates the input histogram.

NVI is an indicator which can have the values of 1 or 2. If NVI = 1, the user supplies known (measured) values of voltage and current. In this case, the numerical technique described in Chapter 2, Section 2.3.3 is used to estimate the field at the plate. If NVI = 2, the program constructs a voltage-current curve for a specified geometry up to a voltage specified by the user. In this study, NVI = 1.

NX is the number of grid points in the X direction

(transverse to the main gas flow) which is used in the numerical techniques that determine the electrical conditions. In this study, NX = 11.

NY is the number of grid points in the Y direction (parallel to the main gas flow) which is used in the numerical techniques that determine the electrical conditions. In this study, NY = 10.

NITER is an indicator whose function depends on NVI. When NVI = 1, the value of NITER determines the maximum value of iterations that the program will make in a loop which converges on the global mass collection efficiency. In this study, NITER = 3.

NCALC is an indicator which can have the values 0 and 1. When NCALC = 0, particle charge is calculated by Eq. 2.30. When NCALC = 1, particle charge is calculated by Eq. 2.32. In this study, NCALC = 1.

NRAPD is an indicator which depends on the rapping puff size distributions. When NRAPD = 1, the computer program uses a built-in distribution. In this study, the effect of rapping re-entrainment was neglected, by bypassing the corresponding output variables.

NEFF is an indicator which determines how the total mass re-entrained at the outlet due to rapping is estimated. In this study, the corresponding output was also bypassed.

NTEMP is an indicator which relates the total mass re-entrained due to rapping to whether the ESP is a cold-side or a hot-side unit. In this study, the corresponding output was bypassed.

NONID is an indicator which specifies the number of combinations of corrections due to non-uniform gas flow, sneakage and re-entrainment. In this study, NONID = 1, i.e., no corrections are applied.

DL is the inlet dust loading (grain ft^{-3}).

PL is the total electric length of the ESP (ft).

ETAO is the estimated global collection efficiency (%). If NVI = 1, ETAO may be the measured collection efficiency, and it is used as a test for convergence in an iteration loop for the global efficiency. A good value for ETAO is either the measured efficiency or the efficiency as calculated by Eqs. 2.40 or 2.41, assuming the average field at the plate to be equal to the average field in the interelectrode

spacing, or scaled down by some factor (between 1-2).

DD is the density of the particles (Kg/m^3). It is used in the program only to convert mass of particles to number of particles, for the estimation of the space-charge effects due to the particulates.

EPS is the dielectric constant of the particles (≥ 1).

VRATIO is the ratio of the peak voltage to the average voltage. In this study, VRATIO = 1.

US is the ionic mobility at standard temperature ($0^{\circ}C$) and pressure (1 atm). In this study, US = 1.65×10^{-4} $m^2 V^{-1} s^{-1}$, as recommended by McDonald (1978 a).

FPATH is a parameter used in the field charging equation which represents the number of ionic mean free paths over which the momentum of the ions will persist and allow the ions to reach the surface of the particle, even though the saturation charge has been reached. In this study, FPATH = 1, as recommended by McDonald (1978 a, b).

EBD is the electrical breakdown strength of the dust layer (V/m). When NVI = 1, this variable is not used for computational purposes.

RHO is the bulk resistivity of the collected layer (Ohm cm), and it is used only to estimate the average field in the particulate layer, by Eq. 2.46.

ASNUCK(I) is an array which contains information on gas sneakage and/or re-entrainment due to causes other than rapping. The index I runs from one to NONID, and the value of ASNUCK is represented by a correction factor given by Eqs. 2.56 and 2.57.

AZIGGY(I) is an array which contains information on non-uniformity of gas flow. In this study, AZIGGY(I) = 0.

AZNUMS(I) is an array containing the number of baffled stages in the ESP. In this study, AZNUMS(I) = 1. When ASNUCK(I) = AZIGGY(I) = 0 and AZNUMS(I) = 1, ideal efficiencies are obtained.

ENDPT(I) is an array of particle diameters corresponding to points on a curve of inlet mass cumulative percent versus particle diameter. The index I runs from one to NENDPT. The midpoints between successive particle diameters represent NENDPT-1 average particle diameters used in the program to characterize the different size bands.

PRCU(I) is an array containing values of cumulative percent undersize corresponding to points on a curve of inlet mass cumulative percent versus particle diameter. The index I runs from 1 to NENDPT, when NDIST = 1.

D50 is the median mass diameter of a log-normal inlet particle size distribution (μm), when NDIST = 2.

SIGMAP is the geometric standard deviation of a log-normal inlet particle size distribution, when NDIST = 2.

NUMSEC is the number of electrical sections in the direction of gas flow. In this study, NUMSEC = 1.

LSECT(I) is an array of values of the number of incremental lengths to be considered in each electrical section. The index I runs from one to NUMSEC, and in this study, LSECT(1) = 8.

AS(NSECT) is the total collection area for a given electrical section (ft^2). The index NSECT runs from one to NUMSEC, and in this study, AS(1) = 20.99.

VOS(NSECT) is the applied voltage in each electrical section (V).

TCS(NSECT) is the total current in each electrical section (A).

WLS(NSECT) is the total discharge wire length in a given electrical section (ft). In this study, WLS(1) = 18.95.

ACS(NSECT) is the corona wire radius for each electrical section (in). In this study, ACS(1) = 3.0906×10^{-2}.

BS(NSECT) is the wire-to-plate spacing in a given electrical section (in). In this study, BS(1) = 3.189.

NWS(NSECT) is the number of discharge electrodes in each electrical section. In this study, NWS(1) = 15.

SYS(NSECT) is one-half the wire-to-wire spacing in each electrical section (in). In this study, SYS(1) = 2.992.

VGS(NSECT) is the total gas volume flow rate in each electrical section (acfm).

VGASS(NSECT) is the gas velocity in a given electrical section (fts^{-1}).

TEMPS(NSECT) is the gas temperature in each electrical section (^{o}F).

PS(NSECT) is the gas pressure (absolute) in a given electrical section (atm). In this study, PS(1) = 1.

VISS(NSECT) is the gas viscosity in each electrical section ($Kg\ m^{-1}s^{-1}$).

LINCS(NSECT) is the incremental length in each electrical section (ft).

In this study, LINCS(1) = 1.0376. Values around one foot are recommended by McDonald (1978 a, b).

Typical input data is shown in pp. A14.

The output data is fundamentally divided into five sections. First, the input data is printed out. This is seen in page A14 . The second part concerns the incremental analysis of precipitator performance, and is shown in pp. A15. Here, the input data is converted to SI units, and it is self-explanatory. The other variables are (for each incremental length):

ROVRI - the ratio of total charge density to ionic charge density;

ERAVG - the average electric field in the inter-electrode spacing (Vm^{-1});

EPLT - the electric field at the plate (Vm^{-1});

AFID - the average free ion density (m^{-3});

CMCD - the average current density at the plate, calculated from the appropriate boundary condition of the numerical estimation of the electrical conditions ($nA\ cm^{-2}$).

MMD - the mass median diameter of the precipitated material (μm);

WEIGHT - the amount of precipitated material per volume of gas (Kg m_{gas}^{-3});

DUST LAYER - the rate of dust deposition at the plates (mm min^{-1});

J(PART) - the average current density at the plate due to particles (Am^{-2});

J(ION) - the average current density at the plate due to ions (Am^{-2}).

INCR. NO. - the increment number for which the calculations were performed.

The third part of the output data concerns the charging rates for each particle size in each incremental length, as shown in pp. A15. The charging rates are expressed as a fraction of the saturation charge. Eq. 2.32 was used to calculate the particle charges, and for the smaller particles the charge due to diffusion charging is significant. Under these conditions, the ratio of actual charge to saturation charge may exceed one. Particle diameters are in meters.

The fourth part of the output data concerns the actual charges acquired by the different particle sizes in the various incremental lengths, in coulomb. These are shown in pp. A16.

The last set of output data refers to the actual performance of the ESP, as a function of particle sizes, averaged over the entire length. This is shown in pp. A16. The first column shows the particle sizes (m) of the inlet histogram. The second column shows the Cunningham correction factor for each particle size. The next two columns show the inlet and outlet differential mass distributions. The last three columns show the effective ideal (no-rap) collection efficiencies (%), migration velocities (cm s^{-1}) and penetrations (%), for each particle size.

The last table shows information regarding the mean mass diameters (μm) and geometric standard deviations of both inlet and outlet distributions, and the least squares correlation coefficients (where appropriate), as discussed in Chapter 5. Also shown is the precipitation rate parameter, obtained by back-calculation from the Deutsch Equation (as applied to the entire ESP length) and the calculated global collection efficiency.

The data discussed above is only part of the data handling capability of the SRI computer program, since it is restricted to the case of estimation of precipitator performance under ideal conditions. The complete computer program as presented by McDonald (1978 a) contains the main program and 20 subroutines, with a total of 2240 cards.

In this study, the program was simplified, consisting of the main program and 13 subroutines, with a total of 1408 cards[1].

---

[1] A copy of the version of the program as used in the present study is available from Prof. R.J. Munz, Department of Chemical Engineering, McGill University, Montreal.

E.P.A. ESP MODEL
I.E.R.L.-R.T.P. AND SO.R.I.
REVISION: JAN.1,1978

PRINTOUT OF INPUT DATA FOR DATA SET NUMBER 1

DATA ON CARD NUMBER 1

NENDPT=20 NDATA= 1

DATA ON CARD NUMBER 2

LAB-ESP: CuO

DATA ON CARD NUMBER 3

NEST= 1 NDIST= 2 NVI= 1 NX=11 NY=10 NITER= 3 NCALC= 1 NRAPD= 1 NEFF= 1 NTEMP= 1 NONID= 1

DATA ON CARD NUMBER 4

DL= 0.002003RN/ACF PL= 8.3000FT ETAD= 70.00000% DD= 6400.00KG/M**3 EPS= 2.700E+01
VRATIO= 1.0000 US=0.000165M**2/V-SEC FPATH = 1.0000 EBD= 224000.V/M RHOCGS= 1.10E+08OHM-CM

DATA ON CARD NUMBER 5

ASNUCK(1)=0.0 AZIGGY(1)=0.0 AZNUMS(1)= 1.0

DATA ON CARD NUMBER 6

ENDPT(1)=	0.800UM	ENDPT(2)=	2.400UM	ENDPT(3)=	4.000UM	ENDPT(4)=	5.600UM	ENDPT(5)=	7.200UM
ENDPT(6)=	8.800UM	ENDPT(7)=	10.400UM	ENDPT(8)=	12.000UM	ENDPT(9)=	14.000UM	ENDPT(10)=	16.000UM

DATA ON CARD NUMBER 7

ENDPT(11)=	18.000UM	ENDPT(12)=	20.000UM	ENDPT(13)=	23.000UM	ENDPT(14)=	26.000UM	ENDPT(15)=	29.000UM
ENDPT(16)=	32.000UM	ENDPT(17)=	36.000UM	ENDPT(18)=	40.000UM	ENDPT(19)=	46.000UM	ENDPT(20)=	54.000UM

DATA ON CARD NUMBER 8

D50= 13.6000UM SIGMAP= 1.5900

DATA ON CARD NUMBER 9

NUMSEC= 1 LSECT(1)= 8

DATA ON CARD NUMBER 10

AS(1)= 2.0990E+01FT**2 VOS(1)= 2.5700E+04V TCS(1)= 2.0000E-04A WLS(1)= 1.8950E+01FT
ACS(1)= 3.0906E-02IN BS(1)= 3.1890E+00IN NWS(1)= 1.5000E+01

DATA ON CARD NUMBER 11

SYS(1)= 2.9920E+00IN VGS(1)= 6.5262E+02FT**3/MIN VGASS(1)= 1.6404E+01FT/SEC TEMPS(1)= 8.2400E+01F
PS(1)= 1.0000E+00ATM VISS(1)= 1.8400E-05KG/M-SEC LINCS(1)= 1.0376E+00FT

INCREMENTAL ANALYSIS OF PRECIPITATOR PERFORMANCE

LAB-ESP:-SCA=32.2FT2/1000ACFM;J=10.7UA/FT2

CALCULATION IS IN SECTION NO.= 1 AND THE SECTION LENGTH IS= 2.5317M

COLLECTION AREA= 1.952E+00M2
WIRE TO PLATE= 9.100E-02M
CURRENT/M= 3.460E-05AMP/M
1/2 WIRE TO WIRE= 7.600E-02M
TEMPERATURE= 300.778K
IONMOBILITY= 1.817E-04M2/VOLT-SEC
DUST WEIGHT= 1.414E-06KG/SEC

APPLIED VOLTAGE= 2.570E+04VOLTS
CORONA WIRE-RADIUS= 7.850E-04M
CURRENT DENSITY= 1.025E-04AMP/M2
GAS FLOWRATE= 3.087E-01M3/SEC
PRESSURE= 1.000ATM
MEAN THERMAL SPEED= 4.462E+02M/SEC
LENGTH INCR.=0.31646782M

TOTAL CURRENT= 2.000E-04AMPS
CORONA WIRE LENGTH= 5.780E+00M
DEPOSIT E FIELD= 1.127E+02VOLT/M
GAS VELOCITY= 5.003E+00M/SEC
VISCOSITY= 1.840E-05KG/M-SEC
PART. PATH PARAM.= 5.768E-08M
INPUT EFF./INCR.= 13.97

RDVRI	ERAVG	EPLT	AFID	CMCD	MMD	WEIGHT	DUST LAYER	J(PART)	J(ION)	INCR. NO
1.0010	3.173E+05	1.5134E+05	1.1098E+13	10.2	1.55E-05	4.358E-07	3.308E-05	1.08E-10	1.02E-04	1
1.0008	3.173E+05	1.5134E+05	1.1100E+13	10.2	1.51E-05	5.444E-07	4.132E-05	1.99E-10	1.02E-04	2
1.0006	3.173E+05	1.5134E+05	1.1102E+13	10.2	1.45E-05	5.347E-07	4.059E-05	2.38E-10	1.02E-04	3
1.0004	3.173E+05	1.5134E+05	1.1104E+13	10.2	1.40E-05	4.815E-07	3.655E-05	2.43E-10	1.02E-04	4
1.0003	3.173E+05	1.5134E+05	1.1105E+13	10.2	1.35E-05	4.163E-07	3.160E-05	2.32E-10	1.02E-04	5
1.0002	3.173E+05	1.5134E+05	1.1106E+13	10.2	1.29E-05	3.526E-07	2.676E-05	2.12E-10	1.02E-04	6
1.0002	3.173E+05	1.5134E+05	1.1107E+13	10.2	1.25E-05	2.953E-07	2.241E-05	1.90E-10	1.02E-04	7
1.0001	3.173E+05	1.5134E+05	1.1107E+13	10.2	1.21E-05	2.459E-07	1.866E-05	1.68E-10	1.02E-04	8

EST.EFFICIENCY= 70.00 UNCORRECTED COMPUTED EFFICIENCY= 72.19

INCREMENTAL ANALYSIS OF PRECIPITATOR PERFORMANCE

LAB-ESP:-SCA=32.2FT2/1000ACFM;J=10.7UA/FT2

CALCULATION IS IN SECTION NO.= 1 AND THE SECTION LENGTH IS= 2.5317M

COLLECTION AREA= 1.952E+00M2
WIRE TO PLATE= 9.100E-02M
CURRENT/M= 3.460E-05AMP/M
1/2 WIRE TO WIRE= 7.600E-02M
TEMPERATURE= 300.778K
IONMOBILITY= 1.817E-04M2/VOLT-SEC
DUST WEIGHT= 1.414E-06KG/SEC

APPLIED VOLTAGE= 2.570E+04VOLTS
CORONA WIRE-RADIUS= 7.850E-04M
CURRENT DENSITY= 1.025E-04AMP/M2
GAS FLOWRATE= 3.087E-01M3/SEC
PRESSURE= 1.000ATM
MEAN THERMAL SPEED= 4.462E+02M/SEC
LENGTH INCR.=0.31646782M

TOTAL CURRENT= 2.000E-04AMPS
CORONA WIRE LENGTH= 5.780E+00M
DEPOSIT E FIELD= 1.127E+02VOLT/M
GAS VELOCITY= 5.003E+00M/SEC
VISCOSITY= 1.840E-05KG/M-SEC
PART. PATH PARAM.= 5.768E-08M
INPUT EFF./INCR.= 14.79

RDVRI	ERAVG	EPLT	AFID	CMCD	MMD	WEIGHT	DUST LAYER	J(PART)	J(ION)	INCR. NO
1.0010	3.173E+05	1.5135E+05	1.1097E+13	10.2	1.55E-05	4.358E-07	3.308E-05	1.08E-10	1.02E-04	1
1.0008	3.173E+05	1.5135E+05	1.1100E+13	10.2	1.51E-05	5.443E-07	4.132E-05	1.99E-10	1.02E-04	2
1.0006	3.173E+05	1.5135E+05	1.1102E+13	10.2	1.45E-05	5.347E-07	4.059E-05	2.38E-10	1.02E-04	3
1.0004	3.173E+05	1.5135E+05	1.1104E+13	10.2	1.40E-05	4.815E-07	3.655E-05	2.43E-10	1.02E-04	4
1.0003	3.173E+05	1.5135E+05	1.1105E+13	10.2	1.35E-05	4.163E-07	3.160E-05	2.32E-10	1.02E-04	5
1.0002	3.173E+05	1.5135E+05	1.1106E+13	10.2	1.29E-05	3.526E-07	2.676E-05	2.12E-10	1.02E-04	6
1.0002	3.173E+05	1.5135E+05	1.1107E+13	10.2	1.25E-05	2.953E-07	2.241E-05	1.90E-10	1.02E-04	7
1.0001	3.173E+05	1.5135E+05	1.1107E+13	10.2	1.21E-05	2.459E-07	1.866E-05	1.68E-10	1.02E-04	8

CHARGING RATES FOR PARTICLE SIZES FROM SUBROUTINE CHGSUM

CLASSICAL FIELD CHARGE USED FOR PARTICLE CHARGING

INCREMENT NO. Q/QSATF FOR INDICATED PARTICLE SIZES

	0.1500E-05	0.3200E-05	0.4800E-05	0.6400E-05	0.8000E-05	0.9600E-05	0.1120E-04	0.1300E-04
1	0.5047	0.4476	0.4252	0.4129	0.4051	0.3998	0.3956	0.3921
2	0.6995	0.6301	0.6035	0.5891	0.5800	0.5737	0.5691	0.5651
3	0.8123	0.7356	0.7065	0.6909	0.6811	0.6743	0.6693	0.6650
4	0.8867	0.8047	0.7739	0.7575	0.7471	0.7400	0.7347	0.7302
5	0.9397	0.8537	0.8216	0.8044	0.7937	0.7863	0.7808	0.7762
6	0.9797	0.8904	0.8571	0.8394	0.8283	0.8207	0.8151	0.8103
7	1.0110	0.9189	0.8847	0.8665	0.8551	0.8473	0.8416	0.8367
8	1.0363	0.9417	0.9067	0.8881	0.8765	0.8685	0.8627	0.8577

	0.1500E-04	0.1700E-04	0.1900E-04	0.2150E-04	0.2450E-04	0.2750E-04	0.3050E-04	0.3400E-04
1	0.3891	0.3968	0.3849	0.3830	0.3812	0.3797	0.3786	0.3774
2	0.5617	0.5591	0.5569	0.5548	0.5527	0.5511	0.5498	0.5485
3	0.6614	0.6586	0.6563	0.6540	0.6518	0.6501	0.6487	0.6470
4	0.7264	0.7239	0.7211	0.7187	0.7164	0.7146	0.7131	0.7117
5	0.7722	0.7692	0.7667	0.7642	0.7619	0.7600	0.7585	0.7570
6	0.8061	0.8031	0.8006	0.7980	0.7956	0.7937	0.7921	0.7906
7	0.8325	0.8291	0.8267	0.8241	0.8217	0.8197	0.8181	0.8166
8	0.8535	0.8502	0.8475	0.8449	0.8424	0.8404	0.8388	0.8372

	0.3800E-04	0.4300E-04	0.5000E-04
1	0.3763	0.3753	0.3741
2	0.5473	0.5461	0.5448
3	0.6460	0.6449	0.6434
4	0.7104	0.7091	0.7076
5	0.7557	0.7543	0.7529
6	0.7892	0.7879	0.7863
7	0.8152	0.8137	0.8122
8	0.8358	0.8343	0.8328

CHARGE ACCUMULATED ON PARTICLE SIZES IN EACH INCREMENT

INCREMENT	CHARGE FOR INDICATED PARTICLE SIZES							
	0.1600E-05	0.3200E-05	0.4800E-05	0.6400E-05	0.8000E-05	0.9600E-05	0.1120E-04	0.1300E-04
1	0.31832E-15	0.11204E-15	0.24138E-15	0.41673E-15	0.63979E-15	0.90745E-15	0.12226E-14	0.16327E-14
2	0.44121E-16	0.15497E-15	0.34259E-15	0.59454E-15	0.91464E-15	0.13028E-14	0.17588E-14	0.23530E-14
3	0.51237E-16	0.18559E-15	0.40109E-15	0.69731E-15	0.10740E-14	0.15312E-14	0.20686E-14	0.27692E-14
4	0.55928E-16	0.20304E-15	0.43936E-15	0.76445E-15	0.11781E-14	0.16803E-14	0.22708E-14	0.30407E-14
5	0.59274E-16	0.21540E-15	0.46640E-15	0.81185E-15	0.12515E-14	0.17854E-14	0.24133E-14	0.32320E-14
6	0.61794E-16	0.22465E-15	0.48657E-15	0.84715E-15	0.13062E-14	0.18635E-14	0.25191E-14	0.33741E-14
7	0.63769E-16	0.23184E-15	0.50202E-15	0.87449E-15	0.13485E-14	0.19240E-14	0.26010E-14	0.34839E-14
8	0.65363E-16	0.23760E-15	0.51472E-15	0.89631E-15	0.13822E-14	0.19722E-14	0.26662E-14	0.35714E-14
	0.1500E-04	0.1700E-04	0.1900E-04	0.2150E-04	0.2450E-04	0.2750E-04	0.3050E-04	0.3400E-04
1	0.21573E-14	0.27543E-14	0.34237E-14	0.43622E-14	0.56377E-14	0.70759E-14	0.86767E-14	0.10750E-13
2	0.31140E-14	0.39808E-14	0.49536E-14	0.63185E-14	0.81745E-14	0.10269E-13	0.12601E-13	0.15622E-13
3	0.36667E-14	0.46895E-14	0.58375E-14	0.74486E-14	0.96401E-14	0.12113E-13	0.14868E-13	0.18437E-13
4	0.40272E-14	0.51516E-14	0.64138E-14	0.81854E-14	0.10595E-13	0.13315E-13	0.16345E-13	0.20271E-13
5	0.42911E-14	0.54770E-14	0.68195E-14	0.87040E-14	0.11268E-13	0.14161E-13	0.17385E-13	0.21562E-13
6	0.44697E-14	0.57186E-14	0.71208E-14	0.90890E-14	0.11767E-13	0.14789E-13	0.18156E-13	0.22519E-13
7	0.46154E-14	0.59053E-14	0.73534E-14	0.93862E-14	0.12152E-13	0.15274E-13	0.18751E-13	0.23258E-13
8	0.47314E-14	0.60538E-14	0.75386E-14	0.96228E-14	0.12458E-13	0.15659E-13	0.19225E-13	0.23846E-13
	0.3900E-04	0.4300E-04	0.5000E-04					
1	0.13391E-13	0.17096E-13	0.23044E-13					
2	0.19472E-13	0.24878E-13	0.33557E-13					
3	0.22985E-13	0.29374E-13	0.39631E-13					
4	0.25275E-13	0.32303E-13	0.43588E-13					
5	0.26885E-13	0.34364E-13	0.46371E-13					
6	0.28080E-13	0.35892E-13	0.48436E-13					
7	0.29002E-13	0.37072E-13	0.50029E-13					
8	0.29736E-13	0.38010E-13	0.51296E-13					

PARTICLE SIZE RANGE STATISTICS

CORRECTIONS FOR NONIDEALITIES USING SET NO. 1 OF CORRECTION PARAMETERS

SIZE	CCF	INLET%	OUTLET%	NO-RAP EFF.	NO-RAP W	NO-RAP P
1.600E-06	1.091	0.009	0.0270	18.4344	3.222	81.5656
3.200E-06	1.045	0.407	1.0264	29.7989	5.595	70.2011
4.800E-06	1.030	2.369	5.1530	39.5027	7.947	60.4973
6.400E-06	1.023	5.726	10.7421	47.8313	10.290	52.1687
8.000E-06	1.018	8.881	14.3736	54.9955	12.626	45.0045
9.600E-06	1.015	10.753	15.0164	61.1657	14.957	38.8343
1.120E-05	1.013	11.215	13.5166	66.4837	17.286	33.5163
1.300E-05	1.011	13.133	13.4114	71.5965	19.904	28.4035
1.500E-05	1.010	11.208	9.5265	76.3642	22.809	23.6358
1.700E-05	1.009	9.023	6.3824	80.3291	25.713	19.6709
1.900E-05	1.008	6.997	4.1199	83.6273	28.615	16.3727
2.150E-05	1.007	7.421	3.4738	86.9821	32.241	13.0179
2.450E-05	1.006	4.746	1.6875	90.1124	36.590	9.8876
2.750E-05	1.005	2.990	0.8076	92.4890	40.938	7.5110
3.050E-05	1.005	1.874	0.3846	94.2937	45.283	5.7063
3.400E-05	1.004	1.461	0.2175	95.8585	50.352	4.1415
3.800E-05	1.004	0.790	0.0816	97.1287	56.144	2.8713
4.300E-05	1.003	0.570	0.0373	98.1831	63.381	1.8169
5.000E-05	1.003	0.430	0.0148	99.0424	73.509	0.9576

EFFICIENCY-STATED=72.19 COMPUTED= 72.1918 CONVERGENCE OBTAINED

ADJUSTED NO-RAP EFF. = 72.1918
MMD OF INLET SIZE DISTRIBUTION= 1.360E+01
SIGMAP OF INLET SIZE DISTRIBUTION= 1.590E+00
MMD OF EFFLUENT UNDER NO-RAP CONDITIONS= 1.067E+01
SIGMAP OF EFFLUENT UNDER NO-RAP CONDITIONS= 1.527E+00
LOG-NORMAL GOODNESS OF FIT= 1.000
PRECIPITATION RATE PARAMETER UNDER NO-RAP CONDITIONS= 20.239

SIGMAG= 0.0 WITH 0.0 SNEAKAGE OVER 1.000 STAGES

REFERENCES

McDonald, J.R. (1978 a) - "A Mathematical Model of Electrostatic Precipitation, Revision 1, Volume I: Modelling and Programming."
Contract SRI/EPA 68-02-2114
EPA - 600/7-78-111a

McDonald, J.R. (1978 b) - "A Mathematical Model of Electrostatic Precipitation, Revision 1, Volume II: User Manual."
Contract SRI/EPA 68-02-2114
EPA-600/7-78-111b

APPENDIX B

B.1 Electrical Characteristics of Laboratory-Scale ESP with Clean Plates

The experimental data on voltage-current characteristics obtained with laboratory air at room temperature, pressure and humidity are shown in Fig. B.1, where (i) is the secondary current as read from the power supply control board. It is observed that an increased humidity reduces the current obtained at the same voltage level. This is consistent with a reduction in the equivalent ion mobility, as explained in Chapter 2, because the mobility of H_2O ions is smaller than that of O_2 ions (Oglesby et al., 1978).

Fig. B.2 shows the relationship between the total current as measured by the ammeter at the power supply control board (i) and as measured by the milliameters directly connected to the ESP plates ($i_1 + i_2$), under the three experimental conditions for which the measurements were taken, and the agreement is excellent. The current measured by the milliammeters at the collection plates is used to generate the current distribution along the ESP length. These results are shown in Fig. B.3, where the current to the first 1.25m long plate (i_I) is directly measured by one of the milliammeters (i_1). The second milliammeter (i_2) measures the current from the opposite 1.25m long plate plus the current from

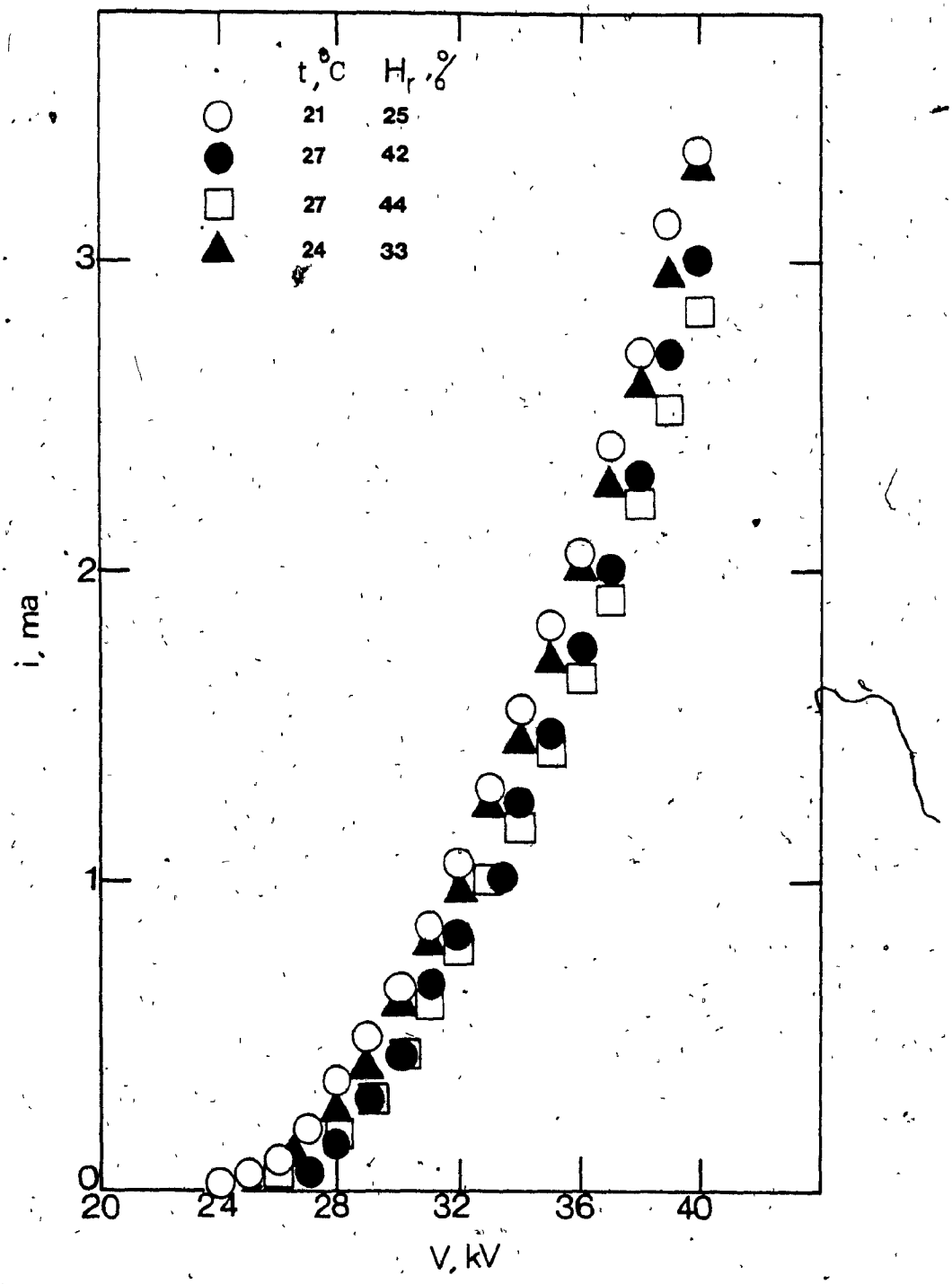


Figure B.1 Clean-plate voltage-current characteristics of laboratory-scale ESP

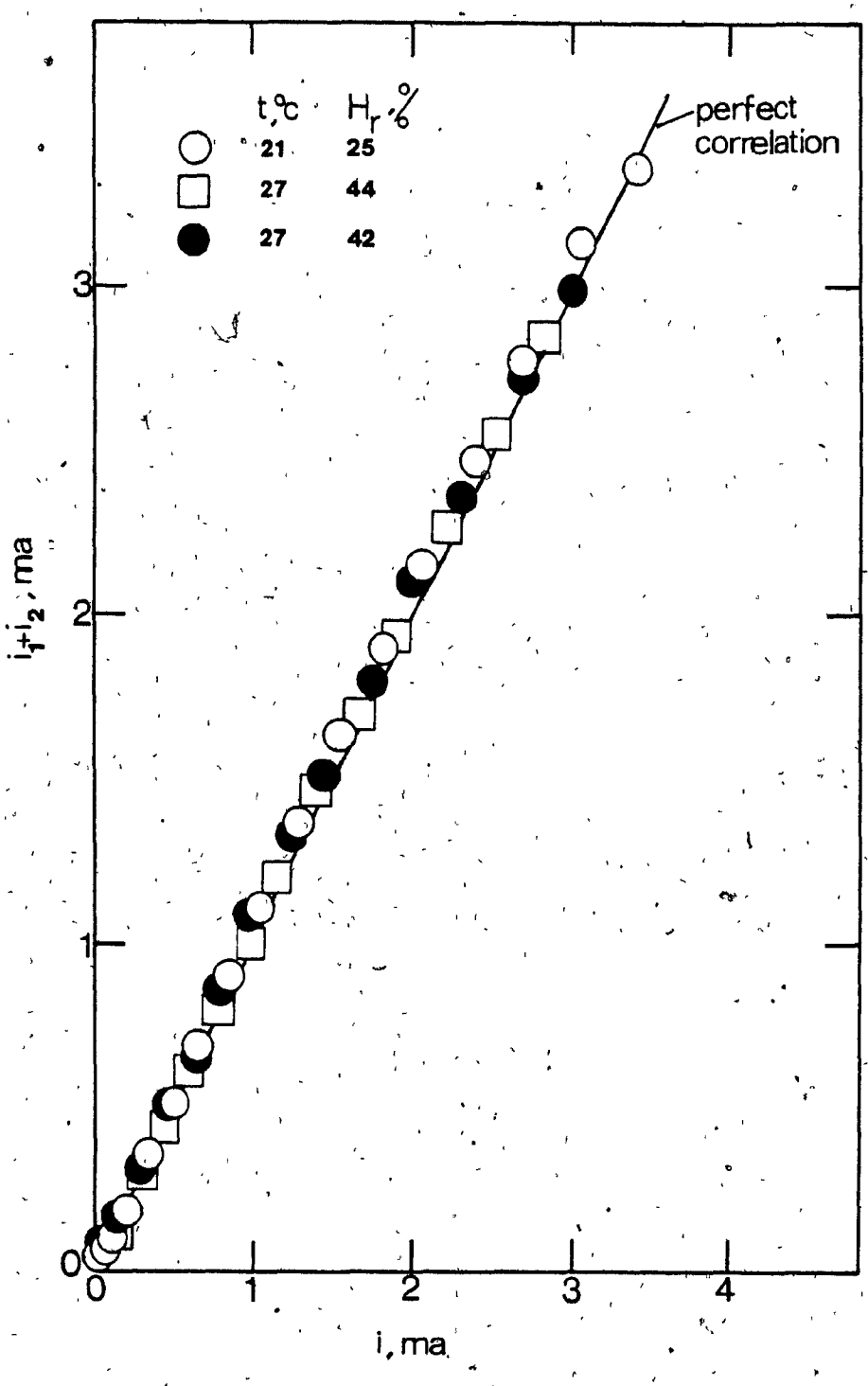


Figure B.2 Relation between total secondary current (i) from the power supply and along the ESP length ($i_1 + i_2$)

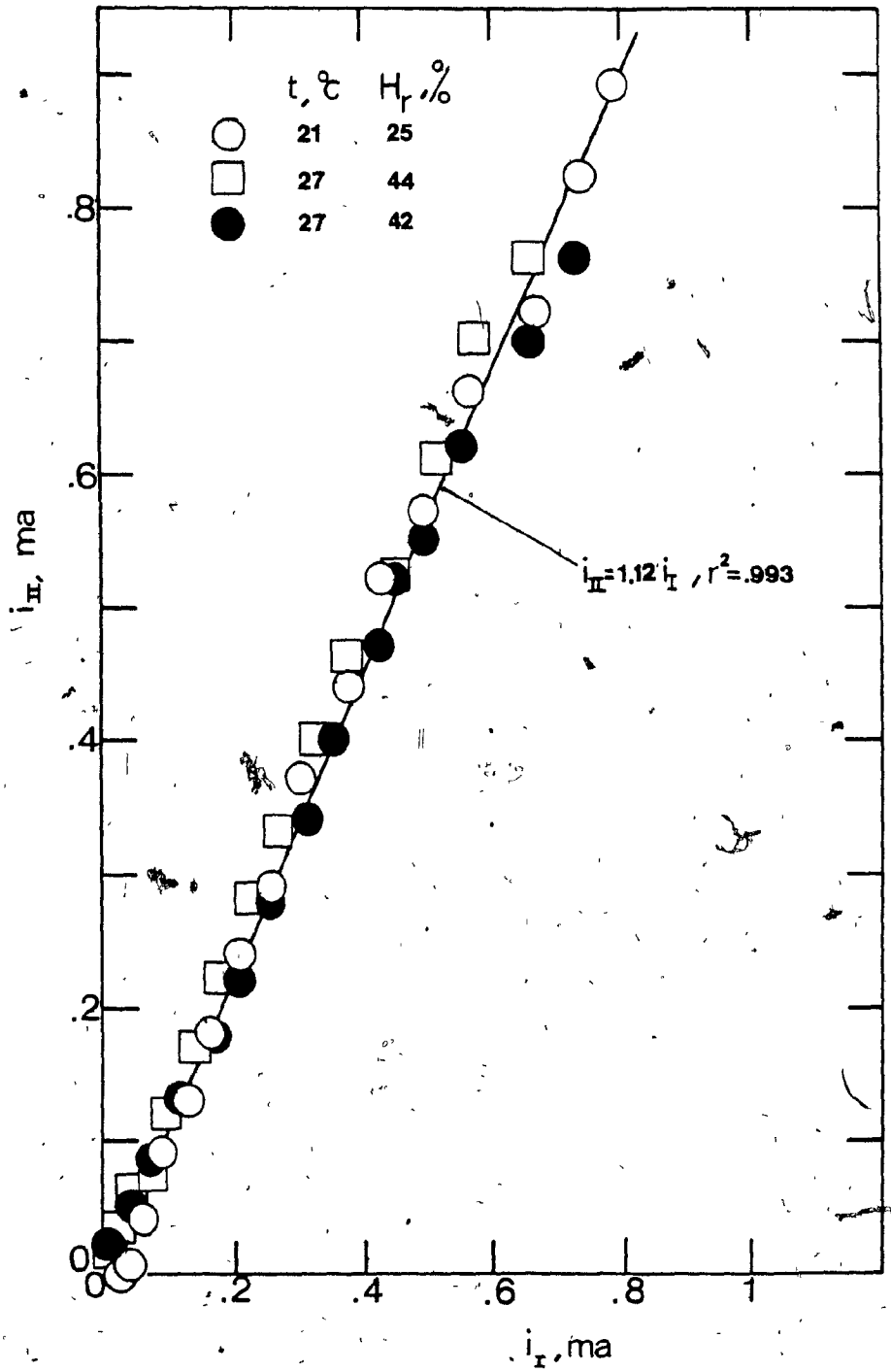


Figure B.3 Relation between current to the first plate (i_I) and current to the second plate (i_{II})

the two longer 1.28m plates which are placed in series with the shorter plates. Then, assuming symmetry, the current to one of the longer plates (i_{II}) is given by $(i_2 - i_1)/2$.

A linear least-squares fitting of the data of Fig. B.3 shows that the current to the second plates is larger by about 12% than the current to the first plates. This is probably due to the facts that the second plate is longer and that the eighth corona wire from the ESP inlet is 3cm downstream of the beginning of the longer plates, such that it will contribute to their current somewhat more significantly than to the current of the first (shorter) plates.

Fig. B.4 shows the hysteresis effect observed when the voltage-current characteristics are determined by increasing or decreasing the applied voltage. The current observed when decreasing the voltage is always smaller. Since the relative humidity did not change during the time required to obtain the data for each ascending-descending method, the reason for the observed discrepancy must be another cause, which at present is not known. In any case, the effect is small.

The corona onset voltage was experimentally determined by measuring very small currents with a microammeter. An applied voltage of 21 KV produces a current of about 2μA.

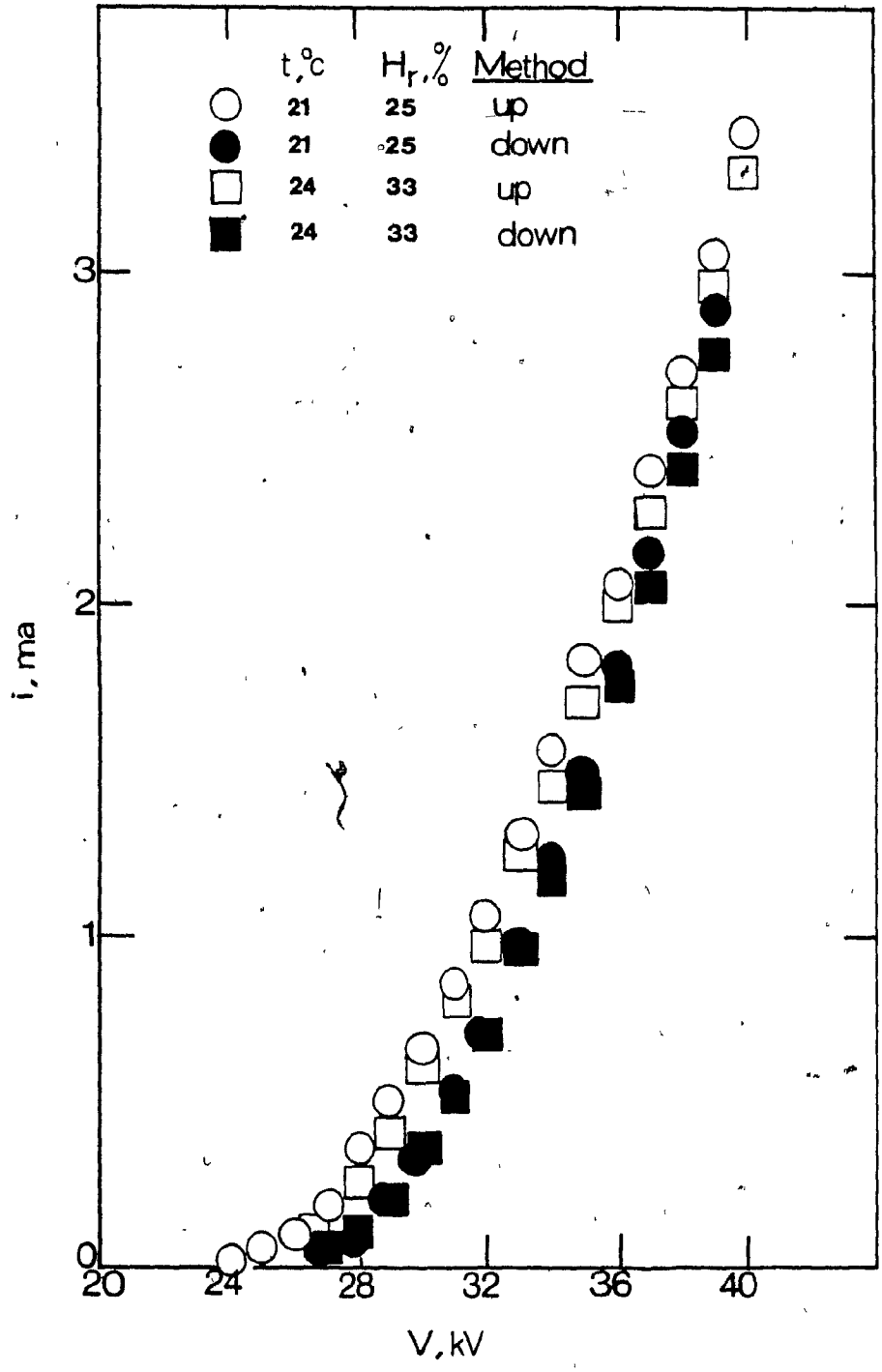


Figure B.4 Hysteresis of clean-plate voltage-current characteristics

Below 21 KV the readings are unstable. If the corona onset voltage is estimated from Eqs. 2.6 and 2.8 (Chapter 2), then the assumption of smooth wires gives $V_o \sim 25$ KV. The lower experimental value is probably due to two effects (Robinson, 1965): the effect of some wire roughness and the effect of the two neighbourless wires near the inlet and outlet of the ESP which both tend to decrease V_o. The corona onset value is only informative, since it was not used in this study.

B.2 Gas Flow Characteristics

The Venturi meter used for gas flow measurements was constructed according to ASME design (Bean, 1971). One difference with respect to the ASME design is that the Venturi meter was fabricated of welded sheet metal instead of being machined. The critical dimensions of the Venturi meter are: ratio of throat diameter to pipe diameter = 0.45; throat area = $3.763 \times 10^{-3} m^2$; included angle of smaller cone = 21^o; included angle of larger cone = 10^o; length of smaller cone = 25.5cm.

Since the Venturi discharge coefficient may be a function of Reynolds number and type of Venturi, it was experimentally determined at four different flow rates, using a Pitot (Prandtl type, i.e. static-dynamic probe) and micromanometer assembly.

In the micromanometer, Meriam fluid of specific gravity one was used. The thickness of the Pitot tube probe was 3.1mm, and traversing was done immediately downstream from the ESP outlet contraction. The discharge coefficient of the standard Pitot tube was taken as 0.99, as recommended by Smith et al. (1977), and the velocity at any sampling point was found from:

$$v = 0.99 \sqrt{\frac{2\ \Delta P}{\rho_{air}}} \qquad (B.1)$$

where (ΔP) is the differential pressure given by the micromanometer and ρ_{air} is air density at the sampling point conditions. The blower was turned on and the temperature was allowed to stabilize. This is necessary due to an initial heating-up of the blower. The temperature was read from a thermometer located near the sampling station. All measurements for the Venturi calibration were performed at about 26°C and near atmospheric pressure.

Fig. B.5 shows the four horizontal profiles and one vertical profile obtained with four different pressure differentials through the Venturi meter. The reason the profiles are shown as the product (vr) as a function of distance from the center (r) is for convenience in obtaining the average velocity by (Foust et al., 1960):

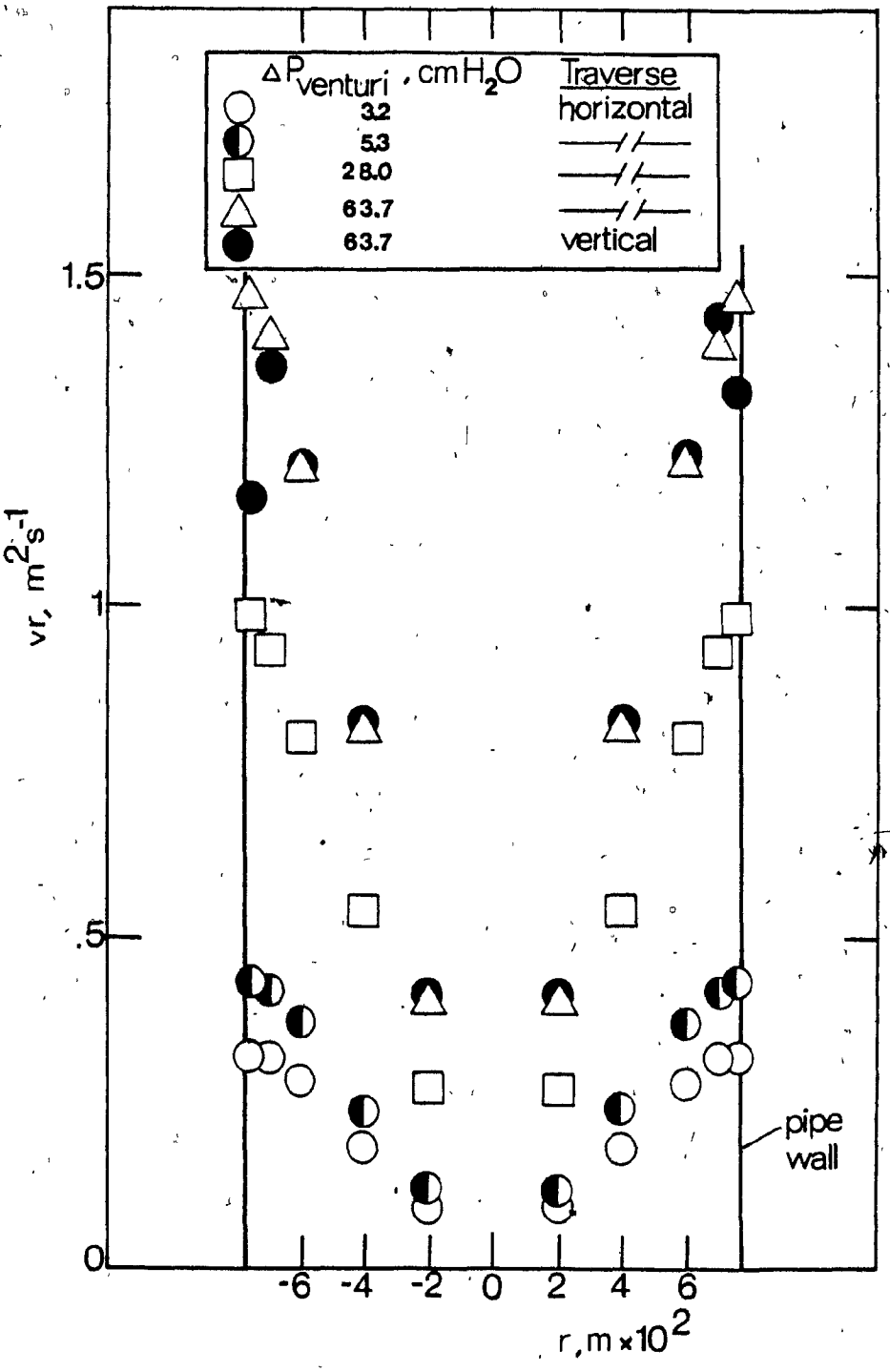


Figure B.5 Velocity profiles at the ESP outlet, used to calibrate the Venturi meter

$$v_{av} = \frac{2}{R^2} \int_0^R vr\, dr \qquad (B.2)$$

which is valid for a symmetrical profile around the center of the pipe of radius (R). For unsymmetrical profiles, the average velocity is calculated for each side of the tube.

From the integration of the velocity profiles, an average velocity (v_{av}) was determined for each pressure differential at the Venturi meter. The corresponding values were converted to volume flow rates by multiplying by the pipe flow area. The Venturi meter discharge coefficient (C_V) was found from the standard Venturi equation (Perry et al., 1973), which for this particular Venturi is:

$$C_V = \frac{Q}{5.43 \times 10^{-3} \gamma} \sqrt{\frac{\rho_{air}}{\Delta P}} \qquad (B.3)$$

where (C_V) is the discharge coefficient, (Q) is volumetric flow rate, (γ) is expansion coefficient, ρ_{air} is air density at upstream pressure and (ΔP) is the difference between the upstream and downstream pressures at the Venturi. The expansion coefficient was estimated at between 0.99 - 1.00 for the measured range of pressure differentials at the Venturi meter, and Eq. B.3 reduces to:

$$C_v = \frac{Q}{5.40 \times 10^{-3}} \sqrt{\frac{\rho_{air}}{\Delta P}} \qquad (B.4)$$

Table B.1 shows the discharge coefficient as a function of throat Reynolds number, determined by graphical integration of the velocity profiles, using the trapezoidal rule (Fig. B.5).

Table B.1

Venturi Discharge Coefficient

Re(throat) x 10^{-5}	Traverse	C_v
1.0	Horizontal	0.946
1.3	"	0.960
2.9	"	0.944
4.5	Horizontal + Vertical	0.956

The average discharge coefficient is $C_v = 0.95 \pm 0.01$, and is practically independent of the experimental range of Re.

For smooth Venturis in this range of Re, the discharge coefficient should be around 0.96-0.99 (Streeter et al., 1975); the lower experimental value is probably due to non-recoverable friction losses due to the rougher internal surface of the fabricated Venturi meter.

Velocity profiles were determined at the ESP inlet using both a standard 3.1mm diameter Prandtl Pitot tube and micromanometer assembly, and a hot-wire anemometer (DISA probe type SS P14, Thermo-Systems Inc., Cleveland Ave. North, St. Paul, Minnesota). The hot-wire anemometer was calibrated with the Pitot tube, using linearization techniques described in the manufacturer's literature, at the center point of the channel flow.

Sampling was performed with a traversing guide, at predetermined positions at the ESP inlet, by using the appropriate sampling ports. The location of the ports and the corresponding sampling points are shown in Fig. B.6.

The velocity profiles at the ESP inlet for the final choice of guiding vanes positioning at the inlet expansion and with the plenum chamber installed are shown in Figs. B.7, B.8, B.9 and B.10.

The relative turbulence intensities as determined by hot-wire anemometry at the ESP inlet are shown in Figs. B.11 and B.12.

B.3 Calibration of the Tafa Feeder with Copper Oxide

The Tafa vibrating feeder was calibrated for use with the copper oxide described in Chapter 5. The reason for the calibration is to determine the accuracy of the sampling system.

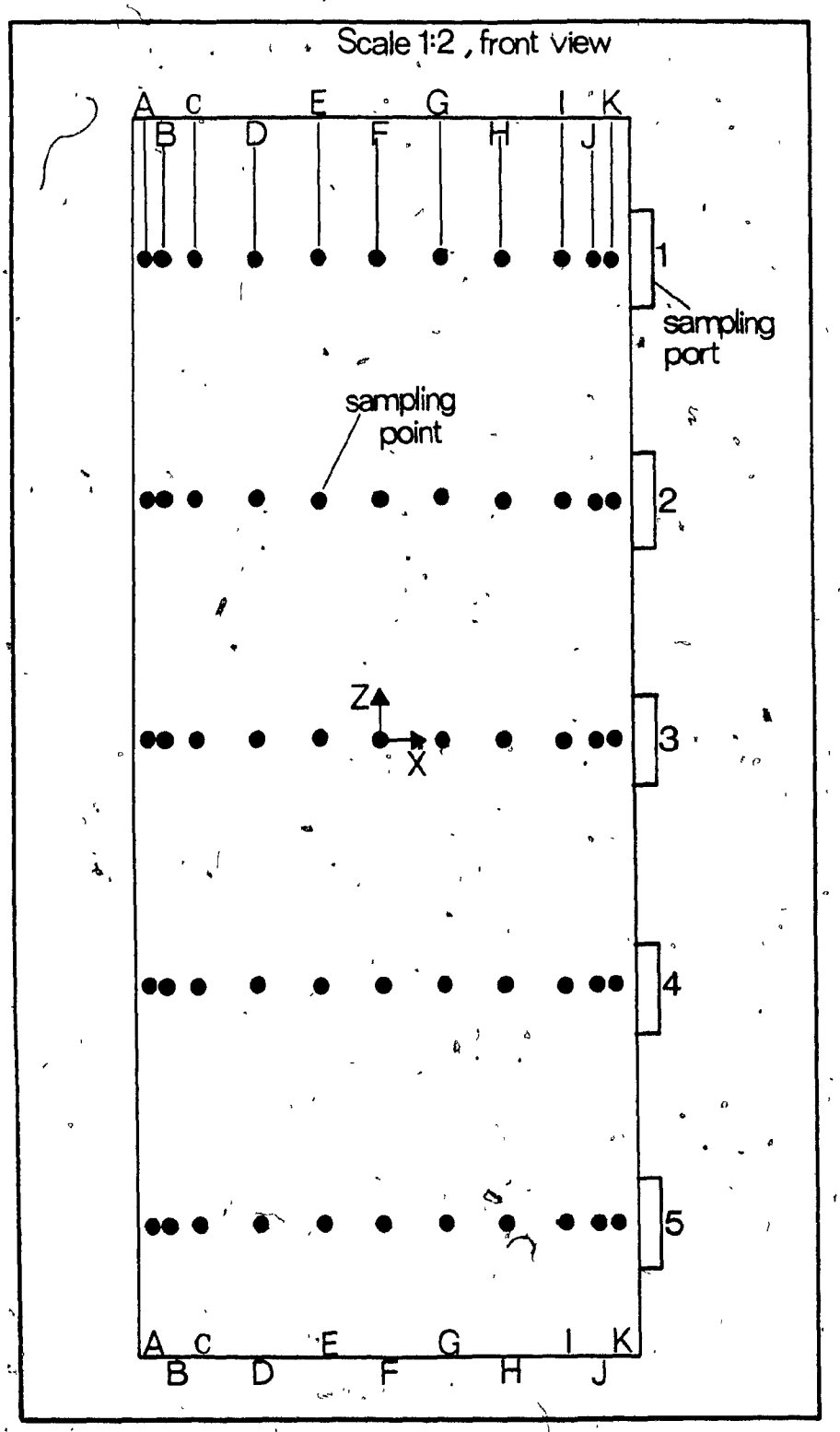


Figure B.6 Sampling location at the ESP inlet for velocity and turbulence measurements

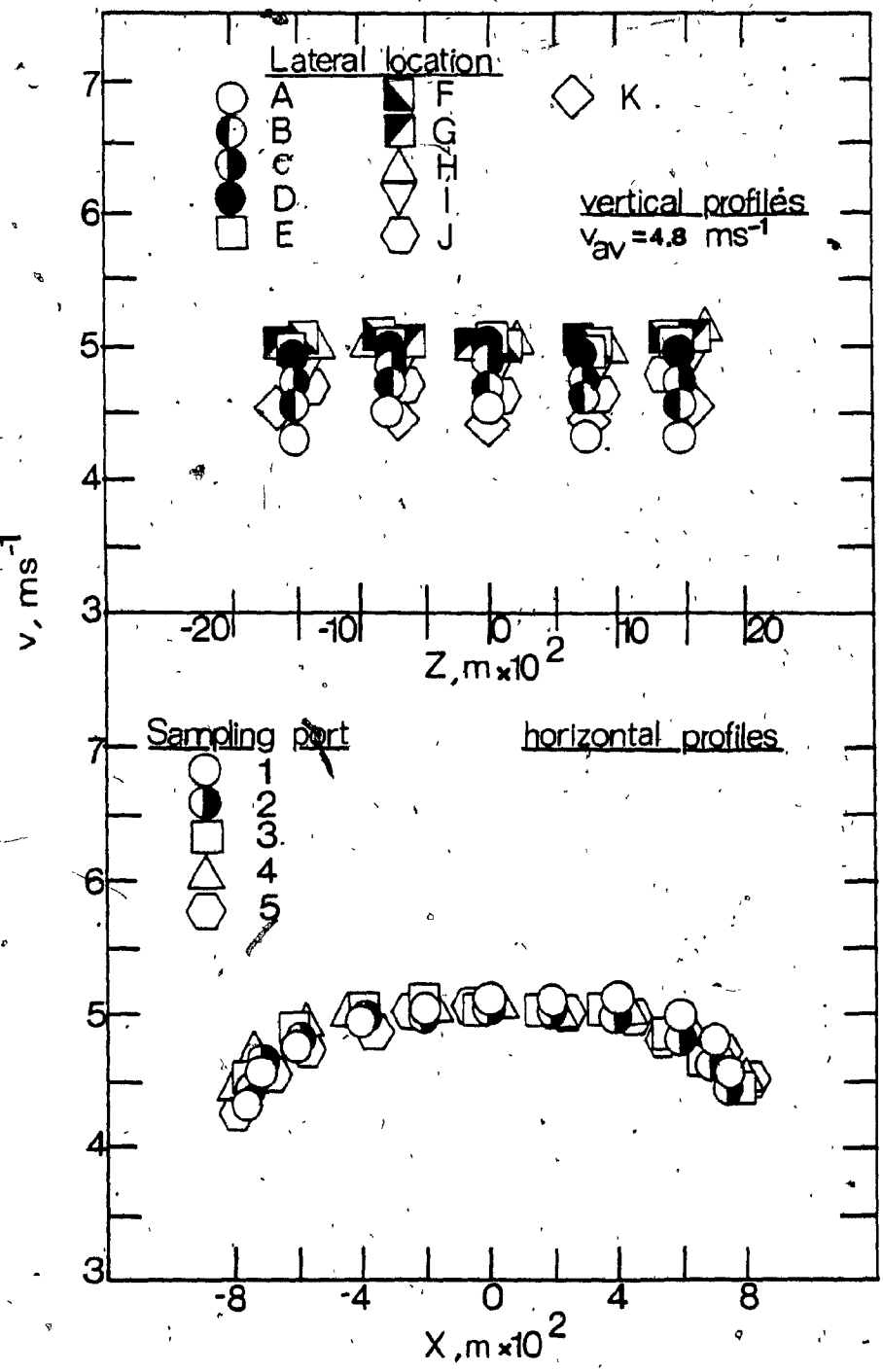


Figure B.7 Velocity profiles at the ESP inlet, obtained with a pitot tube at an average velocity of 4.8 ms^{-1}

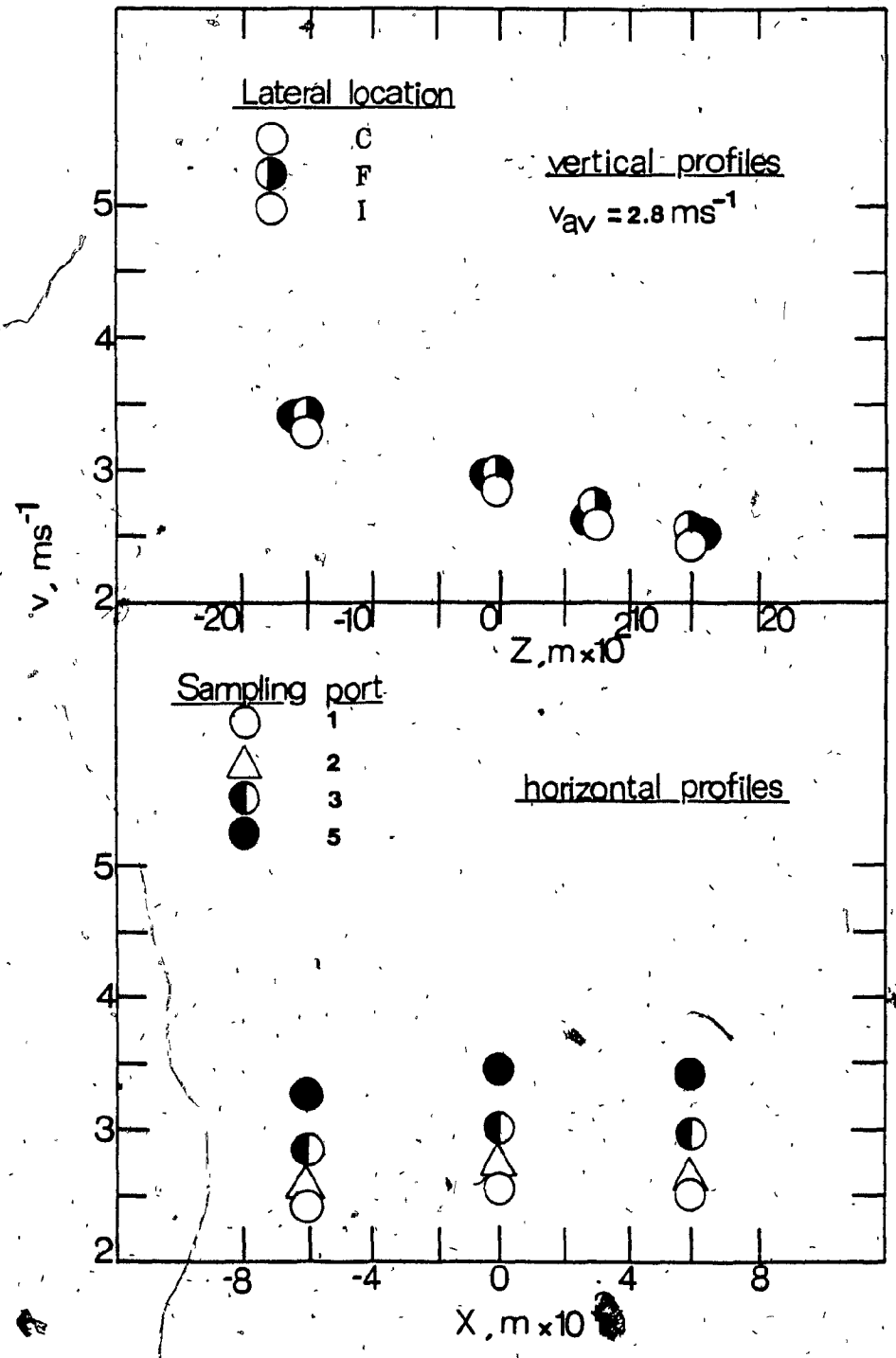


Figure B.8 Velocity profiles at the ESP inlet, obtained with a pitot tube at an average velocity of 2.8 ms^{-1}

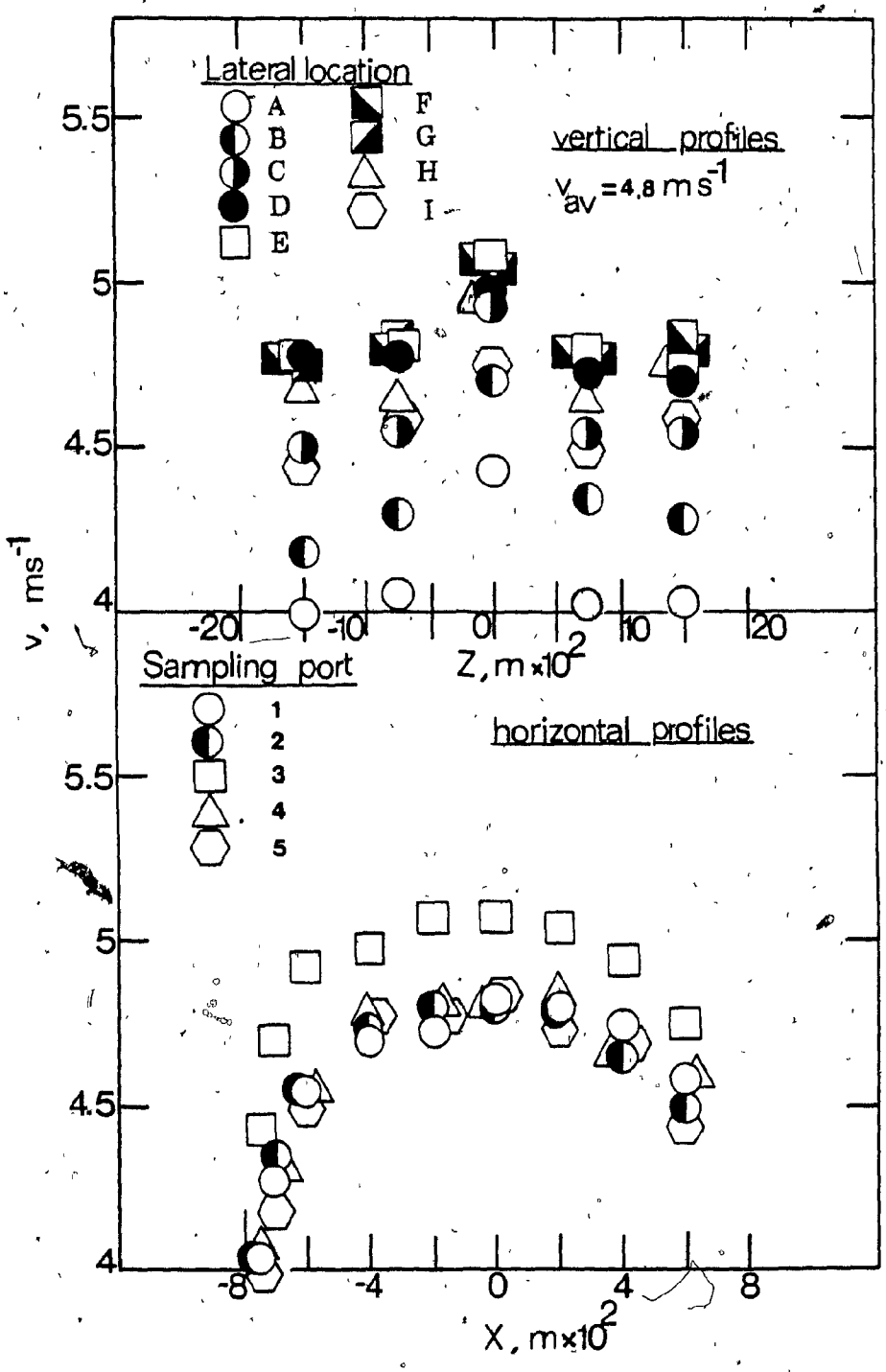


Figure B.9 Velocity profiles at the ESP inlet, obtained with a hot-wire anemometer at an average velocity of 4.8 ms^{-1}

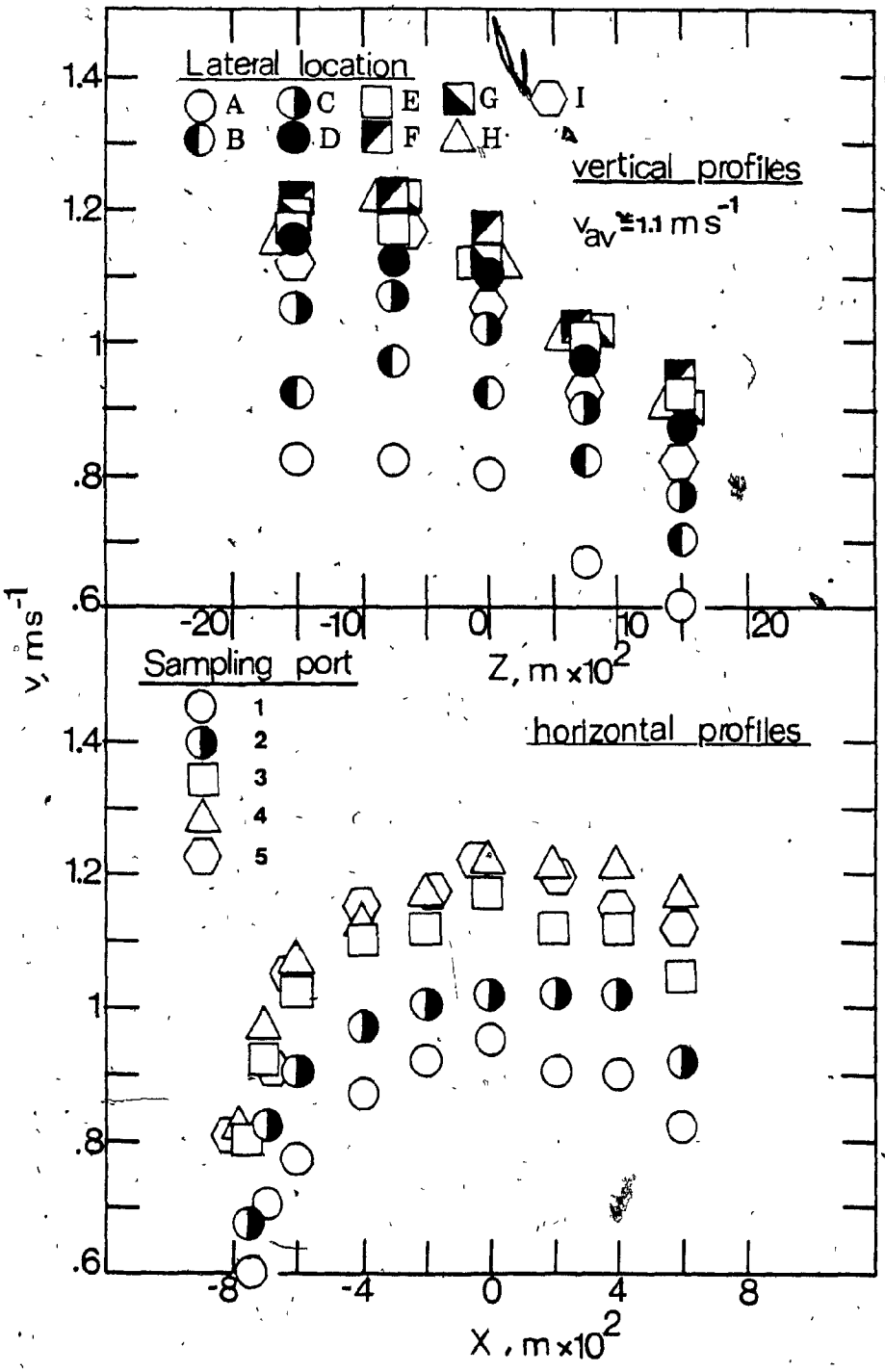


Figure B.10 Velocity profiles at the ESP inlet, obtained with a hot-wire anemometer at an average velocity of 1.1 ms^{-1}

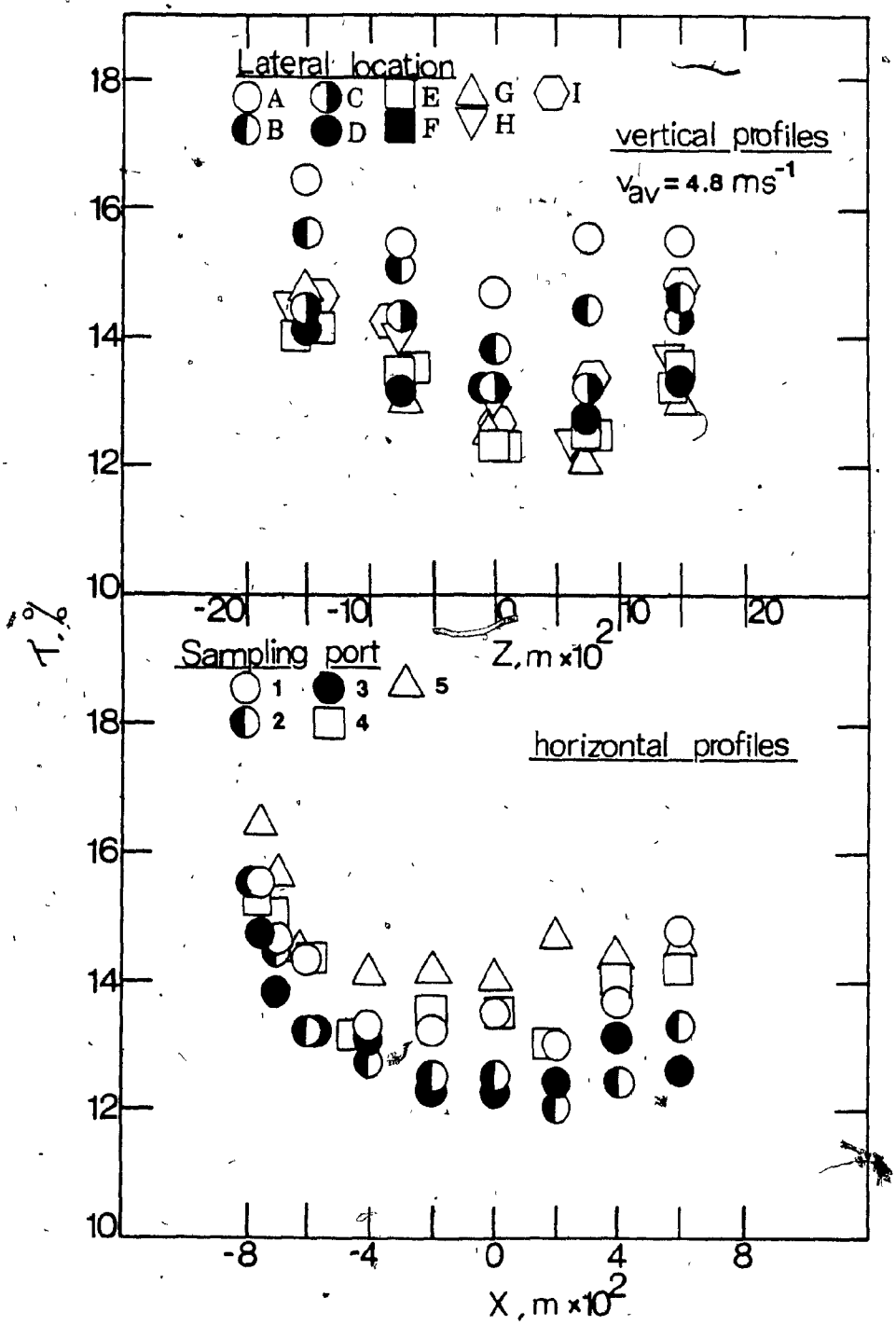


Figure B.11 Relative turbulence intensities at the ESP inlet, at an average velocity of 4.8 ms^{-1}

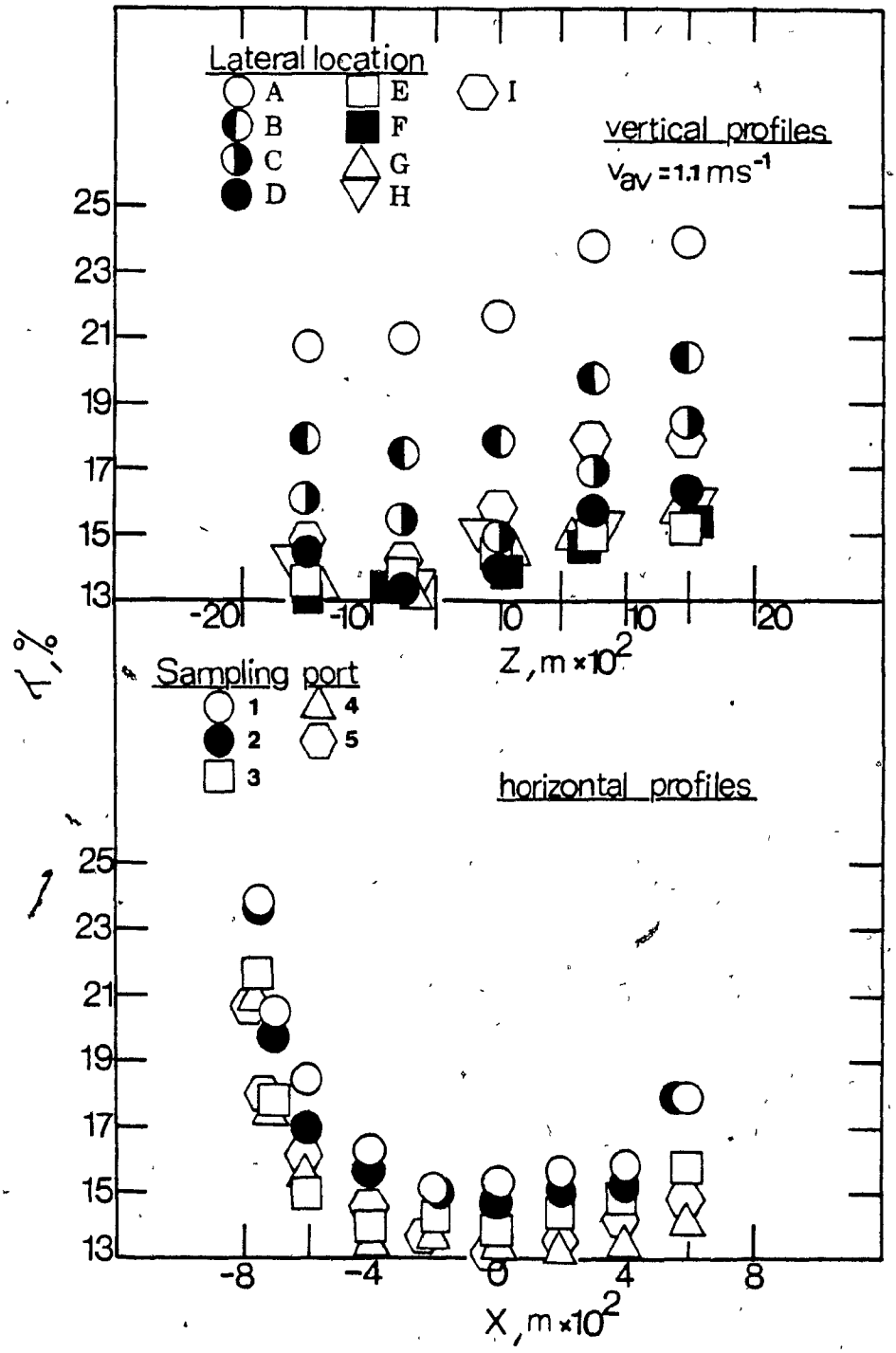


Figure B.12 Relative turbulence intensities at the ESP inlet, at an average velocity of 1.1 ms^{-1}

A sampling container was designed to collect the dust pneumatically conveyed by the Tafa feeder, and the input voltage to the feeder was measured by a digital voltmeter. The sampling reservoir was a polyethylene bottle with an inlet port and an outlet high surface area paper filter.

It was found that the collection efficiency of the sampling container was 100% over all conditions tested. Sampling times varied from 5 min at the lower voltages to 2 min at the higher voltage. To avoid plugging of the outlet line from the feeder at high feed rates, the air flow through the feeder was increased correspondingly. Table B.2 shows the approximate Tafa feeder rotameter flow rates necessary to avoid line plugging at the various input voltages to the feeder, using the copper oxide described in Chapter 5.

Table B.2

Tafa Feeder Conditions for CuO

(1atm, 25°C)

Input Voltage (ac V)	Air Flowrate ($lmin^{-1}$)
50-70	4-6
70-80	6-10
80-90	10-14
90-110	>14

Fig. B.13 shows the calibration curve for the Tafa feeder rotameter, as determined with both dry and wet test meters, at room temperature and pressure, using dry air from a compressed air tank.

Fig. B.14 shows the output rate of CuO from the Tafa Feeder, at various input voltages to the vibrating ramp. The number of samples varied from 5 at the higher voltages to 17 at the lower voltages. The high uniformity of feed rates obtained with the Tafa feeder and CuO is apparent from Fig. B.13. Below about 65 Vac, the feed rate declines sharply and no feed could be obtained at an applied voltage of 45 Vac or less. At all voltages above 60 V, the 95% confidence intervals represent less than four percent of the average value, while at 60 V it represents about 8% of the average value.

B.4 Calibration Curve of the Wright Feeder Rotameter

Fig. B.15 shows the calibration curve for the rotameter used to measure the air flow rate through the Wright feeder, obtained at atmospheric conditions of pressure and temperature, using dry compressed air and a dry test meter.

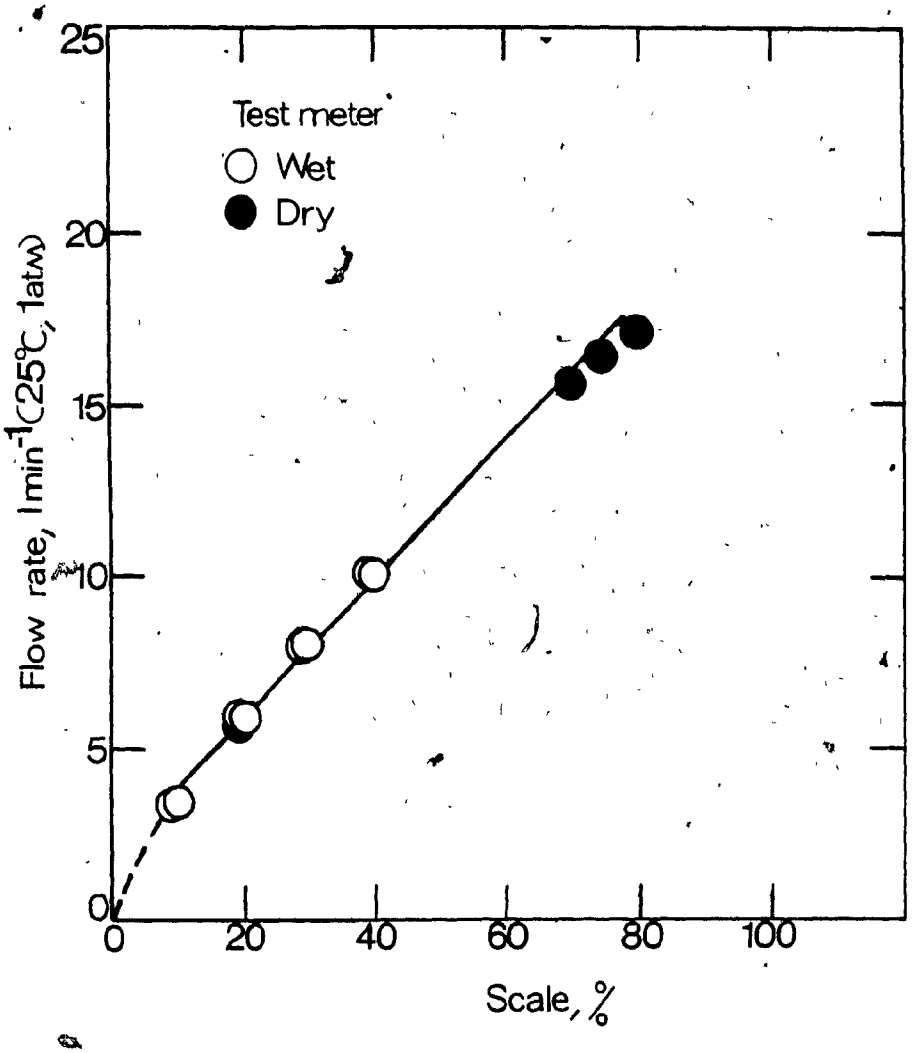


Figure B.13 Calibration curve of Tafa feeder rotameter, at ~25°C and 1 atm

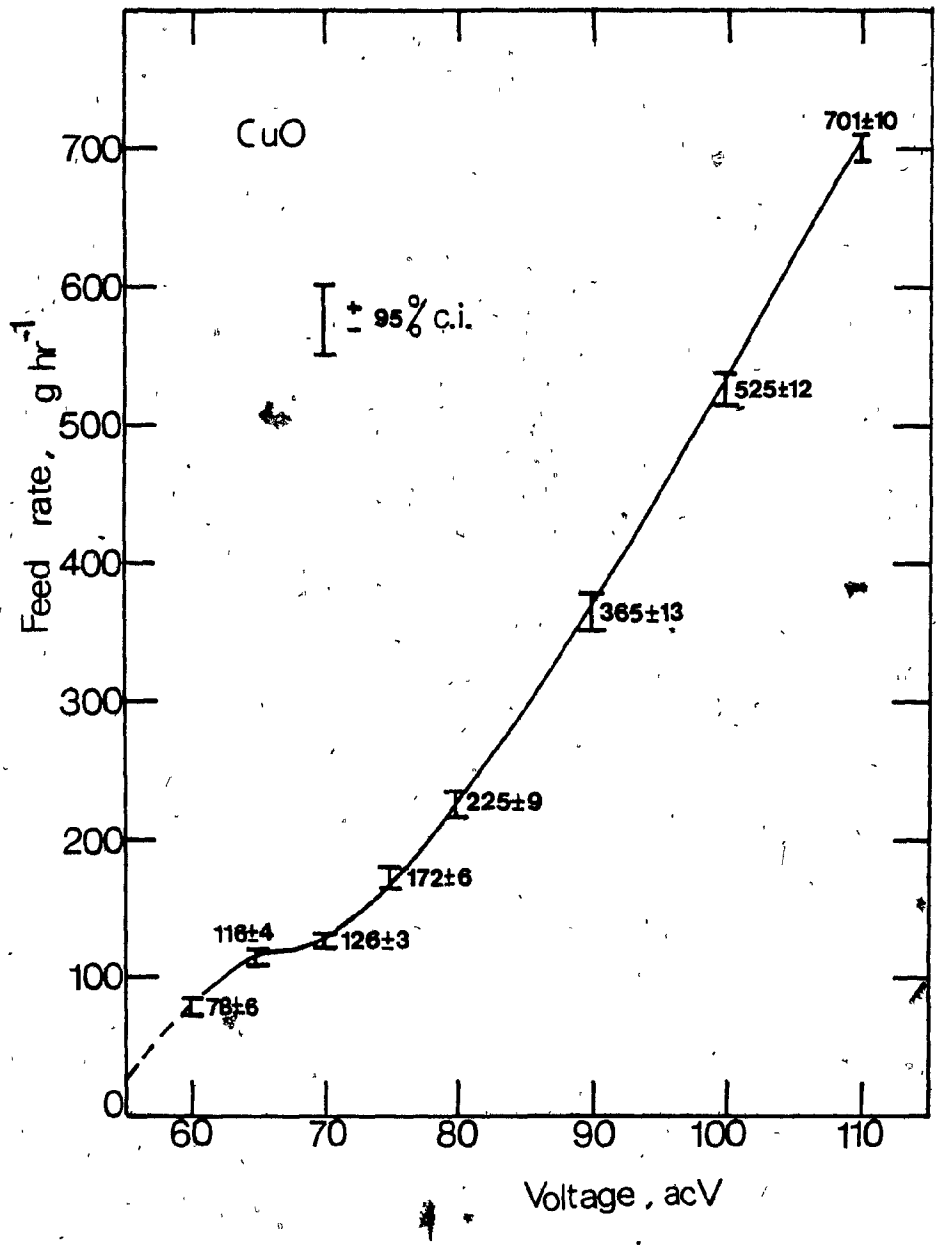


Figure B.14 Calibration curve of Tafa feeder, for CuO

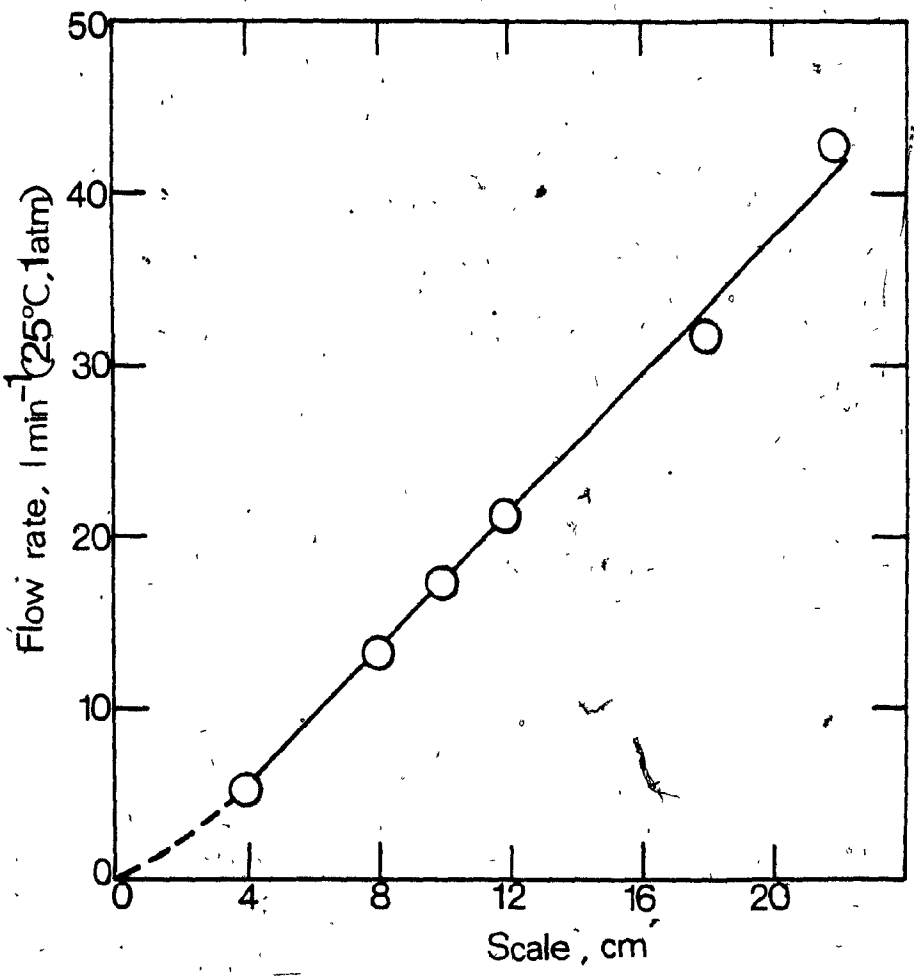


Figure B.15 Calibration curve of Wright feeder rotameter at ~25°C and 1 atm

REFERENCES

Bean, H.S. (ed.) (1971) - "Fluid Meters: Their Theory and Application", ASME, 6th edition, pp. 230-234.

Foust, A.S., Wenzel, L.A., Clump, C.W., Maus, L, and Anderson, L.B. (1960) - "Principles of Unit Operations", John Wiley and Sons, Inc., pp.408-409.

Oglesby, S., Jr., and Nichols, G.B. (1978) - "Electrostatic Precipitation", Marcel Dekker, Inc., pp. 24.

Perry, H.R., and Chilton, C.H. (eds.) (1973) - "Chemical Engineers' Handbook", McGraw-Hill, 5th ed., pp. 5-10, 5-11.

Robinson, M. (1965) - "Corona Starting Voltages for Parallel Wire-Plate Electrodes", IEEE, Int. Convention Record 13, part 7, pp. 73-76.

Smith, W.B., Cushing, K.M., and McCain, J.D. (1977) - "Procedures Manual for Electrostatic Precipitation Evaluation", SRI/EPA Contract 68-02-2131, EPA - 600/7-77-059, June, pp. 124.

Streeter, V.L. and Wylie, E.B. (1975) - "Fluid Mechanics", McGraw-Hill, 6th ed., pp. 467.

APPENDIX C

C.1 Calibration Curve of Sampling Rotameter

The rotameter used to measure the air flow of the sampling train at the ESP outlet was [illegible]ch a dry test meter. Fig. C.1 is the ca[illegible]ion.

The required position [illegible] rotameter float when sampling under vacuum was determined by reading the pressure at the rotameter using a mercury manometer, and applying the standard rotameter equation (Perry et al., 1973).

C.2 Velocity Profiles and Sampling Points at the ESP Outlet

The location of the sampling points at the 15.4cm i.d. outlet aluminium pipe was at centroids of circular sections of equal area, as recommended by Smith et al. (1977), and is given in Fig. C.2.

Also shown in this figure are the measured velocity profiles at the outlet sampling station, at various air flow rates through the ESP.

The isokinetic sampling flow rates were determined by the gas velocity in the duct and the sampling nozzle diameter.

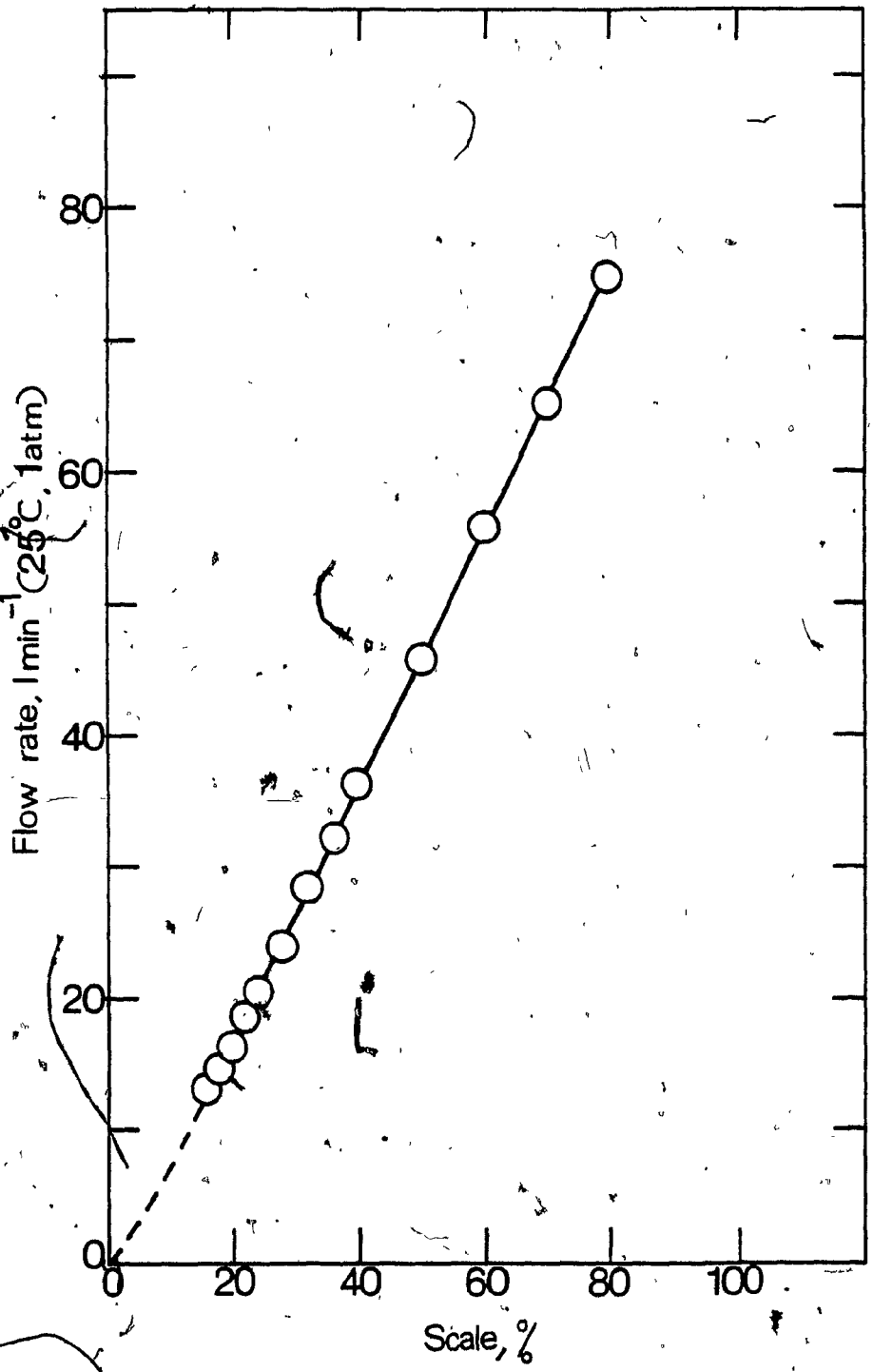


Figure C.1 Calibration curve of sampling rotameter at ~25°C and 1 atm

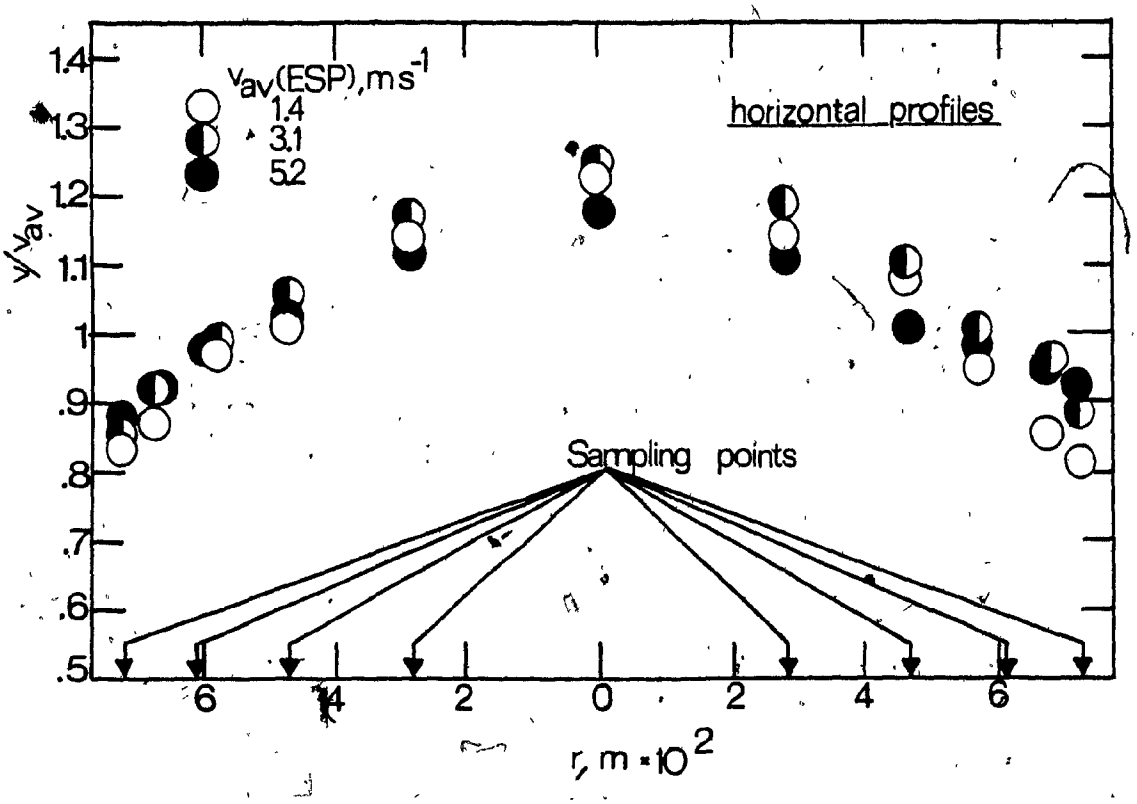


Figure C.2 Velocity profiles at the sampling station at the ESP outlet and location of dust sampling points

C.3 Particle Size Statistics: Conversion of Number to Weight Basis

The raw number frequency data used for the purpose of illustrating the different methods of converting number to weight based size distributions, discussed in Chapter 5, Section 5.3.3, is given in Table C.1. Also shown are the non-cumulative weight fractions determined by the direct conversion method (Eq. 5.4, Chapter 5). The count frequency represents a composite distribution of CuO particles, and is used here as an example. The arithmetic mean mass diameter was directly calculated from the tabulated values (Eq. 5.6, Chapter 5). The least squares fitting technique used for the estimation of the parameters of the log-normal approximation to the measured distribution requires the use of the extremes of the size intervals, since it is based on a cumulative distribution. Table C.1 gives the upper sizes of the different particle size classes, together with the respective value of the (T) variable, determined by using Eq. 5.13. As expected, the arithmetic means are somewhat larger than the geometric means.

For the trial and error solution of optimizing the likelihood function described by Eq. 5.26, a grid of the estimates of the distribution coefficients (MND and σ_g) is given in Table C.2, together with the values obtained for the logarithmic likelihood function. The values were arbitrarily

Table C.1

- Raw Data from Optical Microscope: Direct Conversion Method
(Cuprio Oxide Composite Sample)

Particle	1.6	3.2	4.8	6.4	8.0	9.6	11.2	12.8	14.4	16.0	17.6	19.2	20.8	22.4	24.0	25.6
Diameter (D_i), um	(0.8)	(2.4)	(4.0)	(5.6)	(7.2)	(8.8)	(10.4)	(12.0)	(13.6)	(15.2)	(16.8)	(18.4)	(20.0)	(21.6)	(23.2)	(24.8)	(26.4)
Frequency (n_i)	158	207	587	942	813	583	344	237	154	89	59	37	21	12	8	7	
% Frequency[1]	3.71	4.86	13.79	22.12	19.09	13.69	8.08	5.57	3.62	2.09	1.39	0.87	0.49	0.28	0.19	0.16	
% Cumulative Frequency Undersize	0.00	3.71	8.57	22.36	44.48	63.57	77.27	85.35	90.91	94.53	96.62	98.00	98.87	99.37	99.65	99.84	100.00
$D_i^3 n_i (x 10^{-3})$	0.647	6.78	64.9	247	416	516	483	497	460	365	322	262	189	135	111	117	
% Weight[2]	0.02	0.16	1.55	5.89	9.92	12.31	11.52	11.85	10.97	8.71	7.68	6.25	4.51	3.22	2.65	2.79	
Value of T[3]	-1.78 578	-1.36 795	-0.75 986	-0.13 951	0.34 654	0.74 753	1.05 157	1.33 544	1.60 124	1.82 807	2.05 419	2.28 057	2.49 530	2.69 723	2.94 817		

(1) $$\frac{n_i \times 100}{\sum_{i=1}^{16} n_i}$$

(2) $$\frac{n_i D_i^3 \times 100}{\sum_{i=1}^{16} n_i D_i^3}$$

(3) Eq. 5.13 (Chapter 5)

displaced by adding the constant ($+1.011 \times 10^4$) to all entries.

Table C.2

Logarithmic Likelihood Function for CuO

MND(μm)	6.23	6.42	6.62	6.89	7.10	7.32	7.54	7.77
σ_g								
1.49	0	125	231	335	386	414	419	400
1.54	147	257	348	437	480	-	-	-
1.58	235	331	409	487	524	543	-	-
1.63	278	362	430	498	585	547	547	-
1.68	290	361	421	480	508	-	-	-
1.73	270	336	-	-	-	-	-	-

The values of the mean arithmetic and geometric number and mass diameters, as well as the geometric standard deviations estimated by the different methods are given in Table C.3.

Table C.3

Particle Size Statistical Data from Table C.1

Method	MND_a (μm)	MND (μm)	MMD_a (μm)	MMD (μm)	σ_g
Direct	8.3	(7.4) [1]	13.8	(12.8) [1]	-
Least Squares	(7.9) [2]	7.1	(14.9) [2]	13.6	1.59
Maximum Likelihood	(8.0) [2]	7.1	(16.3) [2]	14.6	1.63

[1] Eq. 5.9 (Chapter 5)

[2] ARITHMETIC MEAN = GEOM. MEAN $\exp\left|(\ln \sigma_g)^2/2\right|$

Although there is some difference in the results obtained by the different methods, this is inconsequential for purposes of the computer simulation using the SRI computer program described in Appendix A and Chapter 2, as shown in Section 5.4.1 of Chapter 5, Table 5.4.

The generation of the number and mass distributions using the estimated values of the geometric mean and standard deviation follows the method outlined in Section 5.3.3, using Eqs. 5.27 - 5.32. Table C.4 gives the estimated percent number and weight distributions, from the data given in Table C.3. The particle diameters were extended to the

maximum value of 54μm, which approximately corresponds to the maximum particle diameter observed for the coarser oxides (this should be expected since these oxides were sieved through a 53μm sieve).

Fig. C.3 shows the number differential distributions based on the direct, least-squares and maximum likelihood methods.

Fig. C.4 shows the cumulative size distributions on a number and weight basis.

Eq. 5.2 and Fig. 5.6 (Chapter 5) can be used to determine the accuracy to which the microscope derived data represents the size distribution by either weight or number.

To estimate the standard error, an average size distribution is chosen instead of the composite frequencies given in Table C.1, since a lower error will be obtained by using the composite values due to the much larger number of particles. This error would not be representative of the actual error when performing a typical size distribution measurement involving a count of between 500-700 particles. Since the frequencies displayed in Table C.1 are the composite counts of seven independent measurements (Table C.6), the average distribution was found by dividing each number frequency by the factor seven. Very similar results are

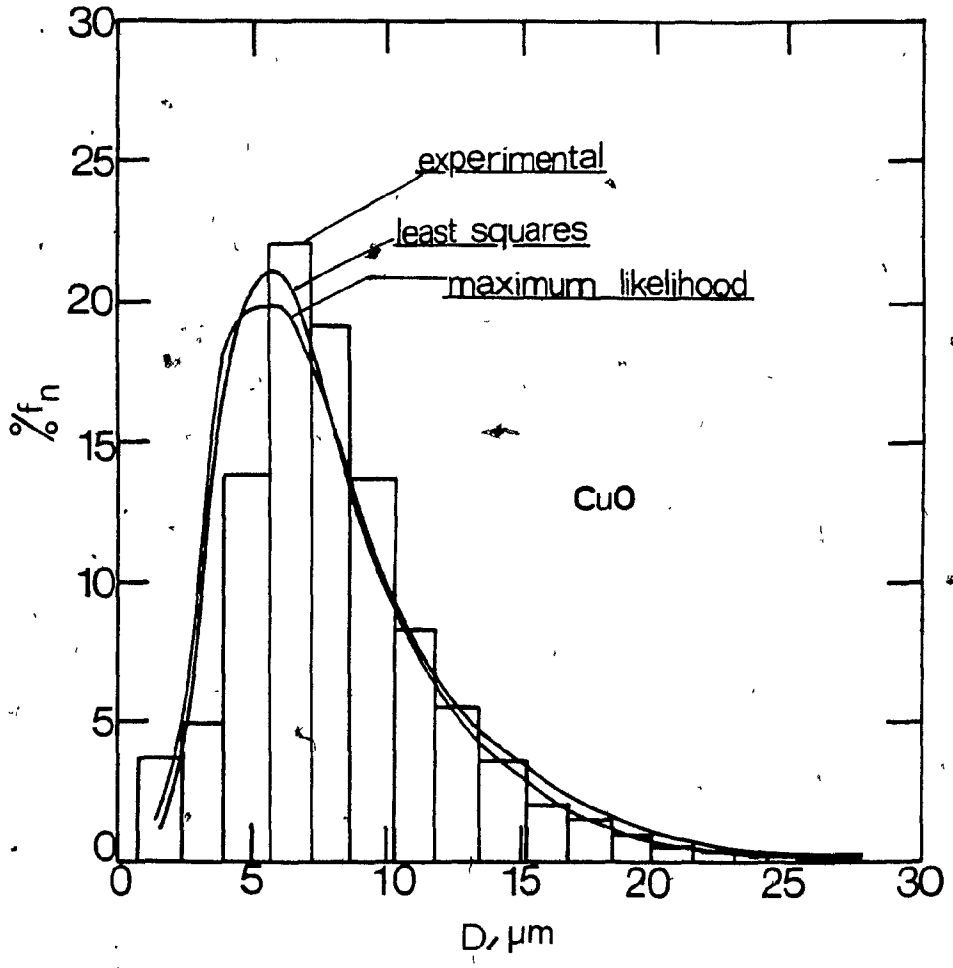


Figure C.3 Comparison between log-normal approximations and experimental number frequency data for CuO

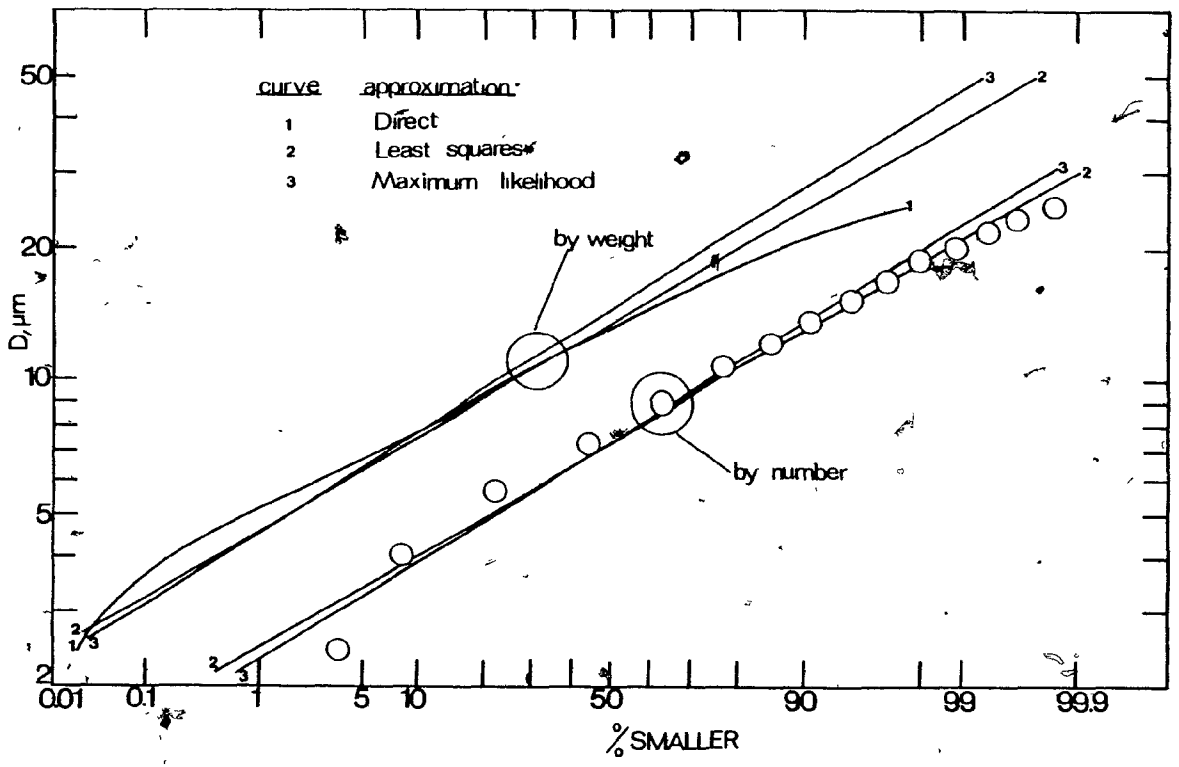


Figure C.4 Comparison between different methods of converting from number to weight basis, on a cumulative scale (CuO)

Table C.4

Generation of Number and Weight Distributions (CuO)

D (μm)	1.6 (0.8)	3.2 (2.4)	4.8 (4.0)	6.4 (5.6)	8.0 (7.2)	9.6 (8.8)	11.2 (10.4)	13.0 (12.1)	15.0 (14.0)	17.0 (16.0)	19.0 (18.0)	21.5 (20.3)	24.5 (23.0)	27.5 (26.0)	30.5 (29.0)	34.0 (32.3)	38.0 (36.0)	43.0 (40.5)	50.0 (46.5)	(54.0)
% Cumulative Frequency Undersize	0[1]	1.05	11.24	31.09	51.79	68.25	79.74	87.26	92.90	96.03	97.76	98.72	99.43	99.74	99.88	99.943	99.979	99.993	(~100)	100
	0[2]	1.34	12.07	31.40	51.14	66.94	78.21	85.80	91.71	95.14	97.12	98.27	99.17	99.59	99.79	99.89	99.95	99.975	99.989	(100)
% Frequency	1.05[1]	10.19	19.85	20.70	16.46	11.49	7.52	5.64	3.13	1.73	0.96	0.71	0.31	0.14	0.063	0.036	0.014	0.007	(~0)	
	1.34[2]	10.73	19.33	19.74	15.80	11.27	7.59	5.91	3.43	1.98	1.15	0.90	0.42	0.20	0.10	0.060	0.025	0.014	(0.011)	
% Cumulative Weight Undersize	0[1]	0.01	0.45	2.92	8.77	17.74	28.52	39.71	53.76	63.88	72.83	79.77	87.14	91.86	94.84	96.72	98.19	98.99	99.57	(100)
	0[2]	0.01	0.41	2.53	7.47	15.10	24.48	34.50	46.65	57.48	66.61	74.03	82.37	88.10	91.97	94.57	96.75	98.03	99.05	(100)
% Weight	0.01[1]	0.44	2.47	5.85	8.97	10.78	11.19	13.05	11.12	8.95	6.94	7.37	4.72	2.98	1.88	1.47	0.80	0.58	(0.43)	
	0.01[2]	0.40	2.12	4.96	7.63	9.38	10.02	12.15	10.83	9.13	7.42	8.34	5.73	3.87	2.60	2.18	1.28	1.02	(0.95)	

(1) Least-Squares Method

(2) Maximum Likelihood Method

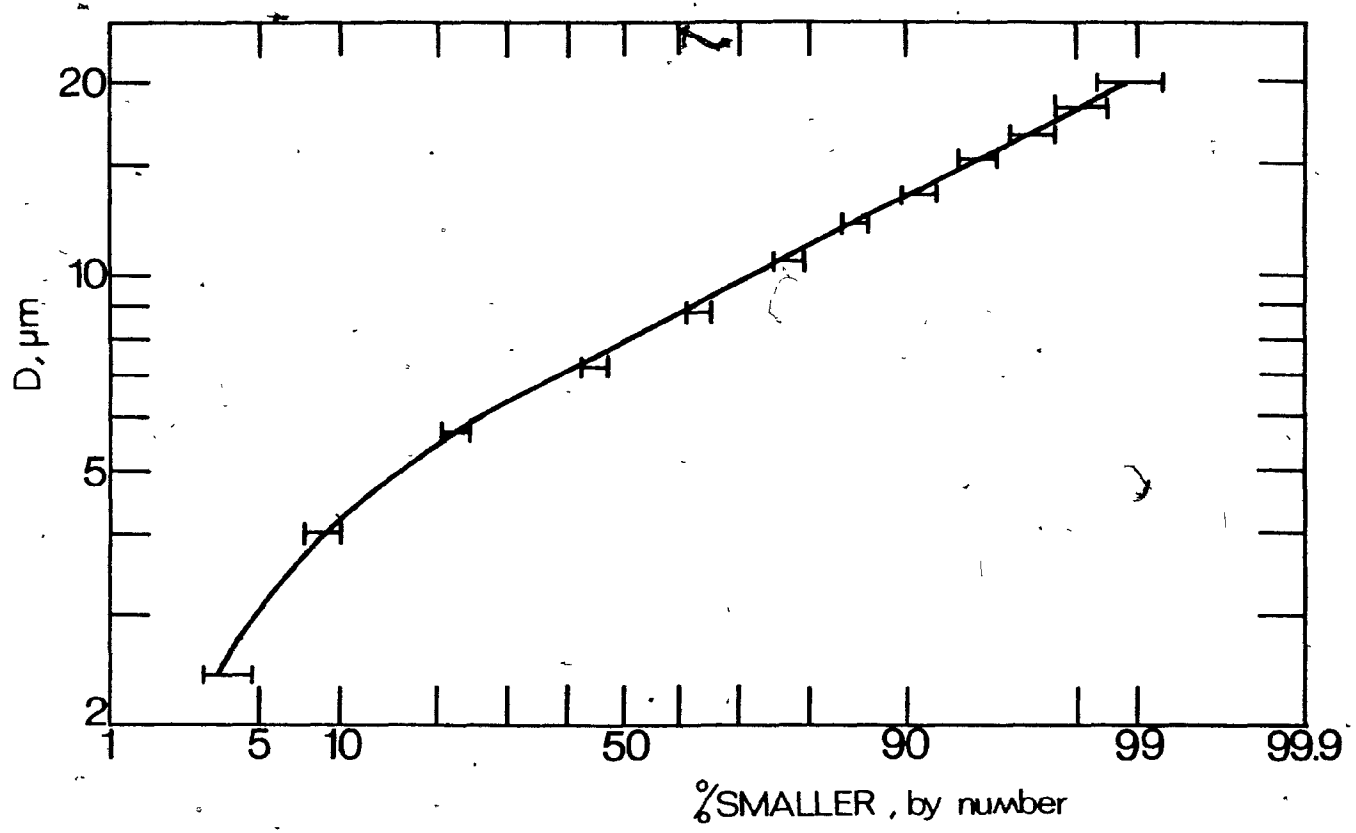


Figure C.5 Binomial standard deviations of a typical cumulative CuO size distribution, by number

obtained by using any of the actually observed distributions. Fig. C.5 shows the binomial deviations for each size class of this average size distribution on a number basis.

The maximum standard error on the cumulative frequencies on a number basis was around 2% for all the size distributions measured using the optical microscope.

Fig. C.6 shows the estimated accuracy obtained in converting the number based size distribution of Fig. C.5 into a weight based distribution, by using both the direct conversion and least-squares method. As expected, the poorer accuracies result for the larger particles, due to the low frequency of occurrence and to the significant weight contribution. Slightly better accuracies are obtained by using a log-normal approximation to the particle size distribution than by directly converting the number based to a weight based distribution, since less weight is given to the larger particles actually counted and sized under the microscope. Also, as long as at least 5 particles are counted per size class, the minimum accuracy to be expected in transforming the number based to weight based distributions is around ±3%.

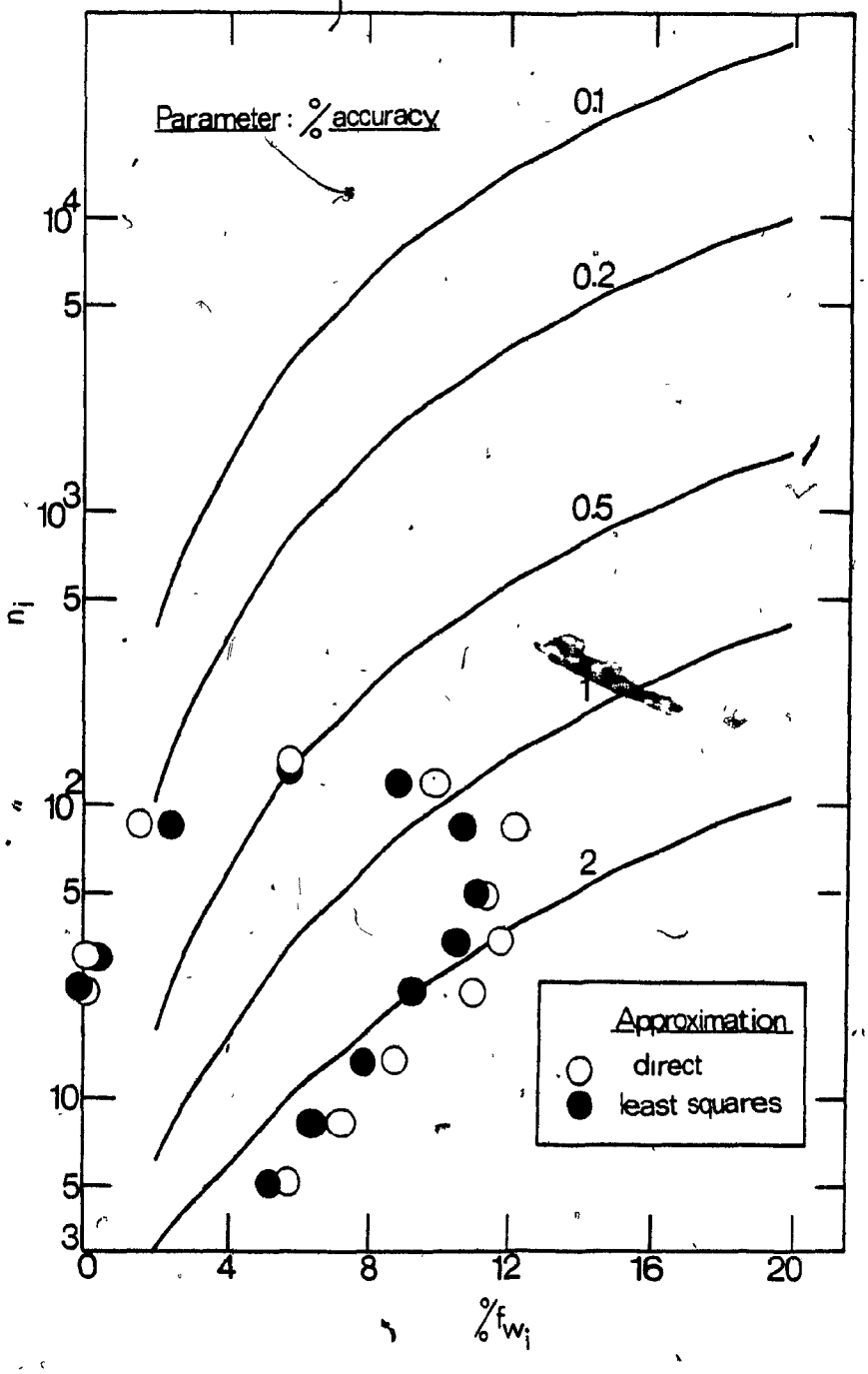


Figure C.6 Accuracy of converting a typical CuO size distribution from a number to a weight basis, according to the method of Yamate et al. (1977)

C.4 Effect of Sedimentation in Changing the Inlet Size Distribution

An estimate of the change in the size distribution of the dusts at the ESP inlet due to sedimentation occurring prior to the ESP was obtained by measuring the size distribution of the sedimented dust. For purposes of illustration, the following data was obtained with cupric oxide powder, which had a relatively large size and high density of $6.4 gcm^{-3}$, with an average velocity at the ESP inlet of $1.2 ms^{-1}$.

Table C.5 gives the optical microscope raw data for the sedimented dust. Also shown are the respective weight fractions as estimated from the direct conversion of number to weight based distribution and from the least-squares estimation method.

Since the collection efficiency prior to the ESP inlet was 49.4% (Fig.5.2, Chapter 5), for every 100g of CuO leaving the powder feeder, only 51.6g enter the ESP. The sedimented dust can then be subtracted from the undisturbed dust, in each corresponding size band. The results are shown in Table C.5, where the data on the undistorted size distribution of CuO given in Tables C.1 and C.4 was taken into account. Fig. C.7 shows the distributions on a weight basis after sedimentation prior to the ESP inlet, and the different methods of converting the number based to a weight based distribution yield very similar results.

Table C.5

Effect of Sedimentation in Distorting the Inlet Size Distribution (CuO)

D (μm)	1.6	3.2	4.8	6.4	8.0	9.6	11.2	12.8	14.4	16.0	17.6	19.2	20.8	22.4	24.0				
Observed Frequency	33	64	88	110	106	77	64	50	31	25	14	20	14	6	6				
% Weight (Direct Conversion)	0.01	0.20	0.93	2.74	5.17	6.49	8.56	10.00	8.82	9.71	7.27	13.52	12.00	6.42	8.16				
Sedimented Weight (per 100g)	0.005	0.10	0.46	1.35	2.55	3.21	4.23	4.94	4.36	4.80	3.59	6.68	5.93	3.17	4.03				
Correct % Weight (Inlet) (1)	0.03	0.12	2.13	8.90	14.46	17.84	14.30	13.75	12.96	7.67	7.84	–	–	–	–				
D²(μm)	1.6	3.2	4.8	6.4	8.0	9.6	11.2	13.0	15.0	17.0	19.0	21.5	24.5	27.5	30.5	34.0	38.0	43.0	50.0
% Weight (Least Squares)	0.01	0.25	1.14	2.59	4.14	5.43	6.30	8.47	8.51	8.10	7.44	9.70	7.94	6.36	5.03	5.07	3.65	3.65	(6.22)
Sedimented Weight (per 100g)	0.005	0.12	0.56	1.28	2.05	2.68	3.11	4.18	4.20	4.00	3.68	4.79	3.92	3.14	2.48	2.50	1.80	1.80	(3.07)
Correct % Weight (Inlet) (2)	0.03	0.56	3.33	7.97	12.07	14.13	14.10	15.48	12.07	8.64	5.69	4.50	1.43	–	–	–	–	–	–
Generated Distribution (2)	0.01	0.58	3.98	9.71	14.06	15.27	14.01	14.03	9.99	6.70	4.33	3.71	1.83	0.90	0.44	0.27	0.11	0.06	(0.07)

(1) Direct Conversion

(2) Least Squares Log-Normal

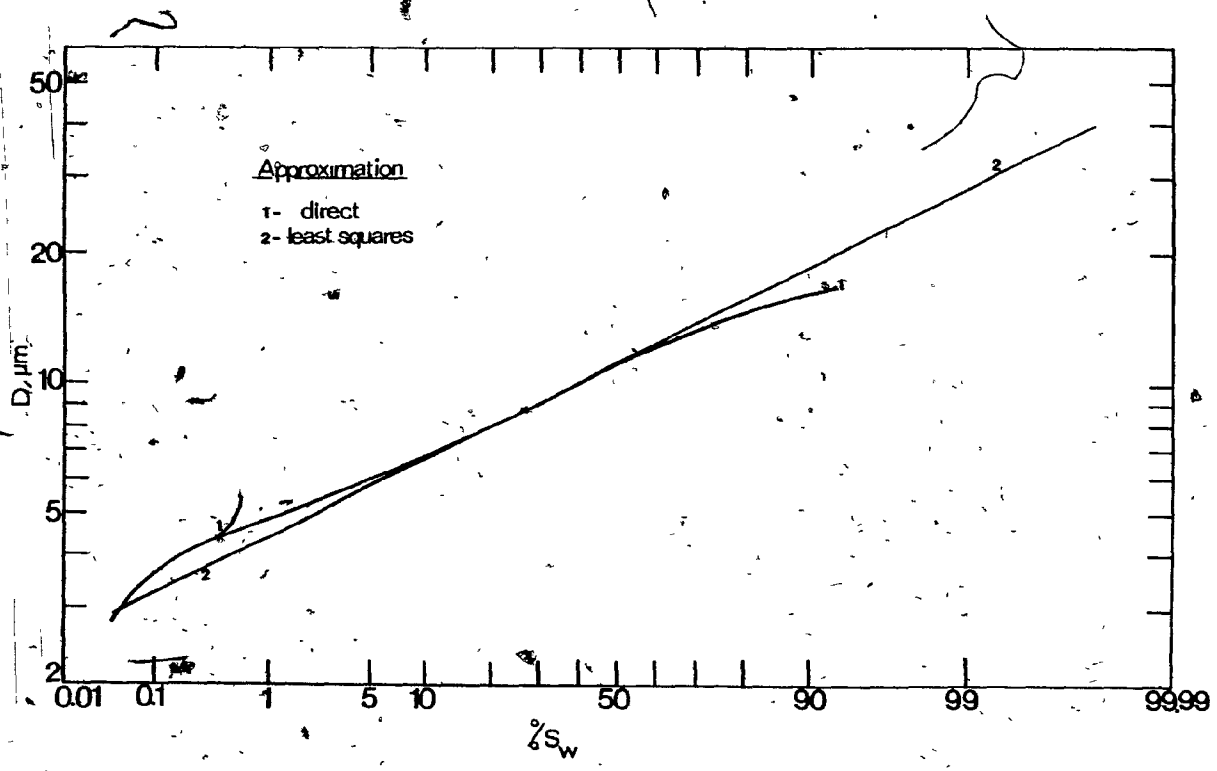


Figure C.7 Typical particle size distribution of CuO, after sedimentation prior to the ESP inlet

As is seen from Fig. C.7, the mean mass diameter of cupric oxide at the ESP inlet was reduced from about 13.6μm to 11.1μm, at an average velocity of 1.2 ms^{-1}. The distribution also became narrower, since the geometric standard deviation was reduced from 1.6 to 1.5. The observed reduction in mean size at various air velocities is shown in Fig. 5.3, Chapter 5, for cupric oxide.

C.5 Use of the X-Ray Sedimentometer

As an illustration on the use of the X-Ray Sedigraph 5000D, described in Chapter 5, section 5.3.2.2, the industrial (Noranda) dust is here considered. The expressions to be taken into account are the following (Micromeritics Instrument Corporation Instruction Manual, Sedigraph 5000D Particle Size Analyser, Norcross, Georgia):

$$Re_p = \frac{D\, v_t \rho_o}{\mu} \qquad (C.3)$$

$$v_t = \frac{D^2(\rho - \rho_o)g}{18\mu} \qquad (C.4)$$

$$R = \frac{2.0542(\rho - \rho_o)}{(50/D)^2 \mu} \times 10^{-4} \qquad (C.5$$

Eq. C.3 represents the Reynolds number for the particle of diameter (D) moving in a fluid of density (ρ_o) and viscosity (μ) with a terminal velocity (v_t). Eq. C.4 is the expression for the terminal velocity in Stokes regime ($Re_p < 1$). Eq. C.5 represents the rate setting to be entered into the instrument, where (D) is in micron. The rate setting controls the rate of sedimentation cell movement built into the instrument to provide the proper settling distance for a given particle diameter.

For purposes of calculation, the starting (maximum) diameter should be used in the above expressions.

The density of the particles to be analysed was determined by a gas picnometer (Micromeritics, Model 1302, Norcross, Georgia), using nitrogen as the non-adsorbed gas, to be 3.2 ± 0.1 gcm^{-3} (one standard deviation). With D = 50 μm as the starting diameter, using Calgon 0.05 % as the dispersing medium (ρ_o = 995 Kg m^{-3}, $\mu = 0.768 \times 10^{-3}$ Kg $m^{-1}s^{-1}$, at the operating temperature of 32°C), the rate has a value of 595 and the maximum Re is about 0.3. The applicability of Stokes law is then verified.

A more concentrated dispersing medium of 0.5% sodium hexametaphosphate in water was also used. The experimental results obtained with the industrial (Noranda) dust using the two dispersing liquids are shown in Fig. C.8. The use of

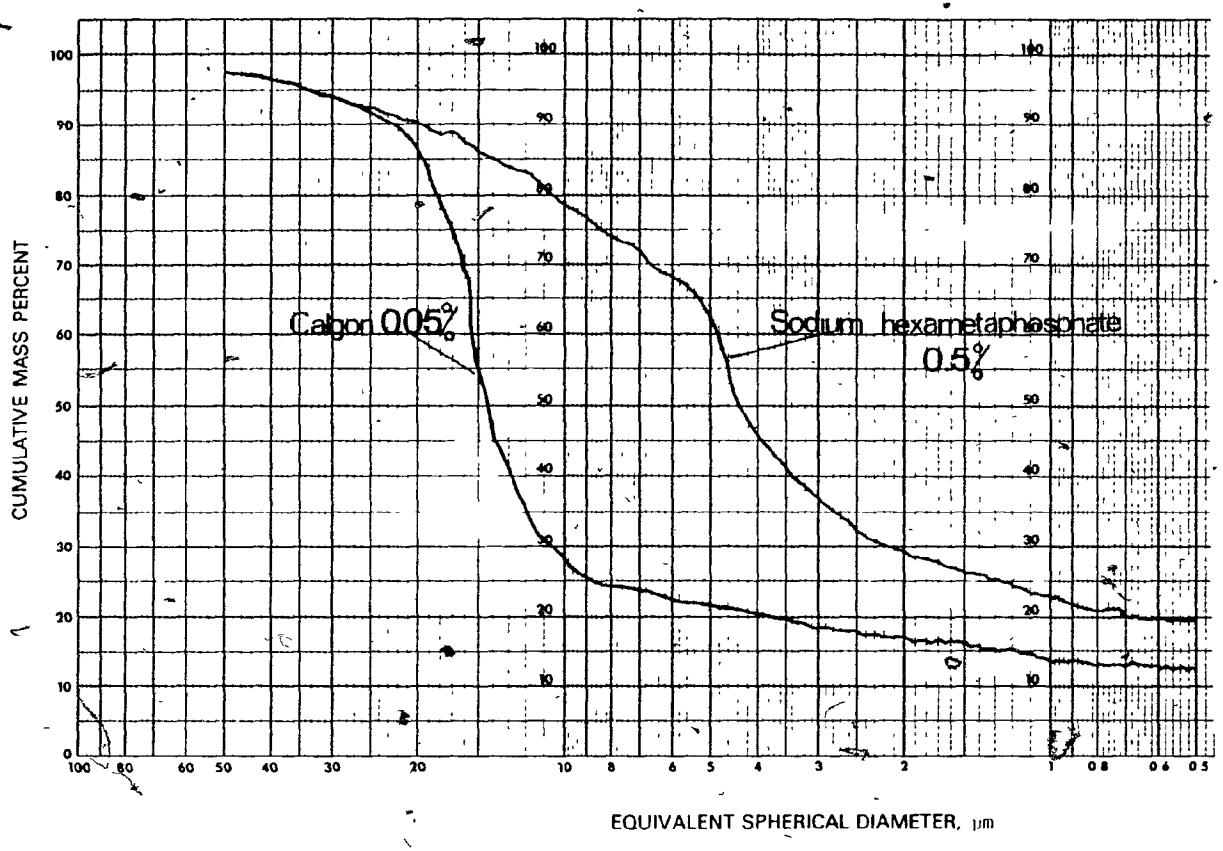


Figure C.8 Effect of dispersing medium in the size distribution of the Noranda dust, obtained with the X-ray Sedigraph 5000D

ultrasonic vibration did not improve the degree of dispersion obtained. The different behaviour observed with this dust using the two dispersing mediums was not found for any of the other powders used in this work.

C.6 Optical Microscope Raw Data for the Coarser Oxides

Table C.6 gives the observed frequencies of CuO, at various input voltages to the Tafa vibrating feeder, as measured by the optical microscope. The composite frequencies were used in Section C.3 as an example on the conversion of a number to a weight based distribution.

Table C.7 gives the observed frequencies of MgO and TiO_2, as well as the composite frequencies. The composite frequencies were determined by dividing the total number of counts in each size range by the total global count.

C.7 The Wright Feeder - Minicyclone System

A minicyclone was designed and built to reduce the mean particle size of alumina obtained by using the Wright dust feeder. A standard design was employed (Crawford, 1976), as shown in Fig. C.9. The cyclone was machined from aluminium with a plexiglass dust hopper, and it was designed for easy dismantling, if necessary, for cleaning.

Table C.6

Optical Microscope Raw Data for Cupric Oxide

Input Voltage (ac V) \ D(μm)	1.6	3.2	4.8	6.4	8.0	9.6	11.2	12.8	14.4	16.0	17.6	19.2	20.8	22.4	24.0	25.6	Total Count
0	3.68	5.18	11.54	19.90	18.06	16.22	8.70	6.35	3.51	2.17	1.51	1.17	1.00	0.50	0.33	0.17	598
0	3.65	5.64	16.09	24.05	16.25	10.45	8.13	5.64	4.15	2.49	1.33	1.00	0.50	0.33	0.17	0.17	603
70	3.11	4.59	12.13	20.49	22.30	15.57	8.69	4.92	2.62	2.30	1.31	0.98	0.49	0.16	0.16	0.16	610
80	3.68	5.28	13.44	22.40	20.16	14.08	8.64	5.28	3.36	1.44	0.96	0.48	0.32	0.16	0.16	0.16	625
90	4.98	5.81	14.95	23.42	17.77	11.46	7.64	5.32	3.49	1.99	1.50	0.83	0.33	0.17	0.17	0.17	602
100	4.19	4.19	13.69	21.10	17.87	14.49	7.25	6.44	5.31	1.93	1.45	0.97	0.48	0.32	0.16	0.16	621
110	2.67	3.34	14.69	23.54	21.20	13.52	7.51	5.01	2.84	2.34	1.67	0.67	0.33	0.33	0.17	0.17	599
Composite	3.71	4.86	13.79	22.12	19.09	13.69	8.08	5.57	3.62	2.09	1.39	0.87	0.49	0.28	0.19	0.16	4258

Table C.7

Optical Microscope Raw Data for MgO and T_iO_2

D (μm)	1.6	3.2	4.8	6.4	8.0	9.6	11.2	12.8	14.4	16.0	17.6	19.2	20.8	22.4	24.0	25.6	27.2	28.8	Total Count
MgO (1)	4.52	43.37	18.27	11.55	6.63	4.12	3.01	2.61	1.81	1.31	1.00	0.80	0.60	0.40	-	-	-	-	996
MgO (2)	3.66	33.08	20.73	12.20	8.84	7.16	4.88	2.74	2.29	1.22	0.91	0.76	0.91	0.61	-	-	-	-	656
MgO Composite	4.18	39.29	19.25	11.80	7.51	5.33	3.75	2.66	2.00	1.27	0.97	0.79	0.73	0.48	-	-	-	-	1652
T_iO_2 (1)	4.01	22.37	20.26	15.65	12.24	7.92	5.72	3.71	2.61	1.50	1.00	0.60	0.60	0.50	0.50	0.50	0.20	0.10	997
T_iO_2 (2)	5.50	22.39	20.37	15.60	11.74	8.62	5.14	4.04	2.57	1.28	1.10	0.92	0.37	0.37	-	-	-	-	545
T_iO_2 Composite	4.54	22.37	20.30	15.63	12.06	8.17	5.51	3.83	2.59	1.43	1.04	0.71	0.52	0.45	0.32	0.32	0.13	0.06	1542

(1) From Feeder Bin

(2) After Feeder

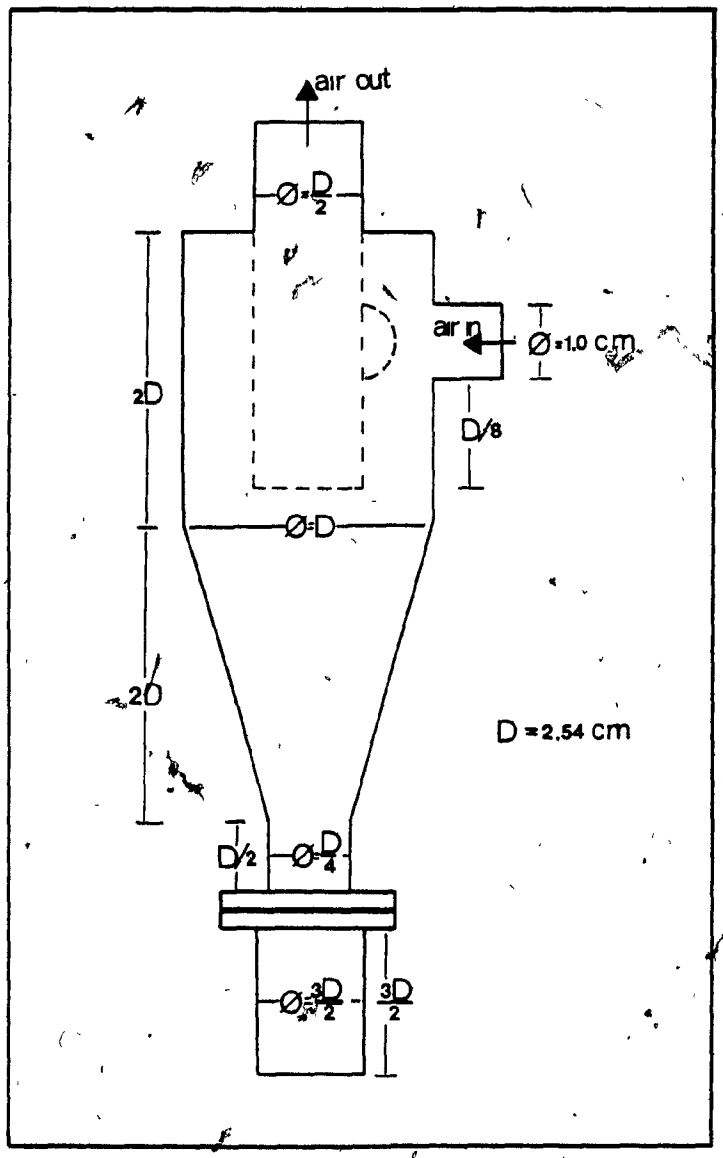


Figure C.9 Schematic diagram of minicyclone

It is known that theoretical equations for the calculation of cyclone cut-points (particle diameter for which the collection efficiency is 50%) may be inappropriate for minicyclones (Chan et al., 1977 and John et al., 1980). Since the minicyclone was not calibrated, its true fractional efficiency curve is not known. An estimation was obtained using standard theories (Crawford, 1976). An experimental estimation was also obtained by sampling the small alumina emitted from the Wright feeder with and without the minicyclone, using the Andersen MKIII cascade impactor (Chapter 5).

The global mass collection efficiency of the minicyclone was determined by weighing the Wright feeder dust container at the beginning and end of the feed cycle, together with the alumina collected in the cyclone hopper. The global collection efficiency of the cyclone was measured to be approximately 60% for the fine alumina, at an air flow rate through both Wright feeder and minicyclone of 15 $l\ min^{-1}$. Since sampling was not performed immediately upstream of the minicyclone (when on-line) or of the Wright feeder (with the cyclone off-line), the results on fractional efficiencies should only be regarded as an approximation, since preferential size deposition might have occurred between the dust injection and sampling ports, respectively, at the Venturi throat and ESP inlet.

Fig. C.10 shows the measured fractional collection efficiency of the minicyclone and the theoretical prediction as based on standard cyclone theory. Since most of the mass of the alumina particles at the exit of the minicyclone belongs to agglomerates, the density of the agglomerates was assumed to be between the bulk density of the packed plug of alumina in the Wright feeder, i.e. 0.9 gcm^{-3}, and half the true density of the alumina particles (Chapter 5, section 5.4.2). The results shown in Fig. C.10 from the Andersen impactor and the theoretical curve are both based on this assumption.

The scatter in the data of Fig. C.10 does not allow any definite conclusion to be reached as to the cut-point of the minicyclone, but it seems to be around 4 - 7μm. The global efficiencies predicted from standard theory are in the range 54.6 - 55.1%, in good agreement with the measured value. The theoretical values of the global cyclone efficiencies are based on the measured size distribution of alumina at the exit of the Wright feeder, when operated at an air flow rate of 15ℓmin^{-1}, and as determined by the Andersen impactor.

The optical microscope was also used to estimate the size distribution of alumina at the ESP inlet, and Table C.8 gives the observed number and weight frequencies. Table C.9 gives the observed weights and weight frequencies using the Andersen cascade impactor.

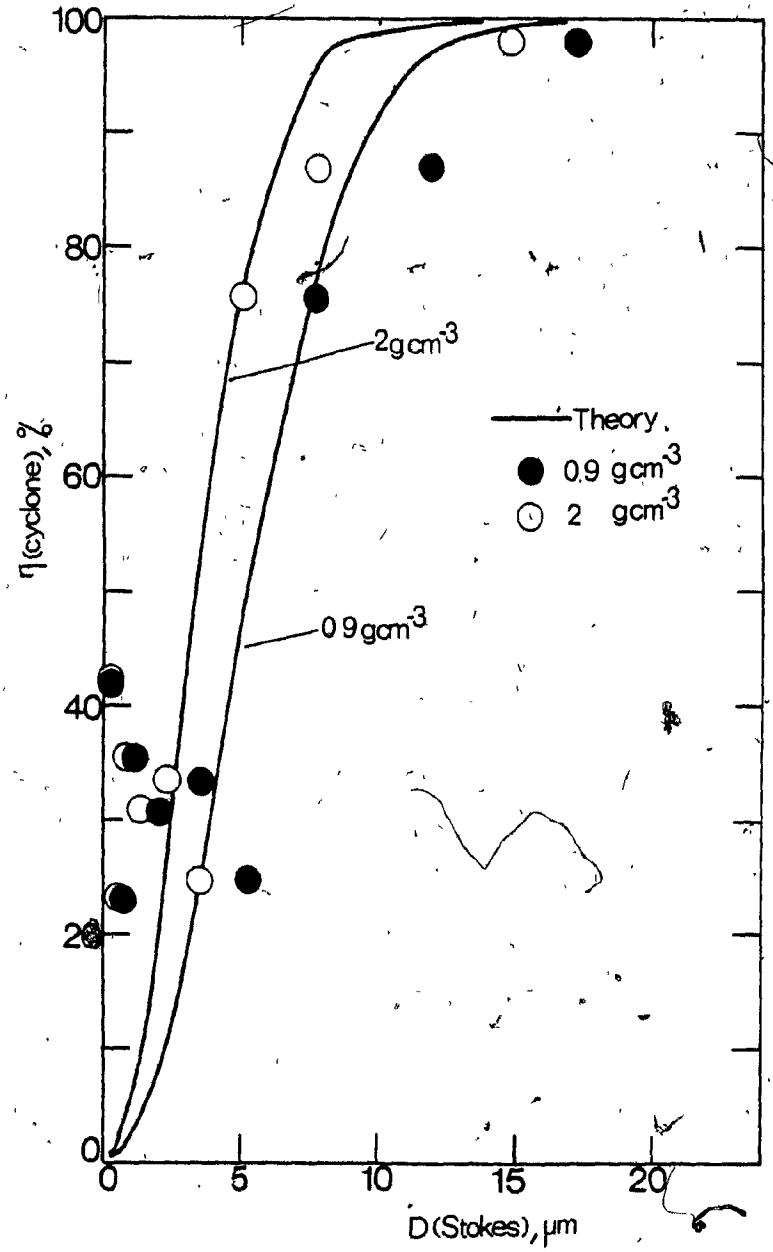


Figure C.10 Fractional efficiency curves of the mini-cyclone, with alumina, at 15 ℓ min^{-1}

Table C.8

Optical Microscope Raw Data for Alumina

D (μm)	0.8	1.6	3.2	4.8	6.4	8.0	9.6	Total Count
% Frequency(1)	48.29	35.69	9.10	4.37	1.46	0.73	0.36	2746
% Weight(1)	1.22	7.21	14.71	23.84	18.88	18.44	15.71	
% Frequency(2)	60.81	24.33	9.50	3.80	1.09	0.34	0.14	3498
% Weight(2)	2.15	6.89	21.53	29.06	19.76	12.04	8.57	

(1) Cyclone Off-Line

(2) Cyclone On-Line

Table C.9

Cascade Impactor Raw Data for Alumina

Stage No.	(1)	Collected Mass (mg)/Weight Frequency (%)			
1	3.16/28.81	0.06/1.36	0.05/1.28	0.13/1.83	0.04/1.23
2	1.00/9.12	0.19/4.32	0.12/3.08	0.16/2.26	0.10/3.07
3	1.10/10.03	0.14/3.18	0.25/6.41	0.55/7.76	0.21/6.44
4	0.88/8.02	0.81/18.41	0.60/15.38	0.94/13.26	0.47/14.42
5	1.47/13.40	0.98/22.27	0.87/22.31	1.59/22.43	0.73/22.39
6	1.93/17.59	1.24/28.18	1.17/30.00	2.27/32.02	1.01/30.98
7	1.25/11.39	0.87/19.77	0.69/17.69	1.29/18.19	0.58/17.79
8	0.12/1.09	0.07/1.59	0.13/3.33	0.09/1.27	0.10/3.07
Backfilter	0.06/0.55	0.04/0.92	0.02/0.52	0.07/0.98	0.02/0.61
Sampling Time (min)	120	120	96	150	90
Total Mass (mg)	10.97	4.40	3.90	7.09	3.26
Concentration (mg am^{-3})	6.44	2.58	2.86	3.33	2.55

(1) Without the minicyclone

Fig. C.11 shows how the estimated accuracy in converting from the alumina number based with the cyclone on-line to a weight based distribution changed with the number of particles counted, i.e. with the size range. A much wider variation in accuracy was obtained with the fine alumina than with the coarser oxides, as may be seen by comparing Figs. C.6 and C.11. Furthermore, much lower accuracies were obtained for the fine alumina above a particle diameter of about 4.8μm, despite the much larger relative count.

The high sensitivity of the alumina size distribution to the presence of the larger particles is demonstrated in Fig. C.12, where the change in the mass median diameter is plotted with respect to percentage of total count. The curve was obtained by considering only particles below a specific size range, say 9.6μm, graphically determining the median size using the data of Table C.8, reducing the size range to 8μm, redetermining the median and so on. The high sensitivity of the median mass diameter to the inclusion of the larger particles is apparent from Fig. C.12. No such sensitivity was observed for the coarser oxides, since the weight of the larger particles was much less important.

The Wright feeder was also used without the mini-cyclone to feed the industrial (Noranda) dust to the ESP inlet. The weights and weight frequencies on each collection

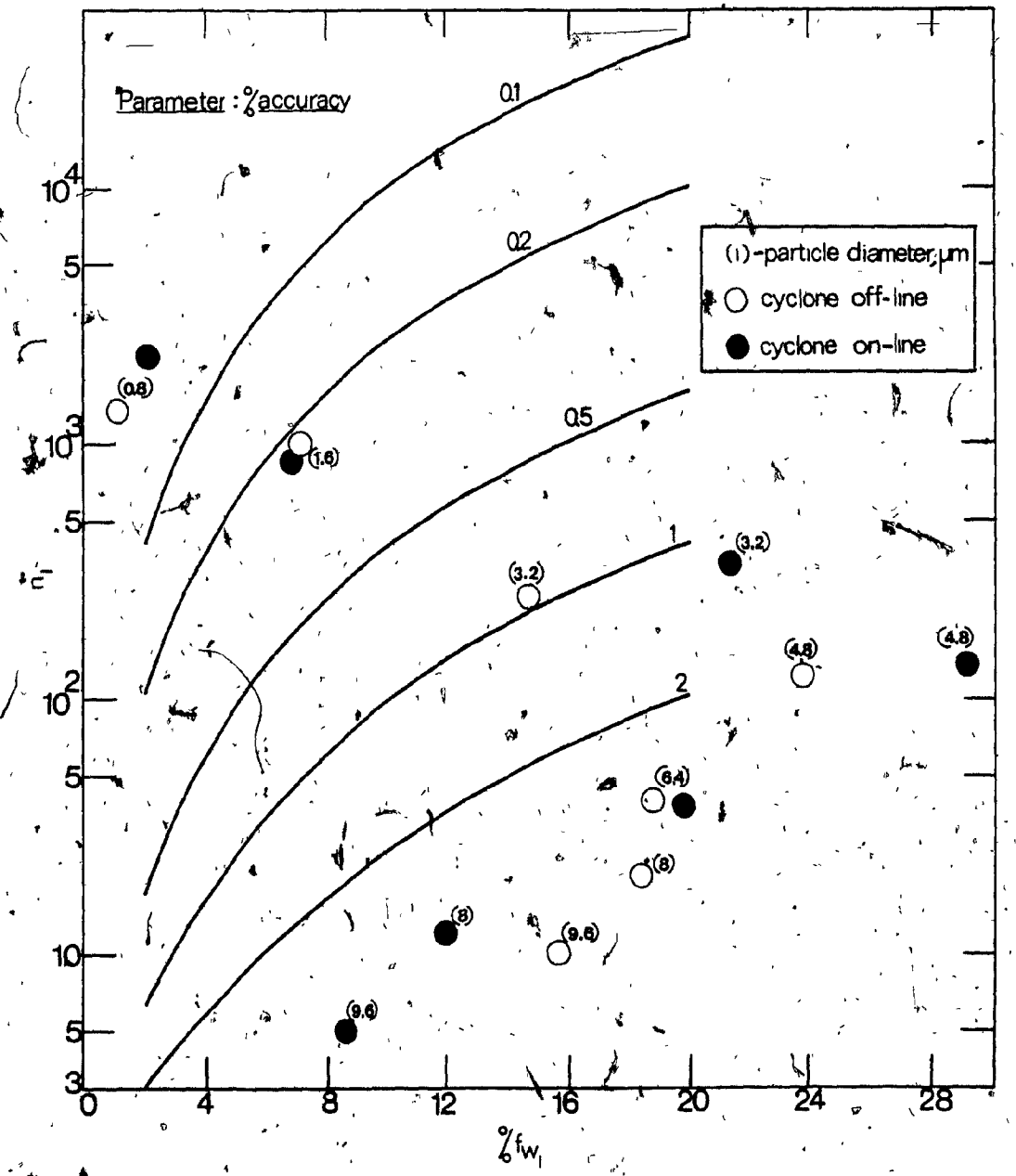


Figure C.11 Accuracy of converting optical microscope derived alumina size distributions, from a number to a weight basis, according to the method of Yamate et al. (1977)

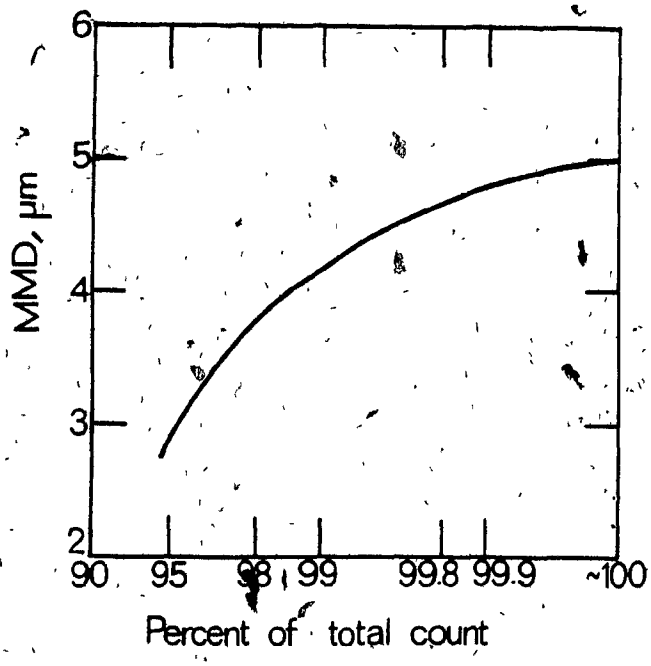


Figure C.12 Sensitivity of the MMD of alumina to the proportion of total count (optical microscope data)

stage of the Andersen cascade impactor are given in Table C.10.

Table C.11 gives the corresponding cumulative weight percentages undersize for copper, lead, zinc and cadmium, as determined by AAS analysis of the dust collected on the impactor substrates. The criteria of a minimum of approximately 1 mg of dust to be analysed was followed; this explains the type of data in the first column of each element. The values shown in Table C.11 are already corrected to account for leaching of the elements (Cu, Pb, Zn and Cd) from the glass fibers of the impactor substrates and backfilter.

Table C.10

Cascade Impactor Raw Data for Overall Noranda Dust

Stage No.	Collected Mass (mg)/Weight Frequency (%)		
1	0.52/8.60	1.39/9.29	1.59/9.16
2	0.23/3.80	1.02/6.82	1.22/7.03
3	0.50/8.26	1.62/10.83	1.90/10.95
4	0.54/8.93	1.34/8.96	1.67/9.63
5	0.84/13.88	2.13/14.24	2.55/14.70
6	1.76/29.09	4.03/26.94	4.89/28.18
7	1.65/27.27	3.11/20.79	2.88/16.60
8	0.01/0.17	0.26/1.74	0.42/2.42
Backfilter	0/0	0.06/0.40	0.23/1.33
Sampling Time (min)	72	144	144
Total Mass (mg)	6.05	14.96	17.35
Concentration (mg m^{-3})	5.92	7.32	7.98 (1)

(1) Impactor Flow Rate of 15.1 ℓmin^{-1}

Table C.11

Cascade Impactor Raw Data for Elements of Noranda Dust

Stage No.	Copper			Lead			Zinc			Cadmium		
1	-	72.00	65.70	-	93.54	93.27	-	92.19	92.11	-	92.97	92.22
2	-	53.41	47.49	-	86.55	87.59	-	84.95	86.58	-	86.45	86.44
3	51.16	41.88	35.36	81.58	75.48	77.21	81.23	73.97	75.75	83.61	76.00	76.17
4	-	26.59	27.44	-	64.57	67.22	-	62.92	63.74	-	65.54	65.90
5	30.75	15.76	17.41	61.55	49.53	51.66	60.19	46.79	47.03	64.44	50.03	51.15
6	17.83	4.24	3.96	31.85	22.47	20.95	31.69	19.87	16.19	33.67	23.27	20.94
7	-	-	-	-	-	-	-	-	-	-	-	-
8	0	-	-	0	-	-	0	-	-	0	-	-
Sampling Time (min)	72	144	144	72	144	144	72	144	144	72	144	144
Total Weight of Element (mg)	0.39	0.45	0.38	1.86	4.53	4.63	0.75	1.65	1.70	0.90	1.86	2.01
Elemental Concentration (mgm^{-3})	0.38	0.22	0.17	1.82	2.22	2.13	0.73	0.81	0.78	0.88	0.91	0.92

REFERENCES

Chan, T., and Lippmann, M. (1977) - "Particle Collection Efficiencies of Air Sampling Cyclones: An Empirical Theory", Env. Science & Technology, 11, no. 4, April pp. 377-382.

Crawford, M. (1976) - "Air Pollution Control Theory", McGraw-Hill, pp. 280-287.

John, W., and Reischl, G. (1980) - "A Cyclone for Size-Selective Sampling of Ambient Air", J.APCA, 30, no. 8, August, pp. 872-876.

Perry, R.H., and Chilton, C.H. (eds.)(1973) - "Chemical Engineers' Handbook", McGraw-Hill, 5th ed., pp. 5-16.

Smith, W.B., Cushing, K.M., and McCain, J.D. (1977) - "Procedures Manual for Electrostatic Precipitator Evaluation", SRI Contract 68-02-2131, EPA-600/7-77-059, June, pp. 143-148.

Yamate, G. and Stockham, J.D. (1977) - "Sizing Particles using the Microscope" in "Particle Size Analysis", Stockham and Fochtam (eds.), Ann Arbor Science, pp. 23-33.